TECHNISCHE UNIVERSITÄT WIEN
Vienna University of Technology

Diese Dissertation haben begutachtet:

_____   _____
Prof. Dr. A. Toschi   Prof. Dr. M. Fabrizio

DISSERTATION

New routes towards a theoretical treatment of nonlocal electronic correlations

ausgeführt zum Zwecke der Erlangung des akademischen Grades eines
Doktors der technischen Wissenschaften unter der Leitung von

Prof. Dr. Alessandro Toschi

E 138 - Institut für Festkörperphysik
eingereicht an der Technischen Universität Wien
Fakultät für Physik

von

Dipl.Ing. Georg Rohringer

Matrikelnummer: 0027402
Kolschitzkygasse 6/7, 1040 Wien

Wien, am 22. November 2013

Abstract

The central focus of this thesis is the theoretical description of *non-local* electronic correlations characterizing the physics of important classes of materials such as, for example, transition metal oxides or rare earth compounds. From the theoretical side, in the last two decades, a big step forward was achieved by the development of dynamical mean field theory (DMFT), which accounts, non-perturbatively, for a relevant part of the electronic correlations, namely the *local* ones. In that way, it was possible to theoretically understand several important effects arising in correlated materials, as the Mott metal-insulator transition.

However, many fascinating phenomena such as, e.g., unconventional superconductivity or quantum criticality, originate from (or are at least strongly affected by) *non-local* correlations, which are not captured in the framework of DMFT. This thesis aims precisely at the development and the application of novel methods for including non-local electronic correlation effects at all length scales beyond DMFT. These extensions of DMFT are mostly based on the calculations of two-particle local vertex quantities. Specifically, the Dynamical Vertex Approximation (DΓA) requires as input the local irreducible vertex (Γ) of DMFT, and we demonstrate its applicability by analyzing the anti-ferromagnetic phase-transition in the Hubbard model.

Finally, a completely new method for considering non-local correlations, based on the generating functional for the one-particle irreducible vertex functions, is introduced. This novel approach, including a larger number of Feynman diagrams, might further improve over the DΓA, and, in perspective, lead to a unifying theoretical description of the non-local electronic correlation effects beyond DMFT.

Für meine Eltern
Erika & Günter

Contents

Deutsche Kurzfassung

Die vorliegende Dissertation befasst sich mit der Entwicklung und Anwendung neuer quantenfeldtheoretischer Methoden zur Behandlung nicht-lokaler elektronischer Korrelationen. In den letzten Jahrzehnten haben korrelierte Materialien stetig an Bedeutung gewonnen. Dies liegt einerseits an den faszinierenden physikalischen Effekten, die auf elektronischen Korrelationen basieren, wie zum Beispiel Hochtemperatursupraleitung oder quantenkritisches Verhalten, andererseits aber auch an zahlreichen möglichen technologischen Anwendungen dieser Stoffe. Die Entwicklung entsprechender Theorien zur Beschreibung elektronischer Korrelationen stellt daher eine der wesentlichen Herausforderungen für die theoretische Festkörperphysik dar.

Die Dynamik der Elektronen in einem Festkörper stellt ein kompliziertes quantenmechanisches Vielteilchenproblem dar. Eine exakte Lösung dieses Problems, d.h. eine Berechnung der entsprechenden Vielteilchenwellenfunktion für die $\sim 10^{23}$ Elektronen, ist selbst unter Vernachlässigung der Bewegung der Atomkerne (Born-Oppenheimer-Näherung) nicht möglich. Die wesentliche Schwierigkeit für die theoretische Behandlung liegt in der Coulomb Wechselwirkung zwischen den Teilchen. Dadurch ist das Verhalten eines einzelnen Elektrons stark von dem der anderen Elektronen abhängig. Die Eigenzustände derartiger Systeme, die man auch als *korreliert* bezeichnet, können nicht durch eine einfache Slaterdeterminante dargestellt werden. Daher sind fortgeschrittene Techniken zur Lösung dieses Vielteilchenproblems erforderlich. In dieser Dissertation werden neue Vielteilchenmethoden entwickelt, untersucht und auf konkrete Probleme angewandt.

Die *dynamische Molekularfeld-Theorie* (DMFT) ist seit zwei Jahrzehnten eine der erfolgreichsten Methoden zur theoretischen Beschreibung von stark korrelierten Elektronen-Systemen. Hierbei wird das Kristallgitter, in dem sich die Elektronen bewegen und miteinander wechselwirken, durch einen einzigen Gitterplatz, an dem die Teilchen interagieren, ersetzt. Der Rest des Gitters wird durch ein System von nicht wechselwirkenden Teilchen beschrieben, das an diesen Gitterplatz gekoppelt ist. Für dieses vereinfachte System ist es nun möglich

eine (numerische) Lösung zu finden. Auf diese Weise werden (rein) *lokale* Korrelationen, d.h. Korrelationen zwischen Elektronen am selben Gitterplatz, sehr gut beschrieben. Ein Teil dieser Dissertation ist der Anwendung von DMFT zur Beschreibung optischer Eigenschaften von zwei Materialien aus einer Klasse von Hochtemperatursupraleitern (Kupraten) gewidmet.

Den vielleicht interessantesten physikalischen Phänomenen liegen allerdings oft (auch) *nicht-lokale* Korrelationen zugrunde. Dazu zählen Magnetismus, (quanten)kritische Phänomene, (schwache) Lokalisierung oder unkonventionelle Supraleitung. In dieser Arbeit sollen die theoretischen Grundlagen für eine Beschreibung dieser Effekte auf dem Niveau einfacher Modelle gelegt werden.

Kapitel 1 gibt eine kurze Einführung in die Physik stark korrelierter Elektronen-Systeme sowie einen Überblick über die entsprechenden state-of-the-art Methoden für deren theoretische Behandlung. Danach werden in **Kapitel 2** die grundlegenden quantenmechanischen Modelle zur Analyse von Systemen stark wechselwirkender Teilchen vorgestellt. Des weiteren werden die Green-Funktionen eingeführt, welche die wesentlichen Objekte für eine quantenfeldtheoretische Beschreibung der elektronischen Struktur von Festkörpern beziehungsweise der entsprechenden Modelle darstellen. Der Schwerpunkt liegt hierbei auf einer ausführlichen Beschreibung von Zweiteilchen-Green-Funktionen, da diese in der Literatur bisher nur vereinzelt Beachtung gefunden haben.

In **Kapitel 3** werden lokale elektronische Korrelationen diskutiert. Diese können mittels DMFT theoretisch sowohl qualitativ als auch quantitativ sehr genau beschrieben werden. Zur Demonstration der Leistungsfähigkeit dieser Theorie präsentieren wir eine DMFT Studie des Hochtemperaturverhaltens der optischen Leitfähigkeit sowie des optischen spektralen Gewichts zweier Hochtemperatursupraleiter aus der Materialfamilie der Kupraten. Der Vergleich mit den entsprechenden experimentellen Daten ist ein gutes Beispiel für die Anwendbarkeit von DMFT zur Beschreibung realer Materialien. Der Rest von Kapitel 3 ist der systematischen Untersuchung von lokalen Zweiteilchen-Green-Funktionen in DMFT gewidmet, die in der bisherigen Literatur kaum behandelt wurden. Dies liegt hauptsächlich an der Komplexität dieser Objekte und weniger an ihrer Bedeutung für die Beschreibung korrelierter Systeme: In der Tat stellen Zweiteilchen-Greenfunktionen nicht nur die Basis zur theoretischen Berechnung experimentell messbarer Antwort-Funktionen dar, sondern sie sind auch ein wesentliches Ingredienz für die Konstruktion (Feynman) diagrammatischer Erweiterungen von DMFT, um über DMFT hinausgehende Korrelationen zu inkludieren.

Solche Erweiterungen von DMFT werden in **Kapitel 4** ausführlich diskutiert. Das Ziel ist hierbei neben den lokalen Korrelationen von DMFT vor allem auch *nicht-lokale* Kor-

relationen auf allen Längenskalen zu berücksichtigen. Wie schon anfangs erwähnt, sind diese für viele interessante Effekte in korrelierten Materialien verantwortlich. Nach einer kurzen Erläuterung von Clustermethoden, die im wesentlichen kurzreichweitige Korrelationen beschreiben können, wird eine allgemeine Darstellung der Gemeinsamkeiten aller diagrammatischer Erweiterungen von DMFT zur Inklusion langreichweitiger Korrelationen präsentiert. Das Hauptaugenmerk liegt hierbei auf der Dynamischen Vertex Approximation (DΓA), die auf der lokalen Näherung des vollständig irreduziblen Zweiteilchenvertex beruht. Ihre Anwendbarkeit zur theoretischen Beschreibung nicht-lokaler Korrelationen wird an der Berechnung der Einteilchen-Green-Funktionen für einen Benzen-Ring demonstriert. Des weiteren wird eine vereinfachte Version von DΓA zur Analyse des kritischen Verhaltens des drei-dimensionalen Hubbard Modells angewandt. Der letzte Abschnitt dieses Kapitels ist einem neuen, vielversprechenden Ansatz zur Beschreibung nicht-lokaler Korrelationen gewidmet, der auf dem einteilchenirreduziblen erzeugenden Funktional für die Green-Funktionen beruht. Diese neue Methode erlaubt auch einen ersten, systematischen, Vergleich der bestehenden diagrammatischen Methoden, der den Abschluß dieses Kapitels bildet.

Zuletzt wird in **Kapitel 5** ein Überblick über die wesentlichen Inhalte und Resultate dieser Arbeit gegeben. Ein Ausblick auf mögliche Erweiterungen der hier vorgestellten Theorien sowie deren Anwendung auf ungelöste Probleme stark korrelierter Elektronen-Systeme schließen die Dissertation ab.

List of Publications

- G. Rohringer, A. Toschi, H. Hafermann, K. Held, V. I. Anisimov, and A. A. Katanin, *One-particle irreducible functional approach: A route to diagrammatic extensions of dynamical mean-field theory*, Phys. Rev. B, **88**, 115112 (2013).

- T. Schäfer, G. Rohringer, O. Gunnarsson, S. Ciuchi, G. Sangiovanni, and A. Toschi, *Divergen Precursors of the Mott-Hubbard Transition at the Two-Particle Level*, Phys. Rev. Lett., **110**, 246405 (2013).

- G. Rohringer, A. Valli, and A. Toschi, *Local electronic correlations at the two-particle level*, Phys. Rev. B, **86**, 125114 (2012).

- G. Rohringer, A. Toschi, A. A. Katanin, and K. Held, *Critical Properties of the Half-Filled Hubbard Model in Three Dimensions*, Phys. Rev. Lett., **107**, 256402 (2011).

- A. Toschi, G. Rohringer, A. A. Katanin, and K. Held, *Ab initio calculations with the dynamical vertex approximation*, Annalen der Physik, **523**, 698 (2011).

- K. Held, C. Taranto, G. Rohringer, and A. Toschi, *Hedin Equations, GW, GW+DMFT, and All That*, Lecture Notes of the Autumn School 2011 Hands-on LDA+DMFT, Forschungszentrum Jülich GmbH (publisher) (2011).

- D. Nicoletti, O. Limaj, P. Calvani, G. Rohringer, A. Toschi, G. Sangiovanni, M. Capone, K. Held, S. Ono, Yoichi Ando, and S. Lupi, *High-Temperature Optical spectral Weight and Fermi-liquid Renormalization in Bi-based Cuprate Superconductors*, Phys. Rev. Lett., **105**, 077002 (2010).

Preprint:

- C. Taranto, S. Andergassen, J. Bauer, K. Held, A. A. Katanin, W. Metzner, G. Rohringer, and A. Toschi, *From infinite to two dimensions thorugh the functional renormalization group*, http://arxiv.org/abs/1307.3475.

Chapter 1

Introduction and Scope

"Die einzige Regel, die ihr immer beherzigen müsst, lautet: Dort wo schon Einer steht kann kein Zweiter stehen." ("The only rule, which you have to take to your heart, ends in: No second person can stand on the place, where already another person is standing"), Hermann Schwab, pastor of St. Leopold, Klosterneuburg, 1962-1996.

This statement was one of the first instructions which I got from pastor Hermann Schwab when I started my service as altar boy in St. Leopold almost 25 years ago. At that time, I laughed about this ascertainment since it seemed self-evident to me. Only many years later I understood that an intrinsic truth is inherent in this sentence, recognizing that it represents a very basic example for what we call *correlations*: The behavior of one entity affects the behavior of the other one(s). Indeed, correlations are present almost everywhere in everyday life, in the overcrowded underground (where we can literally feel them), in the traffic jam on our way into the weekend, and also in a game of chess where disregarding the correlation effects between the pieces will result in a quick loss.

Let us stress that the origin of correlations is deeply rooted in the *interaction* between entities, but, at the same time, one should always keep in mind that the two concepts are not equivalent. This is very well exemplified by the situation of a very long traffic jam: Here is indeed no direct "interaction" between the first and the last car, which might be several kilometers away from each other. However, the standstill of the first car clearly influences the behavior of the last one, which, of course, has to stop as well, demonstrating that the two vehicles are correlated.

On the other hand, it should be also emphasized that correlations coincide neither with the concept of a fixed *order* in a system. Resorting once more to the example of cars on a highway, one can define an "ordered state", e.g., as the situation where all the cars are

driving with exactly the same speed in queue. In absence of an external perturbation, such as an accident, the single driver will not "feel" any correlation with the others: he will just continue to keep his velocity and position in the chain. In fact, if all the other drivers also follow this behavior, he can just consider them all together as some kind of "homogeneous cloud", which forces him to keep his velocity and position (relative to this field), while the behavior of any other specific single car does not concern him, as long as the driver does not cause a perturbation of this "cloud" by, e.g., a change in his speed. As we will see in the following, the "ordered state" situation corresponds in a more scientific context to what we call mean field theory, where the direct mutual interaction between two entities is replaced by an interaction between one entity and a mean field formed by the other ones. It is clear that this simplification allows for describing an ordered state within the assumption that no fluctuations from the specific order considered takes place. This corresponds, however, to the neglect of correlation effects, which can become crucial in many important situations.

As the title of the present thesis suggests, we are not interested here in correlations between people or cars but rather in correlations between electrons in a solid. In order to formalize better the physics we are concerned with, let us start by considering the general Hamiltonian for a solid state system. Since our main focus is on the electronic behavior, we neglect the dynamics of the atomic nuclei which constitute the crystal lattice of the system, so that their presence will just generate the static periodic potential in which the electrons are bound. This is tantamount to the so-called Born-Oppenheimer approximation [1] and corresponds to the assumption of an infinite mass for the atomic nuclei[1]. We will furthermore neglect any relativistic corrections since we will mostly focus on energies around 1 eV, much lower than $m_e c^2 \sim 10^9$ eV, the energy of the electron rest mass. Let us just remark that in specific situations beyond the scope of this thesis, in particular for systems with partially filled f-orbitals of heavy atoms, the treatment of spin-orbit coupling will become also important for an accurate description of the electronic structure.

Within the framework of the Born-Oppenheimer approximation and by neglecting all relativistic effects, the Hamiltonian for describing the dynamics of the electrons in a solid is written as:

$$\hat{H} = \underbrace{\sum_{i=1}^{N} \left[\frac{\hat{\mathbf{p}}_i^{\,2}}{2m} + V(\hat{\mathbf{r}}_i) \right]}_{\hat{H}_0} + \underbrace{\sum_{i=1}^{N} \sum_{j=i+1}^{N} \frac{e^2}{|\hat{\mathbf{r}}_i - \hat{\mathbf{r}}_j|}}_{\hat{H}_I}, \tag{1.1}$$

---

[1]The mass of a single proton or neutron in the nucleus is indeed about a factor 2000 larger than the corresponding electron mass, justifying in most cases the Born-Oppenheimer assumption.

where the lattice-periodic potential $V(\hat{\mathbf{r}})$, generated by the atomic nuclei, is given by:

$$V(\hat{\mathbf{r}}) = -\sum_l \frac{Z_l e^2}{|\mathbf{R}_l - \hat{\mathbf{r}}|}. \tag{1.2}$$

Z_l is the number of protons of the l-th nucleus at the position $\mathbf{R}_l$. The Hamiltonian (1.1) consists of a *non-interacting* part $\hat{H}_0$, which describes the kinetic energy of the electrons and their interaction with the external potential generated by the atomic nuclei of the lattice, and an interacting term $\hat{H}_I$ corresponding to the Coulomb interaction among the electrons themselves. Since this interaction contribution is far from being negligible, (strong) correlation effects could be expected in all these systems. Interestingly, this is not the case for most materials. Specifically, in compounds with partially filled bands exhibiting s- or p-character, the electron-electron interaction is usually well screened, since these orbitals are rather extended. Hence, the electrons belonging to these valence states can be considered "on average" as pretty far away from each other In this situation, one can reasonably expect that for such materials mean field theories, where the actual two-particle repulsion between the electrons $\hat{H}_I$ is replaced by an interaction between the single electron and an effective field generated by the other electrons, will work quite well. In fact, it is known that the physics of s- and p-electron systems can be understood qualitatively and quantitatively rather well by methods where the electronic correlations beyond mean-field are either neglected or taken into account only rudimentarily.

In this respect, one of the most widespread and successful approaches, aiming at a solution of the Hamiltonian (1.1), is the density functional theory (DFT) [2]. It is based on the Hohenberg-Kohn theorem [2] which states that all observables of the system described by this Hamiltonian are uniquely determined by the corresponding ground-state density $\rho_0(\mathbf{r})$. Hence, observables such as, e.g., the total energy E, can be considered as a functional of this ground state density $\rho_0(\mathbf{r})$, i.e., $E \equiv E[\rho(\mathbf{r})]$. On the other hand, the so-called V-representability theorem [3] states that there exists a unique non-interacting system (i.e., where $\hat{H}_I \equiv 0$) defined by the one-particle potential $V_0(\mathbf{r})$, which exhibits the same ground state density. Such density $\rho_0(\mathbf{r})$ can be explicitly written in terms of these one-particle eigenstates $\phi_i(\mathbf{r})$, i.e., $\rho_0(\mathbf{r}) = \sum_{i=1}^{N} |\phi_i(\mathbf{r})|^2$. This way the *auxiliary* potential $V_0(\mathbf{r})$ can be understood as a functional of $\rho_0(\mathbf{r})$, i.e., $V_0 = V_0[\rho]$. For this reason, given $V_0[\rho]$ the ground-state density $\rho_0(\mathbf{r})$ can be obtained iteratively by an self-consistent solution of the corresponding one-particle Schrödinger equation.

There are, however, two main obstacles in the DFT approach just described: (i) The func-

tional $V_0[\rho]$ is not known for the interacting Hamiltonian (1.1). Hence, approximations for it are needed. Usually, one performs such an approximation for a corresponding energy-functional $E_0[\rho]$, the functional derivative of which yields $V_0[\rho] = \delta E_0[\rho]/\delta\rho$. The most common among these functionals is expressed in the so-called local density approximation (LDA) [4,5] where $E_0[\rho]$ is represented by just a local functional of the density $\rho(\mathbf{r})$. Let us stress that there is no systematic way for deriving these functionals. In fact, experience in the calculation of real materials has shown, that different types of functionals are appropriate for different classes of compounds [6–8]. (ii) The second problem of DFT is that it, in principle, yields only the ground-state density of the system (and of course all observables which can be calculated from it). However, no information about the energy-spectrum of the Hamiltonian (1.1) should be extracted from this method. In fact, from the formal point of view, one should keep in mind that the one-particle states of the auxiliary non-interacting system do not represent one-particle levels of the real electrons: Because of the correlations originated by the interaction term $\hat{H}_I$ in Eq. (1.1), the system cannot be described by means of a single Slater determinant of single-particle wave-functions. Nevertheless, in practice, it turns out that for a large number of materials such a single-particle description holds, and the energy-eigenvalues of the auxiliary non-interacting system can be indeed interpreted as the band-structure of the compound, as it is confirmed experimentally by angle-resolved photoemission spectroscopy (ARPES). However, in this respect, DFT does not constitute an exact method, as it is for the calculation of the ground-state density, but rather corresponds to a sort of static mean-field approximation. This explains why, eventually, DFT methods work pretty well for systems where correlation effects are rather week due to the screening of the strong Coulomb repulsion, as it is, precisely, the case for the above mentioned materials with partially filled s- and p-orbitals. For the same reason, DFT typically fails in describing the spectral properties of solids with partially filled d- and f-shells, even from a qualitative point of view. For instance, for some compounds of this class, DFT predicts a metallic behavior with sizable spectral weight at the Fermi energy, while they are found to be insulating in experiments. This observation indicates that correlation effects are rather strong in the presence of d- or f-valence states. In fact, this is indeed expected for these systems, from a general point of view, as it will be briefly recalled in the following.

In contrast to the above described s- and p-compounds, the valence orbitals of systems with partially filled d- or f-shells are indeed rather narrow in space, especially for the case of $3d$ and $4f$ orbitals.[2] Hence, the screening mechanism for the Coulomb repulsion between

---

[2]This latter "trend" can be understood as follows": Differently from $3d$ and $4f$ orbitals the radial wave functions of the $4d$ and $5f$ orbitals have a node. Consequently, electrons occupying $3d$ and $4f$ shells are much

Figure 1.1: Periodic table. The elements which are mainly responsible for partially filled d- and f- orbitals are red- and violet-rimmed, respectively.

two electrons residing in one of these orbitals becomes inefficient. Such a situation is often encountered in the outer orbitals of transitions metal atoms (d-systems) or of lanthanide and actinide elements (f-systems), which are marked by the red- and violet-rimmed boxes, respectively, in the periodic table in Fig. 1.1. Typical examples for such compounds are oxides of the transitions metals from the titanates to the cuprates or heavy fermion systems such as Cerium.

While the high degree of correlation in these solids makes any kind of mean-field treatment insufficient, even for a qualitative theoretical understanding, their physics is typically characterized by fascinating and technologically relevant phenomena such as the Mott metal-to-insulator transition (MIT) in V_2O_3 [10–16], high-temperature superconductivity in the cuprates [17], giant magneto-resistance in the manganites [18, 19] or the volume collapse in Ce [20, 21]. In this light, the mismatch between experimental data and theoretical predictions based on DFT for d- and f-systems calls for many-body methods, which are capable

---

closer to the atomic nucleus with respect to $4d$ and $5f$ electrons, as one can also infer, more quantitatively, from the ratios between the corresponding average radial location of the electrons in the respective shells, i.e., $\langle \hat{r} \rangle_{3d}/\langle \hat{r} \rangle_{4d} \sim 0.5$ and $\langle \hat{r} \rangle_{4f}/\langle \hat{r} \rangle_{5f} \sim 0.57$ (in the hydrogen atom). For a more detailed explanation of this point see Ref. [9].

of taking into account the strong correlations among d-electrons and f-electrons. It should be, however, stressed that the analytical and computational effort of many-body methods applied to solid state systems is considerably larger than that of DFT. Hence, applying them directly to the general solid state Hamiltonian (1.1) is in most cases too difficult. This calls for simplified model Hamiltonians, built to capture the basic physics of the system under considerations. Let us stress that, even within these simplified model Hamiltonians, the goal of a complete theoretical understanding of all correlation effects is far from being achieved. Against this background, the main scope of the present thesis is the application and the further development of theoretical tools for improving the description of electronic correlations for these basic model Hamiltonians, with the help of the most advanced techniques of quantum field theory for non-relativistic systems.

The thesis is organized as follows: in **chapter 2** we first explain how a simplified model can be derived from the full Hamiltonian for electrons in a crystal as given in Eq. (1.1), by taking into account only the most relevant degrees of freedom. This will lead us to the so-called Hubbard model, which represents the perhaps most transparent model for describing correlated electrons on a lattice, and the Anderson impurity model (AIM) as its local counterpart. Then, we will recall the technique of the n-particle Green's functions which constitute the most important objects for a theoretical description of the dynamics of lattice electrons in the framework of quantum field theory. Since a comprehensive discussion of the general properties of these functions, at least beyond the more standard one-particle level, is still lacking in the literature, we aim at filling this gap, by presenting a thorough analysis of all symmetry features of the one- and more-particle Green's functions and their interpretation in terms of Feynman diagrams in the second part of this chapter. Specifically, the concept of irreducibility of one- and two-particle Green's functions will be highlighted, as it represents the foundation of several of the most modern quantum field theoretical methods aiming at an accurate description of correlations on all length scales in many electron systems. Finally, we will give explicit expressions for the one- and the two-particle Green's functions in the extreme cases of a non-interacting system and a system without dispersion, i.e., the so-called "atomic limit".

Chapter 3 of the thesis is dedicated to the discussion of *local correlations*, i.e., correlations of two-electrons on the same lattice site. In this respect the dynamical mean field theory (DMFT) [22–25] represents a big step forward in the theoretical understanding as it is capable of treating the (purely) local part of the correlations, which is in many cases the most important one, non-perturbatively. Therefore, at the beginning of this chapter we will introduce DMFT and discuss its strengths and limitations. In order to exemplify its applicability

to the description of real correlated materials, we present a DMFT study of ours for the hight-temperature behavior of the optical spectral weight in two Bi-based high-temperature superconducting cuprate compounds. Thereafter, we turn to one of the main topics of this thesis which is the analysis of (local) two-particle Green's functions. This is very important because it allows not only for the calculation of thermodynamic response functions of the considered system at the DMFT level, but also constitutes the basic ingredient for several diagrammatic extensions of DMFT, aiming at an inclusion of nonlocal correlations effects. The final part of this section considers an attractive model for lattice electrons, analyzing it in terms of an exact mapping on the corresponding repulsive case. This might be relevant for the physics of ultra-cold atoms in optical lattices as well as for an effective low-energy description of some characteristic features of the high-temperature superconducting cuprates. In **chapter 4**, we discuss cases where DMFT provides a rather poor approximation, since nonlocal correlations become important. This is the case for low-dimensional systems or systems in the vicinity of second-order phase-transitions. Aiming at an accurate theoretical description of such situations, we consider different extension of DMFT, which allow for a treatment of spatial correlations beyond the local DMFT ones. Specifically we review the dynamical vertex approximation (DΓA) [26–30] which is based on the locality of the fully irreducible two-particle vertex function and demonstrate its applicability by studying a simple nanoscopic system. Next, we introduce a simplified version of DΓA (i.e., ladder DΓA), which takes into account ladder scattering processes in only one channel. We illustrate its ability to capture nonlocal correlation effects by applying it to the problem of the critical behavior of the half-filled three-dimensional single-band Hubbard model [31]. Thereafter, we turn to extension of DMFT which are based on the functional integral technique [32,33] such as the dual fermion (DF) approach [34,35], which we briefly review. Considering the limitations of both, DΓA and DF in their present ladder implementation, we propose a new scheme, coined one-particle irreducible approach (1PI) [36], which aims at unifying the existing methods and allows for a discussion of differences and similarities in the currently adopted diagrammatic approaches.

Finally, in **chapter 5**, we recapitulate the main results obtained in this thesis, and we try to highlight the possible pathways for further theoretical developments of the methods and of the physical understanding, which can be inspired by our findings.

Let us stress, at the end of this introduction, that several results of this thesis have already been published in different peer-reviewed journals. An explicit Reference to the publication (a complete list of which is reported on page xi) will be given at the beginning of the corresponding result section of the thesis. Furthermore, we will mark with different

style/indentation when extended parts of the text have been taken from the publication with only small changes.

Chapter 2

Quantum Field Theory description of correlated electron systems

„Mache die Dinge so einfach wie möglich - aber nicht einfacher.“(A. Einstein)

In this chapter, we introduce first the models for describing correlated electrons, which will be used throughout the entire thesis: (i) the Hubbard Hamiltonian, as the simplest lattice model for treating electronic correlations, and (ii) the Anderson impurity model (AIM) for the description of the local correlations between electrons at a single lattice site. We will then introduce the methods of quantum field theory (QFT) which provide the essential theoretical tools for analyzing these models. More specifically, the n-particle Green's functions and their representation in terms of Feynman diagrams constitute the central objects of our theoretical description. In this framework, the various symmetry properties of the Hamiltonians under consideration will be discussed in great detail, since they lead to important simplifications of the mathematical structure of the Green's functions and allow for a better understanding of their physical content. Finally, at the end of the chapter, exact analytic solutions for the Green's functions in the limiting cases of non-interacting and completely localized ("atomic limit") electrons will be presented, as these provide an important guidance to the interpretation of the more complex theoretical calculations, discussed in the following chapters.

Solving the Schrödinger equation for Hamiltonian (1.1) of the general solid stat problem,

introduced in the previous chapter,

$$\hat{H}\psi(\mathbf{r}_1,\ldots,\mathbf{r}_N) = E\psi(\mathbf{r}_1,\ldots,\mathbf{r}_N) \tag{2.1}$$

is an unfeasible task if one considers the case of a macroscopic number of particles ($N \sim 10^{23}$). Furthermore, even assuming that one could really calculate the many-particle wave function $\psi(\mathbf{r}_1,\ldots,\mathbf{r}_N)$, which contains the complete information about the system under considera-tion, this would not be a useful quantity to work with. Indeed, we are not interested to determine the behavior of every single electron of our system but rather to obtain a descrip-tion of our many body system, which can be compared with the experimental observations. This specifically means that our theoretical approach should allow for the calculation of the most important thermodynamic and spectral observables, such as the spectral function $A(\omega,\mathbf{k})$, the optical conductivity $\sigma(\omega)$, the (dynamic) spin susceptibility $\chi_s(\omega,\mathbf{q})$, the specific heat, and so forth. These are determined by the response of the system to an excitation of one or two particles rather than bey the configuration of each single particle in the system. Therefore, a formalism which allows for adding and removing electrons to the many particle state under consideration would be advantageous. Note that this situation is analogous to relativistic quantum electrodynamics, where the (infinitely many) negative energy solutions of the Dirac equation are assumed to be occupied, defining the vacuum state of the system, while the interesting physics occurs when adding single electrons or positrons to this state. Since the number of occupied states is infinite in the relativistic case, it is inevitable to re-sort to the formalism of second quantization in order to get a consistent formulation of the theory. In fact, in our (non-relativistic) situation the number of occupied states is still finite though typically very large ($\sim 10^{23}$). Hence, while a description within a first quantization formalism would be still possible, it is much more convenient to adopt the technique of sec-ond quantization also in this situation. Furthermore, this approach allows also for changing the number of particles in the system as required by statistical mechanics calculations in the grand canonical ensemble. The Hamiltonian (1.1) rewritten in second quantization reads as [21]:

$$\hat{\mathcal{H}} = \sum_{\sigma} \int d^3r \; \hat{\psi}_{\sigma}^{\dagger}(\mathbf{r}) \left[-\frac{\hbar^2}{2m}\Delta + V(\mathbf{r}) \right] \hat{\psi}_{\sigma}(\mathbf{r}) - \mu \overbrace{\sum_{\sigma} \int d^3r \; \hat{\psi}_{\sigma}^{\dagger}(\mathbf{r})\hat{\psi}_{\sigma}(\mathbf{r})}^{\hat{\mathcal{N}}} +$$
$$+ \frac{1}{2}\sum_{\sigma\sigma'} \int d^3r\,d^3r' \; \hat{\psi}_{\sigma}^{\dagger}(\mathbf{r})\hat{\psi}_{\sigma'}^{\dagger}(\mathbf{r}')\frac{e^2}{|\mathbf{r}-\mathbf{r}'|}\hat{\psi}_{\sigma'}(\mathbf{r}')\hat{\psi}_{\sigma}(\mathbf{r}), \tag{2.2}$$

where the operator $\hat{\psi}_\sigma^{(\dagger)}(\mathbf{r})$ (creates) annihilates an electron with spin σ at position $\mathbf{r}$. Notice, that we have added a contribution $\mu\hat{\mathcal{N}}$ in Eq. (2.2) containing the chemical potential μ and the (particle-) number operator $\hat{\mathcal{N}}$, which is necessary, when performing calculations in the grand-canonical ensemble.

Instead of analyzing the N-particle wavefunction $\psi(\mathbf{r}_1,\ldots,\mathbf{r}_N)$ (which, as previously discussed, is not a useful object to work with), we will consider the n-particle Green's function $G_{n,\sigma_1\ldots\sigma_{2n}}(\tau_1,\mathbf{r}_1,\ldots,\tau_{2n},\mathbf{r}_{2n})$ defined as

$$G_{n,\sigma_1\ldots\sigma_{2n}}(\tau_1,\mathbf{r}_1,\ldots,\tau_{2n},\mathbf{r}_{2n}) = \left\langle \mathrm{T}\left(\hat{\psi}_{\sigma_1}^\dagger(\tau_1,\mathbf{r}_1)\ldots\hat{\psi}_{\sigma_{2n}}(\tau_{2n},\mathbf{r}_{2n})\right)\right\rangle, \qquad (2.3)$$

where an odd/even index always corresponds to a creation/annihilation operator $\hat{\psi}_\sigma(\tau_i,\mathbf{r}_i)/$ $\hat{\psi}_\sigma^\dagger(\tau_i,\mathbf{r}_i)$ which corresponds to the convention, where the creation and annihilation operators appear in alternating order. T is the time-ordering operators which arranges the $2n$ creation and annihilation operators according to their imaginary time argument starting from left with the operator, which exhibits the largest imaginary time argument. In addition, due to the fermionic nature of the operators $\hat{\psi}_\sigma$ and $\hat{\psi}_\sigma^\dagger$, a minus sign has to be added to the sequences of operators which represent an odd permutation of the original order. Since we are only dealing with systems in thermal equilibrium, we adopt the Matsubara formalism [33, 37, 38] which considers the imaginary time variables $\tau_i \in [0,\beta]$ ($\beta = \frac{1}{T}$, T ...temperature) and the (imaginary) time dependent field operators $\hat{\psi}_\sigma^{(\dagger)}(\tau_i,\mathbf{r}_i)$ in the (Matsubara) Heisenberg representation

$$\hat{\psi}_\sigma(\tau_i,\mathbf{r}_i) = e^{\tau_i\hat{\mathcal{H}}}\hat{\psi}_\sigma(\mathbf{r}_i)e^{-\tau_i\hat{\mathcal{H}}}, \qquad\qquad \hat{\psi}_\sigma^\dagger(\tau_i,\mathbf{r}_i) = e^{\tau_i\hat{\mathcal{H}}}\hat{\psi}_\sigma^\dagger(\mathbf{r}_i)e^{-\tau_i\hat{\mathcal{H}}}. \qquad (2.4)$$

We also recall that the averaging $\langle\ldots\rangle$ in Eq. (2.3) is performed using the (equilibrium) density operator for the grand canonical ensemble

$$\langle\ldots\rangle = \frac{1}{Z}\mathrm{Tr}\left(e^{-\beta\hat{\mathcal{H}}}\ldots\right) \quad\text{with}\quad Z = \mathrm{Tr}\left(e^{-\beta\hat{\mathcal{H}}}\right). \qquad (2.5)$$

The calculation of n-particle Green's functions for the lowest values of $n = 1,2$ is the central problem of quantum field theory in many-particle systems. The explicit expression for these Green's functions allows for an evaluation of the most important thermodynamic quantities as well as for a calculation of expectation values for physical observables. In order to give a physical illustration of the meaning of a Green's function let us take a closer look at the

easiest, one-particle, case:

$$G_{1,\sigma_1\sigma_2}(\tau_1, \mathbf{r}_1, \tau_2, \mathbf{r}_2) = \left\langle \mathrm{T}\left(\hat{\psi}^\dagger_{\sigma_1}(\tau_1, \mathbf{r}_1)\hat{\psi}_{\sigma_2}(\tau_2, \mathbf{r}_2)\right)\right\rangle. \tag{2.6}$$

Assuming that $\tau_2 > \tau_1$ one sees that the operator $\hat{\psi}^\dagger_{\sigma_1}(\tau_1, \mathbf{r}_1)$ adds an electron with spin σ_1 at the (Matsubara) time τ_1 and the position $\mathbf{r}_1$ to the system. This electron then propagates through the system until it is annihilated at the (later) time τ_2 and the position $\mathbf{r}_2$ by the operator $\hat{\psi}_{\sigma_2}(\tau_2, \mathbf{r}_2)$. Analogously, the other time order $\tau_2 < \tau_1$ describes the propagation of a hole from $\mathbf{r}_2$ to $\mathbf{r}_1$. Hence, the one-particle Green's function describes the behavior of the system when adding one particle or hole which acts as a probe for the interaction which are present in the system. Analogously, one can interpret the two-particle Green's functions (for instance, as measuring the effect of a perturbation of and observable such as, e.g., the density of the system) , which explains the dominant role of these quantities in the theoretical many-particle physics.

Unfortunately, it is still far too difficult to calculate even the one-particle Green's function for the Hamiltonian (2.2) exactly. Besides the possibility of deriving approximate solutions directly for Eq. (2.2) [see the discussion about density functional theory in Cap. 1], one often tries first to find simpler basic models which, however, should still capture the most important physical aspects of the original system (see next section). Furthermore, as we will discuss explicitly in this chapter, the symmetries of the system often allow for important simplifications in the calculations of the Green's functions. Eventually, the calculation of the Green's functions, even for the simplified model, has to be performed in a given approximation scheme. For methods based on the QFT the application of (Feynman) diagrammatic techniques is often helpful or necessary: It does not only allow for a systematic definition of the approximation scheme, but it also leads to a deeper understanding of the physical processes described by these functions.

2.1   Models

2.1.1   The Hubbard model

In this thesis we aim at developing theoretical tools for the description of systems with partially filled d- or f-shells. Since, as we discussed in the introduction (Cap. 1), these orbitals are very narrow, the Coulomb interaction between the electrons is not well screened, differently from the case of s- or p-orbitals. Hence, a simple mean field treatment of the

solid state Hamiltonian (2.2) will not yield satisfactory results. However, as we mentioned above, a more precise treatment of (2.2), which takes into account the strong correlations between the electrons, is presently not feasible, neither analytically nor numerically. This observation calls for the construction of a simpler model which, nevertheless, contains the most important physical aspects of the original one, i.e., the kinetic energy of the particles and their interaction. One of the most simple models, which meets this claim, is the Hubbard model. In this section, we will derive the corresponding Hubbard Hamiltonian, starting from the full solid-state one in second quantization, Eq. (2.2), demonstrating the validness of such a strongly simplified modeling for describing electrons in strongly correlated orbitals. The derivation presented below is mainly based on [33].

In order to restrict the Hamiltonian (2.2) to the most important degrees of freedom, i.e., to the energy regions crucial for the physics of the system ($E \approx E_{\mathrm{F}}$), it is convenient to expand first the creation and annihilation operators $\hat{\psi}_\sigma^\dagger(\mathbf{r})$ and $\hat{\psi}_\sigma(\mathbf{r})$ in terms of eigenstates of the non-interacting part $\hat{H}_0$ of the full solid state Hamiltonian, given in Eq. (1.1). We recall here that, since the potential $\hat{V}(\mathbf{r})$ is generated by the distribution of nuclear charges located at the sites of a periodic lattice, it fulfills the periodicity condition

$$\hat{V}(\mathbf{r}) = \hat{V}(\mathbf{r} + \mathbf{R}), \tag{2.7}$$

where $\mathbf{R}$ is a lattice vector. Hence, according to the Bloch theorem [33, 39], the one-particle eigenstates of $\hat{H}_0$ can be written as Bloch wave functions $\psi_{\mathbf{k}n}(\mathbf{r})$ where n is the band index and $\mathbf{k}$ is a crystal momentum vector located in the first Brillouin zone. The corresponding energies are given by $\varepsilon_{\mathbf{k}n}$, and the wave function $\psi_{\mathbf{k}n}(\mathbf{r})$ can be written as:

$$\psi_{\mathbf{k}n}(\mathbf{r}) = e^{i\mathbf{k}\mathbf{r}} u_{\mathbf{k}n}(\mathbf{r}), \tag{2.8}$$

where $u_{\mathbf{k}n}(\mathbf{r})$ hast the symmetry of the lattice, i.e., $u_{\mathbf{k}n}(\mathbf{r}+\mathbf{R}) = u_{\mathbf{k}n}(\mathbf{r})$ for an arbitrary lattice vector $\mathbf{R}$. Since the $\psi_{\mathbf{k}n}(\mathbf{r})$ are a complete set of eigenfunctions of a hermitian operator it is possible to expand every wave function $\psi_\sigma(\mathbf{r})$ or wave operator $\hat{\psi}_\sigma(\mathbf{r})$ in terms of these basis states:

$$\hat{\psi}_\sigma^{(\dagger)}(\mathbf{r}) = \frac{V}{(2\pi)^3} \int_{\mathrm{BZ}} d^3k \sum_n \psi_{\mathbf{k}n}^{(*)}(\mathbf{r}) \hat{a}_{\mathbf{k}n\sigma}^{(\dagger)}, \tag{2.9}$$

where the operator $\hat{a}_{\mathbf{k}n\sigma}^{(\dagger)}$ (creates) annihilates an electron with a crystal momentum $\mathbf{k}$, a spin σ and an energy $\varepsilon_{\mathbf{k}n}$. V is here the volume of the unit cell and "BZ" denotes the first Brillouin

zone. Considering that:

$$\hat{H}_0\psi_{\mathbf{k}n}(\mathbf{r}) = \left(-\frac{\hbar^2}{2m}\Delta + \hat{V}(\mathbf{r})\right)\psi_{\mathbf{k}n}(\mathbf{r}) = \varepsilon_{\mathbf{k}n}\psi_{\mathbf{k}n}(\mathbf{r}) \qquad (2.10)$$

one can express the solid-state Hamiltonian (2.2) as

$$\hat{\mathcal{H}} = \frac{V}{(2\pi)^3}\int_{\mathrm{BZ}} d^3k \sum_{n\sigma}(\varepsilon_{\mathbf{k}n} - \mu)\hat{a}^\dagger_{\mathbf{k}n\sigma}\hat{a}_{\mathbf{k}n\sigma} + \hat{\mathcal{V}}_{ee} \qquad (2.11)$$

where $\hat{\mathcal{V}}_{ee}$ denotes the interaction part of the Hamiltonian[1].

One typically speaks of a *nearly free electron system* if the potential $\hat{V}(\mathbf{r})$ is only weakly depending on $\mathbf{r}$, i.e., $\hat{V}(\mathbf{r}) \sim V_0(=0)$. In this case the corresponding Bloch wave functions $\psi_{\mathbf{k}n}(\mathbf{r})$ become simple plane waves $[u_{\mathbf{k}n}(\mathbf{r})=1]$ and the dispersion $\varepsilon_{\mathbf{k}n}$ is that of free electron $\varepsilon_{\mathbf{k}n} = \frac{(\mathbf{k}+\mathbf{G}_n)^2}{2m}$ where $\mathbf{G}_n$ is a reciprocal lattice vector (with $\mathbf{k}$ located within the first Brillouin zone). In real systems, such a situation can be observed for the outermost electrons in the elemental metals drawn from groups I-IV of the periodic table. For this specific case, the (rather strong) Coulomb potential of the atomic nuclei is screened by the inner core electrons leading to an almost free (itinerant) behavior of the valence electrons [39].

Since the Bloch wave-function $\psi_{\mathbf{k}n}(\mathbf{r})$ as well as the energies $\varepsilon_{\mathbf{k}n}$ are periodic functions of $\mathbf{k}$, i.e., $u_{(\mathbf{k}+\mathbf{G})n}(\mathbf{r}) = u_{\mathbf{k}n}(\mathbf{r})$ and $\varepsilon_{(\mathbf{k}+\mathbf{G})n} = \varepsilon_{\mathbf{k}n}$ with any reciprocal lattice vector $\mathbf{G}$, one can represent them in terms of a Fourier series:

$$\psi_{\mathbf{k}n}(\mathbf{r}) = \sum_{\mathbf{R}} e^{i\mathbf{k}\mathbf{R}}\phi_n(\mathbf{r}-\mathbf{R}), \qquad \phi_n(\mathbf{r}-\mathbf{R}) = \frac{V}{(2\pi)^3}\int_{\mathrm{BZ}} d^3k\, e^{-i\mathbf{k}\mathbf{R}}\psi_{\mathbf{k}n}(\mathbf{r}), \qquad (2.12)$$

where the sum on the right-hand side of the left equation runs over all lattice vectors $\mathbf{R}$. From a mathematical point of view Eq. (2.12) is just an orthogonal transformation between two basis sets in the subspace of eigenfunctions of $\hat{H}_0$ corresponding to the band index n, namely the Bloch basis $\{\psi_{\mathbf{k}n}(\mathbf{r})\}$ and the well-known *Wannier basis* $\{\phi_n(\mathbf{r}-\mathbf{R})\}$ [39]. In general the Wannier states are not eigenstates of the Hamiltonian $\hat{H}_0$, since they they can be seen as a linear combination of of Bloch-eigenstates $\psi_{\mathbf{k}n}$ corresponding to different $\mathbf{k}$ and, hence, to different eigenenergies $\varepsilon_{\mathbf{k}n}$. Only in a situation of an almost completely flat band $\varepsilon_{\mathbf{k}n} = \varepsilon_n$, i.e., if the energy eigenvalue is independent of the crystal momentum $\mathbf{k}$ the Wannier functions are eigenfunctions to the energy ε_n. Such a behavior can be observed for systems

---

[1]Let us recall that, for the non-interacting system in the ground state ($\hat{\mathcal{V}}_{ee} = 0$, $T = 0$), all the levels $\{\mathbf{k}n\sigma\}$ with $\varepsilon_{\mathbf{k}n} \leq \varepsilon_F = \mu$ are occupied while the states with a higher energy are empty.

with a rather large lattice constant and electrons which are tightly bound to the corresponding atomic nuclei. In this case the potential $\hat{V}(\mathbf{r})$ can be considered, to a first approximation, as sum of the potentials of all atomic nuclei of the lattice which do not overlap. Hence, an eigenfunction of the lattice system is just a linear combination of atomic wave functions centered a the different lattice sites $\mathbf{R}$. That means, that in such a situation, the Wannier functions defined in Eq. (2.12) can be considered as atomic-like wave functions centered at the various lattice sites $\mathbf{R}$. Therefore, this so-called *tight binding description* works best for systems with rather localized states, which is specifically the case of the partially filled d- or f-shells in transition metals and rare earths, which we are interested in.

Hence, in our perspective, it is useful to adopt the tight binding representation, i.e., to rewrite the full Hamiltonian (2.2) in terms of Wannier states. Therefore, similarly to Eq. (2.9), we expand the wave-operator in terms of Wannier functions:

$$\hat{\psi}_\sigma^{(\dagger)}(\mathbf{r}) = \sum_{\mathbf{R}_i, n} \phi_n^{(*)}(\mathbf{r} - \mathbf{R}_i)\hat{c}_{in\sigma}^{(\dagger)}, \tag{2.13}$$

where $\hat{c}_{in\sigma}^{(\dagger)}$ (creates) annihilates an electron in the Wannier state (or, in a shorter notation, "orbital") n at the lattice site $\mathbf{R}_i$. Inserting this representation into Eq. (2.2) yields the solid state Hamiltonian in the tight binding representation:

$$\hat{\mathcal{H}} = \sum_\sigma \sum_{ij,mn} (-t_{ij}^{mn} - \mu\delta_{ij}\delta_{mn})\hat{c}_{im\sigma}^\dagger \hat{c}_{jn\sigma} + \sum_{\sigma\sigma'} \sum_{ijkl} \sum_{mnop} U_{ijkl}^{mnop} \hat{c}_{im\sigma}^\dagger \hat{c}_{jn\sigma'}^\dagger \hat{c}_{ko\sigma'} \hat{c}_{lp\sigma}. \tag{2.14}$$

The indices $\{i, j, k, l\}$ correspond to lattice sites while the indices $\{m, n, o, p\}$ label different Wannier (orbital) states. The quantities t_{ij}^{mn} and U_{ijkl}^{mnop} are given by

$$t_{ij}^{mn} = -\int d^3r\, \phi_m^*(\mathbf{r} - \mathbf{R}_i) \left(-\frac{\hbar^2}{2m}\Delta + \hat{V}(\mathbf{r}) \right) \phi_n(\mathbf{r} - \mathbf{R}_j) = \tag{2.15}$$

$$= -\delta_{mn} \frac{V}{(2\pi)^3} \int d^3k\, e^{i\mathbf{k}(\mathbf{R}_i - \mathbf{R}_j)}\varepsilon_{\mathbf{k}n}$$

$$U_{ijkl}^{mnop} = \frac{1}{2}\int d^3r \int d^3r'\, \phi_m^*(\mathbf{r} - \mathbf{R}_i)\phi_n^*(\mathbf{r}' - \mathbf{R}_j)\frac{e^2}{|\mathbf{r} - \mathbf{r}'|}\phi_o(\mathbf{r}' - \mathbf{R}_k)\phi_p(\mathbf{r} - \mathbf{R}_l). \tag{2.16}$$

We note that up to now now no approximations have been used, i.e., the Hamiltonian (2.14) is the exact solid-state Hamiltonian in second quantization written in the tight binding representation, that means in the basis of the Wannier states. It includes all energy bands as well as the full Coulomb interaction $(\mathcal{V}_{ee})$ between two electrons. In order to extract a more

manageable model from Eq. (2.14), which nevertheless contains the essential physics we want
to describe, approximations have to be performed, as discussed in the following:

- In the present thesis we will restrict ourselves to the case of low-temperatures ($T \ll T_\mathrm{F}$)
  and, hence, low energy excitations around the Fermi level. Therefore, we will consider
  only energy bands, whose one-particle energies $\varepsilon_{\mathbf{k}n}$ are located at the Fermi level. As a
  further simplification, we assume that only one band crosses the Fermi level and all the
  other ones are well separated and far away from this "target" band. Hence, from now
  on *we will drop all band indices* assuming that we restrict ourselves to the one target
  band n_0 at the Fermi level.

- Since our main interest is focused on systems with partially filled d- and f-shells the
  Wannier functions are very localized, i.e., the function $\phi_n(\mathbf{r} - \mathbf{R}_i)$ has a maximum at
  $\mathbf{r} = \mathbf{R}_i$ and decays rapidly with increasing distance $|\mathbf{r} - \mathbf{R}_i|$ from the nucleus. In the
  atomic limit where $\varepsilon_{\mathbf{k}n} = \varepsilon_n$ does not depend on $\mathbf{k}$ one has $t_{ij} = \varepsilon \delta_{ij}$, meaning that
  no inter-atomic transport is possible. Since the pure atomic limit, obviously, cannot
  describe the most interesting phenomena of solid state physics, one should allow at least
  for a weak hybridization of neighboring sites, e.g., we restrict t_{ij} to the nearest neighbor
  hopping only [i.e., for each i the sum over j runs only over the nearest neighbors of i in
  Eq. (2.14)]. For systems with translational invariance, the hopping term in Eq. (2.14)
  can be parameterized by a single quantity: $t_{ij} = t$ if i and j are nearest neighbors in
  the lattice and $t_{ij} = 0$ otherwise.

- Finally, we want to simplify also the interaction part of the Hamiltonian (2.14). Since
  we assume that our electrons are strongly localized, we will focus on contributions to
  U_{ijkl} where the indices are either equal or, at most, nearest neighbors, as it was the
  case for t_{ij}.

  - The *direct terms* $V_{ij} := U_{ijji}$ with $i \neq j$: This contribution describes the essentially
    classical (electrostatic) interaction between two charges sitting at the lattice sites
    $\mathbf{R}_i$ and $\mathbf{R}_j$. It takes the form

    $$\sum_{\sigma\sigma'} \sum_{i \neq j} V_{ij} \hat{n}_{i\sigma} \hat{n}_{j\sigma'}, \tag{2.17}$$

    where $\hat{n}_{i\sigma} = \hat{c}_{i\sigma}^\dagger \hat{c}_{i\sigma}$ is the particle density at the lattice site i with spin σ. In certain
    materials such a density-density-type interaction gets rather strong and leads to
    instabilities in the charge distribution know as charge density waves [40].

- *exchange coupling contributions* U_{ijij} with $i \neq j$: One can express the corresponding contribution in the Hamiltonian in terms of spin and charge operators

$$\hat{\mathbf{S}}_i = \begin{pmatrix} \hat{c}_{i\uparrow}^\dagger & \hat{c}_{i\downarrow}^\dagger \end{pmatrix} \frac{1}{2} \boldsymbol{\sigma} \begin{pmatrix} \hat{c}_{i\uparrow} \\ \hat{c}_{i\downarrow} \end{pmatrix}, \qquad \hat{n}_i = \sum_\sigma \hat{n}_{i\sigma} = \sum_\sigma \hat{c}_{i\sigma}^\dagger \hat{c}_{i\sigma}, \qquad (2.18)$$

where $\boldsymbol{\sigma}$ denotes the vector of the three Pauli matrices $[\boldsymbol{\sigma} = (\sigma_x, \sigma_y, \sigma_z)]$. A straightforward calculation yields:

$$\sum_{\sigma\sigma'} \hat{c}_{i\sigma}^\dagger \hat{c}_{j\sigma'}^\dagger \hat{c}_{i\sigma'} \hat{c}_{j\sigma} = -2 \left(\hat{\mathbf{S}}_i \cdot \hat{\mathbf{S}}_j + \frac{1}{4} \hat{n}_i \hat{n}_j \right), \qquad (2.19)$$

and, with the definition $J_{ij}^F = U_{ijij}$, the term corresponding to U_{ijij} in Eq. (2.14) can be rewritten as

$$\sum_{i \neq j} \sum_{\sigma\sigma'} U_{ijij} \hat{c}_{i\sigma}^\dagger \hat{c}_{j\sigma'}^\dagger \hat{c}_{i\sigma'} \hat{c}_{j\sigma} = -2 \sum_{i \neq j} J_{ij}^F \left(\hat{\mathbf{S}}_i \cdot \hat{\mathbf{S}}_j + \frac{1}{4} \hat{n}_i \hat{n}_j \right). \qquad (2.20)$$

For $J_{ij}^F > 0$ ($J_{ij}^F < 0$) such a contribution induces a ferromagnetic (antiferromagnetic) coupling between neighbor spins, since a parallel alignment leads to a reduction of energy, as one can infer from Eq. (2.20). Hence, we observe that, an effective magnetic interaction can originate in a quite general way from the purely repulsive Coulomb repulsion.

- *Local interaction term* U_{iiii}: If the overlap between Wannier functions centered at neighboring sites is very small, V_{ij} and J_{ij}^F (as well as all other matrix elements U_{ijkl} with at least two different indices) are exponentially suppressed. In such a situation only the "on-site" part U_{iiii} of the Coulomb interaction, i.e., the so-called Hubbard interaction $U := 2U_{iiii}$ becomes the predominant interaction mechanism. Extracting the corresponding term from Eq. (2.14) leads to:

$$\sum_i \sum_{\sigma\sigma'} U_{iiii} \hat{c}_{i\sigma}^\dagger \hat{c}_{i\sigma'}^\dagger \hat{c}_{i\sigma'} \hat{c}_{i\sigma} = \sum_i U n_{i\uparrow} n_{i\downarrow}. \qquad (2.21)$$

Taking into account only the local interaction part of the Hamiltonian (2.14) and restricting oneself to the case of nearest neighbor hopping only, one arrives at the so-called **Hubbard model**:

$$\hat{\mathcal{H}}_{\text{Hubbard}} \equiv \hat{\mathcal{H}} = -t \sum_{\langle ij \rangle, \sigma} \hat{c}_{i\sigma}^\dagger \hat{c}_{j\sigma} + U \sum_i \hat{n}_{i\uparrow} \hat{n}_{i\downarrow} - \mu(\hat{n}_\uparrow + \hat{n}_\downarrow), \qquad (2.22)$$

where $\langle . \rangle$ denotes a summation over nearest neighbors.

This *single band Hubbard model* (an its generalizations to multi-orbital systems and/or more general hopping terms) is frequently used in solid state theory as the basic Hamiltonian to describe strongly correlated systems. The reason for this is that it already includes the two most important energy scales characterizing the physics of correlated electrons:

- The *kinetic energy* of the electrons which is given by the parameter t considering the electronic hopping processes from one site to its nearest neighbors.

- The *potential energy* of the electrons due to the strong local electrostatic repulsion, which originates from the Coulomb interaction between charged particles occupying the same (narrow) orbital and is parameterized by U in Eq. (2.22)].

Hence, we can see, that the two important contributions appearing in the original lattice model (1.1), namely the kinetic energy of an electron moving in the field generated by a periodic potential ($\hat{H}_0$) and the Coulomb repulsion between two electrons ($\hat{H}_I$) are –to some extent– captured by the corresponding contributions of the much simpler Hubbard model. Before going in to discuss the quantum field theory methods need for treating the Hubbard Hamiltonian, we recapitulate here the main approximations performed in our derivations:

- We restricted ourselves to only **one band** n_0 at the Fermi level, assuming that all the electrons in the other bands have energies far below or far above the Fermi energy. However, we should not forget that these neglected electrons still have interactions with the electrons in the target band at the Fermi level. Even though the effects of these interactions are small in many cases, they are in generally not negligible. In particular, it is not possible to calculate "ab-initio" the interaction parameter U for a given material just by applying the definition given in Eq. (2.16), since we are neglecting the electrons in all the bands aside from the target band at the Fermi level. These electrons, not explicitly present in the Hubbard model, screen the Coulomb interaction in the target band and, hence, lead to a modification (in general a reduction) of the Coulomb parameter with respect to the "bare" quantity calculated in Eq. (2.16). Since these screening effects are specific for each material and depend on the form of the bands below and above the Fermi level as well as on their separation from the target band one cannot construct the parameter U in general. While in the last years quite accurate methods (e.g., the constrained RPA, or its locally unscreened variant, see Refs. [21, 41]) for calculating U for the Hubbard model by partly including the screening effects, starting from ab-initio density functional calculations of a specific

compound, have been developed, in this thesis we will consider, generally, the Hubbard U as a merely phenomenological parameter.

- We restricted ourselves to the **purely local Coulomb interaction** U between two electrons at the same lattice site, neglecting all the other contributions originated from the full Coulomb interaction, some of which have been explicitly discussed previously in this section. While this approximation evidently considers the largest part of the Coulomb interaction, the other contributions may not be negligible in every situation [40]. This aspect will be, however, not explicitly considered in this thesis.

- We will almost always refer to rather localized situations, where we can restrict our hopping terms t_{ij} to **nearest neighbor hopping** t **only**. However, such restriction can be easily lifted by just including further hopping terms t' (next-nearest-neighbor hopping), t'' (next-next-nearest-neighbor-hopping), etc. to the model. While in several parts of the thesis we will stick to nearest-neighbor hopping only, we will also present results taking into account further hopping contributions, e.g., in Sec. 3.1.1.

Up to now we did not talk explicitly about the specific lattice we are considering. In principle, the above-mentioned approximations can be applied to all Bravais lattices in one, two or three dimensions. As we will mainly perform model calculations, we will restrict ourselves to the typical case of a simple cubic lattice in two or three dimension. Nevertheless, we want to stress that the methods described in this thesis can be applied to any general type of lattice symmetry.

Turning to the solution of the Hubbard model, it is important to recall, that despite its apparent simplicity, its Green's functions cannot be calculated exactly, neither analytically nor numerically. The difficulties originate from the following issues:

- An analytical solution is prevented by the fact the two parts of the Hamiltonian of Eq. (2.22) are diagonal in two different bases. The hopping term (t) is diagonal in momentum space [see Eq. (2.11)] as it is usually the case for the kinetic energy contribution to the Hamiltonian. On the other hand, the interaction term (U) is diagonal in real space, since the Hubbard interaction between two electrons is active only if both particles are located at the same lattice site i [see Eq. (2.21)]. From a more physical point of view, one can say that the first term of the Hubbard model tends evidently to *delocalize* the electrons, i.e., to make them itinerant, while the second contribution gives rise to a *localization* of the particles. Especially if t and U are of the same order
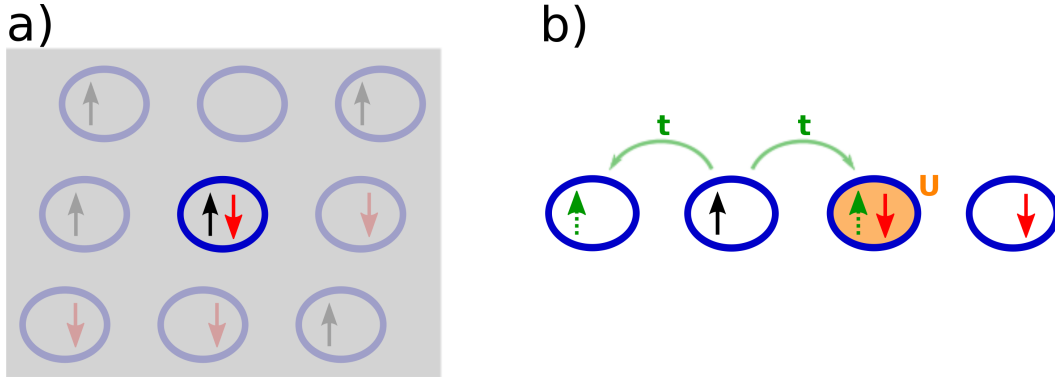
Figure 2.1: a) Local correlations at one lattice site; b) Non-local correlations due to a local interaction.

of magnitude this competition between itinerancy and localization has rendered hitherto an analytical solution of the Hamiltonian in Eq. (2.22) in arbitrary dimensions impossible.

- For a numerical solution of the system one has to restrict oneself to a finite lattice and represent the Hamiltonian as a matrix in a specific basis, e.g., the local basis where the interaction is diagonal. However, since one has four possible states $[\{|0\rangle, |\uparrow\rangle, |\downarrow\rangle, |\uparrow\downarrow\rangle\}$ corresponding to an unoccupied, singly occupied with an $\uparrow$- or $\downarrow$-electron or doubly occupied state] at each lattice site, the Hilbert space of the system grows as 4^N, where N is the number of lattice sites. Hence, even for a lattice with N = 1000 sites, which is rather small compared to the corresponding number in a realistic crystal (N $\sim 10^{23}$), the dimension of the Hilbert space is $\approx 10^{600}$ which makes a numerical solution evidently impossible. Therefore, one has to stick to rather small systems of (at best) 100 sites, the numerical solution of which suffers from (not always controllable) finite size effects.

The state of affairs discussed above calls for an approximation of the theoretical treatment of the Hubbard Hamiltonian, aiming at preserving its physical content as best as possible. A reasonable simplification for the Hubbard model can be found by analyzing the different "types" of correlations which occur in this system. (i) *Local correlations* describe the correlations between (two) electrons at the same lattice site while the rest of the lattice acts just as a "reservoir" where particles can be taken out or put in without any restrictions. This situation is illustrated in Fig. 2.1a: In order to single out the local correlations one assumes that the hopping of an electron from/to at least one of the sites in the gray shaded area to/from the site in the center is always possible, irrespective of the occupation of the neighboring sites. Hence, the fluctuations of the number and the spin of the electron(s) at

the lattice site in the center are only determined by the interaction between the particles at this site. Such local correlations are predominant in several physical cases and will be discussed in detail in Cap. 3. (ii) Despite the locality of the electron-electron interaction also *non-local correlations* can become important, as in the situation illustrated schematically in Fig. 2.1b. Whether an electron can hop unhindered away from the second site in this figure depends on the occupation of the neighboring sites. If this is already occupied, one has to pay an energy U if a second electron moves to this place which makes such an hopping process more unlikely compared to the transfer of the particle to an empty site (hopping to the left in Fig. 2.1b). It is obvious that such an effect becomes only important in the cases, where the number of nearest neighbors in the lattice is small, i.e., if for low-dimensional systems. Other situations where non-local correlations play a crucial role for the physics of the system and methods how to treat them are discussed in Cap. 4.

Neglecting non-local correlations at all might lead to reasonable simplifications for the Hubbard Hamiltonian in many situations. Hence, a corresponding model for the description of the local correlations in the lattice is presented in the next section.

2.1.2 The Anderson Impurity model (AIM)

The AIM describes a non-interacting bath of conduction electrons which hybridize with an interacting impurity. The corresponding Hamiltonian reads:

$$\hat{\mathcal{H}} = \sum_{\ell\sigma} \varepsilon_\ell \hat{a}^\dagger_{\ell\sigma} \hat{a}_{\ell\sigma} + \sum_{\ell\sigma} V_\ell (\hat{c}^\dagger_\sigma \hat{a}_{\ell\sigma} + \hat{a}^\dagger_{\ell\sigma} \hat{c}_\sigma) + U\hat{n}_\uparrow \hat{n}_\downarrow - \mu(\hat{n}_\uparrow + \hat{n}_\downarrow), \qquad (2.23)$$

where $\hat{a}^\dagger_{\ell\sigma}(\hat{a}_{\ell\sigma})$ creates (annihilates) an electron with spin σ at the bath-level of energy ε_ℓ, $\hat{c}^\dagger_\sigma(\hat{c}_\sigma)$ creates (annihilates) an electron at the impurity site $(\hat{n}_\sigma = \hat{c}^\dagger_\sigma \hat{c}_\sigma)$, V_ℓ parameterizes the hybridization between the bath and the impurity, and U is the on-site repulsion between two electrons at the impurity.

The AIM is analogous to a lattice model with only one interacting site embedded in a non-interacting electronic bath represented by the rest of the lattice [42]. In this respect the AIM is equivalent to Fig. 2.1a, and, hence, constitutes a crucial ingredient for the description of the purely local correlations in the lattice system. A method, whose implementation relies on this observation is the dynamical mean field theory (DMFT) which will be discussed in chapter 3.

The AIM has, however, its own physical importance [42]. It was originally introduced by P. W. Anderson [43] in order to describe local magnetic moments (represented by the impurity)

in metals (modeled by the non-interacting electron bath). In order to get a better under-
standing of the physical phenomena which are described by the AIM, we present a short
discussion of the physics of local moments in this section. However, the reader should keep
in mind that this topic is not in the scope of the present work, for which the AIM is used as
an auxiliary system for describing the purely local part of the correlations in the Hubbard
model.

Let us first focus on the case $U = \mu = 0$, i.e., the situation where a non-interacting impurity
hybridizes with a band ε_ℓ of conduction electrons. In the limit where the hybridization
vanishes, $V_\ell = 0$, the impurity density of states, $A(\omega)$ (which is, of course, independent
from the spin), is given by just a delta peak at the Fermi level ($\mu = 0$), i.e., $A(\omega) = \delta(\omega)$.
If we assume to start with one, e.g., $\uparrow$-electron at the impurity, this singly occupied state
exhibits an infinite lifetime, i.e., the system has a net magnetic moment. Switching on the
hybridization V_ℓ leads to a broadening of the peak as[2]:

$$A(\omega) = \frac{1}{\pi} \frac{\mathrm{Im}\Delta}{\omega^2 + [\mathrm{Im}\Delta]^2}, \tag{2.24}$$

where Δ denotes the hybridization function, which will be calculated explicitly in Sec. 2.2.7.1
[see Eq. (2.210)]. The localized magnetic state has now a finite life-time proportional to the
inverse of $\mathrm{Im}\Delta$. Hence, the magnetic moment will disappear for large enough values of this
quantity.

Let us now turn to the interacting AIM $U \neq 0$. Starting from the case of a *free impurity*
$V_\ell = 0$, i.e, from the so-called "atomic limit" where no hybridization of the impurity with the
bath exists (see also Sec. 2.2.7.2) , it is straightforward to obtain a criterion for the existence
of a local magnetic moment. In fact, in this situation one has to consider four possible states:
(i) The impurity is empty; (ii) and (iii) The impurity is occupied by one electron with spin
σ; (iv) The impurity is occupied by two electrons with opposite spins (double occupation).
According to the Hamiltonian in Eq. (2.23), the corresponding energies of these four states
are 0 for the empty impurity, $-\mu$ for the singly occupied impurity, and $U - 2\mu$ for double
occupation. The system exhibits a non-zero magnetic moment when a single electron with
spin σ resides at the impurity. Hence, in order to turn this singly occupied state into the

---

[2]Let us not that, in principle, for any non-interacting system one would *always* find a δ-like contribution to
the density of states for each *eigenstate* of the system. However, the a_ℓ and c do *not* represent an eigenbasis
of the Hamiltonian (2.23), and, hence, the corresponding density of states for the impurity is a Lorentzian
rather than a δ-like peak.

ground state of the system, one has to impose the following condition on the parameters:

$$0 \leq \mu \leq U. \tag{2.25}$$

For $\mu \ll 0$ the ground state is that with no electrons at the impurity, i.e., at low temperatures it is almost always empty, while for $\mu \gg U$ it is occupied by two electrons. These situations correspond both to non-magnetic ground states.

In a more general situation with $\Delta \neq 0$, such a non-magnetic ground state can be observed for $\mu \lesssim \Delta$ or $\mu \gtrsim U - \Delta$, i.e., if the empty or the doubly occupied state is near the Fermi surface. In the latter cases charge fluctuations become more important than spin fluctuations and the number of electrons at the impurity is not an integer number. The fluctuating magnetic moment disappears, it is dissolved in the in the metallic host and one speaks of an *intermediate valence* or *mixed valence* of the impurity atom.

On the contrary, for the formation of a local magnetic moment in the interacting AIM, one has to impose the following condition on its parameters:

$$0 \ll \mu \pm \Delta \ll U. \tag{2.26}$$

Within this condition, the impurity is almost always singly occupied and has a localized magnetic moment, although its orientation in obviously not fixed. In this regime, the charge fluctuations are suppressed and, hence, the AIM can be mapped onto the so-called Kondo model. This model describes the interaction of conduction electrons in a metallic host with the spin of the impurity site, with an antiferromagnetic Heisenberg coupling of the type $\mathcal{J}\left(\hat{\mathbf{S}} \cdot \hat{\mathbf{s}}_\ell\right)$, where $\hat{\mathbf{S}}$ represents the spin operator for the localized state at the impurity and $\hat{\mathbf{s}}_\ell$ is the spin operator of the conduction electrons. Historically, the Kondo Hamiltonian was first used by J. Kondo in order to explain the minimum occurring in the electrical resistivity as a function of temperature in a metal with magnetic impurities [42].

2.2 Green's functions and Symmetries

In this section we introduce the formalism for the one- and the two-particle Green's functions for the models described in the previous section 2.1 and discuss some of their general properties. As already said, the knowledge of these Green's functions allows for the calculation of physical, (e.g., spectral, mechanical, thermodynamical,etc.) properties of the system under consideration. Specifically, from *one-particle* Green's function of a lattice model, one can

extract the spectral function $A(\omega, \mathbf{k})$, which is directly measured in (angle resolved) photo-emission spectroscopy (ARPES) experiments. It corresponds to the spectrum of one-particle excitations in the system under considerations and can also describe the renormalization of specific physical properties, such as the electronic mass, due to the interaction between the particles. More generally, the knowledge of the one-particle Green's function is sufficient for the calculation of the expectation value of any one-particle observable, such as the density or the spin, of the correlated system.

As a matter of fact, also *two-particle* Green's functions contain quite valuable information. They allow for calculating the linear response of the system to a small external perturbation such as, e.g., an electric field [optical conductivity $\sigma(\omega))$], a magnetic field [spin susceptibility $\chi_s(\omega, \mathbf{q})$], pressure (compressibility), etc. In particular, we will consider the *local* two-particle Green's functions (i.e., those for the AIM), because they do not only allow for the calculation of the local response functions, but are a crucial ingredient for any two-particle analysis in the DMFT framework. More specifically, they are a necessary input for calculating frequency- and momentum-dependent response functions in the framework of DMFT, as we will see in Cap. 3. Furthermore, the local vertex functions, which can be extracted from the local two-particle Green's functions, constitute the basic brick for the different diagrammatic extensions of the dynamical mean field theory aiming at the inclusion of nonlocal correlations beyond DMFT. Such nonlocal correlations are important, e.g., for describing a system close to a second order phase-transition as it will be discussed Cap. 4.

Despite its importance, a thorough and systematic analysis of the local two-particle Green's functions has been addressed only sporadically in the textbooks [38, 44] and the previous literature [45–47]. Hence, mostly following the detailed analysis of our recent work [48], we will present a systematic analysis of n-particle Green's functions and their general properties (symmetries) in the framework of a unifying derivation and formalism, with a special focus on the one- and the two-particle cases. This will provide for a deeper understanding of the general structure and, as a consequence, also the physical content of the Green's functions. Furthermore, we will show how the symmetries of the system lead to a reduction of the complexity or, more precisely, to a decrease of the number of arguments of the Green's functions. Such simplification is obviously of crucial importance for all numerical algorithms, especially those performed at the two-particle level, since the corresponding numerical effort pushes the actual computer and memory resources to its limit. Finally, the symmetries of the system also often serve as a consistency check for Green's functions calculated by means of approximated methods, and, hence, provide a test for these approximations.

We can start from the definition of the n-particle Green's function already given in Eq. (2.3),

and here reported, for convenience, in its most general form:

$$
\begin{aligned}
G_{n,i_1\ldots i_{2n}}(\tau_1,\ldots,\tau_{2n}) &= \left\langle \mathrm{T}\left[\hat{c}^\dagger_{i_1}(\tau_1)\hat{c}_{i_2}(\tau_2)\ldots\hat{c}^\dagger_{i_{2n-1}}(\tau_{2n-1})\hat{c}_{i_{2n}}(\tau_{2n})\right]\right\rangle = \\
&= \frac{1}{Z}\mathrm{Tr}\left(e^{-\beta\hat{\mathcal{H}}}\mathrm{T}\left[\hat{c}^\dagger_{i_1}(\tau_1)\hat{c}_{i_2}(\tau_2)\ldots\hat{c}^\dagger_{i_{2n-1}}(\tau_{2n-1})\hat{c}_{i_{2n}}(\tau_{2n})\right]\right),
\end{aligned}
\tag{2.27}
$$

where

$$
Z = \mathrm{Tr}\left(e^{-\beta\hat{\mathcal{H}}}\right) \quad \text{and} \quad \hat{c}^{(\dagger)}_{i_j}(\tau) = e^{\tau\hat{\mathcal{H}}}\hat{c}^{(\dagger)}_{i_j}e^{-\tau\hat{\mathcal{H}}}.
\tag{2.28}
$$

analogously to Eqs. (2.3), (2.4) and (2.5) for the solid state Hamiltonian (2.2). T is the time-ordering operator which in the case of fermions has the property:

$$
T\left[\hat{c}^{(\dagger)}_{i_j}(\tau_j)\hat{c}^{(\dagger)}_{i_k}(\tau_k)\right] = \hat{c}^{(\dagger)}_{i_j}(\tau_j)\hat{c}^{(\dagger)}_{i_k}(\tau_k)\theta(\tau_j-\tau_k) - \hat{c}^{(\dagger)}_{i_k}(\tau_k)\hat{c}^{(\dagger)}_{i_j}(\tau_j)\theta(\tau_k-\tau_j).
\tag{2.29}
$$

That means T sorts the $2n$ fermionic creation and annihilation operators according to their imaginary time argument (starting with the largest on the left-hand side) and attributes a minus sign to contributions, which constitute an odd permutation of the original sequence of the operators given in the definition of the Green's function in Eq. (2.27). The indices i_j represent the set of all degrees of freedom of the system such as space coordinate/lattice site/momentum, orbital, spin, etc., i.e., $i_j\widehat{=}(\mathbf{r}_j/\mathbf{R}_j/\mathbf{k}_j, l_j, \sigma_j, \ldots)$. For instance, specializing $i_j\widehat{=}(\mathbf{r}_j, \sigma_j)$ [or $i_j\widehat{=}(\mathbf{k}_j, \sigma_j)$ after a Fourier transform] one recovers the specific definition of the n-particle Green's function for the solid state Hamiltonian as given in Eq. (2.3). For the Hubbard model i_j has to be chosen as $i_j\widehat{=}(\mathbf{R}_j, \sigma_j)$ [or $i_j\widehat{=}(\mathbf{k}_j, \sigma_j)$ after a Fourier transform] while for the AIM we are typically only interested in the Green's function for the correlated impurity site (in which case all operators $\hat{c}^{(\dagger)}_{i_j}$ refer to the impurity site), $i_j\widehat{=}\sigma_j$.

2.2.1 General properties of the Green's functions

In this section we recapitulate very basic and general properties for the n-particle Green's functions of a system of interacting fermions, which are not based on any specific symmetry of the underlying model. The boundary conditions discussed in Sec. 2.2.1.1 follow mainly from the cyclic property of the trace appearing in the definition of the Green's functions [Eq. (2.27)], while the crossing symmetry discussed in Sec. 2.2.1.2 is a consequence of the indistinguishability of identical fermionic particles. Finally, we will shortly analyze the behavior of the Green's functions under the operation of complex conjugation in Sec. 2.2.1.3.

2.2.1.1   Boundary conditions

We recall here the boundary conditions for the n-particle Green's functions with respect to their imaginary-time arguments: In contrast to the case of real times, one has to restrict the domain of definition for the imaginary times τ_i in the n-particle Green's function, Eq. (2.27), to a certain interval, the size of which is determined by the inverse temperature β. This can be easily seen when explicitly performing the trace in Eq. (2.27) by summing over a complete Eigenbasis $|n\rangle$ of the Hamiltonian $\hat{\mathcal{H}}$. Assuming without loss of generality (w.l.o.g.) that τ_1 is the largest and τ_{2n} is the smallest imaginary time argument of the n-particle Green's functions one gets the so-called Lehmann representation [38]:

$$G_{n,i_1\ldots i_{2n}}(\tau_1,\ldots,\tau_{2n}) = \frac{1}{Z}\sum_m e^{-(\beta+\tau_{2n}-\tau_1)E_m}\langle m|\hat{c}_{i_1}^\dagger e^{-\tau_1\hat{\mathcal{H}}}\ldots e^{\tau_{2n}\hat{\mathcal{H}}}\hat{c}_{i_{2n}}|m\rangle, \qquad (2.30)$$

where E_m is the m-th eigenvalue of the Hamiltonian $\hat{\mathcal{H}}$ and $|m\rangle$ the corresponding eigenstate. For an infinitely large system the number of states $|m\rangle$ is also infinite and the spectrum of $\hat{\mathcal{H}}$ is unbounded, i.e., the eigenenergies E_m become arbitrarily large. Hence, in order to make the (infinite) sum over m in Eq. (2.30) converging, one has to ensure that the contribution $e^{-(\beta+\tau_{2n}-\tau_1)E_m}$ leads to an exponential suppression of the corresponding matrix-element in the sum rather than an (exponential) enhancement. This requires that

$$\beta + \tau_{2n} - \tau_1 > 0. \qquad (2.31)$$

Taking into account that τ_1 was assumed to be the largest and τ_{2n} the smallest imaginary time argument of the n-particle Green's function, one obtains

$$\tau_{2n} + \beta > \tau_1 > \ldots > \tau_i \ldots > \tau_{2n}, \qquad (2.32)$$

i.e., all time arguments have to be located within an interval of the length β. Fig. 2.2 illustrates this state of affairs exemplarily for the one-particle Green's function $G_{1,i_1i_2}(\tau_1,\tau_2)$ where the gray shaded area between the two solid diagonal lines represents the domain of definition for $G_{1,i_1i_2}(\tau_1,\tau_2)$ in the (τ_1,τ_2) plane.

Further restrictions (or, more precisely, simplifications) for the n-particle Green's functions can be achieved by considering the cyclic property of the trace, appearing in Eq. (2.27). Assuming again that τ_1 is the largest and τ_{2n} the smallest imaginary time argument and using
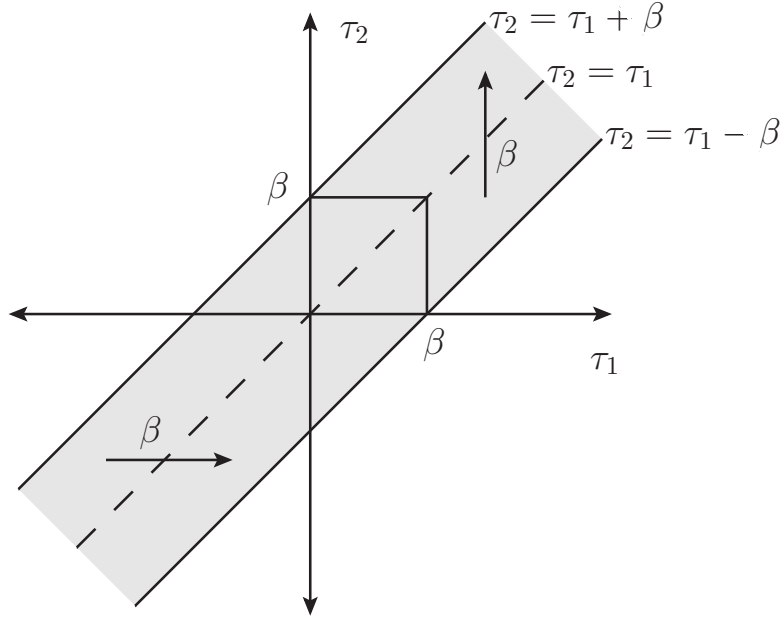
Figure 2.2: Domain of definition for $G_{1,i_1 i_2}(\tau_1, \tau_2)$. The figure is readapted from Ref. [48].

definition (2.28) for the time-dependent creation and annihilation operators one obtains:

$$\mathrm{Tr}\left[e^{-\beta\hat{\mathcal{H}}}e^{\tau_1\hat{\mathcal{H}}}\hat{c}_{i_1}^{\dagger}e^{-\tau_1\hat{\mathcal{H}}}\hat{c}_{i_2}(\tau_2)\ldots\hat{c}_{i_{2n-1}}^{\dagger}(\tau_{2n-1})e^{\tau_{2n}\hat{\mathcal{H}}}\hat{c}_{i_{2n}}e^{-\tau_{2n}\hat{\mathcal{H}}}\right]=$$

$$=\mathrm{Tr}\left[e^{-\beta\hat{\mathcal{H}}}\hat{c}_{i_2}(\tau_2)\ldots\hat{c}_{i_{2n-1}}^{\dagger}(\tau_{2n-1})e^{\tau_{2n}\hat{\mathcal{H}}}\hat{c}_{i_{2n}}e^{-\tau_{2n}\hat{\mathcal{H}}}e^{(\tau_1-\beta)\hat{\mathcal{H}}}\hat{c}_{i_1}^{\dagger}e^{-(\tau_1-\beta)\hat{\mathcal{H}}}\right]= \qquad (2.33)$$

$$=\mathrm{Tr}\left[e^{-\beta\hat{\mathcal{H}}}e^{(\tau_{2n}+\beta)\hat{\mathcal{H}}}\hat{c}_{i_{2n}}e^{-(\tau_{2n}+\beta)\hat{\mathcal{H}}}e^{\tau_1\hat{\mathcal{H}}}\hat{c}_{i_1}^{\dagger}e^{-\tau_1\hat{\mathcal{H}}}\hat{c}_{i_2}(\tau_2)\ldots\hat{c}_{i_{2n-1}}^{\dagger}(\tau_{2n-1})\right].$$

One the other hand, the very same term as in the second [third] line of Eq. (2.33) appears also in the definition of the time-ordered product in Eq. (2.27), when one performs the transformation $\tau_1 \to \tau_1 - \beta$ $[\tau_{2n} \to \tau_{2n} + \beta]$. However, one gets a different sign compared to Eq. (2.33), since the transfer of the operator $\hat{c}_{i_1}^{\dagger}(\tau_1)$ $[\hat{c}_{i_{2n}}(\tau_{2n})]$ from the first [last] to the last [first] position of the trace involves $2n-1$, i.e., an odd number, of commutations of fermionic operators. Hence, one obtains the following identities for the n-particle Green's function, known as the Kubo-Martin-Schwinger (KMS) boundary conditions [49, 50]:

$$G_{n,i_1\ldots i_{2n}}(\tau_1, \ldots, \tau_{2n}) = -G_{n,i_1\ldots i_{2n}}(\tau_1 - \beta, \ldots, \tau_{2n}) \qquad (2.34a)$$

$$G_{n,i_1\ldots i_{2n}}(\tau_1, \ldots, \tau_{2n}) = -G_{n,i_1\ldots i_{2n}}(\tau_1, \ldots, \tau_{2n} + \beta). \qquad (2.34b)$$

Note that these relations only holds if τ_1 $[\tau_{2n}]$ is the largest [smallest] time argument. Otherwise, the transformation $\tau_1 \to \tau_1 - \beta$ $[\tau_{2n} \to \tau_{2n} + \beta]$ would lead to a set of imaginary

times $\tau_1, \ldots, \tau_{2n}$ which does not fulfill the necessary condition (2.32) and, hence, is not located within the domain of definition of the n-particle Green's function. The horizontal and the vertical arrows, respectively, in Fig. 2.2 illustrate such allowed transformations of the imaginary time arguments for the one-particle Green's function (the transformation should not lead to a (τ_1, τ_2)-point outside the gray-shaded stripe).

By implication of Eqs. (2.34) all imaginary time arguments can be restricted to the interval $[0, \beta]$. Indeed, the value of G_n for all other combinations of time arguments [that are allowed according to Eq. (2.32)] can be constructed by repeated application of Eq. (2.34a) [Eq. (2.34b)] for the respectively largest [smallest] time argument. Eventually, the anti-periodicity condition Eq. (2.34) allows us to express the n-particle Green's function as Fourier expansion:

$$G_{n, i_1 \ldots i_{2n}}(\tau_1, \ldots, \tau_{2n}) = \frac{1}{\beta^{2n}} \sum_{\{\nu_i\}} e^{i(\nu_1 \tau_1 + \ldots - \nu_{2n} \tau_{2n})} \widetilde{G}_{n, i_1 \ldots i_{2n}}(\nu_1, \ldots, \nu_{2n}), \tag{2.35a}$$

$$\widetilde{G}_{n, i_1 \ldots i_{2n}}(\nu_1, \ldots, \nu_{2n}) = \int_0^\beta d\tau_1 \ldots \int_0^\beta d\tau_{2n} \, e^{-i(\nu_1 \tau_1 + \ldots - \nu_{2n} \tau_{2n})} G_{n, i_1 \ldots i_{2n}}(\tau_1, \ldots, \tau_{2n}), \tag{2.35b}$$

where $\nu_i = \frac{\pi}{\beta}(2n_i + 1)$ are fermionic Matsubara frequencies. Note that the (discrete) Fourier representation Eq. (2.35a) extends the n-particle Green's functions "antiperiodically" from the regime defined by Eq. (2.32) to the entire τ-space, i.e., to the $\mathbb{R}^{2n}$, circumventing any restrictions as imposed by Eq. (2.32)[3].

2.2.1.2 Crossing symmetry

The crossing symmetry is a manifestation of the Fermi-Dirac statistics, and, hence, of the Pauli principle, for indistinguishable fermions. Therefore, strictly speaking, the designation of this property as "symmetry" is in some sense misleading, since it is not connected to the invariance of the Hamiltonian with regard to any (unitary) transformation. Its origin is rather founded in the time-ordering of the creation and annihilation fermionic operators in Eq. (2.27). According to the definition of the time-ordered product in Eq. (2.29), the order of the fermionic operators chosen for the definition of the Green's function plays no role, *except* for an overall sign. Specifically, exchanging two creation or annihilation operators within the time-ordered product in Eq. (2.27) does not change the Green's function except

---

[3]This, of course, would not have been the only choice. One could, e.g., put G_n to 0 for all combinations of τ_i not fulfilling condition (2.32).

for an additional minus sign:

$$G_{n,i_1...i_j...i_k...i_{2n}}(\tau_1,...,\tau_j,...,\tau_k,...\tau_{2n}) = -G_{n,i_1...i_k...i_j...i_{2n}}(\tau_1,...,\tau_k,...,\tau_j,...\tau_{2n}). \quad (2.36)$$

We want to stress that the numbers j and k, indicating the position of the corresponding operators in the trace, must have the same parity, i.e., both have to be even or odd integer numbers. The latter case corresponds to an exchange of two $\hat{c}^\dagger$ operators, i.e., to exchanging two outgoing electrons, while the first possibility represents the commutation of two $\hat{c}$ operators, i.e., the permutation of two incoming electrons. A different parity of j and k would correspond to exchanging a creation with an annihilation operator, leading to a sequence of such operators, which is not captured by the definition of G_n in Eq. $(2.27)^4$. Hence, such permutations are not applicable for the formulation of the crossing symmetry. As an obvious corollary, there is no crossing relation for the one-particle Green's function, while for the two-particle case one obtains:

$$G_{2,i_1i_2i_3i_4}(\tau_1,\tau_2,\tau_3,\tau_4) =$$
$$= -G_{2,i_3i_2i_1i_4}(\tau_3,\tau_2,\tau_1,\tau_4) = -G_{2,i_1i_4i_3i_2}(\tau_1,\tau_4,\tau_3,\tau_2) = G_{2,i_3i_4i_1i_2}(\tau_3,\tau_4,\tau_1,\tau_2),$$
$$(2.37)$$

which allows for important simplifications when working with two-particle Green's functions. Let us finally note that relations analogous to Eqs. (2.36) and (2.37) can be obviously also formulated in Fourier space [see Eq. (2.35b)].

2.2.1.3 Complex conjugation

For the complex conjugation of the n-particle Green's function we consider the general relation $\langle m|A_1...A_n|m\rangle^* = \langle m|A_n^\dagger...A_1^\dagger|m\rangle$ for the complex conjugation of a matrix element of a product of operators and apply it to the definition of the Green's function in Eq. (2.27). This straightforwardly leads to the identity:

$$G^*_{n,i_1...i_{2n}}(\tau_1,...,\tau_{2n}) = G_{n,i_{2n}...i_1}(-\tau_{2n},...,-\tau_1), \quad (2.38)$$

---

[4] Remember that the creation and annihilation operators in the definition of the n-particle Green's function have to appear in alternating order where the first one is a creation operator. An exchange of a creation with an annihilation operator would lead to a sequence which is not conform with this requirement and, hence, does not match the definition of the n-particle Green's function in Eq. (2.27).

where we again used the cyclic property of the trace. Performing a Fourier transform of Eq. (2.38) yields

$$G^*_{n,i_1\ldots i_{2n}}(\nu_1,\ldots,\nu_{2n}) = G_{n,i_{2n}\ldots i_1}(-\nu_{2n},\ldots,-\nu_1), \tag{2.39}$$

providing an additional useful exact (and general) relation for the n-particle Green's function.

2.2.2   Symmetries

In this section we will analyze the impact of symmetries of the system on the Green's functions. Though the main focus here and in the following chapters is on the Hubbard model and the AIM, most of the results reported in this section hold also in more general situations, e.g., for the full solid state Hamiltonian (2.2). As already discussed, in the AIM the interesting information is provided by the (local) impurity Green's functions, i.e., the operators $\hat{c}^{(\dagger)}$ in definition (2.27) correspond exclusively to creation and annihilation operators for electrons at the impurity site, while for the Hubbard model one has to calculate in principle Green's functions among different sites. Hence, for the two models under consideration the general index i_j, introduced at the beginning of Sec. 2.2 will correspond to the following two sets of quantum numbers, respectively:

- AIM: $i_j \widehat{=} \sigma_j$,

- Hubbard model: $i_j \widehat{=} (\mathbf{R}_j, \sigma_j)$ or $i_j \widehat{=} (\mathbf{k}_j, \sigma_j)$,

where $\mathbf{R}_j$ denotes a lattice vector and $\mathbf{k}_j$ is a momentum vector located in the first Brillouin zone.

From a formal point of view the main difference between the two models are the spatial degrees of freedom (lattice site $\mathbf{R}_i$ and momentum $\mathbf{k}$, respectively) present in the (translational invariant) Hubbard model, but missing in the AIM. On the other hand, due to the same (spatially local) nature of the electronic interaction, both models share significant similarities with respect to symmetries concerning their time- and spin-degrees of freedom. Hence, in order to avoid redundancy by presenting almost equivalent derivations for both models, we perform most of the calculations for the local AIM only, i.e., we consider $i_j \widehat{=} \sigma_j$, for the general index i_j in Eq. (2.27). The Hubbard model will be treated explicitly exclusively in situations where a symmetry directly concerns the spatial degrees of freedom, as it is the case, e.g., for the lattice translational invariance, the point group symmetry of the lattice, or the space inversion symmetry.

Let us now discuss the general method which will be used for analyzing most of the symmetry properties of the n-particle Green's functions. For this purpose, it proves convenient to adopt

an (admittedly) unusual notation where G_n is (re)defined as an explicit "function" of the creation and annihilation operators *and* the Hamiltonian, i.e.,

$$
\begin{aligned}
G_n(\hat{c}^\dagger, \hat{c}, \hat{\mathcal{H}}) :=& G_{n,i_1\ldots i_{2n}}(\tau_1,\ldots,\tau_{2n}) = \\
=& \left\langle \mathrm{T}\left[\hat{c}^\dagger_{i_1}(\tau_1)\hat{c}_{i_2}(\tau_2)\ldots\hat{c}^\dagger_{i_{2n-1}}(\tau_{2n-1})\hat{c}_{i_{2n}}(\tau_{2n})\right]\right\rangle.
\end{aligned}
\tag{2.40}
$$

Note that, for the sake of a better readability, we use the same symbol G_n for this new expression. In the next step we consider a similarity transformation, represented by an invertible operator $\hat{\mathcal{U}}$ (e.g., the spin rotation operator), which transforms the creation and annihilation operators according to [51]:

$$
\hat{c}'^\dagger_{i_j} = \hat{\mathcal{U}}^{-1}\hat{c}^\dagger_{i_j}\hat{\mathcal{U}} \qquad\qquad \hat{c}'_{i_j} = \hat{\mathcal{U}}^{-1}\hat{c}_{i_j}\hat{\mathcal{U}}.
\tag{2.41}
$$

We can then define the "transformed" Green's function G'_n, i.e., the Green's function written in terms of the transformed fermionic operators [$c'^\dagger, c'$ instead of $c^\dagger, c$ in Eq. (2.40)], as:

$$
\begin{aligned}
G'_{n,i_1\ldots i_{2n}}(\tau_1,\ldots,\tau_{2n}) :=& G_n(\hat{c}'^\dagger, \hat{c}', \hat{\mathcal{H}}) = \\
=& \left\langle \mathrm{T}\left[\hat{c}'^\dagger_{i_1}(\tau_1)\hat{c}'_{i_2}(\tau_2)\ldots\hat{c}'^\dagger_{i_{2n-1}}(\tau_{2n-1})\hat{c}'_{i_{2n}}(\tau_{2n})\right]\right\rangle.
\end{aligned}
\tag{2.42}
$$

Physically G'_n corresponds to the Green's function G_n transformed with the active (similarity) transformation $\hat{\mathcal{U}}$. Considering that

$$
\hat{c}'^{(\dagger)}_{i_j}(\tau) = e^{\tau\hat{\mathcal{H}}}\hat{c}'^{(\dagger)}_{i_j}e^{-\tau\hat{\mathcal{H}}},
\tag{2.43}
$$

the transformed Green's function can be written schematically as

$$
G'_{n,i_1\ldots i_{2n}}(\tau_1,\ldots,\tau_{2n}) = \left\langle \ldots e^{\tau_j\hat{\mathcal{H}}}\ \underbrace{\hat{\mathcal{U}}^{-1}\hat{c}^{(\dagger)}_{i_j}\hat{\mathcal{U}}}_{\hat{c}'^{(\dagger)}_{i_j}}\ e^{-\tau_j\hat{\mathcal{H}}}e^{\tau_k\hat{\mathcal{H}}}\ \underbrace{\hat{\mathcal{U}}^{-1}\hat{c}^{(\dagger)}_{i_k}\hat{\mathcal{U}}}_{\hat{c}'^{(\dagger)}_{i_k}}\ e^{-\tau_k\hat{\mathcal{H}}}\ldots\right\rangle.
\tag{2.44}
$$

According to the associative law one can interpret this matrix element also in a different way:

$$
G'_{n,i_1\ldots i_{2n}}(\tau_1,\ldots,\tau_{2n}) = \left\langle \ldots e^{\tau_j\hat{\mathcal{H}}}\hat{\mathcal{U}}^{-1}\hat{c}^{(\dagger)}_{i_j}\ \overbrace{\hat{\mathcal{U}}e^{-\tau_j\hat{\mathcal{H}}}e^{\tau_k\hat{\mathcal{H}}}\hat{\mathcal{U}}^{-1}}^{e^{-\tau_j\hat{\mathcal{H}}'}e^{\tau_k\hat{\mathcal{H}}'}}\ \hat{c}^{(\dagger)}_{i_k}\hat{\mathcal{U}}\ e^{-\tau_k\hat{\mathcal{H}}}\ldots\right\rangle,
\tag{2.45}
$$

where $\hat{\mathcal{H}}'$ is defined as:

$$
\hat{\mathcal{H}}' = \hat{\mathcal{U}}\hat{\mathcal{H}}\hat{\mathcal{U}}^{-1}.
\tag{2.46}
$$

a)

b)
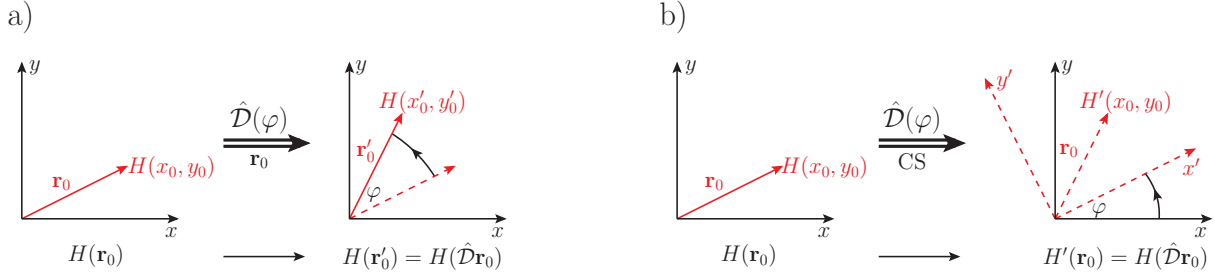
Figure 2.3: a) illustrates the change of the value of H under an (active) rotation of its argument, i.e., the coordinate vector $\mathbf{r}_0$. (b) After rotating the frame of reference (together with the vector $\mathbf{r}_0$!) the system is described by the Hamiltonian function H' instead of H. Evaluating this new function for the original coordinate vector $\mathbf{r}_0$ yields the same result as the evaluation of H for the rotated vector $\mathbf{r}_0'$ in a). Note that the coordinates of the vector $\mathbf{r}_0$ in the last panel are the same as in the first one. However, in the last panel they are given with respect to the rotated frame of reference.

This holds for left- and the rightmost operators inside the matrix element as well, due to the cyclic property of the trace:

$$\left\langle e^{-\beta\hat{\mathcal{H}}}e^{\tau_1\hat{\mathcal{H}}} \underbrace{\hat{\mathcal{U}}^{-1}\hat{c}_{i_1}^\dagger\hat{\mathcal{U}}}\ldots\underbrace{\hat{\mathcal{U}}^{-1}\hat{c}_{i_{2n}}\hat{\mathcal{U}}} e^{-\tau_{2n}\hat{\mathcal{H}}} \right\rangle = \left\langle \overbrace{\hat{\mathcal{U}}e^{-\tau_{2n}\hat{\mathcal{H}}}e^{-\beta\hat{\mathcal{H}}}e^{\tau_1\hat{\mathcal{H}}}\hat{\mathcal{U}}^{-1}} \hat{c}_{i_1}^\dagger\hat{\mathcal{U}}\ldots\hat{\mathcal{U}}^{-1}\hat{c}_{i_{2n}} \right\rangle, \tag{2.47}$$

where we assumed w.l.o.g. that τ_1 is the largest and τ_{2n} is the smallest time argument. The above considerations can be more concisely expressed, eventually, by means of the following relation[5]:

$$G_n(\hat{c}'^\dagger, \hat{c}', \hat{\mathcal{H}}) = G_n(\hat{c}^\dagger, \hat{c}, \hat{\mathcal{H}}'). \tag{2.48}$$

This equation has a simple interpretation (consider, e.g., a spin rotation for $\hat{\mathcal{U}}$): The left-hand side describes the Green's function for creation and annihilation operators which are transformed with an *active* transformation $\hat{\mathcal{U}}$, but expressed in the *old* reference system (see example below). The right-hand side represents the same transformation but for the reference system which means that now the Hamiltonian has to be transformed with the corresponding *passive* (or inverse) transformation. In this sense Eq. (2.48) is just an expression of the obvious fact that the description of similarity transformations in terms of active and passive ones must coincide.

Let us illustrate the arguments discussed in the last paragraph for a simple classical model defined in $\mathbb{R}^2$ by the Hamiltonian function $H(\mathbf{r})$, $\mathbf{r} \in \mathbb{R}^2$. As similarity transformation we

---

[5]We recall that the partition function Z is invariant under any similarity transformation of the Hamiltonian due to the cyclic property of the trace.

consider rotations $\hat{\mathcal{U}} = \hat{\mathcal{D}}(\varphi)$ about the z axis through an angle φ. In Fig. 2.3a we *actively* rotate the vector $\mathbf{r}_0$ onto a new vector $\mathbf{r}_0' = \hat{\mathcal{D}}\mathbf{r}_0$. Hence, the value of the Hamiltonian function H changes from $H(\mathbf{r}_0)$ to $H(\mathbf{r}_0')$ when transforming the vector $\mathbf{r}_0$, which corresponds to the active transformation of the operators $\hat{c}$ and $\hat{c}^\dagger$ discussed above [see Eq. (2.41)]. On the other hand, one can rotate the coordinate system (CS) through the angle φ as it is illustrated in Fig. 2.3b. The coordinates of a point with respect to the original coordinate system can be obtained from the coordinates of the same physical point with respect to the new reference system by means of the transformation $\hat{\mathcal{D}}$, i.e., $\mathbf{r} = \hat{\mathcal{D}}\mathbf{r}'$. Therefore, the Hamiltonian in the rotated frame of reference is given by $H' = H \circ \hat{\mathcal{D}}$. Inserting now the *original* coordinate vector $\mathbf{r}_0$ into the new function H', as it is illustrated in Fig. 2.3b, one retains the same result as for the direct transformation of the vector $\mathbf{r}_0$, i.e., $H'(\mathbf{r}_0) = H(\hat{\mathcal{D}}\mathbf{r}_0)$.

Coming back to our specific purpose, we recall that $\hat{\mathcal{U}}$ can be coined a *symmetry* of the system if it commutes with $\hat{\mathcal{H}}$, and, hence, the transformed Hamiltonian is equal to the original one:

$$[\hat{\mathcal{U}}, \qquad \hat{\mathcal{H}}] = 0 \qquad \Longrightarrow \qquad \hat{\mathcal{H}}' = \hat{\mathcal{H}}. \qquad (2.49)$$

Therefore, according to Eq. (2.48), in this case the transformed Green's function G_n' will coincide with the original one:

$$G'_{n,i_1\ldots i_{2n}}(\tau_1, \ldots, \tau_{2n}) = G_{n,i_1\ldots i_{2n}}(\tau_1, \ldots, \tau_{2n}). \qquad (2.50)$$

This equation constitutes the basis for deriving formally all symmetry properties of the Green's functions, which will be discussed in the following subsections.

2.2.2.1 Time and Space translation symmetry

If the Hamiltonian $\hat{\mathcal{H}}$ is time-independent (as it is the case for both the Hubbard model and the AIM) the Green's functions do not depend explicitly on the $2n$ times $\tau_1 \ldots \tau_{2n}$ but only on time differences, e.g., of the form $\tau_i - \tau_{2n}$. For proving this statement, we consider the time translational operator $\hat{\mathcal{T}}_\tau$ for the similarity transformation $\hat{\mathcal{U}}$ discussed above [see, e.g., Eq. (2.41)]:

$$\hat{\mathcal{U}} = \hat{\mathcal{T}}_\tau := e^{-\tau\hat{\mathcal{H}}}. \qquad (2.51)$$

The corresponding transformed creation and annihilation operators [see Eq. (2.41)] are given by

$$\hat{c}_\sigma'^\dagger(\tau) = e^{\tau\hat{\mathcal{H}}}\hat{c}_\sigma^\dagger e^{-\tau\hat{\mathcal{H}}} \qquad\qquad \hat{c}_\sigma'(\tau) = e^{\tau\hat{\mathcal{H}}}\hat{c}_\sigma e^{-\tau\hat{\mathcal{H}}}. \tag{2.52}$$

For the specific choice $\tau = -\tau_{2n}$ the transformed Green's function, i.e., the Green's function for the transformed operators as given in Eq. (2.42), reads

$$G'_{n,\sigma_1...\sigma_{2n}}(\tau_1, \ldots, \tau_{2n}) = \left\langle e^{-\beta\hat{\mathcal{H}}} e^{(\tau_1-\tau_{2n})\hat{\mathcal{H}}} \hat{c}_{\sigma_1}^\dagger\, e^{-(\tau_1-\tau_{2n})\hat{\mathcal{H}}}\, e^{(\tau_2-\tau_{2n})\hat{\mathcal{H}}} \hat{c}_{\sigma_2} e^{-(\tau_2-\tau_{2n})\hat{\mathcal{H}}} \cdots \right.$$
$$\left. \cdots e^{(\tau_{2n-1}-\tau_{2n})\hat{\mathcal{H}}} \hat{c}_{\sigma_{2n-1}}^\dagger e^{-(\tau_{2n-1}-\tau_{2n})\hat{\mathcal{H}}} \hat{c}_{\sigma_{2n}} \right\rangle, \tag{2.53}$$

where we assume w.l.o.g. that $\tau_1 > \tau_2 > \ldots > \tau_{2n-1} > \tau_{2n}$. Since the time translation operator $\hat{\mathcal{T}}_\tau$ commutes with our (time-independent) Hamiltonian and, hence, can be classified as a "symmetry" of the system, the transformed Green's function must coincide with the original one [see Eq. (2.50)]. This observation can be expressed by the following equation:

$$G_{n,\sigma_1...\sigma_{2n}}(\tau_1, .., \tau_{2n}) = G_{n,\sigma_1...\sigma_{2n}}(\tau_1 - \tau_{2n}, .., \tau_{2n-1} - \tau_{2n}, 0). \tag{2.54}$$

Together with the antiperiodicity of G_n [Eqs. (2.34)], the time translational invariance [Eq. (2.54)] leads to a useful simplification of the Fourier transform of G_n [see Eq. (2.35b)]:

$$\widetilde{G}_{n,\sigma_1...\sigma_{2n}}(\nu_1, \ldots, \nu_{2n}) = \int_0^\beta d\tau_1 \ldots \int_0^\beta d\tau_{2n}\, e^{-i(\nu_1\tau_1+...-\nu_{2n}\tau_{2n})} G_{n,\sigma_1...\sigma_{2n}}(\tau_1, \ldots, \tau_{2n}) =$$
$$= \int_0^\beta d\tau_1 \ldots \int_0^\beta d\tau_{2n}\, e^{-i(\nu_1\tau_1+...-\nu_{2n}\tau_{2n})} G_{n,\sigma_1...\sigma_{2n}}(\tau_1 - \tau_{2n}, \ldots, \tau_{2n-1} - \tau_{2n}, 0). \tag{2.55}$$

Hence, by means of the transformation $\tau_i = \tau_i' + \tau_{2n}, i = 1, \ldots, 2n-1$, one introduces new time variables τ_i', the integration over which has to be performed in the interval $[-\tau_{2n}, \beta - \tau_{2n}]$. However, as discussed at the end of Sec. 2.2.1.1, $G_{n,\sigma_1...\sigma_{2n}}(\ldots, \tau_i, \ldots)$ is an antiperiodic function with with respect to τ_i with period β^6. Accordingly, an integral of this function over any interval of the length β is equal to the integral from 0 to β. Finally, one can perform the integration on the remaining time τ_{2n}, which appears now in the phase factor

---

[6]Consequently, the combination $e^{\pm i\nu_i\tau_i}G_{n,\sigma_1...\sigma_{2n}}(\ldots, \tau_i, \ldots)$ is periodic in τ_i (with periodicity β) since $e^{\pm i\nu_i\beta} = -1$ for all fermionic Matsubara frequencies ν_i.

$e^{-i(\nu_1-\nu_2+\ldots+\nu_{2n-1}-\nu_{2n})\tau_{2n}}$ only, yielding the (energy) conservation relation:

$$\int_0^\beta d\tau_{2n}\, e^{-i(\nu_1-\nu_2+\ldots+\nu_{2n-1}-\nu_{2n})\tau_{2n}} = \beta\delta_{(\nu_1-\nu_2+\ldots+\nu_{2n-1}-\nu_{2n})0}. \tag{2.56}$$

Relabeling all integration variables back to τ_i one obtains:

$$\widetilde{G}_{n,\sigma_1\ldots\sigma_{2n}}(\nu_1,\ldots,\nu_{2n}) = \int_0^\beta d\tau_1 \ldots \int_0^\beta d\tau_{2n-1} \left(\int_0^\beta d\tau_{2n}\, e^{-i(\nu_1-\nu_2+\ldots+\nu_{2n-1}-\nu_{2n})\tau_{2n}}\right) \times$$

$$\times\, e^{-i(\nu_1\tau_1-\ldots+\nu_{2n-1}\tau_{2n-1})} G_{n,\sigma_1\ldots\sigma_{2n}}(\tau_1,\ldots,\tau_{2n-1},0) \tag{2.57}$$

$$= \beta\delta_{(\nu_1-\nu_2+\ldots+\nu_{2n-1})\nu_{2n}} G_{n,\sigma_1\ldots\sigma_{2n}}(\nu_1,\ldots,\nu_{2n-1}),$$

where the $2n-1$ frequency Green's function $G_{n,\sigma_1\ldots\sigma_{2n}}(\nu_1,\ldots,\nu_{2n-1})$ is defined as:

$$G_{n,\sigma_1\ldots\sigma_{2n}}(\nu_1,\ldots,\nu_{2n-1}) = \int_0^\beta d\tau_1 \ldots \int_0^\beta d\tau_{2n-1}\, e^{-i(\nu_1\tau_1-\ldots+\nu_{2n-1}\tau_{2n-1})} G_{n,\sigma_1\ldots\sigma_{2n}}(\tau_1,\ldots,\tau_{2n-1},0). \tag{2.58}$$

The discussion above shows, that in Fourier space it is sufficient to consider the Green's function G_n which depends only on $2n-1$ rather than on $2n$ frequencies. Physically, this represents simply a direct manifestation of the energy conservation, due to the time-translational invariance of the system.

Since the Hamiltonian of the Hubbard model is also time independent, the very same relations derived above for the AIM, are also applicable to the frequency dependence of G_n. In addition, in the Hubbard model case, one has typically an analogue symmetry for the spatial degrees of freedom, i.e., the lattice translational invariance: The system is invariant under a shift by a lattice vector $\mathbf{R}$. The corresponding operator $\hat{\mathcal{U}} = \hat{\mathcal{T}}_{\mathbf{R}}$ can be defined for any lattice vector $\mathbf{R}$ via its action on the creation and annihilation operators:

$$\hat{c}'^\dagger_{\mathbf{R}_i}(\mathbf{R}) = \hat{\mathcal{T}}_{\mathbf{R}}^{-1}\hat{c}^\dagger_{\mathbf{R}_i}\hat{\mathcal{T}}_{\mathbf{R}} = \hat{c}^\dagger_{\mathbf{R}_i+\mathbf{R}} \qquad \hat{c}'_{\mathbf{R}_i}(\mathbf{R}) = \hat{\mathcal{T}}_{\mathbf{R}}^{-1}\hat{c}_{\mathbf{R}_i}\hat{\mathcal{T}}_{\mathbf{R}} = \hat{c}_{\mathbf{R}_i+\mathbf{R}}. \tag{2.59}$$

Setting $\mathbf{R} = \mathbf{R}_{2n}$, it is straightforward to derive a relation analogous to Eq. (2.54), but for the lattice vectors $\mathbf{R}_i$ instead of the times τ_i:

$$G_{n,\mathbf{R}_1\ldots\mathbf{R}_{2n}} = G_{n,(\mathbf{R}_1-\mathbf{R}_{2n})\ldots(\mathbf{R}_{2n-1}-\mathbf{R}_{2n})\mathbf{R}_0}, \tag{2.60}$$

where $\mathbf{R}_0$ denotes the origin of the coordinate system, e.g., $\mathbf{R}_0 = (0,0,0)^{\mathrm{T}}$ in the three-dimensional case. Note that, for the sake of readability, we have suppressed the spin indices

σ_i and the time arguments τ_i in Eq. (2.60) since there is no difference between the Hubbard model and the AIM regarding these degrees of freedom.

Performing the Fourier transform with respect to the $\mathbf{R}_i$ one obtains:

$$
\begin{aligned}
\widetilde{G}_{n,\mathbf{k}_1\ldots\mathbf{k}_{2n}} &= \sum_{\mathbf{R}_1\ldots\mathbf{R}_{2n}} e^{i(\mathbf{k}_1\mathbf{R}_1-\mathbf{k}_2\mathbf{R}_2+\ldots+\mathbf{k}_{2n-1}\mathbf{R}_{2n-1}-\mathbf{k}_{2n}\mathbf{R}_{2n})} G_{n,\mathbf{R}_1\ldots\mathbf{R}_{2n}} = \\
&= \frac{(2\pi)^d}{V}\delta(\mathbf{k}_1 - \mathbf{k}_2 + \ldots + \mathbf{k}_{2n-1} - \mathbf{k}_{2n}) G_{n,\mathbf{k}_1,\ldots,\mathbf{k}_{2n-1}},
\end{aligned}
\tag{2.61}
$$

where the (simplified) $2n - 1$-momenta Green's function $G_{n,\mathbf{k}_1\ldots\mathbf{k}_{2n-1}}$ is defined as:

$$
G_{n,\mathbf{k}_1,\ldots,\mathbf{k}_{2n-1}} = \sum_{\mathbf{R}_1\ldots\mathbf{R}_{2n-1}} e^{i(\mathbf{k}_1\mathbf{R}_1-\mathbf{k}_2\mathbf{R}_2+\ldots-\mathbf{k}_{2n-1}\mathbf{R}_{2n-1})} G_{n,\mathbf{R}_1\ldots\mathbf{R}_{2n-1}\mathbf{R}_0},
\tag{2.62}
$$

and V is the volume of the unit cell of the underlying lattice, e.g., $V = a^d$ for the Hubbard model on a d-dimensional cubic lattice with lattice constant a.

Physically the δ-function in Eq. (2.61) corresponds to the momentum originated by the space-translational invariance of the system.

2.2.2.2   SU(2) symmetry

A further simplification concerning the spin dependence of the n-particle Green's functions can be achieved by taking into account the SU(2) symmetry of the Hamiltonian. Formally a system is SU(2) symmetric, if the Hamiltonian commutes with all generators of this group, i.e., the spin operators in the three spatial dimensions:

$$
[\hat{\mathcal{H}}, \hat{\mathcal{S}}_i] = 0, \text{for } i = x, y, z.
\tag{2.63}
$$

The spin operators $\hat{\mathcal{S}}_i$ are defined as the total spin of the system in the 3 directions, the general i-component of which reads:

$$
\hat{\mathcal{S}}_i = \sum_j \hat{\mathcal{S}}_{i,j} = \sum_j \frac{1}{2} \sum_{\sigma\sigma'} \hat{c}_{j\sigma'}^\dagger \sigma_i^{\sigma'\sigma} \hat{c}_{j\sigma},
\tag{2.64}
$$

where the sum over j indicates a sum over all lattice sites in the Hubbard model and over the bath sites and the impurity in the AIM, respectively, and $\sigma_i^{\sigma'\sigma}$ denotes the Pauli matrices

$$\sigma_x = \begin{pmatrix} 0 & 1 \\ 1 & 0 \end{pmatrix} \qquad \sigma_y = \begin{pmatrix} 0 & -i \\ i & 0 \end{pmatrix} \qquad \sigma_z = \begin{pmatrix} 1 & 0 \\ 0 & -1 \end{pmatrix}. \qquad (2.65)$$

It is a straightforward task to show that both Hamiltonians under consideration (Hubbard and AIM) fulfill Eq. (2.63) in their paramagnetic phase[7]. Turning to the discussion of the effects of the SU(2) symmetry on the Green's functions, similarly to the analysis of the time translation invariance, we will present the following derivations only for the AIM since the generalization to the lattice system is trivial.

A first consequence of the SU(2) symmetry is that the total spin of the n-particle Green's function is conserved. While this assertion holds for any arbitrary direction we will discuss it w.l.o.g. only for the z-component of the spin, i.e., for the component pointing in the direction of the quantization axis. For this specific choice the property of spin conservation of the n-particle Green's function can be expressed as:

$$\overbrace{\sigma_1 + \sigma_3 + \ldots + \sigma_{2n-1}}^{S_z \text{ of the outgoing particles}} = \overbrace{\sigma_2 + \sigma_4 + \ldots + \sigma_{2n}}^{S_z \text{ of the incoming particles}}, \qquad (2.66)$$

where the numerical index $1, 2, \ldots, 2n$ classifies the position of the spin in the trace [see Eq. (2.27)]. This means that the total spin (in z-direction) of he incoming particles (corresponding to the annihilation operators $\hat{c}_{\sigma_{2i}}$) must coincide with the total spin of the outgoing ones (represented by the creation operators $\hat{c}^\dagger_{\sigma_{2i-1}}, i = 1 \ldots n$). One can prove this statement by the following argument.

Since $\hat{S}_z$ is an hermitian operators we can divide the entire Hilbert space into orthogonal subspaces defined by the corresponding eigenvalues S_z. Hence, the n-particle Green's function, as defined in Eq. (2.27), can be represented as:

$$G_{n,\sigma_1\ldots\sigma_{2n}}(\tau_1, \ldots, \tau_{2n}) = \frac{1}{Z} \sum_{S_z} \sum_\alpha \langle S_z, \alpha | e^{-\beta\hat{\mathcal{H}}} e^{\tau_1\hat{\mathcal{H}}} \hat{c}^\dagger_{\sigma_1} e^{-\tau_1\hat{\mathcal{H}}} \ldots e^{\tau_{2n}\hat{\mathcal{H}}} \hat{c}_{j_{2n}\sigma_{2n}} e^{-\tau_{2n}\hat{\mathcal{H}}} | S_z, \alpha \rangle, \qquad (2.67)$$

where $\sum_\alpha$ denotes the trace over all states $|S_z, \alpha\rangle$ in the subspace defined by the value of S_z.

---

[7]Adding, e.g., a magnetic field to the Hamiltonian would break this symmetry and, hence, the following analysis does not hold in such a case.

Since $[\hat{\mathcal{H}}, \hat{S}_z] = 0$, an operator of the form $e^{\gamma \hat{\mathcal{H}}}$, $\gamma \in \mathbb{C}$, cannot change the value of S_z, i.e.,

$$e^{\gamma \hat{\mathcal{H}}} |S_z, \alpha\rangle = |S_z, \alpha'\rangle. \tag{2.68}$$

On the other hand the commutation relations between the creation and annihilation operators, respectively, and $\hat{S}_z$ read:

$$[\hat{S}_z, \hat{c}_{j\sigma}^\dagger] = \sigma \hat{c}_{j\sigma}^\dagger, \qquad\qquad [\hat{S}_z, \hat{c}_{j\sigma}] = -\sigma \hat{c}_{j\sigma}, \tag{2.69}$$

where $\sigma = \pm\frac{1}{2}$ corresponds to spin-$\uparrow$ and spin-$\downarrow$, respectively. From Eq. (2.69) immediately follows that

$$\hat{c}_{j\sigma}^\dagger |S_z, \alpha\rangle = |S_z + \sigma, \alpha'\rangle \quad \text{and} \quad \hat{c}_{j\sigma} |S_z, \alpha\rangle = |S_z - \sigma, \alpha'\rangle. \tag{2.70}$$

Eqs. (2.68) and (2.70) allow us to calculate the matrix-element $\langle S_z, \alpha| \ldots |S_z, \alpha\rangle$ in Eq. (2.67):

$$\langle S_z, \alpha| e^{-\beta \hat{\mathcal{H}}} e^{\tau_1 \hat{\mathcal{H}}} \hat{c}_{j_1 \sigma_1}^\dagger e^{-\tau_1 \hat{\mathcal{H}}} \ldots e^{\tau_{2n} \hat{\mathcal{H}}} \hat{c}_{j_{2n} \sigma_{2n}} e^{-\tau_{2n} \hat{\mathcal{H}}} |S_z, \alpha\rangle =$$
$$= \langle S_z, \alpha|S_z + \sigma_1 - \sigma_2 + \ldots + \sigma_{2n-1} - \sigma_{2n}, \alpha'\rangle = C_{S_z, \alpha\alpha'} \delta_{(\sigma_1 - \sigma_2 + \ldots + \sigma_{2n-1} - \sigma_{2n})0}, \tag{2.71}$$

where $C_{S_z, \alpha\alpha'}$ is some constant depending on S_z, α and α'. The last equality, which follows from the fact that states corresponding to different S_z are orthogonal, represents exactly the requirement of spin conservation (along an arbitrary z-axis) which was postulated at the beginning of this paragraph in Eq. (2.66).

The spin conservation leads to a further, significant, simplification of the n-particle Green's functions. In fact, Eq. (2.66) allows for an even stronger restriction of (spin) variables than the corresponding decimation of frequency and momentum arguments due to time/space translational invariance, as a consequence of the discrete and bounded nature of the spin degrees of freedom ($\sigma = \pm\frac{1}{2}$).

Specifically, the *one-particle* Green's functions depends only on *one* spin variable, which allows for the simplified definition:

$$G_{1,\sigma_1}(\nu_1) := \delta_{\sigma_1 \sigma_2} G_{1,\sigma_1 \sigma_2}(\nu_1), \tag{2.72}$$

i.e., only the diagonal part in spin space ($\sigma_1 = \sigma_2$) contributes.

The situation, obviously, is a bit more involved for the *two-particle* Green's functions. Here,

among the $2^4\!=\!16$ possible combinations of spins only the following $2\!\times\!3\!=\!6$ remain,

$$\sigma_1 = \sigma_2 = \sigma_3 = \sigma_4, \qquad (\sigma_1 = \sigma_2) \neq (\sigma_3 = \sigma_4), \qquad (\sigma_1 = \sigma_4) \neq (\sigma_2 = \sigma_3), \qquad (2.73)$$

with $\sigma_1 =\uparrow$ or $\sigma_1 =\downarrow$, because for all the others the two-particle Green's functions vanish due to Eqs. (2.66) and (2.71), respectively. This observation suggests to adopt the following definitions at the two-particle level:

$$G_{2,\sigma\sigma'}(\nu_1, \nu_2, \nu_3) := G_{2,\sigma\sigma\sigma'\sigma'}(\nu_1, \nu_2, \nu_3) \qquad G_{2,\overline{\sigma\sigma'}}(\nu_1, \nu_2, \nu_3) := G_{2,\sigma\sigma'\sigma\sigma'}(\nu_1, \nu_2, \nu_3), \qquad (2.74)$$

which cover all six cases mentioned above since for $\sigma = \sigma'$ the two definitions in Eqs. (2.74) of course coincide. Moreover, considering the crossing symmetry relation (2.37), one can easily show that $G_{2,\sigma\sigma'}$ and $G_{2,\overline{\sigma\sigma'}}$ are, in general, related in the following way:

$$G_{2,\overline{\sigma\sigma'}}(\nu_1, \nu_2, \nu_3) = -G_{2,\sigma\sigma'}(\nu_1, \nu_4, \nu_3), \qquad (2.75)$$

where $\nu_4\!=\!\nu_1\!-\!\nu_2\!+\!\nu_3$ is determined by energy conservation. Note that for $\sigma\!=\!\sigma'$, Eq. (2.75) represents a constraint for the frequency arguments rather than for the spin.

As a next step, we have to analyze how the n-particle Green's functions behave under a rotation, i.e., under a generic SU(2) transformation. To this end, we consider the operator $\hat{\mathcal{U}} = \hat{\mathcal{D}}$ which performs such an *active rotation* of a (many-particle) state vector $|\{n_{i\sigma}\}\rangle$ through an angle φ about an axis the direction of which is defined by a unit vector $\mathbf{n}$:

$$\hat{\mathcal{U}} = \hat{\mathcal{D}}(\mathbf{n}, \varphi) = e^{-i\varphi\mathbf{n}\cdot\hat{\boldsymbol{S}}}, \quad \mathbf{n} \in \mathbb{R}^3, \|\mathbf{n}\|_2\!=\!1 \text{ and } \varphi \in [0, 2\pi), \qquad (2.76)$$

where $\|\cdot\|_2$ denotes the Euclidean norm in $\mathbb{R}^3$. For our purposes it turns out convenient to introduce the "Pauli-spinors"

$$\hat{\mathbf{c}} := \begin{pmatrix} \hat{c}_\uparrow \\ \hat{c}_\downarrow \end{pmatrix} \qquad\qquad \hat{\mathbf{c}}^\dagger := \begin{pmatrix} \hat{c}_\uparrow^\dagger \\ \hat{c}_\downarrow^\dagger \end{pmatrix}, \qquad (2.77)$$

containing the two spin components of an annihilation and a creation operator at the impurity site. Performing the transformation (i.e., in this case the rotation), given in Eq. (2.41), for the "spinor" yields:

$$\hat{\mathbf{c}}'^\dagger(\mathbf{n}, \varphi) = e^{i\varphi\mathbf{n}\cdot\hat{\boldsymbol{S}}}\hat{\mathbf{c}}^\dagger e^{-i\varphi\mathbf{n}\cdot\hat{\boldsymbol{S}}} \qquad\qquad \hat{\mathbf{c}}'(\mathbf{n}, \varphi) = e^{i\varphi\mathbf{n}\cdot\hat{\boldsymbol{S}}}\hat{\mathbf{c}} e^{-i\varphi\mathbf{n}\cdot\hat{\boldsymbol{S}}}. \qquad (2.78)$$

In order to calculate $\hat{\mathbf{c}}'^{(\dagger)}(\mathbf{n}, \varphi)$, we differentiate Eqs. (2.78) with respect to φ which yields the following ordinary differential equation for $\hat{\mathbf{c}}'^{(\dagger)}(\mathbf{n}, \varphi)$:

$$\frac{d}{d\varphi}\hat{\mathbf{c}}'^{(\dagger)}(\mathbf{n}, \varphi) = ie^{i\varphi\mathbf{n}\cdot\hat{\boldsymbol{S}}}[\mathbf{n}\cdot\hat{\mathbf{S}}, \hat{\mathbf{c}}^{(\dagger)}]e^{-i\varphi\mathbf{n}\cdot\hat{\boldsymbol{S}}} = {}^{(\pm)}\frac{1}{2}i\mathbf{n}\cdot\boldsymbol{\sigma}^{(\mathrm{T})}\hat{\mathbf{c}}'^{(\dagger)}(\mathbf{n}, \varphi), \qquad (2.79)$$

with the initial value

$$\hat{\mathbf{c}}'^{(\dagger)}(\mathbf{n}, 0) = \hat{\mathbf{c}}^{(\dagger)}. \qquad (2.80)$$

$\boldsymbol{\sigma}^{(\mathrm{T})} = (\sigma_x^{(\mathrm{T})}, \sigma_y^{(\mathrm{T})}, \sigma_z^{(\mathrm{T})})$ denotes the vector of the (transposed) Pauli matrices. Note, that $\mathbf{n}\cdot\boldsymbol{\sigma}^{(\mathrm{T})}$ is the scalar product of two vectors in $\mathbb{R}^3$, while the components of $\boldsymbol{\sigma}^{(\mathrm{T})}$ are two-dimensional matrices acting on the spinors $\hat{\mathbf{c}}^{(\dagger)}$.

The solution of Eq. (2.79) is given by

$$\hat{\mathbf{c}}'^{(\dagger)}(\mathbf{n}, \varphi) = e^{{}^{(\pm)}i\frac{\varphi}{2}\mathbf{n}\cdot\boldsymbol{\sigma}^{(\mathrm{T})}}\hat{\mathbf{c}}^{(\dagger)} = \left[\cos\left(\frac{\varphi}{2}\right)\mathbb{1}{}^{(\pm)}i\sin\left(\frac{\varphi}{2}\right)\mathbf{n}\cdot\boldsymbol{\sigma}^{(\mathrm{T})}\right]\hat{\mathbf{c}}^{(\dagger)}. \qquad (2.81)$$

Since $\hat{\mathcal{D}}$ commutes with the Hamiltonian the Green's function should not change under such a rotation, as it was shown in Eqs. (2.49) and (2.50) for a general symmetry transformation. That means that the rotated Green's G'_n functions [see Eq. (2.42)]:

$$G'_{n,\sigma_1\ldots\sigma_{2n}}(\tau_1, \ldots, \tau_{2n}) = \left\langle \mathrm{T}\left[\hat{c}'^{\dagger}_{\sigma_1}(\tau_1)\hat{c}'_{\sigma_2}(\tau_2)\ldots\hat{c}'^{\dagger}_{\sigma_{2n-1}}(\tau_{2n-1})\hat{c}'_{\sigma_{2n}}(\tau_{2n})\right]\right\rangle, \qquad (2.82)$$

should coincide with the original one $(G'_n = G_n)$. In order to calculate the rotated Green's function G'_n, we can insert the relation obtained in Eq. (2.81) for $\hat{c}'^{(\dagger)}_\sigma$ into Eq. (2.82). While in principle this could be done for the general case of a generic $\mathbf{n}$ and φ, it is much more convenient to evaluate Eq. (2.81) for specific values of $\mathbf{n}$ and φ.[8] In particular, we can choose the SU(2) transformation $\hat{\mathcal{D}}$ to be a rotation about the y-axis, i.e., $\mathbf{n} = (0, 1, 0)^{\mathrm{T}}$ which yields[9]:

$$\begin{pmatrix} \hat{c}'^{(\dagger)}_\uparrow \\ \hat{c}'^{(\dagger)}_\downarrow \end{pmatrix} = \begin{pmatrix} \cos(\frac{\varphi}{2}) & -\sin(\frac{\varphi}{2}) \\ \sin(\frac{\varphi}{2}) & \cos(\frac{\varphi}{2}) \end{pmatrix} \begin{pmatrix} \hat{c}^{(\dagger)}_\uparrow \\ \hat{c}^{(\dagger)}_\downarrow \end{pmatrix}, \qquad (2.83)$$

For the rotation angle φ we consider the following two specific cases:

- $\boldsymbol{\varphi = \pi}$: Physically this choice of φ corresponds to a rotation of the spins by 180 degrees,

---

[8]We note that all relevant rotational symmetry relations for the one- and two-particle Green's functions can be obtained without such a restriction, but a general treatment would not provide any additional information.

[9]We omit the arguments $\mathbf{n}$ and φ of $\hat{c}^{(\dagger)}_\sigma$ for the sake of a better readability.

i.e., to a spin-flip process, which can be directly obtained from Eq. (2.83):

$$\hat{c}_{\sigma}'^{(\dagger)} = -2\sigma\hat{c}_{(-\sigma)}^{(\dagger)}, \qquad (2\sigma = \pm 1). \tag{2.84}$$

Inserting this into Eq. (2.82) and considering that $G_n' = G_n$ shows, that the Green's functions do not change by flipping *all* spins:

$$G_{n,\sigma_1...\sigma_{2n}}'(\tau_1, \ldots, \tau_{2n}) = G_{n,(-\sigma_1)...(-\sigma_{2n})}(\tau_1, \ldots, \tau_{2n}) = G_{n,\sigma_1...\sigma_{2n}}(\tau_1, \ldots, \tau_{2n}), \tag{2.85}$$

where we considered that $\prod_{i=1}^{2n}(2\sigma_i) \equiv +1$ due to spin conservation [Eq. (2.66)]. Accordingly, the *one-particle* Green's function $G_{1,\sigma_1}(\nu_1)$ does not exhibit any spin dependence at all and, hence, can be redefined as:

$$G_1(\nu_1) := G_{1,\uparrow}(\nu_1) = G_{1,\downarrow}(\nu_1). \tag{2.86}$$

For the *two-particle* Green's function, in turn, a rotation of all spins through an angle π gives rise to the relations:

$$G_{2,\uparrow\uparrow}(\nu_1, \nu_2, \nu_3) = G_{2,\downarrow\downarrow}(\nu_1, \nu_2, \nu_3) \qquad G_{2,\uparrow\downarrow}(\nu_1, \nu_2, \nu_3) = G_{2,\downarrow\uparrow}(\nu_1, \nu_2, \nu_3). \tag{2.87}$$

Hence, taking into account the crossing relation (2.75), from the six possible spin combinations for the two-particle Green's function considered in Eq. (2.73) only two are really relevant, namely $G_{2,\uparrow\uparrow}$ and $G_{2,\uparrow\downarrow}$. All the others either lead to vanishing contributions or can be obtained from the latter ones by means of the crossing or the SU(2) symmetry relations.

- $\varphi = \frac{\pi}{2}$: Physically this choice of φ corresponds to rotate the spins by 90 degrees, i.e., to transform a spin in z-direction into a spin in x-direction, which can be directly inferred from Eq. (2.83):

$$\hat{c}_{\sigma}'^{(\dagger)} = \frac{1}{\sqrt{2}}\left(\hat{c}_{\sigma}^{(\dagger)} - 2\sigma\hat{c}_{(-\sigma)}^{(\dagger)}\right), \qquad (2\sigma = \pm 1). \tag{2.88}$$

For this transformation a general discussion in terms of the n-particle Green's function is not possible because one has to take into account concretely its spin dependence, i.e., one has to consider each spin combination separately. Hence, we focus on the one- and the two-particle cases which are relevant for this thesis.

For the *one-particle* Green's function this transformation does not provide any new information.This was, however, to be expected from Eq. (2.86) since the one-particle

Green's function does not depend on the direction of the spin at all.

For the *two-particle* Green's functions, on the contrary, the SU(2) rotation through $\frac{\pi}{2}$ yields a relations between $G_{2,\uparrow\uparrow}$ and $G_{2,\uparrow\downarrow}$. In fact, inserting Eq. (2.88) into Eq. (2.82) and considering $G'_n = G_n$, spin conservation [Eq. (2.66)], the invariance under spin flips [Eq. (2.87)] as well as the crossing relation [Eq. (2.75)] yields:

$$
\begin{aligned}
G_{2,\uparrow\uparrow}(\nu_1, \nu_2, \nu_3) &= G_{2,\uparrow\downarrow}(\nu_1, \nu_2, \nu_3) + G_{2,\overline{\uparrow\downarrow}}(\nu_1, \nu_2, \nu_3) = \\
&= G_{2,\uparrow\downarrow}(\nu_1, \nu_2, \nu_3) - G_{2,\uparrow\downarrow}(\nu_1, \nu_4, \nu_3),
\end{aligned}
\tag{2.89}
$$

where $\nu_4 = \nu_1 - \nu_2 + \nu_3$ (energy conservation). Hence, in the SU(2) symmetric case only one of the six spin combinations, for which the two-particle Green's function does not vanish [as discussed in Eq. (2.73)] is independent, namely $G_{2,\uparrow\downarrow}$ while all the others can be derived from the latter. In particular, $G_{2,\uparrow\uparrow}$ can be calculated from $G_{2,\uparrow\downarrow}$ by means of Eq. (2.89), while on the other hand, the knowledge of $G_{2,\uparrow\uparrow}$ is *not* sufficient for determining $G_{2,\uparrow\downarrow}$. In fact, the latter case, i.e., when only $G_{2,\uparrow\uparrow}$ is known, Eq. (2.89) provides just a constraint on $G_{2,\uparrow\downarrow}$.[10]

2.2.2.3   Time and Space Reversal Symmetry

In classical physics a system is said to be invariant under time reversal if the Hamiltonian function H does not change under the transformation $\mathbf{p} \to -\mathbf{p}$. As a consequence, if a trajectory $x(t)$ is a solution of the equation of motion, $x(-t)$, i.e., the reversed motion, is also a solution.

In standard quantum mechanics the time-reversal operator $\hat{T}$ is an anti-unitary operator. For spinless particles or a system *without* spin-dependent interactions it is simply represented by complex conjugation of the wave function[11]:

$$
\hat{T}\psi(x) = K\psi(x) := \psi^*(x),
\tag{2.90}
$$

---

[10]Physically, this observation can be understood in the following way: As it will be discussed in Sec. 2.2.4 the two-particle Green's function is connected to the scattering amplitude between two electrons. No restriction exist for scattering events between one $\uparrow$-electron and one $\downarrow$-electron. However, if two $\uparrow$-electrons are involved, the Pauli principle does not allow for scattering processes where *both* particles occupy the same quantum state, as it is, e.g., the case for the (lowest order) constant U contribution to the scattering amplitude. Hence, the scattering events contained in $G_{2,\uparrow\uparrow}$ represent just a subset of all possible scattering events contained in $G_{2,\uparrow\downarrow}$ (or $G_{2,\overline{\uparrow\downarrow}}$).

[11]We recall that, if the systems exhibits any spin-dependent interactions, such as, e.g., spin-orbit coupling $\boldsymbol{\sigma} \cdot \hat{\mathbf{L}}$ or the coupling to a magnetic field $\boldsymbol{\sigma} \cdot \mathbf{B}$, the time reversal operator reads as $\hat{T} = \sigma_2 \otimes K$ where K denotes the complex conjugation.

where K denotes the complex conjugation. Therefore, the system is invariant under time reversal, if the (time-independent) Hamiltonian is a *real function* of the momentum operator $\hat{p}$ and the position operator $\hat{x}$. This is, in fact, usually the case for systems without spin-orbit coupling and without interaction with a magnetic field, i.e., for Hamiltonians of the form $\hat{\mathcal{H}} = \frac{\hat{p}^2}{2m} + V(\hat{x})$ with a real potential V. In such a case, all eigenfunctions $\psi(x) = \langle x|\psi\rangle$ in space representation can be chosen to be real, i.e., $\psi(x) = \psi^*(x)$.

An analogous situation occurs, obviously, also in the framework of quantum field theory. In the occupation number basis $|\{n_j\}\rangle$ $\big[\{n_j\}\hat{=}\{n_1, \ldots, n_j, \ldots\}, \, n_j = 0, 1$ for fermions$\big]$, the matrix elements of a creation or annihilation operator $\hat{c}_i^{(\dagger)}$ for an arbitrary state i is purely real:

$$\langle\{n'_j\}|\hat{c}_i^\dagger|\{n_j\}\rangle = (1 - n_i)\delta_{n'_i(n_i+1)} \qquad \langle\{n'_j\}|\hat{c}_i|\{n_j\}\rangle = n_i\delta_{n'_i(n_i-1)}, \qquad (2.91)$$

or equal 0 if the occupation of all states $j \neq i$ is not the same for $|\{n\}\rangle$ and $|\{n'\}\rangle$), i.e., $n'_j \neq n_j$ for at least one $j \neq i$. Furthermore, under our assumption that the Hamiltonian $\hat{\mathcal{H}}$ is a real function of the creation and annihilation operators $\hat{c}_i^\dagger$ and $\hat{c}_i$, its representation in the occupation number basis will be evidently a purely real matrix:

$$\langle\{n'_j\}|\hat{\mathcal{H}}|\{n_j\}\rangle^* = \langle\{n'_j\}|\hat{\mathcal{H}}|\{n_j\}\rangle, \qquad (2.92)$$

which also holds for any operator $e^{\alpha\hat{\mathcal{H}}}$, $\alpha \in \mathbb{R}$ (e.g., $\alpha = \beta, \pm\tau$). If one performs, then, the trace in the definition of the Green's function [Eq. (2.27)] by summing over the occupation number basis, each single contribution is just a matrix element of a product of operators $\hat{c}_i^{(\dagger)}$ and $e^{\alpha\hat{\mathcal{H}}}$. Hence, according to Eqs. (2.91) and (2.92) all these matrix elements are purely real and thus the same holds for the specific case of G_n as a function of imaginary times[12]:

$$G^*_{n,\sigma_1\ldots\sigma_{2n}}(\tau_1, \ldots, \tau_{2n}) = G_{n,\sigma_1\ldots\sigma_{2n}}(\tau_1, \ldots, \tau_{2n}). \qquad (2.93)$$

Eq. (2.93) obviously holds for systems where the Hamiltonian is a real function of the creation and annihilation operators such as the AIM and the single-band Hubbard model. On the contrary, this condition will be violated by Hamiltonian contributions like the spin-orbit coupling (which nevertheless preserves the time reversal invariance of the system) or by the coupling to an external magnetic field (which breaks explicitly the time reversal symmetry). Eventually, combining the expression for the complex conjugation of the Green's function

---

[12]This property could be also proven by resorting to the functional integral representation of the Green's function [52].

derived in Sec. 2.2.1.3 [Eq. (2.38)] with Eq. (2.93), leads to the following relation for the Green's function of a the AIM:

$$G_{n,\sigma_1...\sigma_{2n}}(\tau_1,\ldots,\tau_{2n}) = G_{n,\sigma_{2n}...\sigma_1}(-\tau_{2n},\ldots,-\tau_1) = G_{n,\sigma_{2n}...\sigma_1}(\beta-\tau_{2n},\ldots,\beta-\tau_1), \quad (2.94)$$

where the last equality follows from anti-periodic nature of the imaginary times Green's function [see Eqs. (2.34)]. Performing the Fourier transform according to Eq. (2.58) yields:

$$G_{n,\sigma_1...\sigma_{2n}}(\nu_1,\ldots,\nu_{2n-1}) = G_{n,\sigma_{2n}...\sigma_1}(\nu_{2n},\ldots,\nu_2), \quad (2.95)$$

where $\nu_{2n}=\nu_1-\nu_2\ldots+\nu_{2n-1}$ is determined by the requirement of energy conservation. For the one-particle Green's function Eq. (2.95) reduces to the trivial relation $G_1(\nu_1) = G_1(\nu_1)$ since it depends only on one frequency, while for the two-particle Green's function, Eq. (2.95) gives rise to further simplifying restrictions on its frequency dependence.

Applying the discussion above to the Hubbard model leads to a relation analogous to Eqs. (2.94) and (2.95), for the AIM, which reads ,in terms of the space coordinates, as:

$$G_{n,\mathbf{R}_1...\mathbf{R}_{2n}} = G_{n,\mathbf{R}_{2n}...\mathbf{R}_1}, \quad (2.96)$$

where we have suppressed the time- and the spin dependence of the Green's function since it exactly coincides with that of the AIM discussed above. When performing the Fourier transform as defined in Eqs. (2.61) and (2.62) one gets the relation

$$G_{n,\mathbf{k}_1...\mathbf{k}_{2n-1}} = G_{n,(-\mathbf{k}_{2n})...(-\mathbf{k}_2)}, \quad (2.97)$$

where $\mathbf{k}_{2n}=\mathbf{k}_1-\mathbf{k}_2+\ldots+\mathbf{k}_{2n-1}$ is given by the requirement of momentum conservation. Eq. (2.97) exhibits, hence, a similar behavior for the momenta $\mathbf{k}_i$ as Eq. (2.95) does for the frequencies. The only difference is, however, that the momenta are reversed, i.e., $\mathbf{k} \to -\mathbf{k}$, as it is expected under time reversal. We note, furthermore, that if the system, on the other hand, features additionally *space inversion symmetry* as well, i.e., the Hamiltonian does not change under the transformation $\mathbf{R} \to -\mathbf{R}$, which is the case for our Hubbard Hamiltonian, then also the momenta exhibit exactly the same behavior as the frequencies under time and space inversion, i.e.,

$$G_{n,\mathbf{k}_1...\mathbf{k}_{2n-1}} = G_{n,\mathbf{k}_{2n}...\mathbf{k}_2}, \quad (2.98)$$

where $\mathbf{k}_{2n} = \mathbf{k}_1 - \mathbf{k}_2 + \ldots + \mathbf{k}_{2n-1}$ (momentum conservation).

2.2.2.4 Point group symmetry of the lattice

This section concerns obviously only the Hubbard model (there does not exist a lattice for the AIM). The point group of a lattice consists of all rotations under which the lattice is mapped on itself. A classification of the 7 possible crystal systems and the 14 Bravais lattices can be found in the literature [39] but it is not relevant for the results presented in the next chapters. We will restrict ourselves here to the specific case, considered in this thesis, namely the *simple cubic lattice*. One element of the point group of a simple cubic lattice was already discussed in the last section, that is the inversion of the lattice. This symmetry reduces the number of non-equivalent $\mathbf{k}$ points by a factor of two. In addition one has to consider all possible rotations that leave the lattice invariant. In d dimension this leads to a reduction of the full Brillouin zone $[-\frac{\pi}{a}, \frac{\pi}{a}]^d$ by a factor of $2^d d!$ corresponding to the d possible reflections $\mathbf{k}_i \to -\mathbf{k}_i$ and the $d!$ permutations of the of the d momentum arguments. Hence, for the two-dimensional case the size of such a *"irreducible Brillouin zone"* is just $\frac{1}{4}$ times the size of the full Brillouin zone, while for three dimensions the point group symmetries lead to a reduction by a factor of $\frac{1}{48}$.

2.2.2.5 Particle-Hole symmetry

In addition to general symmetry properties, it is also interesting to discuss explicitly the specific case in which the Hubbard model and the AIM exhibit a further symmetry, which is called particle-hole symmetry. As the name says, the corresponding unitary symmetry operator exchanges creation and annihilation operators, i.e., "particles" and "holes". The situation is completely analog to the particle-antiparticle symmetry of the relativistic quantum electrodynamics. In fact, the particle-hole transformation operator corresponds in some sense to the charge conjugation transformation between electrons and positrons know from relativistic quantum field theory. Intuitively, one would expect that exchanging particles and holes can represent a symmetry for the Hubbard model and the AIM only for specific subsets of parameters defining these models. More precisely, the Hubbard Hamiltonian must exhibit (i) a symmetric density of states (DOS), which is the case of a bipartite lattice (such as the simple cubic lattice) with only nearest neighbor hopping. Furthermore, (ii) the system has to be *half-filled*, i.e., there is one electron per lattice site, which corresponds to the choice $\mu = \frac{U}{2}$ for the chemical potential. For a more detailed discussion of the particle-hole symmetry of the Hubbard model we refer to the literature [53–55] and to the end of this section. Analogously, for the AIM a particle-hole symmetry transformation can be also defined, if the AIM exhibits (i) a symmetric bath and (ii) is half filled, i.e., there has to be one electron at

the impurity site. As for the Hubbard model, the latter condition can be fulfilled by choosing $\mu = \frac{U}{2}$. The validity of these conditions can be easily proved as follows , starting from the general definition of the AIM:

$$\hat{\mathcal{H}} = \sum_{\ell\sigma} \varepsilon_\ell \hat{a}^\dagger_{\ell\sigma} \hat{a}_{\ell\sigma} + \sum_{\ell\sigma} V_\ell(\hat{c}^\dagger_\sigma \hat{a}_{\ell\sigma} + \hat{a}^\dagger_{\ell\sigma} \hat{c}_\sigma) + U\hat{n}_\uparrow \hat{n}_\downarrow - \mu(\hat{n}_\uparrow + \hat{n}_\downarrow),$$

where the sum over ℓ (bath sites) ranges from 2 to N and $\ell = 1$ denotes the impurity (i.e., $\hat{a}^{(\dagger)}_{1\sigma} = \hat{c}^{(\dagger)}_{2\sigma}$). The particle-hole transformation we are considering for the AIM is defined by the unitary operator $\hat{\mathcal{U}} = \hat{\mathcal{W}}$:

$$\hat{\mathcal{W}} = (\hat{a}^\dagger_{N\uparrow} - \hat{a}_{N\uparrow})\dots(\hat{a}^\dagger_{2\uparrow} - \hat{a}_{2\uparrow})(\hat{c}^\dagger_\uparrow + \hat{c}_\uparrow)(\hat{a}^\dagger_{N\downarrow} - \hat{a}_{N\downarrow})\dots(\hat{a}^\dagger_{2\downarrow} - \hat{a}_{2\downarrow})(\hat{c}^\dagger_\downarrow + \hat{c}_\downarrow). \qquad (2.99)$$

Calculating the action of this transformation on the creation and annihilation operators yields:

$$\hat{\mathcal{W}}^\dagger \hat{c}^\dagger_\sigma \hat{\mathcal{W}} = -\hat{c}_\sigma \qquad\qquad \hat{\mathcal{W}}^\dagger \hat{c}_\sigma \hat{\mathcal{W}} = -\hat{c}^\dagger_\sigma \qquad (2.100a)$$

$$\hat{\mathcal{W}}^\dagger \hat{a}^\dagger_{\ell\sigma} \hat{\mathcal{W}} = \hat{a}_{\ell\sigma} \qquad\qquad \hat{\mathcal{W}}^\dagger \hat{a}_{\ell\sigma} \hat{\mathcal{W}} = \hat{a}^\dagger_{\ell\sigma}. \qquad (2.100b)$$

Hence, the annihilation and creation operators are interchanged under the transformation $\hat{\mathcal{W}}$, justifying the denotation of $\hat{\mathcal{W}}$ as "particle-hole" transformation.

Eqs. (2.100) give rise to the following transformation of the AIM Hamiltonian:

$$\hat{\mathcal{W}}^\dagger \hat{\mathcal{H}} \hat{\mathcal{W}} = \sum_{\ell\sigma}(-\varepsilon_\ell)\hat{a}^\dagger_{\ell\sigma}\hat{a}_{\ell\sigma} + \sum_{\ell\sigma} V_\ell(\hat{c}^\dagger_\sigma \hat{a}_{\ell\sigma} + \hat{a}^\dagger_{\ell\sigma}\hat{c}_\sigma) + U\hat{n}_\uparrow \hat{n}_\downarrow +$$
$$- (U - \mu)(\hat{n}_\uparrow + \hat{n}_\downarrow) + 2\sum_\ell \varepsilon_\ell + U - 2\mu. \qquad (2.101)$$

Comparing this expression with the original Hamiltonian in Eq. (2.23) or at the beginning of this section shows that, indeed, $\hat{\mathcal{W}}$ *does not* represent a symmetry for a generic AIM: The sign of the energy levels ε_ℓ of the bath as well as chemical potential $[\mu \to (U - \mu)]$ are changed under the transformation[13]. However, $\hat{\mathcal{W}}$ constitutes nevertheless a symmetry for a certain subclass of AIMs defined by specific constraints on its parameters which will be discussed in the following:

- $\varepsilon_\ell = -\varepsilon_{\ell+\frac{N}{2}}$ for $\ell = 2\dots\frac{N}{2}$, which means that the bath levels are distributed symmetrically around 0 (here $\frac{N}{2}$ denotes just the integer part of the division).

---

[13] The additional constant term $2\sum_\ell \varepsilon_\ell + U - 2\mu$ can be of course neglected.

- $V_\ell = V_{\ell+\frac{N}{2}}$ for $\ell = 2 \ldots \frac{N}{2}$, i.e., the hybridization between the bath and the impurity should be the same for the positive and the corresponding negative bath energies.

In fact, it is clear that with the restrictions on the parameters ε_ℓ and V_ℓ stated above the negative energy sector of the bath becomes completely equivalent to the positive one. At this stage, if we are interested only to the impurity Green's functions, we can perform the index transformation $\ell \leftrightarrow (\ell + \frac{N}{2})$ which changes the minus sign in front of ε_ℓ in Eq. (2.101) back into a plus sign as in the original Hamiltonian (2.23). The original Hamiltonian in Eq. (2.101) is finally retrieved simply by choosing $\mu = \frac{U}{2}$, as mentioned above.

Next, we calculate the (particle-hole) transformed n-particle Green's function

$$G'_{n,\sigma_1 \ldots \sigma_{2n}}(\tau_1, \ldots, \tau_{2n}) = \left\langle \mathrm{T}\left[\hat{c}'^\dagger_{\sigma_1}(\tau_1)\hat{c}'_{\sigma_2}(\tau_2)\ldots\hat{c}'^\dagger_{\sigma_{2n-1}}(\tau_{2n-1})\hat{c}'_{\sigma_{2n}}(\tau_{2n})\right]\right\rangle, \qquad (2.102)$$

where

$$\hat{c}'^\dagger_\sigma = \hat{\mathcal{W}}^\dagger \hat{c}^\dagger_\sigma \hat{\mathcal{W}} = -\hat{c}_\sigma, \qquad\qquad \hat{c}'_\sigma = \hat{\mathcal{W}}^\dagger \hat{c}_\sigma \hat{\mathcal{W}} = -\hat{c}^\dagger_\sigma. \qquad (2.103)$$

Restricting oneself to AIMs with an symmetric bath as described above, $\hat{\mathcal{W}}$ represents a symmetry of the system. Hence, the transformed Green's function must coincide with the original one, i.e.,

$$G'_{n,\sigma_1 \ldots \sigma_{2n}}(\tau_1, \ldots, \tau_{2n}) = G_{n,\sigma_1 \ldots \sigma_{2n}}(\tau_1, \ldots, \tau_{2n}). \qquad (2.104)$$

Inserting the transformed creation and annihilation operators Eq. (2.103) into the definition of the transformed Green's function Eq. (2.102) leads to

$$G'_{n,\sigma_1 \ldots \sigma_{2n}}(\tau_1, \ldots, \tau_{2n}) = \left\langle \mathrm{T}\left[\hat{c}_{\sigma_1}(\tau_1)\hat{c}^\dagger_{\sigma_2}(\tau_2)\ldots\hat{c}_{\sigma_{2n-1}}(\tau_{2n-1})\hat{c}^\dagger_{\sigma_{2n}}(\tau_{2n})\right]\right\rangle. \qquad (2.105)$$

This expression does not match any longer the definition of the n-particle Green's function in Eq. (2.27), but we can use the crossing symmetry to invert the order of the creation and annihilation operators in Eq. (2.105) to restore the correct sequence according to the definition of the n-particle Green's function. It is easy to prove that one obtains an additional factor $(-1)^n$ due to the anti-commutative nature of fermionic operators[14]. Hence, since $\hat{\mathcal{W}}$ constitutes a symmetry of the Hamiltonian, one has $G'_n = G_n$ [Eq. (2.50)], yielding the

---

[14]In order to invert the order of $2n$ operators one needs $(2n-1)+(2n-2)+\ldots+2+1 = 2n^2-n$ exchanges of fermionic operators which leads to a factor $(-1)^{2n^2-n} = (-1)^n$.

following relation for the n-particle Green's function:

$$G_{n,\sigma_1\ldots\sigma_{2n}}(\tau_1,\ldots,\tau_{2n}) = (-1)^n G_{n,\sigma_{2n}\ldots\sigma_1}(\tau_{2n},\ldots,\tau_1). \qquad (2.106)$$

Next, we recall the formula for the complex conjugation of the Green's function [Eq. (2.38)]

$$G^*_{n,\sigma_1\ldots\sigma_{2n}}(\tau_1,\ldots,\tau_{2n}) = G_{n,\sigma_{2n}\ldots\sigma_1}(-\tau_{2n},\ldots,-\tau_1),$$

and combine it with Eq. (2.106) which gives rise to the following relation for the n-particle Green's function in the particle-hole symmetric case:

$$G^*_{n,\sigma_1\ldots\sigma_{2n}}(\tau_1,\ldots,\tau_{2n}) = (-1)^n G_{n,\sigma_1\ldots\sigma_{2n}}(-\tau_1,\ldots,-\tau_{2n}). \qquad (2.107)$$

Transforming Eq. (2.107) to Fourier space leads to

$$G^*_{n,\sigma_1\ldots\sigma_{2n}}(\nu_1,\ldots,\nu_{2n-1}) = (-1)^n G_{n,\sigma_1\ldots\sigma_{2n}}(\nu_1,\ldots,\nu_{2n-1}), \qquad (2.108)$$

which states that the local Green's function is a purely real or a purely imaginary function depending on whether n is an even or an odd number. Specifically, the one-particle Green's function exhibits solely an imaginary part, i.e.,

$$G^*_1(\nu_1) = -G_1(\nu_1), \qquad (2.109)$$

while the two-particle Green's function is purely real:

$$G^*_{2,\sigma\sigma'}(\nu_1,\nu_2,\nu_3) = G_{2,\sigma\sigma'}(\nu_1,\nu_2,\nu_3). \qquad (2.110)$$

Taking into account also the time reversal symmetry of the system [Eq. (2.93)], i.e., that the Green's functions G_n in Eq. (2.107) are purely real at the imaginary time axis, leads to a further relation which reads as:

$$G_{n,\sigma_1\ldots\sigma_{2n}}(\tau_1,\ldots,\tau_{2n}) = (-1)^n G_{n,\sigma_1\ldots\sigma_{2n}}(-\tau_1,\ldots,-\tau_{2n}), \qquad (2.111)$$

the Fourier representation of which is given by

$$G_{n,\sigma_1\ldots\sigma_{2n}}(\nu_1,\ldots,\nu_{2n-1}) = (-1)^n G_{n,\sigma_1\ldots\sigma_{2n}}(-\nu_1,\ldots,-\nu_{2n-1}). \qquad (2.112)$$

Eq. (2.111) is related to another important property of the one-particle Green's function in the time space. The local electronic density of the system, i.e., the average number of electrons at the impurity site (n), can be calculated from this Green's function as:

$$\lim_{\tau \to 0+} G_1(\tau, 0) = \langle \hat{n}_\sigma \rangle = \frac{\langle \hat{n} \rangle}{2} = \frac{n}{2} \qquad \lim_{\tau \to 0+} G_1(-\tau, 0) = \frac{\langle \hat{n} \rangle}{2} - 1 = \frac{n}{2} - 1. \qquad (2.113)$$

According to Eq. (2.107), $G_1(-\tau, 0) = -G_1(\tau, 0)$, which implies that

$$\frac{n}{2} = -\left(\frac{n}{2} - 1\right) \qquad \Longrightarrow \qquad n = 1. \qquad (2.114)$$

This equation shows that for the specific restrictions on the parameters ε_ℓ, V_ℓ and μ of the AIM, made in this section, the system is indeed *half-filled*, i.e., there is on average one electron at the impurity $(n{=}1)$.

For the Hubbard model on a simple (hyper)cubic lattice some additional consideration has to be done. The particle-hole transformation corresponding to Eq. (2.103) reads in this case as

$$\hat{c}'^\dagger_{\mathbf{R}_i} = \hat{\mathcal{W}}^\dagger_{\mathrm{H}} \hat{c}^\dagger_{\mathbf{R}_i} \hat{\mathcal{W}}_{\mathrm{H}} = e^{\pm i\mathbf{\Pi}\mathbf{R}_i} \hat{c}_{\mathbf{R}_i}, \qquad \hat{c}'_{\mathbf{R}_i} = \hat{\mathcal{W}}^\dagger_{\mathrm{H}} \hat{c}_{\mathbf{R}_i} \hat{\mathcal{W}}_{\mathrm{H}} = e^{\pm i\mathbf{\Pi}\mathbf{R}_i} \hat{c}^\dagger_{\mathbf{R}_i}, \qquad (2.115)$$

where $\hat{\mathcal{W}}_{\mathrm{H}}$ denotes the particle-hole transformation for the Hubbard model and $\mathbf{\Pi}$ refers to the (total antiferromagnetic) vector $\mathbf{\Pi} = (\pi, \ldots, \pi)^{\mathrm{T}}$ in d dimensions with the lattice constant $a = 1$ for the underlying (hyper)cubic lattice. The additional factor $e^{\pm i\mathbf{\Pi}\mathbf{R}_i}$ in Eq. (2.115) is a manifestation of the bipartite nature of a simple cubic lattice, allowing for a division into two sub-lattices A and B, whereupon (w.l.o.g.) $e^{+i\mathbf{\Pi}\mathbf{R}_i} = \pm 1$ depending on whether $\mathbf{R}_i$ is located in sub-lattice A or B. Hence, for the Green's function of the Hubbard model we obtain a relation analogous to Eq. (2.107):

$$G^*_{n,\mathbf{R}_1\ldots\mathbf{R}_{2n}} = (-1)^n G_{n,\mathbf{R}_1\ldots\mathbf{R}_{2n}} \prod_{i=1}^{2n} e^{i\mathbf{\Pi}\mathbf{R}_i}, \qquad (2.116)$$

where we again suppress the spin and time arguments, since they are exactly the same as in Eq. (2.107) for the AIM. Performing the Fourier transform of Eq. (2.116) leads to:

$$G^*_{n,\mathbf{k}_1\ldots\mathbf{k}_{2n-1}} = (-1)^n G_{n,(\mathbf{\Pi}-\mathbf{k}_1)\ldots(\mathbf{\Pi}-\mathbf{k}_{2n-1})}. \qquad (2.117)$$

Hence, in the case of a particle-hole symmetry of the underlying Hubbard model, the momentum-

dependent Green's functions are *purely real* or *purely imaginary* only for some specific $\mathbf{k}$ vectors[15]. These $\mathbf{k}$ vectors are either given by the requirement that $\pi - k_i = k_i$, which means that $k_i = \frac{\pi}{2}$ or –due to the point group symmetry of the lattice– by the constraint $\pm k_i = \pi \pm k_{P(i)}$ where $P(i)$ denotes an arbitrary permutation of the d coordinates. The latter condition defines some high-symmetry points, lines or planes in the d-dimensional $\mathbf{k}$ space. For instance, in the specific case of a simple square lattice in $d = 2$ dimensions one has $\pm k_x = \pi \pm k_y$. This defines a square centered in the origin rotated through 45 degrees about the z-axis (with corners at $(\pm \pi, 0) and (0, \pm \pi)$], which coincides exactly with the non-interacting Fermi-surface for the half filled two-dimensional Hubbard model. Hence, in the $d = 2$ case with particle-hole symmetry, the one-particle Green's function is purely imaginary for all $\mathbf{k}$ points on the corresponding Fermi surface according to Eq. (2.116). On the contrary in $d = 3$, even when the model is particle-hole symmetric, the set of $\mathbf{k}$ vectors, where the one-particle Green's function is purely imaginary, does not *cover* the entire two-dimensional Fermi-surface, but only some specific one-dimensional subset of it.

2.2.2.6   The SU(2)$_\mathbf{P}$ [and SO(4)] symmetry of the half-filled AIM

In this section we will discuss a symmetry which originates from *combining* the SU(2) and the particle-hole invariance of the (half-filled) system. To this end, we constrain the particle-hole transformation $\hat{\mathcal{W}}$, discussed in Sec. 2.2.2.5 [Eq. (2.99)] to one spin species, e.g., the $\downarrow$-electrons, while the $\uparrow$-electrons are now untouched by the transformation. The corresponding operator $\hat{\mathcal{W}}_p$ reads as

$$\hat{\mathcal{W}}_p = (\hat{a}_{\mathrm{N}\downarrow}^\dagger - \hat{a}_{\mathrm{N}\downarrow}) \dots (\hat{a}_{2\downarrow}^\dagger - \hat{a}_{2\downarrow})(\hat{c}_\downarrow^\dagger + \hat{c}_\downarrow). \tag{2.118}$$

For the AIM, one can show that, under the same constraints on the bath parameters ε_ℓ and V_ℓ and the chemical potential μ, which are described in Sec. 2.2.2.5 (page 47) for the (full) particle-hole transformation[16], the transformation $\hat{\mathcal{W}}_p$ provides a mapping of the half-filled repulsive Hubbard model $(U > 0)$ onto the attractive one $(-U < 0)$, i.e,

$$\hat{\mathcal{H}}' = \hat{\mathcal{W}}_p^\dagger \hat{\mathcal{H}}(U) \hat{\mathcal{W}}_p = \hat{\mathcal{H}}(-U), \tag{2.119}$$

where $\hat{\mathcal{H}}(U)$ and $\hat{\mathcal{H}}(-U)$ denote the Hamiltonians exhibiting a positive (repulsive) and the corresponding negative (attractive) value of U, respectively. Hence, the partial particle hole

---

[15]For the local Green's functions instead, the same conditions of the AIM are valid.

[16]$\varepsilon_\ell = -\varepsilon_{\ell + \frac{\mathrm{N}}{2}}$, $V_\ell = V_{\ell + \frac{\mathrm{N}}{2}}$, and $\mu = \frac{U}{2}$.

transformation $\hat{\mathcal{W}}_p$ itself does not represent a symmetry of the AIM but maps its repulsive version ($U > 0, \mu = \frac{U}{2}$) onto its attractive version ($-U, \mu = -\frac{U}{2}$) and vice versa. This mapping between the repulsive and the attractive system will be discussed in more detail later in Sec. 2.2.5, where also a more precise derivation of Eq. (2.119) will be provided. In the present section, however, we will focus on a different aspect of the transformation $\hat{\mathcal{W}}_p$. Though $\hat{\mathcal{W}}_p$ does not represent a symmetry of the system itself, it gives rise to an additional symmetry which is connected with the rotational invariance of the spin degrees of freedom. In fact, considering the rotation operator $\hat{\mathcal{D}}$ in Eq. (2.76), one can define a, corresponding, new transformation $\hat{\mathcal{D}}_p$ as:

$$\hat{\mathcal{D}}_p = \hat{\mathcal{W}}_p^\dagger \hat{\mathcal{D}} \hat{\mathcal{W}}_p. \tag{2.120}$$

It is obvious that $\hat{\mathcal{D}}_p$ constitutes a symmetry of the transformed Hamiltonian $\hat{\mathcal{H}}' = \hat{\mathcal{W}}_p^\dagger \hat{\mathcal{H}}(U) \hat{\mathcal{W}}_p = \hat{\mathcal{H}}(-U)$ since $[\hat{\mathcal{D}}, \hat{\mathcal{H}}] = 0$, i.e.,

$$[\hat{\mathcal{D}}_p, \hat{\mathcal{H}}'] = [\hat{\mathcal{W}}_p^\dagger \hat{\mathcal{D}} \hat{\mathcal{W}}_p, \hat{\mathcal{W}}_p^\dagger \hat{\mathcal{H}} \hat{\mathcal{W}}_p] = \hat{\mathcal{W}}_p^\dagger [\hat{\mathcal{D}}, \hat{\mathcal{H}}] \hat{\mathcal{W}}_p \equiv 0. \tag{2.121}$$

Furthermore, it is convenient to split the Hamiltonian $\hat{\mathcal{H}}$ of the AIM, defined in Eq. (2.23), into a non-interacting and an interacting part:

$$\hat{\mathcal{H}} = \hat{\mathcal{H}}_0 + U\hat{\mathcal{H}}_\text{I}, \tag{2.122}$$

where the two contributions $\hat{\mathcal{H}}_0$ and $\hat{\mathcal{H}}_\text{I}$ are defined as:

$$\hat{\mathcal{H}}_0 = \sum_{\ell\sigma} \varepsilon_\ell \hat{a}_{\ell\sigma}^\dagger \hat{a}_{\ell\sigma} + \sum_{\ell\sigma} V_\ell(\hat{c}_\sigma^\dagger \hat{a}_{\ell\sigma} + \hat{a}_{\ell\sigma}^\dagger \hat{c}_\sigma), \qquad \hat{\mathcal{H}}_\text{I} = \left(\hat{n}_\uparrow - \frac{1}{2}\right)\left(\hat{n}_\downarrow - \frac{1}{2}\right). \tag{2.123}$$

Note that the term $\mu(\hat{n}_\uparrow + \hat{n}_\downarrow)$ with $\mu = \frac{U}{2}$ has been explicitly included in the definition of $\hat{\mathcal{H}}_\text{I}$.

Eq. (2.119) implies that:

$$\hat{\mathcal{H}}_0' = \hat{\mathcal{W}}_p^\dagger \hat{\mathcal{H}}_0 \hat{\mathcal{W}}_p = \hat{\mathcal{H}}_0, \qquad\qquad \hat{\mathcal{H}}_\text{I}' = \hat{\mathcal{W}}_p^\dagger \hat{\mathcal{H}}_\text{I} \hat{\mathcal{W}}_p = -\hat{\mathcal{H}}_\text{I}, \tag{2.124}$$

which means that only the sign of the interacting part $\hat{\mathcal{H}}_\text{I}$ changes under the transformation $\hat{\mathcal{W}}_p$ while $\hat{\mathcal{H}}_0$ is invariant. Taking furthermore into account that both parts of the Hamiltonian $\hat{\mathcal{H}}$ commute with the SU(2) (rotation) transformation $\hat{\mathcal{D}}$ separately, i.e.,

$$[\hat{\mathcal{D}}, \hat{\mathcal{H}}_0] = 0, \qquad\qquad [\hat{\mathcal{D}}, \hat{\mathcal{H}}_\text{I}] = 0, \tag{2.125}$$

it is obvious that they also commute with the new transformation $\hat{\mathcal{D}}_p$. Hence, we come to the conclusion that not only $\hat{\mathcal{D}}$ but also $\hat{\mathcal{D}}_p$ constitutes a symmetry of the particle-hole symmetric system which can be expressed as:

$$[\hat{\mathcal{D}}_p, \hat{\mathcal{H}}] = 0. \tag{2.126}$$

According to the definition of the rotation operator $\hat{\mathcal{D}}$ in Eq. (2.76), one can construct the transformed rotation operator $\hat{\mathcal{D}}_p$ by means of the transformed generators $\hat{\boldsymbol{S}}_p$:

$$\hat{\boldsymbol{S}}_p = \hat{\mathcal{W}}_p^\dagger \hat{\boldsymbol{S}} \hat{\mathcal{W}}_p, \tag{2.127}$$

where $\hat{\boldsymbol{S}}$ denotes the vector of spin operators as defined in Eq. (2.63). The calculation of the so-called "pseudospin" operators [53, 55] $\hat{\boldsymbol{S}}_p$ is now straightforward and yields:

$$\hat{\mathcal{S}}_{p,x} = -\frac{1}{2}\left(\hat{c}_\uparrow^\dagger \hat{c}_\downarrow^\dagger + \hat{c}_\downarrow \hat{c}_\uparrow\right), \tag{2.128a}$$

$$\hat{\mathcal{S}}_{p,y} = -\frac{1}{2i}\left(\hat{c}_\uparrow^\dagger \hat{c}_\downarrow^\dagger - \hat{c}_\downarrow \hat{c}_\uparrow\right), \tag{2.128b}$$

$$\hat{\mathcal{S}}_{p,z} = \frac{1}{2}\left(\hat{c}_\uparrow^\dagger \hat{c}_\uparrow + \hat{c}_\downarrow^\dagger \hat{c}_\downarrow - 1\right). \tag{2.128c}$$

Note that in Eqs. (2.128) only the symmetry operators at the impurity are stated while for a complete definition of $\hat{\boldsymbol{S}}$ a sum over the corresponding operators for the bath sites is needed as well [see also the definition of the spin operators in Eq. (2.63)]. However, the latter differ from the one for impurity, given in Eqs. (2.128), only by the sign in front of the first two equations [Eqs. (2.128a) and (2.128b)]. The generators of the pseudospin rotation can be interpreted physically as follows: $\hat{\mathcal{S}}_{p,z}$ represents simply the (charge) density operator of the system (or, more precisely, the deviation of the density from its half-filling value 1). The x- and y-component of the pseudospin $\hat{\mathcal{S}}_{p,x}$ and $\hat{\mathcal{S}}_{p,x}$, instead, correspond to local Cooper pair operators, describing the superconducting order parameter of the system. In this respect, the equivalence of all three components of the pseudospin in the local AIM, is a manifestation of the equivalence of the density and the superconducting fluctuations in the half-filled system, as it will be discussed in more detail at the end of this section [see, e.g., Eq. (2.139)].

It is now straightforward to show that these new "pseudospin" operators $\hat{\mathcal{S}}_{p,i}$ commute with the spin operators $\hat{\mathcal{S}}_j$. Furthermore, the unitary transformation $\hat{\mathcal{W}}_p$ preserves the commutator algebra of the SU(2) symmetry group leading to *two* independent SU(2) groups [SU(2)$_\text{S}$ for

the spin and $SU(2)_P$ for the pseudospin], whose entire algebra is defined as follows:

$$[\hat{\mathcal{S}}_i, \hat{\mathcal{S}}_j] = i\varepsilon_{ijk}\hat{\mathcal{S}}_k, \qquad [\hat{\mathcal{S}}_{p,i}, \hat{\mathcal{S}}_{p,j}] = i\varepsilon_{ijk}\hat{\mathcal{S}}_{p,k}, \qquad [\hat{\mathcal{S}}_i, \hat{\mathcal{S}}_{p,j}] = 0. \qquad (2.129)$$

Combining the two $SU(2)$ symmetry groups leads to[17] $SO(4) \simeq SU(2)_S \times SU(2)_P / Z_2$, explaining why the particle-hole symmetric AIM can by considered as $SO(4)$ symmetric.

Below the impact of a pseudospin rotation $\hat{\mathcal{D}}_p$ on the Green's functions will be analyzed. Since the pseudospin operator is obtained from the spin operator just by the transformation Eq. (2.120), the corresponding calculations are completely equivalent to those concerning the usual spin. In fact, considering the discussion in Sec. 2.2.2.2 in the paragraph below Eq. (2.78), one can obtain the analogous results for the pseudospin by transforming the spinors and operators by means of the partial particle-hole transformation $\hat{\mathcal{W}}_p$. To this end, we define the following (pseudo)spinors:

$$\hat{\mathbf{c}}_p := \begin{pmatrix} -\hat{c}_\uparrow \\ \hat{c}_\downarrow^\dagger \end{pmatrix} = \hat{\mathcal{W}}_p^\dagger \hat{\mathbf{c}} \hat{\mathcal{W}}_p, \qquad \hat{\mathbf{c}}_p^\dagger := \begin{pmatrix} -\hat{c}_\uparrow^\dagger \\ \hat{c}_\downarrow \end{pmatrix} = \hat{\mathcal{W}}_p^\dagger \hat{\mathbf{c}}^\dagger \hat{\mathcal{W}}_p, \qquad (2.130)$$

where $\hat{\mathbf{c}}$ and $\hat{\mathbf{c}}^\dagger$ have been specified in Eq. (2.77). For constructing the pseudospin rotation operator $\hat{\mathcal{D}}_p$, one can proceed in completely the same as for the spin rotation operator in Sec. 2.2.2.2, paragraph between Eqs. (2.78) and (2.83). Indeed, considering a pseudospin rotation about the y-axis through an angle φ for the operators $\hat{\mathbf{c}}_p$ and $\hat{\mathbf{c}}_p^\dagger$ yields:

$$\begin{pmatrix} -\hat{c}_\uparrow' \\ \hat{c}_\downarrow'^\dagger \end{pmatrix} = \begin{pmatrix} \cos(\frac{\varphi}{2}) & -\sin(\frac{\varphi}{2}) \\ \sin(\frac{\varphi}{2}) & \cos(\frac{\varphi}{2}) \end{pmatrix} \begin{pmatrix} -\hat{c}_\uparrow \\ \hat{c}_\downarrow^\dagger \end{pmatrix}, \quad \begin{pmatrix} -\hat{c}_\uparrow'^\dagger \\ \hat{c}_\downarrow' \end{pmatrix} = \begin{pmatrix} \cos(\frac{\varphi}{2}) & -\sin(\frac{\varphi}{2}) \\ \sin(\frac{\varphi}{2}) & \cos(\frac{\varphi}{2}) \end{pmatrix} \begin{pmatrix} -\hat{c}_\uparrow^\dagger \\ \hat{c}_\downarrow \end{pmatrix}, \quad (2.131)$$

for the transformed (pseudo)spinor $\hat{\mathbf{c}}_p'^{(\dagger)}$. Eq. (2.131) can be simply obtained from the corresponding equation for the spin rotation (2.83) by applying $\hat{\mathcal{W}}_p^\dagger$ and $\hat{\mathcal{W}}_p$ to the creation and annihilation operators [see Eq. (2.130)] in the latter relation.

Since $\hat{\mathcal{D}}_p$ represents a symmetry of the system, as usual, the following relation holds for the Green's function[18]:

$$G'_{n,\sigma_1...\sigma_{2n}}(\tau_1, \ldots, \tau_{2n}) = G_n(\hat{c}'^\dagger, \hat{c}', \hat{\mathcal{H}}) = G_{n,\sigma_1...\sigma_{2n}}(\tau_1, \ldots, \tau_{2n}). \qquad (2.132)$$

---

[17] Z_2 is the cyclic group of degree 2. A representation is, e.g., the set $\{1, -1\}$ with the ordinary multiplication as group operation [56, 57].

[18] The following discussion about the impact of the symmetry transformation $\hat{\mathcal{D}}_p$ on the Green's functions follows the same steps as the corresponding analysis for the $SU(2)$ symmetry operators $\hat{\mathcal{D}}$ in Sec. 2.2.2.2.

Similarly as for the spin rotation, we will consider two values of the angle φ:

- **$\varphi = \pi$:** Physically this choice of φ corresponds to transform the creation into annihilation operators and vice versa, plus an additional spin flip, as it can be directly obtained from Eqs. (2.131):

$$\hat{c}'^{\dagger}_{\sigma} = 2\sigma\hat{c}_{(-\sigma)}, \qquad\qquad \hat{c}'_{\sigma} = 2\sigma\hat{c}^{\dagger}_{(-\sigma)}, \qquad (2.133)$$

where $2\sigma = \pm 1$. Inserting these expressions into the Green's function G'_n and re-doing the spin flips by means of SU(2) symmetry, one retrieves exactly the same expression as for the (full) particle hole transformation already discussed in Sec. 2.2.2.5 [see in particular Eq. (2.103)]. Hence, we refer to this section for the investigation of the pseudospin rotation through π.

- **$\varphi = \frac{\pi}{2}$:** This choice of φ corresponds to the following transformation of the creation and annihilation operators [see Eq. (2.131)]:

$$\hat{c}'_{\sigma} = \frac{1}{\sqrt{2}}\left(\hat{c}_{\sigma} + 2\sigma\hat{c}^{\dagger}_{(-\sigma)}\right), \qquad \hat{c}'^{\dagger}_{\sigma} = \frac{1}{\sqrt{2}}\left(\hat{c}^{\dagger}_{\sigma} + 2\sigma\hat{c}_{(-\sigma)}\right), \qquad (2\sigma = \pm 1). \qquad (2.134)$$

For this transformation we restrict ourselves to the most relevant case of the two-particle Green's function. Inserting Eq. (2.134) into Eq. (2.132), and considering spin conservation [Eq. (2.66)], the invariance under spin flips [Eq. (2.87)], the crossing relation [Eq. (2.75)], time reversal invariance [Eq. (2.94)] as well as the particle hole symmetry [Eq. (2.108)] yields:

$$G_{2,\uparrow\uparrow}(\tau_1, \tau_2, \tau_3, \tau_4) = G_{2,\uparrow\downarrow}(\tau_1, \tau_4, \tau_2, \tau_3) - G_{2,\uparrow\downarrow}(\tau_1, \tau_2, \tau_4, \tau_3), \qquad (2.135)$$

or after a Fourier transform

$$G_{2,\uparrow\uparrow}(\nu_1, \nu_2, \nu_3) = G_{2,\uparrow\downarrow}(\nu_1, \nu_4, -\nu_2) - G_{2,\uparrow\downarrow}(\nu_1, \nu_2, -\nu_4) \qquad (2.136)$$

where $\nu_4 = \nu_1 - \nu_2 + \nu_3$ is defined by the requirement of energy conservation.

A similar derivation can be given also for the Hubbard Hamiltonian. However, since for the partial particle-hole transformation of lattice systems also the phase factors $e^{i\boldsymbol{\Pi}\mathbf{R}_i}$ occur [compare with Eq. (2.115) for the (full) particle-hole transformation], the generalization of the above AIM results to the Hubbard Hamiltonian is more involved than for the symmetries

in the previous sections. As the related equations are not relevant for this thesis we will avoid such complications here.

Let us finally investigate, instead, the impact of the $SU(2)_P$ symmetry on important physical quantities, such as the dynamic (one-frequency) local *susceptibilities*. These objects represent the time/frequency dependent autocorrelation functions for a selected physical observable $\hat{A}$ and read as:

$$\chi_{\hat{A}}(\omega) = \frac{1}{2} \int_0^\beta d\tau \, e^{i\omega\tau} \chi_{\hat{A}}(\tau) = \frac{1}{2} \int_0^\beta d\tau \, e^{i\omega\tau} \left\langle \left(\hat{A}(\tau) - \langle \hat{A} \rangle \right) \left(\hat{A}(0) - \langle \hat{A} \rangle \right) \right\rangle$$
$$= \frac{1}{2} \int_0^\beta d\tau \, e^{i\omega\tau} \left\langle \hat{A}(\tau) \hat{A}(0) \right\rangle - \frac{1}{2} \beta \delta_{\omega 0} \langle \hat{A} \rangle^2, \tag{2.137}$$

where $\langle \ldots \rangle$ and $\hat{A}(\tau)$ are defined analogously to Eqs. (2.27) and (2.28) for the Green's functions. $\chi_{\hat{A}}(\tau)$ describes the tendency of the system to "remember" the initial value of the observable $\hat{A}$ after a certain time τ. If, e.g., $\hat{A} = \hat{\mathcal{S}}_i$ is the spin in i-direction, $\chi_{\hat{\mathcal{S}}_i}(\tau)$ indicates whether the system exhibits locally a stable magnetic moment or not, corresponding to a constant or a decreasing behavior of the local susceptibility with respect to τ.

Let us now consider the susceptibilities for the generators $\hat{\mathcal{S}}_i$ and $\hat{\mathcal{S}}_{p,i}$ of the $SU(2)_S$ spin and the $SU(2)_P$ pseudospin group, respectively. It is easy to show that all the expectation values of these operators vanish in the half-filled case and, hence, one has to consider only the first contribution in the second line of Eq. (2.137)[19]. It is well known that in the $SU(2)_S$ symmetric case considered here the susceptibilities for each of the three spin directions $\hat{\mathcal{S}}_i, i = x, y, z$ coincide, i.e.,

$$\chi_{\hat{\mathcal{S}}_x}(\omega) = \chi_{\hat{\mathcal{S}}_y}(\omega) = \chi_{\hat{\mathcal{S}}_z}(\omega) =: \chi_m(\omega). \tag{2.138}$$

This equation should also hold for the pseudospins $\hat{\mathcal{S}}_{p,i}$ which is obviously the case for $\chi_{\hat{\mathcal{S}}_{p,x}}(\omega) = \chi_{\hat{\mathcal{S}}_{p,y}}(\omega)$. However, the equation $\chi_{\hat{\mathcal{S}}_{p,x}}(\omega) = \chi_{\hat{\mathcal{S}}_{p,z}}(\omega)$ leads to a relation between the so-called charge susceptibility $\chi_d(\omega) = \chi_{\hat{\mathcal{S}}_{p,z}}(\omega)$ and the particle-particle susceptibility $\chi_{pp}(\omega) = \chi_{\hat{\mathcal{S}}_{p,x}}(\omega)$ which measures the formation of electron (Cooper) pairs at the impurity, and, hence, constitutes a hallmark of superconductivity. Therefore, one expects that the following relation holds:

$$\chi_d(\omega) \equiv \chi_{pp}(\omega), \tag{2.139}$$

which can be explicitly proven by means of Eq. (2.135) when restricting the time arguments

---

[19]For $\hat{\mathcal{S}}_{p,z} = \hat{n} - 1$ consider that $\langle \hat{n} \rangle = 1$ since we are at half filling.

of the Green's functions entering this equation in the following way ($\tau_1 = \tau$):

$$\lim_{\tau_4 \to 0} \lim_{\tau_3 \to \tau_4+} \lim_{\tau_2 \to \tau-} G_{2,\uparrow\uparrow}(\tau, \tau_2, \tau_3, \tau_4) = \lim_{\tau_4 \to 0} \lim_{\tau_3 \to \tau_4+} \lim_{\tau_2 \to \tau-} \left[G_{2,\uparrow\downarrow}(\tau, \tau_4, \tau_2, \tau_3) - G_{2,\uparrow\downarrow}(\tau, \tau_2, \tau_4, \tau_3) \right].$$
(2.140)

Resorting to the definition of the Green's function in τ space one has

$$\langle \hat{n}_\uparrow(\tau) \hat{n}_\uparrow(0) \rangle = \langle \hat{c}_\uparrow^\dagger \hat{c}_\downarrow^\dagger(\tau) \hat{c}_\downarrow \hat{c}_\uparrow(0) \rangle - \langle \hat{n}_\uparrow(\tau) \hat{n}_\downarrow(0) \rangle + \frac{\langle \hat{n} \rangle}{2},$$
(2.141)

which coincides exactly with Eq. (2.139) after performing the Fourier transform with respect to τ.

2.2.3 Definitions and Symmetry relations: An overview

This section is devoted to provide a concise list of the definitions of all relevant one- and two-particle quantities specifically used in this thesis as well as a compact summary of their symmetry properties. For this reason, here, we will present the final equations only (making reference to the more general results of the previous section).

The *one-particle* Green's function is defined as

$$G_{1,i_1 i_2}(\tau_1, \tau_2) = \left\langle \mathrm{T} \left[\hat{c}_{i_1}^\dagger(\tau_1) \hat{c}_{i_2}(\tau_2) \right] \right\rangle.$$
(2.142)

For the Hubbard model $i_j = (\mathbf{R}_j, \sigma_j)$ while for the AIM $i_j = \sigma_j$. Performing the Fourier transform under consideration of all symmetries, i.e., omitting all the unnecessary indices, leads to the definition

$$G(\nu, \mathbf{k}) = \sum_{\mathbf{R}_i} \int_0^\beta d\tau \, e^{-i(\nu\tau - \mathbf{k}\mathbf{R}_i)} G_{1,(\mathbf{R}_i \sigma)(\mathbf{R}_0 \sigma)}(\tau, 0),$$
(2.143)

where $\mathbf{R}_0$ denotes the origin of the of the lattice, i.e., $\mathbf{R}_0 = (0, 0, 0)^{\mathrm{T}}$ in the three-dimensional case. The corresponding definition for the AIM can be easily obtained from Eq. (2.143) by "deleting" all spatial degrees of freedom, i.e., $\mathbf{R}_i$ and/or $\mathbf{k}$, in this and the following equation(s). The properties of the **one-particle** Green's function can be summarized as follows:

- $G^*(\nu, \mathbf{k}) = G(-\nu, \mathbf{k})$: general rule for complex conjugation [Eq. (2.39 in Sec. 2.2.1.3].

- $G(\nu, -\mathbf{k}) = G(\nu, \mathbf{k})$: space reversal symmetry [Eqs. (2.97) and (2.98) in Sec. 2.2.2.3].

- $G^*(\nu, \mathbf{k}) = -G(\nu, \mathbf{\Pi} - \mathbf{k})$, where $\mathbf{\Pi} = (\pi, \dots, \pi)^{\mathrm{T}}$: particle-hole symmetry if $\mu = \frac{U}{2}$ [Eqs. (2.109) and (2.117) in Sec. 2.2.2.5].

Note that the boundary conditions, the time- and space-translation invariance as well as the SU(2) [and the SU(2)$_\mathrm{P}$] symmetry are already implicitly included in the definition of the one-particle Green's function by considering it as function of *only one* frequency and momentum without any spin dependence. While, as mentioned in Sec. 2.2.1.2, there is no crossing symmetry in the one-particle case, the time reversal symmetry only yields the trivial relation $G(\nu, \mathbf{k}) = G(\nu, \mathbf{k})$.

For the **two-particle** Green's function we restrict ourselves for the sake of simplicity to the AIM (or, equivalently, to the local Green's function of the Hubbard model), for which numerical results are discussed in the next chapter. However, the generalization to the non-local degrees of freedom of the Hubbard model is, in most of the cases, straightforward. Let us recall first the most general definition of the two-particle Green's function:

$$G_{2,\sigma_1\sigma_2\sigma_3\sigma_4}(\tau_1, \tau_2, \tau_3, \tau_4) = \left\langle \mathrm{T}\left[\hat{c}^\dagger_{\sigma_1}(\tau_1)\hat{c}_{\sigma_2}(\tau_2)\hat{c}^\dagger_{\sigma_3}(\tau_3)\hat{c}_{\sigma_4}(\tau_4)\right]\right\rangle. \tag{2.144}$$

Usually one does not work with the two-particle Green's function directly but considers, as we will also do in the next chapters, the following combination of one- and two-particle Green's functions:

$$\chi_{\sigma_1\sigma_2\sigma_3\sigma_4}(\tau_1, \tau_2, \tau_3, \tau_4) := G_{2,\sigma_1\sigma_2\sigma_3\sigma_4}(\tau_1, \tau_2, \tau_3, \tau_4) - G_{1,\sigma_1\sigma_2}(\tau_1, \tau_2)G_{1,\sigma_3\sigma_4}(\tau_3, \tau_4), \tag{2.145}$$

which is coined *generalized susceptibility*[20]. Its one-particle ("bubble") contribution [second term on the right-hand side of Eq. (2.145)] is referred to as *bare susceptibility*

$$\chi_{0,\sigma_1\sigma_2\sigma_3\sigma_4}(\tau_1, \tau_2, \tau_3, \tau_4) = -G_{1,\sigma_1\sigma_4}(\tau_1, \tau_4)G_{1,\sigma_3\sigma_2}(\tau_3, \tau_2), \tag{2.146}$$

which describes the independent propagation of one particle/hole. This means that Eq. (2.145) can be rewritten as:

$$\chi_{\sigma_1\sigma_2\sigma_3\sigma_4}(\tau_1, \tau_2, \tau_3, \tau_4) = G_{2,\sigma_1\sigma_2\sigma_3\sigma_4}(\tau_1, \tau_2, \tau_3, \tau_4) + \chi_{0,\sigma_1\sigma_4\sigma_3\sigma_2}(\tau_1, \tau_4, \tau_3, \tau_2). \tag{2.147}$$

Taking into account the time translation invariance of the system we can set $\tau_4 = 0$ and

---

[20]*Physical* susceptibilities, depending on just one time/frequency arguments, as defined in Eq. (2.137), can be obtained from the corresponding generalized susceptibilities by taking the limits $\tau_2 \to \tau_1-$, $\tau_4 \to \tau_3-$ and, finally, $\tau_4 \to 0$.

consider susceptibilities depending only on three times [see Eq. (2.54) in Sec. 2.2.2.1]. Furthermore, the restrictions on the spin degrees of freedom imposed by the SU(2) symmetry [Eq. (2.73) and below in Sec. 2.2.2.2] suggest to replace the four-spin object by a quantity depending on two spins only. Hence, it proves convenient to introduce the following definitions, as it was done for the two-particle Green's function G_2 [Eq. (2.74) in Sec. 2.2.2.2], also for the susceptibilities:

$$\chi_{\sigma\sigma'}(\tau_1, \tau_2, \tau_3) := \chi_{\sigma\sigma\sigma'\sigma'}(\tau_1, \tau_2, \tau_3, 0) \tag{2.148a}$$

$$\chi_{\overline{\sigma\sigma'}}(\tau_1, \tau_2, \tau_3) := \chi_{\sigma\sigma'\sigma'\sigma}(\tau_1, \tau_2, \tau_3, 0). \tag{2.148b}$$

While for $\sigma = \sigma'$ both definitions of course coincide, $\chi_{\overline{\sigma\sigma'}}$ is equal to the two-particle Green's function $G_{2,\overline{\sigma\sigma'}}$ in the other case ($\sigma \neq \sigma'$), since the term which should be subtracted according to Eq. (2.145) vanishes ($G_{1,\sigma\sigma'} = 0$ for $\sigma \neq \sigma'$). However, using the crossing symmetry [Eqs. (2.37) in Sec. 2.2.1.2] one can show that the quantity defined in Eq. (2.148b) can be derived from the one in Eq. (2.148a) by means of a permutation of the time or - in Fourier space - frequency arguments as shown in in Sec. 2.2.2.2, Eq. (2.75). Hence, we will consider explicitly Eq. (2.148a) only, making reference to Eq. (2.148b) just in some specific cases.

After taking the Fourier transform, the generalized susceptibility χ depends only on three fermionic Matsubara frequencies ν_1, ν_2 and ν_3 ($\nu_4 = \nu_1 - \nu_2 + \nu_3$ in the four-frequency object $\widetilde{G}_2$) as a consequence of time-translation symmetry [Eq. (2.58) in Sec. 2.2.2.1]. Here, it is convenient to introduce the two following frequency conventions, which are known as particle-hole (ph) and particle-particle (pp) notation, respectively:

$$
\begin{array}{llll}
\boldsymbol{ph}: & \nu_1 = \nu & \boldsymbol{pp}: & \nu_1 = \nu & \text{(2.149a)} \\
& \nu_2 = \nu + \omega & & \nu_2 = \omega - \nu' & \text{(2.149b)} \\
& \nu_3 = \nu' + \omega & & \nu_3 = \omega - \nu & \text{(2.149c)} \\
& \nu_4 = \nu' & & \nu_4 = \nu', & \text{(2.149d)}
\end{array}
$$

where $\nu = \frac{\pi}{\beta}(2n+1)$ and $\nu' = \frac{\pi}{\beta}(2n'+1)$ are fermionic Matsubara frequencies and $\omega = \frac{\pi}{\beta}(2m)$ is a bosonic Matsubara frequency. Taking into account that that the creation/annihilation operators are connected with outgoing/incoming electrons and incoming/outgoing holes, respectively, the choice of the frequency convention has a clear physical motivation in both cases:

- In the ph-case one considers the scattering process of an electron with energy $\nu + \omega$ and a hole with energy $-\nu$, i.e., the transferred energy of this process is ω.
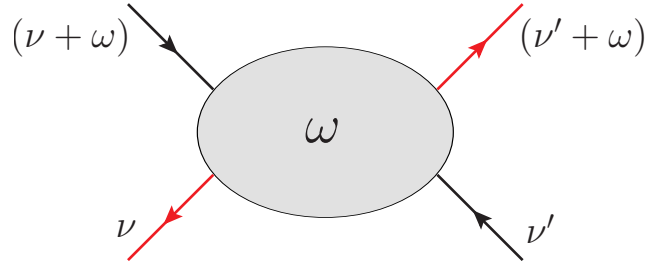
- In the *pp*-case we look at the scattering of two electrons with energies ν' and $\omega - \nu'$. Again the transferred energy of this process is ω.
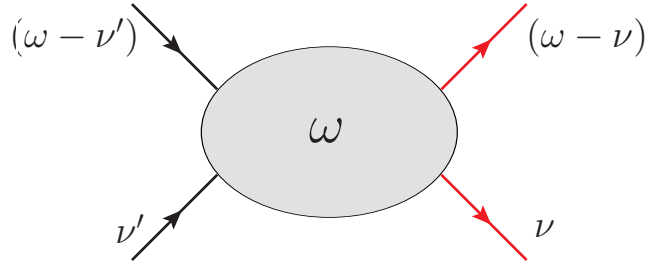
Hence, we define the Fourier transform of the generalized susceptibility in a twofold way, adopting the two frequency conventions discussed above:

$$\chi_{\sigma\sigma'}^{\nu\nu'\omega} := \chi_{ph,\sigma\sigma'}^{\nu\nu'\omega} := \chi\Big(\underbrace{\nu\sigma, (\nu'+\omega)\sigma'}_{\text{outgoing electrons}}; \underbrace{\nu'\sigma', (\nu+\omega)\sigma}_{\text{incoming electrons}}\Big) :=$$

$$:= \int_0^\beta d\tau_1 d\tau_2 d\tau_3 \, \chi_{\sigma\sigma'}(\tau_1, \tau_2, \tau_3) e^{-i\nu\tau_1} e^{i(\nu+\omega)\tau_2} e^{-i(\nu'+\omega)\tau_3},$$

$$(2.150a)$$

$$\chi_{pp,\sigma\sigma'}^{\nu\nu'\omega} := \chi\Big(\underbrace{\nu\sigma, (\omega-\nu)\sigma'}_{\text{outgoing electrons}}; \underbrace{(\omega-\nu')\sigma, \nu'\sigma'}_{\text{incoming electrons}}\Big) :=$$

$$(2.150b)$$

$$:= \int_0^\beta d\tau_1 d\tau_2 d\tau_3 \, \chi_{\sigma\sigma'}(\tau_1, \tau_2, \tau_3) e^{-i\nu\tau_1} e^{i(\omega-\nu')\tau_2} e^{-i(\omega-\nu)\tau_3},$$

Since in the full two-particle Green's function both particle-hole and particle-particle scattering processes are simultaneously included, it is possible to express χ_{pp} in terms of χ_{ph} and vice versa:

$$\chi_{pp,\sigma\sigma}^{\nu\nu'\omega} = \chi_{ph,\sigma\sigma'}^{\nu\nu'(\omega-\nu-\nu')} \qquad\qquad \chi_{ph,\sigma\sigma}^{\nu\nu'\omega} = \chi_{pp,\sigma\sigma'}^{\nu\nu'(\omega+\nu+\nu')}. \qquad (2.151)$$

Symmetry	Relation in *ph*-notation	Reference
Crossing symmetry	$\chi_{\overline{\sigma\sigma'}}^{\nu\nu'\omega} - \delta_{\sigma\sigma'}\chi_0^{\nu(\nu+\omega)(\nu'-\nu)} = -\chi_{\sigma\sigma'}^{\nu(\nu+\omega)(\nu'-\nu)} + \chi_0^{\nu\nu'\omega}$	Sec. 2.2.1.2, Eq. 2.37
Complex conjugation	$\left(\chi_{\sigma\sigma'}^{\nu\nu'\omega}\right)^* = \chi_{\sigma'\sigma}^{(-\nu')(-\nu)(-\omega)} \stackrel{\mathrm{SU(2)}}{=} \chi_{\sigma\sigma'}^{(-\nu')(-\nu)(-\omega)}$	Sec. 2.2.1.3, Eq. 2.39
SU(2) symmetry	$\chi_{\sigma\sigma'}^{\nu\nu'\omega} = \chi_{(-\sigma)(-\sigma')}^{\nu\nu'\omega} = \chi_{\sigma'\sigma}^{\nu\nu'\omega}$ $\chi_{\sigma\sigma}^{\nu\nu'\omega} = \chi_{\sigma(-\sigma)}^{\nu\nu'\omega} - \chi_{\sigma(-\sigma)}^{\nu(\nu+\omega)(\nu'-\nu)} + \chi_0^{\nu\nu'\omega}$	Sec. 2.2.2.2, Eqs. 2.87, 2.89
Time reversal symmetry	$\chi_{\sigma\sigma'}^{\nu\nu'\omega} = \chi_{\sigma'\sigma}^{\nu'\nu\omega} \stackrel{\mathrm{SU(2)}}{=} \chi_{\sigma\sigma'}^{\nu\nu'\omega}$	Sec. 2.2.2.3, Eq. 2.95
Particle-hole symmetry $\left(\mu = \frac{U}{2}\text{ only}\right)$	$\left(\chi_{\sigma\sigma'}^{\nu\nu'\omega}\right)^* = \chi_{\sigma\sigma'}^{\nu\nu'\omega}$	Sec. 2.2.2.5, Eqs. 2.108-2.110
SU(2)$_\mathrm{P}$ symmetry $\left(\mu = \frac{U}{2}\text{ only}\right)$	$\chi_{\sigma\sigma}^{\nu\nu'\omega} = \chi_{\sigma(-\sigma)}^{\nu(-\nu'-\omega)(\nu'-\nu)} - \chi_{\sigma(-\sigma)}^{\nu(-\nu'-\omega)\omega} + \chi_0^{\nu\nu'\omega}$	Sec. 2.2.2.6, Eq. 2.136

Table 2.1: Summary of the symmetry relations for the susceptibilities in *ph*-notation.

In reason of this, we will focus mainly on $\chi \equiv \chi_{ph}$ and consider explicitly χ_{pp} in specific cases only.

The corresponding susceptibility χ_0 does not exhibit any spin dependence at all, since it is just the product of two one-particle Green's functions. Indeed, performing the Fourier transform of Eq. (2.146), we obtain

$$\widetilde{\chi}_0(\nu_1, \nu_2, \nu_3, \nu_4) = -\beta^2 G(\nu_1)G(\nu_2)\delta_{\nu_1\nu_4}\delta_{\nu_2\nu_3} =: \chi_0(\nu_1, \nu_2, \nu_3)\beta\delta_{\nu_1\nu_4}. \tag{2.152}$$

Using the frequency conventions introduced above for the susceptibilities we arrive at the

following definitions:

$$\chi_0^{\nu\nu'\omega} := \chi_{0,ph}^{\nu\nu'\omega} := -\beta G(\nu)G(\nu+\omega)\delta_{\nu\nu'} \qquad \chi_{0,pp}^{\nu\nu'\omega} := -\beta G(\nu)G(\omega-\nu)\delta_{\nu\nu'}. \qquad (2.153)$$

Eventually, for the sake of conciseness, we have summarized in Tab. 2.1 the most important symmetry-properties of the generalized susceptibilities discussed in this chapter for the *ph*-notation, reporting also the reference to the corresponding sections, where they are derived and discussed in more detail. Note that the boundary conditions, the time-translation invariance as well as (partially) also the SU(2) symmetry are already intrinsically included in the definition of the generalized susceptibility by considering it as a function of *only three* frequencies and *two* spins. Finally, we note here that, by means of Eqs. (2.151) and (2.153), it is straightforward to derive relations analogue to the ones given in Tab. 2.1 also in particle-particle notation. The corresponding results can be found in Appendix A.

Let us finally illustrate how the physical susceptibilities $\chi_{\sigma\sigma'}(\omega)$ and $\chi_{pp,\sigma\sigma'}(\omega)$, can be obtained from the generalized ones. As already discussed at the end of Sec. 2.2.2.5 (see, in particular, page 55), these one-frequency objects describe the (linear) response of a system to an external perturbation. Specifically, these response functions can be calculated from the corresponding generalized susceptibilities by a summation over all the fermionic variables, as follows:

$$\chi_{\sigma\sigma'}(\omega) = \frac{1}{\beta^2}\sum_{\nu\nu'}\chi_{\sigma\sigma'}^{\nu\nu'\omega}, \qquad\qquad \chi_{pp,\sigma\sigma'}(\omega) = \frac{1}{\beta^2}\sum_{\nu\nu'}\chi_{pp,\sigma\sigma'}^{\nu\nu'\omega}. \qquad (2.154)$$

The corresponding density, magnetic and particle-particle susceptibilities, considered in Sec. 2.2.2.5, page 55, are then defined as $\chi_d(\omega) = \chi_{\uparrow\uparrow}(\omega) + \chi_{\uparrow\downarrow}(\omega)$, $\chi_m(\omega) = \chi_{\uparrow\uparrow}(\omega) - \chi_{\uparrow\downarrow}(\omega)$ and $\chi_{pp}(\omega) = \chi_{pp,\uparrow\downarrow}(\omega)$. Let us remark that, analogously to Eq. (2.154), also the bare response function $\chi_{0,(pp)}(\omega)$ can be defined as the ν,ν'-sum of the corresponding bare susceptibility $\chi_{0,(pp)}^{\nu\nu'\omega}$.

2.2.4 Green's functions and Feynman diagrams

In this section we will use the technique of Feynman diagrams [32,33,38], i.e., a diagrammatic representation of the perturbative expansion around the non-interacting case $U = 0$, to gain further insight into the structure of the one- and the two-particle Green's functions. This will allow for a deeper understanding of the physical content of the Green's functions and will prove also important for the development of new approximation schemes, well beyond

$$G_0(\nu)$$

Figure 2.4: Diagrammatic elements for the AIM. The corresponding diagrammatic elements for the Hubbard model can be obtained by simply replacing the local non-interacting Green's function $G_0(\nu)$ with the corresponding (**k** dependent) non-interacting Green's function of the lattice model $G_0(\nu, \mathbf{k})$.

perturbation theory, for the calculation of the Green's functions in the intermediate-to-strong interaction case. The basic elements of the diagrammatic technique are depicted in Fig. 2.4 for the impurity (local) Green's function of the AIM. $G_0(\nu)$ denotes the bare one-particle impurity Green's function, i.e., the local Green's function for the non-interacting system ($U = 0$) while the interaction, which is given just by a purely local repulsion U in the case of the Hubbard model and the AIM, is represented by a dot which connects four Green's function lines corresponding to the two incoming and two outgoing fermions, respectively. We recall, that energy (=frequency), momentum and spin have to be conserved at each vertex, i.e., the sum of these quantities for the incoming particles must coincide with the sum for the outgoing ones. Furthermore, if both incoming particles exhibit the same spin the corresponding contribution of the diagram on the right-hand side of Fig. 2.4 vanishes due to the specific structure of the interaction term[21].

Let us stress that, because of the local nature of the electronic interaction, the diagrammatic structure of the AIM and the Hubbard model exhibit important similarities. Hence, in order to avoid redundancy by presenting almost "equivalent" diagrams and equations for both models, we introduce the following unifying notation for the time/space and the frequency/momentum arguments, respectively: All results, obtained for the (purely local!) AIM hold also for the Hubbard model when replacing the (imaginary) time τ with the four-vector $(\tau, \mathbf{R}_i)$, where $\mathbf{R}_i$ is a lattice vector, or accordingly in Fourier space, replacing the (Matsubara) frequency ν with $(\nu, \mathbf{k})$, where $\mathbf{k}$ is a momentum vector located in the first Brillouin zone. For time integrations and frequency summations, respectively, one has to consider the

---

[21]The interaction term is given for both models by $U\hat{n}_\uparrow\hat{n}_\downarrow$, i.e., the interaction takes place only for particles with opposite spins. This is obviously a direct consequence of the "local" nature of the interaction and of the Pauli principle.
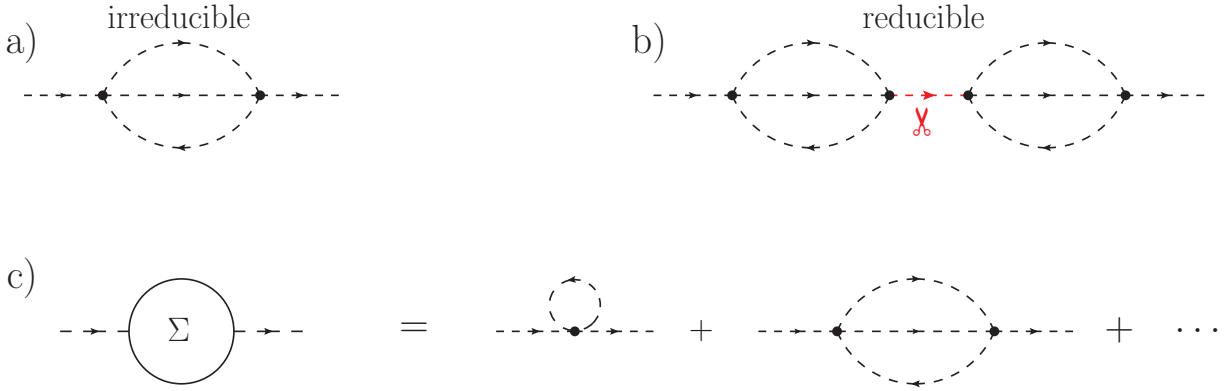
Figure 2.5: a) Irreducible diagram for the one-particle Green's function; b) Reducible diagram: the diagram falls apart if one cuts the red dashed line; c) Summing up irreducible diagrams (without external legs), yields the so-called self-energy.

generalizations

$$\int_0^\beta d\tau \, e^{-i\nu\tau} \Longrightarrow \sum_{\mathbf{R}_i} \int_0^\beta d\tau \, e^{-i(\nu\tau - \mathbf{k}\mathbf{R}_i)} \quad \text{and} \quad \frac{1}{\beta} \sum_\nu \Longrightarrow \frac{1}{\beta} \sum_\nu \frac{1}{V_{\text{BZ}}} \int_{\text{BZ}} d^d k, \quad (2.155)$$

where BZ denotes the first Brillouin zone and V_{BZ} its volume (e.g., $V_{\text{BZ}} = \frac{1}{(2\pi)^d}$ for the simple cubic lattice in d dimensions with the lattice constant $a = 1$ which will be mainly considered in this thesis). Derivations and equations, where the differences between the Hubbard model and the AIM cannot be taken into account by a mere replacement of a frequency variable by a four-vector containing frequency and momentum will be accentuated explicitly in this section.

2.2.4.1 One-particle Green's functions

Since the diagrammatic techniques for treating the *one-particle* Green's function can be found in the textbooks [32, 33, 38], we just summarize the most important features here. The set of all Feynman diagrams for the one-particle Green's function can be divided into two classes according to the topological structure of the diagrams. A diagram is called *one-particle irreducible* if it cannot be split into two sub-diagrams by cutting *one* internal Green's function line G_0 (Fig. 2.5a) otherwise it is coined *reducible* (Fig. 2.5b). Summing up all irreducible diagrams as depicted in Fig. 2.5c and amputating the external legs yields the so-called *self-energy* of the system. All reducible diagrams in turn can be constructed by connecting an arbitrary number of irreducible diagrams with G_0 lines. Summing up all
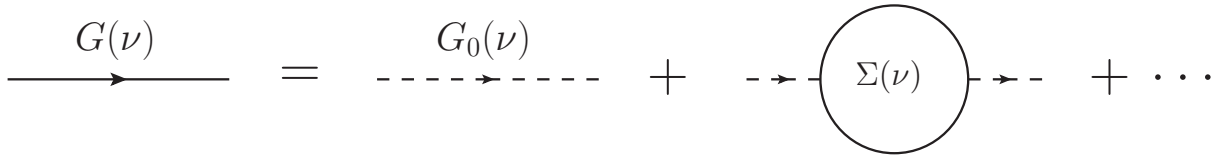
Figure 2.6: Diagrammatic representation of the Dyson equation.

contributions (reducible and irreducible) one obtains the Dyson equation:

$$G(\nu) = G_0(\nu) + G_0(\nu)\Sigma(\nu)G_0(\nu) + \ldots = \frac{1}{[G_0(\nu)]^{-1} - \Sigma(\nu)}, \tag{2.156}$$

which is illustrated diagrammatically in Fig. 2.6). A continuous line denotes the full interacting Green's function $G(\nu)$ of the system.

We can now introduce corrections to the bare Green's functions G_0 which constitute self-energy diagrams such as the one depicted in Fig. 2.5a. Summing up all such contributions one can replace the bare Green's function G_0 by the full interacting one G as it is shown in Fig. 2.7a. Hence, it is possible to construct all Feynman diagrams for the self-energy also in terms of the full, instead of the non-interacting, Green's function. However, in order to avoid double-counting, when working with the full G, one has to restrict oneself to a subset of diagrams coined *skeleton diagrams*. They are characterized by the fact that their internal Green's function lines do not contain any self-energy insertions (see, e.g., Fig. 2.7b). This is necessary since the full Green's function already takes into account *all* possible one-particle self-energy corrections and, hence, a diagram as depicted in Fig. 2.7c would lead to a double counting of such terms.

2.2.4.2   Two-particle Green's function

The two-particle Green's function will be discussed exclusively in terms of skeleton diagrams, i.e., all the lines represent full interacting Green's functions G.

For a non-interacting system ($U = 0$), the Wick's theorem [38] states that the two-particle Green's functions can be represented as a sum of products of one-particle Green's functions, i.e.,

$$G_{2,\sigma\sigma'}^{(U=0)}(\nu, \nu + \omega, \nu' + \omega) = \beta G_0(\nu)G_0(\nu')\delta_{\omega 0} - \beta G_0(\nu)G_0(\nu + \omega)\delta_{\nu\nu'}\delta_{\sigma\sigma'}. \tag{2.157}$$

For the calculation of the susceptibility one has to subtract the first summand on the right-
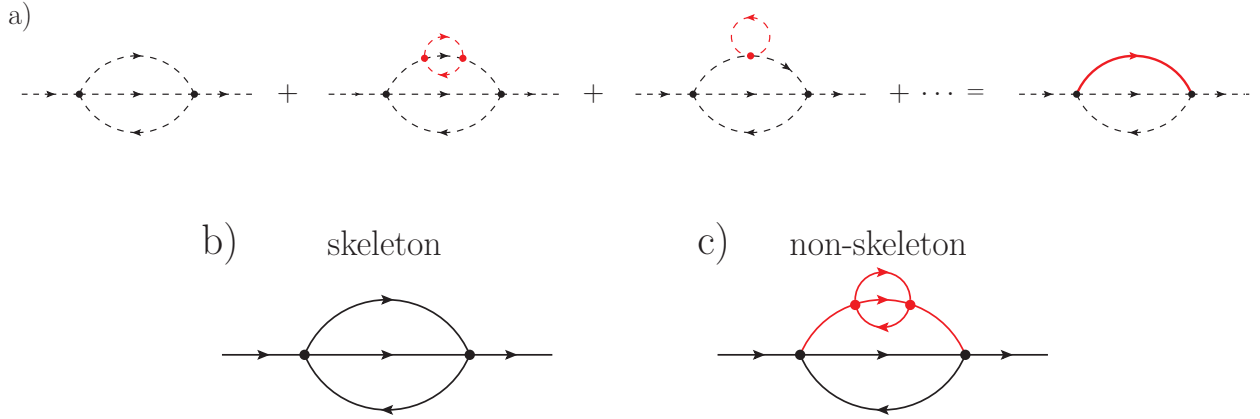
Figure 2.7: a) Dressing the internal lines of a self-energy diagram; b) A skeleton diagram; c) A non-skeleton diagram where one of the internal Green's functions is dressed by a self-energy correction.

Figure 2.8: Diagrammatic representation of $\chi_{\sigma\sigma'}^{\nu\nu'\omega}$. The figure is readapted from Ref. [48].

hand side of Eq. (2.157) which yields:

$$\chi_{(U=0),\sigma\sigma'}^{\nu\nu'\omega} = -\beta G_0(\nu)G_0(\nu+\omega)\delta_{\nu\nu'}\delta_{\sigma\sigma'} = \chi_0^{\nu\nu'\omega}\delta_{\sigma\sigma'}, \tag{2.158}$$

justifying the denomination of a product of Green's functions as χ_0. For the interacting case ($U \neq 0$), in addition to the dressing of the bare Green's function G_0 by the self-energy (see Fig. 2.6, $G_0 \to G$) in Eqs. (2.157) and (2.158), another important term arises. This describes the scattering processes between *two* particles or a particle and a hole, respectively. Hence, one will naturally decompose the susceptibility χ into two parts, which are shown diagrammatically in Fig. 2.8 and analytically read as:

$$\chi_{\sigma\sigma'}^{\nu\nu'\omega} = -\beta G(\nu)G(\nu+\omega)\delta_{\nu\nu'}\delta_{\sigma\sigma'} - G(\nu)G(\nu+\omega)F_{\sigma\sigma'}^{\nu\nu'\omega}G(\nu')G(\nu'+\omega). \tag{2.159}$$

One can see that in addition to the so-called *unconnected* part of the generalized suscepti-
bility, already present in Eq. (2.158) for the non-interacting case $U = 0$, a vertex part, i.e., a
term containing the so-called full vertex function F, occurs in Eq. (2.159) for the generalized
susceptibility at $U \neq 0$. Since this contribution to the susceptibility does not decompose into
a product of two one-particle Green's functions, we refer to it as *connected* part. In the Fermi
liquid regime, where one-particle excitations are unambiguously defined, the vertex function
F can be interpreted physically as scattering amplitude between two quasi-particles [38].
Considering the definition of the bare susceptibility [Eq. (2.153)] we can express the full
generalized susceptibility χ as:

$$\chi_{\sigma\sigma'}^{\nu\nu'\omega} = \chi_0^{\nu\nu'\omega}\delta_{\sigma\sigma'} - \frac{1}{\beta^2}\sum_{\nu_1\nu_2}\chi_0^{\nu\nu_1\omega}F_{\sigma\sigma'}^{\nu_1\nu_2\omega}\chi_0^{\nu_2\nu'\omega}. \tag{2.160}$$

For the other spin combination ($\overline{\uparrow\downarrow}$), the almost same definition holds, differing from the $\uparrow\downarrow$
susceptibility only with respect to the factor $\delta_{\sigma\sigma'}$ in χ_0:

$$\chi_{\overline{\sigma\sigma'}}^{\nu\nu'\omega} = \chi_0^{\nu\nu'\omega} - \frac{1}{\beta^2}\sum_{\nu_1\nu_2}\chi_0^{\nu\nu_1\omega}F_{\overline{\sigma\sigma'}}^{\nu_1\nu_2\omega}\chi_0^{\nu_2\nu'\omega}. \tag{2.161}$$

Analogous definitions can be introduced for the particle-particle notation.

"Topological" structure of the diagrams for the vertex function F

In the following we will discuss the "topological" structures of diagrams for the full vertex
function F. Let us recall that F represents the connected part of the generalized susceptibility
without the outer legs, i.e., the four (one-particle) Green's functions which constitute the two
incoming and the two outgoing particles have been singled out as one can see in Eq. (2.159).
If we consider *one-particle irreducibility*, as we did for the self-energy in a previous paragraph
(see Fig. 2.5), it turns out that all contributions to F exhibit this property, i.e., the two-
particle vertex function does not contain any *one-particle reducible* diagram. This state of
affairs is illustrated in Figs. 2.9a,b where such, hypothetical, one-particle reducible diagrams
for the two-particle vertex function are drawn. However, one sees immediately that diagrams
as depicted in Fig. 2.9a are forbidden due to a violation of particle conservations at the red
vertices, while the diagram shown in Fig. 2.9b contains spurious non-skeleton contributions
(red box) and, hence, is not included in the diagrammatic technique[22]. Let us stress that

---

[22]The one-particle reducible part of the latter diagram represents, in fact, an outer leg of F which is
amputated.
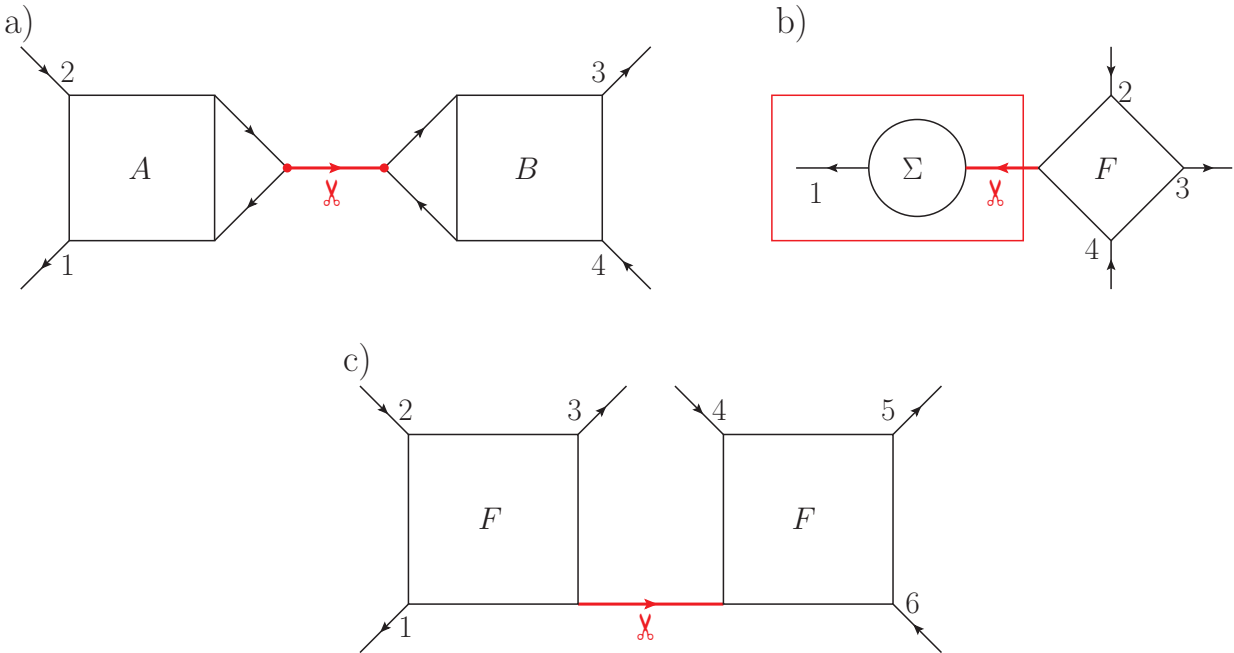
Figure 2.9: a) Hypothetical one-particle reducible diagram for F: This diagram vanishes due to a violation of particle conservation at the red vertices. b) Hypothetical one-particle reducible diagram for F: This diagram does not contribute since the Green's function inside the red box contains a self-energy correction which is not allowed for skeleton diagrams. c) One-particle reducible contribution to the three-particle vertex function. The numbers $1 \ldots 6$ denote the incoming/outgoing particles.
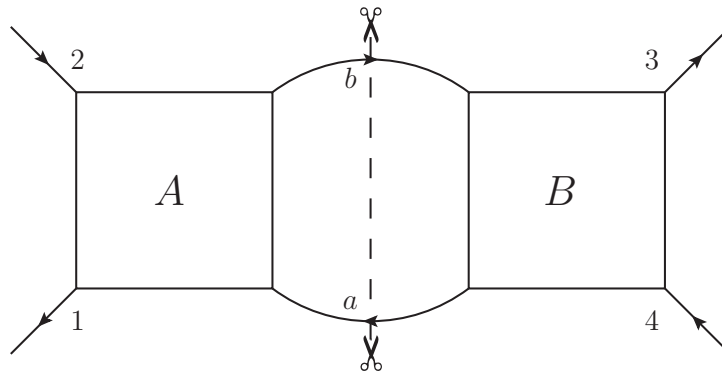
Figure 2.10: Schematic representation of a generic particle-hole reducible diagram contributing to the (full) scattering amplitude F. The figure is readapted from Ref. [48].

the nonexistence of one-particle reducible diagrams is an intrinsic characteristic of the two-particle vertex functions. Indeed, for three- and more-particle vertices such diagrams appear as it is illustrated in Fig. 2.9c.

Parquet equation

Since the property of one-particle irreducibility does not play any discriminating role for two-particle vertex functions (differently from the one-particle case) if we aim at a classification of these two-particle diagrams, we should turn to the concept of *two-particle irreducibility*. This leads to a classification of diagrams with respect to the way they can be split into two parts by cutting *two* internal Green's function lines.

- *Fully irreducible:* These diagrams of F cannot be split into two parts by cutting two internal Green's function lines. They correspond somehow to the self-energy diagrams at the one-particle level, which are one-particle irreducible.

- *Reducible:* A diagram of F is reducible if it can be split into two parts by cutting *two* internal Green's function lines. However, at the two-particle level the concept of reducibility is "richer" than at the one-particle level. In fact, there are more possibilities of cutting lines than in the one-particle case, and, therefore, the notion of reducibility always refers to one of these possibilities, i.e., to a specific channel. The channel specifies, in which way two of the four outer legs of a given diagram can be separated from the other two. Labeling the outer legs with 1, 2, 3, 4, where 1 and 3 denote outgoing particles while 2 and 4 refer to the incoming ones, it is clear that three different possibilities exist: Diagrams where (1 3) can be separated from (2 4) are coined particle-particle (pp) reducible, while the other two cases, i.e., (1 2) from (3 4) and (1 4) from (2 3), are referred to as particle-hole longitudinal (ph) and particle-hole transversal ($\overline{ph}$) reducible diagrams, respectively. An example for a diagram which is reducible in the longitudinal particle-hole channel is shown in Fig. 2.10 where (1 2) can be separated from (3 4) by cutting the internal lines a and b.

It should be stressed that each diagram is either fully irreducible or reducible in exactly one channel, i.e., no diagrams that are reducible in two or more channels can exist. This can be easily seen by the following argument: Consider a diagram that is reducible in the longitudinal particle-hole channel (ph) as that shown in Fig. 2.10. It is clear that the subdiagram A can be separated from B by cutting the Green's function lines a and b. Let us assume that the diagram is reducible in the (1 4)-(2 3) channel [=transversal particle-hole channel ($\overline{ph}$)] as well, i.e., it can be split into two parts, one containing the outer legs 1 and 4 the other one containing 2 and 3, by cutting two internal lines. This would be only possible if the subdiagrams A and B could be split into two parts by cutting only one internal line. But this is impossible since it would lead to subdiagrams with three outer legs, which
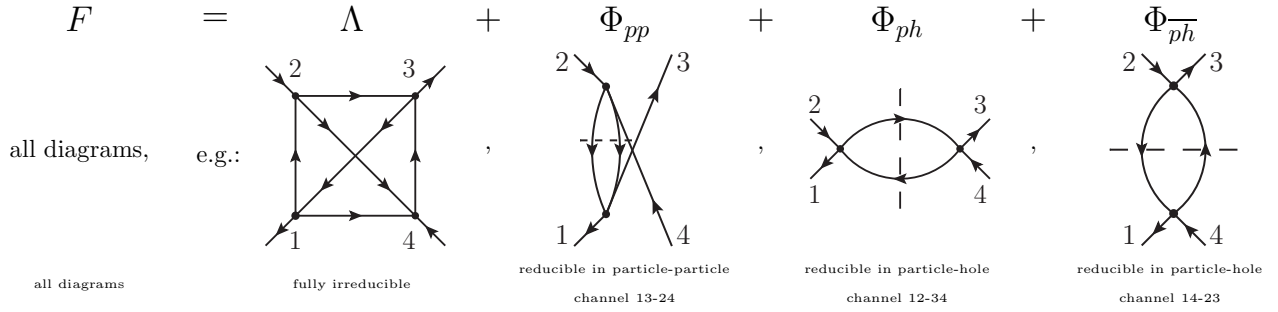
Figure 2.11: Diagrammatic illustration of the parquet decomposition of the full vertex function F. For each of the four contributions (fully irreducible, reducible in channel ph, $\overline{ph}$ and pp) one low-order diagram is shown. The figure is reproduced from Ref. [48].

violates particle conservation as it was already discussed previously in the paragraph about one-particle reducibility (see Fig. 2.9a). Therefore, it is proven that each diagram is *either* fully irreducible or reducible in –at most– one channel (i.e., in the ph, $\overline{ph}$, or pp channel). As a consequence one can decompose the complete vertex function F into four parts: a fully two-particle irreducible one (Λ) and the (two-particle) reducible contributions (Φ_r) in the three different channels:

$$F = \Lambda + \Phi_{pp} + \Phi_{ph} + \Phi_{\overline{ph}}. \tag{2.162}$$

which has been written in a schematic notation, omitting spin and frequency arguments. This equation (2.162), which expresses the decomposition of F, is called *parquet equation*. It is schematically illustrated in Fig. 2.11 with one low-order diagram shown for each of the contributions. The parquet equation is the two-particle analogon of the classification of the one-particle diagrams as reducible and irreducible ones (defining the self-energy). Hence, in principle it represents just a "classification" scheme of all connected (two-particle) diagrams, which are divided this way into four classes.

Bethe-Salpeter equations

While one can easily calculate the full vertex function F from the generalized susceptibility χ by means of Eq. (2.160), in order to work with the parquet equation, one needs additional relations connecting F and the reducible vertices Φ_r. This can be achieved by defining new quantities Γ_r:

$$F = \Phi_r + \Gamma_r, \quad r = pp, ph, \overline{ph}. \tag{2.163}$$

Since F contains all diagrams and Φ_r contains all the diagrams which are reducible in the given channel r, Γ_r is the set of all diagrams, which are *irreducible* in the respective channel.

Since each diagram is either fully irreducible or reducible in a given channel, we have that $\Gamma_r = \Lambda + \Phi_{j_1} + \Phi_{j_2}$, $j_1, j_2 \neq r$. In this way the diagram depicted in Fig. 2.10 belongs to $\Gamma_{\overline{ph}}$ and Γ_{pp} since it is reducible in the longitudinal particle-hole (ph) channel.

The Γ_r vertices, in turn, can be calculated from F by means of an integral equation, the so called Bethe-Salpeter-equation:

$$F = \Gamma_r + \int \Gamma_r (GG)_r F \qquad \Longleftrightarrow \qquad \Phi_r = \int \Gamma_r (GG)_r F, \qquad (2.164)$$

where the integral symbol denotes an integration/summation over all internal degrees of freedom (e.g., frequencies, spin, momentum, ...). $(GG)_r$ denotes the product of two one-particle Green's function with corresponding frequency arguments according to the respective channel r.

The interpretation of Eq. (2.164) is very simple: F is the sum of all diagrams which are irreducible in the given channel r (Γ_r) and the diagrams that are reducible in this channel (Φ_r). The reducible diagrams, in turn, can be represented in terms of the irreducible ones Γ_r and the set of all diagrams F: Connecting these two building blocks with two Green's function lines one obtains diagrams that are reducible in the channel r as it is illustrated for $r = ph$ in Fig. 2.12a. We should note here, that when considering an arbitrary (ph) reducible diagram, its splitting into two subdiagrams can be realized in different ways (Figs. 2.12b and c for a specific case). However, the Bethe-Salpeter requirement that the left subdiagram belongs to the irreducible vertex Γ_r guarantees the uniqueness of the division (Fig. 2.12c). This way, taking one of the building blocks irreducible avoids any possible double counting of diagrams.

Let us also stress that a decomposition of the vertex F according to Eqs. (2.163) and (2.164) is in any case not unique, in the sense that it can obviously be performed independently for all three channels.

Symmetries of F, Γ_r and Λ

The symmetry properties of the *full vertex F* almost coincide with that for the generalized susceptibility[23]. In fact, combining the decomposition of the generalized susceptibilities as given in Eqs. (2.160) and (2.161) with the symmetry relations for χ reported in Tab. 2.1 yields analogous equations for F which are summarized in Tab. 2.2. As it was the case for χ

---

[23]Since F can be obtained from χ by subtracting all unconnected contributions χ_0 and amputating the outer legs G, one can obtain the symmetry relations for F by substituting it for χ in Tab. 2.1 and removing all χ_0's from the equations.
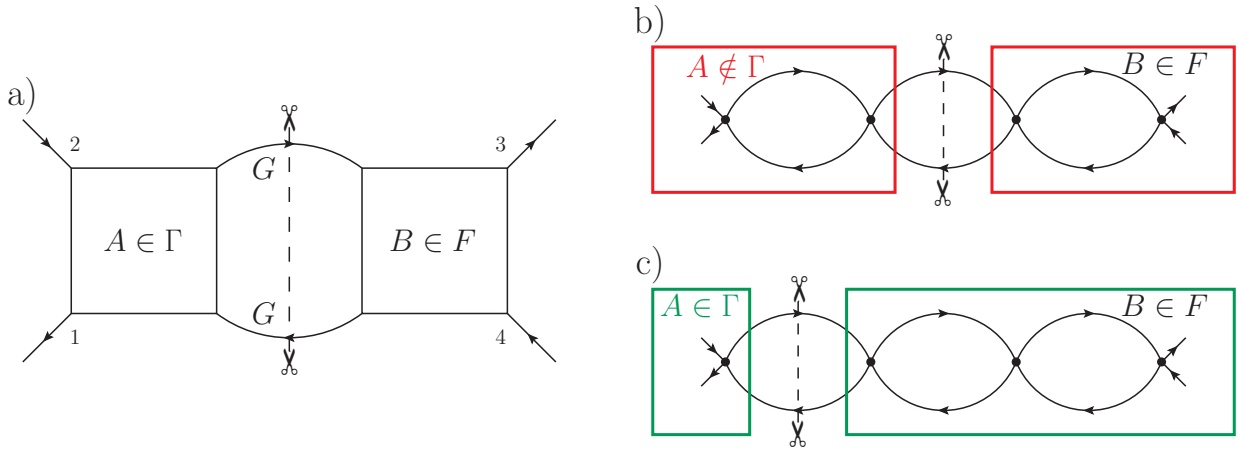
Figure 2.12: Diagrams $\mathcal{D} \in \Phi_{ph}$ which are reducible in the longitudinal particle-hole channel [ph, $\Gamma \equiv \Gamma_{ph}$]: a) Each diagram which is constructed according to Eq. (2.164) is reducible in the ph channel. b) Splitting of a ph reducible diagram into two parts A and B (red boxes) both of which are not irreducible in the ph channel. c) Splitting of a ph reducible diagram into two parts (green boxes) one of which (A) is irreducible in the ph channel.

the time translation symmetry as well as partly the SU(2) symmetry are already taken into account by defining the vertex as a function of only three frequencies and two spin variables, and, hence, they do not give rise to any further constraints on F. For the symmetry relations of the vertex function F in particle-particle (pp) notation we refer the reader to Appendix A.

The *irreducible vertex functions* Γ_r exhibit the same symmetry properties as the full vertex F *except* for the crossing symmetry[24]. This can be easily understood by a closer inspection of the last two diagrams (ph and $\overline{ph}$) in Fig. 2.11: Exchanging, e.g., the two incoming electrons (2 and 4) transforms the ph diagram (third diagram in Fig. 2.11) into the corresponding $\overline{ph}$ diagram (fourth diagrams in Fig. 2.11) and vice versa. Hence, the crossing symmetry does not represent a constraint for Γ_{ph} and $\Gamma_{\overline{ph}}$, respectively, but rather yields the following relation between these two channels:

$$\Gamma_{ph,\overline{\sigma\sigma'}}^{\nu\nu'\omega} = -\Gamma_{\overline{ph},\sigma\sigma'}^{\nu(\nu+\omega)(\nu'-\nu)}. \tag{2.165}$$

At the same time, the particle-particle channel Γ_{pp} is not connected to any other channel and, hence, fulfills a crossing relation on its own which is completely equivalent to the crossing relation of the full vertex function F in particle-particle notation (see Tab. A.2 in Appendix

---

[24]Therefore, a list of all symmetries for Γ_r can be simply obtained by replacing F with Γ_r in Tabs. 2.2 and A.2, respectively, except for the crossing symmetry

Symmetry	Relation in *ph*-notation	Reference
Crossing symmetry	$$F_{\sigma\sigma'}^{\nu\nu'\omega} = -F_{\sigma\sigma'}^{\nu(\nu+\omega)(\nu'-\nu)}$$	Sec. 2.2.1.2, Eq. 2.37
Complex conjugation	$$\left(F_{\sigma\sigma'}^{\nu\nu'\omega}\right)^* = F_{\sigma'\sigma}^{(-\nu')(-\nu)(-\omega)} \overset{\mathrm{SU(2)}}{=} F_{\sigma\sigma'}^{(-\nu')(-\nu)(-\omega)}$$	Sec. 2.2.1.3, Eq. 2.39
SU(2) symmetry	$$F_{\sigma\sigma'}^{\nu\nu'\omega} = F_{(-\sigma)(-\sigma')}^{\nu\nu'\omega} = F_{\sigma'\sigma}^{\nu\nu'\omega}$$ $$F_{\sigma\sigma}^{\nu\nu'\omega} = F_{\sigma(-\sigma)}^{\nu\nu'\omega} + F_{\sigma(-\sigma)}^{\nu\nu'\omega} = F_{\sigma(-\sigma)}^{\nu\nu'\omega} - F_{\sigma(-\sigma)}^{\nu(\nu+\omega)(\nu'-\nu)}$$	Sec. 2.2.2.2, Eqs. 2.87, 2.89
Time reversal symmetry	$$F_{\sigma\sigma'}^{\nu\nu'\omega} = F_{\sigma'\sigma}^{\nu'\nu\omega} \overset{\mathrm{SU(2)}}{=} F_{\sigma\sigma'}^{\nu'\nu\omega}$$	Sec. 2.2.2.3, Eq. 2.95
Particle-hole symmetry $\left(\mu = \frac{U}{2} \text{ only}\right)$	$$\left(F_{\sigma\sigma'}^{\nu\nu'\omega}\right)^* = F_{\sigma\sigma'}^{\nu\nu'\omega}$$	Sec. 2.2.2.5, Eqs. 2.108-2.110
SU(2)$_{\mathrm{P}}$ symmetry $\left(\mu = \frac{U}{2} \text{ only}\right)$	$$F_{\sigma\sigma}^{\nu\nu'\omega} = F_{\sigma(-\sigma)}^{\nu(-\nu'-\omega)(\nu'-\nu)} - F_{\sigma(-\sigma)}^{\nu(-\nu'-\omega)\omega}$$	Sec. 2.2.2.6, Eq. 2.136

Table 2.2: Summary of the symmetry relations for for the vertex function F in *ph*-notation.

A):

$$\Gamma_{pp,\sigma\sigma'}^{\nu\nu'\omega} = -\Gamma_{pp,\sigma\sigma}^{\nu(\omega-\nu')\omega}. \tag{2.166}$$

Note that we adopt here the "natural" notation for the irreducible vertices, i.e, the particle-hole notation for Γ_{ph} and $\Gamma_{\overline{ph}}$ and the particle-particle notation for Γ_{pp}.

Finally, when considering the *fully irreducible vertex* Λ, we observe that, as F, by definition it cannot be divided into different channels. Consequently, it fulfills exactly the same symmetry relations as given in Tabs. 2.2 and A.2 for F, i.e., replacing F with Λ in these tables yields the symmetry relations for the fully irreducible vertex.

Spin diagonalization

In the SU(2)-symmetric case it is sufficient to consider three spin combinations for the generalized susceptibilities and the vertex functions, i.e., $\uparrow\uparrow$, $\uparrow\downarrow$, and $\overline{\uparrow\downarrow}$ [see Eqs. (2.73) and (2.74)]. As we have discussed before, at the level of the full vertex F or the fully irreducible vertex Λ, the $\overline{\uparrow\downarrow}$ vertex can be expressed through the $\uparrow\downarrow$ vertex by means of the crossing symmetry. However, since at the level of the irreducible vertices Γ_r the corresponding crossing relation connects two different channels [ph and $\overline{ph}$, see Eq. (2.165)], it is convenient to treat for the moment $\Gamma_{r,\overline{\uparrow\downarrow}}$ as independent quantity. This way, we have three spin combinations for each of the three channels, which would lead to nine different Γ's. However, considering the crossing- and the SU(2)-symmetry, it turns out that only three of them are independent, i.e., one for each channel. In practice, we will follow the usual choice [44–46] of considering *four* irreducible vertex functions, i.e., two for the ph- and two for the pp-case, respectively, which allows for a more "symmetric" formalism:

$$\Gamma_d^{\nu\nu'\omega} = \Gamma_{ph,\uparrow\uparrow}^{\nu\nu'\omega} + \Gamma_{ph,\uparrow\downarrow}^{\nu\nu'\omega} \tag{2.167a}$$

$$\Gamma_m^{\nu\nu'\omega} = \Gamma_{ph,\uparrow\uparrow}^{\nu\nu'\omega} - \Gamma_{ph,\uparrow\downarrow}^{\nu\nu'\omega} \tag{2.167b}$$

$$\Gamma_s^{\nu\nu'\omega} = \Gamma_{pp,\uparrow\downarrow}^{\nu\nu'\omega} - \Gamma_{pp,\overline{\uparrow\downarrow}}^{\nu\nu'\omega} \tag{2.167c}$$

$$\Gamma_t^{\nu\nu'\omega} = \Gamma_{pp,\uparrow\downarrow}^{\nu\nu'\omega} + \Gamma_{pp,\overline{\uparrow\downarrow}}^{\nu\nu'\omega}. \tag{2.167d}$$

Let us stress again that, in principle, in the pp-case it would be sufficient to consider only $\Gamma_{pp,\uparrow\downarrow}$ rather than Γ_s and Γ_t. In fact, taking into account the crossing relation (2.166) one gets

$$\Gamma_s^{\nu\nu'\omega} = \Gamma_{pp,\uparrow\downarrow}^{\nu\nu'\omega} + \Gamma_{pp,\uparrow\downarrow}^{\nu(\omega-\nu')\omega}, \qquad \Gamma_t^{\nu\nu'\omega} = \Gamma_{pp,\uparrow\downarrow}^{\nu\nu'\omega} - \Gamma_{pp,\uparrow\downarrow}^{\nu(\omega-\nu')\omega}, \tag{2.168}$$

which means that Γ_s and Γ_t are just the symmetric and the antisymmetric part of the vertex function $\Gamma_{pp,\uparrow\downarrow}$ with respect to the frequency argument ν'. It is also useful to rewrite Γ_s and Γ_t by means of the SU(2) symmetry relations given in Tab. A.2:

$$\Gamma_s^{\nu\nu'\omega} = \Gamma_{pp,\uparrow\downarrow}^{\nu\nu'\omega} + \Gamma_{pp,\uparrow\downarrow}^{\nu(\omega-\nu')\omega} = 2\Gamma_{pp,\uparrow\downarrow}^{\nu\nu'\omega} - \Gamma_{pp,\uparrow\uparrow}^{\nu\nu'\omega} \tag{2.169a}$$

$$\Gamma_t^{\nu\nu'\omega} = \Gamma_{pp,\uparrow\downarrow}^{\nu\nu'\omega} - \Gamma_{pp,\uparrow\downarrow}^{\nu(\omega-\nu')\omega} = \Gamma_{pp,\uparrow\uparrow}^{\nu\nu'\omega}. \tag{2.169b}$$

For convenience, we will use the same definitions at the level of F and Λ as well. However, exploiting all symmetry relations of Tab. 2.2 shows that only $F_{\uparrow\downarrow}$ ($\Lambda_{\uparrow\downarrow}$) is an independent function while all the others can be represented in terms of the latter.

Within this four-channel formalism we can now easily derive the Bethe-Salpeter equations for the four vertex functions defined in Eqs. (2.167), explicitly including their spin and frequency dependence. It turns out that the Bethe-Salpeter equations couple the ↑↑ and the ↑↓ vertex functions. However, resorting to the definitions in Eqs. (2.167) leads to a decoupling, i.e., one obtains one independent Bethe-Salpeter equation for each of the four vertex functions Γ_d, Γ_m, Γ_s and Γ_t. For the –rather lengthy– calculations of the Γ_r and the Λ_r, $r = d, m, s, t$, we refer to Appendices B and C.

2.2.5   Mapping onto the attractive model

If the particle-hole transformation $\hat{\mathcal{W}}$, discussed in Sec. 2.2.2.5 [Eq. (2.99)], is done for one spin species only it is called *partial* particle hole transformation $\hat{\mathcal{W}}_p$. It was already introduced in Sec. 2.2.2.6 where the pseudospin symmetry of the particle-hole symmetric AIM was discussed. While in this part of the thesis $\hat{\mathcal{W}}_p$ just served as a kind of auxiliary quantity, used to establish the connection between the $SU(2)$ spin and the $SU(2)_P$ pseudospin symmetry of the particle-hole symmetric AIM, this section is devoted to the analysis of $\hat{\mathcal{W}}_p$ itself. Though the basic definitions and results for the symmetry operation $\hat{\mathcal{W}}_p$ have already been given in Sec. 2.2.2.6, we will recall some of them in following for convenience.

A partial particle-hole transformation provides a mapping of the half-filled repulsive Hubbard model ($U > 0$) onto the attractive one ($-U < 0$) as it is discussed exhaustively in the literature [54, 58–67] for the Hubbard Hamiltonian. In this section we will consider the corresponding transformation for the AIM, similar as it was done in the case of the (full) particle-hole transformation in Sec. 2.2.2.5.

Let us recall the partial particle-hole transformation for the ↓-electrons, defined in Eq. (2.118):

$$\hat{\mathcal{W}}_p = (\hat{a}_{N\downarrow}^\dagger - \hat{a}_{N\downarrow}) \ldots (\hat{a}_{2\downarrow}^\dagger - \hat{a}_{2\downarrow})(\hat{c}_\downarrow^\dagger + \hat{c}_\downarrow).$$

The action of this transformation on the creation and annihilation operators is given by

$$\hat{\mathcal{W}}_p^\dagger(\hat{c}_\downarrow^\dagger, \hat{c}_\downarrow)\hat{\mathcal{W}}_p = (-1)^{(N-1)}(\hat{c}_\downarrow, \hat{c}_\downarrow^\dagger)$$
$$\hat{\mathcal{W}}_p^\dagger(\hat{c}_\uparrow^\dagger, \hat{c}_\uparrow)\hat{\mathcal{W}}_p = (-1)^{N}(\hat{c}_\uparrow^\dagger, \hat{c}_\uparrow)$$

(2.170a)

$$\hat{\mathcal{W}}_p^\dagger(\hat{a}_{\ell\downarrow}^\dagger, \hat{a}_{\ell\downarrow})\hat{\mathcal{W}}_p = (-1)^{N}(\hat{a}_{\ell\downarrow}, \hat{a}_{\ell\downarrow}^\dagger)$$
$$\hat{\mathcal{W}}_p^\dagger(\hat{a}_{\ell\uparrow}^\dagger, \hat{a}_{\ell\uparrow})\hat{\mathcal{W}}_p = (-1)^{N}(\hat{a}_{\ell\uparrow}^\dagger, \hat{a}_{\ell\uparrow}).$$

(2.170b)

Indeed one can see, that under $\hat{\mathcal{W}}_p$ the interchange of creation and annihilation operators

takes place only for $\sigma = \downarrow$ while the $\uparrow$ operators are not modified by the transformation [except for a phase factor $(-1)^N$]. Hence, the name "partial" particle hole transformation for the unitary operator $\hat{\mathcal{W}}_p$ is well justified.

Using Eqs. (2.170) it is straightforward to derive the behavior of the AIM Hamiltonian under the transformation $\hat{\mathcal{W}}_p$:

$$
\begin{aligned}
\hat{\mathcal{W}}_p^\dagger \hat{\mathcal{H}} \hat{\mathcal{W}}_p = & \sum_\ell \left[\varepsilon_\ell \hat{a}_{\ell\uparrow}^\dagger \hat{a}_{\ell\uparrow} - \varepsilon_\ell \hat{a}_{\ell\downarrow}^\dagger \hat{a}_{\ell\downarrow} \right] + \sum_{\ell\sigma} V_\ell (\hat{c}_\sigma^\dagger \hat{a}_{\ell\sigma} + \hat{a}_{\ell\sigma}^\dagger \hat{c}_\sigma) - \\
& - U\hat{n}_\uparrow \hat{n}_\downarrow - [(\mu - U)\hat{n}_\uparrow - \mu\hat{n}_\downarrow) + \sum_{\ell=2}^{N} \varepsilon_\ell - \mu.
\end{aligned}
\tag{2.171}
$$

Next, we proceed by imposing the same constraints on the parameters of the AIM as we did for the particle-hole transformation in Sec. 2.2.2.5 on page 47: (i) We assume that the bath levels are distributed symmetrically around 0, i.e., $\varepsilon_\ell = -\varepsilon_{\ell+\frac{N}{2}}$ for $\ell = 2 \ldots \frac{N}{2}$; (ii) The hybridization between the bath and the impurity should be the same for the positive and the corresponding negative bath energy, which means that $V_\ell = V_{\ell+\frac{N}{2}}$ for $\ell = 2 \ldots \frac{N}{2}$. (iii) The chemical potential μ is chosen as $\mu = \frac{U}{2}$. According to this restrictions on ε_ℓ, V_ℓ and μ, it is clear that the positive and the negative energy sector of the bath are completely equivalent which suggests to perform the index transformation $\ell \leftrightarrow (\ell + \frac{N}{2})$ in Eq. (2.171), but now for the $\downarrow$ spins only. Thus the minus sign in front of $\varepsilon_\ell \hat{a}_{\ell\downarrow}^\dagger \hat{a}_{\ell\downarrow}$ changes back into the plus sign as in the original Hamiltonian. Therefore, considering that $\mu = \frac{U}{2}$, one "retrieves" almost the original AIM Hamiltonian, whit the only, crucial, difference, that the sign of U in the interacting part of the Hamiltonian has changed. Hence, when considering the particle-hole symmetric constraints on ε_ℓ, V_ℓ and μ, one can express the transformed Hamiltonian as in Eq. (2.119):

$$
\hat{\mathcal{H}}' = \hat{\mathcal{W}}_p^\dagger \hat{\mathcal{H}}(U) \hat{\mathcal{W}}_p = \hat{\mathcal{H}}(-U),
$$

where $\hat{\mathcal{H}}(U)$ and $\hat{\mathcal{H}}(-U)$ denote the Hamiltonians exhibiting a positive and the corresponding negative value of U, respectively. Hence, the partial particle hole transformation $\hat{\mathcal{W}}_p$ does not represent a symmetry of the AIM but, indeed, maps its repulsive version $(U > 0, \mu = \frac{U}{2})$ onto the attractive one $(-U, \mu = -\frac{U}{2})$ and vice versa.

The transformation $\hat{\mathcal{W}}_p$ allows us to establish some useful and interesting relations between the Green's functions for the repulsive and the attractive AIM. For this purpose, it turns out convenient to extend the notation of the Green's functions by adding a superscript U or $(-U)$ that indicates whether the calculations have been done for the repulsive or the corresponding

attractive system. As usual, we start from the definition of the transformed Green's function

$$G'_{n,\sigma_1\ldots\sigma_{2n}}(\tau_1,\ldots,\tau_{2n}) = \left\langle \mathrm{T}\left[\hat{c}'^\dagger_{\sigma_1}(\tau_1)\hat{c}'_{\sigma_2}(\tau_2)\ldots\hat{c}'^\dagger_{\sigma_{2n-1}}(\tau_{2n-1})\hat{c}'_{\sigma_{2n}}(\tau_{2n})\right]\right\rangle, \tag{2.172}$$

where

$$\hat{c}'^\dagger_\sigma = \hat{\mathcal{W}}^\dagger_p \hat{c}^\dagger_\sigma \hat{\mathcal{W}}_p \qquad\qquad \hat{c}'_\sigma = \hat{\mathcal{W}}^\dagger_p \hat{c}_\sigma \hat{\mathcal{W}}_p. \tag{2.173}$$

Note that in this case the transformed Green's function G'_n *does not* coincide with the original one G_n since $\hat{\mathcal{W}}_p$ does *not* constitute a symmetry of the system. Instead, we can use the general identity, Eq. (2.48), derived at the beginning of Sec. 2.2.2:

$$G'_n = G_n(\hat{c}'^\dagger, \hat{c}', \hat{\mathcal{H}}) = G_n(\hat{c}^\dagger, \hat{c}, \hat{\mathcal{H}}'), \tag{2.174}$$

in order to obtain relations between the Green's functions for the attractive and the repulsive AIM [$\hat{\mathcal{H}}\hat{=}\hat{\mathcal{H}}(U)$ and $\hat{\mathcal{H}}'\hat{=}\hat{\mathcal{H}}(-U)$].

Let us first stick to the case where all spins are pointing in the same direction, i.e., $\sigma_1 = \sigma_2 = \ldots = \sigma_{2n}$. Due to the SU(2) symmetry of the system we can restrict ourselves to ↑-spins, w.l.o.g. Since the ↑-spin operators $\hat{c}^{(\dagger)}_\uparrow$ are unaffected by the partial particle-hole transformation, the transformed Green's functions G'_n is equal to the original one (and not, as for a symmetry, to the one containing the transformed Hamiltonian!). Hence, according to Eq. (2.174) the Green's functions with all spins pointing in the same direction exactly coincide for the repulsive and the attractive Hubbard model:

$$G'_{n,\sigma\ldots\sigma}(\tau_1,\ldots,\tau_{2n}) = G^U_{n,\sigma\ldots\sigma}(\tau_1,\ldots,\tau_{2n}) = G^{(-U)}_{n,\sigma\ldots\sigma}(\tau_1,\ldots,\tau_{2n}), \tag{2.175}$$

which obviously also holds in frequency space.

For the following analysis of other spin combinations, we restrict ourselves to the one- and the two-particle Green's functions since the effects of the transformation $\hat{\mathcal{W}}_p$ depend strongly on their spin structures which becomes increasingly involved for more-particle Green's functions (despite, of course, the case discussed above, where all spins point in the same direction).

Since in the *one-particle* case all spins have to point in the same direction, Eq. (2.175) immediately tells us that the one-particle Green's function does not change when going from U to $(-U)$, i.e,

$$G^U(\nu) = G^{(-U)}(\nu). \tag{2.176}$$

For the *two-particle* case Eq. (2.175) states that $G^U_{2,\sigma\sigma}$ and $G^{(-U)}_{2,\sigma\sigma}$ coincide. However, an interesting non-trivial relation can be obtained from the transformation of $G_{2,\uparrow\downarrow}$. Considering Eq. (2.172) for this case one gets

$$G'_{2,\uparrow\downarrow}(\tau_1,\tau_2,\tau_3,\tau_4) = \left\langle \mathrm{T}\left[\hat{c}'^\dagger_\uparrow(\tau_1)\hat{c}'_\uparrow(\tau_2)\hat{c}'^\dagger_\downarrow(\tau_3)\hat{c}'_\downarrow(\tau_4)\right]\right\rangle = \left\langle \mathrm{T}\left[\hat{c}^\dagger_\uparrow(\tau_1)\hat{c}_\uparrow(\tau_2)\hat{c}_\downarrow(\tau_3)\hat{c}^\dagger_\downarrow(\tau_4)\right]\right\rangle.$$
(2.177)

Interchanging the last two-operators, which yields an additional minus sign according to the crossing symmetry, restores the correct order of creation and annihilation operators that matches the definition of the Green's functions in Eq. (2.27). This gives rise to the relation:

$$- G^U_{2,\uparrow\downarrow}(\tau_1,\tau_2,\tau_4,\tau_3) = G^{(-U)}_{2,\uparrow\downarrow}(\tau_1,\tau_2,\tau_3,\tau_4),$$
(2.178)

and after a Fourier transform:

$$- G^U_{2,\uparrow\downarrow}(\nu_1,\nu_2,-\nu_4) = G^{(-U)}_{2,\uparrow\downarrow}(\nu_1,\nu_2,\nu_3),$$
(2.179)

where $\nu_4 = \nu_1 - \nu_2 + \nu_3$ is given by the requirement of energy conservation.

For the derivation of the corresponding relation for the Hubbard model, we refer the reader to the discussion of the (full) particle-hole transformation for the lattice system in Sec. 2.2.2.5, page 49. Similarly as for the full particle-hole transformation $\hat{\mathcal{W}}_\mathrm{H}$, the partial particle-hole transformation $\hat{\mathcal{W}}_{\mathrm{H},p}$ for the Hubbard Hamiltonian reads as:

$$\hat{c}'^\dagger_{\mathbf{R}_i,\uparrow} = \hat{\mathcal{W}}^\dagger_{\mathrm{H},p}\hat{c}^\dagger_{\mathbf{R}_i,\uparrow}\hat{\mathcal{W}}_{\mathrm{H},p} = \hat{c}^\dagger_{\mathbf{R}_i,\uparrow}, \qquad \hat{c}'^\dagger_{\mathbf{R}_i,\downarrow} = \hat{\mathcal{W}}^\dagger_{\mathrm{H},p}\hat{c}^\dagger_{\mathbf{R}_i,\downarrow}\hat{\mathcal{W}}_{\mathrm{H},p} = e^{i\mathbf{\Pi R_i}}\hat{c}_{\mathbf{R}_i,\downarrow},$$
(2.180)

$$\hat{c}'_{\mathbf{R}_i,\uparrow} = \hat{\mathcal{W}}_{\mathrm{H},p}\hat{c}_{\mathbf{R}_i,\uparrow}\hat{\mathcal{W}}_{\mathrm{H},p} = \hat{c}_{\mathbf{R}_i,\uparrow}, \qquad \hat{c}'_{\mathbf{R}_i,\downarrow} = \hat{\mathcal{W}}^\dagger_{\mathrm{H},p}\hat{c}_{\mathbf{R}_i,\downarrow}\hat{\mathcal{W}}_{\mathrm{H},p} = e^{i\mathbf{\Pi R_i}}\hat{c}^\dagger_{\mathbf{R}_i,\downarrow},$$
(2.181)

where $\mathbf{\Pi} = (\pi,\ldots,\pi)^\mathrm{T}$. As in Eqs. (2.116) and (2.117) the additional factor $e^{i\mathbf{\Pi R_i}}$ gives rise to the transformation $\mathbf{k} \to \mathbf{\Pi} - \mathbf{k}$ of the momentum arguments of the Green's function. Note, however, that this transformation affects only the $\mathbf{k}$ vectors which correspond to $\downarrow$-creation and annihilation operators, since the corresponding $\uparrow$-operators remain unchanged by the transformation $\hat{\mathcal{W}}_{\mathrm{H},p}$. Hence, formulating Eq. (2.179) for the Hubbard model yields:

$$- G^U_{n,\mathbf{k}_1\mathbf{k}_2(\mathbf{\Pi}-\mathbf{k}_4),\uparrow\downarrow} = G^{(-U)}_{n,\mathbf{k}_1\mathbf{k}_2\mathbf{k}_3,\uparrow\downarrow},$$
(2.182)

where $\mathbf{k}_4 = \mathbf{k}_1 - \mathbf{k}_2 + \mathbf{k}_3$ is given by momentum conservation and the suppressed frequency arguments are completely the same as in the corresponding equation for the AIM [Eq. (2.179)]. Returning to the AIM, we can use the relations connecting the two-particle Green's function

and the generalized susceptibilities (2.147) as well as the definition of frequencies in Eqs. (2.149) in order to express Eq. (2.179) in terms of the χ's:

$$\chi_{U,\uparrow\downarrow}^{\nu\nu'\omega} - \chi_0^{\nu(\nu+\omega)(\nu'-\nu)} = -\chi_{(-U),pp,\uparrow\downarrow}^{\nu(-\nu'-\omega)\omega} + \chi_0^{\nu(\nu+\omega)(-\nu-\nu'-\omega)}. \qquad (2.183)$$

Applying the SU(2) symmetry relation given in Tab. 2.1 for rewriting the left-hand side of this equation yields:

$$-\chi_{U,m}^{\nu(\nu+\omega)(\nu'-\nu)} = -\chi_{(-U),pp,\uparrow\downarrow}^{\nu(-\nu'-\omega)\omega} + \chi_0^{\nu(\nu+\omega)(-\nu-\nu'-\omega)}. \qquad (2.184)$$

Performing the frequency transformation $\nu' \to \nu - \omega$ and $\omega \to \nu' - \nu$ and transforming the right-hand side to the particle-particle notation gives:

$$\chi_{U,m}^{\nu\nu'(-\omega)} = \chi_{(-U),pp,\uparrow\downarrow}^{\nu(\omega-\nu')\omega} - \chi_{0,pp}^{\nu\nu'\omega}. \qquad (2.185)$$

This equation can be interpreted as follows: The inversion $\chi_{U,m}^{\nu\nu'(-\omega)}$ yields, via the Bethe-Salpeter equation, the irreducible vertex $\Gamma_m^{\nu\nu'(-\omega)}$, as discussed in Appendix. B.3. The inversion of the quantity on the right-hand side of Eq. (2.185), instead, gives the irreducible $\uparrow\downarrow$-vertex in the particle-particle channel, i.e., $\Gamma_{(-U),pp,\uparrow\downarrow}^{\nu(\omega-\nu')\omega}$ (see Eq. B.26). Hence, we obtain the relation:

$$\Gamma_{U,m}^{\nu\nu'(-\omega)} = \Gamma_{(-U),pp,\uparrow\downarrow}^{\nu(\omega-\nu')\omega}, \qquad (2.186)$$

If one performs the sum over ν and ν' in Eq. (2.185) in order to obtain the physical (one-frequency) susceptibilities, one observes that the magnetic (spin) fluctuations for the repulsive model are mapped on fluctuations of an electron-pair for the attractive case. This is consistent with the well-known fact that for a lattice model the antiferromagnetic instability for $U > 0$ corresponds to the superconducting instability in the attractive situation.

The relation between the vertex function irreducible in the magnetic channel for the repulsive model and the vertex function irreducible in the particle-particle $\uparrow\downarrow$ channel in the attractive case, stated in Eq. (2.186), can be understood also from a diagrammatic point of view. To this end, we consider in Fig. 2.13a an arbitrary $\uparrow\downarrow$-diagram (for the attractive model) which is *reducible* in the particle-particle channel, i.e., it contributes to $\Phi_{(-U),pp,\uparrow\downarrow}^{\nu\nu'\omega}$. When applying the partial particle-hole transformation to this diagram, the $\downarrow$ Green's functions (plotted in red) are reversed and, accordingly, the corresponding frequency arguments have to change their sign, which yields the diagram depicted in Fig. 2.13b. The latter represents a diagram for the repulsive system which is reducible in the transverse (vertical) particle-hole channel,
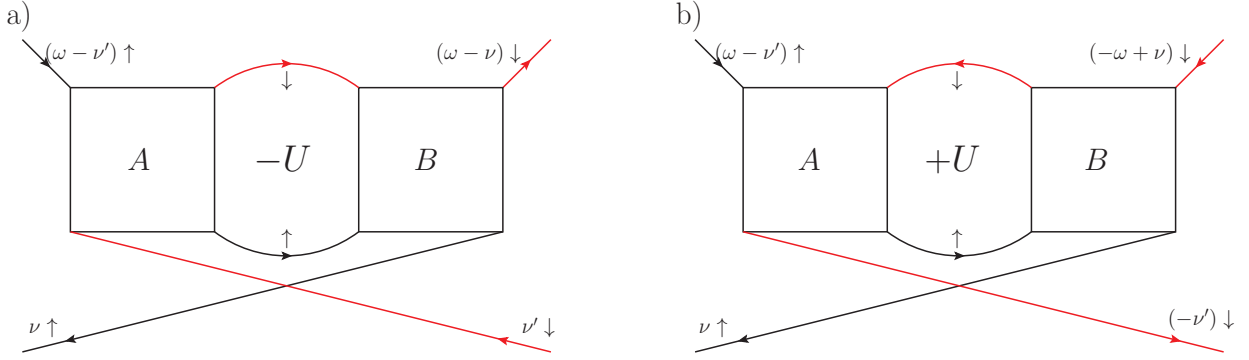
Figure 2.13: a) Example of a reducible diagram in the particle-particle $\uparrow\downarrow$ channel; b) Example of a reducible diagram in the transverse $\uparrow\downarrow$ particle-hole channel; $-U$ denotes the attractive and $+U$ the repulsive model. The figure is reproduced from Ref. [48].

i.e., it belongs to $\Phi_{U,\overline{ph},\uparrow\downarrow}^{\nu(\nu-\omega)(\omega-\nu-\nu')}$. Considering, moreover, that the exchange of two fermions leads to an additional minus-sign, one obtains the following relation between the *pp*- and the (transverse) *ph*-reducible diagrams:

$$\Phi_{(-U),pp,\uparrow\downarrow}^{\nu\nu'\omega} = -\Phi_{U,\overline{ph},\uparrow\downarrow,}^{\nu(\nu-\omega)(\omega-\nu-\nu')}. \tag{2.187}$$

Applying the SU(2) symmetry to this equation yields:

$$\Phi_{(-U),pp,\uparrow\downarrow}^{\nu\nu'\omega} = \Phi_{U,m,\uparrow\downarrow}^{\nu(\omega-\nu')(-\omega)}, \tag{2.188}$$

which evidently holds for the Γ's as well, and, in fact, is equivalent to Eq. (2.186) after the frequency transformation $\nu' \to \omega - \nu'$.

2.2.6 The equation of motion

This section will be devoted to the so-called Schwinger-Dyson equation (or equation of motion) for the Green's function and the electronic self-energy. We start by recalling that, for an interacting system, the Green's functions for different numbers of particles are not independent but connected via exact analytical expressions, called equations of motion [38]. These relations can be readily obtained by differentiating the *n*-particle Green's function, as defined in Eq. (2.27) in its most general form, with respect to one of its imaginary time arguments. Without loss of generality we consider always the derivative with respect to the

first imaginary time τ_1 connected with the first creation operator in Eq. (2.27):

$$\frac{d}{d\tau_1}G_{n,i_1\ldots i_{2n}}(\tau_1,\ldots,\tau_{2n}).\tag{2.189}$$

According to the definition of the time-ordered product of operators in Eq. (2.29) the n-particle Green's function exhibits in general products of the form $\hat{c}_{i_1}^\dagger(\tau_1)\theta(\tau_1-\tau_j)\theta(\tau_k-\tau_1)$ unless τ_1 is the smallest or largest imaginary time argument[25] in Eq. (2.27). Keeping this in mind, one has to apply the product rule for differentiation in Eq. (2.189). Since $\frac{d}{d\tau_1}\theta(\tau_1-\tau_j) = \delta(\tau_1-\tau_j)$ and $\frac{d}{d\tau_1}\theta(\tau_k-\tau_1) = -\delta(\tau_k-\tau_1)$, it is obvious that the contributions where the differentiation acts on the step-function leads again to a n-particle Green's functions albeit with one of the $2n-1$ times $\tau_2\ldots\tau_{2n}$ being equal to τ_1. The other term, $\frac{d}{d\tau}\hat{c}_{i_1}^\dagger(\tau_1)$, can be expressed, instead, by means of the Heisenberg equation of motion [38] for operators:

$$\frac{d}{d\tau}\hat{c}_{i_1}^\dagger(\tau_1) = [\hat{\mathcal{H}},\hat{c}_{i_1}^\dagger(\tau_1)] = [\hat{\mathcal{H}},\hat{c}_{i_1}^\dagger](\tau_1),\tag{2.190}$$

For the sake of clarity, when evaluating the time derivative of G_n, let us consider our general lattice Hamiltonian in a tight binding representation, such as that of Eq. (2.14). For convenience, we will also represent here the site-, orbital- and spin arguments of the creation and annihilation operators in Eq. (2.14) by a single multi-index [see the discussion below Eq. (2.29)], i.e.,:

$$\hat{\mathcal{H}} = \sum_{ij}(-t_{ij}-\mu\delta_{ij})\hat{c}_i^\dagger\hat{c}_j + \sum_{ijkl}U_{ijkl}\hat{c}_i^\dagger\hat{c}_j^\dagger\hat{c}_k\hat{c}_k.\tag{2.191}$$

Considering the general rule for evaluating commutators of products of operators:

$$[\hat{A}\hat{B},\hat{C}] = \hat{A}[\hat{B},\hat{C}] + [\hat{A},\hat{C}]\hat{B} = \hat{A}\{\hat{B},\hat{C}\} - \{\hat{A},\hat{C}\}\hat{B},\tag{2.192}$$

we obtain for Eq. (2.190):

$$\frac{d}{d\tau}\hat{c}_{i_1}^\dagger(\tau_1) = \sum_j(-t_{ji_1}-\delta_{ji_1}\mu)\hat{c}_j^\dagger(\tau_1) + \sum_{ijk}(U_{ijki_1}-U_{iji_1k})\hat{c}_i^\dagger(\tau_1)\hat{c}_j^\dagger(\tau_1)\hat{c}_k(\tau_1).\tag{2.193}$$

For the non-interacting system ($U_{ijkl} \equiv 0$) the operator $\frac{d}{d\tau}\hat{c}_{i_1}^\dagger(\tau_1)$ is replaced by *single* creation operator $\hat{c}_j^\dagger(\tau_1)$ in the trace in Eq. (2.27), which yields again a n-particle Green's function. Hence, in this case the time derivative with respect to its first imaginary time argument yields a closed a differential equation for the n-particle Green's function. This observation will be

---

[25]In that case one has $\hat{c}_{i_1}^\dagger(\tau_1)\theta(\tau_k-\tau_1)$ and $\hat{c}_{i_1}^\dagger(\tau_1)\theta(\tau_1-\tau_j)$, respectively.
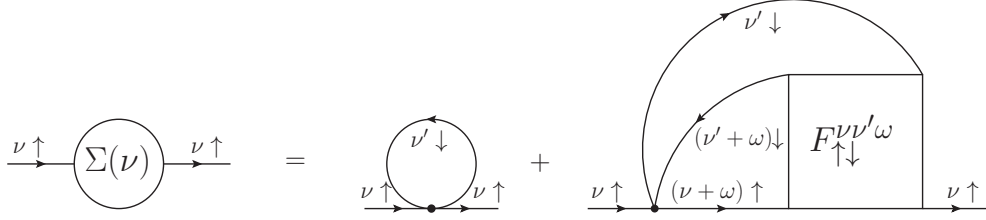
Figure 2.14: Schwinger-Dyson equation of motion. The solid lines represent full interacting Green's functions. The figure is reproduced from Ref. [48].

used in the next section (Sec. 2.2.7) for deriving the non-interacting one-particle Green's function of the AIM.

On the contrary, for the interacting system, a further contribution appears in Eq. (2.193), where $\frac{d}{d\tau}\hat{c}_{i_1}^{\dagger}(\tau_1)$ is replaced by a product of one creation and an additional pair of creation and annihilation operators, giving rise to a $(n+1)$-particle Green's function on the right-hand side of the equation for $\frac{d}{d\tau_1}G_{n,i_1\ldots i_{2n}}(\tau_1,\ldots,\tau_{2n})$. Hence, in the interacting case the equation of motion couples the n-particle Green's function to the $(n+1)$-particle Green's function yielding an infinite chain of equations which is analogous to the so-called BBGKY (Bogoliubov-Born-Green-Kirkwood-Yvon) chain [68] in classical statistical mechanics. The latter consists of interlinked equations of motion for the classical n-particle distribution functions.

In this thesis, however, we are mainly concerned with the equation of motion for the one-particle Green's function of the Hubbard model and the AIM. Following the discussion in this section, the corresponding calculations in this specific cases are straightforward and lead, after a Fourier transform and the application of the Dyson equation [Eq. (2.156)], to:

$$\Sigma(\nu) = \frac{Un}{2} - \frac{U}{\beta^2}\sum_{\nu'\omega}F_{\uparrow\downarrow}^{\nu\nu'\omega}G(\nu')G(\nu'+\omega)G(\nu+\omega), \tag{2.194}$$

which connects the self-energy of the AIM with the vertex function $F_{\uparrow\downarrow}^{\nu\nu'\omega}$ as defined in Eq. (2.159) and Fig. 2.8. The corresponding equation for the Hubbard model can be readily obtained by replacing the Matsubara frequencies ν and ω by four-vectors $(\nu,\mathbf{k})$ and $(\omega,\mathbf{q})$, respectively, in Eq. (2.194). The diagrammatic representation of Eq. (2.194) is depicted in Fig. 2.14.

2.2.7   Analytical calculation of the Green's functions in specific cases

In this section we will give some analytic results for the one- and the two-particle Green's functions in some limiting cases. Specifically, we will discuss non-interacting particles ($U = 0$) and the opposite situation where $t \to 0$ (or, equivalently, $\frac{U}{t} \to \infty$), the so-called "atomic limit", for the Hubbard [see Eq. (2.22)] model and the AIM [see Eq. (2.23)] (in the latter the atomic limit corresponds to $V_\ell \to 0$). From a physical point of view, these extreme assumptions can rarely be used for a quantitative analysis of real systems. However, they allow for a better mathematical and physical understanding of the general structure of one- and two-particle Green's functions, which has been addressed only sporadically hitherto for the two-particle case. Furthermore, they provide quite valuable benchmarks for numerical calculations of more general cases.

2.2.7.1   Non-interacting particle ($U = 0$)

In this case, according to Wick's theorem [38,69], the two- and more-particle Green's functions can be constructed just by summing up all possible products of one-particle Green's functions. In fact, in a completely *uncorrelated* situation all relevant information is contained at the one-particle level. Hence, in the following we refrain from discussing explicitly two- and more-particle Green's functions if $U = 0$.

Hubbard model
In the following we recall the results for the case of non-interacting particles in the Hubbard model on an simple cubic lattice (with the lattice constant $a = 1$). The corresponding Hubbard Hamiltonian reads:

$$\hat{\mathcal{H}}_{(U=0)} = -t \sum_{\langle ij \rangle, \sigma} \hat{c}_{i\sigma}^\dagger \hat{c}_{j\sigma} - \mu \sum_i \hat{n}_i = \frac{1}{(2\pi)^3} \int d^3k \sum_\sigma (\varepsilon_{\mathbf{k}} - \mu) \hat{c}_{\mathbf{k}\sigma}^\dagger \hat{c}_{\mathbf{k}\sigma}. \tag{2.195}$$

In the case of nearest neighbor hopping only $\varepsilon_{\mathbf{k}}$ can be easily calculated by inverting Eq. (2.15) which yields

$$\varepsilon_{\mathbf{k}} = -t \sum_{\langle 0j \rangle} e^{i\mathbf{R}_j \mathbf{k}} = -2t \sum_{i=1}^d \cos(k_i), \tag{2.196}$$

where the sum over j runs over all nearest neighbors of an (arbitrary) lattice site $\mathbf{R}_0$. Here, we have generalized our equation to the case of d dimensions rather than sticking to 3 or 2,

in order to keep the discussion as general as possible.

The calculation of the one-particle Green's function for this Hamiltonian, as defined in Eq. (2.6), can be more easily performed in $\mathbf{k}$ space [33, 38, 68] where our Hamiltonian (2.195) and Green's function are diagonal due to space translational invariance [see Sec. 2.2.2.1, Eqs. (2.61) and (2.62)]. Furthermore, we can omit any spin indices since the Hamiltonian is completely spin-independent and the one-particle Green's function is just the unit-matrix in spin space [Sec. 2.2.2.2, Eqs. 2.72 and 2.86)]. According to Eq. (2.54) we can set $\tau_2 \equiv 0$ and restrict $\tau_1 \equiv \tau$ to the interval $[0, \beta]$ in the definition of the Green's functions, since it depends only on the difference of $\tau_1 - \tau_2$. Hence, we have:

$$G_{1,\sigma_1\sigma_2}(\tau_1, \mathbf{k}_1, \tau_2, \mathbf{k}_2) \equiv G(\tau, \mathbf{k}) = -\frac{1}{Z}\text{Tr}\left(e^{-\beta\hat{\mathcal{H}}}e^{\tau\hat{\mathcal{H}}}\hat{c}_{\mathbf{k}\sigma}e^{-\tau\hat{\mathcal{H}}}\hat{c}_{\mathbf{k}\sigma}^\dagger\right), \quad \tau \in [0, \beta]. \qquad (2.197)$$

For a non-interacting system the time dependent annihilation operator can be calculated explicitly, which yields:

$$e^{\tau\hat{\mathcal{H}}}\hat{c}_{\mathbf{k}\sigma}e^{-\tau\hat{\mathcal{H}}} = \hat{c}_{\mathbf{k}\sigma}(\tau) = e^{-\xi_\mathbf{k}\tau}\hat{c}_{\mathbf{k}\sigma}, \qquad (2.198)$$

where $\xi_\mathbf{k} = \varepsilon_\mathbf{k} - \mu$. The Green's function, hence, becomes:

$$G(\tau, \mathbf{k}) = -e^{-\xi_\mathbf{k}\tau}\frac{\text{Tr}\left(e^{-\beta\hat{\mathcal{H}}}\hat{n}_{\mathbf{k}\sigma}\right)}{\text{Tr}\left(e^{-\beta\hat{\mathcal{H}}}\right)} = -e^{-\xi_\mathbf{k}\tau}\frac{e^{-\beta\xi_\mathbf{k}}}{1 + e^{-\beta\xi_\mathbf{k}}} = -e^{-\xi_\mathbf{k}\tau}f(\xi_\mathbf{k}), \qquad (2.199)$$

where $f(x) = \frac{1}{e^{\beta x}+1}$ is the Fermi function. By means of the transformation $\tau \to it$ (from imaginary to real times) one observes that the time-dependence of the non-interacting Green's function is given by just a pure oscillatory factor $e^{-it\xi_\mathbf{k}}$. This is just the time propagation of a plane wave and, in fact, the non-interacting Green's function describes the free propagation of an added/removed extra electron through the system.

Performing the Fourier transform of (2.199) to fermionic Matsubara frequencies [see Eq. 2.58)] gives:

$$G(\nu, \mathbf{k}) = \int_0^\beta d\tau \; e^{i\nu\tau}G(\tau, \mathbf{k}) = \frac{1}{i\nu + \mu - \varepsilon_\mathbf{k}}. \qquad (2.200)$$

Turning to real frequencies by means of the substitution $\nu \to \omega + i\delta$ ($\delta \to 0+$) shows, that the Green's function becomes singular at exactly the energies $\omega = \varepsilon_\mathbf{k} - \mu$. In fact, on the real axis the one-particle retarded Green's function can be written as:

$$G(\omega, \mathbf{k}) = \frac{1}{\omega + \mu - \varepsilon_\mathbf{k} + i\delta} = \text{P}\frac{1}{\omega + \mu - \varepsilon_\mathbf{k}} - i\pi\delta(\omega + \mu - \varepsilon_\mathbf{k}), \qquad (2.201)$$

where P denotes the principal value when integrating over ω. Hence, in the non-interacting case, the poles of the one-particle Green's function determine the excitation spectrum of the system. It can be shown that this holds to some extent also for interacting systems in the cases where single particle excitations are still well enough defined (Fermi liquid) [38]. In any case, from Eq. (2.201) for the retarded Green's function one can define the so-called spectral function as follows:

$$A(\omega, \mathbf{k}) = -\frac{1}{\pi}\mathrm{Im}G(\omega, \mathbf{k}) \stackrel{U=0}{=} \delta(\omega + \mu - \varepsilon_{\mathbf{k}}). \tag{2.202}$$

While for the non-interacting system $A(\omega, \mathbf{k})$ consists of a collection of divergent peaks at the one-particle energies $\omega = \varepsilon_{\mathbf{k}} - \mu$ [see Eq. (2.202)], it becomes a smoother function in the case of an interacting Hamiltonian, as a consequence of the scattering processes between the electrons. Finally, we recall that summing $A(\omega, \mathbf{k})$ over $\mathbf{k}$ defines the local spectral function:

$$A(\omega) = \sum_{\mathbf{k}} A(\omega, \mathbf{k}), \tag{2.203}$$

which, if the one-particle eigenstates are well defined, counts their number in the energy interval $(\omega, \omega + d\omega)$, and, hence, corresponds to the so-called density of states for $U \to 0$.

AIM

The non-interacting Hamiltonian of the AIM reads (see Eq. (2.23) and Ref. [42]):

$$\hat{\mathcal{H}}_{(U=0)} = \sum_{\ell\sigma} \varepsilon_\ell \hat{a}^\dagger_{\ell\sigma} \hat{a}_{\ell\sigma} + \sum_{\ell\sigma} V_\ell (\hat{c}^\dagger_\sigma \hat{a}_{\ell\sigma} + \hat{a}^\dagger_{\ell\sigma} \hat{c}_\sigma) - \mu \sum_\sigma \hat{c}^\dagger_\sigma \hat{c}_\sigma. \tag{2.204}$$

Since the AIM exhibits bath $(\hat{a}^\dagger_{\ell\sigma}, \hat{a}_{\ell\sigma})$ and impurity $(\hat{c}^\dagger_\sigma, \hat{c}_\sigma)$ degrees of freedom which are coupled via the hybridization V_ℓ, one has to consider three different types of Green's functions:

$$G_{a_m a_\ell}(\tau) = -\langle \hat{a}_{m\sigma}(\tau)\hat{a}^\dagger_{\ell\sigma}\rangle\theta(\tau) + \langle \hat{a}^\dagger_{\ell\sigma}\hat{a}_{m\sigma}(\tau)\rangle\theta(-\tau) \tag{2.205a}$$

$$G_{a_\ell c}(\tau) = G^*_{a_\ell c}(\tau) = G_{ca_\ell}(\tau) = -\langle \hat{c}_\sigma(\tau)\hat{a}^\dagger_{\ell\sigma}\rangle\theta(\tau) + \langle \hat{a}^\dagger_{\ell\sigma}\hat{c}_\sigma(\tau)\rangle\theta(-\tau), \tag{2.205b}$$

$$G_{cc}(\tau) = -\langle \hat{c}_\sigma(\tau)\hat{c}^\dagger_\sigma\rangle\theta(\tau) + \langle \hat{c}^\dagger_\sigma\hat{c}_\sigma(\tau)\rangle\theta(-\tau), \tag{2.205c}$$

where in Eq. (2.205b) the time reversal symmetry, Eq. (2.93), was used. The easiest way to calculate these Green's functions is to differentiate Eqs. (2.205) with respect to the imaginary time variable τ. Taking into account the equations of motion for $\hat{a}_{\ell\sigma}(\tau) = e^{\tau\hat{\mathcal{H}}}\hat{a}_{\ell\sigma}e^{-\tau\hat{\mathcal{H}}}$ and

$\hat{c}_\sigma(\tau) = e^{\tau\hat{\mathcal{H}}}\hat{c}_\sigma e^{-\tau\hat{\mathcal{H}}}$, one gets:

$$\frac{d}{d\tau}\hat{a}_{m\sigma}(\tau) = e^{\tau\hat{\mathcal{H}}}[\hat{\mathcal{H}}, \hat{a}_{m\sigma}]e^{-\tau\hat{\mathcal{H}}} = -\varepsilon_m\hat{a}_{m\sigma}(\tau) - V_m\hat{c}_\sigma(\tau) \tag{2.206a}$$

$$\frac{d}{d\tau}\hat{c}_\sigma(\tau) = e^{\tau\hat{\mathcal{H}}}[\hat{\mathcal{H}}, \hat{c}_\sigma]e^{-\tau\hat{\mathcal{H}}} = -\sum_m V_m\hat{a}_{m\sigma}(\tau) + \mu\hat{c}_\sigma(\tau). \tag{2.206b}$$

Considering furthermore $\frac{d}{d\tau}\theta(\pm\tau) = \pm\delta(\tau)$ leads to the following set of coupled equations for the Green's functions:

$$\frac{d}{d\tau}G_{a_m a_\ell}(\tau) = -\varepsilon_m G_{a_m a_\ell}(\tau) - V_m G_{ca_\ell}(\tau) - \delta(\tau)\delta_{\ell m}, \tag{2.207a}$$

$$\frac{d}{d\tau}G_{ca_\ell}(\tau) = -\sum_m V_m G_{a_m a_\ell}(\tau) + \mu G_{ca_\ell}(\tau), \tag{2.207b}$$

$$\frac{d}{d\tau}G_{cc}(\tau) = -\sum_\ell V_\ell \underbrace{G_{a_\ell c}(\tau)}_{=G_{ca_\ell}(\tau)} + \mu G_{cc}(\tau) - \delta(\tau). \tag{2.207c}$$

This set of equations can be readily solved in frequency space by applying $\int_0^\beta d\tau \, e^{i\nu\tau}$ to both sides of the equations and using partial integration on the left-hand side. The resulting algebraic equations can be easily solved yielding the following expression for the impurity Green's function $G_{cc}(\nu)$:

$$G_{cc}(\nu) = \frac{1}{i\nu + \mu - \Delta(\nu)}, \tag{2.208}$$

where the so-called hybridization function $\Delta(\nu)$ is defined as:

$$\Delta(\nu) = \sum_\ell \frac{V_\ell^2}{i\nu - \varepsilon_\ell}. \tag{2.209}$$

Turning to real frequencies $\nu \to \omega \pm i\delta$ the hybridization function becomes:

$$\Delta(\omega) = \mathrm{P}\sum_\ell \frac{V_\ell^2}{\omega - \varepsilon_\ell} \mp i\pi\underbrace{\sum_\ell \delta(\omega - \varepsilon_\ell)}_{\rho_b(\omega)}, \tag{2.210}$$

where $\rho_b(\omega)$ is the density of states of the bath electrons. Calculating the spectral function according to Eq. (2.202), where we restrict ourselves for the sake of simplicity to the half-filled case $\mu = 0$, one obtains:

$$A(\omega) = \frac{1}{\pi}\frac{\mathrm{Im}\Delta(\omega)}{\omega^2 + [\mathrm{Im}\Delta(\omega)]^2}. \tag{2.211}$$

Hence, the sharp delta peak at $\omega = 0$, corresponding to the density of states of the impurity gets broadened by the imaginary part of the hybridization [Im$\Delta(\omega)$] with the bath [42], as it was already discussed in Sec. (2.1.2).

Let us finally note that the impurity Green's function G_{cc} represents the most significant Green's function in the contest of the AIM, since the interaction will be later imposed on the impurity site only. More formally, resorting to the path integral formulation of the Green's functions, one can show that the bath degrees of freedom can be always integrated out, which is an alternative way to derive the hybridization function $\Delta(\nu)$.

2.2.7.2   Atomic limit $[t(V) \to 0]$

In the atomic limit ($t = 0$ for the Hubbard model and $V_\ell = 0$ for the AIM) the relevant energy scales are evidently the Hubbard interaction U and the temperature $T = \frac{1}{\beta}$. We recall also here that the atomic limit of the Hubbard model and the AIM do coincide, because the local interacting problem is completely decoupled from the rest of the system (whatever this is). In order to illustrate the corresponding physics in a concise way, we will restrict the discussion to the case of half-filling, i.e., $\mu = \frac{U}{2}$, where the effect of electronic correlations is maximal, though the generalization to average impurity occupations different from 1 (corresponding to $\mu \neq \frac{U}{2}$) is rather straightforward [47].

The Hamiltonian of the "atomic" problem then reads:

$$\hat{\mathcal{H}}_{(t \to 0)} = U \left[\hat{n}_\uparrow \hat{n}_\downarrow - \frac{1}{2}(\hat{n}_\uparrow + \hat{n}_\downarrow) \right], \tag{2.212}$$

This Hamiltonian, and as a consequence also the Green's functions, is now diagonal (i.e., purely local) in real space, which is why we stick to the real-space representation in this case. The corresponding one-particle Green's function, which depends only on τ, reads:

$$G(\tau) = -\frac{1}{Z} \text{Tr} \left(e^{-\beta \hat{\mathcal{H}}} e^{\tau \hat{\mathcal{H}}} \hat{c}_\sigma e^{-\tau \hat{\mathcal{H}}} \hat{c}_\sigma^\dagger \right), \quad \tau \in [0, \beta]. \tag{2.213}$$

Since the system is interacting, we *cannot* calculate the time-evolution for the operator $\hat{c}_\sigma(\tau)$ explicitly as we did in the previous section for the non-interacting system. However, when restricting oneself to a single site, the Hilbert space is only four-dimensional and spanned by the basis $\{|0\rangle, |\uparrow\rangle, |\downarrow\rangle, |\uparrow\downarrow\rangle\}$. Hence, in this (rather special atomic limit) situation we can easily evaluate the trace in Eq. (2.213) via the Lehmann representation [38, 47, 70] by just summing over the four basis-states and using the fact that the Hamiltonian (2.212) is

diagonal in this basis, i.e.,

$$\hat{\mathcal{H}}\{|0\rangle, |\uparrow\rangle, |\downarrow\rangle, |\uparrow\downarrow\rangle\} = \{0|0\rangle, -\frac{U}{2}|\uparrow\rangle, -\frac{U}{2}|\downarrow\rangle, 0|\uparrow\downarrow\rangle\}. \tag{2.214}$$

A straightforward calculation yields:

$$G(\tau) = -\frac{e^{(\tau-\beta)\frac{U}{2}} + e^{-\tau\frac{U}{2}}}{1 + e^{-\beta\frac{U}{2}}}. \tag{2.215}$$

After a Fourier transform this equation reads as:

$$G(\nu) = \frac{1}{i\nu - \frac{U^2}{4i\nu}} = \frac{1}{2}\left[\frac{1}{i\nu + \frac{U}{2}} + \frac{1}{i\nu - \frac{U}{2}}\right]. \tag{2.216}$$

The corresponding spectral function $A(\omega) = \frac{1}{\pi}\text{Im}G(\omega)$, where ω is a real frequency, is given by

$$A(\omega) = \frac{1}{2}\left[\delta\left(\omega + \frac{U}{2}\right) + \delta\left(\omega - \frac{U}{2}\right)\right]. \tag{2.217}$$

The particularly simple form of $A(\omega)$ in the atomic limit represent an ideal starting point to illustrate in a specific case the different roles played by electronic correlations at the one- and the two-particle level. In fact, the spectral function $A(\omega)$ [Eq. (2.201)] of the atomic limit corresponds formally to one-particle excitation energies $\varepsilon = \pm\frac{U}{2}$, which are totally independent from T. On the other hand, one would obtain exactly the same local spectral function (or local one-particle Green's function) as in Eq. (2.217) for a *non-interacting* (spinless) two-site Hubbard model at half-filling with periodic boundary conditions, by choosing the hopping parameter as $t = \frac{U}{4}$. As for the Fourier transform one has only two **k** points in this (one-dimensional) system, i.e., $\mathbf{k}_1 = 0$ and $\mathbf{k}_2 = \pi$. According to Eq. (2.196) this corresponds to the "dispersion" $\varepsilon_1 := \varepsilon_{\mathbf{k}_1} = -\frac{U}{2}$ and $\varepsilon_2 := \varepsilon_{\mathbf{k}_2} = \frac{U}{2}$. Hence, considering Eqs. (2.202) and (2.203), the local spectral function of this *non-interacting* system is indeed equivalent to the spectral function for the *interacting* atomic limit in Eq. (2.217). At the same time the two physical situations are completely different, as as it can be seen, by comparing the eigenenergies of the four possible eigenstates. For the atomic limit they are reported in Eq. (2.214), while for our two-site toy- model they are given by:

$$\hat{\mathcal{H}}_{2-\text{site}}\{|0\rangle, |\mathbf{k}_1\rangle, |\mathbf{k}_2\rangle, |\mathbf{k}_1, \mathbf{k}_2\rangle\} = \{0|0\rangle, -\frac{U}{2}|\mathbf{k}_1\rangle, +\frac{U}{2}|\mathbf{k}_2\rangle, 0|\mathbf{k}_1, \mathbf{k}_2\rangle\}. \tag{2.218}$$

Interestingly, the states with two (and, of course, zero) electrons exhibit the same energy,

i.e., 0, for both systems. However, the physical origin of this value is quite different in the two cases: In the non-interacting model the energy of the state with two particles stems from adding up the two one-particle energies $-\frac{U}{2}$ and $+\frac{U}{2}$. On the contrary, the energy of the doubly occupied state in the atomic limit does not originate from summing the energies of two independent particles but from the interaction between them[26]. In other words, the single-particle energies in the atomic limit do depend on whether the impurity site is empty or singly occupied. Such information is intrinsically beyond any one-particle description and represents a clear manifestation of correlations. This can be, more formally, understood by resorting to the diagrammatic representation of the one-particle Green's function and the Dyson equation [see Eq. (2.156)]. Considering that $G_0(\nu) = \frac{1}{i\nu}$ in the non-interacting atomic case ($t = 0$, $U = 0$), the additional contribution in the denominator of Eq. (2.216), $\frac{U^2}{4i\nu}$, should be connected to the self-energy of the system. Indeed, taking into account the contribution $\mu = \frac{U}{2}$ from the chemical potential one obtains for the self-energy of a single half filled atom:

$$\Sigma(\nu) = \frac{U}{2} + \frac{U^2}{4i\nu}. \tag{2.219}$$

In contrast to the self-energy $\Sigma_{(U=0)}(\nu) = 0$ for the non-interacting case, the self-energy in Eq. (2.219) exhibits a rather strong frequency dependence: It *diverges* for $\nu \to 0$, which well exemplifies the inapplicability of a an independent particle description for the system.

The fundamental difference between the interacting atomic limit and the non-interacting two-site Hubbard model discussed above becomes, however, immediately evident in the two- and more-particle Green's functions. In fact, while in the non-interacting case, they can be obtained by summing up products of one-particle Green's functions, this is not possible for the interacting atomic limit. On the contrary, it is a typical hallmark of correlations that higher-order correlation functions (e.g., here two- and more-particle Green's functions) do not factorize but rather contain a (connected) vertex part F (even diverging for $T \to 0$), such as defined in Eq. (2.159) and Fig. 2.8. In fact, the non-vanishing of the vertex part in a two-particle Green's function can be regarded as the "defining" property of electronic correlations. In this respect, the atomic limit provides a simple, analytically solvable, model system, from which one can gain a basic understanding of electronic correlations, and which can serve as a benchmark for numerical methods for treating more general situations.

For the actual calculation of the generalized susceptibility and the vertex function in the

---

[26]*Both* single particle states $|\uparrow\rangle$ and $|\downarrow\rangle$ exhibit the one-particle energy $-\frac{U}{2}$. Hence, adding them up in the doubly occupied state would lead to an energy $-U$, but the term $U\hat{n}_\uparrow\hat{n}_\downarrow$ in the Hamiltonian puts this energy level back to 0 since the Coulomb energy $+U$ has to be paid if both electrons are at the same site.

atomic limit [47, 48, 70], we start from the definition of the two-particle Green's function. Note that we present only the derivation for the two-particle Green's function in the $\uparrow\downarrow$ sector $(G_{2,\uparrow\downarrow})$, since $G_{2,\uparrow\uparrow}$ can be calculated analogously or can be even deduced from the latter by means of a SU(2) symmetry relation as given in Tab. 2.1. Let us recall the definition of G_2 as a function of imaginary times τ_i:

$$G_{2,\uparrow\downarrow}(\tau_1, \tau_2, \tau_3, 0) = \frac{1}{Z}\text{Tr}\left(\text{T}\left[\hat{c}_\uparrow^\dagger(\tau_1)\hat{c}_\uparrow(\tau_2)\hat{c}_\downarrow^\dagger(\tau_3)\hat{c}_\downarrow(0)\right]\right), \qquad (2.220)$$

where $Z = 2(1 + e^{\frac{\beta U}{2}})$ for the atomic limit. In the next step we use the definition $\hat{c}_\sigma^{(\dagger)}(\tau) = e^{\beta\hat{\mathcal{H}}}\hat{c}_\sigma^{(\dagger)}e^{-\beta\hat{\mathcal{H}}}$ for the creation and annihilation operators and the action of the Hamiltonian on the four states of the system, which is given above in Eq. (2.214), to evaluate the trace in Eq. (2.220). The time ordering operator produces six distinct terms corresponding to the six possible arrangements of τ_1, τ_2 and τ_3. By evaluating the trace in Eq. (2.220), one can see that –in the atomic limit– for each of the six time orders only one of the four basis states yields a non-vanishing contribution[27]. The explicit calculation of the trace for all six time sequences is then straightforward and yields:

$$\begin{aligned}
G_{2,\uparrow\downarrow}(\tau_1, \tau_2, \tau_3, 0) = \frac{1}{Z}\Big[& e^{\frac{U}{2}(+\tau_1-\tau_2+\tau_3)}\theta(\tau_1-\tau_2)\theta(\tau_2-\tau_3) \\
& +e^{\frac{U}{2}(+\tau_1+\tau_2-\tau_3)}\theta(\tau_1-\tau_3)\theta(\tau_3-\tau_2) \\
& +e^{\frac{U}{2}(-\tau_1+\tau_2+\tau_3)}\theta(\tau_3-\tau_1)\theta(\tau_1-\tau_2) \\
& -e^{\frac{U}{2}(\beta+\tau_1-\tau_2-\tau_3)}\theta(\tau_2-\tau_1)\theta(\tau_1-\tau_3) \\
& -e^{\frac{U}{2}(\beta-\tau_1-\tau_2+\tau_3)}\theta(\tau_2-\tau_3)\theta(\tau_3-\tau_1) \\
& -e^{\frac{U}{2}(\beta-\tau_1+\tau_2-\tau_3)}\theta(\tau_3-\tau_2)\theta(\tau_2-\tau_1)\Big].
\end{aligned} \qquad (2.221)$$

where $0 \leq \tau_1, \tau_2, \tau_3 \leq \beta$ and $Z = 2(1 + e^{\frac{\beta U}{2}})$. Now one can perform the Fourier transform of this function:

$$\begin{aligned}
G_{2,\uparrow\downarrow}(\nu, \nu+\omega, \nu'+\omega) &= \int_0^\beta d\tau_1 d\tau_2 d\tau_3 e^{-i\nu\tau_1}e^{i(\nu+\beta)\tau_2}e^{-i(\nu'+\omega)\tau_3}G_{2,\uparrow\downarrow}(\tau_1, \tau_2, \tau_3, 0) = \\
&= \chi_{\uparrow\downarrow}^{\nu\nu'\omega} + \beta G(\nu)G(\nu')\delta_{\omega 0},
\end{aligned} \qquad (2.222)$$

---

[27]Specifically, (i) since the rightmost operator $\hat{c}_\downarrow$ annihilates an electron with spin $\downarrow$ only the eigenstates $|\downarrow\rangle$ and $|\uparrow\downarrow\rangle$ yield a finite contribution; (ii) which of the two eigenstates eventually survives in the final result depends on the order of the $\uparrow$-operators. For the sequence $\hat{c}_\uparrow^\dagger \ldots \hat{c}_\uparrow$ the state has to contain an $\uparrow$-electron as well and, hence, the only state contributing from the trace is $|\uparrow\downarrow\rangle$. For the time orders which lead to the sequence $\hat{c}_\uparrow \ldots \hat{c}_\uparrow^\dagger$ of the $\uparrow$-operators the state must not contain an $\uparrow$-electron, and, hence, the only state contributing to the trace is $|\downarrow\rangle$.

where the one-particle Green's function G for the atomic limit has been derived in Eq. (2.216). The explicit evaluation of the Fourier transform in Eq. (2.222) is now, though lengthy, straightforward. The vertex function $F_{\uparrow\downarrow}$ can be obtained from $\chi_{\uparrow\downarrow}$ by dividing the latter through the product of four Green's functions, i.e., $G(\nu)G(\nu+\omega)G(\nu')G(\nu'+\omega)$, and multiplying with (-1) [see Eq. (2.159)]. The final result for $F_{\uparrow\downarrow}$ reads as[28]:

$$
F_{\uparrow\downarrow}^{\nu\nu'\omega} = U - \frac{U^3}{8}\frac{\nu^2 + (\nu+\omega)^2 + (\nu'+\omega)^2 + (\nu')^2}{\nu(\nu+\omega)(\nu'+\omega)\nu'} - \frac{3U^5}{16}\frac{1}{\nu(\nu+\omega)(\nu'+\omega)\nu'} +
$$

$$
- \beta\frac{U^2}{4}\frac{1}{1+e^{\beta U/2}}\frac{2\delta_{\nu(-\nu'-\omega)} + \delta_{\omega 0}}{(\nu+\omega)^2(\nu'+\omega)^2}\left((\nu+\omega)^2 + \frac{U^2}{4}\right)\left((\nu'+\omega)^2 + \frac{U^2}{4}\right) + \quad (2.223)
$$

$$
+ \beta\frac{U^2}{4}\frac{1}{1+e^{-\beta U/2}}\frac{2\delta_{\nu\nu'} + \delta_{\omega 0}}{\nu^2(\nu'+\omega)^2}\left(\nu^2 + \frac{U^2}{4}\right)\left((\nu'+\omega)^2 + \frac{U^2}{4}\right).
$$

The meaning of the several contributions to $F_{\uparrow\downarrow}$ can be easier understood by considering the limit $T \to 0$, i.e., $\beta \to \infty$. In this case, the terms in the first line do not change at all, since it is independent[29] of β. The expression in the third line of Eq. (2.223), instead, even diverges when $\beta \to \infty$ since $\beta(1+e^{-\frac{\beta U}{2}})^{-1} \xrightarrow{\beta\to\infty} \beta \to \infty$. More specifically, this divergence occurs for the (ν, ν')-independent background $\omega = 0$ ($\delta_{\omega 0}$) and for the main diagonal $\nu = \nu'$ ($\delta_{\nu\nu'}$), and follows a $\beta = \frac{1}{T}$ Curie-Weiss law. As we will discuss in more detail in Sec. 3.2.1, such a $\frac{1}{T}$ divergent behavior is a hallmark of the formation of long-living local magnetic moment in the system, which corresponds to the onset of a Mott-insulating phase for sufficiently large values of the Hubbard interaction U. In this respect we can gain further insight by considering the explicit evaluation of the trace for calculating the two-particle Green's function. As discussed in the paragraph after Eq. (2.220) only the states $|\downarrow\rangle$ and $|\uparrow\downarrow\rangle$ contribute to the trace. According to Eq. (2.214) the state $|\downarrow\rangle$ is one of the ground states of the system while $|\uparrow\downarrow\rangle$ represent an excited state. In the limit $\beta \to \infty$ only the ground state should contribute to the calculation of the vertex function $F_{\uparrow\downarrow}$, consistent with the fact that in this limit the system exhibits a magnetic moment.

Let us turn to the second line of Eq. (2.223). One can clearly see that it vanishes for $\beta \to \infty$ due to the exponential factor $(1 + e^{\frac{\beta U}{2}})^{-1}$. As a consequence, such a contribution should originate exclusively from the excited state $|\uparrow\downarrow\rangle$ in the trace. This is also consistent with the term $\delta_{\nu(-\nu'-\omega)}$, describing the local scattering of the two particles with energies $\nu + \omega$ and

---

[28]The result of Eq. (2.223) has been also derived in Ref. [70], albeit with a small typo, and for a more general case, i.e., for an arbitrary filling and with a magnetic field, in Ref. [47].

[29]In fact, β enters the terms in the first line of Eq. (2.223) only implicitly via the definition of the Matsubara frequencies ν, ν' and ω.

ν' in the excited state $|\uparrow\downarrow\rangle$. It is obvious that particle-particle scattering events are strongly suppressed by the repulsive interaction U at low temperatures, and, hence, the corresponding part of the vertex function diminishes.

The $\uparrow\uparrow$-vertex can be calculated in principle in the same way as $F_{\uparrow\downarrow}$. However, it is much simpler to derive it from the SU(2) symmetry relation $F_{\uparrow\uparrow}^{\nu\nu'\omega} = F_{\uparrow\downarrow}^{\nu\nu'\omega} - F_{\uparrow\downarrow}^{\nu(\nu+\omega)(\nu-\nu')}$ as given in Tab. 2.2). An easy calculation yields for $F_{\uparrow\uparrow}$:

$$F_{\uparrow\uparrow}^{\nu\nu'\omega} = \beta \frac{U^2}{4} \frac{\delta_{\nu\nu'} - \delta_{\omega 0}}{\nu^2(\nu'+\omega)^2} \left(\nu^2 + \frac{U^2}{4}\right) \left((\nu'+\omega)^2 + \frac{U^2}{4}\right). \tag{2.224}$$

This vertex function is concentrated on the planes $\nu = \nu'$ and $\omega = 0$ in the three-dimensional frequency space spanned by (ν, ν', ω). Similarly as the term in the third line of Eq. (2.223) it diverges as $\beta = \frac{1}{T} \to \infty$, for the very same reason as for $F_{\uparrow\downarrow}$. Finally, we want to stress here that, due to the particularly simple structure of $F_{\uparrow\uparrow}$ in the atomic limit, the corresponding irreducible particle-particle vertex $\Gamma_t = \Gamma_{pp,\uparrow\uparrow}$ can be calculated analytically. For this purpose we make the Ansatz:

$$\Gamma_{pp,\uparrow\uparrow}^{\nu\nu'\omega} = \Gamma_t^{\nu\nu'\omega} = \gamma(\nu',\omega) \left[\delta_{\nu\nu'} - \delta_{\nu(-\nu'+\omega)}\right] = \gamma(\nu,\omega) \left[\delta_{\nu\nu'} - \delta_{\nu(-\nu'+\omega)}\right], \tag{2.225}$$

and rewrite $F_{\uparrow\uparrow}^{\nu\nu'\omega}$ in the particle-particle notation:

$$\begin{aligned} F_{pp,\uparrow\uparrow}^{\nu\nu'\omega} &= \beta \frac{U^2}{4} \frac{\delta_{\nu\nu'} - \delta_{\nu(-\nu'+\omega)}}{\nu^2(\omega-\nu)^2} \left(\nu^2 + \frac{U^2}{4}\right) \left((\omega-\nu)^2 + \frac{U^2}{4}\right) = \\ &= -\beta \frac{1}{G(\nu)G(\omega-\nu)} \frac{U^2}{4\nu(\omega-\nu)} \left[\delta_{\nu\nu'} - \delta_{\nu(-\nu'+\omega)}\right] = \\ &= -\beta \frac{1}{G(\nu')G(\omega-\nu')} \frac{U^2}{4\nu(\omega-\nu)} \left[\delta_{\nu\nu'} - \delta_{\nu(-\nu'+\omega)}\right]. \end{aligned} \tag{2.226}$$

Inserting now the equations (2.225) and (2.226) for $F_{pp,\uparrow\downarrow}$ and $\Gamma_{pp,\uparrow\downarrow} = \Gamma_t$ into the corresponding Bethe-Salpeter Eq. (B.14a) yields:

$$\begin{aligned} F_t^{\nu\nu'\omega} &= \Gamma_t^{\nu\nu'\omega} - \frac{1}{2\beta} \gamma(\nu',\omega)(-\beta) \frac{U^2}{4\nu(\omega-\nu)} \underbrace{\sum_{\nu_1} \left[\delta_{\nu_1\nu'} - \delta_{\nu_1(-\nu'+\omega)}\right]\left[\delta_{\nu(-\nu_1+\omega)} - \delta_{\nu\nu_1}\right]}_{-2\left[\delta_{\nu\nu'} - \delta_{\nu(-\nu'+\omega)}\right]} = \\ &= \Gamma_t^{\nu\nu'\omega} - \frac{U^2}{4\nu(\omega-\nu)} \Gamma_t^{\nu\nu'\omega} \end{aligned}$$

$$\tag{2.227}$$

Hence, in the triplet channel the connection between the full vertex F_t and the irreducible one Γ_t reduces to the simple algebraic relation:

$$\Gamma_t^{\nu\nu'\omega} = \frac{1}{1 - \frac{U^2}{4\nu(\omega-\nu)}} F_t^{\nu\nu'\omega}. \qquad (2.228)$$

This equation illustrates very well that one has to expect *divergences* in the irreducible vertices. Specifically, in the atomic limit, Γ_t will exhibit a divergence for particular values of the interaction strength (U) and Matsubara frequencies fulfilling the condition:

$$\frac{U^2}{4} = \nu(\omega - \nu), \qquad (2.229)$$

provided that $\omega > 0$. In fact, we will see in the next chapter (Sec. 3.2.2) that such kind of divergences appear in irreducible vertex functions not only in the atomic limit and even at $\omega = 0$ (in the other channels). Their nature is fundamentally different from the infinities of the full vertex F, which takes place exactly at the Mott transition and originating from the formation of the local magnetic moment. In fact, it will be shown that the first divergences of Γ_r can rather be interpreted as non-perturbative "precursors" of the Mott transition itself [71], appearing well inside the metallic regime of the system.

Chapter 3

Local correlations

„In der Mitte wirst du am sichersten gehen.“(Ovid)

In many significant situations the physics of a bulk correlated electron system is dominated by local correlations, i.e., correlations between two electrons at the same lattice site. From a theoretical viewpoint, neglecting nonlocal correlations and considering only the local ones corresponds to a quantum extension of the classical Weiss mean field theory. This extension is known as dynamical mean field theory (DMFT). This approach has become one of the most successful tools for treating correlated electron systems in the last 20 years and allows for a direct calculation of one-particle quantities, such as Green's and spectral functions. As a standard application of DMFT for explaining correlation effects, we present a specific study of the optical spectral weight in the cuprate high-temperature superconductors. The main part of this chapter is, however, dedicated to the analysis of (local) two-particle quantities in the framework of DMFT, i.e., of the local generalized susceptibilities and local vertex functions. While a systematic DMFT analysis at the two-particle level was hitherto missing in the literature, this represents a very important issue, because the two-particle vertices represent the main ingredient for (i) calculating momentum-dependent response functions at the DMFT level and (ii) treating nonlocal spatial correlations at all length scales by means of diagrammatic extensions of DMFT.

In the last section of the previous chapter (Sec. 2.2.7) it has been recalled that non-interacting many-particle systems allow in general for an analytic solution, i.e., an explicit analytic calculation of the one- and more-particle Green's functions. The corresponding results for the one-particle Green's functions of the Hubbard model and the AIM are given in Eqs.

(2.200) and (2.208). On the contrary, in the case of interacting particles only very specific and/or very simple systems, such as the atomic limit discussed in section 2.2.7.2, are exactly solvable.

On the contrary, for a general case, direct numerical simulations of correlated electrons on a lattice are, at present, usually restricted to small clusters of about ~ 100 sites due to the exponential growth of the Hilbert space with the system size. Hence, in general, approximations are needed in order to treat Hamiltonians exhibiting a two- (or even more)-particle interaction term. As for the Hubbard model [Eq. (2.22)] and the AIM [Eq. (2.23)] a perturbative expansion in the interaction might be only applicable (depending on the temperature and doping regime considered) if the interaction parameter U is much smaller than the energy scale of the non-interacting part of the Hamiltonian, i.e., the hopping parameter t and the hybridization function $\Delta(\nu)$, respectively [see Eqs. (2.209) and (2.210)]. In particular, second order phase transitions cannot be described by any kind of plain lowest order perturbation theory, not even in classical statistical mechanics [72].

One of the most important attempts to attack the problem of strongly correlated systems is the *mean-field* approach which was invented by P. E. Weiss [73] as a theory of magnetism, and was applied successfully, in particular, for treating the Ising model [74]. For long time, it was the *only* theory of phase transitions, and L. D. Landau even suggested that mean-field theory was essentially exact for describing critical phase transitions [75, 76]. Nowadays, we know that this is not the case except for sufficiently large values of the spatial dimensionality or for systems with infinite-range interactions [77].

For introducing the concept of mean-fields theories in general, let us discuss, exemplarily, the mean-field solution of the classical Ising model on a d-dimensional lattice. The corresponding model Hamiltonian , in absence of an external magnetic field, is given by:

$$\mathcal{H} = -\frac{1}{2}\mathcal{J}\sum_{\langle ij\rangle} s_i s_j, \tag{3.1}$$

where $\langle\cdot\rangle$ denotes the summation over nearest-neighbor sites, and the (classical) spin at the lattice i can take the values $s_i = \pm 1$. Obviously, $\mathcal{J} > 0$ favors energetically ferromagnetic alignment of the spins while for $\mathcal{J} < 0$ the system has a tendency towards an antiferromagnetic ordering. The numerical value of the parameter $\mathcal{J}$ has to be renormalized by the coordination number z, i.e., the number of nearest neighbors on the lattice:

$$\mathcal{J} = \frac{\mathcal{J}^*}{z}, \tag{3.2}$$

in order to render the average energy per lattice site independent of z, i.e., it also remains finite if $z \to \infty$. This is, e.g., the case for a simple cubic lattice in infinite spatial dimensions[1]. The variable $\mathcal{J}^*$, in turn, is just a constant which is independent from the dimensionality or the coordination number of the system.

Let us now consider the thermal expectation value for s_i which, in some sense, corresponds to the one-particle Green's function in the quantum mechanical case. The corresponding expression reads as:

$$\langle s_i \rangle = \frac{\sum_{\{s_j = \pm 1\}} e^{\frac{\beta \mathcal{J}}{2} \sum_{\langle kl \rangle} s_k s_l} s_i}{\sum_{\{s_j = \pm 1\}} e^{\frac{\beta \mathcal{J}}{2} \sum_{\langle kl \rangle} s_k s_l}}, \tag{3.3}$$

where the normalization factor in the denominator corresponds to the partition function Z of the system and $\sum_{\{s_j = \pm 1\}}$ indicates that the summation over the (two, $s_i = \pm 1$) possible spin configurations is performed for all spins, i.e., all lattice sites, in the system. Even when restricting oneself to a d-dimensional simple cubic lattice, the sums in Eq. (3.3) cannot be performed analytically due to the interacting nature of the Hamiltonian (3.1). The idea of the mean-field approximation is now to replace the interaction between the single spins by an interaction of the spins with an effective external field, generated by the spins themselves. To this end we rewrite the interaction term in the Hamiltonian (3.1) in the following way:

$$s_k s_l = \underbrace{s_k \langle s_l \rangle + \langle s_k \rangle s_l}_{\text{interaction with } h_{\text{eff}}} + \underbrace{(s_k - \langle s_k \rangle)(s_l - \langle s_l \rangle)}_{\text{interaction between fluctuations}} - \underbrace{\langle s_k \rangle \langle s_l \rangle}_{\text{constant energy shift}} . \tag{3.4}$$

The first two terms on the right-hand side of this equation describe the interaction of a spin with an effective field (h_{eff}) generated by the mean value of a neighboring spin, while the third contribution represents the interaction between the fluctuations of neighboring spins around their mean field values. The last summand in Eq. (3.4) is just a constant contribution to the total energy and can be neglected here.

A mean-field treatment of the Ising model corresponds to neglecting the fluctuation term (i.e., the third summand) in Eq. (3.4). Considering the proper scaling of the parameter $\mathcal{J}$ [24] in Eq. (3.2) one can show, that this assumption becomes even exact in the limit of an infinite coordination number ($\to \infty$) or dimension ($d \to \infty$) [24]. It is, however, important to emphasize that for any finite ($d = 1, 2, 3$) dimensions the neglect of the fluctuation term constitutes just an *approximation*, namely a "mean-field" approximation.

---

[1]Here, in the specific case of a hypercubic lattice geometry, $z = 2d \to \infty$ in the limit of infinite dimensions.
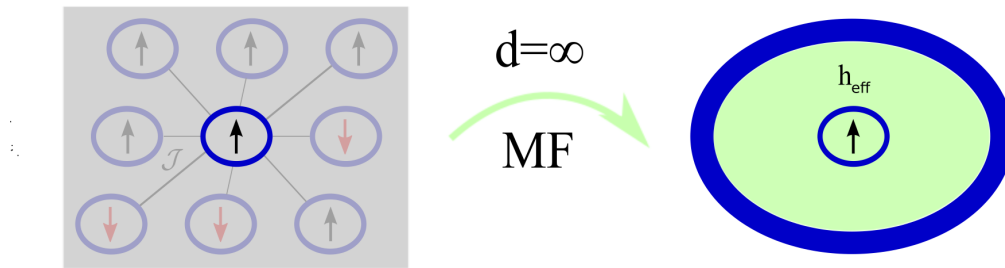
Figure 3.1: Schematic representation of the mean field approximation for the Ising model. An $\uparrow$-spin corresponds to $s_i = +1$, the $\downarrow$-spin to $s_i = -1$. The effective field h_{eff} is given by $h_{\text{eff}} = \mathcal{J}zm = \mathcal{J}^*m$.

In the next step we take into account the homogeneity of the systems which implies that $\langle s_i \rangle = \langle s \rangle \equiv m$, independent from the lattice site i. In this context m represents the expectation value for the magnetic moment per lattice site. We now insert the decomposition of $s_k s_l$, as given in Eq. (3.4), into Eq. (3.3). Applying our mean-field assumptions, i.e., neglecting the third summand in Eq. (3.4), yields:

$$\langle s_i \rangle = m = \frac{\sum_{\{s_j = \pm 1\}} e^{\beta \mathcal{J} m z \sum_k s_k} s_i}{\sum_{\{s_j = \pm 1\}} e^{\beta \mathcal{J} m z \sum_k s_k}} + O\left(\frac{1}{z}\right). \tag{3.5}$$

One can see that the contribution $\mathcal{J}mz = \mathcal{J}^*m \equiv h_{\text{eff}}$ acts as an effective magnetic field for the spin s_k in the exponent of Eq. (3.5). Hence, the mean-field treatment of the Ising model corresponds to replacing the interaction between one specific spin and its neighbors by an interaction between this spin with an effective mean-field generated by the other spins, as it is illustrated in Fig. 3.1. This way, our original two-particle problem from Eq. (3.1) has been reduced to a single-particle description. The mean field h_{eff} has to be determined self-consistently from Eq. (3.5). Indeed, performing all the sums in the latter relation leads to:

$$m = \tanh(\beta h_{\text{eff}}), \qquad\qquad h_{\text{eff}} = \mathcal{J}^*m. \tag{3.6}$$

This relation is the required self-consistency condition between the mean magnetization m and the effective interaction h_{eff}, which, in this simple case, can be solved graphically or semi-analytically. Within this mean-field framework, it is then relatively easy to derive, e.g., all correlations functions and the (meand-field) critical behavior ("Gaussian" critical
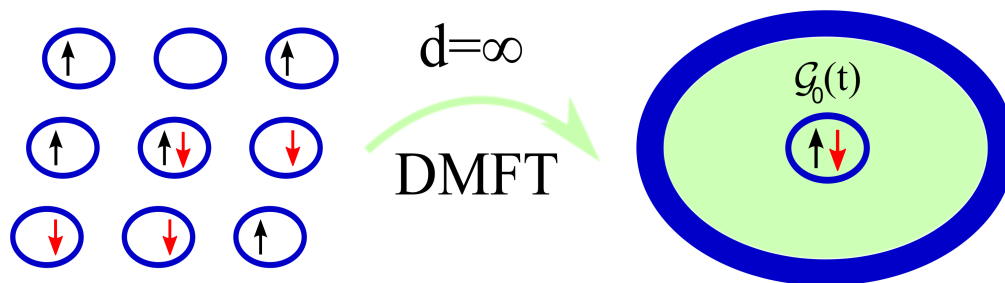
Figure 3.2: Mapping of the Hubbard model onto an effective single site problem embedded in a *time-dependent* mean-field $\mathcal{G}_0(t)$.

exponents) [33, 72, 78] of the Ising model.

The method described above represents evidently a *static* mean-field approach, i.e., the average over s_i is taken with respect to both space and time. This is appropriate for a classical system such as the Ising model, where no dynamical spin fluctuations can occur. However, for a corresponding quantum system, local quantum fluctuations might give rise, beyond the spatial correlations generated by the third term on the right-hand side of Eq. (3.4), also to purely temporal correlation effects, calling for a corresponding extension of the mean field scheme presented above [22].

3.1 Dynamical mean-field theory (DMFT) and the limit of infinite dimensions

The main focus of this thesis is on the quantum Hubbard Hamiltonian defined in Eq. (2.22), which represents one of the most basic models for describing correlated electron systems. As already mentioned before, in spite of its rather simple form, the solution of the Hubbard model for the non-trivial cases, where $U \neq 0$ and $t \neq 0$, remains a formidable theoretical challenge. In particular, in the situation where the kinetic energy scale t and the interaction energy scale U are of the same order of magnitude, a perturbative treatment [79, 80] of one of these two parts of the Hamiltonian yields very poor results. Much better results for the non-perturbative regime has been obtained by applying to this quantum model similar steps as those of the mean-field theory for the Ising model. Specifically one can replace, also for the Hubbard model, the actual lattice of interacting sites by one interacting site, which is coupled to a mean-field generated by the electrons at the remaining sites. This procedure, which corresponds to performing a spatial average, is indicated schematically in Fig. 3.2. The crucial difference with respect to the static mean-field approach for the

DMFT-flow

$$G^{\mathrm{new}}(\nu) = \sum_{\mathbf{k}} G(\nu, \mathbf{k})$$

$$G_0(\nu, \mathbf{k})$$

| AIM $\mathcal{G}_0(\nu)$ | Impurity-solver | $G(\nu)$ | Inverse Dyson Eq. | $\Sigma(\nu)$ | Dyson equation | $G(\nu, \mathbf{k})$ |
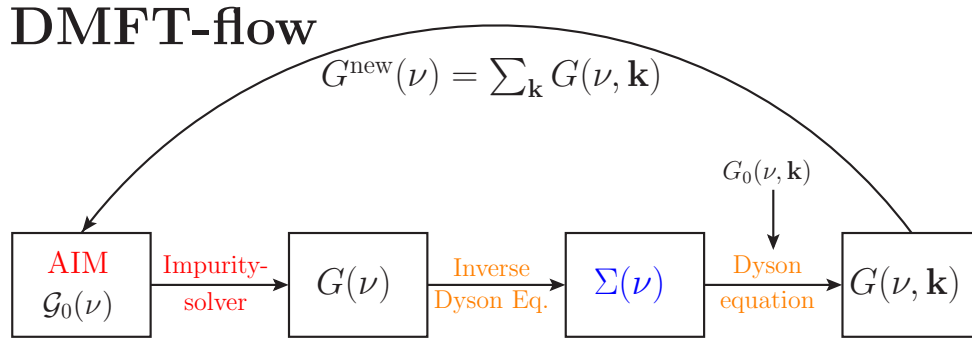
Figure 3.3: Flow diagram of DMFT. $G(\nu, \mathbf{k}) \widehat{=} G_{\mathrm{DMFT}}(\nu, \mathbf{k})$ in this figure.

(classical) Ising model is, however, that we keep now the time dependence of the mean-field $\mathcal{G}_0(t)$, which well explains the denotation of this approach as "*dynamical* mean field theory" (DMFT) [22, 24, 25]. In this way, within DMFT, we are able to describe the purely local part of the electronic correlations (i.e., temporal or quantum local fluctuations), neglecting only the nonlocal ones in space[2].

As already mentioned in the discussion of the Ising model, the observable $\langle s_i \rangle$ corresponds to the Green's function $G(\nu, \mathbf{k})$ in case of the Hubbard model. Similarly, $\mathcal{G}_0(t)$ is the time-dependent counterpart of the static mean-field h_{eff} as one can easily infer from a comparison of Figs. 3.1 and 3.2. However, the Hubbard model analog to the relation between the observable and the mean-field, which is just the algebraic equation $h_{\mathrm{eff}} = \mathcal{J} z \langle s_i \rangle = \mathcal{J}^* \langle s_i \rangle$ in the Ising case [see Eq. (3.6)], cannot be written (and solved!) so easily. In this respect, a breakthrough was achieved in a seminal paper by Georges and Kotliar [81], who realized that a given dynamical mean-field representation of the Hubbard model on the right-hand side of Fig. 3.2 corresponds to the solution of an AIM. In fact, in the latter, one interacting site is hybridized with a non-interacting bath which can be described by a hybridization function $\Delta(\nu)$ or, equivalently, by a local non-interacting Green's function $\mathcal{G}_0(\nu)$, which is just the Fourier transform of $\mathcal{G}_0(t)$ [see Eqs. (2.208) and (2.209), where $G_{cc}(\nu) \widehat{=} \mathcal{G}_0(\nu)$]. The crucial advantage of this identification is, that it is easy to set up a systematic scheme for the practical application of DMFT, as it is also illustrated in the flow diagram in Fig. 3.3:

1) Starting from an AIM defined by the hybridization function $\Delta(\nu)$ or the corresponding non-interacting Green's function $\mathcal{G}_0(\nu)$ one has to calculate the interacting local Green's function $G(\nu)$ by means of an impurity solver (such as, e.g., exact diagonalization (ED) [24], quantum Monte Carlo (QMC) [82, 83], numerical renormalization group

---

[2]For a discussion of local and nonlocal correlations in the Hubbard model see also Sec. 2.1.1.

(NRG) [84] or density matrix renormalization group (DMRG) [85–87]). Let us stress that this step corresponds to a numerically "exact" solution of a correlated system and, hence, all local correlations of the AIM are taken into account.

2) One extracts the local[3] self-energy of the AIM, $\Sigma(\nu)$ from $G(\nu)$ by means of the Dyson equation [Eq. (2.156)] for the AIM. Let us note that $\Sigma(\nu)$ is exactly the part of $G(\nu)$ which describes the (purely local) correlations in the system. In fact, $\Sigma(\nu) \equiv 0$ for the non-interacting case $U = 0$ and it diverges in the atomic limit [for $T = 0$, see Eq. (2.219)].

3) We turn now to the original lattice problem, we are interested in, which is defined by the bare dispersion $\varepsilon_{\mathbf{k}}$ or the bare lattice Green's function $G_0(\nu, \mathbf{k})$ as given in Eq. (2.200). The DMFT expression for the interacting lattice Green's function is then given by:

$$G_{\mathrm{DMFT}}(\nu, \mathbf{k}) = \frac{1}{i\nu - \varepsilon_{\mathbf{k}} + \mu - \Sigma(\nu)}. \tag{3.7}$$

One can see that the (purely) local correlations are included in this DMFT lattice Green's function via the local self-energy $\Sigma(\nu)$ of the related AIM. Let us stress that $G_{\mathrm{DMFT}}(\nu, \mathbf{k})$ corresponds to the expectation value $\langle s_i \rangle$ in the Ising model.

4) In the last step we extract the local part of the DMFT Green's function [Eq. (3.7)] and compare it to the local Green's function of the corresponding AIM. If

$$\sum_{\mathbf{k}} G_{\mathrm{DMFT}}(\nu, \mathbf{k}) = G(\nu), \tag{3.8}$$

then the DMFT cycle already converged. Otherwise we update the mean field $\mathcal{G}_0(\nu)$ by means of the Dyson equation:

$$\mathcal{G}_0^{\mathrm{new}}(\nu) = \left[\sum_{\mathbf{k}} G_{\mathrm{DMFT}}(\nu, \mathbf{k}) \right]^{-1} + \Sigma(\nu). \tag{3.9}$$

Then we iterate the cycle starting again from step 1) with the new mean-field $\mathcal{G}_0^{\mathrm{new}}(\nu)$ until convergence is reached. Let us note that Eq. (3.9), i.e., the relation between

---

[3]Note that, in this chapter, for the *local* quantities, i.e., the one- and the two-particle Green's functions, the self-energy and the vertices, the same notation as in Cap. 2 will be used, i.e., *no* additional subscript "loc" will be added to them (in contrast to Cap. 4, where such a subscript will be attached to all local quantities). This should, however, not lead to any confusion in the present chapter, since the only $\mathbf{k}$-dependent quantity, which occurs here, is the DMFT Green's function $G_{\mathrm{DMFT}}(\nu, \mathbf{k})$.

a)
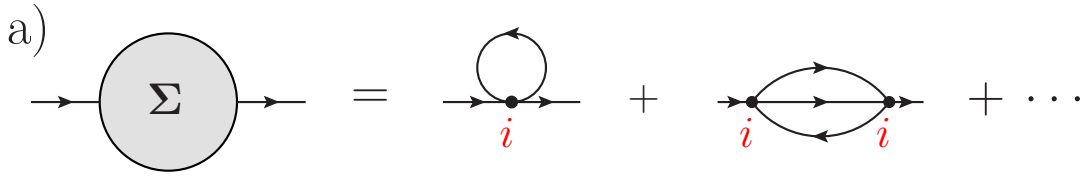
Figure 3.4: Skeleton diagrams for the DMFT self-energy. The DMFT self-energy is purely local, being built by purely local skeleton diagrams only, exactly as in the cas of the impurity self-energy of the AIM. (i denotes here the index of the lattice site $\mathbf{R}_i$.)

the Green's function of the Hubbard model (in the DMFT approximation) and the non-interacting local Green's function $\mathcal{G}_0(\nu)$, represents the quantum counterpart of the self-consistency equation $h_{\mathrm{eff}} = \mathcal{J}z\langle s_i\rangle = \mathcal{J}^*\langle s_i\rangle$ [see Eq. (3.6)] for the Ising model, which relates the mean field h_{eff} to the expectation value of the observable s_i, i.e., the mean magnetization $m \equiv \langle s_i\rangle$.

From the above discussion, it should be clear that correlations enter the DMFT cycle via the exact solution the AIM, a full interacting quantum many body problem, which is nevertheless numerically treatable since only *one* interacting site is involved. Still, in most of the cases the calculation of the local Green's function of the AIM is the numerical bottleneck of the DMFT algorithm, in particular for complicated many-orbital problems.

From a more theoretical perspective, in the discussion of the Ising model at the beginning of this chapter we stated that the corresponding mean field solution gets exact in the limit of an infinite coordination number $z \to \infty$. An analogous conclusion can be drawn [22] for the DMFT solution of the Hubbard model. While we refer to Refs. [24,88–91] for a rigorous derivation of this statement, we sketch briefly here the main ingredients of ingredients of the proof.

First of all, in order to render the average kinetic and potential energy independent of the dimension of the system, we have to introduce a proper scaling for the corresponding parameters t and U, analogous to Eq. (3.2) for the scaling of $\mathcal{J}$ in the Ising model:

$$t = \frac{t^*}{\sqrt{z}}, \qquad\qquad\qquad U = U^*, \qquad\qquad (3.10)$$

where t^* and U^* are constants independent from the coordination number or the dimension of the lattice. One observes that the interaction parameter U, due to its locality in space, remains unchanged when changing z or d, while the hopping t has to be rescaled with $\sqrt{z}$ in order to keep the kinetic energy finite in the limit $z \to \infty$. With the scaling in Eq. (3.10) one

can show that all skeleton diagrams[4], for the self-energy of the Hubbard model are purely local in the limit of an infinite coordination number z. This state of affairs is illustrated explicitly in Fig. 3.4. Hence, it becomes clear also from this diagrammatic point of view that the DMFT self-energy of the Hubbard model formally does coincides with the local self-energy of an corresponding AIM in the limit of infinite coordination number or dimension. Hence, the DMFT approach of Figs. 3.2 and 3.3 can be formally seen as the exact solution of our quantum many-body problem in this limit.

Let us stress, that for a finite coordination number the DMFT Green's function $G_{\mathrm{DMFT}}(\nu, \mathbf{k})$ in Eq. (3.7) represents just an approximation for the real Green's function of the Hubbard model. This observation leads to significant consequences for two- and more-particle Green's functions: While the DMFT self-consistency guarantees that the local part of the *one-particle* DMFT lattice Green's function coincides with the *one-particle* local AIM Green's function, i.e., $\sum_{\mathbf{k}} G_{\mathrm{DMFT}}(\nu, \mathbf{k}) = G(\nu)$, for any coordination number z, this holds in the *two- and more-particle* case only for $z \to \infty$. For instance, we find that, for any finite coordination number z:

$$\sum_{\mathbf{kk'q}} G_{2,\mathbf{kk'q}}^{\mathrm{DMFT}}(\nu, \nu', \omega) \neq G_2(\nu, \nu', \omega), \tag{3.11}$$

where $G_{2,\mathbf{kk'q}}^{\mathrm{DMFT}}(\nu, \nu', \omega)$ can be caluclated via the standard Bethe-Salpeter procedure described, e.g., in Ref. [24]. This violation of the two-particle self-consistency for the DMFT solution at finite z (or d) can also lead to certain difficulties concerning the asymptotic behavior of the self-energy obtained with ladder diagrammatic extensions of DMFT, as it will be discussed in Sec. 4.3.1. Despite this, we recall that for calculating spectral functions, DMFT represents one of the most powerful tools at disposal for treating strongly correlated electron systems. In many important cases, it allows for an accurate many-body quantitative description of the properties of real correlated materials, which are missed by more conventional ab-initio DFT treatments (see Cap. 1). This will be demonstrated in the following section for a specific case.

3.1.1 A DMFT case study: Optical spectral weight in the cuprates

*Parts of the results and the discussion presented in the following section have been already published in the APS Journal "Physical Review Letters": PRL **105**, 077002 (2010).*

---

[4]Skeleton diagrams are constructed from full interacting Green's functions rather than from bare ones and, hence, must not contain self-energy corrections of the internal lines. For a more detailed discussion of this issue we refer to Sec. 2.2.4.1.
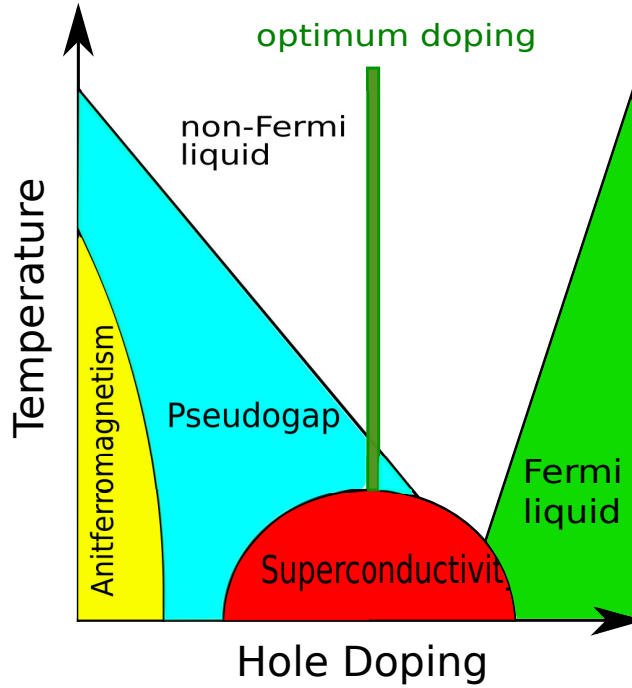
Figure 3.5: Schematic phase-diagram of the hole-doped cuprates as a function of temperature and doping level. The green bar indicates the parameter regime for which the experimental and theoretical study of the two specific Bi-based cuprate compounds discussed in the text was performed.

In this section we present a DMFT study of the optical conductivity $\sigma(\omega, T)$ and the related (partial) sum rule (optical spectral weight) $W(\Omega_c, T)$ for the two Bi-based high-temperature superconducting cuprate compounds $Bi_2Sr_{1.6}La_{0.4}CuO_6$ and $Bi_2Sr_2CaCu_2O_8$. This was motivated by new infrared (IR) optical spectroscopic experimental data for these observables [i.e., $\sigma(\omega, T)$ and $W(\Omega_c, T)$] obtained at increasingly higher temperatures above the superconducting transition temperature T_c of the respective compound at optimum doping[5] (see green bar in the schematic phase-diagram in Fig. 3.5). As it will be shown by a comparison of the theoretical and experimental results, in particular for $W(\Omega_c, T)$ [see Fig. 3.8 below], DMFT provides not only for a qualitative understanding of physical properties of these strongly correlated materials, but it allows also for a quantitative description of the experimental findings.

The topic presented in this section is mainly thought as a demonstrative illustration of the applicability of DMFT to experimentally relevant studies, and, hence, does not represent the main scope of this thesis. For the sake of clarity, however, we will briefly summarize some of

---

[5]That is the amount of hole-doping for which T_c takes its largest value in the phase-diagram of the cuprates (see green bar in Fig. 3.5).
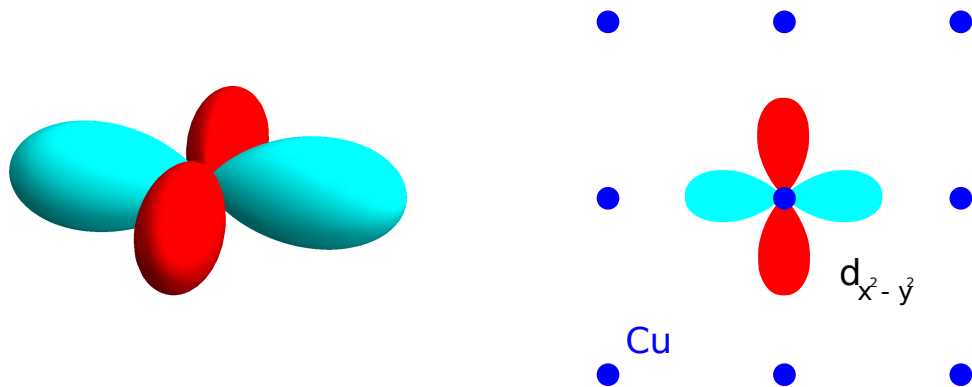
Figure 3.6: Left panel: Copper $3d_{x^2-y^2}$-orbital. Right panel: In our effective model for the Copper-oxygen plane of the cuprates only the $d_{x^2-y^2}$-orbital is taken into account.

the most important facts concerning the high-temperature cuprate superconductors, as well as their optical conductivity sum rules relevant for our DMFT analysis.

Hubbard model for the cuprates. The literature about the cuprates is vast both from the experimental and the theoretical perspective. Hence, we do not aim here at a comprehensive description of the physical properties of this class of materials, but we rather recall the most important facts in a short overview.

In Fig. 3.5 a generic phase-diagram for the cuprates is shown as a function of temperature and hole-doping, where the origin of the coordinate system corresponds to $T = 0$ and $n = 1$ electron per (Cu) lattice site, i.e., without doping (stoichiometric compounds) the system is half-filled. With increasing (hole) doping the insulating antiferromagnetic phase, which is rather typical for strongly correlated electron systems at half filling, turns into a so-called "pseudogap" phase [92]: For specific **k** vectors a gap appears in the spectrum, i.e., the system displays an insulating behavior for these values of the crystal momentum, though no evident long-range order can be individuated in this regime. At *higher temperatures*, this pseudogap phase gradually changes with increasing doping to an "anomalous" metallic state exhibiting non-Fermi liquid behavior. Finally, at a very high concentration of holes, i.e., at a much lower electronic density, the cuprates behave progressively more like a standard Fermi liquid. At *lower temperatures* and intermediate doping levels, however, one observes the appearance of the famous unconventional (d-wave high-T_c) superconductivity [17]. Since the highest critical temperatures for superconductivity in the cuprates largely exceed the condensation temperature of liquid nitrogen (77 K), this class of materials is, of course, a very interesting one from a technological point of view. Hence, it is not surprising that most of the

hitherto existing analyses address the low-temperature behavior, focusing, in particular, on the unconventional superconductivity and the pseudogap state. However, strong correlations also influence the physical properties of these materials at high temperatures, leading, e.g., to interesting effects such as the violation of the Ioffe-Regel limit for resistivity saturation, the quasiparticle thermal decoherence or a linear behavior of the resistivity as a function of temperature [93, 94]. Our investigation, in fact, focuses precisely on the anomalous metal regime *above* the superconducting phase up to very high temperatures (~ 500 K) at optimum doping, as indicated by the vertical green bar in Fig. 3.5.

In order to apply a many-body treatment, such as DMFT, to the specific case of the cuprates, we have to define an appropriate model which covers its basic physics in the parameter regime under consideration. To this end we consider the lattice of these materials: Superconducting cuprates have a layered crystal structure. Cu-O planes alternate with layers containing heavy ions, which act essentially as charge reservoirs. The interesting physics takes place mostly within the Cu-O planes. In the present theoretical investigation, we restrict ourselves to the partially filled Copper $3d_{x^2-y^2}$ orbitals which are rather narrow (see left panel in Fig. 3.6), and, hence, exhibit the strongest correlation effects. In this simplified, but widely used, modelling of the cuprates, the oxygen p_x and p_y bands, as well as spherical and axial orbitals such as Cu $4s$ and Cu $3d_{z^2}$, respectively, are folded down into the Cu $3d_{x^2-y^2}$ state, since the correlation effects are usually rather small for these orbitals. Let us, however, mention that, in general, a single-band description of the cuprates is in many respects not sufficient as it is discussed extensively in the literature [95–98].

Keeping in mind these limitations, we will model the two cuprate compounds under consideration by a two-dimensional single-band Hubbard Hamiltonian on a simple square lattice formed by the Cu atoms, as it is shown schematically in the right panel of Fig. 3.6:

$$H = -\sum_{ij,\sigma} t_{ij} c_{i\sigma}^\dagger c_{j\sigma} + U \sum_i n_{i\uparrow} n_{i\downarrow}, \qquad (3.12)$$

where t_{ij} denotes the hopping amplitude from the lattice site i to the lattice site j. Let us just mention here that this version of the single-band Hubbard model is slightly more general than the corresponding definition in Sec. 2.1.1, Eq. (2.22), since it considers hopping processes between arbitrarily distant sites i and j instead between only nearest neighbors. Specifically, for the two cuprate compounds under consideration, we take into account a nearest neighbor hopping t, a next-nearest neighbor hopping t' (diagonal hopping) and a next-next-nearest
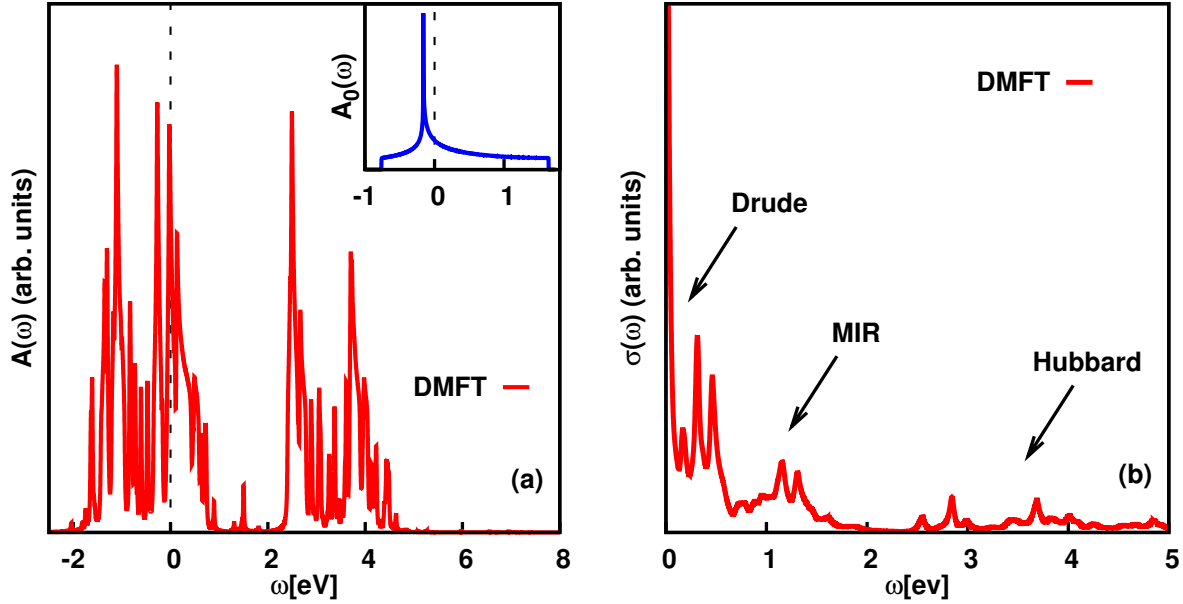
Figure 3.7: (a) **k**-integrated spectral function $A(\omega)$ for the interacting system $Bi_2Sr_{1.6}La_{0.4}CuO_6$ at $T = 100K$ modeled by the Hamiltonian in Eq. (3.12). The inset shows the density of states $A_0(\omega)$ for the corresponding non-interacting system. Dashed lines mark the Fermi levels at $\omega = 0$. (b) Optical conductivity $\sigma(\omega)$ at $T = 100K$. The arrows indicate contributions stemming from optical transitions between different energy intervals of the one-particle spectral function.

neighbor hopping t''. Reasonable numerical values for these parameters[6] are obtained from theoretical calculations (DFT) [98,99] and/or extracted from angular resolved photoemission spectroscopy studies [100]. The parameter U has been chosen[7] according to [99]. As already mentioned, we investigate the system at optimum (hole)doping, i.e., with an average electron density of $n = 0.84$ electrons per Cu-atom (or, more precisely, per Cu $3d_{x^2-y^2}$ orbital).

DMFT calculations Let us first discuss the (one-particle) spectral properties of the system(s) under consideration. To this end we have performed DMFT(ED) calculations, with $N_s = 6(7)$ sites in the ED impurity solver, for $Bi_2Sr_{1.6}La_{0.4}CuO_6$ ($Bi_2Sr_2CaCu_2O_8$). We start by discussing the general features of the DMFT spectral function $A(\omega)$ on the real axis, defined as:

$$A(\omega) = -\frac{1}{\pi} \sum_{\mathbf{k}} G_{\text{DMFT}}(\omega, \mathbf{k}), \tag{3.13}$$

---

[6]Specifically, in our DMFT calculations we used $t = 0.25(0.35)$ eV, $t'/t = -0.2(-0.3)$ and $t''/t' = -0.5(0.0)$ for $Bi_2Sr_{1.6}La_{0.4}CuO_6$ ($Bi_2Sr_2CaCu_2O_8$).

[7]$U = 12t = 3.0(4.2)$ eV for $Bi_2Sr_{1.6}La_{0.4}CuO_6$ ($Bi_2Sr_2CaCu_2O_8$).

where $G_{\mathrm{DMFT}}(\omega, \mathbf{k})$ is given in Eq. (3.7) and ω denotes a real frequency variable.

In Fig. 3.7a the spectral function is shown for the case[8] of $\mathrm{Bi_2Sr_{1.6}La_{0.4}CuO_6}$ at the lowest temperature under consideration ($T = 100K$). The interacting spectrum is characterized by three main features: (i) a (Z-renormalized) quasiparticle peak at the Fermi level $\omega = 0$ (with $Z = \left[1 - \frac{\partial \Sigma(\omega=0)}{\partial \omega}\right]^{-1}$), (ii) the lower Hubbard band, almost "attached" to the coherent peak, and (iii) the upper Hubbard band at $\omega \approx U = 12t = 3.6$ eV which is well separated from the two other main spectral features. The inset in Fig. 3.7a shows the corresponding density of states for the non-interacting system. Notice that the Fermi energy is still relatively far from the van Hove singularity (VHS) for the considered case. Hence, effects stemming from the VHS, such as a strong enhancement of the T-dependence of the chemical potential, are not expected to play a particularly important role here.

Optical conductivity   From the DMFT Green's function $G_{\mathrm{DMFT}}(\omega, \mathbf{k})$ the (DMFT) optical conductivity is computed –except for a purely numerical prefactor– as:

$$\sigma(\omega) \propto \sum_{\mathbf{kk'}} \frac{\partial \varepsilon(\mathbf{k})}{\partial \mathbf{k}} \frac{\partial \varepsilon(\mathbf{k'})}{\partial \mathbf{k'}} \int_{-\infty}^{\infty} d\nu \, \mathrm{Im}\left[G_{\mathrm{DMFT}}(\omega, \mathbf{k})\right] \mathrm{Im}\left[G_{\mathrm{DMFT}}(\omega + \nu, \mathbf{k})\delta_{\mathbf{kk'}}\right] \frac{f(\nu) - f(\omega + \nu)}{\omega},$$

(3.14)

where $f(\nu) = (e^{\nu/T} + 1)^{-1}$ is the Fermi function. Let us just stress here that the expression of the optical conductivity built on a bubble-like convolution of two one-particle Green's functions in Eq. (3.14) becomes rigorously exact, beyond the non-interacting case, only for the single band Hubbard model in infinite dimensions (the pure DMFT limit) [24, 101–104]. This issue will be discussed in more detail at the end of this section.

In Fig. 3.7b the DMFT results for $\sigma(\omega)$ at $T = 100K$ are shown for the compound $\mathrm{Bi_2Sr_{1.6}La_{0.4}CuO_6}$. Considering the corresponding spectrum in Fig. 3.7a, one can easily identify the Drude peak at low energies, stemming from transitions "within" the quasiparticle peak, a mid-infrared (MIR) contribution related to transitions between the quasiparticle peak and the lower Hubbard band as well as high energy contributions at $\omega \sim U$ which are due to transitions from/to the upper Hubbard band.

Let us note that our DMFT data for $A(\omega)$ and $\sigma(\omega)$ in Fig. 3.7 are "spiky" because of exact diagonalization (ED) as impurity solver, which gives rise to a discrete spectrum due to the finite number of bath sites. Therefore, a direct quantitative comparison of frequency resolved observables [such as $A(\omega)$ or $\sigma(\omega)$], calculated from DMFT, with the corresponding experimental data for a given frequency ω is not very insightful. On the other hand, ED

---

[8]Similar results are obtained for the other compound.
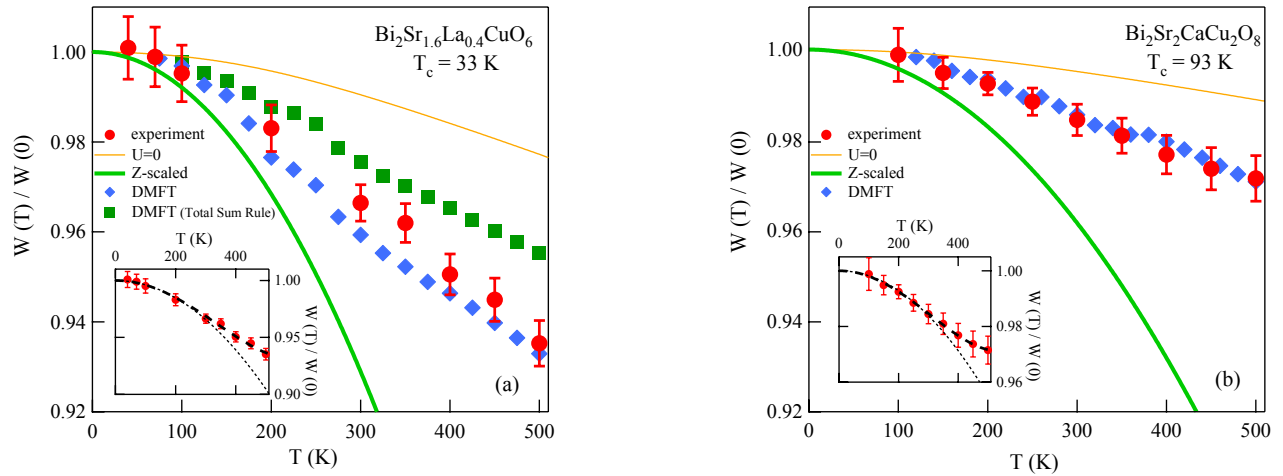
Figure 3.8: Temperature-dependent restricted optical sum rule $W(\Omega_c, T)$ of optimally doped (a) $Bi_2Sr_{1.6}La_{0.4}CuO_6$ and (b) $Bi_2Sr_2CaCu_2O_8$, normalized to the (extrapolated) value at $T = 0$. The experimental data (red circles) are compared with DMFT results for the restricted sum rule (blue diamonds) of the single-band Hubbard model. Also shown are theoretical calculations for the non-interacting system ($U = 0$) and the lowest order Sommerfeld expansion where the coefficient B is simply rescaled by the quasiparticle DMFT weight (Z scaled). In panel (a) DMFT results for the total (one-band) sum rule are displayed for comparison (green squares). In the inset the dotted (dashed) line indicates the fit performed on $W(\Omega_c, T)$ data using Eq. (3.16) up to the second (fourth) order. The figure is reproduced from Ref. [105].

works particularly well for ω-integrated quantities, such as the optical sum rule $W(\Omega_c, T)$, whose behavior and comparison with experiments will be discussed in the next paragraph.

Optical sum rule A quantity which contains essential information about electronic correlations is the (partial) sum rule (or optical spectral weight), which is given by the frequency integral of the optical conductivity up to a cut-off frequency Ω_c:

$$W(\Omega_c, T) = \int_0^{\Omega_c} d\omega \; \sigma(\omega, T). \tag{3.15}$$

For $\Omega_c \to \infty$ the so called f-sum rule is recovered, which implies that W is proportional to the charge density of the system (and therefore independent of the temperature). However, for a finite cut-off Ω_c the temperature behavior of this "restricted" sum rule provides significant information about electronic correlations in the system. Specifically, if Ω_c is chosen[9] in such

---

[9]Experimentally, this frequency Ω_c can be estimated by the position of a minimum in $\sigma(\omega)$, for ω close to the plasma frequency of the system. From a theoretical point of view, the corresponding Ω_c has to be chosen in such a way that the Drude peak and the MIR contribution of $\sigma(\omega)$ [see Fig. 3.7b] contribute to

a way that only the lowest conduction band contributes to W, the sum-rule accounts for the total kinetic energy of the charge carriers in this band. In this respect, it is worth recalling that precisely the reduction of the kinetic energy estimated experimentally from the restricted optical sum rules with respect to the non-interacting theoretical predictions (e.g., from density functional theory) is often used to provide a first quantification of the "correlation degree" of a given material [106–108]. In the particular case of the cuprates, the study of the restricted sum rules has attracted a considerable interest in the last decade [109, 110], because several anomalies have been reported both for the doping dependence of the optical spectral weight [111, 112] as well as for its temperature dependence in the normal and in the superconducting phase [99, 111, 113–118]. In particular, the anomalies reported for the temperature-dependence of the restricted optical sum rule in the normal phase of the cuprates were referred to a particularly enhanced low-temperature increase of the optical spectral weight, attributed mostly to electronic correlations. No attempt was made, at the beginning, to investigate the whole temperature-dependence in the normal phase on a broader temperature interval. This has become possible only more recently, when new infrared/optics experiments were performed by the Roma group of Prof. Lupi and Prof. Calvani, who extended the previous temperature range of their experiments up to 500 K. In particular, in Fig. 3.8 we compare our DMFT data (blue diamonds) for the restricted optical sum rule [$W(T) \equiv W(\Omega_c, T)$] normalized by its value at $T = 0$, i.e., $W(T)/W(0)$, with the corresponding experimental results (red circles) for temperatures up to 500 K. One can clearly see a good agreement between theory and experiment in the whole temperature regime, in contrast to the complete failure of calculations done by neglecting the electronic interactions (U=0). This demonstrates not only the crucial role played by (local) electronic correlations in the high-temperature regime of the cuprates, but it also shows the ability of DMFT to describe quantitatively realistic aspects of strongly correlated materials. We recall here, however, that for a proper theoretical description of other features of the cuprate physics such as, e.g., the onset of unconventional superconductivity, the inclusion of nonlocal correlations beyond DMFT (see Cap. 4) is absolutely needed.

To gain further insight in the specific problem of the optical sum rule at higher temperatures, we have also compared our DMFT results to a (rescaled) Sommerfeld expansion:

$$W(T) \simeq W_0 - BT^2 + CT^4. \tag{3.16}$$

For a non-interacting system such an expansion would certainly work with coefficients $B =$

---

the optical integral $W(\Omega_c, T)$ in Eq. (3.15), yielding a value of roughly 2.5 eV for Ω_c.

B_0 and $C = C_0$ which can be calculated (semi-)analytically in terms, e.g., of the hopping parameters. The question is, however, up to what extent a similar scheme holds also for a correlated system. To a first approximation, assuming that a Fermi liquid (FL) description is still valid, one could expect the Sommerfeld coefficients to be renormalized by correlations as $B = B_0/Z$ and $C = C_0/Z^3$ on the basis of a simple dimensional argument ($B \propto \frac{1}{t} \rightarrow \frac{1}{Zt}$ and $C \propto \frac{1}{t^3} \rightarrow \frac{1}{(Zt)^3}$). As for the comparison, in Fig. 3.8 experimental and DMFT data are plotted together with the curves obtained by a simple rescaling of the non-interacting coefficient B_0 with the quasiparticle renormalization factor Z. The overall agreement in the low-temperature regime appears rather satisfactory, the small deviation observed up to 250-300 K being likely related to the T-dependence of the chemical potential. As for the coefficient C, whose value affects more the high-temperature regime ($T > 300$ K), our analytical calculations demonstrate that the simple dimensional renormalization ($1/Z^3$) is not applicable to the coefficient C_0. In fact, we have seen that its value also depends on frequency- and temperature-dependent scattering terms of $\Sigma(\omega)$, whose role is found to be substantial according to our DMFT calculation. However, as one can observe in the insets of Fig. (3.8), a T^4-fit of our data works up to the highest temperature under consideration, confirming the possibility of a strongly renormalized Fermi liquid description for the high-temperature behavior of the restricted optical sum rule, even though we are in the parameter regime (see green bar in Fig. 3.5) where usually a non-Fermi liquid/anomalous metal behavior of the cuprates would be expected.

Let us conclude this brief illustration of an application of a DMFT calculation to a realistic case, with some more general considerations on the formula used to compute $\sigma(\omega)$ in DMFT, Eq. (3.14). In fact, according to Eq. (3.14), the expression for $\sigma(\omega)$ is obtained only by the product of two Green's functions, which would correspond to the non-interacting contribution of the generalized two-particle (current-current) susceptibility. The latter, in turn, includes generally so-called vertex corrections at all orders, as it is illustrated in Eq. (2.159) and Fig. 2.8. This means, that the optical conductivity should be calculated from a two-particle Green's function rather than from just a product of two one-particle Green's functions. However, it can be shown [24,82,101–104], that, for the single-band Hubbard model in the DMFT limit of infinite coordination number or dimension $z \rightarrow \infty$ ($d \rightarrow \infty$), because of the odd symmetry of the current operator and the locality of the two-particle (irreducible) vertices (inside a ladder resummation), the vertex (i.e., the actual two-particle) part of the generalized susceptibility (i.e., F) vanishes in the calculation of the optical conductivity, and, hence, only the bare bubble term, constructed as the product of two one-particle DMFT Green's functions, survives. While this approximation turns out adequate for the specific

situation under consideration, it should be stressed, that the inclusion of vertex corrections to the bubble-like susceptibility is, in general, decisive for an accurate description of other response functions of correlated systems computed in DMFT. This is well exemplified by recent comparative calculations [119–121] for the local dynamical spin susceptibility in the iron-pnictides, where the inclusion of dynamic vertex corrections is crucial for capturing the main spectral features of the corresponding inelastic neutron scattering experiments. In this context, however, one should note the lack of systematic analyses of the two-particle vertex functions in the DMFT literature. Hence, aiming at filling this gap, we will present our detailed DMFT results for the two-particle Green's and vertex functions of the Hubbard model in the rest of the chapter, starting from the next section.

3.2 DMFT results at the two-particle level

Parts of the results and the discussion presented in the following two sections have been already published in the APS Journal "Physical Review B": PRB **86***, 125114 (2012).*

Apart from the spectral function of a system, which is related to the one-particle Green's function and can be measured experimentally by (angle-resolved) photoemission spectroscopy [(AR)PES], most of the experimentally accessible observables correspond to two-particle Green's functions. Specifically, the (linear) response of a system to a small external perturbation can be usually represented in terms of (generalized) susceptibilities, which have to be extracted from two- instead of one-particle objects [see Eqs. (2.137) and (2.146) for the local case]. Within DMFT such **k**-dependent generalized susceptibilities can be calculated from the Bethe-Salpeter equations in the respective channel [24, 119], i.e., Eqs. (B.6) or (B.18), where the local Green's function in these relations is replaced by $G_{\text{DMFT}}(\nu, \mathbf{k})$ while the irreducible vertex $\Gamma_r^{\nu\nu'\omega}$ is just the local one, obtained from the AIM connected with DMFT solution of the lattice model [see also Eqs. (4.5), (4.6), (4.99) and (4.106) in Cap. 4]. The lowest order contribution to the generalized susceptibility is just the bare DMFT bubble, i.e., the product of two DMFT Green's functions. While this first, "one-particle", part of the generalized susceptibility is sufficient for calculating, e.g., the optical or the thermal conductivity within DMFT (see the discussion in the last section, in particular Eq. (3.14) and Refs. [24, 101, 103, 104]), usually (local) vertex corrections, stemming from $\Gamma_r^{\nu\nu'\omega}$, are essential for an accurate determination of the other response functions within DMFT (see, e.g., Refs. [120, 121]). An increasingly efficient and precise treatment of the vertex corrections, based on a detailed knowledge of the essential properties of the two-particle local vertex func-

tions of DMFT is, hence, highly desirable for the frontier research of correlated electronic systems.

The importance of determining the properties of local (reducible and irreducible) two-particle quantities for the DMFT, i.e., for the AIM connected with the DMFT solution of the Hubbard model, however, goes well beyond the needs for a numerical calculation of momentum- and frequency-dependent response functions at the DMFT level. In fact, reducible and irreducible vertices of the AIM constitute the basic ingredients of the diagrammatic extension of DMFT aiming at an inclusion of spatial correlations at all length scales. Such methods will be analyzed extensively in Cap. 4 (see, in particular, Sec. 4.1.2).

The above considerations clearly show the central role of local two-particle Green's functions, in particular generalized susceptibilities and vertices, for a theoretical description of strongly correlated systems. In spite of such relevance, as we mentioned before, no systematic study of the two-particle quantities has been presented in the DMFT literature hitherto (only very recently we learned about a related study for a Hubbard model exhibiting a dynamical $U(\omega)$, see Ref. [122]). In this section we, hence, perform a thorough investigation of the local reducible and irreducible two-particle vertex functions of DMFT. In particular, we will present our DMFT results for all local two-particle vertex-functions discussed in Sec. 2.2.4.2, i.e., F (full vertex), Γ_r (irreducible in channel r) and Λ (fully irreducible vertex) of the single-band half-filled Hubbard model on a three-dimensional simple cubic lattice, as defined in Eq. (2.22). In the following we will express all energies (in particular U and $T = 1/\beta$) in units of D, which is given by twice the standard deviation of the non-interacting density of states of the lattice system. For the three-dimensional model, this corresponds to $D = 2\sqrt{6}t$ where t represent the hopping amplitude between nearest neighbors. The frequency-dependent local vertex functions have been obtained numerically from the AIM associated to the DMFT solution of the Hubbard model by means of exact diagonalization (ED). Specifically, the DMFT(ED) algorithm used to compute the local two-particle vertex functions exploits the Lehmann representation for the generalized local susceptibilities χ_{ph}, χ_{pp} [Eqs. (2.150a)-(2.150b)] of the AIM, the analytic expression of which has been derived and reported, e.g., in Refs. [26, 50, 70, 123]. From χ_{ph} and χ_{pp}, the full (connected) two particle vertex (F) is easily computed by subtracting the unconnected parts and cutting the other legs [see Eq. (2.159)]. Then, all the two-particle vertices ir-

reducible in one channel (Γ_r) are obtained via inversion of the corresponding Bethe Salpeter equations [see Eq. (2.164), and Eqs. (B.7), (B.19), (B.26) in Appendix B]. Eventually, the knowledge of the Γ_r in all channels ($r = d, m, s, t$) allows us to determine the fully irreducible vertex (Λ) via the (inverse) parquet equation(s) [Fig. 2.11, Eqs. (2.162) and (2.163), and Eqs. (C.1)-(C.6) in Appendix C]. Let us note that the mathematical formalism for the (local) two-particle Green's functions, i.e., for the generalized susceptibilities and the vertices, has been already discussed in Cap. 2 and Appendices A-C, to which we refer the reader in for definitions and analytical relations.

The ED-calculations presented in the following have been performed with $N_s = 5$ (1 impurity and 4 bath) sites in the AIM, keeping (at least) 160 (positive) fermionic and bosonic Matsubara frequencies, which has required, for each determination of the generalized susceptibility, a parallel calculation of about 100.000 CPU-hours on the Vienna Scientific Cluster (VSC). This allowed for a precise calculation of the (Matsubara) frequency structures of the two-particle vertex functions at all levels of the diagrammatics, down to the fully irreducible objects. The accuracy of the calculations has been directly tested by checking the asymptotic behavior and the symmetry properties (see Cap. 2 and Appendix A) of the different vertex functions, as well as by comparing them to the corresponding atomic limit results (see Sec. 2.2.7.2). Furthermore, the numerical robustness of our DMFT(ED) results for reducible and irreducible local vertices has been also successfully verified by comparing with corresponding results obtained with a Hirsch-Fye quantum Monte Carlo algorithm [124] as impurity solver, in a slightly higher temperature regime ($\beta = 20.0$) than that considered here (see Fig. 3.9).

We will present our DMFT results in the following way: we will start analyzing the most conventional (and easiest to compute) among the vertex functions, i.e., the full vertex[10] F, in the next subsection (Sec. 3.2.1). Subsequently, in Sec. 3.2.2 we will make a step deeper in the diagrammatics, presenting our DMFT results for the vertices irreducible in one specific channel (Γ_r), and, finally, in Sec. 3.2.3, results for what can be considered the most fundamental

---

[10]Let us recall that, at the two-particle level, the connected (full) vertex F is one-particle irreducible (1PI), as it has been explicitly discussed in Sec. 2.2.4.2 (see, in particular, page 66) and illustrated in Figs. 2.9a and 2.9b. In fRG [125] and DΓA [26] publications, this vertex is usually denoted as Γ, while in DF it is coined $\gamma^{(4)}$ [34].
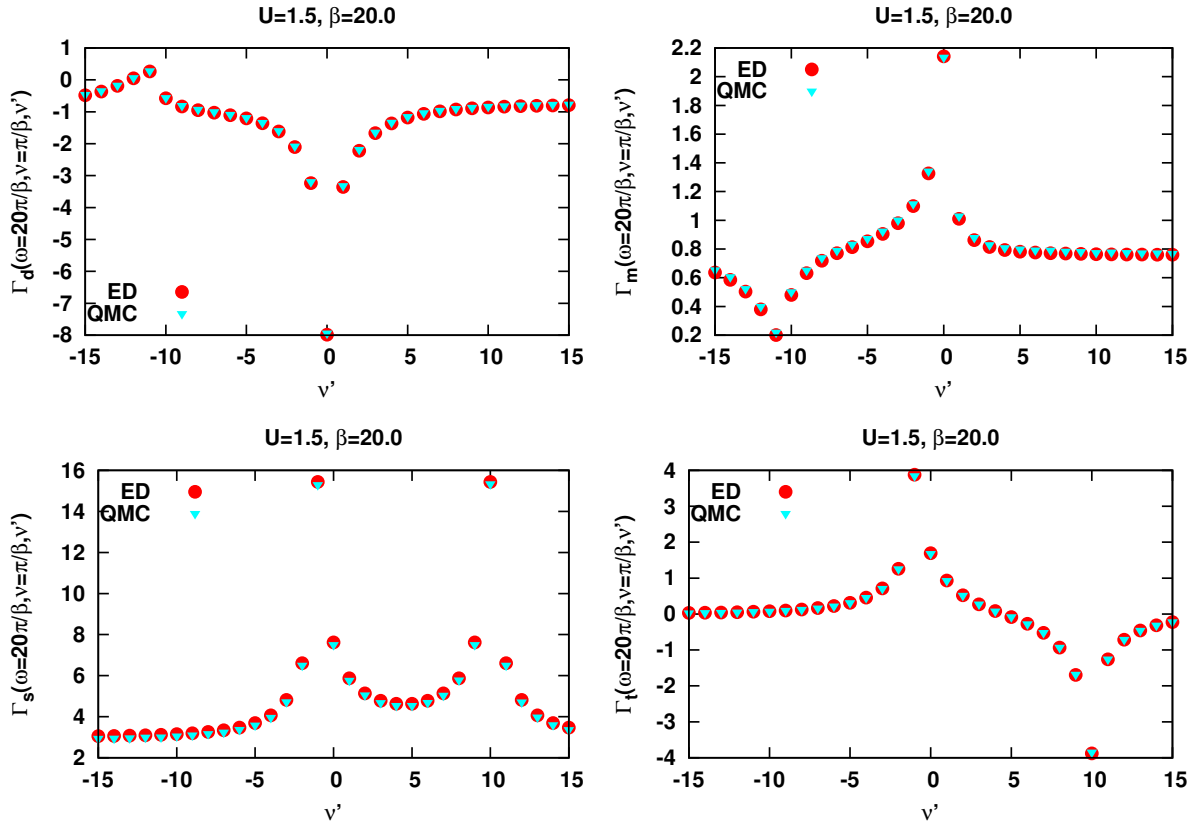
Figure 3.9: Comparison of DMFT(ED) and DMFT(QMC) results of our calculations for the two-particle vertices Γ_r, irreducible in one specific channel $r = d, m, s, t$ for a case with $U = 1.5$ and $\beta = 20.0$.

block of the two-particle diagrammatics, the fully irreducible vertex function Λ, will be presented and discussed.

In all cases, the frequency structure of the local vertices will be first examined at small values of U (e.g., $U = 0.5$), which allows for a direct comparison with perturbation theory. Deviations from the perturbation theory predictions will be also discussed, and in Sec. 3.2.4, their effects on more conventional physical and thermodynamical quantities will be eventually addressed. Finally, the impact of our analysis on possible improvements of numerical calculations of two-particle vertex functions is briefly discussed in Sec. 3.2.5.

3.2.1 DMFT results: Full vertex functions

The full vertex F, which (in the Fermi liquid regime) corresponds physically to the scattering amplitude between two dressed quasi-particles [38] discussed
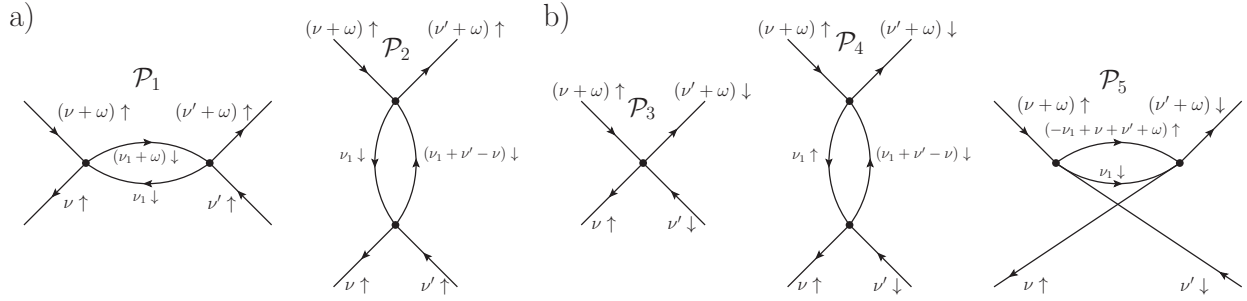
Figure 3.10: a) Lowest order (perturbative) diagrams for $F_{\uparrow\uparrow}$. b) The same for $F_{\uparrow\downarrow}$. The figure is reproduced from Ref. [48].

in Sec. 2.2.4.2 (see, in particular, page 66), contains all connected diagrams with two particles coming in and two particles going out. The relevance of this vertex functions, as well as its application in different application schemes, will be discussed extensively in Cap. 4, see in particular Sec. 4.1.2 and Tab. 4.1, while for further formal details concerning the notations and conventions we refer the reader to Cap. 2, Sec. 2.2.4.2. In Fig. 3.10 the lowest order (in U) diagrams for the two possible spin combinations are shown in the particle-hole frequency convention introduced in Sec. 2.2.3, Eqs. (2.149) and (2.150a) [the corresponding results in the particle-particle notation can be simply obtained via the transformation $\omega \to \omega - \nu - \nu'$, see also Eq. (2.151)]. Let us stress that all internal lines in the vertex diagrams correspond to full interacting Green's functions, and, hence, only skeleton diagrams are considered, as it was already discussed at the beginning of Sec. 2.2.4.2. We recall, moreover, that on the level of F, the singlet- and the triplet-channel are just linear combinations of F_d and F_m [see discussion on page 73 below Eqs. (2.169)]. In terms of Green's functions the lowest order contributions for F read as follows:

$$\mathcal{P}_1 = +\frac{U^2}{\beta} \sum_{\nu_1} G(\nu_1) G(\nu_1 + \omega), \tag{3.17a}$$

$$\mathcal{P}_2 = -\frac{U^2}{\beta} \sum_{\nu_1} G(\nu_1) G(\nu_1 + \nu' - \nu), \tag{3.17b}$$

for the $\uparrow\uparrow$-case and:

$$\mathcal{P}_3 = U, \tag{3.18a}$$

a)

b)
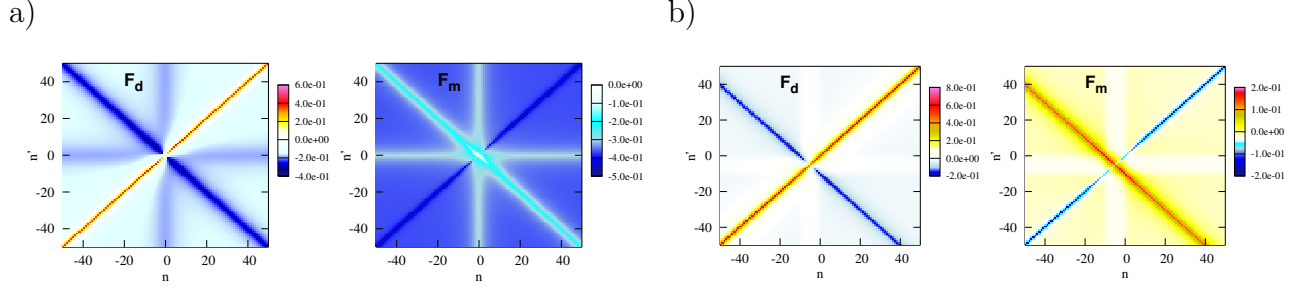
Figure 3.11: Vertex functions vs. the two fermionic frequencies $\nu = \frac{\pi}{\beta}(2n+1)$ and $\nu' = \frac{\pi}{\beta}(2n'+1)$ $(n, n' \in \mathbb{Z})$: density part $F_d^{\nu\nu'\omega}-U$ (left) and magnetic part $F_m^{\nu\nu'\omega}+U$ (right) for $U=0.5$ at half-filling $(\beta = 26.0)$ for fixed $\omega = \frac{\pi}{\beta}(2m)$ $(m \in \mathbb{Z})$; a) $\omega=0$ $(m=0)$, b) $\omega=20\frac{\pi}{\beta}$ $(m=10)$. The figure is readapted from Ref. [48].

$$\mathcal{P}_4 = -\frac{U^2}{\beta} \sum_{\nu_1} G(\nu_1)G(\nu_1 + \nu' - \nu), \tag{3.18b}$$

$$\mathcal{P}_5 = -\frac{U^2}{\beta} \sum_{\nu_1} G(\nu_1)G(-\nu_1 + \nu + \nu' + \omega), \tag{3.18c}$$

for the ↑↓-case. The lowest order contributions for the four different channels, as defined for the Γ's in Eqs. (2.167), hence, are given by:

$$F_d^{\nu\nu'\omega} = F_{ph,\uparrow\uparrow}^{\nu\nu'\omega} + F_{ph,\uparrow\downarrow}^{\nu\nu'\omega} = U + O(U^2) \tag{3.19}$$

$$F_m^{\nu\nu'\omega} = F_{ph,\uparrow\uparrow}^{\nu\nu'\omega} - F_{ph,\uparrow\downarrow}^{\nu\nu'\omega} = -U + O(U^2) \tag{3.20}$$

$$F_s^{\nu\nu'\omega} = F_{pp,\uparrow\downarrow}^{\nu\nu'\omega} - F_{pp,\overline{\uparrow\downarrow}}^{\nu\nu'\omega} = 2U + O(U^2) \tag{3.21}$$

$$F_t^{\nu\nu'\omega} = F_{pp,\uparrow\downarrow}^{\nu\nu'\omega} + F_{pp,\overline{\uparrow\downarrow}}^{\nu\nu'\omega} = 0 + O(U^2). \tag{3.22}$$

The full vertex functions F in the density $(F_d = F_{\uparrow\uparrow} + F_{\uparrow\downarrow})$ and magnetic $(F_m = F_{\uparrow\uparrow} - F_{\uparrow\downarrow})$ channel calculated by means of DMFT are shown for the case $\omega=0$ and $\omega\neq0$ in Fig. 3.11a and Fig. 3.11b, respectively. The x-axis corresponds to the fermionic Matsubara frequency $\nu = \frac{\pi}{\beta}(2n+1)$ $(n \in \mathbb{Z})$ while the y-axis is assigned to $\nu' = \frac{\pi}{\beta}(2n' + 1)$ $(n' \in \mathbb{Z})$. Note that, for the sake of readability of the figure, instead of the absolute values of the Matsubara frequencies just the corresponding indices n and n' are reported. The vertex functions F are calculated for $U = 0.5$ at half-filling, at a temperature value $(\beta = 26.0$, i.e., $T = 0.038)$ close to the critical end-point of the MIT in DMFT [24,82]. It should
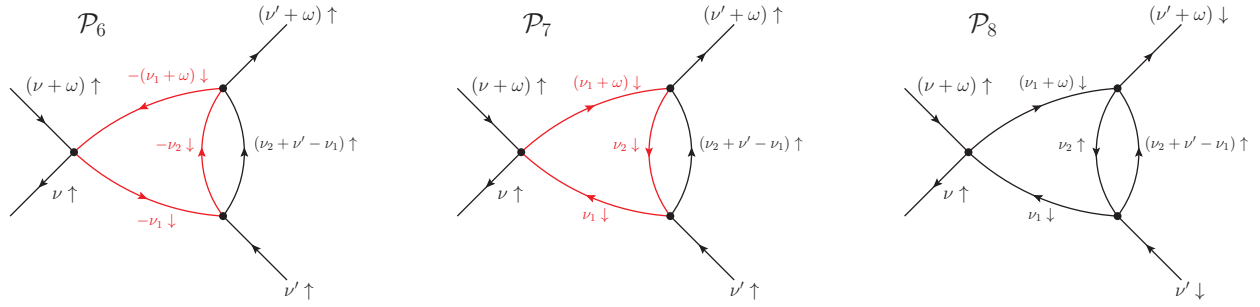
Figure 3.12: Third order (perturbative) diagrams for $F_{\uparrow\uparrow}$ and $F_{\uparrow\downarrow}$. The figure is reproduced from Ref. [48].

be recalled that for the half-filled system all vertex functions are purely real [see Eqs. (2.108) and (2.110)]. Furthermore, here as in the following, the (constant) contribution of the first order diagram $\mathcal{P}_3$ in Fig. 3.10b, namely the Hubbard U, is subtracted in order to better highlight the frequency-dependent structures of the two-particle vertices beyond the standard lowest order perturbative results.

One can now trace the different features of the two-dimensional plot of F back to different types of diagrams. First of all, let us note that a constant background is still present, despite the subtraction of the lowest order term. This constant background stems from higher order diagrams that are independent of ν and ν'. An example in second order perturbation theory is given in Fig. 3.10: The left diagram in Fig. 3.10a ($\mathcal{P}_1$) has no ν- or ν'-dependence and is proportional to $U^2\chi_0(\omega)$, as it also follows from Eq. (3.17a), and will be proportional to $U^2\chi_0(\omega)$ [see Eq. (2.154)]. The same holds also for diagrams of higher order with all possible vertex corrections inside the bubble of $\mathcal{P}_1$: The sum of all diagrams of this family yields the constant background [roughly proportional to $U^2\chi(\omega)$, with $\chi(\omega)$ defined in Eq. (2.154)] observed in Fig. 3.11a for $\omega = 0$. Because of the frequency dependence of $\chi(\omega)$ this feature is progressively reduced with an increasing value of ω as one can observe in Fig. 3.11b.

Secondly, the evident structure along the main diagonal (i.e., the region around the line $\nu = \nu'$) stems from diagrams like the second ones ($\mathcal{P}_2$, $\mathcal{P}_4$) in Fig. 3.10a or b [see also Eqs. (3.17b) and (3.18b)], which describe (at the order considered) scattering processes *reducible* in the transverse particle-hole channel. More specifically, these diagrams, as well as similar diagrams of the

same type but with vertex corrections included, depend only on $(\nu-\nu')$, which means that they give a constant contribution (of the kind $U^2\chi(\nu-\nu')$ along the lines $\nu-\nu' = $const. The largest contribution, however, is expected for the case $\nu - \nu' = 0$ when the scattering between the particle and the hole occurs at the Fermi surface. One can easily identify these structures in Fig. 3.11. For the density-case one obviously has to add the diagrams of the ↑↑- and the ↑↓-channel, which leads to twice the contribution of such diagrams in second order perturbation theory. For the magnetic vertex, instead, these second-order contributions cancel exactly each other, and only higher order contributions to this diagonal line remain, which explains the quantitative difference between the data for the two channels.

Furthermore, one also observes an enhanced scattering amplitude along the secondary diagonal $\nu'=-\nu$. The origin of this structure stems from diagrams like $\mathcal{P}_5$ in Fig. 3.10b [see also Eq. (3.18c)], which build up scattering processes *reducible* in the particle-particle channel. In fact, such diagrams (with and without vertex corrections in the bubble) describe the scattering of two particles with energies $(\nu+\omega)$ and ν'. Hence, the corresponding scattering amplitude is enhanced for total energies at the Fermi level, i.e., for $\nu' = -\nu-\omega$. If $\omega = 0$ this yields the secondary diagonal in the plots shown in Fig. 3.11a, but for the same reason, at finite ω this line is expected to be shifted to $\nu' = -\nu-\omega$. This behavior is shown for case of the tenth bosonic Matsubara frequency, i.e., for $\omega = \frac{\pi}{\beta}(2\times 10) = 20\frac{\pi}{\beta}$, in Fig. 3.11b. Within the chosen particle-hole notation [see Eq. (2.151)], the main diagonal remains unchanged, as it stems from ω-independent diagrams, while the secondary diagonal is shifted downwards compared to Fig. 3.11a. As it will be discussed in more detail later, the existence of this shift should be considered explicitly, when implementing new frequency extrapolation schemes for the vertex F at finite ω.

Finally, we also note a cross-structure (shaped as a "+") in Fig. 3.11a, i.e., one observes an enhanced scattering amplitude compared to the constant background along the lines $\nu = 0$ and $\nu' = 0$. In order to explain the origin of these structures one has to go at least to third order perturbation theory. The contribution of the diagrams shown in Fig. 3.12 reads as:

$$\mathcal{P}_{7,8} = -\frac{U^3}{\beta^2}\sum_{\nu_1\nu_2} G(\nu_1)G(\nu_1+\omega)G(\nu_2)G(\nu_2+\nu'-\nu_1). \qquad (3.23)$$

One sees that it is independent of ν and therefore it gives a constant contribution along the horizontal line $\nu' = $ const. in Fig. 3.11, with a maximum for $\nu' \sim 0$, as only in this situation one has the possibility to have all Green's functions appearing in Eq. (3.23) simultaneously at the Fermi level. In complete analogy, one can construct diagrams that do not depend on ν' (in this case the vertical bubble should be on the left side). At $\omega = 0$ these result in a maximum at $\nu = 0$, which explains the cross-structure observed in F. A more quantitative understanding of the "+"-shaped cross-structure in F requires a closer look at the spin dependence of the third-order diagrams shown in Fig. 3.12: While the only contribution to $F_{\uparrow\downarrow}$ is given by the last diagram in this figure ($\mathcal{P}_8$), for $F_{\uparrow\uparrow}$ one has to include two topologically non-equivalent diagrams ($\mathcal{P}_6$ and $\mathcal{P}_7$). The explicit expression for $\mathcal{P}_7$ is completely equivalent to that for the $\uparrow\downarrow$-vertex (i.e., $\mathcal{P}_8$). As for $\mathcal{P}_6$, its expression one can be obtained from $\mathcal{P}_7$ by simply inverting the (internal) $\downarrow$-lines (and the corresponding frequencies). This leads to:

$$\mathcal{P}_6 = -\frac{U^3}{\beta^2} \sum_{\nu_1\nu_2} G(-\nu_1)G(-\nu_1 - \omega)G(-\nu_2)G(\nu_2 + \nu' - \nu_1). \qquad (3.24)$$

At half-filling one has $G(-\nu) = -G(\nu)$ due to particle-hole symmetry [see Eqs. (2.39) and (2.109) in Cap. 2], which implies $\mathcal{P}_6 = -\mathcal{P}_7$. Hence, the diagrams $\mathcal{P}_6$ and $\mathcal{P}_7$ cancel each other, and only the contribution $\mathcal{P}_8$ to the $\uparrow\downarrow$-vertex remains in this order of perturbation theory. This can be viewed as a manifestation of the so-called Furry's theorem [69, 126] of quantum electrodynamics, which states that -as a results of the electron-positron symmetry- *a closed fermionic loop containing an odd number of Fermions always vanishes.* This also explains the different signs of the cross-structure originated by the diagrams shown in Fig. 3.12: In the density/magnetic channel $F_{\uparrow\downarrow}$ enters with a plus/minus sign which leads to a negative/positive contribution of diagram $\mathcal{P}_8$ w.r.t. the negative background of F as one can directly see by the colored features of the plots in Fig. 3.11a.

Extending our analysis to the finite-ω case, we observe a broadening of the cross-structure of F, with the formation of an horizontal and a vertical band, both extended from $-\omega$ to 0, see Figs. 3.11b and 3.13b. This more general feature can be traced to the sign changes (i.e., their jumps at zero frequen-

a)

b)
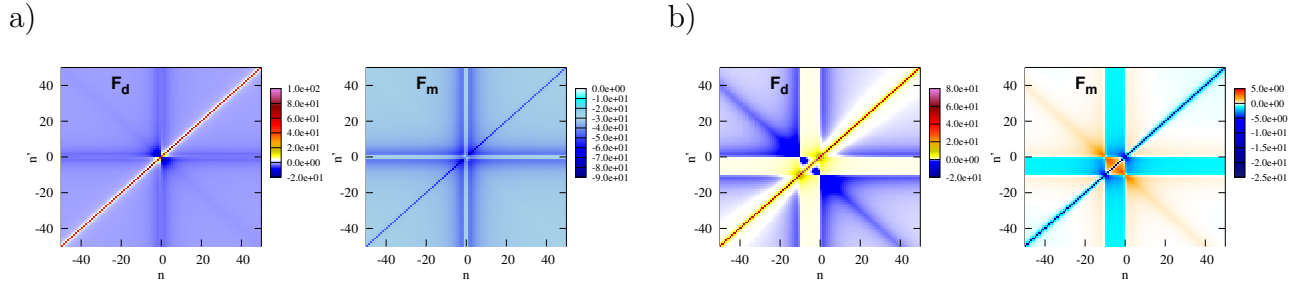
Figure 3.13: The same as in Fig. 3.11, but for $U = 2.0$. The figure b is readapted from Ref. [48].

cies) of the four Green's functions in Eq. (3.23). It is important to note that the combination of this broadened cross-structure with the (shifted) diagonal maxima/minima of the vertex function F generates the appearance of a sort of square-like feature in the frequency plots, the importance of which will be further discussed in Sec. 3.2.5.

In the final part of this section, we investigate how our DMFT-results change, upon increasing the value of the Hubbard interaction beyond the weak-coupling regime. While the quantitative comparison with perturbation theory is obviously deteriorating when increasing U, it is interesting to note that at least the "topology" of the main frequency structure of the vertex F survives qualitatively unchanged also for higher values of U, and -to a good extent-even in the atomic limit.

In Fig. 3.13 we report our results for $U = 2.0$, i.e., *four* times larger than the interaction value considered before. Notice that this value of U lies well beyond the perturbative regime, and corresponds, e.g., to the U for which the maximum of the Néel temperature of the antiferromagnetic instability is predicted by DMFT at half-filling [24, 127].

From a first visual inspection of the plots, it emerges clearly that the main frequency structures of the vertex functions correspond well to those we have just discussed for the perturbative case: One can easily identify similar structures as in the plots of Fig. 3.11 in the same position as before, and even with the same sign for the deviation w.r.t. the lowest order constant contribution. Remarkably, a similar situation can be observed even in the extreme case of the atomic limit ($D = 0$), where an analytic expression of the full vertex functions F_d, F_m can be derived [47, 48, 70, 123] directly from the Lehmann

representation. The corresponding results for the ↑↑- and ↑↓-vertex are reported in Sec. 2.2.7.2, Eqs. (2.224) and (2.223). We reproduce them here for convenience:

$$F_{d,m}^{\nu\nu'\omega} = F_{\uparrow\uparrow}^{\nu\nu'\omega} \pm F_{\uparrow\downarrow}^{\nu\nu'\omega} \tag{3.25}$$

$$F_{\uparrow\uparrow}^{\nu\nu'\omega} = \beta \frac{U^2}{4} \frac{\delta_{\nu\nu'} - \delta_{\omega 0}}{\nu^2(\nu'+\omega)^2} \left(\nu^2 + \frac{U^2}{4}\right) \left((\nu'+\omega)^2 + \frac{U^2}{4}\right) \tag{3.26}$$

$$F_{\uparrow\downarrow}^{\nu\nu'\omega} = U - \frac{U^3}{8} \frac{\nu^2 + (\nu+\omega)^2 + (\nu'+\omega)^2 + (\nu')^2}{\nu(\nu+\omega)(\nu'+\omega)\nu'} - \frac{3U^5}{16} \frac{1}{\nu(\nu+\omega)(\nu'+\omega)\nu'} +$$
$$- \beta \frac{U^2}{4} \frac{1}{1+e^{\beta U/2}} \frac{2\delta_{\nu(-\nu'-\omega)} + \delta_{\omega 0}}{(\nu+\omega)^2(\nu'+\omega)^2} \left((\nu+\omega)^2 + \frac{U^2}{4}\right) \left((\nu'+\omega)^2 + \frac{U^2}{4}\right) +$$
$$+ \beta \frac{U^2}{4} \frac{1}{1+e^{-\beta U/2}} \frac{2\delta_{\nu\nu'} + \delta_{\omega 0}}{\nu^2(\nu'+\omega)^2} \left(\nu^2 + \frac{U^2}{4}\right) \left((\nu'+\omega)^2 + \frac{U^2}{4}\right). \tag{3.27}$$

From the analytical expression of the atomic limit Eqs. (3.25)-(3.27), in fact, one can easily recognize the same main frequency features of the vertex F, appearing in the cases studied with DMFT ($U = 0.5$ and $U = 2.0$). For instance, one immediately identifies the ph and the pp diagonal structures in the terms proportional to $\delta_{\nu\nu'}$ and to $\delta_{\nu(-\nu'-\omega)}$ in Eqs. (3.25), (3.26) and (3.27). Not surprisingly for the atomic limit of repulsive models, however, the magnitude of the pp structure is exponentially suppressed when $T \ll U$, as it can be inferred from the corresponding prefactor. Interestingly, beyond the two diagonal structures, one can recognize in the atomic limit formulas also the (for $\omega \neq 0$ broadened) "+"-shaped cross-structure, which was generated at small U by the third order diagrams, Eq. (3.23). In fact, this structure corresponds –even in the atomic limit– to the term proportional to U^3 in Eq. (3.27). We observe finally, that in the atomic limit the U-dependence of F, though obviously strong, appears simplified with respect to the general case. In particular, one can identify two types of U-dependent contributions to the vertex functions F: (i) The exponentials $e^{\frac{\beta U}{2}}$ stem from the Maxwell-Boltzmann factor, appearing when calculating the trace for a grandcanonical ensemble, while (ii) the powers of U terms originate from the matrix elements. Interestingly, one observes that, due to the absence of any kinetic energy contribution in the atomic limit, the highest power in U occurring in the expression for F [see Eqs. (3.25)] is U^6 (see, in this respect, also the analysis of Ref. [22]).
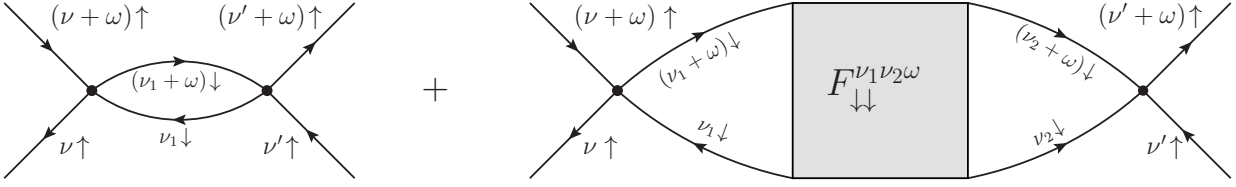
Figure 3.14: The diagram $\mathcal{P}_1$ from Fig. 3.10a supplemented by the corresponding diagrams including all possible vertex corrections.

Divergences of F. The enhancement of the main structures of the vertex function F, i.e., the main ($\nu = \nu'$) and the secondary diagonal ($\nu = -\nu' - \omega$) as well as the constant background, with an increasing value of the Hubbard interaction U from 0.5 to 2.0 (compare Figs. 3.11 and 3.13) gives rise to the question, how the Mott metal-to-insulator transition (MIT) at $U_{\mathrm{MIT}} \approx 3$ affects these features. To this end we return to the bubble diagrams in Fig. 3.10, the contributions of which are responsible for the topology of the vertex functions depicted in Figs. 3.11 and 3.13. As already discussed above, the second-order diagrams from Fig. 3.10 can be (or, for large values of U, have to be) supplemented by vertex corrections, without changing the frequency structure of the corresponding contribution. For instance, in Fig. 3.14 all diagrams, which represent vertex corrections of the bare bubble $\mathcal{P}_1$ in Fig. 3.10a, are independent of ν and ν', and, hence, give rise to the constant background observed in $F_{\uparrow\uparrow}$. One can see that, besides the bare bubble on the left-hand side, bubbles with all possible vertex corrections, i.e., including the full vertex $F_{\downarrow\downarrow} = F_{\uparrow\uparrow}$ arise. Analytically, the diagrams in Fig. 3.14 correspond to:

$$\frac{U^2}{\beta^2} \sum_{\nu_1 \nu_2} \beta G(\nu_1) G(\nu_1 + \omega) \delta_{\nu_1 \nu_2} + G(\nu_1) G(\nu_1 + \omega) F_{\uparrow\uparrow}^{\nu_1 \nu_2 \omega} G(\nu_2) G(\nu_2 + \omega) \equiv -U^2 \sum_{\nu_1 \nu_2} \chi_{\uparrow\uparrow}^{\nu_1 \nu_2 \omega} =$$

$$= -\frac{U^2}{2} \left[\chi_d(\omega) + \chi_m(\omega) \right], \tag{3.28}$$

where SU(2) symmetry was used and $\chi_d(\omega)$ and $\chi_m(\omega)$ are the physical susceptibilities or response functions discussed at the end of Sec. 2.2.2.6, see in particular Eqs. (2.138) and (2.139). Similar expressions are obtained when adding vertex corrections to the bubbles[11] $\mathcal{P}_2$, $\mathcal{P}_4$ and $\mathcal{P}_5$ in Fig. 3.10. While for a precise analytical determination of all the prefactors for χ_d, χ_m and χ_{pp} as functions of the corresponding frequency arguments, i.e., ω for the longitudinal bubbles, $\nu' - \nu$ for the transverse bubbles and $\nu + \nu' + \omega$ for the particle-particle

---

[11]Note that the consideration of vertex corrections gives rise to to diagrams which have no representation in second order perturbation theory, and, hence, are not included in Fig. 3.10. An example is the longitudinal $\uparrow\downarrow$-bubble for which at least a third-order diagram is required.

bubbles, we refer to [128], let us, here, discuss the physical significance of Eq. (3.28) and the considerations above: According to the latter relation, the constant background in Figs. 3.11 and 3.13 is (also) proportional to the local magnetic susceptibility[12] $\chi_m(\omega)$. However, $\chi_m(0)$ diverges at the MIT (at $T = 0$) [24,81,129,130], giving rise to a strong enhancement of the constant background when approaching this phase transition. A similar analysis can be performed for the main diagonal structure ($\nu = \nu'$ in Figs. 3.11 and 3.13) which is connected to the diagrams $\mathcal{P}_2$ and $\mathcal{P}_4$ in Fig. 3.10 (see also related analyses which appeared recently in Refs. [131–133]) . Dressing these transverse bubbles with all possible vertex corrections, similar to the case of the longitudinal bubble illustrated in Fig. 3.14, gives rise to a term $\chi_m(\nu - \nu')$ contributing to F_d and F_m. Hence, the numerical value at the main diagonal $\nu = \nu'$ is governed once again by $\chi_m(0)$ which gets strongly enhanced when approaching the MIT and even diverges at the transition point (at $T = 0$). On the other hand, $\chi_{pp}(\nu + \nu' + \omega)$ becomes very small with increasing values of U (in the repulsive case), and therefore, the corresponding feature in the vertex functions, i.e., the secondary diagonal, gets strongly suppressed, as it has been already discussed for the atomic limit.

The principal message of our analysis of the vertex F can be, hence, summarized as follows: The topology of the vertex functions is, to a large extent, preserved when increasing U, while the numerical values of the vertex functions for $U \gtrsim 1.0$ are completely unrelated to those of lowest order perturbations theory (see Fig. 3.10), and their knowledge requires, therefore, an explicit calculation by means of DMFT. Hence, while for individuating the location of the main features of F (in particular the main diagonal and the constant background) we can still resort to perturbation theory, the corresponding bubbles in the *ph* magnetic channel will become strongly enhanced by increasing U, with diverging maxima/minima exactly at the MIT. This happens because with increasing U, the bubble contributions of perturbation theory are dressed by all higher order corrections, including an infinite resummation of internal vertex corrections as we have also discussed before [see Fig. 3.14 and Eq. (3.28)]. In fact, these corrections correspond to replacing the bare bubble with the full interacting susceptibility χ_r, where, in particular, the divergence of $\chi_m(0)$ at the MIT (for $T = 0$) yields a corresponding divergence of the constant background and the main diagonal in the frequency structure of F.

---

[12]For the repulsive Hubbard model (or AIM) $\chi_d(\omega)$ is rather small compared to $\chi_m(\omega)$, and is, hence, neglected in the qualitative discussion in this section.
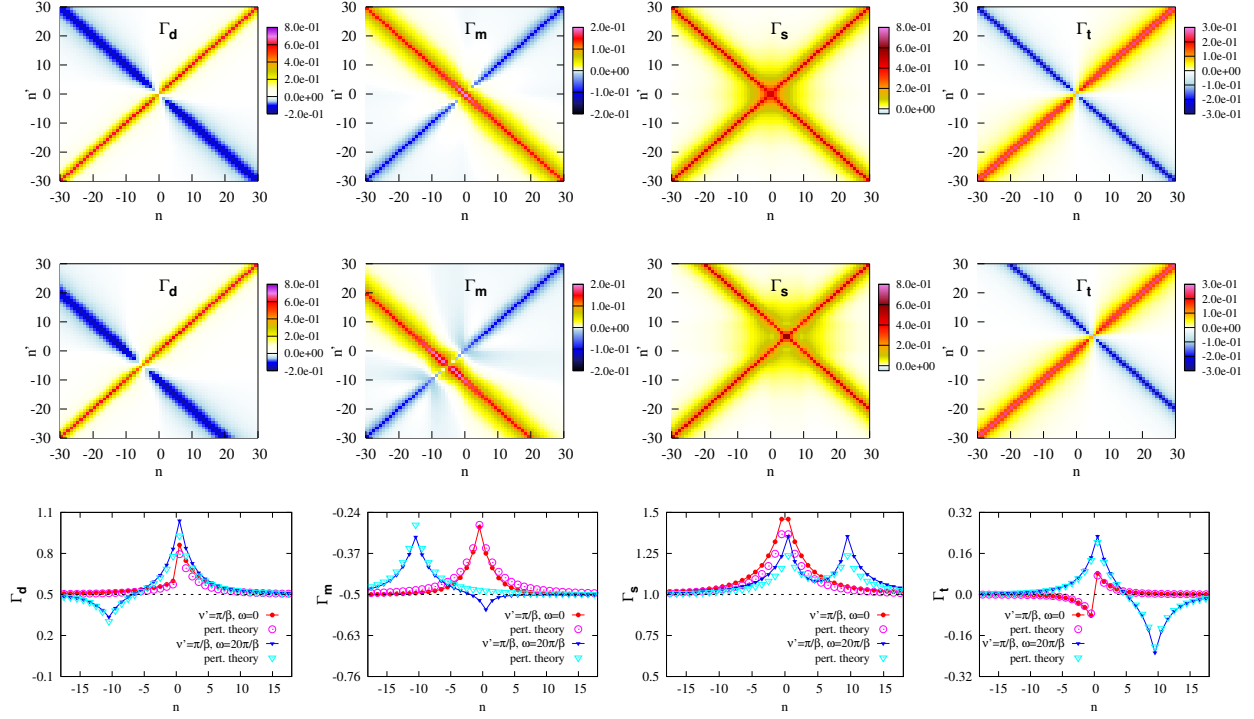
Figure 3.15: Vertex functions irreducible the different channels. First and second row: $\Gamma_d^{\nu\nu'\omega} - U$, $\Gamma_m^{\nu\nu'\omega} + U$, $\Gamma_s^{\nu\nu'\omega} - 2U$, $\Gamma_t^{\nu\nu'\omega}$ for $U = 0.5$ at half-filling ($\beta = 26.0$) for $\omega = 0$ (first row) and $\omega = 20\frac{\pi}{\beta}$ (second row) vs. the two fermionic frequencies ν and ν'. For singlet- and triplet-channel particle-particle notation was adopted. Third row: one-dimensional snapshot of the same vertex functions for $\nu' = \frac{\pi}{\beta}$ ($n' = 0$, fixed) and the two values of ω, compared to the corresponding (lowest order) perturbative results. The figure is readapted from Ref. [48].

3.2.2 Irreducible vertices in one selected channel

At the level of irreducible vertices one has necessarily to consider four independent quantities: the density and the magnetic vertex correspond to the two possible spin combinations in the longitudinal channel (Γ_{ph}), while the singlet and the triplet vertex are linear combinations of the two different spin directions in the particle-particle channel (Γ_{pp}). The transverse channel is not independent, since it can be obtained from the longitudinal one by means of the crossing symmetry [see Eq. (2.165) in Sec. 2.2.4.2 and Eq. (B.13) in Appendix B].

We start with the discussion of the two-dimensional density-plots for the four channels for $U = 0.5$ and two different values of ω ($\omega = 0$ and $\omega = 20\frac{\pi}{\beta}$, Fig. 3.15).
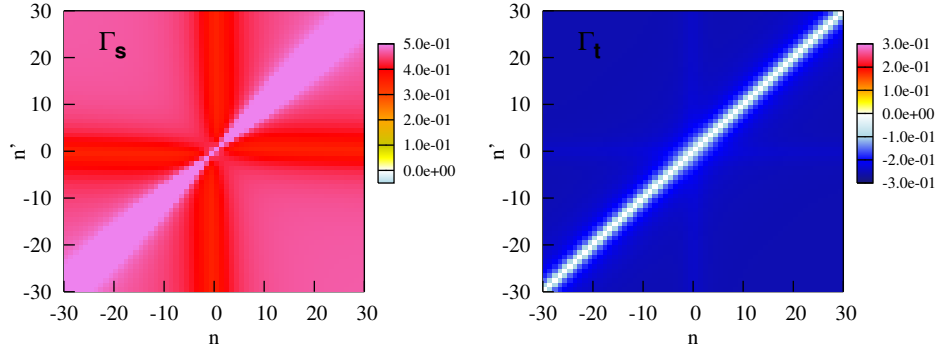
Figure 3.16: Irreducible particle-particle vertices in particle-hole notation: $\Gamma_s^{\nu\nu'(\nu+\nu'+\omega)}-2U$ (left) and $\Gamma_t^{\nu\nu'(\nu+\nu'+\omega)}$ (right) vs. ν and ν' for the same parameters as in Fig. 3.15 (for $\omega=0$). The figure is readapted from Ref. [48].

It is important to recall that for the two particle-particle channels, i.e., the singlet- and the triplet-channel, the particle-particle notation is adopted. For the density- and the magnetic channel (first two plots in each row of Fig. 3.15) one identifies the main and the secondary diagonal as it was the case for the full vertex function F. However, the constant background and the cross-structure in the center are missing. In fact, such features originate from diagrams like $\mathcal{P}_1$ in Fig. 3.10a and $\mathcal{P}_8$ in Fig. 3.12 which are *reducible* in the longitudinal channel and therefore do not contribute to Γ_d and Γ_m.

For the, particle-particle, channel in particle-hole notation one would expect again a constant background, the main diagonal as well as the cross-structure (see Fig. 3.16) but no secondary diagonal since the diagram $\mathcal{P}_5$ in Fig. 3.10b, which is responsible for the latter feature in F, does not contribute to Γ_s and Γ_t, since it is particle-particle reducible.

The situation looks, however, different when adopting particle-particle notation, i.e., $\omega \to \omega - \nu - \nu'$ for the particle-particle irreducible channels: In this case, the first diagram $\mathcal{P}_1$ in Fig. 3.10a, in fact, depends on $\omega - \nu - \nu'$ (instead of being independent of ν and ν' at all) and therefore yields a constant contribution along the lines $\omega = \nu + \nu'$. For the case $\omega = 0$ this contribution reaches a maximum yielding the secondary diagonal structure, as it appears in the density-plots for Γ_s and Γ_t (last two plots in each row of Fig. 3.15). On the other hand, in the particle-particle notation, the diagram $\mathcal{P}_5$ in Fig. 3.10

becomes independent from ν and ν' and, hence, would lead to a constant background. Since this diagram is particle-particle reducible such a contributions is missing in Γ_s and Γ_t which, therefore do not exhibit a constant background as it can be observed in Fig. 3.15.

Let us mention an interesting feature characterizing the triplet vertex Γ_t in the particle-hole notation: The triplet vertex Γ_t coincides with the $\uparrow\uparrow$-vertex. Hence, (in the particle-hole frequency notation) it describes the effective interaction between two incoming electrons with spin $\uparrow$ and energies $\nu + \omega$ and ν', respectively (these are the energies associated with the two annihilation operators in the particle-hole notation). However, for $\nu' = \nu + \omega$ both incoming electrons would be in the same state, which is forbidden by the Pauli-principle. Therefore the triplet vertex is expected to be completely suppressed along this line, as it can be actually observed (for $\omega = 0$) in Fig. 3.16 (right panel).

In the lowest row of Fig. 3.15 one-dimensional slices of the four irreducible vertex functions are shown: ν' is kept fixed to the first fermionic Matsubara frequency in that case, and Γ_r is plotted for two different values of ω as a function of ν. One observes a good agreement with second-order perturbation theory[13] obtaining deviations of the order $U^3 \sim 0.1$. This is to be expected since third order diagrams have not been considered in the perturbation expansion.

At $U = 1.0$ quantitative deviations from perturbation theory results become gradually visible in the "low-frequency" (small ν, ν', if $\omega = 0$) region, see Fig. 3.17, with the possible exception of the triplet channel. To define more generally such "low-frequency" region, however, one should consider the data at *finite* bosonic frequency ($\omega = 20\frac{\pi}{\beta}$), whose quantitative comparison with perturbation theory is shown in the lowest row of Fig. 3.17. Here, one observes that the largest deviations are found in correspondence to the main structures of the vertex functions, i.e., in the proximity of maxima/minima and saddle points of the Γ_r functions (where the exact values deviate already by more than a factor two from perturbation theory). Similarly as for F, however, the position of these frequency structures is unchanged w.r.t. perturbation

---

[13]Let us recall, that here skeleton diagrams (see Sec. 2.2.4.1), of second order in U, have been considered for Γ_r, built from $G(\nu)$. No particular changes are obtained in this regime, by replacing $G(\nu)$ with $\mathcal{G}_0(\nu)$ for the fermionic lines.
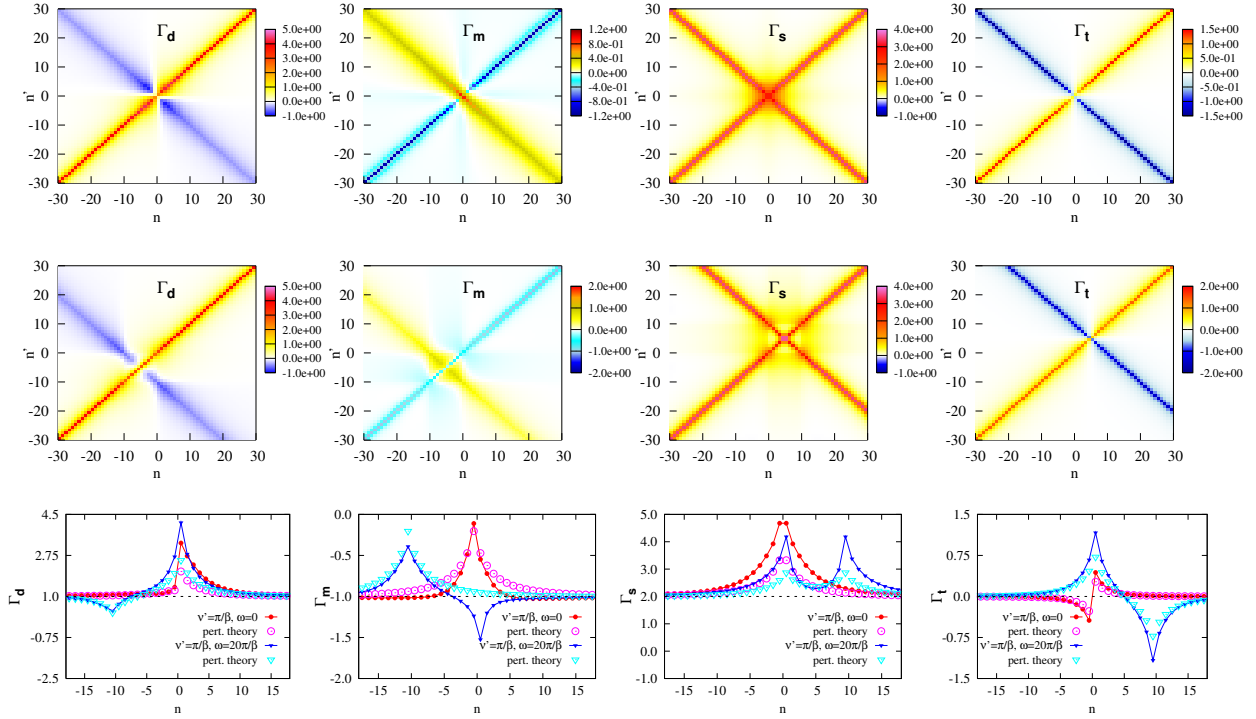
Figure 3.17: Same as in Fig. 3.15 but for U=1.0. The comparison with perturbation theory in the third row shows that, while the most important features of the vertex structures are located exactly at the same position as for U=0.5, the values of the irreducible vertices Γ (with the exception of the triplet channel) deviate already by more than a factor two from perturbation theory in the most significant points of the frequency space, e.g., in the proximity to the maxima and the minima of the vertex functions. At the same time, perturbation theory appears to describe reasonably the region in between the main structures as well as the asymptotic behavior of the vertex (see main text). The figure is readapted from Ref. [48].

theory. Moreover, from the quantitative point of view, perturbation theory still works reasonably well, not only for the asymptotics, but also for the region "in-between" the main vertex structures [128].

This trend is preserved -to some extent- when increasing U further, as it is immediately understandable from the plots for the most general case (i.e., for finite bosonic frequency) Fig. 3.18. At $U = 2.0$ (upper row in Fig. 3.18), the main frequency structures of the four Γ_r are located in the same position as for lower values of U, where perturbation theory was still applicable for their understanding and classification. By a closer inspection of the $U = 2.0$ results, however, some general trends emerge. First, one observes a weakening of the
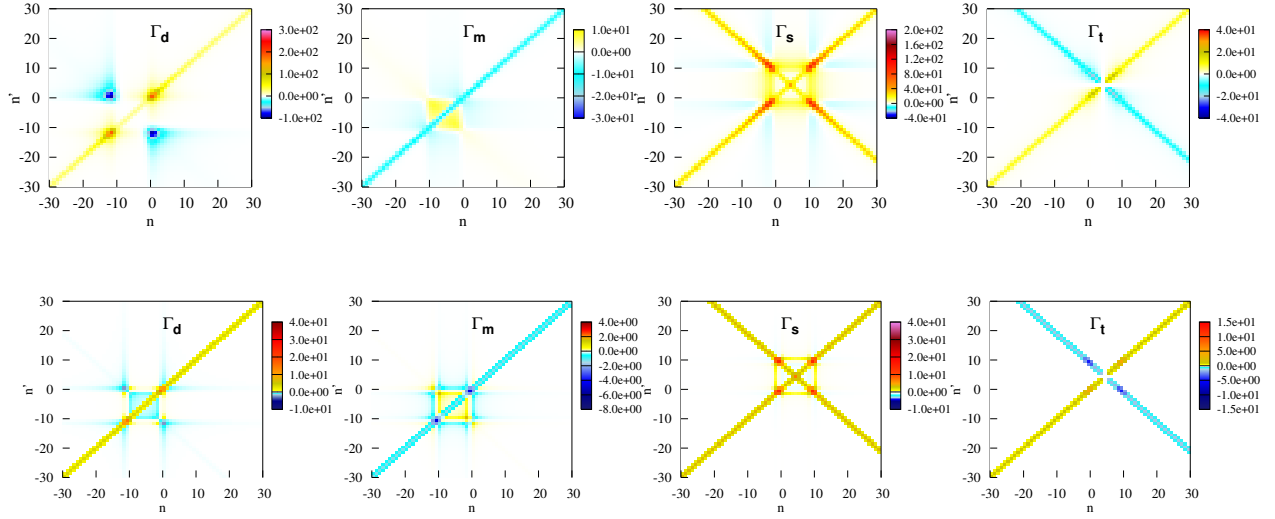
Figure 3.18: Upper row: Same as in Fig. 3.15 but for $U = 2.0$ and at finite $\omega = 20\frac{\pi}{\beta}$. Lower row: atomic limit $(D\!=\!0.0,\ U\beta\!=\!10.0)$ calculation. For singlet- and triplet-channel particle-particle notation was adopted. The figure is readapted from Ref. [48].

secondary diagonal ($\nu = -\nu' - \omega$) in Γ_d and Γ_m in the upper row of Fig. 3.18. This is a consequence of the suppression of particle-particle scattering events in repulsive models, as it was already discussed at the end of section 3.2.1 for the full vertex-function F. Secondly, one can see that, for large values of U, the triplet vertex (last plot in the first row of Fig. 3.18) consists almost completely of the double diagonals. This "$\times$"-structure can be understood in terms of the atomic limit where one can find an exact analytic expression for the triplet vertex, which is reported in Eq. (2.228). Indeed, the latter relation states that $\Gamma_t^{\nu\nu'\omega}$ is proportional to $F_t^{\nu\nu'\omega} = F_{pp,\uparrow\uparrow}^{\nu\nu'\omega} = F_{\uparrow\uparrow}^{\nu\nu'(\omega-\nu-\nu')}$ which consists just of the main ($\nu = \nu'$) and the secondary ($\nu = -\nu' + \omega$) diagonal as one can infer from Eq. (3.26).

Noteworthy, the main features of the vertex functions are preserved also when considering the extreme case of zero bandwidth, i.e, the atomic limit ($D\!=\!0$), shown in the lower row of Fig. 3.18 for a generic choice of $U\beta\!=\!10.0$. One can clearly identify the dominant diagonal- and square-like features at $\omega\!\neq\!0$ whose locations are unchanged w.r.t. to the case of finite D.

The above discussion shows that the "topology" of the vertex functions is to a large extent preserved when increasing U. This, in turn, may be used to build up approximated schemes, beyond the existing ones [134], for parameterizing

the vertex functions, as well as for simplifying two-particle calculations based on DMFT input. One could start from the atomic limit: In this case a good example for such a parametrization is given for the triplet vertex according to its exact expression in the atomic limit [Eq. (2.228)]:

$$\Gamma_t^{\nu\nu'\omega} = f(\nu,\omega)\delta_{\nu\nu'} + g(\nu,\omega)\delta_{\nu(-\nu'+\omega)}. \tag{3.29}$$

A more detailed discussion of the practical applicability of the knowledge of the vertex structures, however, will be given in Sec. 3.2.5.

Divergences of Γ_r. In this section we will discuss divergent features appearing in the vertex functions Γ_r irreducible in one specific channel (r) upon increasing U. As an important premise her, we should stress that *different* kinds of singularities can appear in Γ_r. The first, more conventional, one affects all frequencies (and is even traceable up to the asymptotic region), while the second one, never properly addressed in the DMFT literature before, occurs at low frequencies only. Starting by considering the first kind of divergence, we observe that the progressive enhancement of the main structures of Γ_r, e.g., the main diagonal for Γ_d and Γ_m, with increasing U and their actual ($T = 0$) divergence at the MIT have the very same physical origin as for the full vertices F: For large values of U the bare bubbles from perturbation theory in Fig. 3.10 have to be replaced by the full susceptibilities χ_r with the corresponding frequency dependence. In this way, the divergence of $\chi_m(0)$ leads to the divergence of the corresponding features in Γ_d and Γ_m, i.e., the main diagonal. The only difference between F and Γ_r with respect to this type of infinities is, that in Γ_r all diverging contributions are excluded which are reducible in the specific channel r, as it is, e.g., the case for the constant background, which stems from diagrams as $\mathcal{P}_1$ in Fig. 3.10. Let us emphasize again that these divergent features are not confined to a finite frequency range but extend up to infinity, and hence also affect the asymptotic behavior of the vertex functions in frequency space.

Interestingly, for Γ_r also a completely different kind of singularity can occur at much lower values of U. These second kind of divergences are confined to the low-frequency regime and, hence, do not effect at all the vertex asymptotics. More specifically, such low-frequency divergences of Γ_r arise well before the MIT, i.e, for U values considerably smaller than the critical U of the Mott transition. As already discussed in Sec. 2.2.7.2, such divergences were indeed discovered for the triplet channel in the atomic limit [see Eqs. (2.228) and (2.229)]. In fact, from a purely mathematical point of view, a singular behavior of the irreducible ver-

tex functions is not surprising, since they are obtained by means of a matrix inversion from the generalized susceptibilities. Considering Eqs. (B.6) and (B.18) in Appendix B for the calculation of $\Gamma_r^{\nu\nu'\omega}$ from the matrix inversion of $\chi_r^{\nu\nu'\omega}$ $(r = d, m)$ and $\chi_r^{\nu\nu'\omega} \mp \chi_{0,pp}^{\nu\nu'\omega}$ $(r = s, t)$, respectively, one observes that these relations become undefined if one eigenvalue of the matrix $\chi_r^{\nu\nu'\omega}(\mp\chi_{0,pp}^{\nu\nu'\omega})$ vanishes[14], i.e., in principle $\Gamma_r^{\nu\nu'\omega}$ cannot be calculated for combinations of parameters U and T and the bosonic Matsubara frequency ω, where the corresponding generalized susceptibility corresponds to a singular matrix in the fermionic Matsubara frequencies ν and ν'. In practice, however, one is usually never on top of such a single point in the (U, T) phase diagram but rather in its vicinity, where the lowest eigenvalue of $\chi_r^{\nu\nu'\omega}(\mp\chi_{0,pp}^{\nu\nu'\omega})$ can become arbitrarily small for one specific channel r. Consequently, the corresponding irreducible vertex $\Gamma_r^{\nu\nu'\omega}$ becomes strongly enhanced, since its magnitude is governed by the inverse of this small eigenvalue. As anticipated above, our analysis of the corresponding eigenvectors, and of the frequency structures of Γ_r show that this type of divergence concerns the low-frequency regime of the irreducible vertices Γ_r, marking the difference from the divergences of F and Γ_r due to the Mott transition, which extend to the high-frequency tails of the vertex. As a preamble to the presentation of the numerical data, let us recall that for $U = 0$ the generalized susceptibility coincides with the bare bubble, i.e., with the a diagonal matrix whose elements are just the products of two Green's functions. Hence, for $U = 0$, the eigenvalues of all $\chi_r^{\nu\nu'\omega}$ are always different from zero (for any temperature T), and one expects that the above-discussed singularities can arise (for each T) at a specific value of U in a given channel r and at a certain bosonic Matsubara frequency ω.

In fact, the DMFT analysis in Ref. [71] shows that, for the AIM associated to the DMFT solution of the two-dimensional half-filled Hubbard model on a simple square lattice (with only nearest neighbor hopping), the first divergence encountered by increasing U is due to an eigenvalue of $\chi_r^{\nu\nu'\omega}$ crossing zero in the density channel and for $\omega = 0$ (i.e., for $\Gamma_d^{\nu\nu'(\omega=0)}$)[15]. This sign change of an eigenvalue of $\chi_d^{\nu\nu'(\omega=0)}$ is reflected in a sign-change in the low-frequency structure of the corresponding irreducible vertex ($\Gamma_r^{\nu\nu'(\omega=0)}$, as one can clearly see in Fig. 3.19. Such a singularity is located at $1.27 < U < 1.28$ for $T = 0.1$. The analysis was also performed for different temperatures, allowing to identify a curve $U(T)$ in the U vs. T phase-diagram

---

[14]Note that, for the AIM corresponding to the DMFT solution of a non-frustrated half-filled Hubbard model, $\chi_r^{\nu\nu'\omega}(\mp\chi_{0,pp}^{\nu\nu'\omega})$ is a real symmetric matrix in the indices ν and ν' due to particle-hole symmetry [Eq. 2.110)] and time reversal symmetry [Eq. (2.95)], and, hence, has only real eigenvalues (see also Tabs. 2.1 and A.1).

[15]In the Appendix of Ref. [136], a two-particle vertex divergence has been also reported (for one temperature) whose position would be controlled by U rather than T. This expectation is, however, not verified by our data of Fig. 3.20.
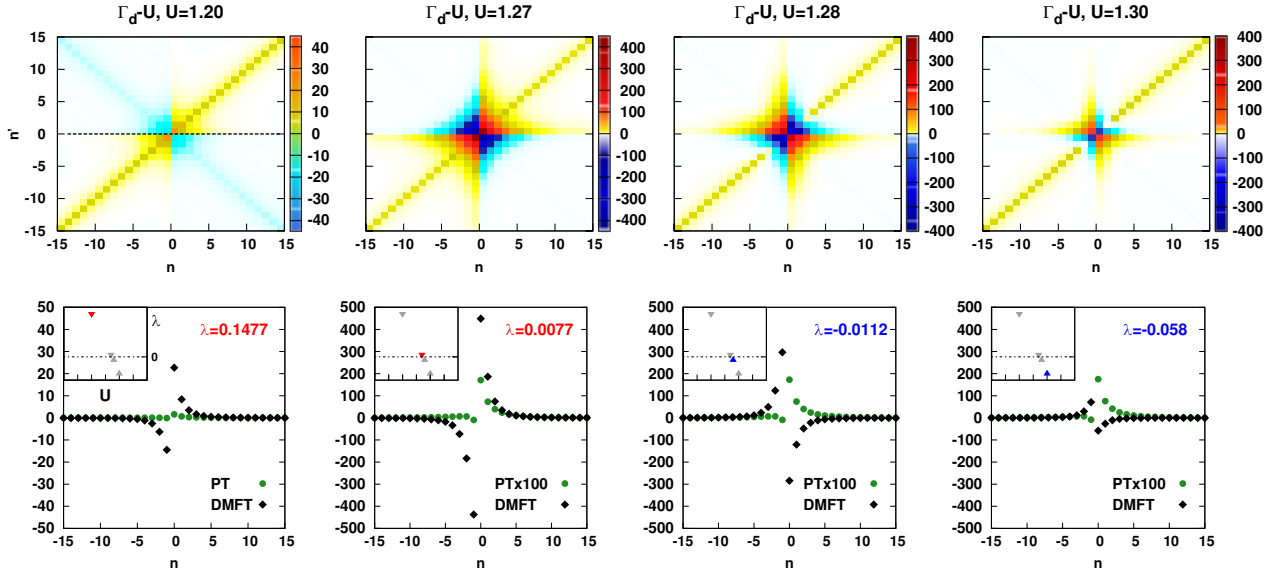
Figure 3.19: Upper row: Evolution of the frequency-dependent two-particle vertex function, irreducible in the density channel, $\Gamma_d^{\nu\nu'(\omega=0)} - U$, for increasing U. The data have been obtained for the fixed temperature $\beta = 10.0$ ($T = 0.1$). Note the characteristic "butterfly"-shaped structure of the low-frequency divergences of $\Gamma_d^{\nu\nu'(\omega=0)}$, which closely resemble the typical low-frequency structures of the fully irreducible vertex $\Lambda_d^{\nu\nu'(\omega=0)}$ (see Sec. 3.2.3). Lower row: Linear snapshot of the same $\Gamma_d^{\nu\nu'(\omega=0)}$ along the path marked by the dashed line in the first panel of the upper row, i.e., as a function of $\nu = \frac{\pi}{\beta}(2n + 1)$ for $\nu' = \frac{\pi}{\beta}$ ($n' = 0$), compared to second-order perturbation theory results, i.e., to $\mathcal{P}_2 + \mathcal{P}_4 + \mathcal{P}_5$ in Fig. 3.10 and Eqs. (3.17) and (3.18). In the legend/insets the closest-to-zero eigenvalue (λ) of $\chi_d^{\nu\nu'(\omega=0)}/\chi_0^{\nu\nu'(\omega=0)}$ is reported for each U. The figure is reproduced from Ref. [71].

of the Hubbard model, at which the first divergence of $\Gamma_d^{\nu\nu'(\omega=0)}$ (which corresponds to the first divergence for all $\Gamma_r^{\nu\nu'\omega}$) can be observed [see red circles (line) in Fig. 3.20]. Remarkably, by further increasing U for a given T, a *second* divergence of $\Gamma_d^{\nu\nu'(\omega=0)}$ is encountered. This divergence appears simultaneously with a divergence in the singlet channel at $\omega = 0$: The corresponding values of U and T are marked by the orange diamonds (line) in the phase-diagram in Fig. 3.20. Though not reported in Ref. [71], it is worth mentioning that for a fixed value of T more and more divergences are found with increasing values of U towards the MIT. These occur in all channels and also at finite values of ω, with the significant exception of the singlet channel (i.e., of the irreducible vertex $\Gamma_m^{\nu\nu'\omega}$). Hence, while an unambiguous interpretation of these type of divergences has not been found yet, the latter observation strongly suggest, that these low-frequency singularities can be understood as a precursor of the MIT, i.e., they are possible related to the formation of a local and instantaneous
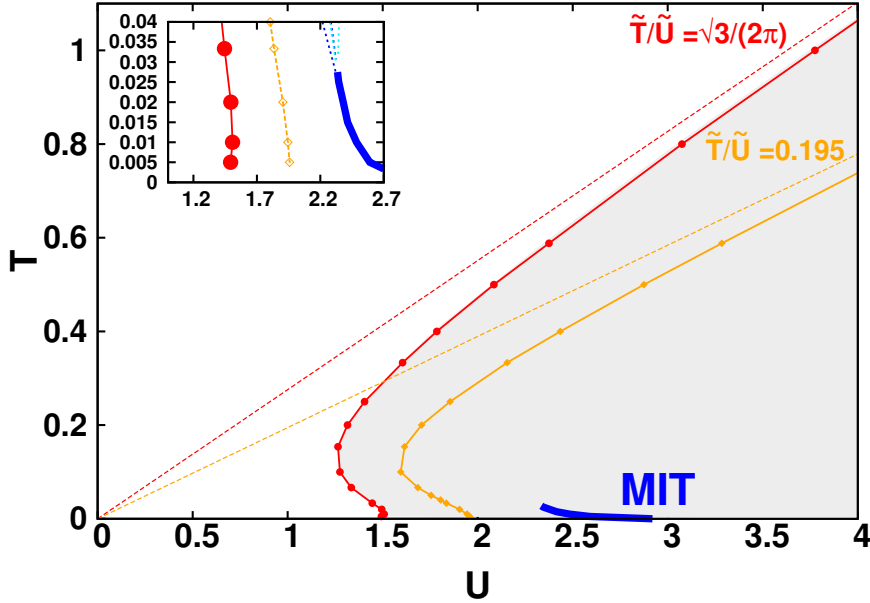
Figure 3.20: Instability lines of the irreducible vertices in the density ($\Gamma_d^{\nu\nu'(\omega=0)}$ red circles) and in the singlet ($\Gamma_s^{\nu\nu'(\omega=0)}$ orange diamonds) channels reported in the DMFT phase diagram of the half-filled Hubbard model (the data from the MIT, blue solid line, are taken from Ref. [82, 135]). The red dashed line indicates the corresponding instability condition ($T = \frac{\sqrt{3}}{2\pi}U$) estimated from the atomic limit. Inset: zoom on the low-temperature region, where also different estimations (dashed light blue [135], dashed blue [82]) of the crossover region are indicated. The figure is readapted from Ref. [71].

magnetic moment, well inside the metallic regime of the Hubbard model. However, since a comprehensive analysis of these singularities is an open issue beyond the scope of this thesis, we refer the interested reader to Ref. [71] for a speculative discussion of possible, more specific, explanations of these singularities (e.g., in terms of a breakdown of perturbation theory and standard Baym-Kadanoff formulations [44], and of a connection with the dynamic transitions observed in the corresponding non-equilibrium calculations [137, 138]).

It should be finally mentioned that the low-frequency divergences of Γ_r, discussed above, can be traced up to large values of U and T and are present also in the case of vanishing bandwidth ($D = 0$), i.e., in the atomic limit. More, specifically, this case allows even for a (semi-)analytical treatment of such vertex singularities. In fact, the atomic limit calculations are quite useful for gaining a deeper insight into the structure of the eigenvalues and eigenvectors of $\chi_r^{\nu\nu'\omega}$ associated with corresponding divergence of $\Gamma_r^{\nu\nu'\omega}$. Similarly as for the triplet channel, see the discussion in Sec. 2.2.7.2, Eqs. (2.228) and (2.229), one can find explicit analytical expressions for the divergence parameter conditions $T(U)$ in the atomic limit also for the

density and the singlet channels. In the following, we will present corresponding calculations for the case $\omega = 0$.

As for the divergence of $\Gamma_d^{\nu\nu'(\omega=0)}$, we should consider the related generalized susceptibility $\chi_d^{\nu\nu'(\omega=0)}$, which can be obtained analytically from the expression for $F_{\uparrow\uparrow}^{\nu\nu'(\omega=0)}$ and $F_{\uparrow\downarrow}^{\nu\nu'(\omega=0)}$ in Eqs. (3.26) and (3.27), the Green's function for the atomic limit in Eq. (2.216) and the definition in Eq. (2.159). By a closer inspection of the ν and ν' dependence of $\chi_d^{\nu\nu'(\omega=0)}$, one observes that most terms are functions of ν^2 and $(\nu')^2$ rather than ν and ν'. Hence, these parts of the generalized susceptibility in the density channel are *invariant* under the transformations $\nu \to -\nu$ and $\nu' \to -\nu'$. This finding suggests the following possible Ansatz for the (normalized) eigenvector connected with vanishing eigenvalues of $\chi_d^{\nu\nu'(\omega=0)}$:

$$E_{d,\bar{\nu}}(\nu) = \frac{1}{\sqrt{2}} \left[\delta_{\nu\bar{\nu}} - \delta_{\nu(-\bar{\nu})} \right], \qquad (3.30)$$

where $\bar{\nu}$ is an arbitrary (fixed) fermionic Matsubara frequency. It is obvious that all parts of $\chi_d^{\nu\nu'(\omega=0)}$ which are invariant under $\nu \to -\nu$ and $\nu' \to -\nu'$ vanish when acting on $E_{d,\bar{\nu}}(\nu)$ as defined in Eq. (3.30). Hence, only the contributions proportional to $\delta_{\nu\nu'}$ and $\delta_{\nu(-\nu')}$ survive, yielding, after a length but straightforward calculation, the following eigenvector equation:

$$\sum_{\nu'} \chi_d^{\nu\nu'(\omega=0)} E_{d,\bar{\nu}}(\nu') = \beta \underbrace{\frac{\bar{\nu}^2 - \frac{3U^2}{4}}{\left(\bar{\nu}^2 + \frac{U^2}{4}\right)^2}}_{\lambda_{d,\bar{\nu}}} E_{d,\bar{\nu}}(\nu). \qquad (3.31)$$

From this relation for can easily extract the analytic condition for the vanishing of the eigenvalue $\lambda_{d,\bar{\nu}}$:

$$\bar{\nu} = \frac{\pi}{\beta}(2\bar{n} + 1) = \frac{\sqrt{3}U}{2} \qquad \Rightarrow \qquad \frac{T}{U} = \frac{\sqrt{3}}{2\pi} \frac{1}{2\bar{n} + 1}, \qquad (3.32)$$

where $\bar{n} \in \mathbb{N}_0$. From Eq. (3.32) it is obvious that the smallest U for which a vanishing eigenvalue, and, hence, a divergence in $\Gamma_d^{\nu\nu'(\omega=0)}$ can be observed, is given by $\bar{n} = 0$, i.e., $\frac{T}{U} = \frac{\sqrt{3}}{2\pi}$. This represent evidently a strong support for the DMFT results of Fig. 3.20, where the dashed red line, denoting our divergence condition for the atomic limit, is approached asymptotically by the numerical DMFT data for the first instability line of the phase diagram, in the regime of large values of U and T. We should note, moreover, that the Ansatz (3.30) for the eigenvector of $\chi_d^{\nu\nu'(\omega=0)}$ is *not* the only one which leads to a vanishing eigenvalue for $\chi_d^{\nu\nu'(\omega=0)}$. However, the DMFT numerical data indicate quite clearly that the form for $E_{d,\bar{\nu}}(\nu)$

in Eq. (3.30) leads to the smallest possible value of U, for which a vanishing eigenvalue of χ_d (and, hence, a divergence of Γ_d) arises.

By increasing U, on the other hand, a similar analysis can be performed for the singlet channel $\chi_s^{\nu\nu'(\omega=0)}$. In this case numerical calculations as well as generic analytical considerations suggest the following structure of the (normalized) eigenvector connected to the vanishing eigenvalue(s):

$$E_s(\nu) = 2B \cos\left(\frac{\beta B}{2}\right) \sqrt{\frac{2B}{\beta[\beta B - \sin(\beta B)]}} \frac{1}{\nu^2 - B^2}, \qquad (3.33)$$

where $B \in \mathbb{R}^+$ is a real positive constant. Applying $\chi_s^{\nu\nu'(\omega=0)}$ to the Ansatz for the eigenvectors in Eq. (3.33) and considering the requirement that the corresponding eigenvalue should vanish, leads to an infinite set of transcendental equations for the two real (positive) variables $U\beta = \frac{U}{T}$ and B, from which only two are independent. They have been solved with help of Mathematica [139], confirming also the large $U - T$ asymptotic linear behavior of the second divergence curve for $\Gamma_s^{\nu\nu'(\omega=0)}$ in the phase diagram in Fig. 3.20 (orange diamonds). Let us note that, very recently, we observed that the very same Ansatz (3.33) for the eigenvector in the singlet case applies also in the density channel, leading to a simultaneous divergence in this channel too.

In conclusion, while the general problem of low-frequency singularities of the DMFT irreducible vertices, as well as their physical interpretation and impact onto numerical algorithms based on irreducible quantities (e.g., parquet), remains completely open, our exact atomic limit results represent an important first step for "supporting" the numerical evidence of vertex divergences in more general cases. Furthermore, they also might provide a guidance to "classify" the numerical low-frequency singularities of Γ_r encountered by increasing U: From the atomic limit results we have learned that two classes of eigenvectors with vanishing eigenvalues of χ_d exist. The first (and simplest) one is given by Eq. (3.32), and the second one (associated with a simultaneous divergence in the singlet channel) is reported in Eq. (3.33). Finally, our findings also demonstrate the existence of an infinite number of singularities in the atomic limit, strongly suggesting that an analogous proliferation of instabilities will be found in the DMFT phase-diagram of the Hubbard model by further approaching the MIT (as it seems also confirmed by preliminary numerical calculations). Possible extensions of analytical studies of the atomic limit out of half-filling as well as corresponding numerical DMFT/DCA calculations will be certainly performed in the immediate future for a clarification of these highly non-perturbative features, which completely surround the Mott-Hubbard MIT in the phase diagram of the Hubbard model.
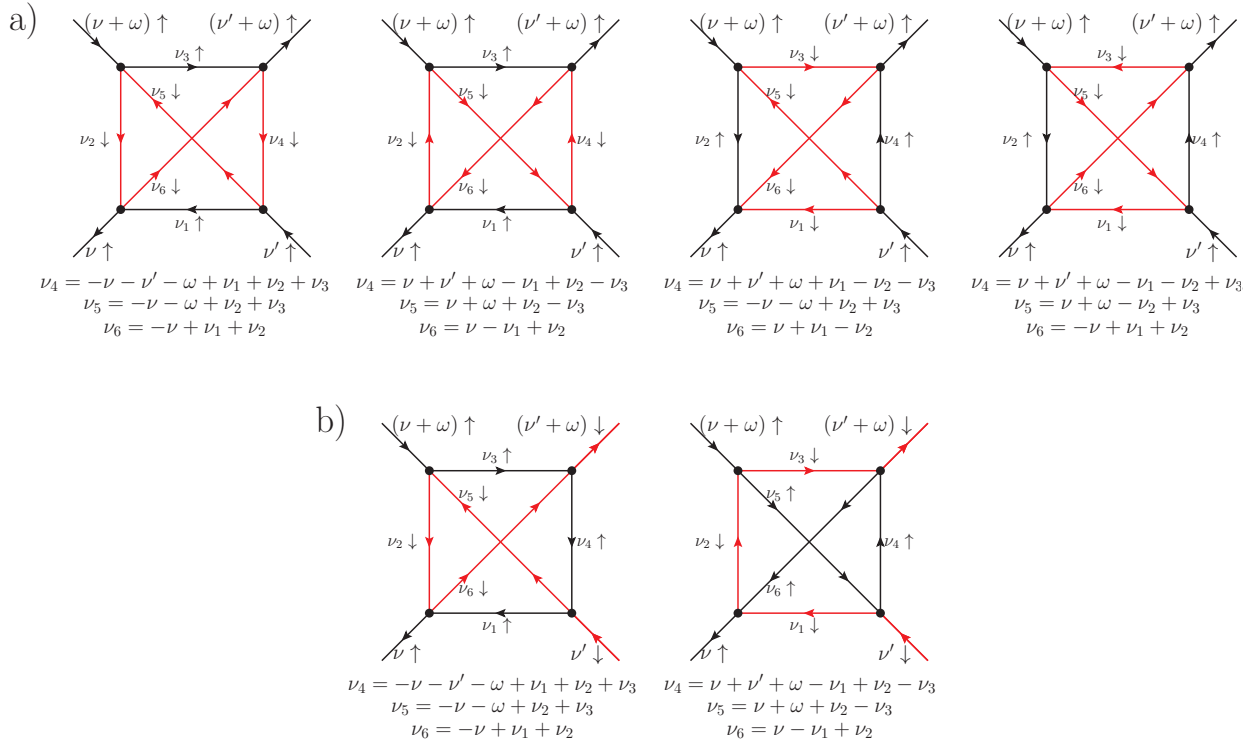
Figure 3.21: U^4-contributions to the perturbative expansion of the fully irreducible vertex ("envelope"-diagrams) in particle-hole notation for $\Lambda_{\uparrow\uparrow}^{\nu\nu'\omega}$ (a) and $\Lambda_{\uparrow\downarrow}^{\nu\nu'\omega}$ (b). The figure is readapted from Ref. [48].

3.2.3   Fully irreducible vertices

In this subsection we present results for the fully irreducible vertex Λ, whose calculation has been performed using formulas reported in Appendix C. We recall here, that the fully irreducible vertex can be viewed as the most fundamental "brick" among the two-particle vertex functions, representing the diagrammatic analog of the self-energy at the two-particle level. Hence, approximations based on this level of the diagrammatics, such as the parquet approximation or the DΓA are extremely appealing from a theoretical point of view. At the same time, the calculation and the manipulation of fully irreducible vertex functions is quite challenging, so that the few calculations [45, 46, 140, 141] based on approximations for Λ just replace the latter with its lowest-order contribution (U), with the only exception of Ref. [142], where the parquet formalism has been combined with the dual fermion theory (see also Sec. 4.4.1).

a)   b)
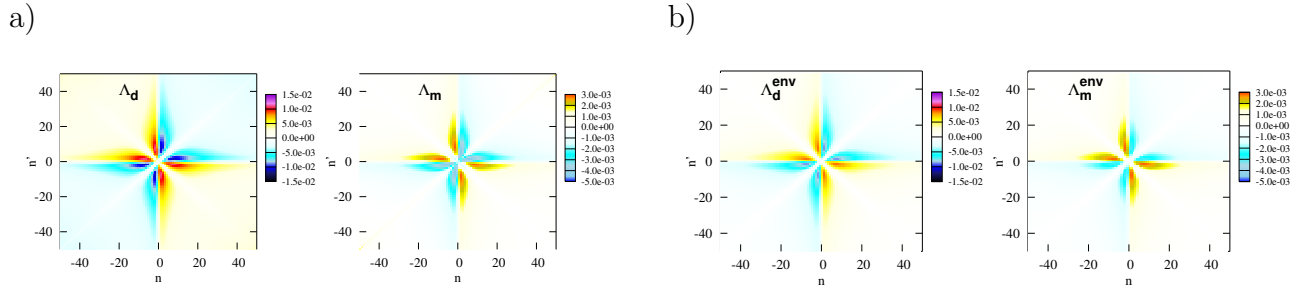
Figure 3.22: a) Fully irreducible vertex functions vs. the two fermionic frequencies ν and ν': density part $\Lambda_d^{\nu\nu'\omega} - U$ (left) and magnetic part $\Lambda_m^{\nu\nu'\omega} + U$ (right) for $U = 0.5$ at half-filling ($\beta = 26.0$) for $\omega = 0$. b) The corresponding 4th-order perturbation theory results ("envelope" diagrams in Fig. 3.21). Note, in all plots, the emergence of a typical "butterfly"-shaped structure at low frequencies and the occurrence of the trivial lowest order $[\pm(2)U]$ asymptotic behavior in all directions of the $\nu - \nu'$ plane. The figure is reproduced from Ref. [48].

Motivated by the lack of studies on the frequency dependence of the fully irreducible local vertices, even at the level of perturbation theory, we will present our numerical and analytical results with more details than in the previous subsections and we also explicitly consider the effects of the frequency dependence of Λ in selected physical and thermodynamical quantities as a function of the Hubbard interaction U.

By definition no channel-dependence of the fully irreducible vertex function Λ can exist, since it is irreducible in *all* channels. Hence, as for F in Sec. 3.2.1, here we also restrict ourselves to the DMFT result for the density and the magnetic vertices, which represent the two possible spin combinations. Diagrammatically, the lowest order contribution to the fully irreducible vertex is the bare Hubbard interaction U (diagram $\mathcal{P}_6$ in Fig. 3.10b). The next terms in the perturbation expansion are already of 4th order: These diagrams have the form of an envelope, and, hence, are usually referred to as "envelope"-diagrams. The envelope-diagrams for the $\uparrow\uparrow$- and the $\uparrow\downarrow$-case are shown in Fig. (3.21).

Let us just mention, here, one interesting feature for the $\uparrow\uparrow$ diagrams, which is specifically relevant for the particle-hole symmetric case: At half-filling the contributions of the first and the second (as well as of the third and the fourth) diagrams in Fig. 3.21a become exactly the same, i.e., one can take only the first and the third diagram and assign a factor two to them.
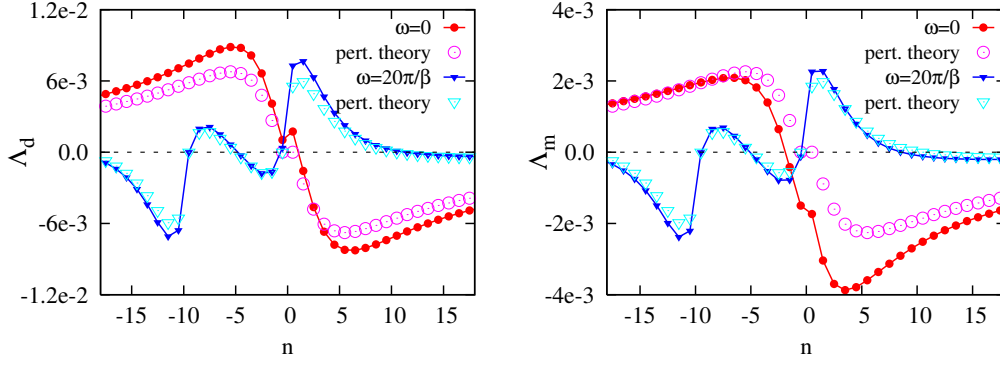
Figure 3.23: (color online). $\Lambda_d^{\nu\nu'\omega} - U$ (left) and $\Lambda_m^{\nu\nu'\omega} + U$ (right) for $U = 0.5$ at half-filling ($\beta = 26.0$) for a selected one-dimensional snapshot at fixed $\omega = 0$ or $\omega = 20\frac{\pi}{\beta}$, $\nu' = \frac{\pi}{\beta}$, as a function of ν. The figure is reproduced from Ref. [48].

This happens because all these diagrams differ only for the direction of the propagators in their closed fermion loops containing four internal electron ↓-lines. This is again analog to Furry's theorem [69, 126] of quantum electrodynamics, which was already discussed in Sec. 3.2.1 below Eq. (3.24) for a third-order contribution to the full vertex function F. In contrast to the situation explained there, where an odd number of fermion lines in a fermionic loop led to a cancellation of diagrams (see also Fig. 3.12), we are dealing here with a closed loop containing an even number of fermions. This leads to a factor 2 for the diagram under consideration rather than to a cancellation.

In Fig. 3.22, eventually, our DMFT results for $\Lambda_d^{\nu\nu'\omega}$ and $\Lambda_m^{\nu\nu'\omega}$ are compared with the U^4-contributions from perturbation theory, given by the envelope diagrams in Fig. 3.21. Algebraically, the contribution stemming from such a diagram is given by:

$$\Lambda_{\text{env}}^{\nu\nu'\omega} = (\pm)\frac{U^4}{\beta^3} \sum_{\nu_1\nu_2\nu_3} G(\nu_1)G(\nu_2)G(\nu_3)G(\nu_4)G(\nu_5)G(\nu_6), \qquad (3.34)$$

where ν_4, ν_5 and ν_6 are functions of ν_1, ν_2 and ν_3 (reported in Fig. 3.21) rather than independent summation variables. We recall, that the lowest order diagram, which is simply given by the bare Hubbard interaction U (diagram $\mathcal{P}_3$ in Fig. 3.10b) here, is subtracted in both cases, i.e., only deviations from this constant contribution are plotted.

From Fig. 3.22 one can see that the characteristic "butterfly"-shaped frequency structure of the DMFT results for $\Lambda_{d,m}^{\nu\nu'\omega}$ closely resembles that of the

envelope diagram. This is expected for a relatively small $U = 0.5$ and it is also demonstrated in Fig. 3.23. There a one-dimensional slice of Λ is plotted (ω *and* ν' are fixed) in comparison with perturbation theory, i.e., the envelope-diagrams. The deviations from the constant term $\pm U$ for $\Lambda_d^{\nu\nu'\omega}$ and $\Lambda_m^{\nu\nu'\omega}$, respectively, are of the order $U^4 \sim 10^{-2}-10^{-3}$ which is perfectly consistent with our numerical data. As we will discuss in the next subsection, this situation can radically change for larger values of U.

Our numerical results show also that, contrary to the case of F and Γ_r, due to the complete absence of reducible contributions, the high-frequency asymptotic value of $\Lambda_{d,m}$ is *always* given by the lowest order terms ($\pm U$). As this asymptotic property is intimately connected with the intrinsic fully irreducible nature of Λ, this result holds evidently independently from the value of U. A consequence for numerical calculations based on this finding will be discussed in Sec. 3.2.5.

Divergences of Λ. Furthermore, let us finally discuss the divergences which can be expected (and observed) in the frequency structures of the fully irreducible vertex $\Lambda_r^{\nu\nu'\omega}$. First, we recall that $\Lambda_r^{\nu\nu'\omega}$ is obtained from $F_r^{\nu\nu'\omega}$ and $\Gamma_r^{\nu\nu'\omega}$ by means of the corresponding explicit parquet relations which are *algebraic* and *linear* in $F_r^{\nu\nu'\omega}$ and $\Gamma_r^{\nu\nu'\omega}$ [see Eqs. (C.1)-(C.2) in Appendix C]. Hence, $\Lambda_r^{\nu\nu'\omega}$ *cannot* exhibit *new* divergences, which are not already present in either the full vertex $F_r^{\nu\nu'\omega}$ or in the vertices $\Gamma_r^{\nu\nu'\omega}$ irreducible in the channel r.

As for the infinities in $F_r^{\nu\nu'\omega}$ (which can be, partially, also found in $\Gamma_r^{\nu\nu'\omega}$), we discussed in Sec. 3.2.1 that they originate from bubble diagrams as depicted in Fig. 3.10, or, more precisely, from the full susceptibilities obtained by dressing the bubbles with all possible vertex corrections. In any case, these diagrams are all *reducible* in one specific channel and, therefore, do not contribute to the *fully irreducible* vertex $\Lambda_r^{\nu\nu'\omega}$. Consequently, also the corresponding divergent features are not present in the fully irreducible vertex functions. In fact, one can explicitly show that all the bubble contributions leading to infinities due to the $T = 0$ divergence of $\chi_m(0)$ when approaching the MIT cancel out in the Parquet equations (C.1)-(C.2) for $\Lambda_r^{\nu\nu'\omega}$, which is consistent with the previous observation of a uniform asymptotic behavior of these vertex functions.

On the other hand, the low-frequency divergences of $\Gamma_r^{\nu\nu'\omega}$, which originate from the matrix inversion of the Bethe-Salpeter equations, persist also in the fully irreducible vertex Λ. Indeed, by a closer inspection of the explicit expression for the parquet equations in Appendix C, it is obvious that no cancellation of these infinities of $\Gamma_r^{\nu\nu'\omega}$ can occur. From another

perspective, when considering the fully irreducible as the most basic among the vertex func-
tions, one can even state that these divergences have their origin in $\Lambda_r^{\nu\nu'\omega}$ rather than in
$\Gamma_r^{\nu\nu'\omega}$, which is also confirmed by the strong enhancement (and a change of sign) of the low-
frequency structures of $\Lambda_r^{\nu\nu'\omega}$ at the corresponding values of the parameters U and T, where
the low-frequency singularities of Γ_r are found.

3.2.4   Effects on physical quantities

In this section, we aim at establishing a connection between the results for
two-particle quantities, we have presented so far, and the more familiar re-
sults at the one-particle level, i.e., those for the self-energy of the system. In
a second step, the connection with some selected physical quantities, which
are typically analyzed in the context of the Hubbard model, will also be illus-
trated. As for the self-energy, this goal can be easily achieved by exploiting
the Schwinger-Dyson equation of motion which is given in Eq. (2.194) and il-
lustrated in Fig. 2.14 in Sec. 2.2.6. Inserting the parquet decomposition [Eq.
(2.162)] into this equation, i.e., splitting up $F_{\uparrow\downarrow}^{\nu\nu'\omega}$ into a fully irreducible and
the three reducible parts allows us to identify four different contributions to
the self-energy stemming from the irreducible and the reducible part of the
full vertex function $F_{\uparrow\downarrow}^{\nu\nu'\omega}$. Specifically, in the upper row of Fig. 3.24 we com-
pare the DMFT self-energy $\Sigma(\nu)$ with its contributions which originate from
the fully irreducible vertex $\Lambda_{\uparrow\downarrow}^{\nu\nu'\omega}$ only and from its lowest order contribution
(U), respectively. For this purpose we used the equation of motion (2.194)
and replaced $F_{\uparrow\downarrow}^{\nu\nu'\omega}$ by $\Lambda_{\uparrow\downarrow}^{\nu\nu'\omega}$ and U, respectively (where the second case simply
yields diagrammatic contributions similar to those of the 2$^{\text{nd}}$-order perturba-
tion theory).
For the relatively small $U = 0.5$ (upper left panel in Fig. 3.24) there is no
visible difference between the self-energies calculated with the frequency-
dependent Λ of DMFT and the bare U. Furthermore, both of them almost
coincide with the exact DMFT local self-energy. This is to be expected here,
since in the perturbative regime the relative difference between the full $\Lambda_{\uparrow\downarrow}^{\nu\nu'\omega}$
and U is extremely small, as we have already noticed in Fig. 3.23. Moreover,
for the rather small value of U under consideration second-order perturbation
theory (i.e., where $F_{\uparrow\downarrow}^{\nu\nu'\omega}$ is replaced by U) should constitute a good approxi-
mation for the exact local DMFT self-energy, as it can also be observed from
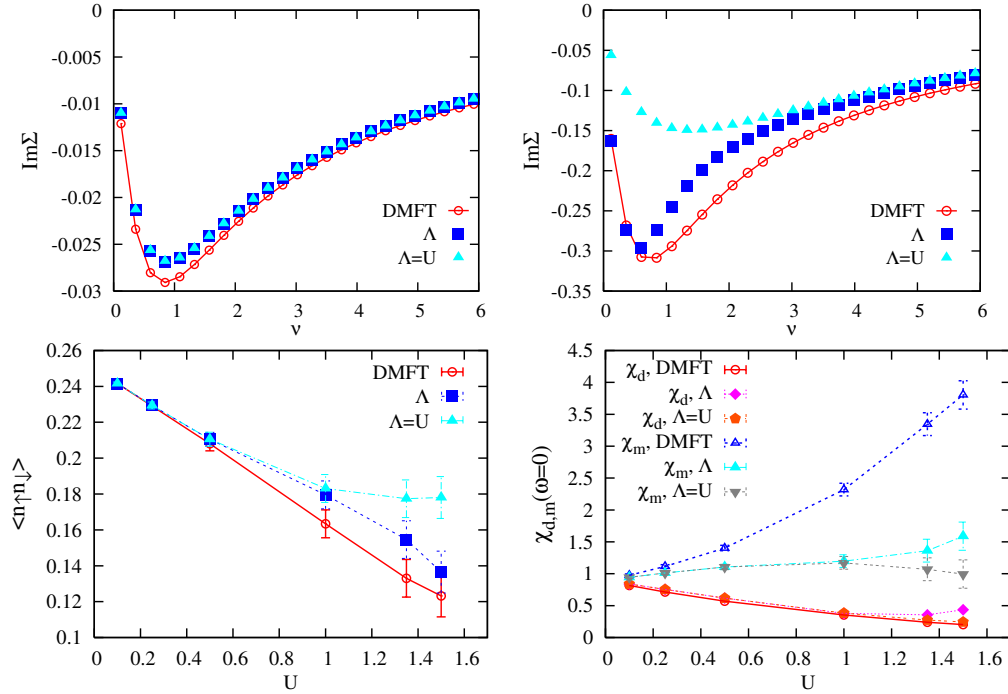
Figure 3.24: Upper row: DMFT self-energy (red circles) compared to the contributions
stemming from $\Lambda_{\uparrow\downarrow}^{\nu\nu'\omega}$ (blue squares) and from U (light-blue triangles) only, respectively,
for $U\!=\!0.5$ (left) and $U\!=\!1.5$ (right); Lower row: double occupancy (left) and susceptibil-
ities (right). The error bars refer to the finite frequency range adopted for the fermionic
frequency summations over ν, ν'.[16] The figure is reproduced from Ref. [48].

the upper left panel in Fig. 3.24.

On the other hand, for a larger value of the Hubbard interaction ($U = 1.5$,
upper right panel in Fig. 3.24) one can see that, while the major part of
the self-energy is still coming from the fully irreducible part of $F_{\uparrow\downarrow}^{\nu\nu'\omega}$, the
frequency dependence of $\Lambda_{\uparrow\downarrow}^{\nu\nu'\omega}$ becomes essential for the calculation of the
self-energy. Hence, setting $\Lambda_{\uparrow\downarrow}^{\nu\nu'\omega} = U$, as it is done, e.g., in the parquet ap-
proximation, would yield results quite far from the correct structure of the
one-particle local self-energy, which appears to be determined, to a major
extent, by frequency-dependent high-order terms of $\Lambda_{\uparrow\downarrow}^{\nu\nu'\omega}$.

Very similar conclusions can be drawn by analyzing the contribution of $\Lambda_{\uparrow\downarrow}^{\nu\nu'\omega}$
to the value of the double occupancy $n_\uparrow n_\downarrow = \frac{1}{\beta U} \sum_\nu \Sigma(\nu)G(\nu)$ as a function of U,
which is shown in the lower left panel of Fig. 3.24. By comparing the results

---

[16]Note: The error bars have been estimated here by comparing the result for the summations over a finite-
frequency range with the exact DMFT results, which can be obtained directly for $n_\uparrow n_\downarrow$ and $\chi_{d,m}^{\nu\nu'\omega}$ from the
ED impurity solver.

obtained with the full DMFT self-energy, with those obtained considering $\Lambda_{\uparrow\downarrow}^{\nu\nu'\omega}$ only, we observe that also in this case the fully irreducible vertex gives a significant contribution to the well-known reduction of the double-occupancy value w.r.t. its not interacting value of $n_\uparrow n_\downarrow = n_\uparrow \times n_\downarrow = 0.25$ with increasing U. Also in this case, however, for $U > 1.0$ the results calculated with the approximation $\Lambda_{\uparrow\downarrow}^{\nu\nu'\omega} = U$ deteriorate very quickly, so that at $U \sim 1.4$ a very incorrect estimate for $n_\uparrow n_\downarrow$ would be obtained by neglecting the frequency dependence of $\Lambda_{\uparrow\downarrow}^{\nu\nu'\omega}$.

The situation appears more articulated, however, when analyzing the case of two-particle local response functions, such as the density $\chi_d(\omega)$ and magnetic $\chi_m(\omega)$ local susceptibilities at zero bosonic frequency ($\omega = 0$) [see also Sec. 2.2.2.6, in particular page 55]. Such thermodynamic quantities contain a very important piece of information for the physics of the Hubbard model as it was already discussed in Secs. 2.2.2.6 and 3.2.1: Approaching the MIT is marked by a constant enhancement of $\chi_m(\omega)$ with increasing U [24]. In fact, a $T = 0$ divergence of $\chi_m \equiv \chi_m(\omega = 0)$ actually signalizes the transition to the Mott-insulating state, as it corresponds to the formation of a stable local magnetic moment in the Mott phase. At the same time, the reduced mobility of the electrons with increasing values of the local Coulomb interaction U is mirrored in a gradual suppression of the local charge fluctuations, and, hence, in a monotonous decrease of $\chi_d \equiv \chi_d(\omega)$, with U. Such trends are naturally well captured by our DMFT calculations, performed via a summation of both Matsubara fermionic frequencies ν, ν' of the generalized susceptibility $\chi^{\nu\nu'\omega=0}$, defined as in Eq. (2.159). Following the same procedure described above, we have extracted the contribution to χ_d and χ_m originated by the fully irreducible vertex $\Lambda_{\uparrow\downarrow}^{\nu\nu'\omega}$ and its lowest-order term (U). While only limited information can be extracted from the χ_d, as it is becoming very small in the non-perturbative region, by analyzing the data for χ_m some relevant difference with the previous cases can be noted. The contribution to χ_m stemming from the irreducible vertices $\Lambda_{\uparrow\downarrow}^{\nu\nu'\omega}$ and reducible diagrams in $F_{\uparrow\downarrow}^{\nu\nu'\omega}$ (i.e., $\Phi_{\uparrow\downarrow}^{\nu\nu'\omega}$) are comparable. The latter contributions appear to become the predominant ones in the region $U > 1.0$ where a stronger enhancement of χ_m is observed. This is not surprising since it is known that for an accurate description of a susceptibility at the corresponding (second-order) phase transition the inclusion of ladder scattering diagrams is crucial. We also note here that the

relative error made by replacing $\Lambda_{\uparrow\downarrow}^{\nu\nu'\omega} = U$ is naturally increasing with U, though remaining weaker than in the previous cases.

3.2.5 Possible algorithmic developments and improvements

After having presented our numerical results for the local vertex function of DMFT, we close this section by discussing here some possible practical applications of our results in improving or developing algorithms for computing the two-particle properties in DMFT, as well as in other many-body methods. Let us briefly recall that the computation of two-particle vertex functions in ED, as well as in QMC, over a large number of frequencies poses evidently significant practical problems (from the stability of the results in the high-energy regime, to the storing of increasingly larger arrays). In this respect, numerical schemes capable to limit the frequency region of the actual calculations of the generalized susceptibility are very useful. A relevant example is the algorithm illustrated in Ref. [143], which allows for a considerable reduction of the size of the frequency region for the numerical calculation of $\chi^{\nu\nu'(\omega=0)}$, aiming at a much faster computation of the q-dependent susceptibilities in DMFT at *zero frequency*. This algorithm is based on the replacement of the calculated high-frequency values of the irreducible vertices Γ_r, with their corresponding asymptotics. In this respect, our results demonstrate that the high-frequency asymptotics of the fully irreducible vertex Λ always reduces to the lowest order perturbative contribution (U). This provides (i) an independent confirmation of the assumptions behind the analytical derivation of the high-frequency behavior of Γ_r of Ref. [143] and (ii) useful information for its possible extension to the *finite frequency ($\omega \neq 0$)* case [128]. Specifically, the analysis of the frequency structure of the irreducible vertices Γ_r at finite bosonic frequency (see, e.g., Figs. 3.15, second row, and 3.18) suggests the way to generalize the results of Ref. [143] to an arbitrary (bosonic) frequency case: One can easily note that the simple double diagonal ("×") structure of Γ_r vertices at zero frequency is replaced by a square-like structure. Hence, the frequency region which one has to calculate exactly will be no longer the low frequency one, but one should rather keep all the vertex values for frequencies belonging to or in the proximity of the square-structure, replacing the remaining ones with the corresponding asymptotics.
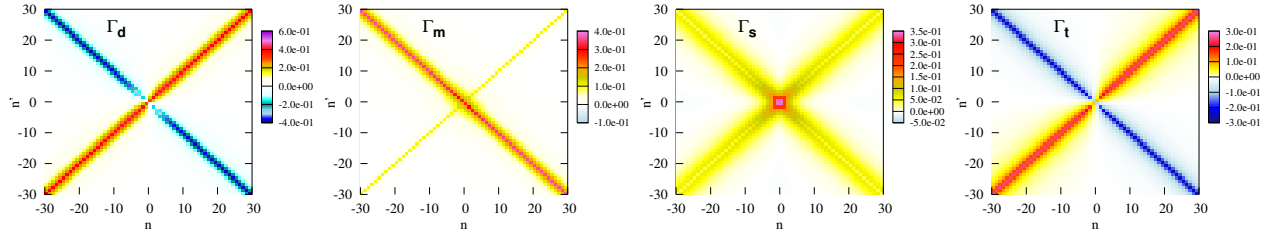
Figure 3.25: Irreducible vertices for the attractive model: $\Gamma_d^{\nu\nu'\omega} - U$, $\Gamma_m^{\nu\nu'\omega} + U$, $\Gamma_s^{\nu\nu'\omega} - 2U$ and $\Gamma_t^{\nu\nu'\omega}$ for $U = -0.5$ at half-filling ($\beta = 26.0$) for $\omega = 0$. The figure is readapted from Ref. [48].

Finally, let us stress here, that many calculations (not only DMFT based) of the Hubbard model aiming to include dynamical vertex corrections may greatly benefit from (approximated) simplifications or parameterizations of the vertex structures, e.g., considering only the most important features of F, Γ or Λ (see, e.g., the proposed parameterization schemes of the vertex function F for functional renormalization group (fRG) calculations on the AIM [134, 144], the Hubbard model [145] or even spin-only models [146]). We also emphasize, here, that the challenge of finding the most efficient vertex parametrization will be also a central issue for algorithmic improvements of the recently proposed DMF²RG scheme [147]. In this light, our results may either guide the construction of such approximations, or –at least– provide a very precise reference for evaluating the correctness of the approximations already in use [134, 148–150].

3.3   DMFT Results for the attractive model

Before analyzing, in the next chapter, the results which can be obtained by using the two-particle local vertex of DMFT for including nonlocal correlations at all length scale within diagrammatic extensions of DMFT, we will devote the last section of this chapter to study the two-particle DMFT vertex functions for the case of an *attractive* interaction ($U < 0$), i.e., for the attractive Hubbard model. To this end we refer the reader also to Sec. 2.2.5, where the mapping between the repulsive and the attractive case by means of a partial particle hole transformation for the half-filled system was discussed.

Obviously, one should keep in mind that an attractive interaction among electrons can represent at most an *"effective"* low-energy description of more
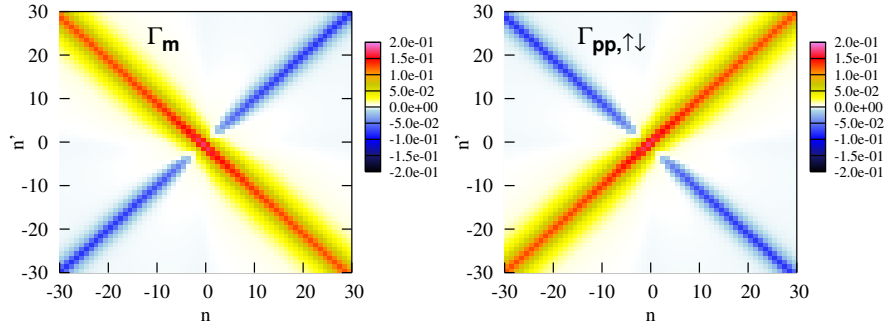
Figure 3.26: $\Gamma_m^{\nu\nu'\omega}$ for $U = +0.5$ (left) and $\Gamma_{pp,\uparrow\downarrow}^{\nu\nu'\omega} = \frac{1}{2}(\Gamma_s^{\nu\nu'\omega} + \Gamma_t^{\nu\nu'\omega})$ for $U = -0.5$ (right), both at half-filling ($\beta = 26.0$) for $\omega = 0$. The figure is readapted from Ref. [48].

complex microscopic phenomena in condensed matter. However, the physics described by the attractive Hubbard model is far from being merely academic. In fact, the latter represents an ideal playground to investigate the physics of the superconducting and charge-density wave ordered phases in the intermediate-to-strong-coupling regime and, more generally, the important problem of the BCS-Bose Einstein crossover [61]. These issues have raised a remarkable interest also because of their possible relevance to the physics of high-temperature superconductivity. Let us recall, e.g., the analyses of the actual role played by the fluctuations of the phase of the superconducting order parameter in the underdoped cuprates [151–154], and the possibility to derive phase-only effective theories [155, 156] to capture a part of the underlying physics of these materials, going beyond [157] the standard BCS assumptions. As for DMFT, its application to the attractive case was very useful to identify [158, 159] the hallmarks of the BCS-Bose Einstein crossover in several thermodynamic and optical properties of correlated systems [160–163]. We should also mention here the novel perspectives opened by the "actual" experimental realization of quantum models with tunable attractive or repulsive interaction, when confining ultra-cold atoms in the interference pattern of laser sources [164, 165]. This exciting new physics is already stimulating novel DMFT studies [166] of the attractive Hubbard model.

Similarly as for the repulsive case, also for the attractive model, previous DMFT studies focused mainly on the one-particle properties. Even the well-known mapping [54] between the repulsive and the attractive Hubbard model (see Sec. 2.2.5), to the best of our knowledge, has never been explicitly ap-

plied to investigate the connections between the repulsive and attractive models at the level of the two-particle vertex functions. Hence, here our aim is to extend our theoretical analysis of Sec. 3.2 also to the $U < 0$ case, identifying and interpreting the observed frequency structures in the vertex functions in terms of the mapping onto the corresponding repulsive case and of the discussions in the previous section(s).

In this respect, let us recall the consequences of the partial particle-hole transformation of the half-filled Hubbard model or, more precisely, of the AIM associated to the DMFT solution of the half-filled Hubbard model, for the properties of the local Green's functions of the system (see Sec. 2.2.5). The (purely imaginary) local one-particle Green's function (and, hence, also the corresponding self-energy) for (half-filled) systems, which differ only in the sign of the Hubbard interaction parameter U, are indeed *identical*, as it is indicated in Eq. (2.176). At the two-particle level the situation is obviously more complicated. While for the ↑↑ case the corresponding two-particle Green's functions, generalized susceptibilities and vertices coincide for the attractive ($-U$) and the corresponding repulsive ($+U$) model [Eq. (2.175)], it is shown in Sec. 2.2.5 that the ↑↓ susceptibility with $U < 0$ is mapped onto the magnetic susceptibility for $U > 0$ [see Eqs. (2.185) and (2.186)]. Physically, this can be understood as follows: Fluctuations of the x- and y-spin component (i.e., the order parameter of the antiferromagnetic phase transition) at positive U are equivalent to fluctuations of the "cooper-pair density" $\hat{c}_\uparrow^\dagger \hat{c}_\downarrow^\dagger$ (i.e., to the superconducting order parameter) at negative U, as it was already demonstrated in the discussion about the SO(4) symmetry of the half-filled Hubbard model and AIM, respectively, in Sec. 2.2.2.6 [see Eqs. (2.127) and (2.128)]. For the lattice model this means that, for any antiferromagnetic instability (with orientation of the magnetic field in the xy-plane) at a given point $(U > 0, T)$ in the phase diagram, there exists a superconducting instability in the corresponding attractive model at $(-U, T)$.

We can now verify our analytical results from Sec. 2.2.5, which we recalled briefly in the previous paragraph, and gain further insight of the vertex structures for $U < 0$, by looking at the corresponding DMFT data. Our DMFT results for the Γ_r's in the four different channels are shown in Fig. 3.25 for the case $U = -0.5$. Comparing it with Fig. 3.15, i.e., the Γ's for the corresponding repulsive case $U = +0.5$, one observes that the triplet-

channel $\Gamma_t^{\nu\nu'\omega}$ is unchanged. This is expected because the triplet channel is identical to the $\uparrow\uparrow$ particle-particle channel $\Gamma_{pp,\uparrow\uparrow}^{\nu\nu'\omega}$, and the $\uparrow$-creation- and annihilation-operators are not affected by the particle-hole transformation [see Eq. 2.170)].

Furthermore, following Eqs. (2.185), (2.186) and (2.188), which state that the magnetic-channel is mapped onto the particle-particle $\uparrow\downarrow$-channel (plus an additional frequency shift), we compare these two channels in Fig. 3.26. Performing the additional transformation $\nu' \to (\omega = 0) - \nu'$ in the plot for $\Gamma_{pp,\uparrow\downarrow}^{\nu\nu'\omega}$ (i.e., reflecting the plot along the $x = \nu$-axis) one sees that the two plots are indeed identical.

Our analytical and numerical results for the case $U < 0$ can be, hence, summarized as follows. The main features of the vertices $\Gamma_r^{\nu\nu'\omega}$ (and logically of the corresponding $F_r^{\nu\nu'\omega}$) appear also for $U < 0$ along the diagonals and originate from reducible processes. As a consequence, also in the attractive case, the "topology" of the vertex functions remains essentially preserved upon increasing U. In contrast to the repulsive case, however, as suggested by Eq. (2.186) and Fig. 3.26, the strong enhancement of the main diagonal structure, identified as an hallmark of the MIT, will be now visible in the *secondary* diagonals ($\nu = -\nu'$) in some of the channels (e.g. magnetic, singlet). Physically, this reflects simply that for $U < 0$, $\chi_{pp,\uparrow\downarrow}(0)$ [instead of $\chi_m(0)$] is diverging at the MIT, since the "insulating" (symmetry broken) phase is now consisting of a collection of preformed local Cooper pairs.

Chapter 4

Nonlocal Correlations beyond DMFT

„Die Mittelmäßigkeit wiegt immer richtig, nur ist ihre Waage falsch."(A. Feuerbach)

In this chapter we discuss the the importance of nonlocal electronic correlations and the development of new methods beyond DMFT to take them into account in theoretical calculations. While cluster extensions of DMFT capture accurately short-range correlations (i.e., those within the cluster size), diagrammatic methods are needed for treating nonlocal electronic correlations on all length scales. The dynamical vertex approximation (DΓA) is an important representative of such methods, and, hence, will be addressed explicitly in this chapter. First, we discuss its basic physical idea and describe its actual implementation. We also present DΓA results for the case of simple nanoscopic systems and we apply a simplified version of the DΓA equations (ladder approximation) to provide an accurate description of the critical properties of the antiferromagnetic phase transition in the three-dimensional Hubbard model beyond the weak coupling regime. In the second part of the chapter, we illustrate other diagrammatic approaches based on the functional integral formalism, such as the dual fermion (DF) theory. Within this framework, eventually a new method based on the one-particle irreducible (1PI) functional for the Green's functions is proposed. This novel 1PI approach aims at improving the treatment of nonlocal correlations with respect to the standard (ladder) implementation of both DF and DΓA, and also allows for a comparison of the diagrammatic content of the existing techniques within a unifying formalism.

4.1   Importance of nonlocal correlations

In the previous chapter, we demonstrated the strength of DMFT in describing correlated electron system on a model level as well as for real materials. However, being a mean field theory

in the space coordinates, DMFT captures only the *local* part of the electronic correlations. While in many situation this constitutes the main contribution, several important physical phenomena have their origin in *nonlocal* electronic correlations. Let us just mention among many the high-temperature superconductivity in the cuprates [17] or pnictides [167, 168], transport through newly engineered hetero- and nanostructures [30, 169–174], the physics and entropy of ultracold atoms trapped in optical lattices [164, 175], or the occurrence of quantum critical points (QCP) in heavy fermion systems [176], which cannot be described accurately in standard DMFT.

The limitations of DMFT are also easily understandable from a purely theoretical point of view: As a mean field theory DMFT considers the effect of electrons at different lattice sites on the electron(s) at one specific site by a (self-consistent) mean field, i.e., it takes an average over all neighbors of this specific site. From this point of view DMFT resembles the classical mean-fields theories even though, in contrast to the latter, it avoids a time average and, hence, takes into account all local quantum fluctuations at the given lattice site. From a statistical point of view, replacing a random variable by an average over its realizations represents a good approximation if the number of samples is large. In fact, if this number approaches infinity, which corresponds to the limit of infinite coordination number $z \to \infty$ or dimensions $d \to \infty$ in DMFT, the approximation gets even exact according to the law of large numbers [177]. Also at high temperatures, where classical thermal fluctuations dominate over the quantum fluctuations, independent of whether local or nonlocal, DMFT will be typically rather accurate. However, in the opposite limits *nonlocal* spatial correlations can become predominant:

- **low dimensional systems:** Considering, e.g., the one-dimensional system depicted in the left panel of Fig. 4.1, one can observe that the mobility of the electron at the second lattice site (from left) depends strongly on the occupation of the two neighboring sites. Indeed, while there is no obstacle that prevents the particle moving to the left, the hopping of this electron to the adjacent site on the right would cost an energy U. Hence, if U is large, the probability for the latter process to happen is very low, which drastically lowers the mobility of the electron at the selected site. Here we see how this system exhibits significant (in this case: short-ranged) nonlocal spatial correlations which, of course, would be washed out by a mean-field description such as DMFT.

- **second-order phase transitions:** In the vicinity to a second-order phase transition to a long-range ordered (e.g., ferromagnetically as it is indicated in the right panel of Fig. 4.1) phase spatial fluctuations on all length scales occur in a system. Specifically,
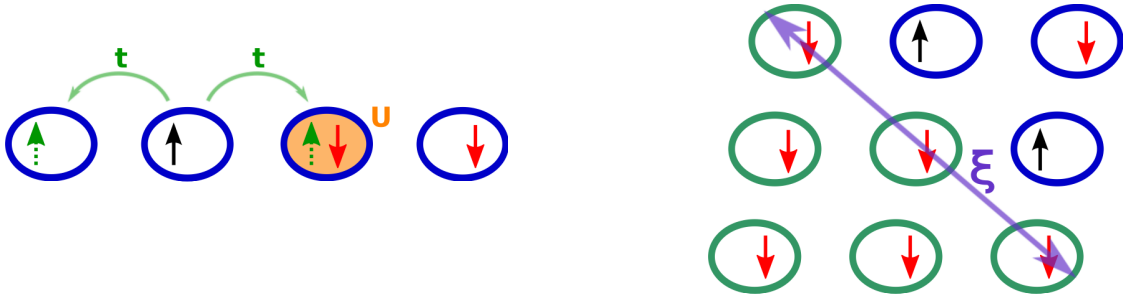
Figure 4.1: Schematic representation of typical situations, where nonlocal spatial correlations play a crucial role (in a lattice model). Left panel: For the low dimensional systems (in this picture one-dimensional) the mobility of an electron at a given site (e.g., the second from the left) depends strongly on the precise configuration of the neighboring sites, which renders a mean-field description problematic. Right panel: In the vicinity of a second-order phase transition to an spatially ordered phase the system is governed by fluctuations on all length scales, making the local description of DMFT a poor approximation in this situation.

exactly at the transition point the correlation length ξ of the fluctuations corresponding to the emergent order, diverges, rendering the local DMFT treatment of this physical phenomenon a very poor approximation.

From the above discussion, it is clear that the inclusion of nonlocal spatial correlations in our calculations is crucial for the understanding of the mechanism of many relevant and exciting physical phenomena at the frontier of the scientific research in condensed matter physics. On the other hand, one would also like to keep the correct treatment of the local correlations, provided by DMFT, since they are essential for an accurate description of the Hubbard Hamiltonian in the intermediate-to-strong coupling regime, as well as for capturing nonperturbatively the physics of the Mott-Hubbard metal-to-insulator transition. This motivates us to search new methods, which add -on the basis of DMFT- nonlocal corrections beyond its spatial mean-field description, and can provide for a better understanding of spatial correlation effects occurring in strongly correlated electron systems. To this end, two main routes have been followed: (i) Different groups have developed self-consistent algorithms for cluster extensions of DMFT, where the single impurity of DMFT is replaced by a cluster of sites, and (ii) diagrammatic extensions, which rely on the Feynman-diagrammatic representation of one- and two-particle Green's functions. Both routes will be discussed in the following with a particular focus on the diagrammatic extensions, which represent one of the principal

Figure 4.2: Cluster extensions of DMFT: The actual lattice problem is replaced by a cluster of interacting sites, which is embedded into a, self-consistently determined, non-interacting bath, allowing for the inclusion of spatial correlations within the cluster size. Cellular DMFT (CDMFT) and dynamical cluster approximation (DCA) correspond to the two possibilities of considering the cluster in real space (CMDFT) or momentum space (DCA), respectively.

topics of this work.

4.1.1 Cluster extensions of DMFT

The basic idea of cluster extensions of DMFT is to replace the actual infinite lattice problem with a finite cluster of N_c interacting sites which hybridizes with a self-consistently determined non-interacting bath (see Fig. 4.2), that accounts for the rest of the lattice. In this respect, these schemes represent the most natural extension of the single site DMFT algorithm to a cluster of sites. Specifically, the cluster can be defined either in real space, leading to the so-called cellular DMFT method (CDMFT) [178, 179], or in momentum space, where the corresponding approach has been coined "dynamical cluster approximation" (DCA) [180–182]. The latter formulation has the advantage of not breaking (when present) the lattice translational symmetry of the system.

In order to better clarify the basic characteristics of these methods, let us first consider the limiting cases of a small and a large number N_c of cluster sites. Taking into account only $N_c = 1$ cluster-site reproduces DMFT, which well justifies the denotation of cluster methods as extension of DMFT. On the other hand, for $N_c \to \infty$ the exact solution of the lattice model is recovered. Hence, in this respect, DCA or CDMFT with $1 < N_c < \infty$ can be considered as methods which "interpolate", systematically, between the DMFT and the exact solution of the lattice problem. For practical calculations, the cluster size has to be restricted obviously to a relatively small value of N_c, by numerical limitations due to the exponential growth of the Hilbert space with the number of sites of the cluster. At present calculations with up to ~ 100 cluster sites are feasible [183, 184], which corresponds, e.g., to $4 - 5$ sites in each
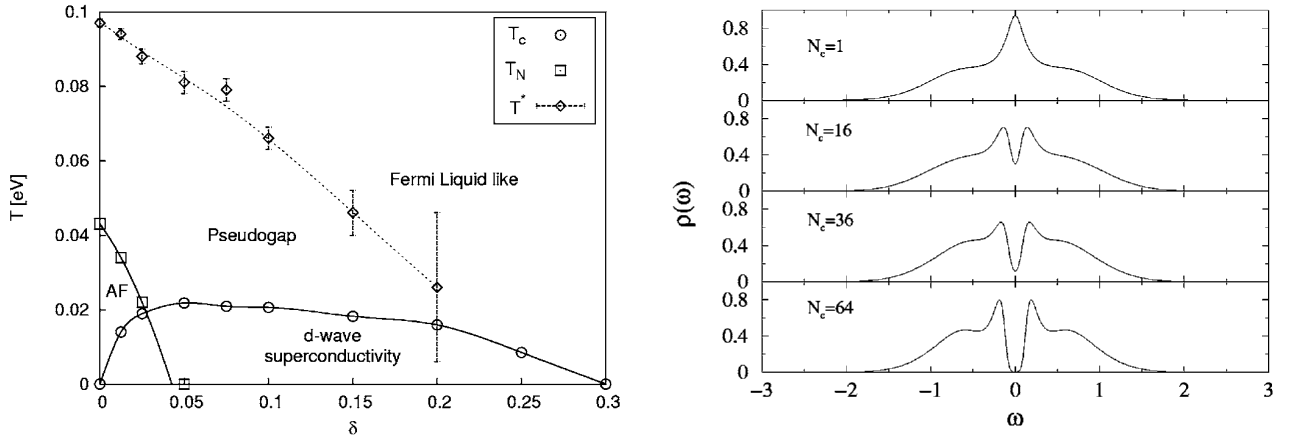
Figure 4.3: Left panel: DCA phase diagram (with $N_c = 4$) for the two-dimensional Hubbard model on a simple cubic lattice. δ represents the amount of hole-doping in the system. The figure is reproduced from Ref. [182]. Right panel: Formation of the pseudogap in the spectrum of the two-dimensional Hubbard model at half-filling. The figure is reproduced from Ref. [187].

direction for the three-dimensional simple cubic lattice[1].

Obviously, cluster extensions of DMFT are capable of treating nonlocal electronic correlations within the cluster size very accurately. In this respect, DCA was quite successful in analyzing the effect of short-range nonlocal correlations on spectral and thermodynamic properties of the two- and three-dimensional Hubbard model, such as, e.g., the formation of a gap in the spectral function at low temperatures (right panel in Fig. 4.3 from Ref. [187] for the half-filled case, and, for the pseudogap occurrence out of half-filling, see Refs. [188, 189]), the d-wave superconductivity for the hole-doped model which might be relevant for the theoretical description of the high-temperature superconducting cuprates (left panel of Fig. 4.3 from Ref. [182]), the momentum space anisotropy in the (nonlocal) self-energy [190], the d-wave symmetry of the effective pairing interaction in the repulsive case [191], and, more recently, the thermodynamics for the three-dimensional model in the vicinity of the antiferromagnetic phase transition [184].

However, as it is easy to imagine, long-range spatial correlations are taken into account only

---

[1]Note that the accuracy of a DCA calculation depends not only on the actual *number* of cluster sites but also on the *geometry* of the cluster, in particular for small cluster sizes or the purpose of extrapolations. It can be indeed shown that for each (small) number N_c of cluster sites a different cluster geometry is advantageous, leading to the so-called Betts clusters which are in general not simple squares or cubes in two and three dimensions, respectively [127, 185, 186].

on a mean-field level by cluster extension of DMFT. This renders a comprehensive description of second-order phase transitions difficult within these approaches. In fact, at a second-order phase transition one observes fluctuations on *all length scales* as the corresponding correlations length ξ diverges. As a matter of course, cluster extensions of DMFT cannot capture directly this physics and, hence, fail in describing critical properties adequately. Even extrapolations of the results to an infinite cluster size ($N_c \to \infty$), which –when properly done on a apecific subset of (Betts) clusters– allow for an estimation of the transition temperature to a magnetically ordered phase [127] or of the Kosterlitz-Thouless T_c for d-wave superconductivity at finite dopings [182], cannot yield accurate predictive results for the critical exponents of the system[2]. Hence, for the description of critical properties of the Hubbard and related models, as well as for the treatment of nonlocal correlations which remains feasible also for realistic systems [192], we aim at the development of complementary methods for taking into account nonlocal correlations on all length scales on the same footing. Such approaches, known as *diagrammatic extension* of DMFT, might be also combined in the future with cluster methods in general multi-scale schemes [193]. Their state-of-the-art development will be presented in the next sections.

4.1.2   Diagrammatic extensions of DMFT

Let us start analyzing the common structure underlying all diagrammatic extensions of DMFT. Though we try to keep the discussion in this section as general as possible, one should keep in mind that we aim at approximate treatments of Hubbard-like Hamiltonians. At this point, a comment on the notation adopted in the following sections is also appropriate: While in the previous two chapters (2 and 3) almost only *local*, i.e., $\mathbf{k}$-independent, one- and two-particle Green's function were considered, in the following we will be also concerned with the corresponding $\mathbf{k}$-*dependent* objects. Hence, in order to avoid any confusion or ambiguity in the denotation of Green's and vertex functions, we will supplement here all local, i.e., $\mathbf{k}$-independent quantities, obtained from an AIM (mostly from that connected with the DMFT solution of the Hubbard model), with an explicit subscript "loc", differently from the previous chapters 2 and 3. As for the $\mathbf{k}$-dependent Green's and vertex functions, we will specify their momentum arguments explicitly, except for the specific situations, where a subsumption of frequencies and momenta into a four-vector is convenient for the sake of a

---

[2]Consider, e.g., the following ascertainment in Ref. [182]: "However, ... these critical exponents (i.e., that of DCA) reflect the behavior at intermediate temperatures. Very close to the transition there must be a region of mean-field behavior."

$$G_0(\nu)$$

Figure 4.4: Diagrammatic elements of the standard perturbative expansion of the Hubbard model. Left: the bare propagator $G_0(\nu, \mathbf{k}) = \frac{1}{i\nu + \mu - \varepsilon_\mathbf{k}}$. Right: The bare Hubbard interaction U.

better readability of the equations.

As indicated in the headline of this section, we will investigate extension of DMFT which are based on the technique of Feynman diagrams. For this purpose we briefly recall the standard diagrammatic perturbation theory for the Hubbard model. In general, two diagrammatic elements are required for expanding the (n-particle) Green's functions of a system into a diagrammatic series. For the case of Hubbard (and related) models these ingredients are depicted in Fig. 4.4 and discussed in the following: (i) A *bare propagator* is needed which is given by the non-interacting Green's functions of the system, $G_0(\nu, \mathbf{k}) = \frac{1}{i\nu + \mu - \varepsilon_\mathbf{k}}$. This is represented by a (dashed) line on the left-hand side of Fig. 4.4. These propagators in turn have to be connected in all possible, but topologically distinct, ways [38] by (ii) the bare *interaction* which, in the case of the one-band Hubbard model, is given just by a constant U (see right panel of Fig. 4.4). Using these diagrammatic elements one can construct all possible diagrams for the self-energy of the system, as it is indicated in Fig. 2.5c. While for a more detailed discussion of the Feynman diagrammatic technique we refer to section 2.2.4 in chapter 2 and the general literature [32, 33, 38, 194], let us stress here that a truncation of the diagrammatic series at a certain order of U yields typically reasonable results only if this interaction parameter is sufficiently small (i.e., much smaller than the bandwidth $W = \varepsilon_\text{max} - \varepsilon_\text{min}$ of the system). In this regime ($U \ll W$) it might be, hence, possible to obtain a good approximation for the self-energy of the system by means of plain perturbation theory up to some finite order in U (depending on, e.g., the temperature).

However, in this thesis we are interested in strongly correlated electron systems, where the Coulomb repulsion between the electrons is not well screened. Hence, as for our models (like the Hubbard model), we consider interaction parameters U which are of the order of - or even larger than - the bandwidth W. In this *nonperturbative* region of the parameter-space one cannot describe the physics of the underlying system by means of perturbation theory up to any finite order in the interaction parameter U. For instance, the mechanism leading to a Mott insulating state in the Hubbard model, which is marked by a divergence of the

a)   b)

G_{DMFT}

G_{loc}

$\gamma_{\mathrm{loc}}^{(4)}$ $\gamma_{\mathrm{loc}}^{(6)}$ $\cdots$
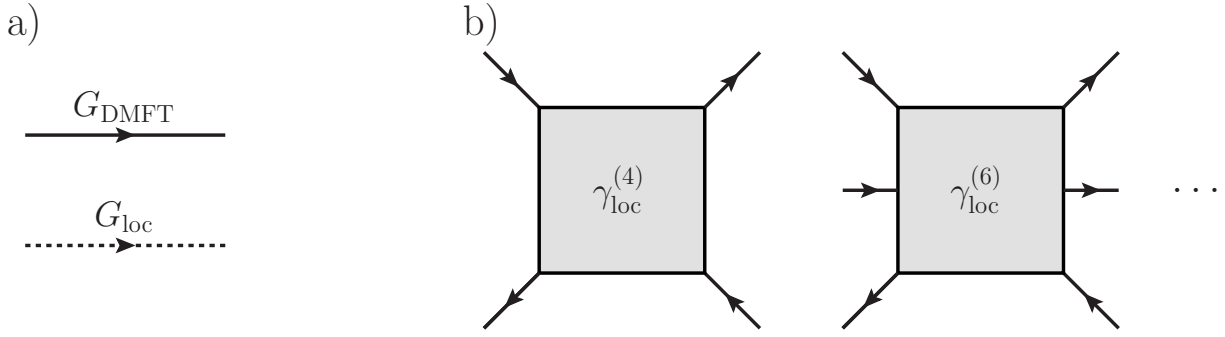
Figure 4.5: Diagrammatic elements for diagrammatic extensions of DMFT; a) The bare
propagators are given by $G \equiv G_{\mathrm{DMFT}}(\nu, \mathbf{k}) = 1/\left[i\nu + \mu - \varepsilon_{\mathbf{k}} - \Sigma_{\mathrm{loc}}(\nu)\right]$ and/or $G_{\mathrm{loc}}(\nu) =$
$1/\left[i\nu + \mu - \Delta(\nu) - \Sigma_{\mathrm{loc}}(\nu)\right]$; b) The interaction part consists of the local n-particle ($n =$
$2, 3, \ldots$) vertex functions $\gamma_{\mathrm{loc}}^{(2n)}$ of DMFT ($2n$ in the superscript of γ_{loc} denotes the number
of outer legs of the corresponding n-particle vertex function).

self-energy for $\nu \to 0$ (at $T = 0$), cannot be captured by a perturbative resummation of a
finite number of diagrams for Σ. In this respect DMFT really represents a big step forward
by allowing for a summation of all the infinitely many purely local Feynman diagrams for
the self-energy, and, hence, for a qualitative description of both sides of the Mott-Hubbard
metal-to-insulator transition. On the other hand, as we already discussed in Sec. 3.1, DMFT
neglects the $\mathbf{k}$ dependence of the self-energy, and, hence, does not take into account any
nonlocal correlation effects. Therefore, it is desirable to recast the perturbation theory for the
self-energy of the Hubbard model in such a way that the DMFT contributions, i.e., all local
correlations, are included already as a starting point of our new perturbative expansion: This
means that DMFT will represent the "lowest-order" of our new diagrammatic techniques,
while nonlocal contributions will be calculated, perturbatively (but not in U!), by means of
selected diagrammatic corrections.

The construction of such a "perturbation" theory around DMFT is the common feature of all
diagrammatic extension of DMFT. The corresponding diagrammatic elements of these new
approaches are depicted in Fig. 4.5:

- **bare propagator:** The DMFT Green's function $G_{\mathrm{DMFT}}(\nu, \mathbf{k})$ or the local DMFT
  Green's function $G_{\mathrm{loc}}(\nu) = \sum_{\mathbf{k}} G_{\mathrm{DMFT}}(\nu, \mathbf{k})$ (after the DMFT self-consistency is reached)
  act as "bare" propagators of the diagrammatic techniques (see Fig. 4.5a). This choice
  ensures a nonperturbative inclusion of all purely *local* correlations of DMFT already
  at the level of lowest (zeroth) order perturbation of the new schemes via the (local)
  DMFT self-energy $\Sigma_{\mathrm{loc}}(\nu)$, which is included in $G_{\mathrm{DMFT}}(\nu, \mathbf{k})$ and $G_{\mathrm{loc}}(\nu)$.
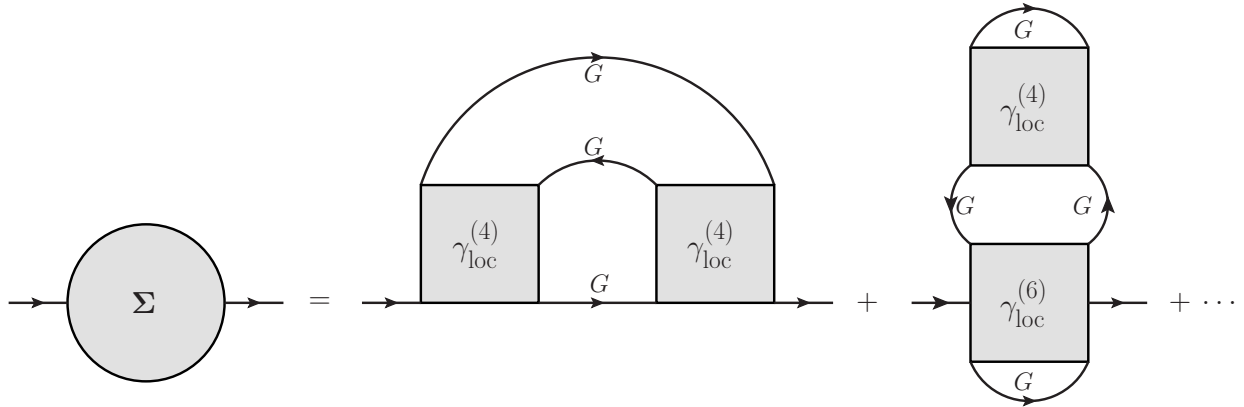
Figure 4.6: Two second-order diagrams for the lattice self-energy $\Sigma(\nu, \mathbf{k})$ built from the diagrammatic elements in Fig. 4.5. G denotes either the DMFT Green's function $G_{\mathrm{DMFT}}(\nu, \mathbf{k})$ or the local DMFT Green's function $G_{\mathrm{loc}}(\nu)$.

- **interaction:** The interaction part of all diagrammatic extension of DMFT is given by the local n-particle vertex functions $\gamma_{\mathrm{loc}}^{(2n)}$ of DMFT (see Fig. 4.5b). Which type of vertex function, i.e., (fully) reducible, one-particle irreducible, two-particle irreducible or even two-particle fully-irreducible, is selected for the construction of diagrams, depends on the specific method under consideration[3]. The common feature of all these vertex functions is that, in contrast to the bare interaction U adopted in ordinary perturbation theory, they exhibit a (in many cases very pronounced) frequency dependence. This means that the interaction between the new "bare particles" (which are, of course, dressed with all local correlation effects) gets strongly nonlocal in time.

We are now in a position to construct diagrams for our $\mathbf{k}$-dependent lattice self-energy $\Sigma(\nu, \mathbf{k})$, using the diagrammatic elements introduced in Fig. 4.5 and discussed above. Exemplarily, two second-order [in $\gamma_{\mathrm{loc}}^{(2n)}$] diagrams are depicted in Fig. 4.6.

It is, however, not possible to sum up all diagrams for the self-energy, considering all higher-order vertex functions, which would correspond, in fact, to the exact solution of the Hubbard model. Hence, approximations are needed. Typically, two types of approximations are involved in all diagrammatic extension of DMFT:

1) **restriction to $\gamma_{\mathrm{loc}}^{(4)}$:** Usually one restricts oneself to the two-particle local vertex function as interaction term, neglecting the three- and more particle contributions. The

---

[3]For this reason, we adopt here the general notation $\gamma_{\mathrm{loc}}^{(2n)}$ for the vertex function aiming at keeping the discussion at this point as general as possible. We will specify the type of vertex function we are using only later, when referring to the specific type of diagrammatic extension of DMFT.

physical argument for this simplification relies on the fact that the original bare in-
teraction among the physical electrons is of a two-particle type. Hence, it is plausible
that approximations made on the level of the two-particle vertex can already contain
the most relevant contributions for the description of nonlocal correlations. However,
it should be stressed that there does not exist a rigorous proof for this statement in the
general case, and, hence, one should carefully check whether the restriction to $\gamma_{\text{loc}}^{(4)}$ is jus-
tified in the specific case under consideration [35, 195]. From a practical point of view,
such an approximation is, however, necessary in many situations (with few exceptions),
since the calculation of three- and more-particle local vertex functions in a general
case is an almost infeasible task even when adopting the most recent continuous-time
quantum Monte Carlo (CTQMC) methods[4].

2) **selection of type of diagrams:** Even within the restriction to the two-particle local
vertex for the new interaction it is not possible to sum up all diagrams for the self-
energy. Besides performing *finite* summations of lowest-order [in $\gamma_{\text{loc}}^{(2n)}$] diagrams[5], one
often considers two schemes which account for an infinite resummation of Feynman
diagrams:

  – *ladder diagrams:* In the vicinity of second-order phase transitions, resummations
    of infinite numbers of diagrams are necessary to describe the effect of the corre-
    sponding critical fluctuations on the physics of the system. However, such infinite
    resummations can be readily performed, if the type of the emergent order is known
    and if there are no competing instabilities to differently ordered phases. In that
    case we can restrict ourselves to the summation of ladder diagrams in the specific
    channel corresponding to the instability under consideration. Analytically, this
    is done by considering a Bethe-Salpeter equation in this specific channel. For a
    detailed discussion of the diagrammatic and analytic structure of ladder diagrams
    and Bethe-Salpeter equations, we refer to section 2.2.4.2 (in particular page 69)
    and appendix B, as well as to sections 4.3 and 4.4.2.1, where the ladder versions
    of the DΓA and 1PI are discussed and compared.

  – *parquet diagrams:* In case one cannot identify a priori the most important fluc-
    tuation channel of the system, or if there are two or more competing instabilities,

---

[4]To the best of our knowledge, the hitherto only calculation of local three-particle vertex functions was
performed in Ref. [123].

[5]Note that nonlocal corrections to the self-energy, arising, e.g., from 2nd-order diagrams, constitute a
sizable contribution only when inserted into a self-consistent scheme [36], and even in that case they can take
into account only short-range correlations [123].

one should construct ladder diagrams in *all* channels, and couple them, in a self-consistent manner. This corresponds analytically to solving the parquet equations for the system [26,44–46]. A diagrammatic and analytical description of this rather complicated set of coupled non-linear integral equations is given in section 2.2.4.2 and appendix C, as well as in the discussion of the full parquet-based version of DΓA of section 4.2.2. Let us just remark here that working with the parquet equations is numerically very demanding. Hence, one usually restricts oneself to ladder approximations whenever it is possible, or, alternatively, if a full parquet treatment is needed but not feasible, one might consider methods based on the functional renormalization group [196], such as the recently proposed DMF^{2}RG in Ref. [147].

After this rather general discussion of the basic ingredients and approximations involved in the diagrammatic extensions of DMFT we will present a short overview over the specific approaches, which were considered in the literature since the invention of DMFT. Historically, one of the first attempts to address the problem of nonlocal correlations beyond DMFT was the so-called $1/d$-method proposed in Ref. [197], which is rather appealing from a purely theoretical point of view. In fact, since DMFT corresponds to the limit of $d \to \infty$, i.e., $1/d = 0$, it is rather obvious to construct nonlocal corrections to the DMFT Green's functions by an expansion of the latter in the "small" parameter $1/d$. However, it turned out that, in the cases of interest, i.e., for $d = 2$ or $d = 3$, keeping just the first few terms of such a series does not improve the DMFT results much and becomes a rather poor approximation if nonlocal correlations are equally or even more important than their local counterparts. A next attempt to include spatial correlations on the top of DMFT was the DMFT+$\Sigma_{\mathbf{k}}$ approach [198–202] which considers nonlocal corrections to the local DMFT self-energy arising from the interaction of non-interacting electrons with spin fluctuations. This theory was constructed mainly for describing the pseudogap behavior of the cuprates and, in this sense, its nature is semi-phenomenological, i.e., it cannot be considered as a purely microscopic approach to the Hubbard model. In this respect we should also mention a more recent extension of DMFT, proposed in Ref. [203], which is based on the mapping of the lattice problem onto a multitude of two-impurity Anderson models, and allows to describe the pseudogap formation in the two-dimensional Hubbard model.

The most important diagrammatic approaches, which were developed in the last five to six years and constitute the main topics of this chapter, are the dynamical vertex approximation (DΓA) in its ladder and its parquet version, the dual fermion (DF) theory and, very

Method	Based on local:	Two-particle level	Diagrams
dual fermion (DF)	full (connected) vertex	F_{loc}	2$^{\text{nd}}$-order, ladder, parquet
one-particle irreducible approach (1PI)	one-particle irreducible vertex	F_{loc}	ladder
DMFT+functional renormalization group (DMF^{2}RG)	one-particle irreducible vertex	F_{loc}	RG flow (parquet-like)
ladder dynamical vertex approximation (ladder DΓA)	two-particle irreducible vertex	$\Gamma_{\text{loc},r}$	ladder
dynamical vertex approximation (DΓA)	two-particle fully irreducible vertex	Λ_{loc}	parquet

Table 4.1: Table of the different diagrammatic methods and the corresponding type (i.e., full, one-particle irreducible, two-particle irreducible or two-particle fully irreducible) of local vertex functions which is required by the method, as well as their two-particle counterparts[6] (F_{loc}, $\Gamma_{\text{loc},r}$ and Λ_{loc}). In the last columns the type(s) of diagrams which have been hitherto considered for the respective approaches are reported.

recently, the one-particle irreducible (1PI) approach, which exhibits a unifying aspect with respect to the other two methods (DΓA and DF). As discussed before, all these schemes are based on the local two-particle vertex functions $\gamma_{\text{loc}}^{(4)}$ and the full or local DMFT Green's functions G_{DMFT} or G_{loc}, respectively.   To get an overall orientation about which type of two-particle vertex and which type of diagrammatic approximation is related to which specific diagrammatic extension of DMFT we refer to Tab. 4.1. Let us mention that the

---

[6]Let us recall that, at the two-particle level, the full connected vertex coincides with the one-particle irreducible one (F_{loc}), as it was already discussed in Sec. 2.2.4.2 (see, in particular, page 66).
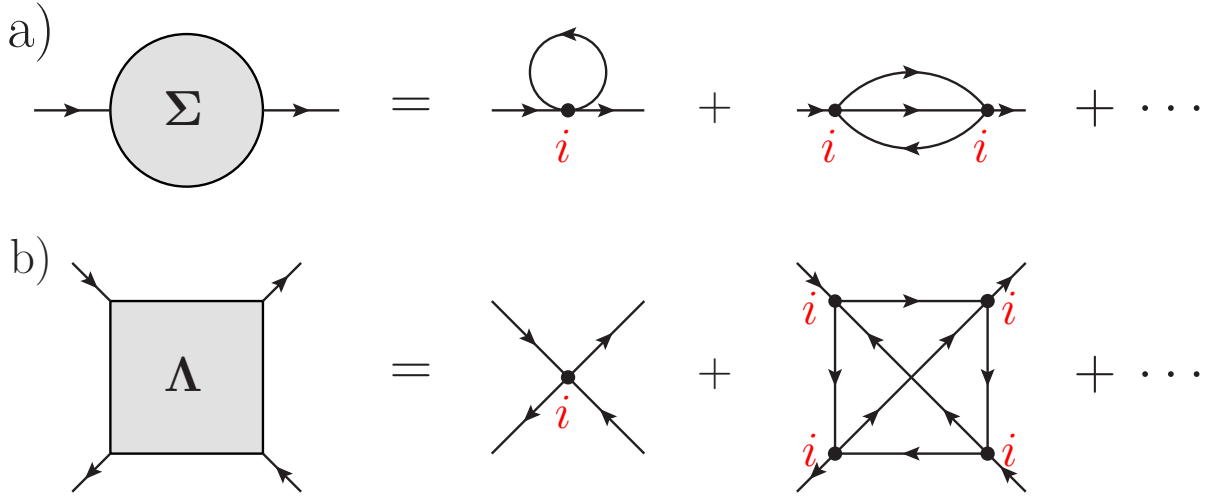
Figure 4.7: a) In DMFT the fully irreducible one-particle vertex, i.e., the self-energy Σ, is purely local (i represents a site index of the lattice); b) In DΓA the fully irreducible two-particle vertex Λ is purely local. Note that all diagrams in this figure are skeleton diagrams, i.e., the lines represent the full interacting Green's functions. The dots in turn correspond to the bare Hubbard interaction U.

recently proposed combination of DMFT and fRG (DMF²RG) [147] also naturally fits in our classification scheme, since here parquet-like diagrams are generated by a renormalization group flow starting from the full two-particle vertex of DMFT. However, we want to point out that the diagrammatic content of DMF²RG cannot be straightforwardly identified as in the other cases (DF, DΓA, 1PI), because corrections to DMFT are not obtained by a direct calculation of a specific subset of diagrams.

In the following chapters we will discuss all methods in Tab. 4.1 (except for DMF²RG, for which we refer the interested reader to Ref. [147]) in more detail and analyze their performance to describe nonlocal correlations beyond DMFT in the system under consideration.

4.2 Dynamical vertex approximation

4.2.1 Basic Idea

For an understanding of the basic idea of the dynamical vertex approximation (DΓA) [26, 27, 29], we make reference once again to the diagrammatic interpretation of DMFT. From the latter perspective, DMFT can be viewed as a method which is based on the locality of the one-particle fully irreducible vertex, i.e., on the complete locality of the self-energy of the
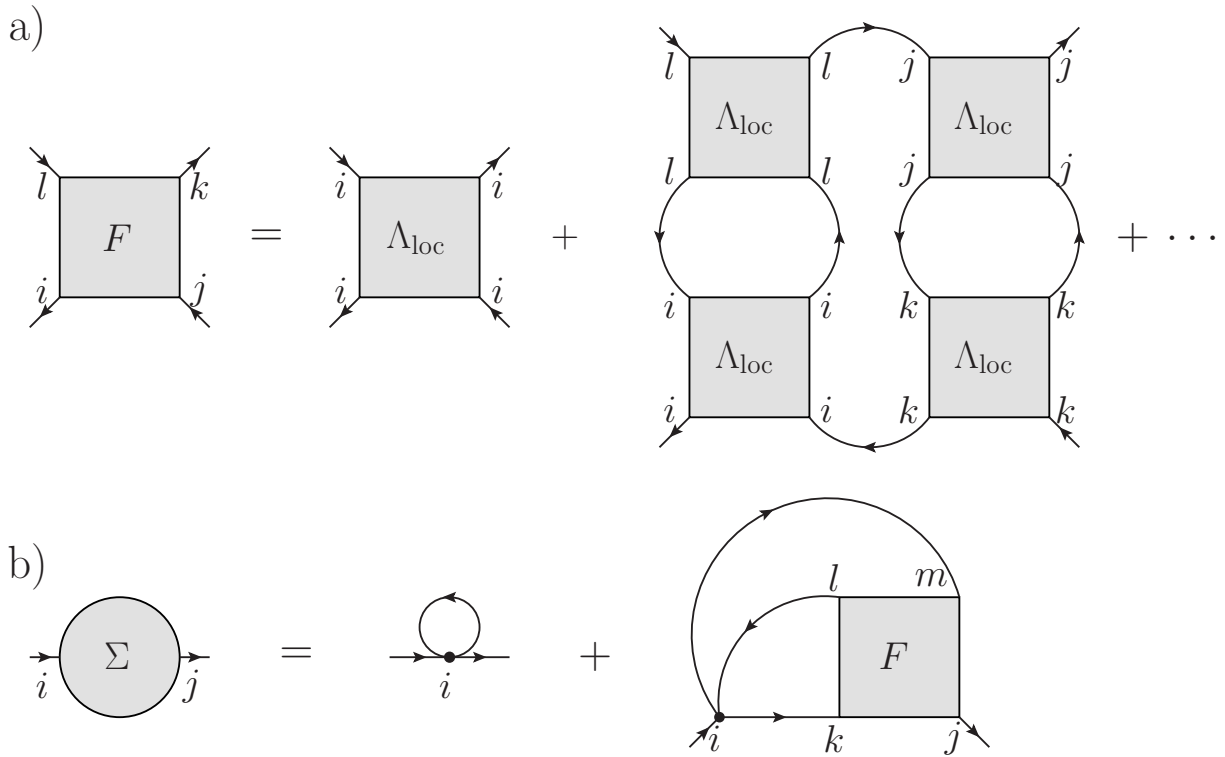
Figure 4.8: a) In DΓA the *nonlocal* full vertex F_{ijkl} is constructed from the local fully irreducible one $\Lambda_{iiii} \equiv \Lambda_{\mathrm{loc}}$ and the nonlocal DMFT Green's function G_{ij} (illustrated by the lines in this figure). b) The nonlocal self-energy Σ_{ij} in turn is calculated from the full vertex F_{ijkl} and the DMFT Green's function G_{ij} by means of the (nonlocal version of the) Schwinger-Dyson equation of motion [see Eq. (2.194)] which is depicted graphically here. (The indices $i, j, k, \ldots$ denote lattice sites here.)

system (see Fig. 4.7a). A very natural generalization of this idea is to raise the concept of locality to the two- or even more-particle level. Hence, in this spirit, the DΓA assumes the *locality of the fully irreducible two-particle vertex* function Λ_{loc}. These local building blocks are then connected by DMFT (nonlocal) Green's functions, yielding a nonlocal reducible vertex F_{ijkl} [or $F_{\mathbf{kk'q}}$ in momentum space, see also the definition of the Fourier transform in Eqs. (2.61) and (2.62)], as it is illustrated in Fig. 4.8a. This vertex in turn leads, via (the **k**-dependent version of) the equation of motion (2.194), to a nonlocal self-energy, as depicted diagrammatically in Fig. 4.8b. Let us point out that for $n = \infty$, i.e., when assuming the ∞-particle vertex to be purely local, the exact solution of the (Hubbard) model is recovered. However, as discussed in the previous section, the calculation of local three- and more-particle vertex functions is numerically very demanding (if not infeasible). Hence, for a practical implementation, we restrict ourselves to the DΓA assumption of complete locality for the

DMFT-flow
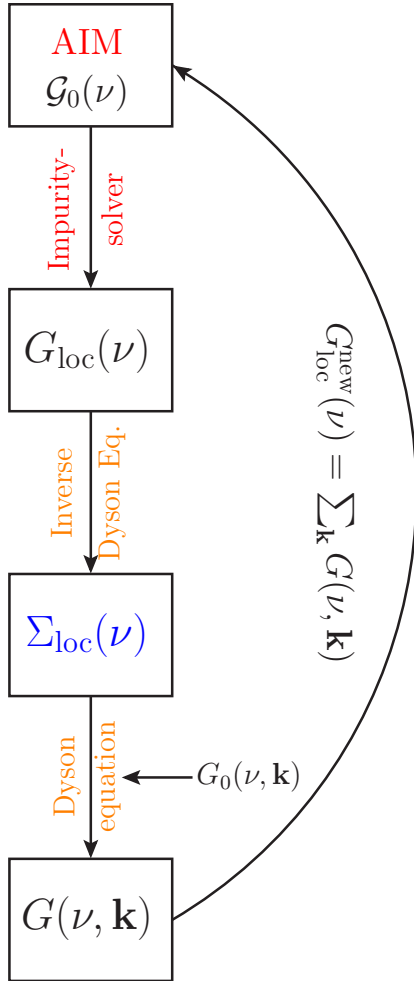
DΓA-flow
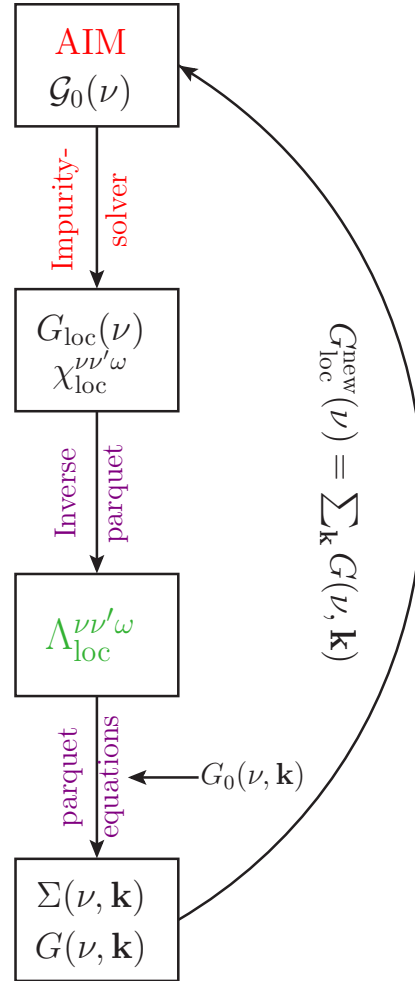
Figure 4.9: Comparison of the flow-diagrams of DMFT and DΓA.

fully irreducible two-particle vertex function Λ, as illustrated in Fig. 4.7b. Before discussing the algorithmic details of DΓA let us recall that conceptually similar methods have been presented in the last years. For instance, a less elaborate version of DΓA has been discussed by Kusonose in Ref. [204], similar techniques have been proposed by Janiŝ *et all.* for the treatment of disordered systems [140, 141], and a multi-scale extension of DΓA has been presented by Slezak *et al.* in Ref. [193].

Let us now turn to the actual implementation, i.e., the flow diagram, of the DΓA, which, for the sake of clarity, is compared with the corresponding flow diagram of DMFT in Fig. 4.9. The DΓA algorithm can be described (in comparison to DMFT) as follows:

1) One has to calculate the local *one- and two-particle*[7] Green's function (or generalized susceptibility) $G_{\text{loc}}(\nu)$ and $\chi_{\text{loc}}^{\nu\nu'\omega}$ for an auxiliary AIM [defined by $\mathcal{G}_0(\nu)$] by means of an impurity solver such as, e.g., exact diagonalization (ED) or quantum Monte Carlo (QMC). Note that in the corresponding step in DMFT only the calculation of the one-particle Green's function $G_{\text{loc}}(\nu)$ is required (see Fig. 4.9).

2) For DΓA one has to extract the local fully irreducible two-particle vertex $\Lambda_{\text{loc}}^{\nu\nu'\omega}$ from $G_{\text{loc}}(\nu)$ and $\chi_{\text{loc}}^{\nu\nu'\omega}$, essentially by inverting the *parquet* equations for the local AIM, as we will discuss in more detail in the next section (see also section 2.2.4.2 and appendices B and C). On the contrary, DMFT requires just the calculation of the local fully irreducible one-particle vertex, i.e., the local self-energy, by inverting the much simpler algebraic Dyson equation of the associated AIM.

3) In the next step the DΓA approximation is applied: This means, one assumes that the fully irreducible vertex of the lattice (Hubbard) model can be replaced by its local counterpart $\Lambda_{\text{loc}}^{\nu\nu'\omega}$, calculated by solving an auxiliary AIM. From $\Lambda_{\text{loc}}^{\nu\nu'\omega}$ and the non-interacting lattice Green's function $G_0(\nu, \mathbf{k})$ one obtains a momentum-dependent lattice vertex $F_{\mathbf{kk'q},\sigma\sigma'}^{\nu\nu'\omega}$ and a momentum-dependent lattice self-energy $\Sigma(\nu, \mathbf{k})$ by solving, self-consistently the parquet equations and the Schwinger-Dyson equation, respectively, for the lattice system. Finally, the lattice Green's function $G(\nu, \mathbf{k})$ can be easily determined from $\Sigma(\nu, \mathbf{k})$ via the Dyson equation. Again, the corresponding procedure is numerically much less demanding in DMFT, where the lattice Green's function is calculated simply by means of the (lattice) Dyson equation from the local self-energy and the bare propagator of the lattice $G_0(\nu, \mathbf{k})$.

4) Finally, we recompute the local part of the lattice Green's function, $\sum_{\mathbf{k}} G(\nu, \mathbf{k})$, and identify it with the local Green's function of a new auxiliary AIM [$\sum_{\mathbf{k}} G(\nu, \mathbf{k}) \equiv G_{\text{loc}}^{\text{new}}(\nu)$], which is defined in this way. In practice, from $G_{\text{loc}}^{\text{new}}(\nu)$ one should extract the corresponding electronic bath $\mathcal{G}_0^{\text{new}}(\nu)$ of the new AIM by solving the "inverse" impurity problem. Let us point out, however, that this is more complicated than the "direct" impurity problem, where the local interacting Green's function $G_{\text{loc}}(\nu)$ is calculated from the Weiss field $\mathcal{G}_0(\nu)$, and requires an iterative procedure[8].

---

[7] For the connection between the full two-particle Green's function G_2 and the generalized susceptibility χ we refer to section 2.2.3, Eqs. (2.145)-(2.150).

[8] For example, $\mathcal{G}_0^{\text{new}}(\nu)$ can be determined from $G_{\text{loc}}^{\text{new}}(\nu) = \sum_{\mathbf{k}} G(\nu, \mathbf{k})$ by solving the impurity model and the local Dyson equation self-consistently in the following way: (i) Starting from an arbitrary local self-energy $\Sigma_{\text{loc}}^{(0)}(\nu)$, one obtains an updated Weiss field through the Dyson equation, i.e., $\mathcal{G}_0^{(1)}(\nu) =$

5) Steps 1-4 are iterated till convergence of $G_{\text{loc}}(\nu)$.

The parquet equations, which are obviously a crucial part of the DΓA algorithm, will be discussed in the next section. Let us here just anticipate that, while the bottleneck of DMFT is the solution of the impurity problem, an additional numerical challenge of DΓA is represented by the numerical solution of the parquet equations. In fact, the full DΓA scheme is numerically very demanding which makes a simplified version of this approach very desirable. This issue will be discussed in section 4.3.

Let us finally mention an interesting point concerning the relation between DMFT and DΓA: Since in the (outer) DΓA self-consistency cycle the AIM is updated, the final solution is in no way connected to DMFT. In fact, though the AIM connected with DMFT might well serve as a reasonable starting point for the first DΓA iteration, other choices of the initial AIM are certainly possible. If viewed (and applied) in this generalized framework, DΓA is not simply adding nonlocal correlations on the top of the local ones of DMFT, as discussed in section 4.1.2, but it generates *all* correlation effects, i.e., local *and* nonlocal, by itself. In fact, a feedback of nonlocal correlations on the local one- and two-particle Green's functions is certainly to be expected in finite dimensions. The latter ones, hence, might strongly differ from their DMFT counterparts in the final DΓA solution depending on the parameter regime considered.

4.2.2 Parquet equations

In the previous section, we have illustrated that important parts of the DΓA algorithm rely on the parquet formalism. While an analytical derivation and explanation, as well as a diagrammatic illustration, have been given in section 2.2.4.2 and appendices B and C, we will now discuss the numerical treatment of these complicated relations [45, 46, 142]. To this end we recall schematically the basic equations of the parquet formalism, i.e., the parquet

---

$\left[\Sigma_{\text{loc}}^{(0)}(\nu) + 1/G_{\text{loc}}^{\text{new}}(\nu)\right]^{-1}$. (ii) Solving the AIM defined by this Weiss field provides a new local Green's function $G_{\text{loc}}^{(1)}(\nu)$ and, hence, also a new self-energy $\Sigma_{\text{loc}}^{(1)}(\nu) = \left[\mathcal{G}_0^{(1)}(\nu)\right]^{-1} - \left[G_{\text{loc}}^{(1)}(\nu)\right]^{-1}$. (i) and (ii) are iterated until $G_{\text{loc}}^{(n)}(\nu) = G_{\text{loc}}^{\text{new}}(\nu)$ [or, equivalently, $\Sigma_{\text{loc}}^{(n)}(\nu) = \Sigma_{\text{loc}}^{(n-1)}(\nu)$] within a given numerical accuracy. This way, the calculated $\mathcal{G}_0^{(n)}$ well represents the Weiss field defining the AIM connected to $G_{\text{loc}}^{\text{new}}(\nu)$.

equation(s), the Bethe-Salpeter equation(s) and the Schwinger-Dyson equation of motion:

$$F = \Lambda + \underbrace{(F - \Gamma_{ph})}_{\Phi_{ph}} + \underbrace{(F - \Gamma_{\overline{ph}})}_{\Phi_{\overline{ph}}} + \underbrace{(F - \Gamma_{pp})}_{\Phi_{pp}}, \tag{4.1a}$$

$$F = \Gamma_r + \int \Gamma_r (GG)_r F, \tag{4.1b}$$

$$\Sigma = \frac{Un}{2} + \int GGGF, \tag{4.1c}$$

where $r = ph, \overline{ph}, pp$ denotes the channel under consideration. For a more explicit form of the parquet and Bethe-Salpeter equations in the three different channels [Eqs. (4.1a) and (4.1b)], including frequency and spin arguments, we refer to Eqs. (C.2), (B.1), (B.8) and (B.14), as well as to Eq. (2.194) for the Schwinger-Dyson equation of motion [Eq. (4.1c)]. As for the nonlocal versions of these three (sets of) equations, let us point out that they can be readily obtained by considering the four vector $k = (\nu, \mathbf{k})$ and $q = (\omega, \mathbf{q})$ in place of the fermionic and bosonic Matsubara frequency ν and ω, respectively.

Let us first discuss the local version of the *inverse parquet* method, which is needed for extracting the local fully irreducible vertex $\Lambda_{\mathrm{loc}}^{\nu\nu'\omega}$ from the local generalized susceptibility $\chi_{\mathrm{loc}}^{\nu\nu'\omega}$ and the local Green's function $G_{\mathrm{loc}}(\nu)$ of a given AIM, which can be directly calculated from the impurity solver of choice, e.g., ED or QMC. The corresponding procedure is illustrated in the left panel of Fig. 4.10 and described in the following:

1) By means of the Bethe-Salpeter equations (B.7) and (B.19) $\Gamma_{\mathrm{loc},r}$ is calculated from χ_{loc} and G_{loc} [for the four different channels and spin combinations $r = d, m, s, t$ as defined, e.g., in Eq. (2.167)].

2) The $\Phi_{\mathrm{loc},r}$ are obtained by means of Eq. (C.1), and, then, the parquet equations (C.2) are solved for Λ_{loc} [for the four different channels and spin combinations which are given in Eqs. (C.2)].

One can see that in the inverse parquet formalism no iteration is required, i.e., the fully irreducible vertex is obtained straightforwardly from the local one- and two-particle Green's functions of the AIM via a one-shot calculation. The situation, however, is much more involved for the following step, i.e., for obtaining all lattice one- and two-particle quantities of the system from a given (purely local) Λ. Let us stress that, besides the non-interacting Green's function $G_0(\nu, \mathbf{k})$, Λ is the *only* input to the parquet equations, from which all reducible and irreducible one- and two-particle quantities, i.e., F, Γ_r, G and Σ, of the lattice

Inverse parquet
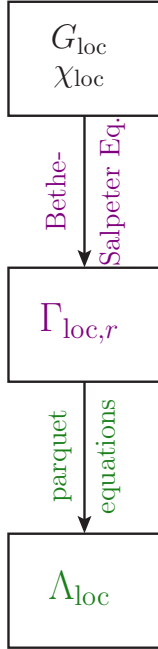
parquet
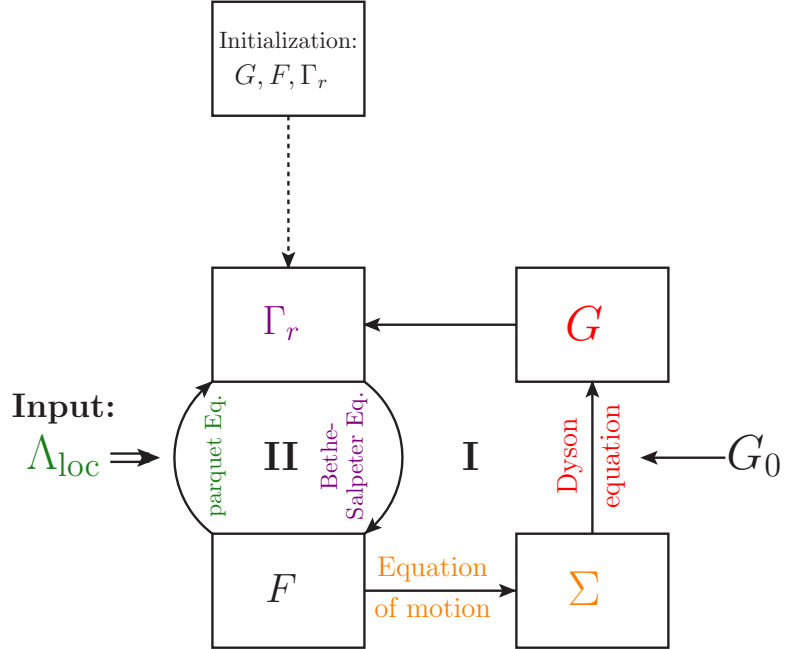
Figure 4.10: Left panel: Flow diagram for the (local) inverse parquet equations, used for extracting the fully irreducible vertex Λ_{loc} from the local one- and two-particle Green's functions (or susceptibilities) G_{loc} and $G_{2,\text{loc}}$ (or $\chi_{\text{loc}}^{\nu\nu'\omega}$). Right panel: Flow diagram for the (lattice) parquet equations of DΓA where from the *only* input Λ_{loc} the full (reducible) vertex F, the vertices Γ_r that irreducible in the different channels $r = ph, \overline{ph}, pp$, the lattice self-energy Σ and the lattice Green's function G are obtained. Let us recall that all local quantities are denoted with a subscript "loc" while all other nomenclature refers to momentum-dependent lattice objects. In this figure, the frequency-, momentum- and spin arguments of the functions are suppressed for the sake of a better readability.

system can be obtained self-consistently. Specifically, the algorithm for solving the parquet equations from a given Λ consists of two nested loops, illustrated in the right panel of Fig. 4.10. Let us give below a short description of this procedure:

1) After initializing the one- and two-particle quantities of the lattice system [F, Γ_r and G (or Σ)], one enters the inner loop (II), where first an updated F is calculated from Γ_r (and, of course G) by means of the Bethe-Salpeter equations. From this F and the Γ_r the reducible vertices Φ_r can be obtained, which in turn allow for updating Γ_r by means of the parquet equations. In this step the input to the parquet equations, i.e., the fully irreducible vertex Λ (which, in the DΓA case, is $\Lambda_{\text{loc}}^{\nu\nu'\omega}$), enters the algorithm. The inner cycle is iterated for a *fixed G* until the convergence for F and Γ_r is reached.

2) From the full vertex F the self-energy Σ can be obtained by means of the Schwinger-Dyson equation of motion.

3) Finally, the Dyson equation allows for updating the Green's function of the system. With this new Green's function we enter again the inner self-consistency loop for F and Γ_r where this Green's function is kept fixed. The outer loop (I) is iterated until the self-consistency for Σ (or G) is reached.

From a numerical point of view it turns out that the algorithm described above is not stable for values of U larger than the bandwidth of the system, i.e., for intermediate-to-strong couplings. This problem was solved very recently by explicitly enforcing the fulfillment of the crossing relations for the vertex-functions which are otherwise violated by the parquet iteration discussed above [46].

4.2.3   First results for nanoscopic systems

The following first results have been obtained in a collaboration and have been also reported in the PhD thesis of A. Valli [30].

Since the full, parquet-based, DΓA scheme is rather complicated and numerically very demanding, it is strongly desirable to perform tests of its applicability for simple systems, which allow for a comparison with exact solutions. To this end the benzene ring, consisting just of six carbon atoms, which is depicted in the upper left panel of Fig. 4.11, was explicitly considered. This structure can be modeled, in a first approximation, by an one-dimensional single-band Hubbard model with six sites and periodic boundary conditions. The hopping amplitude for an electron moving from one site to a neighboring site is given by the parameter t and the Hubbard repulsion between two electrons sitting at the same site of this one-dimensional lattice is denoted as U. The number of electrons per site is set to $n = 1$, since for this specific filling the strongest effects due to local and nonlocal correlations are expected. Let us stress, that we do not pretend to perform a realistic material calculation for the benzene at this point, but we are rather interested in the effects of nonlocal correlations which are expected to be particularly large due to the low dimensionality of the system ($d = 1$).

We start our calculation by extracting the local fully irreducible vertex $\Lambda_{\text{loc},r}^{\nu,\nu'\omega}$ from the AIM, which is related to the DMFT solution of this system. In the right upper panel of Fig. 4.11 a one dimensional slice of $\Lambda_{\text{loc},r}^{\nu\nu'\omega} - U_r$ for fixed values of $\omega = 0$ and $\nu = \pi T$ is shown as a function
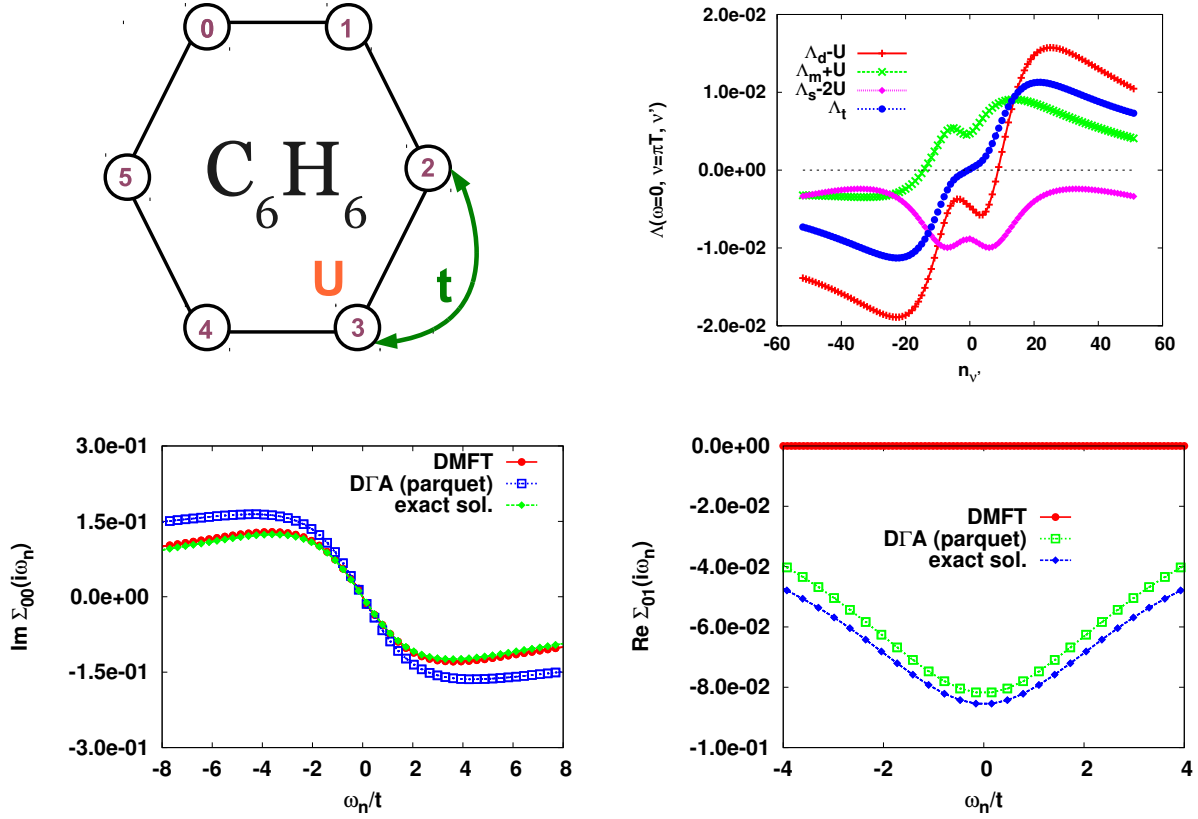
Figure 4.11: DΓA results for nanoscopic systems: Left upper panel: The benzene ring which was considered for the calculation. t is the nearest-neighbor hopping parameter, U represents the local Hubbard interaction and $\beta = 1/T$ corresponds to the inverse temperature. The calculations were performed for $U = 2.0t$ and $\beta = 10.0/t$. Right upper panel: The local DMFT fully irreducible vertex $\Lambda_{\text{loc},r}^{\nu\nu'\omega} - U_r$ ($U_d = U$, $U_m = -U$, $U_s = 2U$ and $U_t = 0$) for fixed values of $\omega = 0$ and $\nu = \pi T$ as a function of ν' (or, more precisely, of the corresponding Matsubara index $n_{\nu'}$). Lower panels: The imaginary part of the local $[\text{Im}\Sigma_{00}(i\omega_n)]$ and the real part of the nonlocal $[\text{Re}\Sigma_{01}(i\omega_n)]$ self-energy in real space for the benzene ring, obtained by means of DΓA in comparison to the corresponding DMFT results and the exact (QMC) solution ($i\omega_n \widehat{=} \nu$ in the main text). The figures are reproduced from Ref. [30].

of ν' (or, more precisely, as a function of the Matsubara index $n_{\nu'}$)[9]. One notes immediately that the (frequency-dependent) deviation of $\Lambda_{\text{loc},r}^{\nu\nu'\omega}$ from its lowest-order contribution U_r is about two orders of magnitude smaller than the interaction parameter U_r itself, which allows for the approximation $\Lambda_{\text{loc},r}^{\nu\nu'\omega} \approx U_r$. Hence, for this system and the specific values for the

---

[9]U_r is the lowest-order (in U) contribution to the fully irreducible vertex $\Lambda_{\text{loc},r}^{\nu\nu'\omega}$ in each channel. Specifically: $U_d = U$, $U_m = -U$, $U_s = 2U$ and $U_t = 0$.

parameters U and T, the full DΓA scheme reduces to the so-called *parquet approximation*, where the fully irreducible vertex Λ_r is replaced by the bare Hubbard interaction U_r as input for the parquet equations. The reason for this negligible small frequency dependence of $\Lambda_{\mathrm{loc},r}^{\nu\nu'\omega}$ is due to the (band)-insulating behavior of the non-interacting system. In fact, the half-filled six-site Hubbard model with nearest neighbor hopping exhibits, for $U = 0$, a large gap in its spectrum at the Fermi level, which leads to a strong suppression of all the frequency-dependent higher-order corrections to $\Lambda_{\mathrm{loc},r}^{\nu\nu'\omega}$.

Let us now compare the results for the local and nonlocal self-energies obtained by means of DΓA with the corresponding ones from DMFT and the exact QMC solution for this system, respectively. First, we want to point out, that for the half-filled case the local part of the self-energy, i.e., $\Sigma_{ii}(\nu)$, is purely imaginary (except for the constant Hartree contribution $\frac{U}{2}$) while the (real-space) self-energy between two neighboring sites, i.e., $\Sigma_{i(i+1)}(\nu)$, is purely real, as can be inferred from the particle-hole symmetry of the system [see Eqs. (2.108) and (2.117)]. The plot in the lower left panel of Fig. 4.11 illustrates that, by comparison with the exact solution, DMFT provides for a qualitatively and quantitatively accurate description of the local self-energy $\Sigma_{ii}(\nu)$, indicating that nonlocal corrections beyond DMFT will not affect strongly the local physics. In fact, we actually observe that DΓA, which, of course, includes also all local DMFT correlations, yields similar results for the local part of the self-energy in the present case. On the contrary, for the nonlocal self-energy $\Sigma_{ij}(\nu)$, the DMFT solution is per definition equal to zero, while DΓA closely resembles the exact QMC solution. These preliminary results demonstrate the applicability and the potential of DΓA for improving the DMFT self-energies by including nonlocal spatial correlation effects beyond DMFT[10].

Before describing, in the next section, an approximate, easier manageable, implementation of DΓA, which is currently used for bulk calculations in two and three-dimensional systems, let us stress that further investigations of more complex molecules are currently under progress. Such benchmarks, where the exact solution is still available, will be very important for testing the validity of the DΓA hypothesis in one of the most unfavorable situations ($d = 1$). Furthermore, it will provide the first actual result obtained within the nanoscopic DΓA scheme (nano-DΓA) recently proposed in Ref. [205] and applied hitherto only at the DMFT level [206, 207].

---

[10]Let us briefly comment here on the deviations between the DΓA self-energy and the one obtained with the exact solution at larger frequencies, which can be observed for both the local and the nonlocal case: These errors stem from the finite frequency interval which is used for solving the Bethe-Salpeter equations and the equation of motion within the parquet approach. However, the size of the mismatch can be systematically reduced by taking into account a larger number of frequencies.

4.3 Dynamical vertex approximation - ladder approximation

As discussed in section 4.2 (see in particular 4.2.2), solving the parquet equations requires a tremendous numerical effort and is (at present) certainly not feasible for realistic multi-orbital systems. Hence, while considerable work will be invested in the next years for the improvement of the full algorithm, at present, simplifications of the DΓA scheme are needed for standard applications of the method. The development of sound and, at the same time, manageable approximations is also highly desirable in view of DΓA treatments of complicated multi-orbital systems [192]. Here, we will illustrate the most commonly used simplification of the full DΓA algorithm, based on ladder diagram resummations ("ladder approximation"), discussing also its physical meaning. To this end, we will start from the exact parquet decomposition of the full lattice vertex $F^{\nu\nu'\omega}_{\mathbf{k}\mathbf{k}'\mathbf{q},\uparrow\downarrow}$ as it is illustrated (for the local case) in Fig. 2.11:

$$F^{\nu\nu'\omega}_{\mathbf{k}\mathbf{k}'\mathbf{q},\uparrow\downarrow} = \Lambda^{\nu\nu'\omega}_{\mathbf{k}\mathbf{k}'\mathbf{q},\uparrow\downarrow} + \Phi^{\nu\nu'\omega}_{pp,\mathbf{k}\mathbf{k}'\mathbf{q},\uparrow\downarrow} + \Phi^{\nu\nu'\omega}_{ph,\mathbf{k}\mathbf{k}'\mathbf{q},\uparrow\downarrow} + \Phi^{\nu\nu'\omega}_{\overline{ph},\mathbf{k}\mathbf{k}'\mathbf{q},\uparrow\downarrow}. \tag{4.2}$$

We recall that the full vertex $F^{\nu\nu'\omega}_{\mathbf{k}\mathbf{k}'\mathbf{q},\uparrow\downarrow}$ can be directly used for calculating the lattice self-energy by means of the (lattice) Schwinger-Dyson equation of motion [see Eq. (2.194) for the local version]. According to the previous section, the DΓA assumption corresponds to replacing $\Lambda^{\nu\nu'\omega}_{\mathbf{k}\mathbf{k}'\mathbf{q},\uparrow\downarrow}$ by its local counterpart $\Lambda^{\nu\nu'\omega}_{\mathrm{loc},\uparrow\downarrow}$, while for all the reducible contributions $\Phi^{\nu\nu'\omega}_{r,\mathbf{k}\mathbf{k}'\mathbf{q},\uparrow\downarrow}$ ($r = pp, ph, \overline{ph}$) the full momentum dependence is kept. In fact, the $\Phi^{\nu\nu'\omega}_{r,\mathbf{k}\mathbf{k}'\mathbf{q},\uparrow\downarrow}$ are obtained by a self-consistent solution of the parquet and the Bethe-Salpeter equations, as discussed in section 4.2.2 for the DΓA. We want to emphasize here, that the momentum dependence of $\Phi^{\nu\nu'\omega}_{r,\mathbf{k}\mathbf{k}'\mathbf{q},\uparrow\downarrow}$ is crucial for describing a second-order phase transitions to a spatially ordered phase such as, e.g., (anti)ferromagnetism, charge density waves, or superconductivity. The vicinity of such an ordering instability is indicated by a strong enhancement of the momentum-dependent two-particle ladder diagrams $\Phi^{\nu\nu'\omega}_{r,\mathbf{k}\mathbf{k}'\mathbf{q},\uparrow\downarrow}$ in the channel r, which is connected to the instability under consideration. Specifically, in the particle-hole channels the nonlocal reducible (ladder) part of the vertex, i.e., Φ_{ph} or $\Phi_{\overline{ph}}$, describes (para)magnons while the corresponding particle-particle ladder Φ_{pp} yields attractive pairing and localization effects [208–210]. Hence, if one knows the leading instability of the system *a priori* one can consider a momentum-dependent ladder $\Phi^{\nu\nu'\omega}_{r,\mathbf{k}\mathbf{k}'\mathbf{q},\uparrow\downarrow}$ only in this relevant channel and restrict oneself to the local approximation for the other ladder(s). This assumption corresponds to the "ladder

approximation" of DΓA.

In the following, we will mainly focus on the repulsive Hubbard model on a bipartite lattice at half-filling with nearest neighbor hopping only. This system is known to exhibit a low-temperature (for two dimensions only at $T = 0$) antiferromagnetically ordered phase. Therefore, antiferromagnetic fluctuations are expected to constitute the main contribution to the nonlocal correlations in this system. Hence, in this situation a restriction to non-local Φ_{ph} and $\Phi_{\overline{ph}}$, while keeping Φ_{pp} local, is quite natural. As will be discussed later in section 4.3.2, we have verified that, for the three-dimensional model and the specific values of the parameters U and β examined there, the difference between the nonlocal and the local particle-particle ladder is negligible compared to the corresponding difference for the particle-hole (in particular the spin) ladders.

Let us now present a short derivation of the equation for the self-energy within the ladder DΓA approach, based on Ref. [26]. As discussed above, applying this approximation to the particle-hole channels (ph and $\overline{ph}$), we assume both Λ and Φ_{pp} to be purely local in Eq. (4.2). Considering furthermore the SU(2) symmetry relation B.13 [which also holds in the nonlocal case when replacing $\nu^{(\prime)} \to (\nu^{(\prime)}, \mathbf{k}^{(\prime)})$ and $\omega \to (\omega, \mathbf{q})$]:

$$\Phi^{\nu\nu'\omega}_{\overline{ph},\mathbf{k}\mathbf{k}'\mathbf{q},\uparrow\downarrow} = -\Phi^{\nu(\nu+\omega)(\nu'-\nu)}_{m,\mathbf{k}(\mathbf{k}+\mathbf{q})(\mathbf{k}'-\mathbf{k})}, \tag{4.3}$$

we obtain the following explicit expression for the full vertex $F^{\nu\nu'\omega}_{\mathbf{k}\mathbf{k}'\mathbf{q},\uparrow\downarrow}$ in the ladder approximation for the DΓA:

$$F^{\nu\nu'\omega}_{\text{lad},\mathbf{k}\mathbf{k}'\mathbf{q},\uparrow\downarrow} = \Lambda^{\nu\nu'\omega}_{\text{loc},\uparrow\downarrow} + \Phi^{\nu\nu'\omega}_{\text{loc},pp,\uparrow\downarrow} + \Phi^{\nu\nu'\omega}_{ph,\mathbf{k}\mathbf{k}'\mathbf{q},\uparrow\downarrow} - \Phi^{\nu(\nu+\omega)(\nu'-\nu)}_{m,\mathbf{k}(\mathbf{k}+\mathbf{q})(\mathbf{k}'-\mathbf{k})}. \tag{4.4}$$

The reducible particle-hole vertices (ladders) for the lattice are calculated by means of the corresponding Bethe-Salpeter equations in the density and magnetic channel [see Eqs. (B.4)], where the local irreducible vertices $\Gamma_{\text{loc},d}$ and $\Gamma_{\text{loc},m}$ are connected by nonlocal DMFT Green's functions $G_{\text{DMFT}}(\nu, \mathbf{k})$. The corresponding equations read:

$$F^{\nu\nu'\omega}_{r,\mathbf{q}} = \Gamma^{\nu\nu'\omega}_{\text{loc},r} + \frac{1}{\beta} \sum_{\nu_1,\mathbf{k_1}} \Gamma^{\nu\nu_1\omega}_{\text{loc},r} G_{\text{DMFT}}(\nu_1,\mathbf{k_1}) G_{\text{DMFT}}(\nu_1+\omega,\mathbf{k_1}+\mathbf{q}) F^{\nu_1\nu'\omega}_{r,\mathbf{q}}, \tag{4.5}$$

where $r = d, m$. Note that, within the ladder DΓA, the vertex $F^{\nu\nu'\omega}_{r,\mathbf{q}}$ defined by Eq. (4.5) does not depend on the momenta $\mathbf{k}$ and $\mathbf{k}'$ of the incoming particle and hole but only on the transferred momentum $\mathbf{q}$. The reason for this is that the irreducible vertex Γ_r in Eq. (4.5) is assumed to be *local*. Hence, the ladder approximation of DΓA can be viewed –in a general
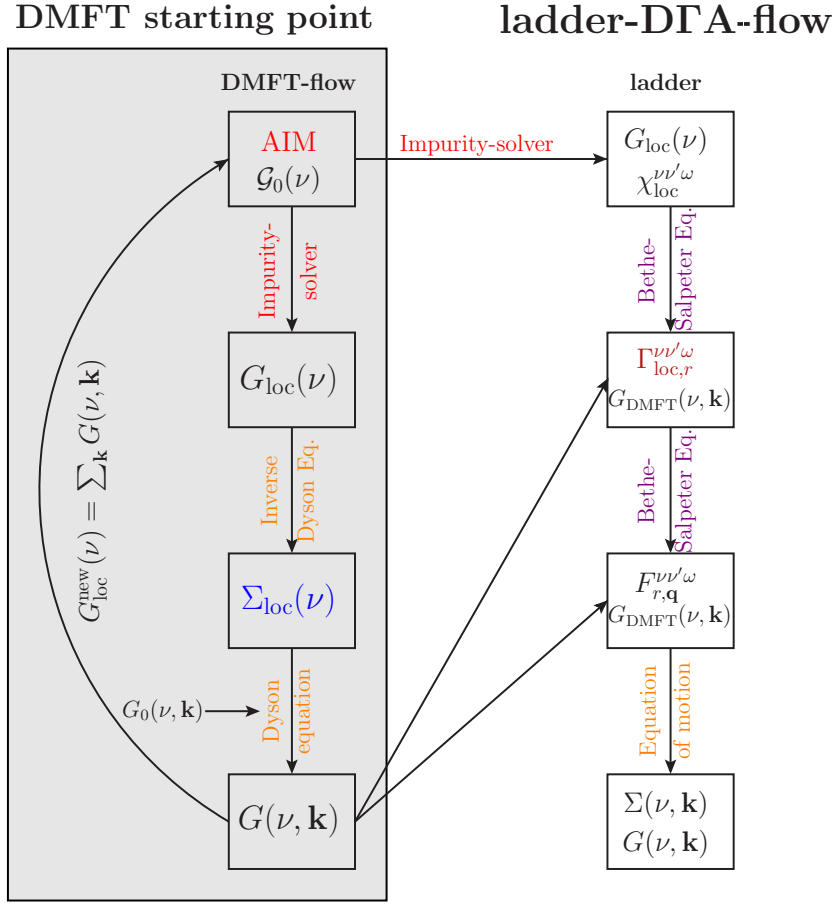
Figure 4.12: Flow diagram for the ladder version of DΓA. The starting point is a converged DMFT solution (DMFT flow-diagram on the left). From DMFT one extracts the local irreducible vertices $\Gamma_{\text{loc},r}^{\nu\nu'\omega}$ in channels $r = d, m$. From the latter and the momentum-dependent DMFT Green's function $G_{\text{DMFT}}(\nu, \mathbf{k})$ one can obtain the nonlocal reducible vertex function $F_{r,\mathbf{q}}^{\nu\nu'\omega}$. Finally the momentum-dependent ladder DΓA self-energy $\Sigma(\nu, \mathbf{k})$ is derived from $F_{r,\mathbf{q}}^{\nu\nu'\omega}$ and $G_{\text{DMFT}}(\nu, \mathbf{k})$ via the equation of motion.

framework– as the scheme where the assumption of complete locality is made at a less deeper level than in the full DΓA, i.e., not for the fully irreducible two-particle vertex Λ, but for the irreducible vertex Γ_r. Such a simplification, however, has a cost, making it problematic to perform ladder calculations within a self-consistent scheme. Technically the problem can be illustrated by considering the parquet equations, where the irreducible vertices, which are local in the ladder DΓA, can be expressed as $\Gamma_{ph} = \Lambda + \Phi_{pp} + \Phi_{\overline{ph}}$ and $\Gamma_{\overline{ph}} = \Lambda + \Phi_{pp} + \Phi_{ph}$. However, since Λ and Φ_{pp} are also supposed to be local, these equations state that Γ_{ph} and $\Gamma_{\overline{ph}}$ should display some nonlocal dependence due to the nonlocality of Φ_{ph} and $\Phi_{\overline{ph}}$. This contradiction prevents the implementation of any standard self-consistency and it is also

partly related to a further problem concerning the asymptotics of the ladder DΓA self-energy which will be discussed in the next section.

Performing a Fourier transform of $F_{r,\mathbf{q}}^{\nu\nu'\omega}$ to real space shows that this vertex function includes only scattering processes of a particle and a hole from one *common* lattice site i to another *common* lattice site j[11]. On the other hand, we want to stress that the scattering amplitude is highly nonlocal in time, i.e., the particle and hole which are scattered can arrive at the initial site i and leave the final site j at different times. This means that retardation effects are fully taken into account by the ladder DΓA while nonlocal scattering effects in space are only partially considered.

As for the practical determination of $F_{r,\mathbf{q}}^{\nu\nu'\omega}$ we note, that usually the corresponding generalized susceptibility $\chi_{r,\mathbf{q}}^{\nu\nu'\omega}$ is considered. This function is easily obtained by means of an analogous Bethe-Salpeter equation [see Eq. (B.6) in appendix B] and reads, in the lattice case:

$$\chi_{r,\mathbf{q}}^{\nu\nu'\omega} = \beta\chi_{0,\mathbf{q}}^{\nu\omega}\delta_{\nu\nu'} - \frac{1}{\beta}\chi_{0,\mathbf{q}}^{\nu\omega}\sum_{\nu_1}\Gamma_r^{\nu\nu_1\omega}\chi_{r,\mathbf{q}}^{\nu_1\nu'\omega}, \tag{4.6}$$

where

$$\chi_{0,\mathbf{q}}^{\nu\omega} = -\sum_{\mathbf{k}}G_{\mathrm{DMFT}}(\nu,\mathbf{k})G_{\mathrm{DMFT}}(\nu+\omega,\mathbf{k}+\mathbf{q}), \tag{4.7}$$

is the **k**-summed bare bubble constructed from DMFT Green's functions[12]. The connection between the susceptibility $\chi_{r,\mathbf{q}}^{\nu\nu'\omega}$ and the corresponding vertex $F_{r,\mathbf{q}}^{\nu\nu'\omega}$ reads as follows:

$$\chi_{r,\mathbf{q}}^{\nu\nu'\omega} = \beta\chi_{0,\mathbf{q}}^{\nu\omega}\delta_{\nu\nu'} - \chi_{0,\mathbf{q}}^{\nu\omega}F_{r,\mathbf{q}}^{\nu\nu'\omega}\chi_{0,\mathbf{q}}^{\nu'\omega}. \tag{4.8}$$

It is important to stress that $F_{r,\mathbf{q}}^{\nu\nu'\omega}$ represents only the full lattice vertex calculated from the Bethe-Salpeter equations in the particle-hole channels. In the ladder version of DΓA it will be, hence, *different* from the lattice vertex defined via the parquet equation (4.4) due to the non-self-consistent treatment of these two sets of relations, i.e., parquet and Bethe-Salpeter. In fact, within the ladder DΓA $F_{r,\mathbf{q}}^{\nu\nu'\omega}$ represents only an auxiliary quantity, used

---

[11]More explicitly, the Fourier transform of the vertex $F_{\mathbf{k}\mathbf{k'}\mathbf{q}}$ to real space (schematically) reads as: $F_{ijlm} = \sum_{\mathbf{k}\mathbf{k'}\mathbf{q}}e^{-i\mathbf{k}\mathbf{R}_i}e^{i(\mathbf{k}+\mathbf{q})\mathbf{R}_j}e^{-i(\mathbf{k'}+\mathbf{q})\mathbf{R}_l}e^{i\mathbf{k'}\mathbf{R}_m}F_{\mathbf{k}\mathbf{k'}\mathbf{q}}$, where i,j,l,m denote the indices of the corresponding lattice vectors $\mathbf{R}_i,\mathbf{R}_j,\mathbf{R}_l,\mathbf{R}_m$. If F does not depend on $\mathbf{k}$ and $\mathbf{k'}$, the summations over these momenta yield δ_{ij} and δ_{lm}, respectively.

[12]Note, that $\chi_{r,\mathbf{q}}^{\nu\nu'\omega}$ is in principle also a $\mathbf{k},\mathbf{k'}$ summed quantity, i.e., $\chi_{r,\mathbf{q}}^{\nu\nu'\omega} = \sum_{\mathbf{k}\mathbf{k'}}\chi_{r,\mathbf{k}\mathbf{k'}\mathbf{q}}^{\nu\nu'\omega}$, where the Bethe-Salpeter equation for the more general object $\chi_{r,\mathbf{k}\mathbf{k'}\mathbf{q}}^{\nu\nu'\omega}$ differs from the corresponding one for $\chi_{r,\mathbf{q}}^{\nu\nu'\omega}$ just by a factor $\delta_{\mathbf{k}\mathbf{k'}}$ in the first summand on the right-hand side of Eq. (4.6). In any case, only the $\mathbf{k}$- and $\mathbf{k'}$-summed susceptibility is needed within ladder DΓA calculations. For the sake of precision, we also point out here the slightly different prefactor in the definition of the local χ_0 in Eq. (2.153) and the corresponding nonlocal quantity in Eq. (4.7).

for determining the reducible vertices Φ_{ph} and $\Phi_{\overline{ph}}$ of the lattice via the relations:

$$\Phi_{d,\mathbf{q}}^{\nu\nu'\omega} = F_{d,\mathbf{q}}^{\nu\nu'\omega} - \Gamma_d^{\nu\nu'\omega}, \qquad\qquad \Phi_{m,\mathbf{q}}^{\nu\nu'\omega} = F_{m,\mathbf{q}}^{\nu\nu'\omega} - \Gamma_m^{\nu\nu'\omega}, \qquad (4.9)$$

which are then, in turn, used for calculating the final full lattice vertex $F_{\mathbf{kk'q},\uparrow\downarrow}^{\nu\nu'\omega}$ of the ladder DΓA approach in Eq. (4.4), and the corresponding ladder DΓA self-energy via the Schwinger-Dyson equation of motion. Substituting Eqs. (4.9) into the expression for the full lattice vertex of the ladder DΓA, Eq. (4.4), yields:

$$F_{\text{lad},\mathbf{kk'q},\uparrow\downarrow}^{\nu\nu'\omega} = \frac{1}{2}\left(F_{d,\mathbf{q}}^{\nu\nu'\omega} - F_{m,\mathbf{q}}^{\nu\nu'\omega}\right) - F_{m,\mathbf{k'}-\mathbf{k}}^{\nu(\nu+\omega)(\nu'-\nu)} - \frac{1}{2}\left(F_{\text{loc},d}^{\nu\nu'\omega} - F_{\text{loc},m}^{\nu\nu'\omega}\right), \qquad (4.10)$$

where $F_{\text{loc},d}^{\nu\nu'\omega}$ and $F_{\text{loc},m}^{\nu\nu'\omega}$ denote the full local vertex functions as defined in section 2.2.4.2. Plugging the vertex function obtained by means of ladder DΓA [Eq. (4.10)] into (the lattice version of) the equation of motion (2.194) yields the expression for the nonlocal self-energy as obtained in Ref. [26]:

$$\Sigma_{\text{lad}}(\nu, \mathbf{k}) = \frac{Un}{2} - \frac{U}{2\beta^2}\sum_{\nu'\omega}\sum_{\mathbf{k'q}}\left(F_{d,\mathbf{q}}^{\nu\nu'\omega} - 3F_{m,\mathbf{q}}^{\nu\nu'\omega} - F_d^{\nu\nu'\omega} + F_m^{\nu\nu'\omega}\right) \times$$
$$\times G_{\text{DMFT}}(\nu', \mathbf{k'})G_{\text{DMFT}}(\nu' + \omega, \mathbf{k'} + \mathbf{q})G_{\text{DMFT}}(\nu + \omega, \mathbf{k} + \mathbf{q}), \qquad (4.11)$$

where a shift of summation variables has been performed in the second summand of $F_{\text{lad},\mathbf{kk'q},\uparrow\downarrow}^{\nu\nu'\omega}$ in order to sum up all contributions stemming from the magnetic vertex $F_{m,\mathbf{q}}^{\nu\nu'\omega}$.

After deriving the relevant relations for the ladder DΓA method, we want to turn our attention now to the flow diagram of the ladder version of DΓA, shown in Fig. 4.12. Let us first mention that, because of the self-consistency issues discussed before, in contrast to the full DΓA scheme, the ladder version of DΓA *always* adopts one- and two-particle Green's functions of DMFT as a starting point. The calculation steps read as follows:

1) A complete DMFT self-consistency cycle has to be performed as indicated in the left-hand box of Fig. 4.12.

2) After the DMFT convergence the local one- and two-particle Green's functions (or generalized susceptibilities), $G_{\text{loc}}(\nu)$ and $\chi_{\text{loc}}^{\nu\nu'\omega}$, are computed from the impurity solver.

3) The irreducible vertices in the channel(s) under consideration, $\Gamma_{\text{loc},r}^{\nu\nu'\omega}$, are calculated via the local Bethe-Salpeter equation(s) [see Eqs. (B.7) and (B.19)].
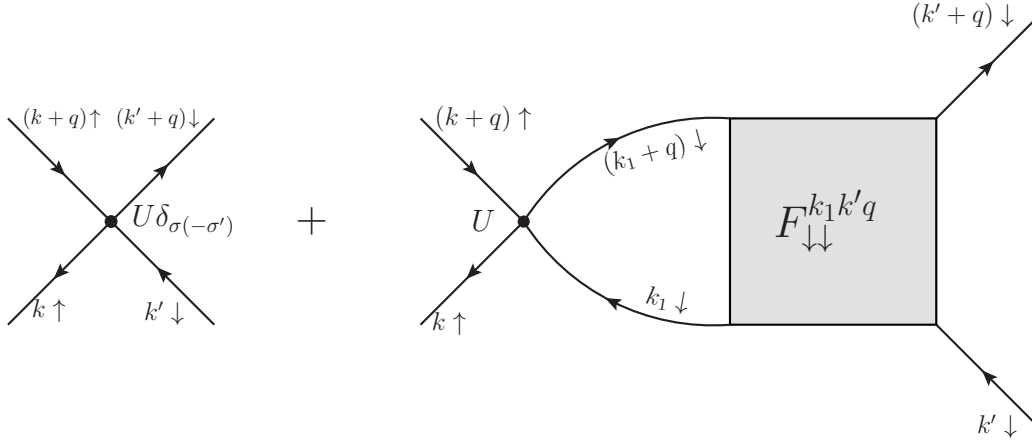
Figure 4.13: Diagrams for $F_{\uparrow\downarrow}^{kk'q}$ that do not depend on ν (and $\mathbf{k}$). Note that the four vector notation $k\widehat{=}(\nu,\mathbf{k})$ and $q\widehat{=}(\omega,\mathbf{q})$ is adopted.

4) The local irreducible vertex functions $\Gamma_{\text{loc},r}^{\nu\nu'\omega}$ and the (momentum-dependent) DMFT Green's function $G_{\text{DMFT}}(\nu,\mathbf{k})$ serve as an input for the (lattice) Bethe-Salpeter equations which, in turn, yield the full vertex functions $F_{r,\mathbf{q}}^{\nu\nu'\omega}$.

5) The self-energy is derived from the DMFT Green's function $G_{\text{DMFT}}(\nu,\mathbf{k})$ and the vertex $F_{r,\mathbf{q}}^{\nu\nu'\omega}$ by means of the equation of motion [see Eq. (4.11)].

One can see that, besides the iteration within the DMFT part of the method, no self-consistency is involved in the ladder version of DΓA. This renders a fixing of the number of particles per lattice site problematic in general, since the chemical potential in the one-particle Green's function of the ladder DΓA is already fixed by the DMFT self-consistency and is not altered within a one-shot ladder DΓA calculation. Furthermore, the violation of the particle conservation by a one-shot calculation of ladder DΓA can be also observed at the two-particle level and becomes manifest in an enhanced asymptotic behavior of the corresponding lattice self-energy. This issue, and a possible solution of this problem, will be discussed in the following section.

4.3.1   Asymptotic behavior and Moriyasque λ corrections

In this section we will discuss the $\frac{1}{i\nu}$-asymptotic behavior of the self-energy $\Sigma(\nu,\mathbf{k})$ obtained by means of ladder DΓA, as it is given in Eq. (4.11). To this end, we consider first the *general* form of the equation of motion [see also Eq. (2.194)] for the Hubbard model, which connects the two-particle vertex function $F_{\mathbf{k}\mathbf{k}'\mathbf{q},\uparrow\downarrow}^{\nu\nu'\omega}$ with the self-energy $\Sigma(\nu,\mathbf{k})$ of the system,

and later on the ladder DΓA approximation for this relation. The general equation of motion reads:

$$\Sigma(k) = \frac{Un}{2} - \frac{U}{\beta^2} \sum_{k'q} F_{\uparrow\downarrow}^{kk'q} G(k')G(k'+q)G(k+q), \tag{4.12}$$

where we adopt the four-vector notation $k \,\widehat{=}\, (\nu, \mathbf{k})$ and $q \,\widehat{=}\, (\omega, \mathbf{q})$ (and analogous for k' and k_1) for the sake of a better readability. Let us now analyze the single contributions to the self-energy with respect to their ν-dependence:

- $G(k+q) \overset{\nu\to\infty}{=} \frac{1}{i\nu} + O\left[\frac{1}{(i\nu)^2}\right]$: Since $G(k+q)$ exhibits already a contribution $\frac{1}{i\nu}$, we have to single out terms which are constant with respect to ν in all the remaining parts of Eq. (4.12) in order to get the $\frac{1}{i\nu}$-asymptotics of the entire expression[13].

- $F_{\uparrow\downarrow}^{kk'q}$: The ν-independent contributions to the vertex-function are given by the diagrams shown in Fig. 4.13. Analytically, these terms can be written as:

$$F_{\uparrow\downarrow}^{kk'q} = \frac{U}{\beta} \sum_{k_1} \left[G(k_1)G(k_1+q) F_{\downarrow\downarrow}^{k_1k'q} + \beta\delta_{k_1k'} \right] + O\left[\frac{1}{i\nu}\right] =$$

$$= -\frac{U}{\beta} \frac{1}{G(k')G(k'+q)} \sum_{k_1} \chi_{\uparrow\uparrow}^{k_1k'q} + O\left[\frac{1}{i\nu}\right], \tag{4.13}$$

where SU(2) symmetry and the definition of χ, as discussed in Eqs. (2.159) and (4.8) and Fig. 2.8, have been used.

Inserting the result from Eq. (4.13) into Eq. (4.12) for the self-energy leads, at the order $\frac{1}{i\nu}$, to:

$$\Sigma(k) = \frac{Un}{2} + \frac{1}{i\nu} \frac{U^2}{\beta^3} \sum_{k_1k'q} \chi_{\uparrow\uparrow}^{k_1k'q} + O\left[\frac{1}{(i\nu)^2}\right]. \tag{4.14}$$

For the exact $\chi_{\uparrow\uparrow}^{k_1k'q}$ [see Eq. (2.150a)]of the AIM or of the Hubbard model, the sum in Eq. (4.14) can be evaluated analytically and yields:

$$\frac{1}{\beta^3} \sum_{k_1k'q} \chi_{\uparrow\uparrow}^{k_1k'q} = \langle n_\uparrow n_\uparrow \rangle - \langle n_\uparrow \rangle \langle n_\uparrow \rangle = \frac{n}{2}\left(1 - \frac{n}{2}\right), \tag{4.15}$$

---

[13]For the substitution $G(k+q) \to \frac{1}{i\nu}$ note also that the largest contribution to the self-energy stems from the $\omega = 0$ term.

in the SU(2) symmetric case, leading to the well-known expression for the $\frac{1}{i\nu}$-asymptotic behavior of self-energy of the AIM and the Hubbard model, respectively[14]:

$$\Sigma(k) = \frac{Un}{2} + U^2\frac{n}{2}\left(1 - \frac{n}{2}\right)\frac{1}{i\nu} + O\left[\frac{1}{(i\nu)^2}\right].\tag{4.16}$$

In the ladder version of DΓA, however, we construct the susceptibility $\chi_r^{kk'q} = \chi_{r,\mathbf{q}}^{\nu\nu'\omega}$ as a ladder consisting of local irreducible vertices $\Gamma_{\text{loc},r}^{\nu\nu'\omega}$ and DMFT Green's functions $G_{\text{DMFT}}(\nu, \mathbf{k})$ [see Eq. (4.6)]. This approximated susceptibility does actually correspond to the definition of the momentum-dependent susceptibility of DMFT [24]. As it is known, however, DMFT used as an approximation for finite dimensional systems is not guaranteed to be self-consistent at the two-particle level. In fact, one observes that the related $\chi_{\uparrow\uparrow}$, as calculated within ladder DΓA or DMFT [see Eq. (4.6) or Ref. [24], respectively], does not fulfill Eq. (4.15), which is reflected in a corresponding violation of the $\frac{1}{i\nu}$-asymptotic behavior of the ladder DΓA self-energy in Eq. (4.16). The deeper reason for this is related to the fact that the ingredients for constructing the ladder diagrams for χ (or F) do not perfectly match any longer in finite dimensions: The irreducible vertex is purely local while the DMFT Green's function exhibits a $\mathbf{k}$-dependence which, in finite dimensions, also leads to a *nonlocal* self-energy. In this way, the Baym-Kadanoff relation (given only schematically without any arguments here) [44]:

$$\Gamma = \frac{\delta\Sigma}{\delta G},\tag{4.17}$$

cannot be satisfied within the ladder DΓA, since the left-hand side of this equation is assumed to be purely local, while one gets a $\mathbf{k}$-dependent quantity on its right-hand side. This problem clearly cannot be overcome by any kind of self-consistency at the one-particle level[15], i.e., for G and Σ, since the main problem of combining a local irreducible vertex Γ and a momentum-dependent Green's functions G remains. Even an outer self-consistency, i.e., some kind of iterative scheme which updates the AIM, possibly useful for other purposes, cannot improve the situation. Hence, alternative ways of restoring the correct asymptotic behavior of the self-energy have been considered within the ladder DΓA approach [27, 28].

Moriyasque λ corrections

In the previous paragraph we pointed out, that the lack of two-particle self-consistency in the

---

[14]In Ref. [211] the asymptotic behavior of the ladder DΓA self-energy was derived in a similar way.

[15]From the above discussion, it should be clear, on the other hand, that a self-consistent treatment of the one- and the two-particle Green's functions, as performed in the full DΓA scheme via the parquet equation, will be sufficient for generating the correct asymptotic behavior of the self-energy in all cases.

construction of the nonlocal susceptibility $\chi_{r,\mathbf{q}}^{\nu\nu'\omega}$ in the ladder DΓA scheme is responsible for the enhanced $\frac{1}{i\nu}$-asymptotic behavior of the corresponding self-energy. Hence, it is obvious, to solve the problem of the wrong high-frequency behavior of $\Sigma(\nu, \mathbf{k})$ by correcting $\chi_{r,\mathbf{q}}^{\nu\nu'\omega}$ "effectively" in such a way that Eq. (4.15) is fulfilled as for the full DΓA scheme. Obviously, it is always desirable to apply effective corrections to physical observable quantities rather than to quite abstract objects such as the generalized susceptibility. To this end, we consider the *physical* susceptibility $\chi_{r,\mathbf{q}}^{\omega}$ defined as:

$$\chi_{r,\mathbf{q}}^{\omega} = \frac{1}{\beta^2} \sum_{\nu\nu'} \sum_{\mathbf{k}\mathbf{k}'} \chi_{r,\mathbf{k}\mathbf{k}'\mathbf{q}}^{\nu\nu'\omega} \equiv \frac{1}{\beta^2} \sum_{\nu\nu'} \chi_{r,\mathbf{q}}^{\nu\nu'\omega}. \tag{4.18}$$

As for the physical interpretation of this function, we refer to the related discussion for the local case in section 2.2.2.6, in particular to page 55. Let us just recall here that for $\omega = 0$ (static limit) $\chi_{r,\mathbf{q}}^{\omega=0}$ corresponds to the thermodynamic response function which describes the response of the system to some external field whose spatial structure is described by a certain $\mathbf{q}$ vector. Specifically, in the magnetic channel ($r = m$), the response of the system to a staggered magnetic field is evidently found at[16] $\mathbf{q} = \mathbf{\Pi}$, while the response to a uniform magnetic field corresponds to $\mathbf{q} = \mathbf{0}$. On the other hand, considering the density ($r = d$) and the particle-particle ($r = pp$) channel, respectively, for $\mathbf{q} = \mathbf{0}$, one gets the response of the system to an external chemical potential or to a pairing field, i.e., the tendency of the system to a charge order or formation of electron pairs. In fact, we recall that the divergence of the corresponding physical susceptibility $\chi_{r,\mathbf{q}}^{\omega=0}$ at a given value of the temperature T and of the Hubbard interaction U (of course for the specific channel r and momentum $\mathbf{q}$), marks the onset of a second-order phase transition to the corresponding spatially ordered phase. In the specific situation considered in the following, the system exhibits a low-temperature (for $d = 2$ only at $T = 0$) antiferromagnetically ordered phase, the transition to which is signaled by the divergence of $\chi_{\mathrm{AF}} \equiv \chi_{m,\mathbf{q}=\mathbf{\Pi}}^{\omega=0}$. Hence, in the following, we will discuss the method of λ corrections exemplarily for this specific situation, though it should be stressed that an adaption of the corresponding equations for systems featuring ferromagnetic, charge-density-wave or pairing (superconducting) instabilities is straightforward.

Specifically, the procedure to define the λ corrections can be derived as follows: Since we aim at correcting the spurious asymptotic behavior of the ladder DΓA self-energy by a modification of the physical susceptibility $\chi_{r,\mathbf{q}}^{\omega}$, we have to rewrite the expression for $\Sigma_{\mathrm{lad}}(\nu, \mathbf{k})$ in Eq. (4.11) in such a way that $\chi_{r,\mathbf{q}}^{\omega}$ enters this relation instead of $F_{r,\mathbf{q}}^{\nu\nu'\omega}$ or $\chi_{r,\mathbf{q}}^{\nu\nu'\omega}$ [for the relation

---

[16] $\mathbf{\Pi} = (\pi, \pi, \ldots)$ is the d-dimensional vector where all components are π.

between $F_{r,\mathbf{q}}^{\nu\nu'\omega}$ and $\chi_{r,\mathbf{q}}^{\nu\nu'\omega}$ see Eq. (4.8)]. Following the derivation presented in Ref. [28], which is analogous to the corresponding calculations for the λ corrections in the 1PI approach in section 4.4.2.1, one obtains:

$$
\Sigma_{\text{lad}}(\nu, \mathbf{k}) = \frac{Un}{2} + \frac{U}{2\beta^2} \sum_{\omega,\mathbf{q}} \Big[\gamma_{d,\mathbf{q}}^{\nu\omega} - 3\gamma_{m,\mathbf{q}}^{\nu\omega} + U\gamma_{d,\mathbf{q}}^{\nu\omega}\chi_{d,\mathbf{q}}^{\omega} + 3U\gamma_{m,\mathbf{q}}^{\nu\omega}\chi_{m,\mathbf{q}}^{\omega} + 2 +
$$
$$
- \sum_{\nu'} \Big(F_d^{\nu\nu'\omega} - F_m^{\nu\nu'\omega} \Big) G_{\text{DMFT}}(\nu', \mathbf{k}')G_{\text{DMFT}}(\nu' + \omega, \mathbf{k}' + \mathbf{q}) \Big] G_{\text{DMFT}}(\nu + \omega, \mathbf{k} + \mathbf{q}),
$$
$$
(4.19)
$$

where the three-point vertex $\gamma_{r,\mathbf{q}}^{\nu\omega}$ is defined in Eq. (4.127). For a more explicit derivation of Eq. (4.19) we refer to the corresponding calculations of the λ corrections within the 1PI approach on page 238 and following.

We observe that, indeed, after rewriting the expression for the self-energy of the ladder DΓA method, the magnetic susceptibility $\chi_{m,\mathbf{q}}^{\omega}$ explicitly enters the equation for $\Sigma_{\text{lad}}(\nu, \mathbf{k})$. Hence, we will modify this physical susceptibility in such a way that the corresponding self-energy in Eq. (4.19) exhibits the correct $\frac{1}{i\nu}$-asymptotic behavior. Following Moriya's theory of "Spin Fluctuations in Itinerant Electron Magnetism" [212], we are now in a position to give a physical motivation for an effective correction of the magnetic susceptibility in the case of a non-self-consistent treatment of spin fluctuations, as in ladder DΓA.

As already discussed above, for the half-filled repulsive Hubbard model on a bipartite lattice $\chi_{m,\mathbf{q}=\mathbf{\Pi}}^{\omega=0}$ is strongly enhanced, which shows that the system exhibits strong antiferromagnetic fluctuations. Hence, in the same spirit of the Moriya theory for itinerant magnetism [212], we will renormalize $\chi_{m,\mathbf{q}}^{\omega}$. Expanding this object for $\omega = 0$ around $\mathbf{q} = \mathbf{\Pi}$ we obtain (see also Eq. (12) in Ref. [28]):

$$
\chi_{m,\mathbf{q}}^{\omega=0} = \frac{A}{(\mathbf{q} - \mathbf{\Pi})^2 + \xi^{-2}},
\tag{4.20}
$$

where A is just some constant and ξ denotes the correlation length of the system, which is a function of the temperature. ξ diverges at the phase transition, determining the related simultaneous divergence of $\chi_{m,\mathbf{q}}^{\omega=0}$ at $\mathbf{q} = \mathbf{\Pi}$. The crucial point is now that, when the generalized susceptibility $\chi_{m,\mathbf{q}}^{\nu\nu'\omega}$ is calculated within DMFT, i.e., from the local irreducible DMFT vertex $\Gamma_{\text{loc},r}^{\nu\nu'\omega}$ and the nonlocal DMFT Green's function $G_{\text{DMFT}}(\nu, \mathbf{k})$, the transition temperature, i.e., the temperature at which the divergence of the corresponding $\chi_{m,\mathbf{q}=\mathbf{\Pi}}^{\omega=0}$ takes place, is overestimated. In fact, this way, one is just calculating the transition temperature of DMFT, which is known to be enhanced compared to the exact solution, since DMFT is a mean field

theory which neglects all spatial fluctuations. These spatial fluctuations, in turn, tend to destroy the order and, hence, to decrease the transition temperature of the antiferromagnetic phase compared to DMFT. From another perspective, this means that, at a given temperature (in the paramagnetic phase), the correlation length ξ calculated by the DMFT ladder is most likely too large, i.e., ξ^{-2} is too small, compared to the exact solution. Hence, a very natural idea in this situation is to correct (the square of) the inverse correlation length ξ^{-2} by just adding a positive constant λ. This method is also applicable for temperatures below the transition temperature of DMFT where ξ, and hence also $\chi_{m,\mathbf{q}=\mathbf{\Pi}}^{\omega=0}$, has become already negative and can be rendered positive by adding the constant λ. In practice, the corrections to $\chi_{m,\mathbf{q}}^{\omega}$ are performed as follows:

$$\left[\chi_{m,\mathbf{q}}^{\omega}\right]^{-1} \to \left[\chi_{m,\mathbf{q}}^{\omega}\right]^{-1} + \lambda = \chi_{m,\mathbf{q}}^{\lambda,\omega}, \tag{4.21}$$

which corresponds to adding λ to ξ^{-2} when considering the explicit form of $\chi_{m,\mathbf{q}}^{\omega}$ (at $\omega = 0$ and $\mathbf{q} = \mathbf{\Pi}$) in Eq. (4.20). In contrast to the standard Moriya theory, the constant λ, in turn, is now fixed by the requirement that the self-energy calculated as in Eq. (4.19) by means of the λ-corrected susceptibility $\chi_{m,\mathbf{q}}^{\lambda,\omega}$ as in Eq. (4.21), exhibits the correct $\frac{1}{i\nu}$-asymptotic behavior. In this respect it is also interesting to consider Eq. (4.15), where the susceptibility is directly related to the $\frac{1}{i\nu}$-high-frequency behavior of the self-energy:

$$\frac{1}{\beta^3} \sum_{\nu\nu'\omega} \sum_{\mathbf{kk'q}} \chi_{\mathbf{kk'q},\uparrow\uparrow}^{\nu\nu'\omega} = \frac{1}{\beta} \sum_{\omega,\mathbf{q}} \chi_{\mathbf{q},\uparrow\uparrow}^{\omega} = \frac{1}{2\beta} \sum_{\omega,\mathbf{q}} \left(\chi_{d,\mathbf{q}}^{\omega} + \chi_{m,\mathbf{q}}^{\omega}\right) \equiv \frac{n}{2}\left(1 - \frac{n}{2}\right), \tag{4.22}$$

where n denotes the number of particles per lattice site (e.g., $n = 1$ for the half-filled case). Since we know that DMFT exhibits the correct asymptotic behavior for the self-energy, it is clear that its corresponding *local* susceptibility fulfills Eq. (4.22), i.e.,

$$\frac{1}{\beta^3} \sum_{\nu\nu'\omega} \chi_{\uparrow\uparrow}^{\nu\nu'\omega} = \frac{n}{2}\left(1 - \frac{n}{2}\right). \tag{4.23}$$

If, hence,

$$\sum_{\mathbf{q}} \chi_{\uparrow\uparrow,\mathbf{q}}^{\omega} = \frac{1}{2}\sum_{\mathbf{q}}\left(\chi_{d,\mathbf{q}}^{\omega} + \chi_{m,\mathbf{q}}^{\omega}\right) = \frac{1}{2}\left(\chi_d^{\omega} + \chi_m^{\omega}\right), \tag{4.24}$$

holds for all values of ω, condition (4.22) is fulfilled also for the nonlocal susceptibilities $\chi_{r,\mathbf{q}}^{\omega}$, $r = d, m$. Condition (4.24), which requires a ω-dependent $\lambda = \lambda(\omega)$, states that the **k**-summed two-particle quantities (susceptibilities) have to be identical to the corresponding

local objects determined from the AIM associated to DMFT. This requirement is nothing else than the self-consistency at the two-particle level which is fulfilled in DMFT only in the limit of infinite dimensions (and, at finite d, by the full parquet-based DΓA). We note that the two-particle self-consistency condition in Eq. (4.24) is evidently stronger than the requirement of charge conservation at the two-particle level in Eq. (4.22), and, hence, implies the latter. However, in our practical calculations, it turned out that the determination of $\lambda(\omega)$ by means of Eq. (4.24) yields the same, ω-independent, λ as the requirement of charge conservation in Eq. (4.22). Let us also remark that the two-particle self-consistency condition (4.24) as well as the requirement of charge conservation in Eq. (4.22) calls, in principle, also for a renormalization of the density susceptibility $\chi_{d,\mathbf{q}}^{\omega}$ by means of the corresponding λ correction via a λ_d. However, for the considered situation of the repulsive half-filled Hubbard model on a simple cubic lattice with nearest neighbor hopping only, nonlocal magnetic fluctuations dominate, while density fluctuations are strongly suppressed by the Hubbard repulsion. Hence, the difference between the nonlocal $\chi_{d,\mathbf{q}}^{\omega}$ and the local χ_d^{ω} is negligible and the λ corrections for $\chi_{d,\mathbf{q}}^{\omega}$ can be neglected ($\lambda_d \equiv 0$). With this further approximation the final equation for determining the value of λ in the λ-corrected magnetic susceptibility can be written as:

$$\frac{1}{2\beta} \sum_{\omega,\mathbf{q}} \chi_{m,\mathbf{q}}^{\lambda,\omega} = \frac{n}{2}\left(1 - \frac{n}{2}\right) - \frac{1}{2\beta} \sum_{\omega,\mathbf{q}} \chi_{d,\mathbf{q}}^{\omega} \approx \frac{n}{2}\left(1 - \frac{n}{2}\right) - \frac{1}{2\beta} \sum_{\omega} \chi_d^{\omega}. \qquad (4.25)$$

Let us finally remark, that it is possible to fulfill both conditions for λ, i.e., (i) $\left[\chi_{m,\mathbf{q}}^{\lambda,\omega}\right]^{-1} = \left[\chi_{m,\mathbf{q}}^{\omega}\right]^{-1} + \lambda > 0$ and (ii) $\Sigma(\nu,\mathbf{k}) \to \frac{U^2}{i\nu}\frac{n}{2}\left(1 - \frac{n}{2}\right)$ for $\nu \to \infty$ [or, equivalently, Eq. (4.25)], by decreasing temperature only down to the corresponding transition temperature of the system. Hence, in two dimension the λ-corrected ladder DΓA calculations can be performed down to $T = 0$ [28], in accordance with the Mermin-Wagner theorem [213], while in $d = 3$ a finite temperature for the phase transition to the antiferromagnetic state occurs. This will be of course lower than the corresponding one in DMFT [31] as a result of the effects of nonlocal correlations included by DΓA. In the next section, a ladder DΓA analysis this phase transition will be discussed in detail.

4.3.2   A (ladder) DΓA case study: Critical behavior of the 3d Hubbard model

Parts of the results and the discussion presented in the following section have been already

In this section we report an analysis of the critical properties of the anti-ferromagnetic instability of the half-filled three-dimensional Hubbard model on a simple cubic lattice with nearest neighbor hopping only, by means of the ladder DΓA approach (with Moriya-corrections). Starting point of our investigation is the corresponding (divergent) antiferromagnetic susceptibility, already introduced in the previous section:

$$\chi_{\text{AF}} = \chi_{m,\mathbf{q}=\mathbf{\Pi}}^{\omega=0} = 2 \int_0^\beta d\tau \, \langle \hat{\mathcal{S}}_{z,\mathbf{\Pi}}(\tau)\hat{\mathcal{S}}_{z,-\mathbf{\Pi}}(0)\rangle \tag{4.26}$$

where the spin operator is defined analogously to Eq. (2.64) in chapter 2, i.e., $\hat{\mathcal{S}}_{z,\mathbf{q}}(\tau) = \frac{1}{2}[\hat{n}_{\mathbf{q}\uparrow}(\tau) - \hat{n}_{\mathbf{q}\downarrow}(\tau)]$ and $\hat{n}_{\mathbf{q}\sigma}(\tau)$ is the Fourier transform of the density operator $\hat{n}_{i\sigma}(\tau)$ with respect to the spatial coordinate i. In the following all the energies (in particular U and T) will be given in terms of the typical energy scale $D = 2\sqrt{6}t$ which corresponds to twice the standard deviation of the non-interacting density of states on a three-dimensional simple cubic lattice. This specific choice renders our results more easily comparable to corresponding ones in other dimensions.

As mentioned in the previous section, the ladder version of DΓA with λ corrections well reproduces the textbook Mermin and Wagner results for the Hubbard model in $d=2$ dimensions yielding a finite, but exponentially large susceptibility at any finite T [28], while the phase transition, which is indicated by $\chi_{\text{AF}} \to \infty$, occurs only at $T = 0$. In $d=3$ the situation is, however, more intriguing, since the antiferromagnetic phase remains stable in a broad region at finite T, allowing for a direct study of the critical properties.

Of particular interest is the analysis of the evolution of the "critical region", where a mean field description of the system is not applicable due to strong nonlocal fluctuations, as a function of the Coulomb repulsion U. To this end, we show the inverse susceptibility χ_{AF}^{-1} as a function of T for different U values in Fig. 4.14. The vanishing of $\chi_{\text{AF}}^{-1} \propto (T - T_N)^\gamma$ marks the onset of the antiferromagnetic long-range order, defining the corresponding transition temperature T_N for a given U. More important is, however, the examination of the critical behavior: While in a mean-field (or DMFT) approach χ_{AF}^{-1} is vanishing linearly close to T_N in accordance with the mean-field (Gaussian) critical
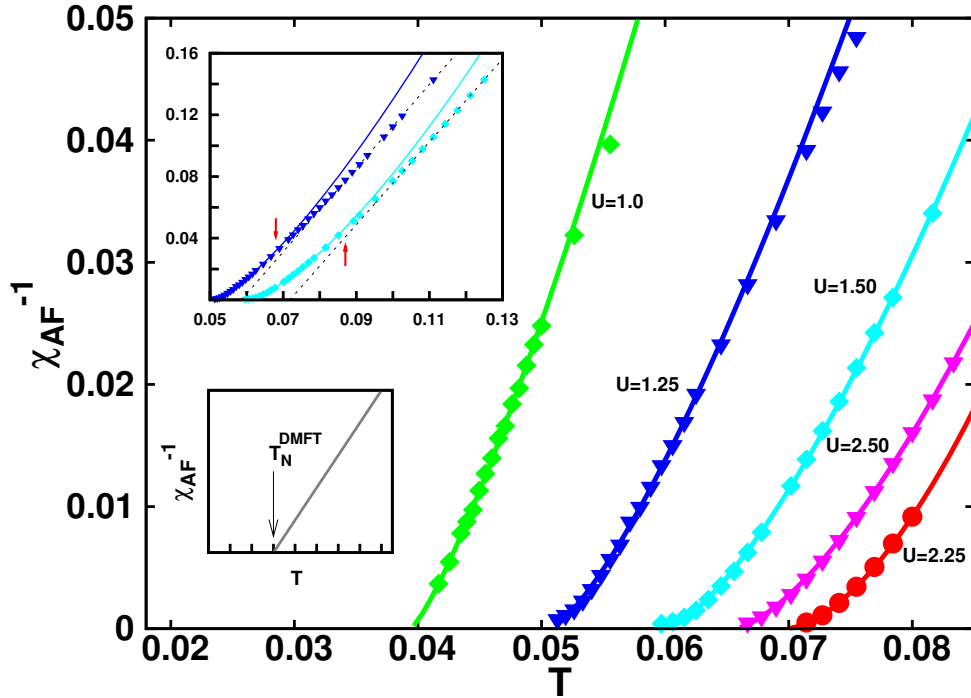
Figure 4.14: Inverse antiferromagnetic susceptibility as a function of T for different U values. Lower inset: Inverse DMFT susceptibility with a mean-field ($\gamma = 1$: linear behavior) critical exponent. Upper inset: larger T interval. Red arrows denote the respective temperatures, at which the devition between χ_{AF}^{-1} and the corresponding linear high-temperature fit becomes larger than 10%. The figure is reproduced from Ref. [31].

exponent $\gamma = 1$ (see lower inset of Fig. 4.14), DΓA data clearly show a bending in the region close to the antiferromagnetic transition (i.e., for $T < T_G$, the so-called Ginzburg temperature [72]), indicating a DΓA critical exponent γ definitely larger than 1. The nonperturbative nature of DΓA also allows for determining the size of the critical region as a function of U from weak to intermediate-to-strong coupling: Our data clearly show that the size of the temperature region where $\chi_{AF}^{-1} \propto |T - T_N|^{\gamma}$ deviates from the linear mean-field behavior, i.e., where γ is different from 1, increases with U. This can be even quantified by calculating χ_{AF} for T much larger then the transition temperature, i.e., $T \gg T_N$, and fitting the high-temperature linear behavior, as it was done in the upper inset of Fig. 4.14 for $U = 1.25$ and $U = 1.5$. In this way T_G has been, hence, estimated as the temperature below which the relative deviation of χ_{AF}^{-1} from the above-mentioned linear fit becomes larger than 10% (red arrows in the upper inset of Fig. 4.14). By this criterion for T_G, the size of the
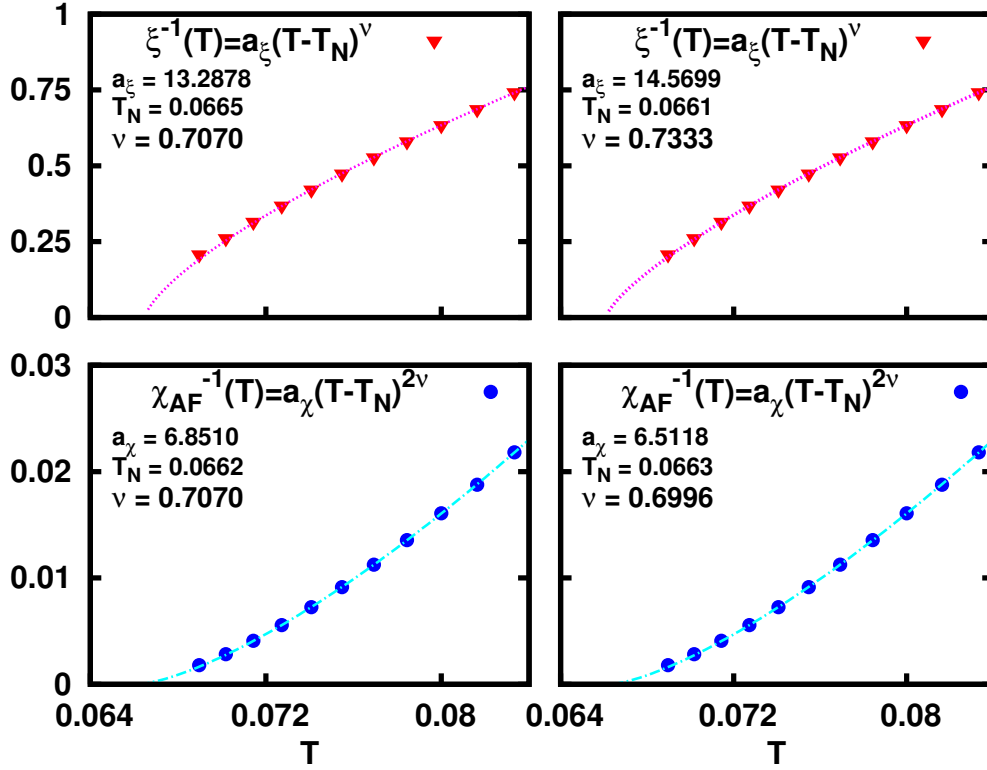
Figure 4.15: Fit of $\chi_{\mathrm{AF}}^{-1}(T)$ and $\xi^{-1}(T)$ for the highest interaction value considered, i.e., $U = 2.5$. Left: fit with fixed $\nu = 0.707$ (Heisenberg-exponent in $d\!=\!3$ [214]). Right: free fit, showing the good compatibility with the $d\!=\!3$ Heisenberg universality class. The figure is reproduced from Ref. [31].

critical region with non-mean-field behavior, i.e., $\Delta T_{\mathrm{crit}} = T_G - T_N$, increases from $\simeq 0.01$ for $U\!=\!1.0$, to $\simeq 0.02$ for $U\!=\!1.25$ and $\simeq 0.025$ for $U\!=\!1.5$, following therefore the dependence determined by the Ginzburg criterion, which implies the inapplicability of the standard Landau-Ginzburg expansion in the temperature region $\Delta T_{\mathrm{crit}} \propto T_N^2$ [72]. For $U < 1.0$ (not shown) the bending of χ_{AF}^{-1} becomes hardly visible, since in this regime T_N follows the RPA-type behavior $T_N \sim \mathrm{e}^{-\frac{D}{U}}$, and therefore the size of the critical region becomes extremely narrow. On the contrary, for $U > 1.5$ the linear behavior becomes confined to temperatures even higher than those shown in Fig. 4.14.

A more quantitative study of the critical behavior requires also a precise evaluation of the critical exponent(s). From the behavior of the antiferromagnetic susceptibility, one can extract the values of the critical exponent ν, which controls the divergence of the antiferromagnetic correlation length ξ [defined as the square root of the inverse mass of the (physical) magnetic susceptibil-
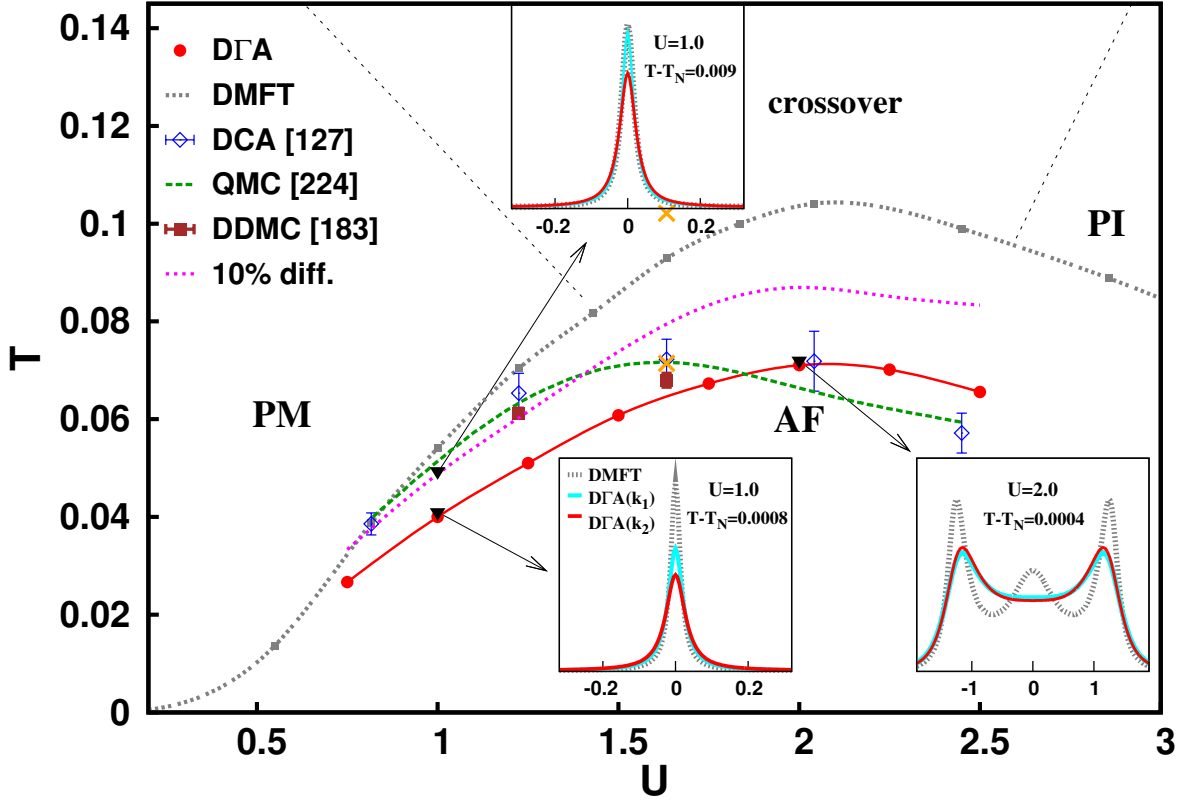
Figure 4.16: Néel temperature in DΓA, compared with the corresponding DMFT, DCA, QMC and DDMC ones. Also shown is the region where corrections to DMFT in form of nonlocal correlations become dominant (violet dashed-dotted line: 10% relative change between the DMFT and the DΓA self-energies at the lowest Matsubara frequency). The orange crosses ("$\times$") mark the U and T values for which a comparison between the ladder DΓA and the DCA self-energy is performed in Fig. 4.17. Insets: DMFT vs. DΓA spectral functions (see text), where $\mathbf{k}_1 = (\frac{\pi}{2}, \frac{\pi}{2}, \frac{\pi}{2})$ and $\mathbf{k}_2 = (\pi, 0, \frac{\pi}{2})$. The figure is readapted from Ref. [31].

ity at $\omega = 0$ and $\mathbf{q} = \mathbf{\Pi}$ as can be inferred from Eq. (4.20)] when $T \to T_N$. This can be computed either from the divergence of χ_{AF} (i.e., directly from the data shown in Fig. 4.14), using the relation[17] $\gamma = 2\nu$, or by extracting the value of ξ from χ_{AF} by fitting its $\mathbf{q}$-dependence for different values of T.[18]

The results of our analysis, shown in Fig. 4.15, demonstrate that DΓA can

---

[17]Note that within Moriyasque DΓA, the critical exponent η is not changed from its MF value (i.e., 0), since the explicitly $\mathbf{q}$-dependent terms of the spin-spin propagator in Eq. (4.20) (but not its mass, which is corrected by λ!) is computed at the level of DMFT.

[18]Specifically, the value of ξ has been computed by fitting the DΓA spin susceptibility $\chi_{m,\mathbf{q}}^{\omega=0}$ with the fitting function $\chi_{\text{fit}}(\mathbf{q}) = A/[4(\sin^2(\frac{q_x-\pi}{2}) + \sin^2(\frac{q_y-\pi}{2}) + \sin^2(\frac{q_z-\pi}{2})) + \xi^{-2}]$ which reduces to Eq. (4.20) for $\mathbf{q} \sim \mathbf{\Pi}$.

describe well the antiferromagnetic criticality of the Hubbard model. For the largest values of $U = 2.5$, indeed, both divergences of χ_{AF} and ξ observed in DΓA can be described (left panels of Fig. 4.15) with high-accuracy by the critical exponent $\nu = 0.707$ of the $d = 3$-Heisenberg antiferromagnetism [214]. This is expected to be the correct exponent, not only because the half-filled Hubbard model can be mapped onto the Heisenberg model in the limit of large U, but also since dimension and symmetry of the order parameter suggest the same universality class. Similar results, though with a lower degree of precision, can be found by directly fitting the value of the ν exponent to χ_{AF}^{-1} and ξ (right panels): For $U = 2.5$, our two fits provide an estimate of $\nu \sim 0.70$ and 0.73, respectively. This shows the Heisenberg universality is still valid also in a parameter region (i.e., at intermediate-to-strong coupling), where the Hubbard model is *not* well approximated by the Heisenberg model. A natural by-product of the calculation of the critical exponents is the determination of T_N at the DΓA level, whose values overall well agree with the most accurate DCA and QMC/DDMC data obtained till 2011 (see Fig. 4.16). While the quantitative agreement is particularly good in the intermediate-to-strong coupling regime, the deviations observed around $U = 1.0$ (smaller T_N in DΓA than in QMC/DCA) might originate from neglecting the relatively small non-local corrections of the charge- and particle-particle-channels, which could affect non-universal quantities such as T_N. On the other hand, also the DCA/QMC finite-size extrapolation is difficult in this region since the antiferromagnetic correlation length is large. In this respect, we refer to a very recent diagrammatic determinant Monte Carlo study [215], where the Néel temperature in the weak coupling regime ($U \sim 1$) was found reduced compared to previous QMC studies, towards the corresponding DΓA values. Let us also mention that the dual fermion approach yields results for the antiferromagnetic Néel temperature of the Hubbard model in three dimensions similar as in the DΓA, with an overestimation of T_N at weak and a possible underestimation at strong couplings [123][19] with respect to older QMC data [216].

In this respect, it is interesting to note here, that very recently an analogous situation has been also observed [195] by performing a ladder dual fermion study of critical properties of

---

[19]Note that, in general, the dual fermion method provides only an upper bound for the Néel temperature of the system.

the Falicov-Kimball model [217]. Within these ladder diagrammatic corrections to DMFT, very accurate predictions for the critical exponents have been obtained, while deviations with respect to lattice QMC data have been observed for non-universal quantities, such as the transition temperature.

Up to now, the focus of our analysis was on *two-particle* quantities of the three-dimensional half-filled Hubbard model, specifically on the (antiferromagnetic) susceptibility $\chi_{AF} = \chi_{m,\mathbf{q}=\mathbf{\Pi}}^{(\lambda),\omega=0}$, used for studying the critical properties of the phase transition to the antiferromagnetic state (i.e., the transition temperature T_N and the critical exponents ν and γ). However, very valuable information is also contained in the *one-particle* Green's function and, in particular, in the electronic self-energy $\Sigma_{\mathrm{lad}}(\nu, \mathbf{k})$, which can be easily obtained in ladder DΓA by means of Eq. (4.19). Hence, in the following, we will present a thorough investigation of $\Sigma_{\mathrm{lad}}(\nu, \mathbf{k})$ and of the related spectral properties of our model. To this end, we start with a comparison of our ladder DΓA results for the self-energy[20] with the corresponding most recent DCA data of Ref. [183]. In order to avoid any complications connected with the analytic continuation of our Matsubara data to the real axis, we perform this comparison on the imaginary frequency axis. In Fig. 4.17, the ladder DΓA self-energy with λ corrections ($\Sigma_{\mathrm{DΓA}}^{\lambda} \equiv \Sigma_{\mathrm{lad}}$) is compared to the corresponding DMFT and DCA data for different cluster sizes. The specific value for the Hubbard interaction parameter considered $U = 1.633$ is quite significant, being located in the intermediate-to-strong coupling regime. As for the temperatures, two values have been taken into account, one below and one above the Néel temperature of DMFT. The corresponding (U, T) points are marked by orange crosses in the phase diagram in Fig. 4.16. In general, for higher temperatures, local and nonlocal short-range correlations are expected to be the predominant, and, hence, DMFT and DCA should yield fairly similar and reliable results in this situation. Indeed, in the upper panels of Fig. 4.17, one observes for a temperature well above the Néel temperature of DMFT ($\beta = 9.798$, see also the upper orange cross in the phase-diagram in Fig. 4.16), that both nonlocal corrections of DCA and DΓA to the DMFT self-energy are overall small, and that the DCA data as a function of cluster size appear already well converged at this rather high temperature. Aiming at a more quantitative analysis, we observe that for a $\mathbf{k}$ point inside the Fermi surface, e.g., the Γ point [$\mathbf{k} = (0, 0, 0)$, upper left panel in Fig. 4.17], a very good agreement is found between the DΓA and the DCA curve for the largest cluster under consideration (100 cluster sites). In addition, com-

---

[20]More specifically, we compare just the imaginary part of the self-energy in Fig. 4.17 since, for the half-filled system and the considered high-symmetry $\mathbf{k}$-points at the Fermi level for which $k_i = \pi - k_{P(i)}$, $i = 1, \ldots, d$, where $P(i)$ denotes an arbitrary permutation of the numbers $\{1, \ldots, d\}$ [see Eq. (2.117) and the discussion below this relation], the real part of $\Sigma(\nu, \mathbf{k})$ is just given by the Hartree term $\frac{Un}{2}$.
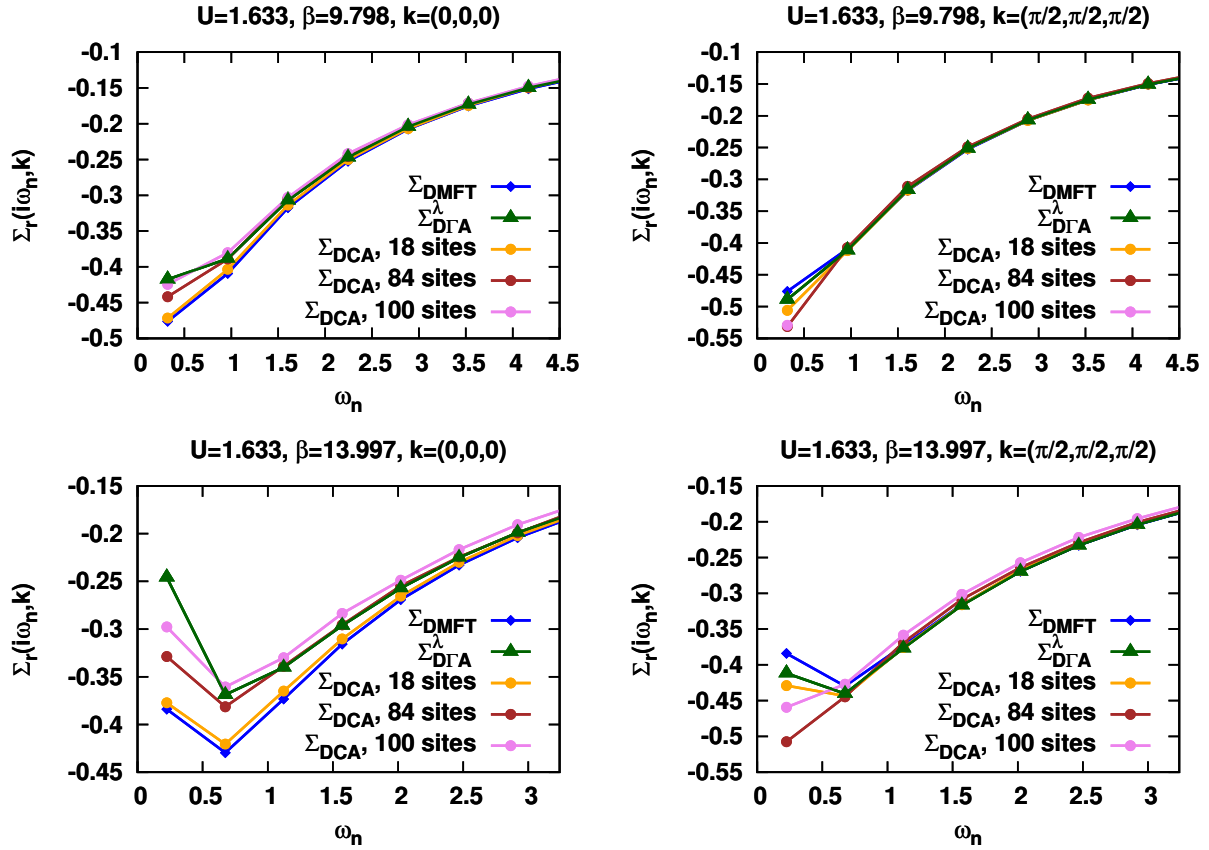
Figure 4.17: Imaginary part of the self-energy obtained with the Moriyasque DΓA ($\Sigma^\lambda_{\text{DΓA}} = \Sigma_{\text{lad}}$) calculated via Eq. (4.19) vs. DMFT and DCA results for different cluster sizes (taken from Ref. [183]). The $(U, T = 1/\beta)$ values for which the results have been obtained are marked by an orange cross ("×") in the phase-diagram in Fig. 4.16.

paring the DCA results for 84 and 100 cluster sites one can see, that the DCA calculations are almost converged as a function of cluster size and tend to match the corresponding DΓA data points. On the contrary, for $\mathbf{k} = (\frac{\pi}{2}, \frac{\pi}{2}, \frac{\pi}{2})$ on the Fermi surface the DΓA self-energy differs from the corresponding (converged) DCA curves for 84 and 100 cluster sites as can be seen in the right upper panel of Fig. 4.17. At the high temperature under consideration, this observation might be related to the neglect of short-range nonlocal contributions to the irreducible density and magnetic vertices $\Gamma_{\text{loc},d}$ and $\Gamma_{\text{loc},m}$ in the ladder version of DΓA. More specifically, the observed underestimation of nonlocal corrections within ladder DΓA could be mitigated by the inclusion of part of these missing nonlocal corrections to $\Gamma_{\text{loc},d}$ and $\Gamma_{\text{loc},m}$, by means of the one-particle irreducible (1PI) scheme (see Secs. 4.4.2 and 4.4.3), especially in the regime of intermediate-to-strong coupling. A more detailed discussion of this issue will be given in Sec. 4.4.3.1 (see, in particular, page 245). Turning to the lower temperature

$\beta = 13.997$, which is located well below the Néel temperature of DMFT for the interaction value $U = 1.633$ (see lower orange cross in Fig. 4.16), one figures out that DCA calculations are not yet converged as a result of nonlocal correlations extended over longer ranges than the available cluster sizes. For the Γ point $\mathbf{k} = (0, 0, 0)$, the evolution of the DCA self-energy with the cluster size looks at least monotonous, tending to the corresponding solution obtained with the (λ-corrected) ladder version of DΓA. On the contrary, at $\mathbf{k} = (\frac{\pi}{2}, \frac{\pi}{2}, \frac{\pi}{2})$ on the Fermi surface one even observes a non-monotonous behavior of the DCA self-energies as a function of cluster size, i.e., $|\Sigma_{\mathrm{DCA}}^{18}| < |\Sigma_{\mathrm{DCA}}^{100}| < |\Sigma_{\mathrm{DCA}}^{84}|$ at the first Matsubara frequency, which, evidently, renders the comparison with DΓA less significant.

As for a more quantitative description of the difference between the DCA and the ladder DΓA self-energies on the Matsubara axis, we can introduce the following measure: We calculate the relative deviation $\frac{1}{N} \sum_n |\mathrm{Im}\, \Sigma_{D\Gamma A}(\mathbf{k}, \omega_n) - \mathrm{Im}\, \Sigma_{DCA}(\mathbf{k}, \omega_n)| / |\mathrm{Im}\, \Sigma_{D\Gamma A}(\mathbf{k}, \omega_n)|$ and sum it over the first $N = 7$ Matsubara frequencies, since for those a difference between the DMFT and the DCA/DΓA self-energy is observable. With respect to the above criterion the relative difference between the DCA and DΓA self-energy is smaller than 5% for all cases depicted in Fig. 4.17. For the lower right panel, i.e., for $\beta = 13.997$ and $\mathbf{k} = (\frac{\pi}{2}, \frac{\pi}{2}, \frac{\pi}{2})$ this is smaller than the DCA difference between the two largest clusters considered (84 and 100 sites), indicating that in this regime the DΓA errors are smaller than the accuracy of the present DCA data. Let us now turn to the investigation of the effects of nonlocal correlations on the spectral properties of the half-filled three-dimensional Hubbard model. As for a quantitative description, we consider the relative differences between the DΓA and the DMFT self-energy at the lowest Matsubara frequency and the point $\mathbf{k}_2 = (\pi, 0, \frac{\pi}{2})$ on the Fermi surface for which the strongest impact of nonlocal correlations is expected and found numerically: $|\Sigma_{\mathrm{DMFT}}(i\nu_1) - \Sigma_{\mathrm{D\Gamma A}}(\mathbf{k}_2, i\nu_1)| / |\Sigma_{\mathrm{DMFT}}(i\nu_1)|$. Note that this quantity, which can be obtained from the Matsubara data for the self-energy, i.e., without an analytic continuation to the real axis, is directly related to the quasiparticle weight Z in the Fermi liquid regime if the linear low-frequency behavior of the self-energy already holds (approximately) at the lowest Matsubara frequency $i\nu_1$. By this one-particle criterion, DMFT is estimated to remain reliable down to the dashed violet line in Fig. 4.16, below which nonlocal DΓA corrections exceed 10%.

While these findings may validate (a posteriori) the usage of DMFT for computing one-particle quantities such as spectral functions in $d = 3$, provided one is not interested in the immediate vicinity of (second-order) magnetic instabilities (i.e., in the region below the dashed violet line in Fig. 4.16), it is important to stress that for two-particle quantities nonlocal correlations play a relevant role in a much larger region of the phase diagram,

i.e., even above the violet line. Let us note that also in the case of single site DMFT for realistic system, such as the pnictides, it has been recently pointed out that local electronic correlations appear more visibly in two- than in one-particle quantities [120]. In our specific case, we observe that the size of the critical region ΔT_{crit}, obtained from the temperature dependence of the antiferromagnetic susceptibility χ_{AF} (i.e., from a two particle quantity), exceeds the violet line at $U > 1.25$. Significant effects of nonlocal correlations may occur even further away from the antiferromagnetic transition, depending on the quantity under consideration. In particular, relevant deviations from the DMFT predictions at even higher-Ts have been reported when analyzing the temperature dependence of the entropy [184].

As for a more physical picture of the impact of nonlocal correlations at the one-particle level, we consider, in the following, the one-particle Green's function on the real frequency axis. To this end we have to perform an analytic continuation of the corresponding self-energy $\Sigma^\lambda_{\text{DGA}} \equiv \Sigma_{\text{lad}}$ which has been obtained as a function of Matsubara frequencies in Eq. (4.19). Let us recall that the analytic continuation procedure of a finite discrete data set on the Matsubara axis is mathematically ill-conditioned, since the accumulation point of the Matsubara frequencies is at $\pm i\infty$. Keeping an eye on this problem, we have performed a Padé fit of our Matsubara data for the self-energy and calculated the **k**-resolved spectral function $A(\omega, \mathbf{k}) = -\frac{1}{\pi} \text{Im} G(\omega, \mathbf{k})$, as defined and discussed in section 2.2.7, for two different **k**-points on the Fermi Surface[21], i.e., $\mathbf{k}_1 = (\frac{\pi}{2}, \frac{\pi}{2}, \frac{\pi}{2})$, $\mathbf{k}_2 = (\pi, 0, \frac{\pi}{2})$. The results for three specific values of U and T have been reported in Ref. [31] and are shown in the insets of Fig. 4.16. At $U = 1.0$ and for a temperature well above the violet line in the phase diagram (upper inset in Fig. 4.16) the effect of nonlocal correlations on the spectrum appears, as expected, moderate: One observes just a small quantitative change in the height of the quasiparticle peak with respect to DMFT for $\mathbf{k}_2$, while for $\mathbf{k}_1$ almost no deviation from DMFT can be seen in the spectrum. The situation of course changes considerably when approaching the second-order transition line. This is because the corresponding (λ-corrected) magnetic susceptibility $\chi^{\lambda,\omega}_{m,\mathbf{q}}$, which explicitly enters in the DΓA equation for $\Sigma^\lambda_{\text{DΓA}} = \Sigma_{\text{lad}}$ [Eq. (4.19)], is diverging at the (red) transition line of Fig. 4.16). Such behavior is particularly evident in the spectra shown in the two lower insets of Fig. 4.16 for temperatures slightly above the T_N of DΓA but far below the violet curve which marks the region of applicability of DMFT for calculating one-particle Green's function. At $U = 1.0$ (left lower inset in Fig. 4.16), a pronounced broadening of the quasiparticle peak occurs in the DΓA spectra compared to DMFT. At $U = 2.0$, the enhanced scattering by nonlocal magnetic fluctuations even qualitatively changes the spectra: the

---

[21]This choice is highly significant, because for these **k**-points (on the Fermi surface) the largest/smallest deviations from the DMFT self-energy are found.
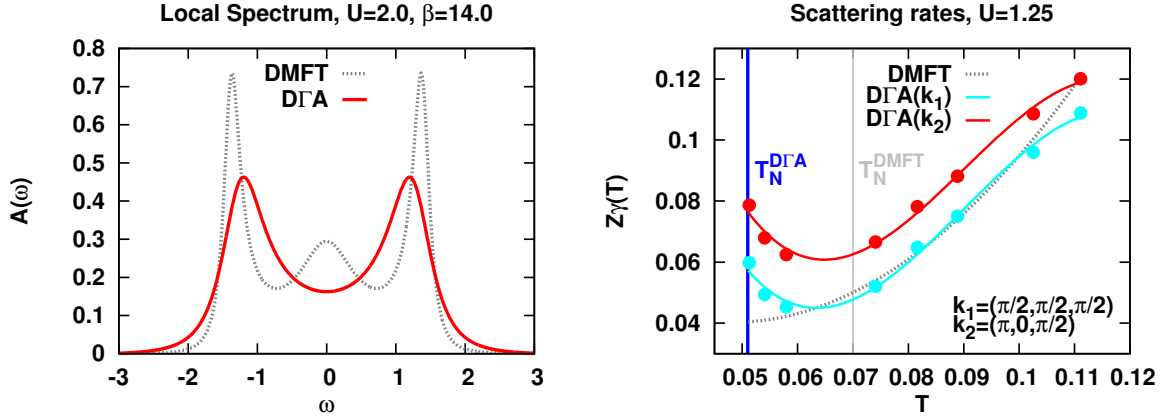
Figure 4.18: Left panel: Local spectral function $A(\omega) = \sum_{\mathbf{k}} A(\omega, \mathbf{k}) = -\frac{1}{\pi} \sum_{\mathbf{k}} \mathrm{Im} G(\omega, \mathbf{k})$ computed with DMFT and DΓA. Right panel: DMFT quasi-particle scattering rates $Z\gamma$ vs the corresponding DΓA results as a function of the temperature for two relevant $\mathbf{k}$-points at the Fermi surface. The continuous curves where obtained by single polynomial fit of the Padé estimation for $Z\gamma$.

(already) damped quasiparticle peak of DMFT is transformed into a "pseudogap" in DΓA in the right lower inset in Fig. 4.16. In principle, one can expect pseudogap behavior very close to the Néel temperature also for an arbitrarily small Hubbard repulsion. The corresponding region gets, however, very narrow at small U: a qualitative estimate according to Eq. (4.19) yields the condition for the pseudogap behavior $\xi > 4\pi v_F^3/(T_N U^2)$ (v_F is an average Fermi velocity), which is only fulfilled in the immediate vicinity of the phase transition at small U, where T_N is exponentially small [31].

In addition to the $\mathbf{k}$-resolved DΓA spectra in the insets of Fig. 4.16 we also present a $\mathbf{k}$-summed, i.e., a local, spectral function in the left panel of Fig. 4.18 for $U = 2.0$ and $\beta = 14.0$, i.e., for the U and T values corresponding to the right lower inset in the phase-diagram. One can see that the most important qualitative feature of the $\mathbf{k}$-resolved DΓA spectra, i.e., the formation of the gap, is preserved also in the local ($\mathbf{k}$-summed) density of states $A(\omega)$, which indicates a significant impact of nonlocal correlations also on local physical observables in this parameter regime.

Let us finally discuss the consequences of nonlocal correlations for the Fermi liquid coefficients in the parameter region, where a quasi-particle description of the system is still applicable, i.e., for small values of U and T. In this region of the phase diagram the (retarded) self-energy on the real axis, $\Sigma(\omega, \mathbf{k})$, can be expanded into a series at $\omega = 0$. For the half-filled system the particle-hole symmetry relations (2.108) and (2.117) and the point group symmetry of the simple cubic lattice (see section 2.2.2.4) imply that $\Sigma^*(i\nu, \mathbf{k}) - \frac{U}{2} = -\Sigma(i\nu, \mathbf{k}) + \frac{U}{2}$ (on

the Matsubara axis) for the two specific $\mathbf{k}$ points on the Fermi surface considered above [i.e., $\mathbf{k}_1 = (\frac{\pi}{2}, \frac{\pi}{2}, \frac{\pi}{2})$ and $\mathbf{k}_2 = (\pi, 0, \frac{\pi}{2})$]. Hence, the expansion of the corresponding $\Sigma(\omega, \mathbf{k})$ on the real frequency axis reads:

$$\Sigma(\omega, \mathbf{k}; T) = \frac{U}{2} - i\gamma(\mathbf{k}; T) - \alpha(\mathbf{k}; T)\omega + O(\omega^2), \tag{4.27}$$

where α is related to the quasiparticle renormalization factor as $Z = (1 + \alpha)^{-1}$. For $U = 1.25$ we extracted from our Padé fits for the self-energies the coefficients $\gamma(\mathbf{k}; T)$ and $Z(\mathbf{k}; T)$ for different temperatures above the Néel temperature of DΓA. Let us note that the extraction of the Fermi liquid coefficients from the Padé fits of the self-energy is numerically a rather delicate procedure, leading to a considerable uncertainty in the results. The DΓA curves in the right panel of Fig. 4.18 have, hence, been fitted to the data points shown in this plot while data points, where the Padé fit exhibited anomalies (e.g., in the sum-rules) and, hence, needs to be double checked, have been excluded. Remarkably, for DMFT such numerical inconsistencies are even larger, since the self-energy is obtained directly from the impurity solver rather than from a momentum integral as in DΓA, which has smoothing effects on the data. Therefore, we present only the fitted curve in the case of DMFT.

In the right panel of Fig. 4.18 the effective scattering rates $Z\gamma$ are shown for the two $\mathbf{k}$ points under consideration and compared to the corresponding DMFT values as a function of temperature. While for a Fermi liquid one typically expects a monotonous increase of $Z\gamma$ with the temperature, as it can be indeed observed for DMFT, the corresponding DΓA results exhibit an evident non-monotonous behavior, with increasing values of $Z\gamma$ at low temperatures when approaching the antiferromagnetic phase transition. This finding is related to the scattering of the electrons by nonlocal magnetic fluctuations which becomes progressively more important at low temperatures and dominates all other effects in the vicinity of the second-order phase transition. These nonlocal magnetic fluctuations and the corresponding scattering are neglected in DMFT. Let us note that qualitatively similar low-temperature nonlocal corrections for the behavior of the Fermi liquid coefficients, in particular of the effective scattering rate, have been reported in a related DCA study in Ref. [190] for the case of the two-dimensional Hubbard model.

We have seen that the ladder DΓA represents a powerful tool for analyzing qualitatively and quantitatively the critical properties of the half-filled Hubbard model. While for universal quantities, such as the critical exponents, one obtains accurate results, one notices deviations with respect to cluster calculations for non-universal quantities, such as the Néel temperature. A similar situation has been recently observed for ladder calculations within

the dual fermion approach [123]. The main limitation of ladder DΓA, however, is the neglect of nonlocal contributions to the irreducible vertex in the specific channel under consideration. This problem matters even more if the system is out of half-filling, since in that case the importance of spin fluctuations compared to the other channels gets gradually reduced with the doping of the system. While a full parquet treatment within the DΓA would certainly overcome this problem, it is numerically very demanding. Hence, in the following we will consider alternative approaches with the aim of including (part of) nonlocal corrections into the irreducible vertices at the ladder level.

4.4   Functional Integral based methods

In this section we will discuss methods for the inclusion of nonlocal correlations beyond the purely local ones, taken into account by DMFT, which are based on the functional integral representation of the n-particle Green's function [32,33], defined (in the operator formalism) in Eq. (2.27):

$$G_{n,i_1\ldots i_{2n}}(\tau_1,\ldots,\tau_{2n}) = \frac{1}{Z}\int D[c_i^+(\tau),c_i(\tau)]\,e^{-\mathcal{S}[c_i^+(\tau),c_i(\tau)]}\,c_{i_1}^+(\tau_1)c_{i_2}(\tau_2)\ldots c_{i_{2n-1}}^+(\tau_{2n-1})c_{i_{2n}}(\tau_{2n}),$$

$$(4.28)$$

where $c_i(\tau)$ and $c_i^+(\tau)$ are the Grassmann fields corresponding to the fermionic operators $\hat{c}_i(\tau)$ and $\hat{c}_i^\dagger(\tau)$, respectively, as given in Eq. (2.28). It should be stressed that, in our convention, similar as for the operators, the variables $c_i^+(\tau)$ and $c_i(\tau)$ are dimensionless. The partition function Z, which serves as normalization factor, reads as $Z = \int D[c_i^+(\tau),c_i(\tau)]\,e^{-\mathcal{S}[c_i^+(\tau),c_i(\tau)]}$, and the indices i_j represent the set of all degrees of freedom of the system under consideration as it was discussed in Sec. 2.2, page 25 below Eq. (2.29), i.e., $i_j\widehat{=}(\mathbf{R}_j,\sigma_j)$ [or $i_j\widehat{=}(\mathbf{k}_j,\sigma_j)$ after a Fourier transform] for the Hubbard Hamiltonian while $i_j\widehat{=}\sigma_j$ for the AIM. $\mathcal{S}$ denotes the imaginary time action which reads as:

$$\mathcal{S}[c_i^+(\tau),c_i(\tau)] = \int_0^\beta d\tau\left[\sum_i c_i^+(\tau)\frac{d}{d\tau}c_i(\tau) + H[c_i^+(\tau),c_i(\tau)]\right],\qquad(4.29)$$

where H is the Hamiltonian functional of the Grassmann fields $c_i^+(\tau)$ and $c_i(\tau)$. For the models which are relevant for this section these Hamiltonian functionals read:

$$H_{\text{Hubbard}}[c_{i\sigma}^+(\tau), c_{i\sigma}(\tau)] = - t \sum_{\langle ij\rangle,\sigma} c_{i\sigma}^+(\tau)c_{j\sigma}(\tau) + U \sum_i c_{i\uparrow}^+(\tau)c_{i\uparrow}(\tau)c_{i\downarrow}^+(\tau)c_{i\downarrow}(\tau) +$$

$$- \mu \sum_{i,\sigma} c_{i\sigma}^+(\tau)c_{i\sigma}(\tau) \tag{4.30}$$

for the lattice system (i.e., the Hubbard model), and

$$H_{\text{AIM}}[c_\sigma^+(\tau), c_\sigma(\tau)] = \sum_\sigma \int_0^\beta d\tau' \, \Delta(\tau - \tau')c_\sigma^+(\tau)c_\sigma(\tau') + U c_\uparrow^+(\tau)c_\uparrow(\tau)c_\downarrow^+(\tau)c_\downarrow(\tau) +$$

$$- \mu \sum_\sigma c_\sigma^+(\tau)c_\sigma(\tau), \tag{4.31}$$

for the AIM, where $\Delta(\tau)$ is the inverse Fourier transform of the hybridization function, defined in Eq. (2.209). To render the Hamiltonian functionals and the action, respectively, diagonal, it is convenient to introduce the Fourier transform with respect to the imaginary time τ (and the space variable $\mathbf{R}_i$ in the case of the Hubbard model) of the fermionic fields $c_{i\sigma}^+(\tau)$ and $c_{i\sigma}(\tau)$. Hence, one defines the following transformation of the Grassmann fields $c_{i\sigma}^+(\tau)$ and $c_{i\sigma}(\tau)$:

$$c_{i\sigma}^{(+)}(\tau) = \frac{1}{\beta} \sum_{\nu,\mathbf{k}} e^{(\mp)\,i(\nu\tau - \mathbf{k}\mathbf{R}_i)}c_{\mathbf{k}\sigma}^{(+)}(\nu), \qquad c_{\mathbf{k}\sigma}^{(+)}(\nu) = \sum_i \int_0^\beta d\tau \, e^{(\pm)\,i(\nu\tau - \mathbf{k}\mathbf{R}_i)}c_{i\sigma}^{(+)}(\tau), \tag{4.32}$$

where ν is a fermionic Matsubara frequency [the sign in the exponent with (without) parentheses is for the creation (annihilation) operators], and $\sum_{\mathbf{k}}$ is a shorthand notation for the momentum integral over the first Brillouin zone, i.e., $\sum_{\mathbf{k}} \hat{=} \frac{1}{(2\pi)^d}\int_{-\pi}^\pi d^dk$ for the Hubbard model on a d-dimensional simple cubic lattice with lattice constant $a = 1$. The corresponding equations for the AIM can be readily obtained by removing all $\mathbf{k}$ and i variables and summations from Eqs. (4.32). In the following also the fields $c_{i\sigma}^+(\nu)$ and $c_{i\sigma}(\nu)$, where the Fourier transform is conducted with respect to the time variable τ only, will be considered; the corresponding transformation is equivalent to Eqs. (4.32) except for $\sum_{\mathbf{k}} e^{\pm i\mathbf{k}\mathbf{R}_i}$ and $\sum_i e^{\pm i\mathbf{k}\mathbf{R}_i}$, respectively[22].

Inserting the Fourier transform of the Grassmann fields c^+ and c, as defined in Eqs. (4.32),

---

[22]Let us also mention that, since $c_{i\sigma}^+(\tau)$ and $c_{i\sigma}(\tau)$ are dimensionless quantities, $c_{\mathbf{k}\sigma}^+(\nu)$ and $c_{\mathbf{k}\sigma}(\nu)$ have the physical dimension of an inverse energy, i.e., $[c_{\mathbf{k}\sigma}^{(+)}(\nu)] = (\text{eV})^{-1}$, see Eqs. (4.32).

into the Gaussian part of the action in Eqs. (4.29), (4.30) and (4.31) yields:

$$\mathcal{S}_{\text{Hubbard}}[c^+, c] = \frac{1}{\beta} \sum_{\nu, \mathbf{k}, \sigma} [-i\nu + \varepsilon_{\mathbf{k}} - \mu] \, c^+_{\mathbf{k}\sigma}(\nu) c_{\mathbf{k}\sigma}(\nu) + U \sum_i \int_0^\beta d\tau \, c^+_{i\uparrow}(\tau) c_{i\uparrow}(\tau) c^+_{i\downarrow}(\tau) c_{i\downarrow}(\tau),$$
(4.33a)

$$\mathcal{S}_{\text{AIM}}[c^+, c] = \frac{1}{\beta} \sum_{\nu, \sigma} [-i\nu + \Delta(\nu) - \mu] \, c^+_\sigma(\nu) c_\sigma(\nu) + U \int_0^\beta d\tau \, c^+_\uparrow(\tau) c_\uparrow(\tau) c^+_\downarrow(\tau) c_\downarrow(\tau). \quad (4.33b)$$

Comparing Eq. (4.33a) with (4.33b) one sees that, concerning the action, the main difference between the Hubbard model and the AIM is the way in which an interacting lattice site is "connected" to the rest of the system, i.e., to the other (interacting) lattice sites in the case of the Hubbard model and to the (non-interacting) bath sites in case of the AIM, respectively. In the following, this observation will be the guideline for separating local and nonlocal degrees of freedom in the Hubbard model[23]. In fact, it is straightforward to express the action of the Hubbard model in terms of the corresponding one for the AIM which reads as:

$$\mathcal{S}_{\text{Hubbard}}[c^+, c] = \sum_i \mathcal{S}_{\text{AIM}}[c_i^+, c_i] - \frac{1}{\beta} \sum_{\nu, \mathbf{k}, \sigma} [\Delta(\nu) - \varepsilon_{\mathbf{k}}] \, c^+_{\mathbf{k}\sigma}(\nu) c_{\mathbf{k}\sigma}(\nu). \quad (4.34)$$

The calculation of the Green's functions by means of the functional integral formalism, as introduced in Eq. (4.28), is typically performed by adding a term containing so-called (fermionic) source-fields $\eta_i(\tau)$ and $\eta_i^+(\tau)$ in the exponent [32]:

$$Z[\eta_i^+(\tau), \eta_i(\tau)] = \int D[c_i^+(\tau), c_i(\tau)] \, e^{-\mathcal{S}[c^+, c] + \sum_i \int_0^\beta d\tau \, [c_i^+(\tau)\eta_i(\tau) + \eta_i^+(\tau)c_i(\tau)]}, \quad (4.35)$$

where, for the sake of generality, we come back for the moment to the notation adopting the generalized index i, the meaning of which depends on the model under consideration[24]. The Green's functions can be now obtained by differentiating $Z[\eta^+, \eta]$ with respect to the

---

[23]Here and in the following we make excessively use of Parseval's theorem [218] which states that the inner product of two functions (or, in our case, Grassmann fields) is invariant under a Fourier transform (except for a possible factor of β concerning the transition from time-integration to frequency-summation), i.e., $\frac{1}{\beta} \sum_{\nu, \mathbf{k}} c^+_{\mathbf{k}\sigma}(\nu) c_{\mathbf{k}\sigma}(\nu) = \int_0^\beta d\tau \sum_i c^+_{i\sigma}(\tau) c_{i\sigma}(\tau)$.

[24]Let us stress here, that in our convention, while $c_i^+(\tau)$ and $c_i(\tau)$ are dimensionless Grassmann fields, $\eta_i^+(\tau)$ and $\eta_i(\tau)$ should have the dimension of an energy ($[\eta_i^+(\tau)] = [\eta_i(\tau)] \equiv$ eV) in order to render the corresponding term in the exponent of Eq. (4.35) dimensionless.

fermionic source fields η and η^+, evaluated at $\eta = 0$ and $\eta^+ = 0$:[25]

$$G_{n,i_1\ldots i_{2n}}(\tau_1,\ldots,\tau_{2n}) = \frac{1}{Z}\frac{\delta^{2n}Z[\eta^+,\eta]}{\delta\eta^+_{i_{2n}}(\tau_{2n})\delta\eta_{i_{2n-1}}(\tau_{2n-1})\ldots\delta\eta^+_{i_2}(\tau_2)\delta\eta_{i_1}(\tau_1)}\bigg|_{\eta^+=0,\eta=0}, \qquad (4.36)$$

where the partition function Z can be expressed as $Z \equiv Z[\eta^+ = 0, \eta = 0]$ in this context. Eq. (4.36) explains the denotation of $Z[\eta^+,\eta]$ as *generating functional* for the n-particle Green's functions. Similarly, one can define a more specialized generating functional $W[\eta^+,\eta]$, from which the *connected* parts of the Green's functions can be directly extracted, as defined in Fig. 2.8 and Eq. (2.159). This functional is simply given by:

$$W[\eta^+,\eta] = \ln Z[\eta,\eta^+]. \qquad (4.37)$$

One can now obtain the connected n-particle Green's function G_n^c by differentiating $W[\eta^+,\eta]$ with respect to the source fields η^+ and η:

$$G^c_{n,i_1\ldots i_{2n}}(\tau_1,\ldots,\tau_{2n}) = \frac{\delta^{2n}W[\eta^+,\eta]}{\delta\eta^+_{i_{2n}}(\tau_{2n})\delta\eta_{i_{2n-1}}(\tau_{2n-1})\ldots\delta\eta^+_{i_2}(\tau_2)\delta\eta_{i_1}(\tau_1)}\bigg|_{\eta^+=0,\eta=0}. \qquad (4.38)$$

Note that the normalization factor $\frac{1}{Z}$ is not needed here, since it is automatically produced by differentiating the logarithm in Eq. (4.37).

In the following sections we are mainly concerned with the calculation of the one-particle Green's function for the Hubbard model, $G(\nu,\mathbf{k})$. This quantity does not exhibits any unconnected parts, i.e., $G_1^c \equiv G_1$, and can be, hence, calculated according to Eqs. (2.57), (2.61) (with lattice constant $a = 1$) and (4.38):

$$G_{1,\mathbf{kk'},\sigma\sigma'}(\nu,\nu') = \frac{\delta^2 W[\eta^+,\eta]}{\delta\eta^+_{\mathbf{k'}\sigma'}(\nu')\delta\eta_{\mathbf{k}\sigma}(\nu)} = \beta\delta_{\nu\nu'}(2\pi)^d\delta^{(d)}(\mathbf{k}-\mathbf{k'})\delta_{\sigma\sigma'}G(\nu,\mathbf{k}), \qquad (4.39)$$

---

[25]Note that, even though the Grassmann fields $\eta^+_{i_j}(\tau_j)$ and $\eta_{i_j}(\tau_j)$ exhibit the physical dimension of an energy, the Green's function in Eq. (4.36) is dimensionless since the operation of functional differentiation involves an integration over τ, i.e., $\int_0^\beta d\tau\, \delta(\tau-\tau_j)c_{i_j}^{(+)}(\tau_j)$, which compensates for the energy dimension of the source fields ($[d\tau] = (\text{eV})^{-1}$ and $[\eta_{i_j}^{(+)}(\tau_j)] = [\delta(\tau-\tau_j)] = \text{eV}$).

where the Fourier transformed source fields $\eta_{\mathbf{k}\sigma}^+(\nu)$ and $\eta_{\mathbf{k}\sigma}(\nu)$ are defined as[26]:

$$\eta_{i\sigma}^{(+)}(\tau) = \sum_{\nu,\mathbf{k}} e^{(\mp)\,i(\nu\tau-\mathbf{k}\mathbf{R}_i)}\eta_{\mathbf{k}\sigma}^{(+)}(\nu), \qquad \eta_{\mathbf{k}\sigma}^{(+)}(\nu) = \sum_i \frac{1}{\beta}\int_0^\beta d\tau\; e^{(\pm)\,i(\nu\tau-\mathbf{k}\mathbf{R}_i)}\eta_{i\sigma}^{(+)}(\tau). \quad (4.40)$$

Let us now discuss the basic idea for the inclusion of nonlocal correlations in the Green's functions of the Hubbard model (beyond the local ones of DMFT) in the framework of the functional integral formalism presented above. To this end, we start from the generating functional [Eq. (4.35)] for the Hubbard model and use the splitting of the lattice action into a local and a nonlocal part, as it was illustrated in Eq. (4.34):[27]

$$Z[\eta^+,\eta] = \int D[c^+,c]\;\exp\left\{-\sum_i \mathcal{S}_{\mathrm{AIM}}[c_i^+,c_i] + \sum_{\nu,\mathbf{k},\sigma}\frac{1}{\beta}\left[\Delta(\nu)-\varepsilon_{\mathbf{k}}\right]c_{\mathbf{k}\sigma}^+(\nu)c_{\mathbf{k}\sigma}(\nu)+ \right.$$
$$\left. + c_{\mathbf{k}\sigma}^+(\nu)\eta_{\mathbf{k}\sigma}(\nu) + \eta_{\mathbf{k}\sigma}^+(\nu)c_{\mathbf{k}\sigma}(\nu)\right\}. \quad (4.41)$$

In the next step a Hubbard-Stratonovich (HS) [33] transformation is performed in order to decouple the term describing the nonlocal degrees of freedom $\mathbf{k}$. For a given set of quantum numbers $(\nu,\mathbf{k},\sigma)$ such a transformation reads:

$$e^{\frac{1}{\beta}[\Delta(\nu)-\varepsilon_{\mathbf{k}}]c_{\mathbf{k}\sigma}^+(\nu)c_{\mathbf{k}\sigma}(\nu)} = [B_{\mathbf{k}\sigma}(\nu)]^{-2}\int d\widetilde{c}_{\mathbf{k}\sigma}^+(\nu)d\widetilde{c}_{\mathbf{k}\sigma}(\nu)\; e^{\pm\frac{1}{\sqrt{\beta}}[\Delta(\nu)-\varepsilon_{\mathbf{k}}]^{\frac{1}{2}}B_{\mathbf{k}\sigma}(\nu)\left[c_{\mathbf{k}\sigma}^+(\nu)\widetilde{c}_{\mathbf{k}\sigma}(\nu)+\widetilde{c}_{\mathbf{k}\sigma}^+(\nu)c_{\mathbf{k}\sigma}(\nu)\right]}$$
$$\times\, e^{-[B_{\mathbf{k}\sigma}(\nu)]^2\widetilde{c}_{\mathbf{k}\sigma}^+(\nu)\widetilde{c}_{\mathbf{k}\sigma}(\nu)}, \quad (4.42)$$

where $B_{\mathbf{k}\sigma}(\nu)$ is an arbitrary complex function [i.e., $B_{\mathbf{k}\sigma}(\nu)\in\mathbb{Z}$] of the variables ν, $\mathbf{k}$ and σ, the dimension of which has to be consistently defined[28]. Also the sign of the exponent in the

---

[26]Note that, in contrast to the Fourier transformation for the physical fields c^+ and c, introduced in Eqs. (4.32), the prefactor $\frac{1}{\beta}$ in Eqs. (4.40) is now assigned to the inverse Fourier transform. Hence, the source fields $\eta_{\mathbf{k}\sigma}^+(\nu)$ and $\eta_{\mathbf{k}\sigma}(\nu)$ in Fourier space exhibit the same physical dimension as the source fields in real space $\eta_{i\sigma}^+(\tau)$ and $\eta_{i\sigma}(\tau)$, namely that of an energy (eV). This is also consistent with the definition of the Fourier transform of the n-particle Green's function in Eq. (2.35b), which should have dimension of $(eV)^{-2n}$ when considering the $2n$-frequency object $\widetilde{G}_{n,i_1\ldots i_{2n}}(\nu_1,\ldots,\nu_{2n})$, Eq. (2.35b), which can be directly obtained from a functional derivative of Z with respect to the Fourier transformed source fields $\eta_{i_j}^{(+)}(\nu_j)$. The corresponding $2n-1$-frequency object, defined in Eq. (2.58), exhibits of course a physical dimension of $(eV)^{-2n+1}$.

[27]There is no factor $\frac{1}{\beta}$ in the second line of Eq. (4.41) since the Fourier transform of the fields η^+ and η is defined without such factor [see Eqs. (4.40)] in contrast to the Fourier transform of the physical fields c^+ and c [see Eqs. (4.32)].

[28]There is only a requirement concerning the dimension of the complex-valued function $B_{\mathbf{k}\sigma}(\nu)$ and the Grassman variable $\widetilde{c}^{(+)}$, namely, that all terms in the exponent of Eq. (4.42) must be dimensionless. This condition is fulfilled if $[B] = [\widetilde{c}^{(+)}]^{-1}$. For instance, if $[\widetilde{c}^{(+)}] = (eV)^{-1}$ as for the Grassmann fields of the real electrons in frequency and momentum representation one has that $[B] = eV$.

first exponential function under the integral is not unambiguously defined ($\pm [\Delta(\nu) - \varepsilon_{\mathbf{k}}]$), since - when expanding the exponential function - the Grassmann integral over the first order term vanishes, while the relevant zeroth- and second-order contributions do not depend on the sign of the exponent. Following the convention of Ref. [36], we choose the plus-sign for this term which is the opposite convention of the dual fermion literature, where the Hubbard-Stratonovich (HS) fields $\widetilde{c}^{(+)}$ are typically labeled $f^{(+)}$ [34].Let us also remark that one can obtain Eq. (4.42) also by means the so-called *covariation splitting formula* [219] rather than a HS transformation, as it is explicitly discussed in Appendix D.

Rewriting $Z[\eta^+, \eta]$ in Eq. (4.41) by applying the Hubbard Stratonovich decoupling in Eq. (4.42) yields:

$$Z[\eta^+, \eta] = \left(\prod_{\nu, \mathbf{k}, \sigma} [B_{\mathbf{k}\sigma}(\nu)]^{-2} \right) \int D[c^+, c] D[\widetilde{c}^+, \widetilde{c}] \, \exp \left\{ -\sum_i \mathcal{S}_{\text{AIM}}[c_i^+, c_i] + \right.$$

$$+ \sum_{\nu, \mathbf{k}, \sigma} \frac{1}{\sqrt{\beta}} [\Delta(\nu) - \varepsilon_{\mathbf{k}}]^{\frac{1}{2}} B_{\mathbf{k}\sigma}(\nu) \left[c_{\mathbf{k}\sigma}^+(\nu)\widetilde{c}_{\mathbf{k}\sigma}(\nu) + \widetilde{c}_{\mathbf{k}\sigma}^+(\nu)c_{\mathbf{k}\sigma}(\nu) \right] +$$

$$\left. - \sum_{\nu, \mathbf{k}, \sigma} [B_{\mathbf{k}\sigma}(\nu)]^2 \widetilde{c}_{\mathbf{k}\sigma}^+(\nu)\widetilde{c}_{\mathbf{k}\sigma}(\nu) + \sum_{\nu, \mathbf{k}, \sigma} \left[c_{\mathbf{k}\sigma}^+(\nu)\eta_{\mathbf{k}\sigma}(\nu) + \eta_{\mathbf{k}\sigma}^+(\nu)c_{\mathbf{k}\sigma}(\nu) \right] \right\}. \quad (4.43)$$

It turns out convenient to choose $B_{\mathbf{k}\sigma}(\nu)$ as[29]

$$B_{\mathbf{k}\sigma}(\nu) = b_\sigma(\nu) [\Delta(\nu) - \varepsilon_{\mathbf{k}}]^{-\frac{1}{2}}, \quad (4.44)$$

since, in this way, the $\mathbf{k}$-integration in the second line of Eq. (4.43) is eliminated in favor of a summation over all lattice sites due to Parseval's theorem, which allows us to combine the contribution

$$\sum_{\nu, \mathbf{k}, \sigma} [\Delta(\nu) - \varepsilon_{\mathbf{k}}]^{\frac{1}{2}} B_{\mathbf{k}\sigma}(\nu) \left[c_{\mathbf{k}\sigma}^+(\nu)\widetilde{c}_{\mathbf{k}\sigma}(\nu) + \widetilde{c}_{\mathbf{k}\sigma}^+(\nu)c_{\mathbf{k}\sigma}(\nu) \right] = \sum_{\nu, i, \sigma} b_\sigma(\nu) \left[c_{i\sigma}^+(\nu)\widetilde{c}_{i\sigma}(\nu) + \widetilde{c}_{i\sigma}^+(\nu)c_{i\sigma}(\nu) \right],$$

$$(4.45)$$

in Eq. (4.43) with $\mathcal{S}_{\text{AIM}}[c_i^+, c_i]$, leading to the following expression for the generating func-

---

[29]$[b] = (\text{eV})^{\frac{1}{2}}[B] = (\text{eV})^{\frac{1}{2}} \left[\widetilde{c}^{(+)} \right]^{-1}$.

tional:

$$Z[\eta^+,\eta] = \widetilde{Z} \int D[\widetilde{c}^+,\widetilde{c}] \ \exp\left\{-\sum_{\nu,\mathbf{k},\sigma}[B_{\mathbf{k}\sigma}(\nu)]^2 \, \widetilde{c}^+_{\mathbf{k}\sigma}(\nu)\widetilde{c}_{\mathbf{k}\sigma}(\nu)\right\} \times$$

$$\times \prod_i \int D[c_i^+,c_i] \ \exp\left\{-\mathcal{S}_{\mathrm{AIM}}[c_i^+,c_i] + \right.$$

$$\left. + \sum_{\nu,\sigma} c_{i\sigma}^+(\nu)\left[\frac{1}{\sqrt{\beta}}b_\sigma(\nu)\widetilde{c}_{i\sigma}(\nu) + \eta_{i\sigma}(\nu)\right] + \left[\frac{1}{\sqrt{\beta}}b_\sigma(\nu)\widetilde{c}^+_{i\sigma}(\nu) + \eta^+_{i\sigma}(\nu)\right]c_{i\sigma}(\nu)\right\},$$

$$(4.46)$$

where $\widetilde{Z} = \left(\prod_{\nu,\mathbf{k},\sigma}[B_{\mathbf{k}\sigma}(\nu)]^{-2}\right)$. The last two lines of Eq. (4.46) can be now identified as the generating functional for the local Green's functions of the AIM at the lattice site i, i.e., $Z_{\mathrm{AIM}}[\widetilde{\eta}_i^+,\widetilde{\eta}_i]$:

$$Z_{\mathrm{AIM}}[\widetilde{\eta}_i^+,\widetilde{\eta}_i] = \int D[c_i^+,c_i]\exp\left\{-\mathcal{S}_{\mathrm{AIM}}[c_i^+,c_i] + \sum_{\nu,\sigma}c_{i\sigma}^+(\nu)\widetilde{\eta}_{i\sigma}(\nu) + \widetilde{\eta}_{i\sigma}^+(\nu)c_{i\sigma}(\nu)\right\}, \quad (4.47)$$

with $\widetilde{\eta}_{i\sigma}^+(\nu) = \beta^{-\frac{1}{2}}b_\sigma(\nu)\widetilde{c}_{i\sigma}^+(\nu) - \eta_{i\sigma}^+(\nu)$ and $\widetilde{\eta}_{i\sigma}(\nu) = \beta^{-\frac{1}{2}}b_\sigma(\nu)\widetilde{c}_{i\sigma}(\nu) + \eta_{i\sigma}(\nu)$. Hence, rewriting the generating functional of the Hubbard model of Eq. (4.46) in terms of the corresponding one for the AIM yields[30]:

$$Z[\eta^+,\eta] = \widetilde{Z}\int D[\widetilde{c}^+,\widetilde{c}] \ \exp\left\{-\sum_{\nu,\mathbf{k},\sigma}[B_{\mathbf{k}\sigma}(\nu)]^2 \, \widetilde{c}^+_{\mathbf{k}\sigma}(\nu)\widetilde{c}_{\mathbf{k}\sigma}(\nu)\right\} \times$$

$$\times \prod_i Z_{\mathrm{AIM}}[\beta^{-\frac{1}{2}}b\widetilde{c}_i^+ + \eta_i^+, \beta^{-\frac{1}{2}}b\widetilde{c}_i + \eta_i] =$$

$$= \widetilde{Z}\int D[\widetilde{c}^+,\widetilde{c}] \ \exp\left\{-\sum_{\nu,\mathbf{k},\sigma}[B_{\mathbf{k}\sigma}(\nu)]^2 \, \widetilde{c}^+_{\mathbf{k}\sigma}(\nu)\widetilde{c}_{\mathbf{k}\sigma}(\nu) + \right.$$

$$\left. + \sum_i W_{\mathrm{AIM}}[\underbrace{\beta^{-\frac{1}{2}}b\widetilde{c}_i^+ + \eta_i^+}_{\widetilde{\eta}_i^+}, \underbrace{\beta^{-\frac{1}{2}}b\widetilde{c}_i + \eta_i}_{\widetilde{\eta}_i}]\right\},$$

$$(4.48)$$

---

[30]Let us remark that the prefactor $\widetilde{Z} = \sum_{\nu,\mathbf{k},\sigma}[B_{\mathbf{k}\sigma}(\nu)]^{-2}$ in Eq. (4.48) is irrelevant, and, hence, can be neglected, for the calculation of the (connected) n-particle Green's functions, which requires only derivatives of the logarithm of $Z[\eta^+,\eta]$ with respect to the fermionic source fields η^+ and η on which $\widetilde{Z}$ does not depend.

where $W_{\mathrm{AIM}} = \ln Z_{\mathrm{AIM}}$ is the generating functional for the connected Green's function of the AIM. By expanding W_{AIM} in Eq. (4.48) in terms of $\widetilde{\eta}_i^+$ and $\widetilde{\eta}_i$ one can see that the new fields $\widetilde{c}^+$ and $\widetilde{c}$, which represent the nonlocal degrees of freedom of the system, are interacting via the local one-, two- and more-particle connected local Green's (or vertex) functions of the AIM. The latter are generated by integrating out the original fermions locally. Differently from the usual HS decoupling of the interaction term [33], here the integral over the original (physical) fields c_i^+ and c_i is *not* Gaussian, since $\mathcal{S}_{\mathrm{AIM}}$ contains an interaction term. Hence, it can not be performed analytically. However, this Grassmann integration corresponds to calculating the one-, two- and more-particle Green's functions for the AIM, for which a numerical solution is possible.

Hence, considering the DMFT solution for the AIM, i.e., the AIM which is determined self-consistently by the DMFT procedure discussed in chapter 3 (Sec. 3.1), the formalism derived above might serve as a starting point for a "perturbative" expansion of the one-particle Green's function of the Hubbard model around the DMFT solution, aiming at a systematic inclusion of nonlocal correlations beyond the local ones of DMFT. In the following two sections, we will discuss two possible methods to do so: (i) We will recall the DF approach and analyze possible problems caused by the inclusion of *one-particle reducible* contributions to the vertex functions in the interaction term [W_{AIM} in Eq. (4.48)]. (ii) We will discuss a new method based on a Legendre transform of W_{AIM}, leading to the generating functional for *one-particle irreducible* (1PI) n-particle local Green's (or, more precisely, vertex) functions. The latter are introduced to overcome the above-mentioned problems in the DF theory due to one-particle reducible vertices.

Let us stress, that, in the following, the DF theory will be discussed in a non-standard way (compared to the corresponding literature) within the framework of generating functionals introduced above, because this allows for a more direct comparison with the newly developed 1PI approach. The advantage of the presented formalism is constituted in the fact, that all Green's functions for the original (physical) fields c^+ and c can be obtained by just calculating the derivative(s) of $Z[\eta^+, \eta]$ with respect to the source fields η^+ and η, independent from all transformations performed for the original functional integral in Eq. (4.35).

4.4.1   Dual Fermion approach

The dual fermion (DF) method was introduced in 2008 by Rubtsov *et al.* [34] as a diagrammatic extension of DMFT based on the functional integral description of the lattice Green's functions. Its basic idea is the splitting of local and nonlocal degrees of freedom

of the Hubbard model by means of an appropriate Hubbard-Stratonovich transformation, similar to that introduced in the previous section in Eq. (4.42). In this way the original lattice electrons c^+ and c are replaced by so-called dual fermions f^+ and f (corresponding to $\widetilde{c}^+$ and $\widetilde{c}$ of the previous section), which interact via the local vertex functions of an auxiliary AIM, e.g., that connected with the DMFT solution of the Hubbard model. These dual particles are already dressed with all local correlation effects of the DMFT and, hence, a perturbation theory in these dual fields adopts DMFT (or another local AIM) as starting point for a perturbative calculation of the Green's functions of the system. In this respect, DF perfectly fits into the general scheme of diagrammatic extensions of DMFT discussed in Sec. 4.1.2. DF has already been applied to improve the DMFT results in several cases, among which is, e.g., the two-dimensional Hubbard model. For this system, DF yields, at the one-particle level, pseudogap-behavior [34, 220] and Fermi-arcs [221] and, at the two-particle level, lattice susceptibilities [222, 223] and second-order phase transitions [35, 123, 195, 224]. In more recent works, DF was used for analyzing non-equilibrium problems [225] and has been also combined with DCA and the parquet formalism, making a first step in the direction of multi-scale methods [142, 193] (see Sec. 4.1.1). In this section, we will, however, focus on some specific aspect and limitation of this method, which serves as a guideline for possible extensions and improvements. Specifically, our considerations will lead to the development of a new approach, based on the one-particle irreducible (1PI) functional, which will be introduced in Sec. 4.4.2. A good starting point for our analysis is a (non-standard) derivation of the dual fermion theory within the framework of the functional integral formalism and the generating functional method developed in the previous section.

Specifically, we can begin by considering Eq. (4.48) and introducing a shift of the fields $\widetilde{c}^+$ and $\widetilde{c}$ in order to get rid of the source fields η^+ and η in the local AIM part of the generating functional:

$$\widetilde{c}^+ = \widetilde{c}'^+ - \sqrt{\beta}b^{-1}\eta^+, \qquad\qquad \widetilde{c} = \widetilde{c}' - \sqrt{\beta}b^{-1}\eta, \qquad\qquad (4.49)$$

where we suppressed all arguments of both the Grassmann fields (i.e., ν, i, σ) and the function b (i.e., ν, σ). For the sake of a better readability we relabel the new variables as $\widetilde{c}'^+ \to \widetilde{c}^+$ and $\widetilde{c}' \to \widetilde{c}$ and obtain the following equation for the generating functional $Z[\eta^+, \eta]$ for the

Green's functions of the Hubbard model:

$$Z[\eta^+, \eta] = \widetilde{Z} \int D[\widetilde{c}^+, \widetilde{c}] \exp \left\{ -\sum_{\nu, \mathbf{k}, \sigma} [B_{\mathbf{k}\sigma}(\nu)]^2 \left[\widetilde{c}_{\mathbf{k}\sigma}^+(\nu) - \sqrt{\beta} b_\sigma^{-1}(\nu) \eta_{\mathbf{k}\sigma}^+(\nu) \right] \times \right.$$
$$\left. \times \left[\widetilde{c}_{\mathbf{k}\sigma}(\nu) - \sqrt{\beta} b_\sigma^{-1}(\nu) \eta_{\mathbf{k}\sigma}(\nu) \right] + \sum_i W_{\mathrm{AIM}}[\beta^{-\frac{1}{2}} b\widetilde{c}_i^+, \beta^{-\frac{1}{2}} b\widetilde{c}_i] \right\}. \tag{4.50}$$

Aiming at an interpretation of this equation, we consider $\eta^+ = \eta \equiv 0$ for which Eq. (4.50) corresponds just to the partition function Z of the Hubbard model. This can be then expressed as $Z = \widetilde{Z} Z_d$, whereupon Z_d is given by the Grassmann integral

$$Z_d = \int D[\widetilde{c}^+, \widetilde{c}] e^{-\mathcal{S}_d[\widetilde{c}^+, \widetilde{c}]}, \tag{4.51}$$

and the dual action $\mathcal{S}_d$ reads as:

$$\mathcal{S}_d[\widetilde{c}^+, \widetilde{c}] = \sum_{\nu, \mathbf{k}, \sigma} [B_{\mathbf{k}\sigma}(\nu)]^2 \widetilde{c}_{\mathbf{k}\sigma}^+(\nu) \widetilde{c}_{\mathbf{k}\sigma}(\nu) - \sum_i W_{\mathrm{AIM}}[\beta^{-\frac{1}{2}} b\widetilde{c}_i^+, \beta^{-\frac{1}{2}} b\widetilde{c}_i]. \tag{4.52}$$

For a better treatment and physical understanding of the "new" particles, i.e., of the "dual fermions", $\widetilde{c}^{(+)}$ arising in Eqs. (4.50), (4.51) and (4.52), we divide the dual action into a "non-interacting" part which is quadratic in $\widetilde{c}^+$ and $\widetilde{c}$ and a remainder, the interacting part, which is of higher (fourth, sixth and, in principle, all) orders in these fields. Since the generating functional W_{AIM} still contains a non-interacting contribution, i.e., one which is quadratic in $\widetilde{c}^+$ and $\widetilde{c}$, it is useful to (Taylor-) expand it with respect to its arguments $\beta^{-\frac{1}{2}} b\widetilde{c}_i^+$ and $\beta^{-\frac{1}{2}} b\widetilde{c}_i$, yielding:

$$W_{\mathrm{AIM}}[b\widetilde{c}_i^+, b\widetilde{c}_i] = \ln Z_{\mathrm{AIM}}[b\widetilde{c}_i^+, b\widetilde{c}_i] = \ln \underbrace{Z_{\mathrm{AIM}}[0, 0]}_{Z_{\mathrm{AIM}}} +$$

$$+ \sum_{\substack{\nu_1 \nu_2 \\ \sigma_1 \sigma_2}} \underbrace{\frac{1}{Z_{\mathrm{AIM}}} \frac{\delta^2 Z_{\mathrm{AIM}}[\widetilde{\eta}_i^+, \widetilde{\eta}_i]}{\delta \widetilde{\eta}_{\sigma_2}^+(\nu_2) \delta \widetilde{\eta}_{\sigma_1}(\nu_1)} \Bigg|_{\widetilde{\eta}^+ = 0, \widetilde{\eta} = 0}}_{\beta G_{\mathrm{loc}}(\nu_1) \delta_{\nu_1 \nu_2} \delta_{\sigma_1 \sigma_2}, \, [(4.36), (4.38), (4.47)]} \left[\beta^{-\frac{1}{2}} b\widetilde{c}_{i\sigma_1}(\nu_1) \right] \left[\beta^{-\frac{1}{2}} b\widetilde{c}_{i\sigma_2}^+(\nu_2) \right] +$$

$$+ \frac{1}{4} \sum_{\substack{\nu_1 \ldots \nu_4 \\ \sigma_1 \ldots \sigma_4}} G_{2, \mathrm{loc}, \sigma_1 \ldots \sigma_4}^c(\nu_1, \ldots, \nu_4) \left[\beta^{-\frac{1}{2}} b\widetilde{c}_{i\sigma_1}(\nu_1) \right] \left[\beta^{-\frac{1}{2}} b\widetilde{c}_{i\sigma_2}^+(\nu_2) \right] \left[\beta^{-\frac{1}{2}} b\widetilde{c}_{i\sigma_3}(\nu_3) \right] \left[\beta^{-\frac{1}{2}} b\widetilde{c}_{i\sigma_4}^+(\nu_4) \right] +$$

$$+ \ldots, \tag{4.53}$$

where ... denotes sixth- and higher-order contributions in the fields $\widetilde{c}^+$ and $\widetilde{c}$. The connected
two-particle Green's function $G^c_{2,\text{loc}}$ reads as:

$$G^c_{2,\text{loc},\sigma_1\ldots\sigma_4}(\nu_1,\ldots,\nu_4) = G_{2,\text{loc},\sigma_1\ldots\sigma_4}(\nu_1,\ldots,\nu_4)+$$
$$- G_{1,\text{loc},\sigma_1\sigma_2}(\nu_1,\nu_2)G_{1,\text{loc},\sigma_3\sigma_4}(\nu_3,\nu_4) + G_{1,\text{loc},\sigma_1\sigma_4}(\nu_1,\nu_4)G_{1,\text{loc},\sigma_2\sigma_3}(\nu_2,\nu_3).$$
$$(4.54)$$

One can see in Eq. (4.53) that the quartic part of W_{AIM} is given by the local two-particle
connected Green's function which is equivalent to the local vertex function *with* outer legs,
i.e.,

$$G^c_{2,\text{loc},\sigma\sigma\sigma'\sigma'}(\nu,\nu+\omega,\nu'+\omega',\nu') = -\beta\delta_{\omega\omega'}G_{\text{loc}}(\nu)G_{\text{loc}}(\nu+\omega)F^{\nu\nu'\omega}_{\text{loc},\sigma\sigma'}G_{\text{loc}}(\nu'+\omega)G_{\text{loc}}(\nu'),$$
$$(4.55a)$$

$$G^c_{2,\text{loc},\sigma\sigma'\sigma\sigma'}(\nu,\nu+\omega,\nu'+\omega',\nu') = -\beta\delta_{\omega\omega'}G_{\text{loc}}(\nu)G_{\text{loc}}(\nu+\omega)F^{\nu\nu'\omega}_{\text{loc},\overline{\sigma\sigma'}}G_{\text{loc}}(\nu'+\omega)G_{\text{loc}}(\nu'),$$
$$(4.55b)$$

according to the definitions of the vertex function F_{loc} in chapter 2, taking into account all
symmetries of the AIM [see Eqs. (2.57), (2.58) and (2.149) for the frequency conventions, Eqs.
(2.73) and (2.74) for the spin dependence, and Eq. (2.159) and Fig. 2.8 for the definition of
the vertex function F_{loc} in Eqs. (4.55)]. G_{loc} denotes the interacting (local) Green's function
of the AIM, defined by the hybridization function $\Delta(\nu)$.

Since it is generally preferable to work with pure vertex functions without outer legs [F_{loc}, in
the case of the two-particle contribution to W_{AIM} in Eq. (4.53)] rather than the connected
two-particle Green's functions $G^c_{2,\text{loc}}$, one chooses $b_\sigma(\nu)$ as the inverse of the full (interacting)
one-particle Green's function of the (local) AIM, i.e.:

$$b_\sigma(\nu) = \sqrt{\frac{1}{\beta}}[G_{\text{loc}}(\nu)]^{-1} = \sqrt{\frac{1}{\beta}}[i\nu - \Delta(\nu) + \mu - \Sigma_{\text{loc}}(\nu)], \qquad (4.56)$$

where $\Sigma_{\text{loc}}(\nu)$ denotes the self-energy of the AIM[31]. In this way all outer legs of the connected
two-particle Green's function will be amputated, which, of course, holds also for the three-
and more-particle connected Green's functions occurring in a further expansion of W_{AIM}.
Moreover, let us point out, that for the choice of b made in Eq. (4.56), $\widetilde{c}^+$ and $\widetilde{c}$ coincide
with the definition of the so-called *dual fermions* f^+ and f of the literature [34].

---

[31]The additional factor $\beta^{-\frac{1}{2}}$ in Eq. (4.56) provides for the correct physical dimension of b, namely, $[b] =$
$(\text{eV})^{\frac{3}{2}}$ (see the discussion in footnotes 28 and 29).

Taking into account Eq. (4.56), one can rewrite the generating functional for the connected Green's function of the AIM, W_{AIM} [Eq. (4.53)], in the following way:

$$W_{\mathrm{AIM}}[b\widetilde{c}_i^+, b\widetilde{c}_i] = \ln Z_{\mathrm{AIM}} - \frac{1}{\beta}\sum_{\nu,\sigma}[G_{\mathrm{loc}}(\nu)]^{-1}\widetilde{c}_{i\sigma}^+(\nu)\widetilde{c}_{i\sigma}(\nu)+$$

$$-\frac{1}{2}\frac{1}{\beta^3}\sum_{\nu\nu'\omega}\sum_{\sigma\sigma'}\left(1-\frac{1}{2}\delta_{\sigma\sigma'}\right)F_{\mathrm{loc},\sigma\sigma'}^{\nu\nu'\omega}\,\widetilde{c}_{i\sigma}^+(\nu)\widetilde{c}_{i\sigma}(\nu+\omega)\widetilde{c}_{i\sigma}^+(\nu'+\omega)\widetilde{c}_{i\sigma'}(\nu') + \ldots,$$

$$\tag{4.57}$$

where the time-reversal symmetry for the vertex function F_{loc} has been used ($F_{\mathrm{loc},\sigma\sigma'}^{\nu\nu'\omega} = F_{\mathrm{loc},\sigma'\sigma}^{\nu'\nu\omega}$, see also Tab. 2.2). Next, we insert relation (4.57) into the expression for the generating functional of the lattice Green's function [Eq. (4.50)]. In order to obtain the Gaussian part with respect to the *dual fermions* $\widetilde{c}^+$ and $\widetilde{c}$, we combine the quadratic term from W_{AIM} in Eq. (4.57) with the corresponding quadratic contribution, explicitly appearing in Eq. (4.50), whereupon B and b are defined in Eqs. (4.44) and (4.56), respectively:

$$-\left\{[B_{\mathbf{k}\sigma}(\nu)]^2 + [b_\sigma(\nu)]^2\,G_{\mathrm{loc}}(\nu)\right\}\widetilde{c}_{\mathbf{k}\sigma}^+(\nu)\widetilde{c}_{\mathbf{k}\sigma}(\nu) =$$

$$= -\frac{1}{\beta}G_{\mathrm{loc}}^{-1}(\nu)\left[(\Delta(\nu)-\varepsilon_{\mathbf{k}})^{-1} + G_{\mathrm{loc}}(\nu)\right]G_{\mathrm{loc}}^{-1}(\nu)\,\widetilde{c}_{\mathbf{k}\sigma}^+(\nu)\widetilde{c}_{\mathbf{k}\sigma}(\nu) =$$

$$= \frac{1}{\beta}\Bigg[\underbrace{\frac{1}{i\nu - \varepsilon_{\mathbf{k}} + \mu - \Sigma_{\mathrm{loc}}(\nu)}}_{G_{\mathrm{DMFT}}(\nu,\mathbf{k})} - G_{\mathrm{loc}}(\nu)\Bigg]^{-1}\widetilde{c}_{\mathbf{k}\sigma}^+(\nu)\widetilde{c}_{\mathbf{k}\sigma}(\nu), \tag{4.58}$$

where $G_{\mathrm{DMFT}}(\nu,\mathbf{k})$ denotes an approximate Green's function for the Hubbard model, constructed with the bare dispersion of the lattice ($\varepsilon_{\mathbf{k}}$) and the local self-energy of the AIM [$\Sigma_{\mathrm{loc}}(\nu)$]. In fact, $G_{\mathrm{DMFT}}(\nu,\mathbf{k})$ formally corresponds to the definition of the DMFT Green's function in chapter 3, Eq. (3.7), if the respective AIM is self-consistently connected to the DMFT solution of the Hubbard Hamiltonian (see Sec. 3.1). However, in DF, the local AIM does *not need to* coincide with the corresponding DMFT solution of the Hubbard model. That is, the hybridization function $\Delta(\nu)$, which uniquely defines the AIM (besides the Hubbard interaction U), is not necessarily determined within a DMFT self-consistency cycle. Nevertheless, the AIM connected with the DMFT solution of the lattice system can be considered as a reasonable starting point for a DF calculation, since in this case all purely local correlations are already included in the Gaussian part of the dual action. In this respect DMFT can be seen as a convenient zeroth-order perturbative approximation for the DF approach, as it has been discussed for general diagrammatic extensions of DMFT in Sec.

4.1.2.

Inserting the expansion of W_{AIM}, obtained in Eq. (4.57), into the expression for the generating functional of the Hubbard model, stated in Eq. (4.50), gives, in consideration of Eq. (4.58), rise to the following relation:

$$Z[\eta^+, \eta] = \widetilde{Z} \int D[\widetilde{c}^+, \widetilde{c}] \exp \left\{ \frac{1}{\beta} \sum_{\nu, \mathbf{k}, \sigma} [G_{\text{DMFT}}(\nu, \mathbf{k}) - G_{\text{loc}}(\nu)]^{-1} \widetilde{c}_{\mathbf{k}\sigma}^+(\nu) \widetilde{c}_{\mathbf{k}\sigma}(\nu) + \sum_i V_{\text{AIM}}[\widetilde{c}_i^+, \widetilde{c}_i] + \right.$$

$$+ \sum_{\nu, \mathbf{k}, \sigma} [\Delta(\nu) - \varepsilon_{\mathbf{k}}]^{-1} G_{\text{loc}}^{-1}(\nu) \left[\eta_{\mathbf{k}\sigma}^+(\nu) \widetilde{c}_{\mathbf{k}\sigma}(\nu) + \widetilde{c}_{\mathbf{k}\sigma}^+(\nu) \eta_{\mathbf{k}\sigma}(\nu) \right]$$

$$\left. - \beta \sum_{\nu, \mathbf{k}, \sigma} [\Delta(\nu) - \varepsilon_{\mathbf{k}}]^{-1} \eta_{\mathbf{k}\sigma}^+(\nu) \eta_{\mathbf{k}\sigma}(\nu) + \sum_i \ln Z_{\text{AIM}} \right\}, \quad (4.59)$$

where the effective interaction $V_{\text{AIM}}[\widetilde{c}_i^+, \widetilde{c}_i]$ between the dual particles is defined, according to Eq. (4.57), as:

$$V_{\text{AIM}}[\widetilde{c}_i^+, \widetilde{c}_i] = -\frac{1}{2} \frac{1}{\beta^3} \sum_{\nu\nu'\omega} \sum_{\sigma\sigma'} \left(1 - \frac{1}{2}\delta_{\sigma\sigma'} \right) F_{\text{loc},\sigma\sigma'}^{\nu\nu'\omega} \; \widetilde{c}_{i\sigma}^+(\nu) \widetilde{c}_{i\sigma}(\nu + \omega) \widetilde{c}_{i\sigma}^+(\nu' + \omega) \widetilde{c}_{i\sigma'}(\nu') + \dots .$$

$$(4.60)$$

Note that the contributions to V_{AIM}, which are of sixth and higher orders in the dual fields $\widetilde{c}^+$ and $\widetilde{c}$, have been neglected, as in the typical DF implementations [see, e.g., Ref. [34] as well as the corresponding discussions in Sec. 4.1.2 and after Eq. (4.63)][32]. Considering the definition of the dual partition function and the dual action in Eqs. (4.51) and (4.52), respectively, motivates the introduction of the *dual Green's functions*, formally analogously to the Green's function for the lattice electrons [Eq. (4.28)]:

$$G_{n,i_1 \dots i_{2n}}^d (\nu_1, \dots, \nu_{2n}) = \frac{1}{Z_d} \int D[\widetilde{c}^+, \widetilde{c}] e^{-\mathcal{S}_d[\widetilde{c}^+, \widetilde{c}]} \; \widetilde{c}_{i_1}^+(\nu_1) \dots \widetilde{c}_{i_{2n}}(\nu_{2n}), \quad (4.61)$$

where $Z_d = Z/\widetilde{Z}$, and the dual action $\mathcal{S}_d$ can be represented using the corresponding effective interaction[33]:

$$\mathcal{S}_d[\widetilde{c}^+, \widetilde{c}] = -\frac{1}{\beta} \sum_{\nu, \mathbf{k}, \sigma} \underbrace{\left[G_{\text{DMFT}}(\nu, \mathbf{k}) - G_{\text{loc}}(\nu) \right]^{-1}}_{G_0^d(\nu, \mathbf{k})} \widetilde{c}_{\mathbf{k}\sigma}^+(\nu) \widetilde{c}_{\mathbf{k}\sigma}(\nu) - \sum_i V_{\text{AIM}}[\widetilde{c}_i^+, \widetilde{c}_i] - \sum_i \ln Z_{\text{AIM}}.$$

$$(4.62)$$

---

[32]To the best of our knowledge, the only DF calculation taking into account the local three-particle vertex has been reported in Ref. [123].

[33]The last contribution $\sum_i \ln Z_{\text{AIM}}$ is just a constant not depending on the fields $\widetilde{c}^+$ and $\widetilde{c}$ and can be neglected, since it drops out in calculations of Green's functions.

a)

b)

$$G_0^d = G_{\mathrm{DMFT}} - G_{\mathrm{loc}}$$

$\gamma_{\mathrm{loc}}^{(4)} = F_{\mathrm{loc}}$

$\gamma_{\mathrm{loc}}^{(6)}$

$\cdots$
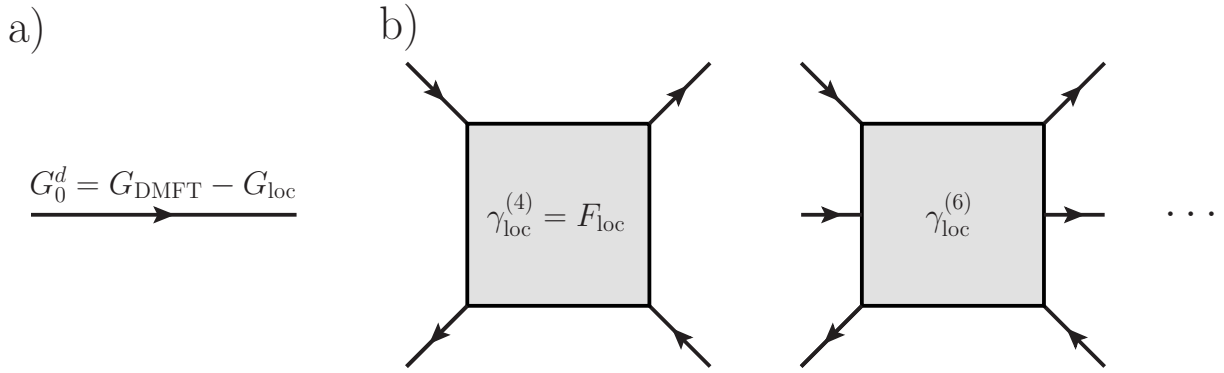
Figure 4.19: Diagrammatic elements of the DF approach: a) The bare propagator of DF is given by the purely *nonlocal* Green's function; b) The interaction part of DF is represented by the local (connected) *n*-particle vertex function $\gamma_{\mathrm{loc}}^{(2n)}$.

 The free dual propagator, i.e., the dual one-particle Green's function for $V_{\mathrm{AIM}} = 0$, G_0^d, is given by the difference $G_{\mathrm{DMFT}} - G_{\mathrm{loc}}$. Hence, if starting from the AIM connected with the DMFT solution of the Hubbard model, the **k**-summation over this bare dual Green's function vanishes because of the DMFT self-consistency condition, justifying the denotation as *purely nonlocal* for this quantity. The dual fermions $\widetilde{c}^+$ and $\widetilde{c}$ are interacting via the effective potential V_{AIM}, Eq. (4.60), which is built from the two- and more-particle local vertex functions of the corresponding AIM. Since these vertices are frequency-dependent, the interaction between the dual fermions is explicitly *nonlocal* in time in contrast to the bare Hubbard interaction U between the original fermions. On the other hand, the dual potential V_{AIM} remains purely local in space, as the original interaction.

We are now in a position to perform diagrammatic perturbation theory for the dual one-particle Green's function $G^d(\nu, \mathbf{k})$ defined in the most general way in Eq. (4.61). The basic diagrammatic elements, i.e., the bare dual Green's function $G_0^d(\nu, \mathbf{k}) = G_{\mathrm{DMFT}}(\nu, \mathbf{k}) - G_{\mathrm{loc}}(\nu)$ and (parts of) the interaction $V_{\mathrm{AIM}}[\widetilde{c}^+, \widetilde{c}]$ between the dual particles, are depicted graphically in Fig. 4.19. Let us remark once again that these diagrammatic bricks of DF fit well into the general scheme for diagrammatic extensions of DMFT discussed in Sec. 4.1.2, as one can also infer from comparing Figs. 4.5 and 4.19. As usual we will construct diagrammatic corrections not directly for the dual Green's function $G^d(\nu, \mathbf{k})$ but for its one-particle irreducible part, i.e., the dual self-energy $\Sigma^d(\nu, \mathbf{k})$ which is defined by the (dual) Dyson equation:

$$\Sigma^d(\nu, \mathbf{k}) = [G_0^d(\nu, \mathbf{k})]^{-1} - [G^d(\nu, \mathbf{k})]^{-1}. \tag{4.63}$$

For practical calculations of the dual self-energy one has to make further simplifications. As

a)   b)
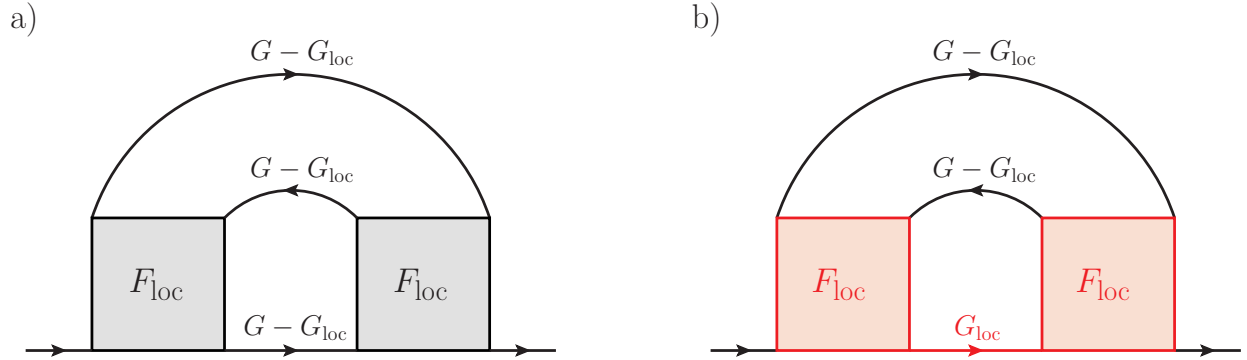
Figure 4.20: a) DF second-order diagram constructed from the local two-particle vertex function only. The figure is readapted from Ref. [36]. b) DF first order diagram constructed from the one-particle reducible part of the three-particle vertex (marked in red). $G \equiv G_{\mathrm{DMFT}}$ for the sake of a better readability.

for general diagrammatic extensions of DMFT, discussed in Sec. 4.1.2, two different types of approximations are involved: *First*, one usually restricts oneself to the two-particle vertex $\gamma_{\mathrm{loc}}^{(2)} = F_{\mathrm{loc}}$ in the interaction part of the dual action [see Eqs. (4.60) and (4.62) as well as Fig. 4.19], since three- and more particle local vertex functions are extremely difficult to calculate numerically. *Secondly*, for the moment, we will discuss only the typical DF implementations, which take into account low-order or ladder diagrams for the perturbation series in the dual space[34]. In Fig. 4.20a we show a second-order diagram for the dual self-energy restricting ourselves to the two-particle vertex function F_{loc}. The Green's functions connecting the vertices are purely nonlocal according to Eq. (4.62) and Fig. 4.19a, i.e., $\sum_{\mathbf{k}} G_0^d(\nu, \mathbf{k}) = 0$. Let us point out that in specific parameter regimes already this second-order (in F_{loc}) diagram for the dual self-energy provides remarkably nonlocal corrections to the local DMFT self-energy[35], which are reported for the two-dimensional half-filled Hubbard model on a square-lattice (with only nearest-neighbor hopping), e.g., in Ref. [221] and Fig. 4.21. More sophisticated implementations of DF, including also ladder diagrams, are even able to describe also the pseudopgap behavior at low U (i.e., $U = 1.0$) [35], not present in the second-order results from Ref. [221] (see Fig. 4.21).

However, despite its successful application for describing nonlocal correlations in the Hubbard model, there are some problematic aspects in DF. In particular, we refer here to a publication [226], that has recently pointed out possible problems arising from the inclusion of *one-particle*

---

[34]We will not consider here the more cumbersome parquet-based approximations in DF, whose first application has been recently reported in Ref. [142].

[35]Note that the dual self-energy has to be transformed to the corresponding self-energy for the real electrons by means of Eq. (4.65), as it will be discussed in detail below.

Im Σ_k
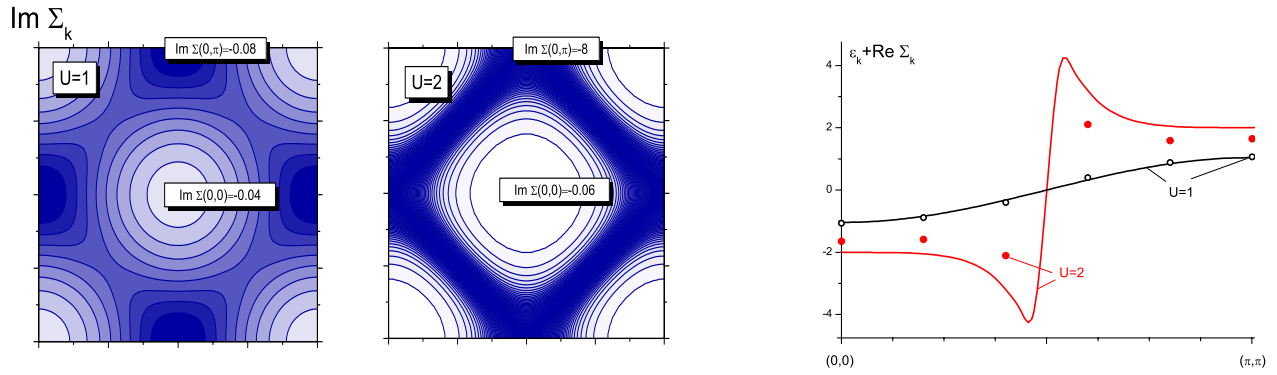
Figure 4.21: Momentum dependent self-energy at the Fermi energy (i.e., $\omega = 0$), obtained within the DF approach, adopting the second-order diagram in Fig. 4.20a. Data are shown at $\beta = 20.0$ and $U = 1.0$ and $U = 2.0$, respectively ($4t \equiv 1.0$). Left panel: Contour plots for Im$\Sigma(\omega = 0, \mathbf{k})$. Right panel: Renormalized dispersion $\varepsilon_{\mathbf{k}} + \text{Re}\Sigma(\omega = 0, \mathbf{k})$, compared with reference data for a 10×10 lattice. The figure is reproduced from Ref. [221].

reducible contributions to the local vertex functions, which represent the interaction between the dual particles. To clarify this, let us first consider the diagram depicted in Fig. 4.20b where one of the nonlocal Green's functions is replaced by a purely local one. This diagram yields an even larger contribution to the dual self-energy than that from Fig. 4.20a, since $G - G_{\text{loc}}$ is smaller than G_{loc} (when the internal $\mathbf{k}$-summation is performed) due to the DMFT self-consistency condition. However, since G_{loc} is not a building element of the dual fermion theory (see Fig. 4.19), the diagram shown in Fig. 4.20b is not included in the typical implementation of DF, where one takes into account only two-particle local vertices as interaction between the dual particles. Indeed, the red part of this diagram represents the *one-particle reducible* contribution to the three-particle vertex, and, hence, this diagram constitutes a correction to the dual self-energy which is of first order in this three-particle vertex. However, numerical calculations including the three-particle vertex are usually not feasible, and, hence, the (rather large) diagrammatic contribution from Fig. 4.20 is usually neglected in standard DF calculations.

On the other hand, the one-particle reducible part of the three- (and also the more-) particle vertex functions gives rise to a further problem: The third-order diagram depicted in Fig. 4.22 contains (besides two two-particle vertex functions F) the *one-particle reducible* contribution to the local three-particle vertex. In terms of real electrons such a diagram would generate a one-particle reducible contribution to the self-energy of the original electrons. This is obviously in contradiction to the definition of the electronic self-energy as *one-particle irreducible* part of the one-particle Green's function. However, with respect to

the dual action given in Eq. (4.62) and the diagrammatic element of DF in Fig. 4.19, respectively, the diagram in Fig. 4.22 is not one-particle reducible since G_{loc} is not present in the perturbation theory for the dual fermions. This contradiction between the real and dual space can be clarified by considering explicitly the transformation between the corresponding Green's functions and self-energies of these two formulations. To this end we simply calculate the (second) derivative of the generating functional $W[\eta^+, \eta] = \ln Z[\eta^+, \eta]$, with $Z[\eta^+, \eta]$ given in Eq. (4.59), with respect to the source fields η^+ and η [see Eq. (4.39)] and consider the definition of the dual Green's function G^d in Eq. (4.61). The result for the one-particle Green's function reads:

$$G(\nu, \mathbf{k}) = G_{\mathrm{loc}}^{-2}(\nu)[\Delta(\nu) - \varepsilon_{\mathbf{k}}]^{-2} G^d(\nu, \mathbf{k}) + [\Delta(\nu) - \varepsilon_{\mathbf{k}}]^{-1}. \qquad (4.64)$$

From this relation one can easily derive the corresponding, exact, relation between the lattice and the dual self-energy which reads:

$$\Sigma_{\mathrm{DF}}(\nu, \mathbf{k}) = \Sigma_{\mathrm{loc}}(\nu) + \frac{\Sigma^d(\nu, \mathbf{k})}{1 + G_{\mathrm{loc}}(\nu)\Sigma^d(\nu, \mathbf{k})}, \qquad (4.65)$$

where $\Sigma_{\mathrm{loc}}(\nu)$ is the self-energy of the AIM. Expanding the denominator in Eq. (4.65) leads to the following expression for the real self-energy:

$$\Sigma_{\mathrm{DF}}(\nu, \mathbf{k}) = \Sigma_{\mathrm{loc}}(\nu) + \Sigma^d(\nu, \mathbf{k}) - \textcolor{red}{\Sigma^d(\nu, \mathbf{k})G_{\mathrm{loc}}(\nu)\Sigma^d(\nu, \mathbf{k})} + \dots. \qquad (4.66)$$

Considering the second-order diagram in Fig. 4.20a for Σ^d in Eq. (4.66), the red term in this equation is exactly equivalent to the diagrammatic contribution stemming from the one-particle reducible vertex depicted in Fig. 4.22. Since these two terms exhibit a different sign they cancel each other, avoiding in this way any one-particle reducible contributions to the real self-energy. One can demonstrate that this exact cancellation works order per order if one considers all diagrams of the theory (i.e., the exact solution). However, when restricting oneself to the local two-particle vertex functions, as in the standard implementations of DF, the term which should be canceled by the transformation formula, Eq. (4.65), is not present in the perturbative expansion of the dual self-energy, and, hence, applying this transformation *introduces* rather than cancels such spurious one-particle reducible contributions in the real self-energy.

Summing up, one can assert that the problems of the DF approach, illustrated in Figs. 4.20 and 4.22 and discussed above, are generated by the *one-particle reducible* contributions to
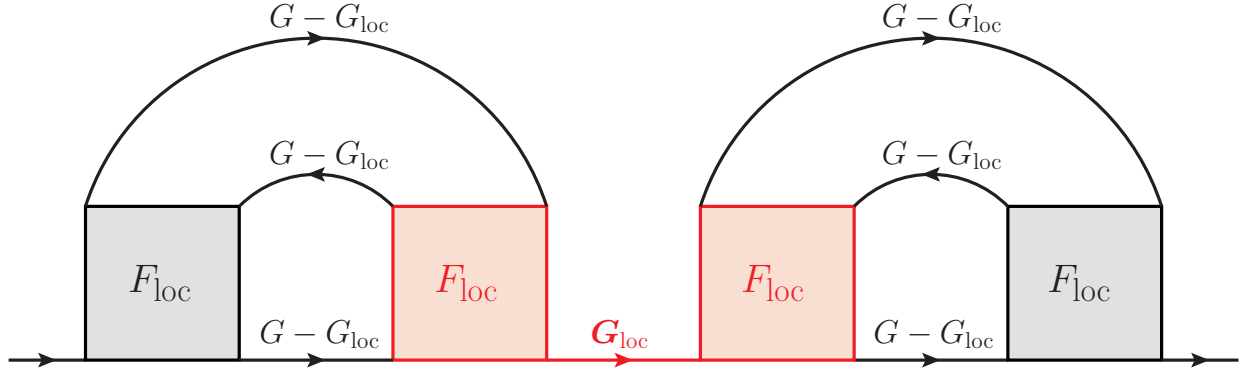
Figure 4.22: Perturbative correction constructed from the one-particle reducible contribution of the local three-particle vertex (red part of the diagram) which gives rise to a reducible contribution to the real self-energy (i.e., the self-energy of the original degrees of freedom). The figure is readapted from Ref. [36].

the three- (and more-) particle vertex functions. Hence, a method which avoids, from the very beginning, the generation of these vertex functions is desirable, aiming at a more concise formulation of the perturbation theory in the dual space. A possible realization of such a method will discussed in the next section.

4.4.2   The one-particle irreducible (1PI) approach

In order to overcome the specific difficulties arising in the DF implementations (perturbative and/or ladder) due to the reducible parts of the local three- and more-particle vertex functions, we aim at a complete elimination of such terms in the perturbative expansion of the self-energy. To this end we consider the Legendre transformation of the generating functional W_{AIM}, discussed in Eqs. (4.47), (4.53) and (4.57):

$$W_{\mathrm{AIM}}[\widetilde{\eta}_i^+, \widetilde{\eta}_i] = \Gamma_{\mathrm{AIM}}[\phi_i^+, \phi_i] - \sum_{\nu,\sigma} \left[\widetilde{\eta}_{i\sigma}^+(\nu)\phi_{i\sigma}(\nu) + \phi_{i\sigma}^+(\nu)\widetilde{\eta}_{i\sigma}(\nu) \right], \qquad (4.67)$$

where the fields ϕ^+ and ϕ will be defined as:

$$\phi_{i\sigma}^+(\nu) = \frac{\delta W_{\mathrm{AIM}}[\widetilde{\eta}_i^+, \widetilde{\eta}_i]}{\delta \widetilde{\eta}_{i\sigma}(\nu)}, \qquad\qquad \phi_{i\sigma}(\nu) = -\frac{\delta W_{\mathrm{AIM}}[\widetilde{\eta}_i^+, \widetilde{\eta}_i]}{\delta \widetilde{\eta}_{i\sigma}^+(\nu)}. \qquad (4.68)$$

The inverse Legendre transformation is given by:

$$\widetilde{\eta}_{i\sigma}^{+}(\nu) = -\frac{\delta\Gamma_{\text{AIM}}[\phi_i^+,\phi_i]}{\delta\phi_{i\sigma}(\nu)}, \qquad\qquad \widetilde{\eta}_{i\sigma}(\nu) = \frac{\delta\Gamma_{\text{AIM}}[\phi_i^+,\phi_i]}{\delta\phi_{i\sigma}^+(\nu)}. \tag{4.69}$$

Let us stress that in Eq. (4.68) ϕ_i^+ and ϕ_i are functionals of the fields $\widetilde{\eta}_i^+$ and $\widetilde{\eta}_i$ [and vice versa for the inverse Legendre transform in Eq. (4.69)][36].

The functional Γ_{AIM} generates the local *one-particle irreducible* (amputated) vertex functions of the AIM [32]. Hence, working with this functional precludes from the beginning the appearance of one-particle reducible contributions in the three- and more-particle vertex functions, which led to the specific problems of DF discussed at the end of the previous section (Sec. 4.4.1). Expanding Γ_{AIM} with respect to ϕ_i^+ and ϕ_i up to the fourth order in these fields yields [32]:

$$\Gamma_{\text{AIM}}[\phi_i^+,\phi_i] = W_{\text{AIM}}[0,0] + \frac{1}{\beta}\sum_{\nu,\sigma}[G_{\text{loc}}(\nu)]^{-1}\phi_{i\sigma}^+(\nu)\phi_{i\sigma}(\nu)+$$

$$- \frac{1}{2}\frac{1}{\beta^3}\sum_{\nu\nu'\omega}\sum_{\sigma\sigma'}\left(1 - \frac{1}{2}\delta_{\sigma\sigma'}\right)F_{\text{loc},\sigma\sigma'}^{\nu\nu'\omega}\phi_{i\sigma}^+(\nu)\phi_{i\sigma}(\nu+\omega)\phi_{i\sigma'}^+(\nu'+\omega)\phi_{i\sigma'}(\nu') + \ldots, \tag{4.70}$$

where ... denotes sixth- and higher-order terms in the fields ϕ_i^+ and ϕ_i, the coefficients of which correspond to the local *one-particle irreducible* (1PI) amputated three- and more particle vertex functions. As a side remark, let us mention that $W_{\text{AIM}}[0,0] = \ln Z_{\text{AIM}}$, as in Eq. (4.53), is in any case just a constant which is not relevant for the calculation of the Green's functions. Comparing the expansion of Γ_{AIM} in Eq. (4.70) with the corresponding one for the functional W_{AIM} in Eqs. (4.53) and (4.57), one observes that the fourth-order (two-particle) terms are equivalent for both functionals, if one chooses $b \propto [G_{\text{loc}}]^{-1}$ in W_{AIM}, as in Eq. (4.56). The reason for this equivalence is founded in the topological structure of the connected two-particle Green's (or vertex) function, discussed in chapter 2, Fig. 2.9: at the two-particle level the full vertex F coincides with the one-particle irreducible one.

Moreover, choosing $b \propto [G_{\text{loc}}]^{-1}$ as in Eq. (4.56) renders also the second-order (one-particle) term of W_{AIM} identical to the corresponding one of Γ_{AIM}, except for a different sign. Let us stress that the amputated Green's functions, i.e., the vertex functions, appear in W_{AIM} *only* for the specific choice of b as in Eq. (4.56), while for Γ_{AIM} the amputation of the outer legs

---

[36]It should be also noted that the fields ϕ_i^+ and ϕ_i (as a function of the Matsubara frequency) exhibit the dimension of an inverse energy, i.e., $(\text{eV})^{-1}$, so that the second term on the right-hand side of Eq. (4.67) becomes dimensionless.

(one-particle Green's functions) is performed by the Legendre transform itself, and, hence, b can be chosen arbitrarily[37].

While the expansion coefficients of W_{AIM} and Γ_{AIM} are equivalent up to the fourth order (two-particle level) in $\widetilde{c}^+/\widetilde{c}$ and ϕ^+/ϕ, respectively (except for a sign in the quadratic term), they become different in their sixth- and higher-order contributions. In fact, the corresponding three- and more-particle vertex functions, which constitute these expansion coefficients, are the full connected ones for W_{AIM} (employed in DF), while –per construction– only their one-particle irreducible counterparts contribute to the Taylor series of Γ_{AIM}. For instance, the three-particle diagram depicted in Fig. 2.9c is contained in the sixth-order term of W_{AIM} but not in Γ_{AIM}, since it is one-particle reducible. Similar examples can be given also for higher-order terms in the expansion of W_{AIM} and Γ_{AIM}, respectively.

Returning to the explicit calculations, we insert the Legendre transform of W_{AIM}, Eq. (4.67), into the expression for the generating functional of the Hubbard model, Eq. (4.50). Since b is arbitrary now, we make the simplest choice which is consistent with the dimensionality requirement in footnotes 29 and 37, i.e., $b = \beta^{-\frac{3}{2}}$. Furthermore, considering Eq. (4.50), $\widetilde{\eta}_i^+$ and $\widetilde{\eta}_i$ are given as:

$$\widetilde{\eta}_{i\sigma}^+(\nu) = \beta^{-2}\widetilde{c}_{i\sigma}^+(\nu), \qquad\qquad \widetilde{\eta}_{i\sigma}(\nu) = \beta^{-2}\widetilde{c}_{i\sigma}(\nu), \qquad\qquad (4.71)$$

and, hence, the generating functional in Eq. (4.50) can be rewritten in the following form:

$$Z[\eta^+, \eta] = \widetilde{Z} \int D[\widetilde{c}^+, \widetilde{c}] \exp\left\{ -\frac{1}{\beta^3} \sum_{\nu,\mathbf{k},\sigma} [\Delta(\nu) - \varepsilon_{\mathbf{k}}]^{-1} \left[\widetilde{c}_{\mathbf{k}\sigma}^+(\nu) - \beta^2\eta_{\mathbf{k}\sigma}^+(\nu)\right] \left[\widetilde{c}_{\mathbf{k}\sigma}(\nu) - \beta^2\eta_{\mathbf{k}\sigma}(\nu)\right] + \right.$$

$$\left. + \sum_i \left(\Gamma_{\text{AIM}}[\phi_i^+, \phi_i] - \frac{1}{\beta^2} \sum_{\nu,\sigma} \left[\widetilde{c}_{i\sigma}^+(\nu)\phi_{i\sigma}(\nu) + \phi_{i\sigma}^+(\nu)\widetilde{c}_{i\sigma}(\nu)\right] \right) \right\}.$$

$$(4.72)$$

Note, that ϕ_i^+ and ϕ_i are functionals of $\widetilde{c}_i^+$ and $\widetilde{c}_i$ or, more precisely, of $\widetilde{\eta}_i^+ = \beta^{-2}\widetilde{c}_i^+$ and $\widetilde{\eta}_i = \beta^{-2}\widetilde{c}_i$, which are defined by Eqs. (4.68). Since Γ_{AIM} depends on ϕ_i^+ and ϕ_i, it is convenient to rewrite the functional integral in Eq. (4.72) in terms of an integration over ϕ_i^+ and ϕ_i instead of $\widetilde{c}_i^+$ and $\widetilde{c}_i$. For this purpose, we use the explicit expressions for $\widetilde{c}_i^+ = \beta^2\widetilde{\eta}_i^+$

---

[37]One just has to make sure that b exhibits the correct dimension as discussed in footnote 29, i.e., $[b] = (\text{eV})^{\frac{3}{2}}$.

and $\widetilde{c}_i = \beta^2 \widetilde{\eta}_i$ in Eqs. (4.69), i.e., the inverse Legendre transformation:

$$\widetilde{c}_{i\sigma}^+(\nu) = -\beta^2 \frac{\delta\Gamma_{\mathrm{AIM}}[\phi_i^+, \phi_i]}{\delta\phi_{i\sigma}(\nu)}, \qquad\qquad \widetilde{c}_{i\sigma}(\nu) = \beta^2 \frac{\delta\Gamma_{\mathrm{AIM}}[\phi_i^+, \phi_i]}{\delta\phi_{i\sigma}^+(\nu)}, \qquad (4.73)$$

between the variables $\widetilde{c}^+/\widetilde{c}$ and ϕ^+/ϕ in Eq. (4.72). Obviously, a transformation of the integration variables in a Grassmann integral requires the multiplication of the integrand with the *inverse* of the determinant of the Jacobian of this transformation [32, 33]. However, while one usually deals with linear transformations, where the Jacobian is just a matrix of ordinary complex numbers, in our case we are concerned with a non-linear transformation: $\delta\Gamma_{\mathrm{AIM}}/\delta\phi_i^+$ and $\delta\Gamma_{\mathrm{AIM}}/\delta\phi_i$ are not just linear functions of ϕ_i^+ and ϕ_i but contain terms of arbitrary order in these fields. Specifically, the Jacobian matrix $M[\phi_i^+, \phi_i]$ corresponding to the variable transformation in Eq. (4.73) reads as:

$$D\begin{pmatrix} \widetilde{c}_{i\sigma}^+(\nu) \\ \widetilde{c}_{i\sigma}(\nu) \end{pmatrix} = \sum_{\nu',\sigma'} \beta^2 \underbrace{\begin{pmatrix} -\frac{\delta^2\Gamma_{\mathrm{AIM}}}{\delta\phi_{i\sigma'}^+(\nu')\delta\phi_{i\sigma}(\nu)} & -\frac{\delta^2\Gamma_{\mathrm{AIM}}}{\delta\phi_{i\sigma'}(\nu')\delta\phi_{i\sigma}(\nu)} \\ \frac{\delta^2\Gamma_{\mathrm{AIM}}}{\delta\phi_{i\sigma'}^+(\nu')\delta\phi_{i\sigma}^+(\nu)} & \frac{\delta^2\Gamma_{\mathrm{AIM}}}{\delta\phi_{i\sigma'}(\nu')\delta\phi_{i\sigma}^+(\nu)} \end{pmatrix}}_{M[\phi_i^+, \phi_i]} D\begin{pmatrix} \phi_{i\sigma'}^+(\nu') \\ \phi_{i\sigma'}(\nu') \end{pmatrix}. \qquad (4.74)$$

Hence, the transformation $(\widetilde{c}^+, \widetilde{c}) \Rightarrow (\phi^+, \phi)$ (for all lattice sites i) leads to the additional contribution:

$$\prod_i \det\left(M[\phi_i^+, \phi_i]\right)^{-1} = \exp\left\{ -\sum_i \ln\det M[\phi_i^+, \phi_i] \right\}, \qquad (4.75)$$

in the integrand of Eq. (4.72). The determinant of the matrix M is taken with respect to the ν and σ indices of the fields ϕ^+ and ϕ.

In order to obtain the functional integral for $Z[\eta^+, \eta]$ in terms of ϕ^+ and ϕ we insert Eqs. (4.73), (4.74) and (4.75) into Eq. (4.72), which yields:

$$Z[\eta^+, \eta] = \widetilde{Z} \int D[\phi^+, \phi] \times$$

$$\times \exp\left\{ -\beta \sum_{\nu,\mathbf{k},\sigma} \left[\frac{\delta\Gamma_{\mathrm{AIM}}[\phi^+, \phi]}{\delta\phi_{\mathbf{k}\sigma}(\nu)} + \eta_{\mathbf{k}\sigma}^+(\nu) \right] \left[\Delta(\nu) - \varepsilon_{\mathbf{k}}\right]^{-1} \left[-\frac{\delta\Gamma_{\mathrm{AIM}}[\phi^+, \phi]}{\delta\phi_{\mathbf{k}\sigma}^+(\nu)} + \eta_{\mathbf{k}\sigma}(\nu) \right] + \right.$$

$$\left. + \sum_i \left[\Gamma_{\mathrm{AIM}}[\phi_i^+, \phi_i] + \sum_{\nu,\sigma} \frac{\delta\Gamma_{\mathrm{AIM}}[\phi_i^+, \phi_i]}{\delta\phi_{i\sigma}(\nu)} \phi_{i\sigma}(\nu) - \phi_{i\sigma}^+(\nu) \frac{\delta\Gamma_{\mathrm{AIM}}[\phi_i^+, \phi_i]}{\delta\phi_{i\sigma}^+(\nu)} - \ln\det M[\phi_i^+, \phi_i] \right] \right\},$$

$$(4.76)$$

where $\delta\Gamma_{\mathrm{AIM}}[\phi^+, \phi]/\delta\phi_{\mathbf{k}\sigma}(\nu)$ and $\delta\Gamma_{\mathrm{AIM}}[\phi^+, \phi]/\delta\phi_{\mathbf{k}\sigma}^+(\nu)$ are defined as the Fourier transforma-

tion of Eqs. (4.73) with respect to the spatial degrees of freedom [see, e.g., Eq. (4.32) and the discussion below this equation].

In the next step, we have to calculate the first and second derivatives of Γ_{AIM} with respect to ϕ^+ and ϕ from Eq. (4.70) and insert them into Eq. (4.76). For this purpose, we restrict ourselves to terms up to the fourth order (in ϕ^+ and ϕ) in the expansion of $\Gamma_{\mathrm{AIM}}[\phi^+, \phi]$ in Eq. (4.70), i.e., to two-particle vertex functions. Hence, we neglect all terms which are of sixth and higher orders in ϕ^+ and ϕ, the expansion coefficients of which are given by the *one-particle irreducible* three- and more-particle vertex functions. Let us recall that this represents one of the (two) typical approximation in the framework of diagrammatic extensions of DMFT, as it has been already outlined in the general introduction about diagrammatic methods in Sec. 4.1.2.

Before entering into the details of the calculations, let us discuss (schematically) the diagrammatic structure of the terms in the second line of Eq. (4.76). We can identify a part proportional to $(\delta_\phi \Gamma_{\mathrm{AIM}})(\delta_{\phi^+} \Gamma_{\mathrm{AIM}})$ (where $\delta_{\phi^{(+)}}$ denotes the functional derivative with respect to the field $\phi^{(+)}$). If one evaluates now this contribution by inserting the explicit expression for (the two-particle part of) Γ_{AIM} [Eq. (4.70)], one finds a term which is proportional to $(F_{\mathrm{loc}})^2 (\phi^+ \phi)^3$. Such contributions build up terms containing local one-particle *reducible* three- (and more)-particle vertices in the considered 1PI diagrammatics[38]. We note here that such contributions are absent in almost all numerical DF calculations, usually restricted to the level of two-particle local vertex functions for the interaction between the dual particles. In this respect, if not taking into account any self-consistency effects, it is clear that the 1PI-scheme allows for the inclusion of the largest possible number of diagrams at the ladder level, starting from a two-particle local vertex approximation.

In principle, one should now practically calculate the first and second derivatives of Γ_{AIM} with respect to ϕ^+ and ϕ, occurring in Eqs. (4.74) and (4.76), directly from Eq. (4.70) and insert them into the generating functional for the Hubbard model after the Legendre transformation [Eq. (4.76)]. However, this would lead (i) to rather complicated contributions up to the sixth order in ϕ^+ and ϕ (corresponding to the local one-particle reducible three-particle vertices), and (ii) to terms of the form $(\eta^+ \phi)(\phi^+ \phi)$, $(\phi^+ \eta)(\phi^+ \phi)$ and $\eta^+ \eta$ in the second line of this equation [(4.76)], which renders the connection between the real Green's function for the Hubbard model and the corresponding Green's functions for the new fields ϕ^+ and ϕ rather complicated[39]. In fact, since η^+ and η couple to terms of third order in ϕ^+ and ϕ, the second

---

[38]Consider, e.g., the one-particle reducible three-particle diagram, shown in Fig. 2.9c, which is clearly proportional to the "product" of two vertex functions F_{loc}, i.e., $\propto (F_{\mathrm{loc}})^2$.

[39]The term $\eta^+ \eta$ is also present in the DF approach [see Eq. (4.59)], and leads to the specific, well known,

functional derivative of Z with respect to η^+ and η in Eq. (4.76), would require the calculation of a three-particle Green's function for the fields ϕ^+ and ϕ ($\langle((\phi^+\phi)^3)\rangle$). Hence, it turns out convenient to first decouple the term which is quadratic in $\left(\pm\delta\Gamma_{\mathrm{AIM}}/\delta\phi^{(+)} - \eta^{(+)}\right)$ [i.e., the second line of Eq. (4.76)] by means of a further Hubbard-Stratonovich transformation [for a given set of quantum numbers $(\nu, \mathbf{k}, \sigma)$]. In order to keep the notation as simple and readable as possible, we now switch to a four-vector notation $k\widehat{=}(\nu, \mathbf{k})$ and $q\widehat{=}(\omega, \mathbf{q})$, already adopted in Sec. 4.3.1 [see Eq. (4.12) and below], for the frequency- and momentum arguments of the fields and the Green's functions and treat the frequency- and momentum-dependency separately only when explicitly needed (e.g., in the case of purely local quantities, which depend only on a frequency). Let us also recall that four-vectors denoted as k contain always a fermionic Matsubara frequencies while the vectors labeled as q exhibit a bosonic frequency. Adopting this convention the above-mentioned Hubbard-Stratonovich decoupling of the term in the second line of Eq. (4.76) is given by:

$$\exp\left\{-\beta\left[\Delta(\nu) - \varepsilon_{\mathbf{k}}\right]^{-1}\left[\frac{\delta\Gamma_{\mathrm{AIM}}[\phi^+, \phi]}{\delta\phi_{k\sigma}} + \eta_{k\sigma}^+\right]\left[-\frac{\delta\Gamma_{\mathrm{AIM}}[\phi^+, \phi]}{\delta\phi_{k\sigma}^+} + \eta_{k\sigma}\right]\right\} =$$

$$= -C^{-2}\int d\psi_{k\sigma}^+ d\psi_{k\sigma}\times$$

$$\times\exp\left\{\sqrt{\beta}\left[\Delta(\nu) - \varepsilon_{\mathbf{k}}\right]^{-\frac{1}{2}}C\left[\left(\frac{\delta\Gamma_{\mathrm{AIM}}}{\delta\phi_{k\sigma}} + \eta_{k\sigma}^+\right)\psi_{k\sigma} + \psi_{k\sigma}^+\left(-\frac{\delta\Gamma_{\mathrm{AIM}}}{\delta\phi_{k\sigma}^+} + \eta_{k\sigma}\right)\right]\right\}\times$$

$$\times\exp\left\{C^2\psi_{k\sigma}^+\psi_{k\sigma}\right\}, \tag{4.77}$$

where $C = C_{k\sigma} \in \mathbb{Z}$ is an arbitrary complex number depending on the variables ν, $\mathbf{k}$ and σ. In the light of the previous discussion of Eq. (4.76), it is useful to choose C as[40]:

$$C_{k\sigma} = \frac{1}{\sqrt{\beta}}\left[\Delta(\nu) - \varepsilon_{\mathbf{k}}\right]^{\frac{1}{2}}. \tag{4.78}$$

This eliminates the corresponding prefactor in the third line of Eq. (4.77), and, hence, the source fields η^+ and η, now coupled linearly to ψ^+ and ψ, do not exhibit any prefactor. However, this way, the fields ϕ^+ and ϕ are not coupled to these source fields anymore. In order to render the equations in a more symmetric form with respect to the fields ϕ^+/ϕ and

---

relation between the real and the dual Green's function and the corresponding self-energies, respectively [34, 221], see Eqs. (4.64) and (4.65).

[40]Similar as for ϕ^+ and ϕ, the fields ψ^+ and ψ have the physical dimension of an inverse energy, i.e., $[\psi^{(+)}] = (\mathrm{eV})^{-1}$. Hence, C must exhibit the dimension of an energy, i.e, $[C] = \mathrm{eV}$.

ψ^+/ψ we introduce the following linear shift of Grassmann variables

$$\psi_{k\sigma}^+ = \psi_{k\sigma}'^+ - \phi_{k\sigma}^+, \qquad\qquad \psi_{k\sigma} = \psi_{k\sigma}' - \phi_{k\sigma}, \qquad (4.79)$$

and insert it, together with the definition of $C = C_{k\sigma}$ in Eq. (4.78), into the Hubbard-Stratonovich decoupling [Eq. (4.77)], which yields:

$$\exp\left\{ -\beta\left[\Delta(\nu) - \varepsilon_\mathbf{k}\right]^{-1}\left[\frac{\delta\Gamma_{\text{AIM}}[\phi^+, \phi]}{\delta\phi_{k\sigma}} + \eta_{k\sigma}^+\right]\left[-\frac{\delta\Gamma_{\text{AIM}}[\phi^+, \phi]}{\delta\phi_{k\sigma}^+} + \eta_{k\sigma}\right]\right\} =$$

$$= -\beta\left[\Delta(\nu) - \varepsilon_\mathbf{k}\right]^{-1} \int d\psi_{k\sigma}^+ d\psi_{k\sigma} \times$$

$$\times \exp\left\{ \frac{1}{\beta}\left[\Delta(\nu) - \varepsilon_\mathbf{k}\right]\left(\psi_{k\sigma}^+ - \phi_{k\sigma}^+\right)\left(\psi_{k\sigma} - \phi_{k\sigma}\right)\right\} \times$$

$$\times \exp\left\{ \frac{\delta\Gamma_{\text{AIM}}}{\delta\phi_{k\sigma}}\left(\psi_{k\sigma} - \phi_{k\sigma}\right) - \left(\psi_{k\sigma}^+ - \phi_{k\sigma}^+\right)\frac{\delta\Gamma_{\text{AIM}}}{\delta\phi_{k\sigma}^+} + \eta_{k\sigma}^+\left(\psi_{k\sigma} - \phi_{k\sigma}\right) + \left(\psi_{k\sigma}^+ - \phi_{k\sigma}^+\right)\eta_{k\sigma}\right\},$$

$$(4.80)$$

where we have relabeled ψ'^+ and ψ' into ψ^+ and ψ for the sake of a better readability.

In the next step, we insert the identity (4.80) into the expression for the generating functional for the Hubbard model in Eq. (4.76). Since the sum over i in the third line of this equation can be rewritten in terms of a $\mathbf{k}$-sum, whereupon, $\sum_i \Gamma_{\text{AIM}}[\phi_i^+, \phi_i]$, in the four-vector notation, is given by:

$$\sum_i \Gamma_{\text{AIM}}[\phi_i^+, \phi_i] = \sum_i \ln Z_{\text{AIM}} + \frac{1}{\beta}\sum_{k,\sigma}[G_{\text{loc}}(\nu)]^{-1}\phi_{k\sigma}^+\phi_{k\sigma} +$$

$$- \frac{1}{2}\frac{1}{\beta^3}\sum_{kkq}\sum_{\sigma\sigma'}\left(1 - \frac{1}{2}\delta_{\sigma\sigma'}\right)F_{\text{loc},\sigma\sigma'}^{\nu\nu'\omega}\phi_{k\sigma}^+\phi_{(k+q)\sigma}\phi_{(k'+q)\sigma}^+\phi_{k'\sigma'} + \ldots \quad (4.81)$$

We can easily combine the terms from Eq. (4.80), inserted in the second line of Eq. (4.76), with the corresponding ones already present in the third line of this equation. First, one recognizes that the contributions $(\delta\Gamma_{\text{AIM}}/\delta\phi)\phi$ and $\phi^+(\delta\Gamma_{\text{AIM}}/\delta\phi^+)$ cancel. Furthermore, considering that

$$\Delta(\nu) - \varepsilon_\mathbf{k} = \underbrace{\left[i\nu + \mu - \varepsilon_\mathbf{k} - \Sigma_{\text{loc}}(\nu)\right]}_{G_{\text{DMFT}}^{-1}(k)} - \underbrace{\left[i\nu + \mu - \Delta(\nu) - \Sigma_{\text{loc}}(\nu)\right]}_{G_{\text{loc}}^{-1}(\nu)}, \qquad (4.82)$$

where $G_{\text{loc}}(\nu)$ and $\Sigma_{\text{loc}}(\nu)$ denote the local Green's function and self-energy of the AIM,

respectively, we arrive at the following expression for the generating functional of the Hubbard model[41]:

$$
Z[\eta^+,\eta] = \widetilde{Z}\overbrace{\prod_{k,\sigma}\{-\beta\left[\Delta(\nu)-\varepsilon_{\mathbf{k}}\right]\}}^{\Pi_{k,\sigma}\,\beta^4}\prod_i Z_{\mathrm{AIM}}\int D[\phi^+,\phi]D[\psi^+,\psi]\times
$$

$$
\times\exp\left\{\frac{1}{\beta}\sum_{k,\sigma}G_{\mathrm{DMFT}}^{-1}(k)\left(\phi_{k\sigma}^+\phi_{k\sigma}+\psi_{k\sigma}^+\phi_{k\sigma}+\phi_{k\sigma}^+\psi_{k\sigma}\right)+\left[G_{\mathrm{DMFT}}^{-1}(k)-G_{\mathrm{loc}}^{-1}(\nu)\right]\psi_{k\sigma}^+\psi_{k\sigma}+\right.
$$

$$
-\frac{1}{\beta^3}\sum_{kk'q}\sum_{\sigma\sigma'}\left(1-\frac{1}{2}\delta_{\sigma\sigma'}\right)F_{\mathrm{loc},\sigma\sigma'}^{\nu\nu'\omega}\left[\psi_{k\sigma}^+\phi_{(k+q)\sigma}\phi_{(k'+q)\sigma'}^+\phi_{k'\sigma'}+\phi_{k\sigma}^+\phi_{(k+q)\sigma}\phi_{(k'+q)\sigma'}^+\psi_{k'\sigma'}+\right.
$$

$$
\left.\left.+\frac{1}{2}\phi_{k\sigma}^+\phi_{(k+q)\sigma}\phi_{(k'+q)\sigma'}^+\phi_{k'\sigma'}\right]-\sum_i\ln\det M[\phi_i^+,\phi_i]+\sum_{k,\sigma}\eta_{k\sigma}^+\left(\psi_{k\sigma}+\phi_{k\sigma}\right)+\left(\psi_{k\sigma}^++\phi_{k\sigma}^+\right)\eta_{k\sigma}\right\}.
$$

$$(4.83)$$

Finally, we want to discuss the structure of the Jacobian $M[\phi_i^+,\phi_i]$. To this end we have to evaluate the second functional derivatives of Γ_{AIM} with respect to the fields ϕ_i^+ and ϕ_i as in Eq. (4.74). The corresponding expressions can be found in appendix E in real- and momentum space. Specifically, considering Eqs. (E.2) suggests to rewrite $M[\phi_i^+,\phi_i]$ in terms of the unit-matrix and a remainder which we will call $D[\phi_i^+,\phi_i]$:

$$
M[\phi_i^+,\phi_i] = \beta G_{\mathrm{loc}}^{-1}(\nu)\left\{\mathbb{1}+D[\phi_i^+,\phi_i]\right\},\tag{4.84}
$$

where $\mathbb{1}$ denotes the unit-matrix in frequency/spin space, i.e., $\mathbb{1}\sim\delta_{\nu\nu'}\delta_{\sigma\sigma'}$, whereupon $D[\phi_i^+,\phi_i]$ is given in appendix F. For further simplifications concerning the term containing $M[\phi_i^+,\phi_i]$ in Eq. (4.83) we consider the following general identity for the logarithm of the determinant of a matrix A:

$$
\ln\det A = \mathrm{tr}\ln A,\tag{4.85}
$$

which holds for any (diagonalizable) $n\times n$ matrix A (also for Grassmann numbers). The trace in Eq. (4.85) is taken with respect to the frequency- and spin variables for each lattice

---

[41]For convenience we also switch the sign of the fields ϕ^+ and ϕ, i.e., $\phi^+\to-\phi^+$ and $\phi\to-\phi$.

site i. Applying Eq. (4.85) to the Jacobian $M[\phi_i^+, \phi_i]$ in Eq. (4.84) yields[42]:

$$
\ln \det M[\phi_i^+, \phi_i] = \operatorname{tr} \ln \left[\beta G_{\text{loc}}^{-1}(\nu) \right] + \operatorname{tr} \ln \left(\mathbb{1} + D[\phi_i^+, \phi_i] \right) =
$$

$$
= \sum_{\nu, \sigma} \ln \left[\beta G_{\text{loc}}^{-1}(\nu) \right] + \operatorname{tr} \ln \left(\mathbb{1} + D[\phi_i^+, \phi_i] \right) =
$$

$$
= \ln Z_{\text{AIM}} + \operatorname{tr} \ln \left(\mathbb{1} + D[\phi_i^+, \phi_i] \right). \tag{4.86}
$$

Inserting this relation into the expression for the generating functional [Eq. (4.83)] leads to a cancellation of $\prod_i Z_{\text{AIM}}$ in the prefactor of the functional integral. Hence, we arrive at the final expression for the generating functional of the Hubbard model represented in the 1PI formalism:

$$
Z[\eta^+, \eta] = \prod_{k,\sigma} \beta^4 \int D[\phi^+, \phi] D[\psi^+, \psi] \times
$$

$$
\times \exp \left\{ \frac{1}{\beta} \sum_{k,\sigma} G_{\text{DMFT}}^{-1}(k) \left(\phi_{k\sigma}^+ \phi_{k\sigma} + \psi_{k\sigma}^+ \phi_{k\sigma} + \phi_{k\sigma}^+ \psi_{k\sigma} \right) + \left[G_{\text{DMFT}}^{-1}(k) - G_{\text{loc}}^{-1}(\nu) \right] \psi_{k\sigma}^+ \psi_{k\sigma} + \right.
$$

$$
- \frac{1}{\beta^3} \sum_{kk'q} \sum_{\sigma\sigma'} \left(1 - \frac{1}{2}\delta_{\sigma\sigma'} \right) F_{\text{loc},\sigma\sigma'}^{\nu\nu'\omega} \left[\psi_{k\sigma}^+ \phi_{(k+q)\sigma} \phi_{(k'+q)\sigma'}^+ \phi_{k'\sigma'} + \phi_{k\sigma}^+ \phi_{(k+q)\sigma} \phi_{(k'+q)\sigma'}^+ \psi_{k'\sigma'} + \right.
$$

$$
\left. + \frac{1}{2} \phi_{k\sigma}^+ \phi_{(k+q)\sigma} \phi_{(k'+q)\sigma'}^+ \phi_{k'\sigma'} \right] - \sum_i \operatorname{tr} \ln \left(\mathbb{1} + D[\phi_i^+, \phi_i] \right) + \sum_{k,\sigma} \eta_{k\sigma}^+ \left(\psi_{k\sigma} + \phi_{k\sigma} \right) + \left(\psi_{k\sigma}^+ + \phi_{k\sigma}^+ \right) \eta_{k\sigma} \right\}.
$$

$$
\tag{4.87}
$$

In order to connect the rather complicated (path-)integral transformations above with our original objective, i.e., the calculation of the one-particle Green's function $G(\nu, \mathbf{k})$ of the Hubbard model, we must evaluate the second functional derivative of $\ln Z[\eta^+, \eta]$ in Eq. (4.87) with respect to $\eta_{k\sigma}^+$ and $\eta_{k\sigma}$ for $\eta_{k\sigma}^+ = 0$ and $\eta_{k\sigma} = 0$, as it was was discussed at the beginning of this section about functional integral based methods in Eq. (4.39). Note that, in order to obtain the one-frequency and one-momentum object $G(\nu, \mathbf{k})$ we have to integrate the general one-particle Green's function in Eq. (4.39) over the second frequency and momentum argument, ν' and $\mathbf{k}'$, respectively:

$$
G(\nu, \mathbf{k}) = \frac{1}{\beta} \sum_{k',\sigma'} \frac{\delta^2 Z[\eta^+, \eta]}{\delta \eta_{k'\sigma'}^+ \delta \eta_{k\sigma}} \bigg|_{\eta_{k'\sigma'}^+ = 0, \eta_{k\sigma} = 0} = \frac{1}{\beta} \frac{\delta^2 Z[\eta^+, \eta]}{\delta \eta_{k\sigma}^+ \delta \eta_{k\sigma}} \bigg|_{\eta_{k\sigma}^+ = 0, \eta_{k\sigma} = 0}, \tag{4.88}
$$

---

[42]For the first summand on the right-hand side of Eq. (4.86) consider the general identities $\langle \hat{n} \rangle = \frac{1}{\beta} \frac{\partial \ln Z}{\partial \mu} = \frac{1}{\beta} \sum_{k,\sigma} G_k = \frac{1}{\beta} \operatorname{tr}(G)$ and $G = \frac{\partial}{\partial \mu} \ln \left(\beta G^{-1} \right)$.

whereupon the last equality, in principle, holds rigorously only for a finite system where the delta-function $(2\pi)^d \delta^{(d)}(\mathbf{k} - \mathbf{k}')$ becomes a Kronecker-delta $\delta_{\mathbf{kk}'}$, due to the discrete nature of the momentum arguments $\mathbf{k}$ in that case. Considering the 1PI representation for the generating functional $Z[\eta^+, \eta]$ in Eq. (4.87) for the calculation of the (real) one-particle Green's function in Eq. (4.88), $G(\nu, \mathbf{k})$ will be expressed as the sum of the four distinct one-particle 1PI Green's functions, given as propagators of the fields ϕ^+, ϕ, ψ^+ and ψ:

$$G(\nu, \mathbf{k}) = \frac{1}{\beta} \left[\langle \phi^+_{k\sigma} \phi_{k\sigma} \rangle + \langle \phi^+_{k\sigma} \psi_{k\sigma} \rangle + \langle \psi^+_{k\sigma} \phi_{k\sigma} \rangle + \langle \psi^+_{k\sigma} \psi_{k\sigma} \rangle \right] . \tag{4.89}$$

The averaging $\langle \cdot \rangle$ is performed using the action $\mathcal{S}^{1\text{PI}}[\phi^+, \phi, \psi^+, \psi]$ of the Hubbard model in the 1PI representation:

$$\langle \rho^+_{k\sigma} \xi_{k\sigma} \rangle := \prod_{k,\sigma} \beta^4 \int D[\phi^+, \phi] D[\psi^+, \psi] e^{-\mathcal{S}^{1\text{PI}}[\phi^+, \phi, \psi^+, \psi]} \rho^+_{k\sigma} \xi_{k\sigma}, \tag{4.90}$$

where $\rho = \phi, \psi$, and $\xi = \phi, \psi$. The action $\mathcal{S}^{1\text{PI}}$ of the 1PI approach can be easily extracted from the generating functional in Eq. (4.87). It is convenient to split it into a "non-interacting" (Gaussian) part and an "interacting part", i.e., $\mathcal{S}^{1\text{PI}} = \mathcal{S}^{1\text{PI}}_0 + \mathcal{S}^{1\text{PI}}_{\text{I}}$, with[43]

$$\mathcal{S}^{1\text{PI}}_0[\phi^+, \phi, \psi^+, \psi] = -\frac{1}{\beta} \sum_{k,\sigma} G_k^{-1} \left(\phi^+_{k\sigma} \phi_{k\sigma} + \psi^+_{k\sigma} \phi_{k\sigma} + \phi^+_{k\sigma} \psi_{k\sigma} \right) + \left[G_k^{-1} - G_{\text{loc},\nu}^{-1} \right] \psi^+_{k\sigma} \psi_{k\sigma}$$

$$\tag{4.91a}$$

$$\mathcal{S}^{1\text{PI}}_{\text{I}}[\phi^+, \phi, \psi^+, \psi] = \frac{1}{\beta^3} \sum_{kk'q} \sum_{\sigma\sigma'} \left(1 - \frac{1}{2}\delta_{\sigma\sigma'} \right) F^{\nu\nu'\omega}_{\text{loc},\sigma\sigma'} \left[\frac{1}{2} \phi^+_{k\sigma} \phi_{(k+q)\sigma} \phi^+_{(k'+q)\sigma'} \phi_{k'\sigma'} + \right.$$

$$\left. + \psi^+_{k\sigma} \phi_{(k+q)\sigma} \phi^+_{(k'+q)\sigma'} \phi_{k'\sigma'} + \phi^+_{k\sigma} \phi_{(k+q)\sigma} \phi^+_{(k'+q)\sigma'} \psi_{k'\sigma'} \right] + \sum_i \text{tr} \ln \left(\mathbb{1} + D[\phi^+_i, \phi_i] \right) .$$

$$\tag{4.91b}$$

For the sake of readability, we have also introduced a new notation for the DMFT and the local Green's function $[G_{\text{DMFT}}(\nu, \mathbf{k})$ and $G_{\text{loc}}(\nu)$, respectively] in Eqs. (4.91), writing the arguments of these two objects as subscripts and omitting the label "DMFT" in the DMFT

---

[43]Let us note that here the "interacting" part still contains a Gaussian contribution (i.e., a summand $\propto \phi^+ \phi$) via the term stemming from the Jacobian, $\sum_i \text{tr} \ln \left(\mathbb{1} + D[\phi^+_i, \phi_i] \right)$, see Eq. (F.4) in appendix F. However, since this term contains a local vertex function $F^{\nu\nu'\omega}_{\text{loc},\sigma\sigma'}$ we assign it to $\mathcal{S}^{1\text{PI}}_{\text{I}}$, so that $\mathcal{S}^{1\text{PI}}_0$ is defined as the action which results from setting $F^{\nu\nu'\omega}_{\text{loc},\sigma\sigma'} = 0$ in Eq. (4.87).

Green's function, i.e.,

$$G_{\text{loc},\nu} := G_{\text{loc}}(\nu), \qquad G_k := G_{\text{DMFT}}(\nu, \mathbf{k}) = \left[G_0^{-1}(\nu, \mathbf{k}) - \Sigma_{\text{DMFT}}(\nu) \right]^{-1}, \qquad (4.92)$$

while G written with its frequency- and momentum arguments, i.e., $G(\nu, \mathbf{k})$, as in Eq. (4.89), represents the (full) interacting one-particle Green's function of the Hubbard model (exhibiting, of course, a nonlocal self-energy). Since in the 1PI representation of the generating functional for the Hubbard model, one deals with two distinct fields, i.e., ϕ and ψ, it is convenient to combine them in the spinors Φ^+ and Φ which are defined as:

$$\Phi_{k\sigma}^+ = \begin{pmatrix} \phi_{k\sigma}^+ \\ \psi_{k\sigma}^+ \end{pmatrix}, \qquad\qquad \Phi_{k\sigma} = \begin{pmatrix} \phi_{k\sigma} & \psi_{k\sigma} \end{pmatrix}. \qquad (4.93)$$

Hence, the spinor Green's function $\mathbf{G}_{k\sigma} = \frac{1}{\beta} \langle \Phi_{k\sigma}^+ \Phi_{k\sigma} \rangle$, which we will refer to as 1PI Green's function in the following, is given by the 2×2-matrix:

$$\mathbf{G}_k = \frac{1}{\beta} \begin{pmatrix} \langle \phi_{k\sigma}^+ \phi_{k\sigma} \rangle & \langle \phi_{k\sigma}^+ \psi_{k\sigma} \rangle \\ \langle \psi_{k\sigma}^+ \phi_{k\sigma} \rangle & \langle \psi_{k\sigma}^+ \psi_{k\sigma} \rangle \end{pmatrix}, \qquad (4.94)$$

where the expectation values are defined as in Eq. (4.90). Note that the sum over all four components of the 1PI Green's function $\mathbf{G}_{k\sigma}$ yields the Green's function $G(\nu, \mathbf{k})$ of the Hubbard model, as one can easily see from Eqs. (4.89) and (4.94).

In the following we will discuss the 1PI action $\mathcal{S}^{\text{1PI}}[\phi^+, \phi, \psi^+, \psi]$ in Eqs. (4.91) and the corresponding 1PI Green's function $\mathbf{G}_{k\sigma}$ [Eq. (4.94)] in terms of a perturbative expansion in Feynman diagrams, aiming at a better physical understanding of the various contributions to $\mathcal{S}^{\text{1PI}}$ and components of $\mathbf{G}_k$, respectively. *First*, it is important to understand what is the "bare" 1PI Green's function, since this object constitutes one of the two basic bricks of diagrammatic perturbation theory (see Sec. 4.1.2). To this end we omit the interaction part of the action [Eq. (4.91b)] for the evaluation of the 1PI Green's function(s) in Eqs. (4.90) and (4.94), which corresponds to neglect the local vertex of the AIM, i.e., $F_{\text{loc},\sigma\sigma'}^{\nu\nu'\omega} = 0$. The corresponding "bare" expectation values for bilinear terms in the fields $\rho = \phi, \psi$ and $\xi = \phi, \psi$ are then calculated similar as in Eq. (4.90) but with the non-interacting action $\mathcal{S}_0^{\text{1PI}}$ instead the full interacting one, i.e.,

$$\langle \rho_{k\sigma}^+ \xi_{k\sigma} \rangle_0 := \prod_{k,\sigma} \beta^4 \int D[\phi^+, \phi] D[\psi^+, \psi] e^{-\mathcal{S}_0^{\text{1PI}}[\phi^+, \phi, \psi^+, \psi]} \rho_{k\sigma}^+ \xi_{k\sigma}. \qquad (4.95)$$
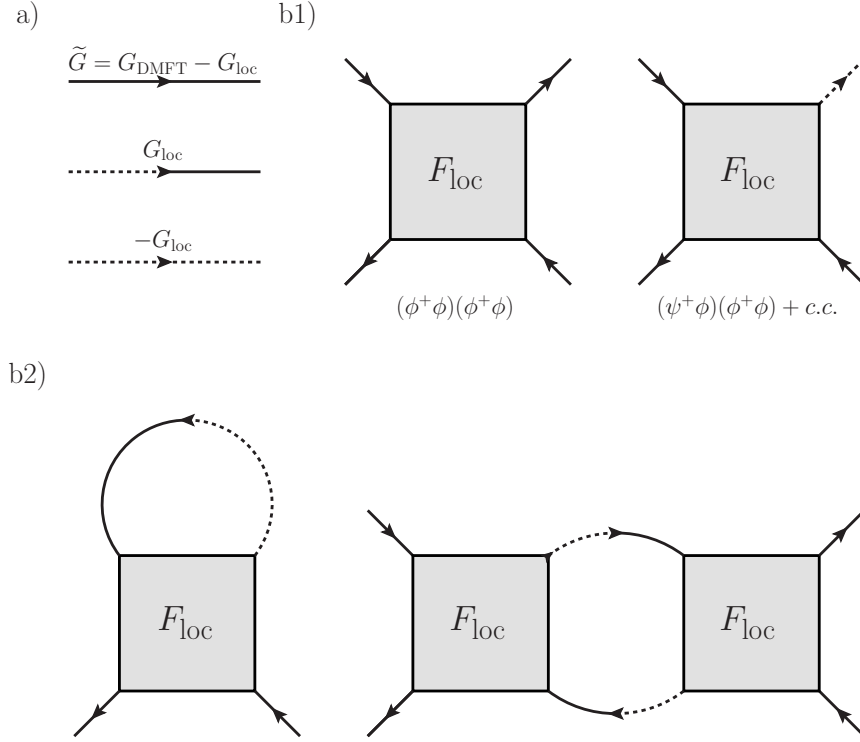
Figure 4.23: Diagrammatic elements of the 1PI approach: a) The bare propagator(s); b1) The interaction terms which are given by the local vertex function F_{loc} [to be multiplied with $\left(1 - \frac{1}{2}\delta_{\sigma\sigma'}\right)$, see Eqs. (4.87) and (4.91b)]; b2) Terms stemming from the Jacobian; The latter are given by combinations of local vertices F_{loc} and local Green's functions G_{loc}, providing for the cancellation of double-counted local contributions. The figure is readapted from Ref. [36].

Considering these definitions, the "bare" 1PI propagator(s) now read(s) as:

$$
\mathbf{G}_{0,k} = \frac{1}{\beta}\langle \Phi_{k\sigma}^+ \Phi_{k\sigma}\rangle_0 = \begin{pmatrix} G_k^{-1} & G_k^{-1} \\ G_k^{-1} & G_k^{-1} - G_{\text{loc},\nu}^{-1} \end{pmatrix}^{-1} = \begin{pmatrix} G_k - G_{\text{loc},\nu} & G_{\text{loc},\nu} \\ G_{\text{loc},\nu} & -G_{\text{loc},\nu} \end{pmatrix}. \quad (4.96)
$$

Summing up all matrix element, which yields the electronic Green's function of the lattice system in the corresponding approximation, shows that the zeroth order perturbation theory in the local vertex F_{loc}, i.e., $F_{\text{loc},\sigma\sigma'}^{\nu\nu'\omega} = 0$, just reproduces the DMFT Green's function $G_k = G_{\text{DMFT}}(\nu, \mathbf{k})$. Hence, similar as for the DF approach, the 1PI method can be considered as a diagrammatic expansion of the full lattice Green's function around the DMFT solution, whereupon the latter already includes all local correlations of the system. In this way, the 1PI approach perfectly fits into the general scheme of diagrammatic extensions of DMFT, outlined previously in Sec. 4.1.2.
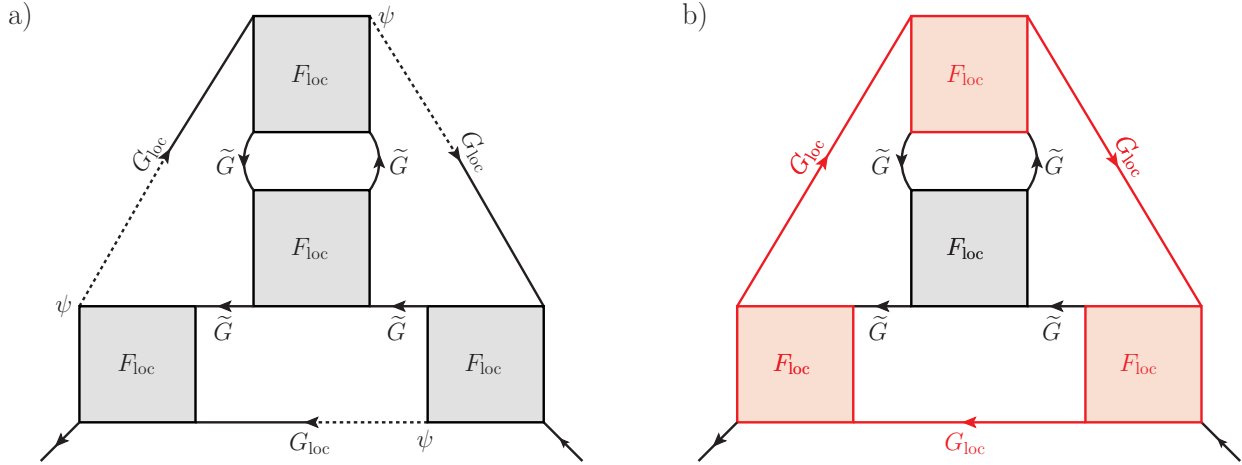
Figure 4.24: a) Fourth-order diagram (in F_{loc}), which is constructed from three interaction terms of type $(\phi^+\phi)(\phi^+\psi)$ (second diagram in Fig. 4.23b1) and one interaction term of type $(\phi^+\phi)(\phi^+\phi)$ (first diagram in Fig. 4.23b1). b) The same diagram appears in second-order perturbation theory, if one includes a (local) three-particle vertex diagram, marked in red in this graphic. However, this diagram is canceled if one expands the Jacobian up to D^3 [corresponding to $(\phi^+\phi)^3$], which leads to a compensation of this doubly counted term. $\widetilde{G} = G_{\text{DMFT}} - G_{\text{loc}}$ and F_{loc} has to be multiplied with $\left(1 - \frac{1}{2}\delta_{\sigma\sigma'}\right)$.

From Eqs. (4.96) and (4.91b) one can now easily derive the diagrammatic elements for the expansion of the 1PI Green's function $\mathbf{G}_k$, which are illustrated graphically in Fig. 4.23. As for the purely Gaussian part of the 1PI formalism, Eq. (4.96) gives rise to three different types of non-interacting ("bare") Green's functions which are also depicted in Fig. 4.23a: The propagator $\widetilde{G}_k = G_k - G_{\text{loc},\nu} = \frac{1}{\beta}\langle\phi^+_{k\sigma}\phi_{k\sigma}\rangle_0$ corresponds to the purely nonlocal electronic fluctuations, while $\frac{1}{\beta}\langle\phi^+_{k\sigma}\psi_{k\sigma}\rangle_0 = \frac{1}{\beta}\langle\psi^+_{k\sigma}\phi_{k\sigma}\rangle_0 = -\frac{1}{\beta}\langle\psi^+_{k\sigma}\psi_{k\sigma}\rangle_0 = G_{\text{loc},\nu}$ describe the local ones, coupled to the nonlocal degrees of freedom via the interaction in the second line of Eq. (4.91b). Let us stress that all these "bare" propagators, in the 1PI approach contain the full local self-energy $\Sigma_{\text{loc}}(\nu)$ of the AIM, and, hence, include all *local* purely self-interaction effects.

As for the "interacting part" of the 1PI action, we discuss the contributions stemming from the Jacobian, i.e., $\sum_i \text{tr}\ln\left(\mathbb{1} + D[\phi^+_i, \phi_i]\right)$, separately from the terms proportional to F_{loc} in Eq. (4.91b). The diagrammatic elements which correspond to the latter are depicted in Fig. 4.23b1. One observes that the interaction term consists of two parts: The first diagram in Fig. 4.23b1 corresponds to the contribution $F_{\text{loc}}(\phi^+\phi)(\phi^+\phi)$ in the interacting part of the 1PI action, Eq. (4.91b). This vertex can be either coupled to both local ($\langle\phi^+\psi\rangle$ or $\langle\psi^+\phi\rangle$) *and* nonlocal propagators ($\langle\phi^+\phi\rangle$) or to nonlocal propagators *only*. On the contrary, the other

contribution to the interaction in Eq. (4.91b), $F_{\text{loc}}\left[(\psi^+\phi)(\phi^+\phi) + (\phi^+\phi)(\phi^+\psi)\right]$, is connected with *at least one* local propagator.

Let us now turn to the Jacobian part of the action, i.e., $\sum_i \text{tr} \ln\left(\mathbb{1} + D[\phi_i^+, \phi_i]\right)$, in Eq. (4.91b). After expanding the logarithm, as done in appendix F, Eq. (F.3), one can rewrite this term as a sum over traces of the single contributions of the corresponding series, i.e., $\sum_i \text{tr} D - \frac{1}{2}\text{tr} D^2 + \ldots$, whereupon the explicit expression for D and D^2 are reported in appendix F, Eqs. (F.4) and (F.5)[44]. $\sum_i \text{tr} D$ (schematically) corresponds to the first (left) graph in Fig. 4.23b2. Such a diagram represents just a purely local correction to the self-energy and is, hence, already included in the self-energy Σ_{loc} of the AIM. This means that this diagram in Fig. 4.23b2 would lead to a double-counting of local contributions to the self-energy. On the other hand, such a diagram is also generated in first order perturbation theory by the second element of the interaction terms in Fig. 4.23b1. Considering the prefactors and signs of both "spurious" contributions, it turns out that they exactly cancel. This avoids a double counting of local correlations at the one-particle level.

In a similar way, the second diagram in Fig. 4.23b2 just constitutes a purely local correction to the local vertex function F_{loc}, and, therefore, would also lead to a double-counting of such vertex contributions. Again, the same diagrams arises from second-order perturbation theory within the 1PI formalism, using the second diagram in Fig. 4.23b1 and G_{loc}, which leads to an cancellation of such spurious terms.

Let us note that the higher-order contributions in D, i.e., D^3, D^4, ..., correspond to local (one-particle irreducible) three- and more particle vertex functions, which can be *constructed just from the local two-particle vertex and local Green's functions*, see, e.g., the red part of diagram 4.24b for D^3. It is obvious that the same local three-particle diagram arises if one expands Γ_{AIM} up to the $(\phi^+\phi)^3$, i.e., if one considers the local, one-particle irreducible, three-particle vertex for Γ_{AIM}. One can show that the latter has the opposite sign with respect to the corresponding contribution stemming from the Jacobian, and hence these two terms cancel. Note that this cancellation takes place already in the interacting part of the action, i.e., the red part of diagram 4.24b does not occur at all in the diagrammatic expansion of the 1PI approach if one expands Γ_{AIM} up to the local three-particle vertex[45]. On the other hand it is clear that diagram 4.24b should contribute to the 1PI (and also to the real) self-energy, and, indeed, this diagram can be constructed just from the diagrammatic element of Γ_{AIM}

---

[44]The $\sum_i$ can be of course rewritten as a sum over momenta as it was done for the functional Γ_{AIM} in Eq. (4.81).

[45]Let us remark that this cancellation does actually occur only for the *exact* functional Γ_{AIM}. Hence, formally, the restriction to, e.g., the two-particle vertex level should be applied only after having considered the occurrence of this cancellation in the action.

restricted to the two-particle vertex level as it is shown in Fig. 4.24a. Summing up, one can state that in the 1PI approach, diagrams from local (one-particle irreducible) three- and more-particle vertex functions, which are built from (local) two-particle vertices and local Green's functions, are generated already at the two-particle vertex level. The equivalent contributions stemming from an explicit consideration of three- and more-particle vertex contributions to Γ_{AIM}, which would lead to a double counting of diagrams such as the one depicted in Fig. 4.24a or b, are canceled by the corresponding contributions of the Jacobian. Let us stress again that this cancellation takes place already for the action of the 1PI approach, not only for the resulting terms in a diagrammatic expansion. Therefore, since we are restricting ourselves to the two-particle vertex for Γ_{AIM}, we have to neglect third- and higher-order contributions in D also in the Jacobian of the Legendre transformation. Let us finally note that the discussion of the Jacobian presented above is, of course, just schematically, while an explicit calculation (at least for the contributions up to the fourth order in ϕ^+ and ϕ, i.e., $\mathrm{tr}D$ and $\mathrm{tr}D^2$) is reported in appendix F.

4.4.2.1   Ladder Approximation in the 1PI approach

*Parts of the results and the discussion presented in following section are based on the publication in the APS Journal "Physical Review Letters": PRL **105**, 077002 (2010).*

Apart from the restriction to the two-particle local vertex in Eq. (4.53), which represents one of the (two) typical simplifications within diagrammatic extensions of DMFT (see Sec. 4.1.2), the practical application of the 1PI method requires a further approximation concerning the type of diagrams adopted for an expansion of the self-energy. In the following, we will restrict ourselves to ladder diagrams which can be constructed from the diagrammatic elements depicted in Figs. 4.23a and 4.23b1. Besides the evaluation of just lowest-order (in F_{loc}) diagrams, ladder-type calculations represent the standard approximation scheme for almost all diagrammatic extensions of DMFT, such as DΓA and DF, as already discussed in Sec. 4.1.2 (see also Tab. 4.1). From a practical point of view, the reason for this is that this type of approximation requires "only" the solution of one Bethe-Salpeter equation in a specific channel, while the more complex parquet treatment is based on the self-consistent numerical solution of the parquet equations and the Bethe-Salpeter equations in *all* channels. Though recently important steps further have been made in this direction [45, 46, 142], the numerical effort for a general treatment of the parquet formalism is still considerable, which renders the restriction to the ladder approximation inevitable in many cases. However, in situations where one (Bethe-Salpeter) channel plays a dominant role, such as, e.g., the magnetic channel
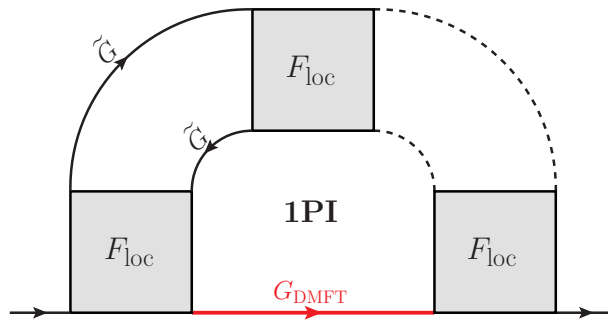
Figure 4.25: Third order (in terms of the local vertex $F_{\mathrm{loc},\sigma\sigma'}^{\nu\nu'\omega}$) self-energy diagram in the 1PI scheme, and ladder extension thereof (indicated by the dashed lines). $\widetilde{G} = G_{\mathrm{DMFT}} - G_{\mathrm{loc}}$. The figure is readapted from Ref. [36].

for the half-filled bipartite lattice, neglecting the (small) nonlocal fluctuations in the other channels is also physically justifiable, as it has been already discussed in section 4.3.

A typical ladder diagram for the 1PI approach is depicted diagrammatically in Fig. 4.25, for the particle-hole channel (ph). As for the explicit derivation of the corresponding analytical expressions, we start from the analysis of all possible bubble-diagrams, which can be constructed from the diagrammatic elements for the 1PI approach shown in Figs. 4.23a and 4.23b1. Considering all possible bubbles (Fig. 4.26), we observe, as a first point, that the bubble (a) with *two* local Green's functions should not appear in our 1PI corrections to the local self-energy, since it is already included in F_{loc} and, hence, it would lead to a double-counting of local vertex diagrams. In fact, as discussed in the previous section (see page 222), the contribution of Fig. 4.26a is canceled by the corresponding counterterms contained in the (inverse of the) determinant of the Jacobian, $J[\phi^+, \phi]$, shown by the second diagram of Fig. 4.23b2. Hence, bubbles with two local Green's function will be not considered for the construction of our ladders.

So far we have not imposed any constraints on our auxiliary AIM, which we used to decouple the local from the nonlocal degrees of freedom in the lattice system. In other words: Hitherto, the hybridization function $\Delta(\nu)$, which defines the AIM [see Eq. (4.33b)], is still arbitrary. For this general case, all the bubble diagrams depicted in Figs. 4.26b, c and d contribute to the ladder. However, considering the specific AIM associated with the DMFT solution of the Hubbard model allows for a further simplification: In this situation all contributions stemming from bubbles with a *single* local Green's function, as depicted in Figs. 4.26b and c, vanish due to the self-consistency condition of DMFT, i.e., $\sum_{\mathbf{k}} \widetilde{G}_k = \sum_{\mathbf{k}} G_{\mathrm{DMFT}}(\nu, \mathbf{k}) - G_{\mathrm{loc}}(\nu) \equiv 0$. Hence, the ladder part of the diagram for the self-energy should necessarily
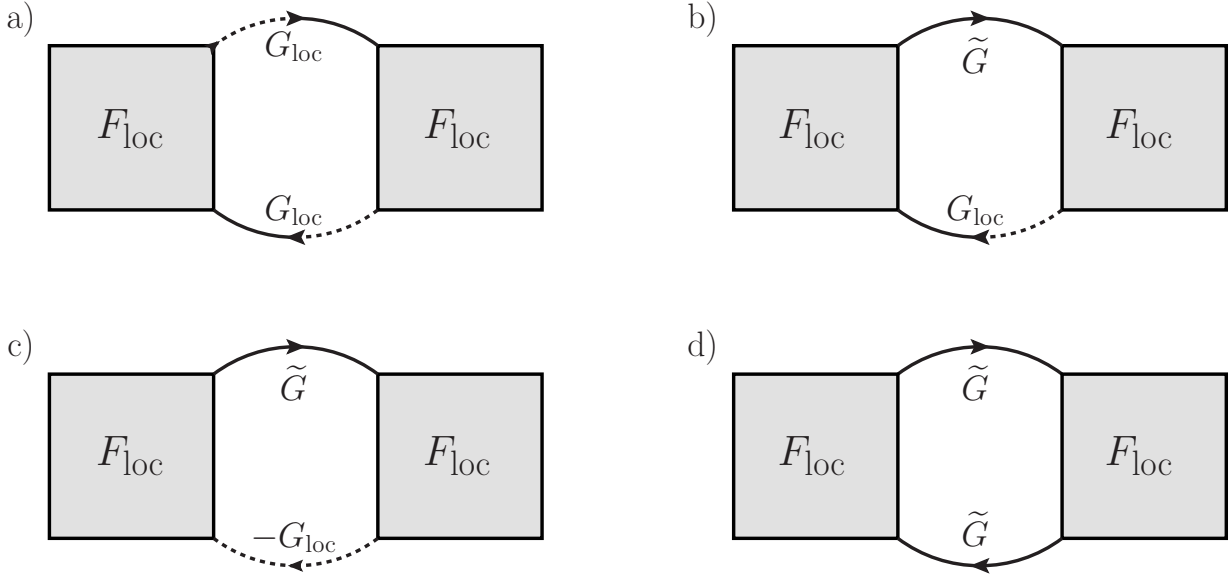
Figure 4.26: Bubble diagrams for the 1PI approach which can be constructed from the diagrammatic elements shown in Figs. 4.23a and 4.23b1. Only the diagram d) contributes to the perturbation series, if one starts from the AIM connected with DMFT. $\widetilde{G} = G_{\text{DMFT}} - G_{\text{loc}}$. The figure is readapted from Ref. [36].

be composed only of bubbles with *two* nonlocal Green's functions $\widetilde{G}_k$ (see Fig. 4.26d). Considering, eventually, the two available vertex functions of the 1PI theory shown in Fig. 4.23b1, it is obvious that the ladder part of a diagram has to be constructed solely from $F_{\text{loc}}(\phi^+\phi)(\phi^+\phi)$ vertices, except for the leftmost and rightmost vertex, which can be either of the type $F_{\text{loc}}(\psi^+\phi + \phi^+\psi)(\phi^+\phi)$, connected by *one local* Green's function G_{loc}, or of the type $F_{\text{loc}}(\phi^+\phi)(\phi^+\phi)$, connected by *only nonlocal* Green's functions $\widetilde{G}$.

The above considerations lead to considerable simplifications concerning the four components of the self-energy (matrix) in the spinor formalism, whose most general form is given by:

$$\boldsymbol{\Sigma} = \begin{pmatrix} \Sigma_{\phi\phi} & \Sigma_{\phi\psi} \\ \Sigma_{\psi\phi} & \Sigma_{\psi\psi} \end{pmatrix}. \tag{4.97}$$

While the ladder has to be the same [i.e., constructed from $\widetilde{G}$ and $F_{\text{loc}}(\phi^+, \phi)(\phi^+\phi)$ only] for all four components of the self-energy, the non-ladder part can be different. In practice, this situation is well exemplified in Fig. 4.27, where exemplarily third-order (ladder) diagrams for the four components of the self-energy are depicted. By a closer inspection of this figure it is obvious that the components $\phi\phi$, $\phi\psi$ and $\psi\phi$ of the self-energy are perfectly equivalent. In fact, for all these three contributions, the Green's function, which does *not* enter the ladder,
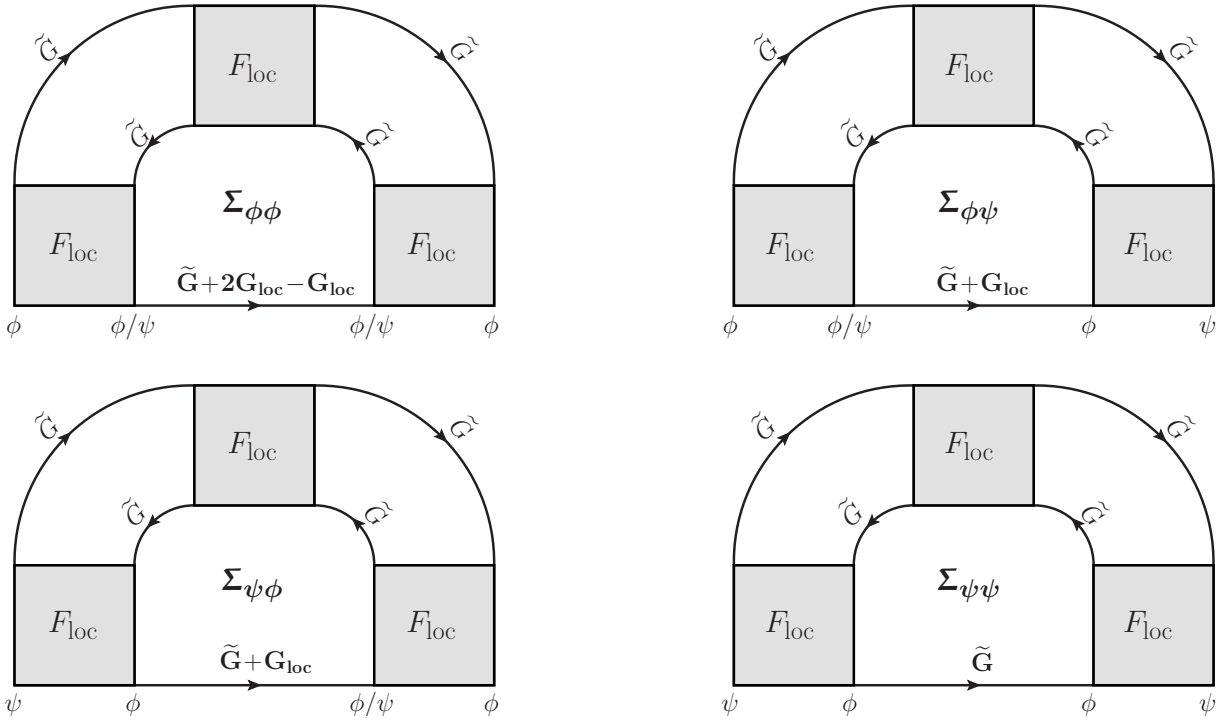
Figure 4.27: The four components of the matrix $\mathbf{\Sigma}$ depicted for diagrams of third order in F_{loc}. $\widetilde{G} = G_{\text{DMFT}} - G_{\text{loc}}$. The figure is readapted from Ref. [36].

is given by $\widetilde{G} + G_{\text{loc}} = G_{\text{DMFT}}$ (or $\widetilde{G} + 2G_{\text{loc}} - G_{\text{loc}} = G_{\text{DMFT}}$ for $\Sigma_{\phi\phi}$), since the fields ϕ and ψ are available for constructing the internal propagator. On the contrary, the $\psi\psi$ component must have the fields ψ at the outer legs of the diagram (see the right diagram in the second row of Fig. 4.27), and, hence, all the inner propagators of the diagram have to be constructed from the fields ϕ *only*, which means that just the nonlocal Green's function $\frac{1}{\beta}\langle\phi^+\phi\rangle = \widetilde{G}$ is available for the inner line which does not enter the ladder. Hence, eventually, one can express the four components of the self-energy of the ladder 1PI by means of only two distinct contributions, which differ just in the Green's function *not* entering the ladder (i.e., $\widetilde{G} + G_{\text{loc}} = G_{\text{DMFT}}$ or $\widetilde{G}$). For convenience, we represent the $\phi\phi$, $\phi\psi$ and $\psi\phi$ elements of $\mathbf{\Sigma}$ as the sum of two terms Σ_1 and Σ_2, corresponding to having $G_{\text{DMFT}} = \widetilde{G} + G_{\text{loc}}$ in the internal (non-ladder) line, while, of course, the $\psi\psi$ component of $\mathbf{\Sigma}$, which contains only $\widetilde{G}$ as internal propagators, is given by Σ_1 only:

$$\Sigma_{\phi\phi,k} = \Sigma_{\phi\psi,k} = \Sigma_{\psi\phi,k} = \Sigma_{1,k} + \Sigma_{2,k},$$
$$\Sigma_{\psi\psi,k} = \Sigma_{1,k}. \tag{4.98}$$

Let us emphasize here once again that both, Σ_1 and Σ_2, contain the *very same* ladder, to be calculated by means of a corresponding Bethe-Salpeter equation. Since we restrict ourselves to the case of a half-filled bipartite lattice, where particle-hole (in particular magnetic) fluctuations dominate, we consider only the particle-hole channels (density and magnetic), as it is illustrated (schematically) in Fig. 4.25. The corresponding Bethe-Salpeter equations are completely analogous to the local ones for the AIM reported in appendix B, Eqs. B.4, except for the replacements of Γ_{loc} with F_{loc} and G_{loc} with $\widetilde{G}$. This leads to the following integral equation for the calculation of the momentum-dependent vertex function $F_{d(m),\mathbf{q}}$ in the 1PI approach:

$$F_{r,\mathbf{q}}^{\nu\nu'\omega} = F_{\text{loc},r}^{\nu\nu'\omega} + \frac{1}{\beta}\sum_{k_1} F_{\text{loc},r}^{\nu\nu_1\omega}\widetilde{G}_{k_1}\widetilde{G}_{k_1+q}F_{r,\mathbf{q}}^{\nu_1\nu'\omega}, \quad r = d,m, \tag{4.99}$$

where again a four-vector notation is adopted, i.e., $k_1\widehat{=}(\nu_1,\mathbf{k}_1)$ and $q\widehat{=}(\omega,\mathbf{q})$. Let us note that $F_{d(m),\mathbf{q}}$, as calculated in Eq. (4.99), is *identical* to the corresponding nonlocal vertex of (ladder) DΓA in Eq. (4.5), which is constructed from the local vertex irreducible in the density (magnetic) channel, $\Gamma_{\text{loc},d(m)}$, [instead of the full local vertex $F_{\text{loc},d(m)}$ in Eq. (4.99)] and the DMFT Green's function $G_{\text{DMFT}} = \widetilde{G} + G_{\text{loc}}$ [instead of the nonlocal propagator $\widetilde{G}$ in Eq. (4.99)]. This can be easily proven by eliminating the full local vertex $F_{\text{loc},d(m)}$ from Eq. (4.99) by means of the local Bethe-Salpeter equation (B.4).

In the next step, we use the nonlocal vertex function $F_{r,\mathbf{q}}$, as constructed in Eq. (4.99) [or, equivalently, in the corresponding DΓA Eqs. (4.5) or (4.6)], for the calculation of the contributions Σ_1 and Σ_2 to the 1PI self-energy, according to the diagrams depicted in Fig. 4.25. Considering the (different) prefactors for the two spin combinations, i.e., $A_d = \frac{1}{2}$ and $A_m = \frac{3}{2}$, we obtain:

$$\Sigma_{1,k} = -\frac{1}{\beta^2}\sum_{k'q}\sum_{r=d,m} A_r F_{\text{loc},r}^{\nu\nu'\omega}\widetilde{G}_{k'}\widetilde{G}_{k'+q}F_{r,\mathbf{q}}^{\nu'\nu\omega}\widetilde{G}_{k+q} - \Sigma_{1,k}^{(2)}, \tag{4.100a}$$

$$\Sigma_{2,k} = -\frac{1}{\beta^2}\sum_{k'q}\sum_{r=d,m} A_r F_{\text{loc},r}^{\nu\nu'\omega}\widetilde{G}_{k'}\widetilde{G}_{k'+q}F_{r,\mathbf{q}}^{\nu'\nu\omega}G_{\text{loc},\nu+\omega}, \tag{4.100b}$$

where $\Sigma_{2,k} \equiv \Sigma_{2,\nu}$ is, in fact, k-independent (1PI correction to the *local* self-energy due to nonlocal corrections). $\Sigma_{1,k}^{(2)}$ is defined as:

$$\Sigma_{1,k}^{(2)} = -\frac{1}{2}\frac{1}{\beta^2}\sum_{k'q}\sum_{r=d,m} A_r F_{\text{loc},r}^{\nu\nu'\omega}\widetilde{G}_{k'}\widetilde{G}_{k'+q}F_{\text{loc},r}^{\nu'\nu\omega}\widetilde{G}_{k+q}. \tag{4.101}$$

The latter contribution accounts for the double-counting of the second-order (in Floc) dia-

gram due to the indistinguishability of identical particles (see the analogous discussion for the Bethe-Salpeter equation in the particle-particle channel in appendix B.3). Note that the corresponding double-counting correction for Σ_2 yields zero due to the DMFT self-consistency condition, i.e., $\Sigma_{2,k}^{(2)} \propto \left(\sum_{\mathbf{k}'} \widetilde{G}_{k'} \right)^2 \equiv 0$.

Inserting the Ansatz (4.98) for the components of the self-energy into the (matrix) Dyson equation gives:

$$\mathbf{G}_k^{-1} = \mathbf{G}_{0,k}^{-1} - \mathbf{\Sigma}_k = \begin{pmatrix} G_k^{-1} - \Sigma_{1,k} - \Sigma_{2,k} & G_k^{-1} - \Sigma_{1,k} - \Sigma_{2,k} \\ G_k^{-1} - \Sigma_{1,k} - \Sigma_{2,k} & G_k^{-1} - G_{\mathrm{loc},\nu}^{-1} - \Sigma_{1,k} \end{pmatrix}. \tag{4.102}$$

In order to obtain the corresponding Green's function $G(\nu, \mathbf{k}) \equiv G_{\mathrm{1PI}}(\nu, \mathbf{k})$ for the lattice system, we have to invert the matrix in Eq. (4.102) and then sum up its components [see Eqs. (4.89) and (4.94)]. This yields:

$$G_{\mathrm{1PI}}(\nu, \mathbf{k}) = \frac{1}{i\nu - \varepsilon_{\mathbf{k}} + \mu - \Sigma_{\mathrm{loc},\nu} - \Sigma_{1,k} - \Sigma_{2,k}}. \tag{4.103}$$

Hence, the total self-energy obtained by means of the 1PI approach is just given by:

$$\Sigma_{\mathrm{1PI},k} = \Sigma_{\mathrm{loc},\nu} + \Sigma_{1,k} + \Sigma_{2,k}. \tag{4.104}$$

We observe that the relationship between the 1PI self-energy (matrix), Eq. (4.97), and the self-energy for the real electrons, Eq. (4.104), is much simpler than the corresponding relation in the DF theory [Eq. (4.65)]. Specifically, the 1PI approach yields no spurious denominator corrections for the lattice self-energy. We also note, that in the dual fermion approach, with the usual restriction to the two-particle local vertex, only the contribution Σ_1 [with the corresponding denominator, given in the Eq. (4.65)] appears, while Σ_2 would correspond to the contributions stemming from the local three-particle (one-particle reducible) vertex, see also Figs. 4.20b and 4.28, which is usually neglected in DF. At the same time, both contributions naturally appear in the 1PI approach already at the two-particle vertex level, providing a possible way-out to the problem of the DF method, discussed at the end of section 4.4.1.

In the following, we will gain a deeper understanding of the diagrammatic contents and the mutual interrelations among the different diagrammatic extensions of DMFT. Such a competitive analysis and understanding, which was missing hitherto in the existing literature, will be obtained by explicitly studying the similarities of DF, DΓA and 1PI (in their ladder
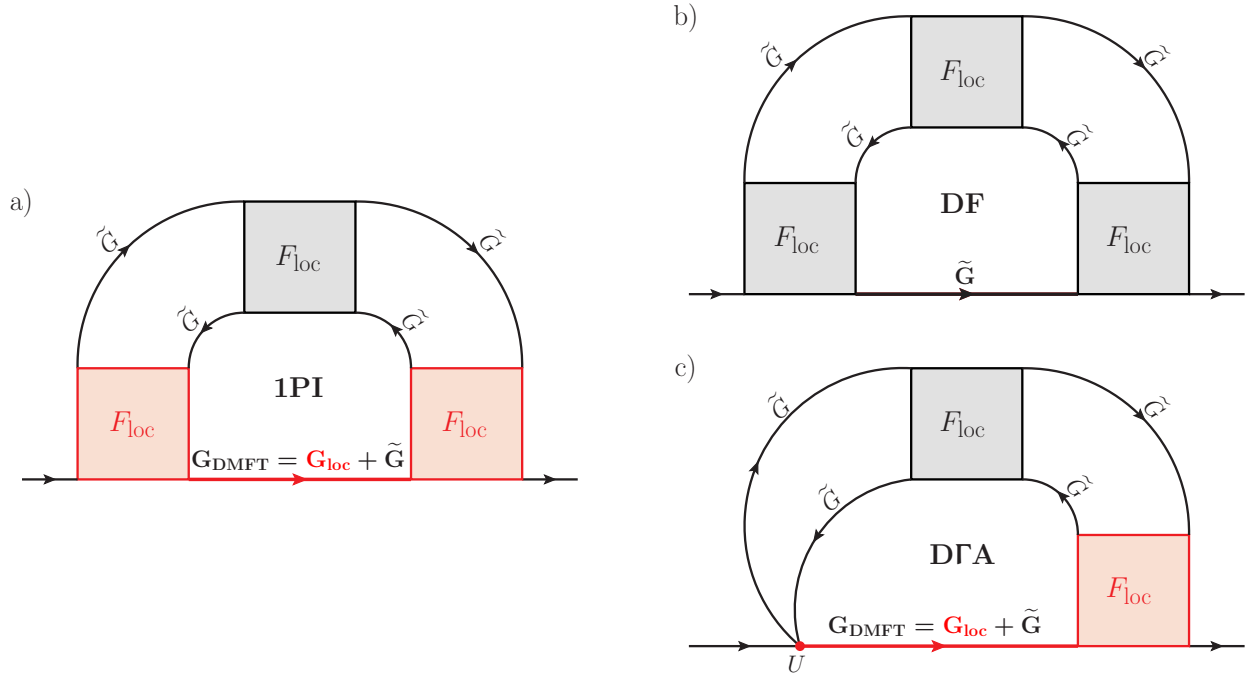
Figure 4.28: Third order (in terms of the local vertex $F_{\mathrm{loc},\sigma\sigma'}^{\nu\nu'\omega}$) diagrams for 1PI (a), DF (b) and its corresponding DΓA counter part (c). The contribution of (a part of) the one-particle reducible three-particle vertex is marked in red in the 1PI and DΓA diagrams. The figure is readapted from Ref. [36].

diagram implementation) in more detail.

Differences between 1PI, DF and DΓA

The different diagrammatic content of the ladder 1PI, ladder DF and ladder DΓA approaches can be readily individuated by a direct inspection of the corresponding diagrams. We will start by considering a typical third-order diagram of the 1PI ladder series, shown in Fig. 4.28a. By comparing it to the corresponding diagram of the DF approach (Fig. 4.28b), it is evident that the latter does not include the term, where the fermionic line at the bottom (bold red line in Fig. 4.28a) corresponds to a local Green's function. We recall, in this respect, that in the dual fermion space the propagation occurs via purely nonlocal Green's functions $\widetilde{G} = G_{\mathrm{DMFT}} - G_{\mathrm{loc}}$, as it can be inferred from Fig. 4.19. Hence, when only the two-particle local vertex is considered as interaction among the dual fermions, there is no way to generate local Green's functions in the DF diagrams for a ladder series. The difference between the diagrams of Fig. 4.28a and Fig. 4.28b corresponds, in fact, to the contribution of the local three-particle vertex in the DF approach (red part in Fig. 4.28a), which is usually neglected. As for the corresponding DΓA diagram (Fig. 4.28c), we observe, that –in contrast to DF– it

does contain the full DMFT Green's function $G_{\mathrm{DMFT}} = \widetilde{G} + G_{\mathrm{loc}}$, yielding, hence, also "mixed" terms with $G_{\mathrm{DMFT}} - G_{\mathrm{loc}}$ propagators in the ladder part of the diagram and one local G_{loc} outside the ladder (bottom of the diagram). Again, analogously to the 1PI diagram, the part of Fig. 4.28c colored in red corresponds to the contribution of the three-particle vertex in the DF approach. At the same time, one should emphasize that the DΓA ladder diagrams, as those depicted in Fig. 4.28c, evidently represent only a subset of the 1PI ladder diagrams. This can be easily understood from a comparison of Fig. 4.28a and Fig. 4.28c: In the 1PI approach, all vertices used for building up the self-energy diagrams are the dynamical ones (F_{loc}), while in DΓA, where the self-energy is explicitly derived from the Schwinger-Dyson equation [see Eqs. (2.194) and (4.11)], one of the vertex functions is replaced by its lowest-order counterpart, i.e., the bare interaction U. Hence, when performing diagrammatic approximations of DMFT *at the ladder level*, the 1PI ladder resummation contains a larger number of diagrams with respect to DF or DΓA. Specifically, it contains all diagrams of the DΓA and DF ladders and additional contributions beyond. On the other hand, we should also keep in mind that the 1PI ladder diagrams themselves represent a subset of the more general set of diagrams, generated by employing the parquet equations for the DΓA instead of the ladder approximation. We will show in the following that the specific 1PI diagram shown in Fig. 4.28 are not contained in ladder DΓA but are generated by the full parquet-based version of DΓA.

To this end, it proves convenient to rewrite Σ_1 and Σ_2 in Eqs. (4.100) by means of the Bethe-Salpeter equation for the nonlocal vertex $F_{r,\mathbf{q}}$ [Eq. (4.99)]. Indeed, a closer inspection of (4.99) and (4.100) shows that both self-energy contributions Σ_1 and Σ_2 contain a term which is completely equivalent to the reducible part of the (nonlocal) Bethe-Salpeter equation (4.99), i.e., to the second summand on the right-hand side of this equation. Hence, one can recast the 1PI ladder self-energies in the following way:

$$
\begin{aligned}
\Sigma_{i,k} &= -\frac{1}{\beta} \sum_q \sum_{r=d,m} A_r \underbrace{\frac{1}{\beta} \sum_{k'} F_{\mathrm{loc},r}^{\nu\nu'\omega} \widetilde{G}_{k'} \widetilde{G}_{k'+q} F_{r,\mathbf{q}}^{\nu'\nu\omega}}_{F_{r,\mathbf{q}}^{\nu\nu\omega} - F_{\mathrm{loc},r}^{\nu\nu\omega},\ \text{see Eq. (4.99)}} G_{i,k+q} - \Sigma_{i,k}^{(2)} = \\
&= -\frac{1}{\beta} \sum_q \sum_{r=d,m} A_r \left(F_{r,\mathbf{q}}^{\nu\nu'\omega} - F_{\mathrm{loc},r}^{\nu\nu'\omega} \right) G_{i,k+q} - \Sigma_{i,k}^{(2)}, \quad i=1,2,
\end{aligned}
\tag{4.105}
$$

where $G_{1,k+q} = \widetilde{G}_{k+q}$ and $G_{2,k+q} = G_{\mathrm{loc},\nu+\omega}$. Eq. (4.105) has a very clear diagrammatic interpretation, which is illustrated in Fig. 4.29: The nonlocal self-energy correction to the local DMFT self-energy, calculated via the ladder approximation within the 1PI approach,
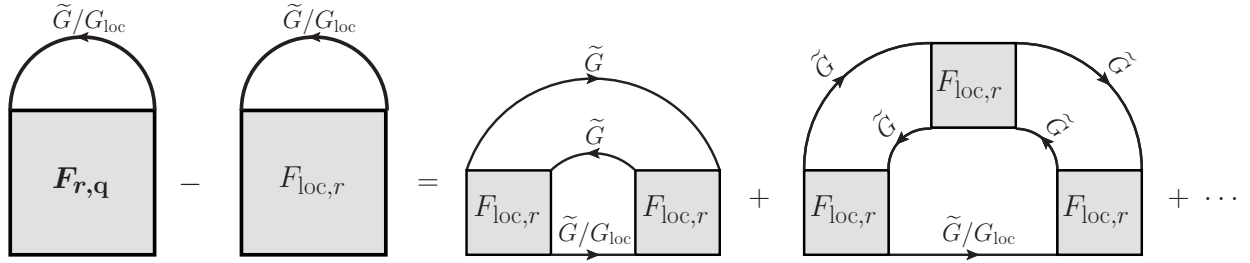
Figure 4.29: Nonlocal (ladder) self-energy corrections within the 1PI approach up to the third order in $F_{\mathrm{loc},r}$: One has to sum up all ladder contributions to $F_{r,\mathbf{q}}$ except for the (purely local) lowest-order term $F_{\mathrm{loc},r}$. Note that for Σ_2 (corresponding to G_{loc} for the non-ladder Green's function) the second-order diagram (first diagram on the right-hand side of this equation) vanishes ($\Sigma_2^{(2)} \equiv 0$).

can be represented as a Hartree diagram, where the "interaction" is given by the nonlocal vertex function $F_{r,\mathbf{q}}$, and the Green's functions is either (i) purely nonlocal (Σ_1) or (ii) solely local (Σ_2) [see the first diagram in Fig. 4.29]. The subtraction of the local vertex $F_{\mathrm{loc},r}$ in Eq. (4.105), which corresponds to the second diagram depicted in Fig. 4.29, accounts for the purely local contribution to the 1PI self-energy already included in DMFT. Due to this subtraction, any possible double-counting of local contributions to the lattice self-energy is prevented.

In order to establish the connection with the DΓA, we will represent $F_{r,\mathbf{q}}$ now in the DΓA way, i.e., in terms of the local vertex, which is *irreducible* in the density (magnetic) channel, $\Gamma_{\mathrm{loc},d(m)}$, instead of the full local vertex [as discussed below Eq. (4.99)]. The corresponding Bethe-Salpeter equations have been already given in the section about the ladder DΓA [Eq. (4.5)] and are here recalled for convenience:

$$F_{r,\mathbf{q}}^{\nu\nu'\omega} = \Gamma_{\mathrm{loc},r}^{\nu\nu'\omega} + \frac{1}{\beta} \sum_{k_1} \Gamma_{\mathrm{loc},r}^{\nu\nu_1\omega} G_{k_1} G_{k_1+q} F_{r,\mathbf{q}}^{\nu_1\nu'\omega}, \quad r = d, m, \tag{4.106}$$

where G denotes, as usual, the lattice DMFT Green's function, which contains the local self-energy Σ_{loc}, i.e., all local correlation effects. Inserting now Eq. (4.106) for $F_{r,\mathbf{q}}$ and its local counterpart [Eq. (B.4)] for F_r into the expressions for the two contributions to the 1PI self-energy in Eq. (4.105), one arrives at the following result:

$$\Sigma_{i,k} = -\frac{1}{\beta} \sum_q \sum_{r=d,m} A_r \frac{1}{\beta} \sum_{k'} \Gamma_{\mathrm{loc},r}^{\nu\nu'\omega} \left(G_{k'} G_{k'+q} F_{r,\mathbf{q}}^{\nu'\nu\omega} - G_{\mathrm{loc},\nu'} G_{\mathrm{loc},\nu'+\omega} F_{\mathrm{loc},r}^{\nu'\nu\omega} \right) G_{i,k+q} - \Sigma_{i,k}^{(2)},$$
$$\tag{4.107}$$

where again $G_{1,k+q} = \widetilde{G}_{k+q}$ and $G_{2,k+q} = G_{\mathrm{loc},\nu+\omega}$. According to Eq. (4.104) one has to sum

up Σ_1, Σ_2 and the local self-energy Σ_{loc} in order to obtain the full lattice self-energy within the ladder 1PI approach, which reads:

$$\Sigma_{1\text{PI},k} = \Sigma_{\text{loc},\nu} - \frac{1}{\beta} \sum_q \sum_{r=d,m} A_r \frac{1}{\beta} \sum_{k'} \Gamma_{\text{loc},r}^{\nu\nu'\omega} \left(G_{k'} G_{k'+q} F_{r,\mathbf{q}}^{\nu'\nu\omega} - G_{\text{loc},\nu'} G_{\text{loc},\nu'+\omega} F_{\text{loc},r}^{\nu'\nu\omega} \right) G_{k+q} - \Sigma_{1,k}^{(2)}$$

(4.108)

This result can be compared to the nonlocal self-energy of the DΓA in section 4.3, Eq. (4.11):

$$\Sigma_{\text{DΓA},k} = \frac{1}{2} U n - \frac{U}{\beta^2} \sum_{k'q} G_{k'} G_{k'+q} \left(A_d F_{d,\mathbf{q}}^{\nu\nu'\omega} - A_m F_{m,\mathbf{q}}^{\nu\nu'\omega} - \frac{1}{2} F_{\text{loc},d}^{\nu\nu'\omega} + \frac{1}{2} F_{\text{loc},m}^{\nu\nu'\omega} \right) G_{k+q}. \quad (4.109)$$

From a first rough comparison of Eqs. (4.108) and (4.109), we can recognize an important difference between $\Sigma_{1\text{PI}}$ and $\Sigma_{\text{DΓA}}$: Apart from (local and second-order) double-counting corrections[46], the bare interaction U in $\Sigma_{\text{DΓA}}$, Eq. (4.109), is *replaced* by the local particle-hole irreducible vertex $\Gamma_{\text{loc},r}$ in $\Sigma_{1\text{PI}}$, Eq. (4.108). What does the formal difference between 1PI and DΓA mean physically? As it is illustrated in Fig. 4.30, the additional diagrams present in 1PI correspond to considering *nonlocal* corrections to the irreducible vertex in the selected channel, while in ladder DΓA calculations perfect locality of this vertex is assumed. It is important to recall, that the assumption of locality of the irreducible vertex in a given channel (e.g., density or magnetic) is not implied at all for the general assumptions of DΓA, in its full parquet-based version. Here, nonlocal corrections to these vertices are indeed generated via the self-consistent solution of the parquet equations, starting from a fully irreducible local vertex. Therefore, even if, in general, the inclusion of a larger number of diagrams does not guarantee on itself an improvement of a given approximation, in our case the additional nonlocal corrections for the irreducible (density- and magnetic-) vertices are physically justifiable by reason of the diagrams which would be generated by the full (parquet-based) DΓA approach.

Let us finally present an analytically more thorough comparison between $\Sigma_{\text{DΓA}}$ and $\Sigma_{1\text{PI}}$. To this end we introduce the following notations for products of two Green's function [see Eq.

---

[46]Double counting corrections are required for the first (and the second) summand inside the parenthesis in Eqs. (4.108) and (4.109), respectively.
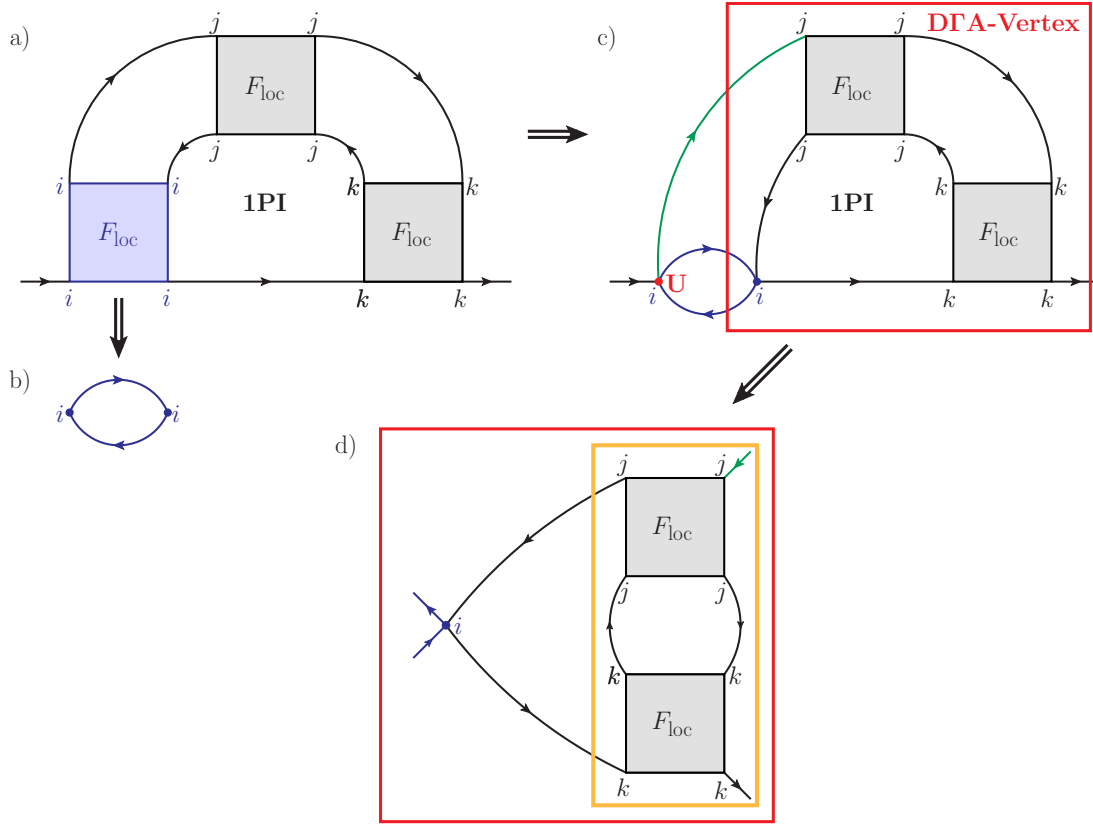
Figure 4.30: We show explicitly how a 1PI diagram can be expressed in a similar form as in DΓA, where there is always a bare U at the left-hand side of the diagrams (i, j, k denote lattice sites). We start from the specific 1PI diagram a) and consider the particular contribution to the leftmost vertex shown in b), so that a) becomes c). Because of the DΓA requirement of a bare U on the leftmost side (see Fig. 4.28c), the entire red box should be interpreted correspondingly as a DΓA-generated reducible vertex. This red box, in turn, can be deformed to d), where the yellow box clearly contains nonlocal ($j \neq k$) contributions to the vertex irreducible in the longitudinal channel (Γ_r). Such nonlocal contributions to Γ_r are, hence, generated within DΓA only via the full parquet implementation of the method. The figure is readapted from Ref. [36].

(4.7)]:

$$\chi_{0,\mathbf{q}}^{\nu\omega} = -\sum_{\mathbf{k}} G_k G_{k+q}, \tag{4.110a}$$

$$\chi_{0,\text{loc}}^{\nu\omega} = -G_{\text{loc},\nu} G_{\text{loc},\nu+\omega}, \tag{4.110b}$$

$$\widetilde{\chi}_{0,\mathbf{q}}^{\nu\omega} = -\sum_{\mathbf{k}} \widetilde{G}_k \widetilde{G}_{k+q} = \chi_{0,\mathbf{q}}^{\nu\omega} - \chi_{0,\text{loc}}^{\nu\omega}. \tag{4.110c}$$

Note that, apart from a factor β, the definition of the local bare susceptibility in Eq. (4.110b) coincides with the diagonal elements of the matrix $\chi_0^{\nu\nu'\omega}$ defined in Eq. (2.153). Let us also point out that the last equality in Eq. (4.110c) follows from the DMFT self-consistency condition $\sum_{\mathbf{k}} G_k = \sum_{\mathbf{k}} G_{k+q} \equiv G_{\mathrm{loc},\nu}$. Considering the definitions in Eqs. (4.110), one can rewrite Eqs. (4.108) and (4.109) for the 1PI and DGA self-energy, respectively, as well as the Bethe-Salpeter equation (4.106), by replacing the term $\sum_k G_k G_{k+q}$ with $-\sum_\nu \chi_{0,\mathbf{q}}^{\nu\omega}$ in these relations. Considering that, according to Eq. (4.110c), $\chi_{0,\mathbf{q}}^{\nu\omega} = \widetilde{\chi}_{0,\mathbf{q}}^{\nu\omega} + \chi_{0,\mathrm{loc}}^{\nu\omega}$, it is clear that the nonlocal contributions to the 1PI and the DΓA self-energies are generated from $\widetilde{\chi}_{0,\mathbf{q}}^{\nu\omega}$. Hence, it is convenient to expand the (momentum-dependent) self-energies (and, of course, also the momentum-dependent vertex $F_{r,\mathbf{q}}$) in terms of this purely nonlocal susceptibility. Taking into account contributions up to the first order in $\widetilde{\chi}_{0,\mathbf{q}}^{\nu\omega}$, we obtain:

$$\Sigma_{\mathrm{1PI},k}^{(2)} = \Sigma_{\mathrm{loc},\nu} + \Sigma_{1,k}^{(2)} = \Sigma_{\mathrm{loc},\nu} + \frac{1}{2}\frac{1}{\beta^2} \sum_{\nu'q} \sum_{r=d,m} A_r F_{\mathrm{loc},r}^{\nu\nu'\omega} \widetilde{\chi}_{0,\mathbf{q}}^{\nu'\omega} F_r^{\nu'\nu\omega} \widetilde{G}_{k+q}, \qquad (4.111)$$

for the corresponding 1PI self-energy with $\Sigma_{1,k}^{(2)}$ defined as in Eq. (4.101), and

$$\Sigma_{\mathrm{D\Gamma A},k}^{(2)} = \Sigma_{\mathrm{loc},\nu} + \frac{1}{\beta^2} \sum_{\nu'\nu''q} A_d F_{\mathrm{loc},d}^{\nu\nu''\omega} \widetilde{\chi}_{0,\mathbf{q}}^{\nu''\omega} \left(\overline{F}_{\mathrm{loc},d}^{\nu''\nu'\omega} - \frac{U}{2}\delta_{\nu''\nu'} \right) + A_m F_{\mathrm{loc},m}^{\nu\nu''\omega} \widetilde{\chi}_{0,\mathbf{q}}^{\nu''\omega} \left(\overline{F}_{\mathrm{loc},m}^{\nu''\nu'\omega} + \frac{U}{2}\delta_{\nu''\nu'} \right)$$
$$\qquad (4.112)$$

for the DΓA case. $\overline{F}_{\mathrm{loc}}$ is defined as:

$$\overline{F}_{\mathrm{loc},d(m)}^{\nu\nu'\omega} = \pm U \left[\delta_{\nu\nu'} + \frac{1}{\beta}\chi_{0,\mathrm{loc}}^{\nu\omega}\Gamma_{\mathrm{loc},d(m)}^{\nu\nu'\omega} \right]^{-1} = \pm U \sum_{\nu''} F_{\mathrm{loc},d(m)}^{\nu\nu''\omega} \left[\Gamma_{\mathrm{loc},d(m)}^{\nu''\nu'\omega} \right]^{-1}, \qquad (4.113)$$

where the matrix inversions are taken with respect to the fermionic Matsubara frequencies ν, ν' and ν''.

Comparing Eqs. (4.111) and (4.112) one observes two differences: (i) The factor $1/2$ in Eq. (4.111), which avoids double counting of diagrams in the 1PI self-energy, is replaced by an explicit subtraction of the double counting terms $\pm U/2$ in Eq. (4.112) for the DΓA. The reason for this is the "asymmetric" form of the DΓA self-energy correction compared to the 1PI one (bare U in DΓA vs. the full vertex in 1PI on the left-hand side of the self-energy diagrams, see Fig. 4.28). Specifically, the ladder for the (local) vertex $\overline{F}_{\mathrm{loc},d(m)}^{\nu\nu'\omega}$ exhibits always a bare U as leftmost (or rightmost) vertex[47]. Hence, it does not fulfill the crossing

---

[47]On the contrary, the ladder series for the full local vertex $F_{\mathrm{loc},d(m)}$ is exclusively built from irreducible vertices $\Gamma_{\mathrm{loc},d(m)}$, whose crossing properties [see Eq. (2.165)] render the full ladder (i.e., the full $F_{\mathrm{loc},d(m)}$) crossing symmetric.

symmetry, which is responsible for the double-counting of diagrams, apart from its lowest-order contribution U which, therefore, has to be corrected by a factor $1/2$. (ii) The second, more important, difference between the two expressions is that $\overline{F}_{\mathrm{loc},d(m)}^{\nu\nu'\omega}$ in Eq. (4.112) is replaced by $F_{\mathrm{loc},d(m)}^{\nu\nu'\omega}$ in $\Sigma_{1\mathrm{PI}}^{(2)}$. In fact, the difference between $\overline{F}_{\mathrm{loc},d(m)}^{\nu\nu'\omega}$ and $F_{\mathrm{loc},d(m)}^{\nu\nu'\omega}$ marks a particular set of nonlocal corrections to the self-energy, automatically generated in the 1PI ladder diagrams, but neglected in the ladder approximation of the DΓA.

The interpretation of the ladder 1PI expressions derived in this section can be summarized as follows: Within the ladder approximation, the 1PI approach includes terms, beyond *all* the ladder diagrams of DF and DΓA, *not* present in either of the two diagrammatic extension of DMFT. In the latter approaches, these terms would be generated by going *beyond* the ladder approximation to DΓA and *beyond* the two-particle local vertex in DF, respectively. At the same time, the numerical effort of performing a ladder 1PI calculation is obviously much smaller compared to the full (parquet-based) DΓA, or to the DF with the three-particle vertex. In this sense, the 1PI approach seems to be the one, which better utilizes, in building a ladder resummation, the information contained in the local two-particle vertex functions of DMFT.

Asymptotic behavior of the 1PI ladder self-energy

In this paragraph we analyze the $\frac{1}{i\nu}$-asymptotic behavior of the ladder 1PI self-energy $\Sigma_{1\mathrm{PI},k}$ with respect to the DΓA one. In general, performing a high-temperature expansion of the (exact) lattice self-energy $\Sigma(\nu,\mathbf{k})$ yields [see also Sec. 4.3.1 and Eq. (4.16)]:

$$\Sigma(\nu,\mathbf{k}) = \frac{Un}{2} + U^2\frac{n}{2}\left(1 - \frac{n}{2}\right)\frac{1}{i\nu} + \mathrm{O}\left(\frac{1}{[i\nu]^2}\right), \tag{4.114}$$

where $n = n_\uparrow + n_\downarrow$ denotes the average number of electrons per lattice site in the system. We recall that the DMFT self-energy $\Sigma_{\mathrm{loc},\nu}$, which coincides with a "numerically exact" one of an AIM with the same density, exhibits always the correct $\frac{1}{i\nu}$-asymptotic behavior reported in Eq. (4.114). On the contrary, as we have observed (and discussed) in Sec. 4.3.1, the $\frac{1}{i\nu}$-contribution to the lattice self-energy calculated within the DΓA formalism shows a deviation from the result in Eq. (4.114). As will be shown in the following, also the 1PI the self-energy, if calculated via a ladder resummation, exhibits the same violation of the high-frequency behavior of Σ. As for the DΓA, the enhanced asymptotics of 1PI calls for an effective treatment of of the self-consistency at the two-particle level. In this respect the situation is pretty similar to the corresponding issue in the DΓA. Therefore, as a first attempt, it is obvious to start by enforcing the required self-consistency effectively via the

Moriya λ corrections (see Sec. 4.3.1 and Refs. [27, 28]). Before discussing this in the next subsection, we focus here on the explicit (analytical) comparison of the asymptotic behavior of the 1PI and the DΓA self-energies. Specifically, we note that $\Sigma_{1,k}$, as given, e.g., in Eq. (4.107), is proportional to $\widetilde{G}_{k+q} = G_{k+q} - G_{\mathrm{loc},\nu+\omega}$, where G_{k+q} again denotes the DMFT Green's function $G_{\mathrm{DMFT}}(\nu + \omega, \mathbf{k} + \mathbf{q})$. Since both, G_{k+q} and $G_{\mathrm{loc},\nu+\omega}$, exhibit the same $\frac{1}{i\nu}$-asymptotic behavior, the latter term cancels out and $\widetilde{G}_{k+q} \overset{\nu\to\infty}{\longrightarrow} \frac{1}{(i\nu)^2}$. Hence, as for the $\frac{1}{i\nu}$-asymptotic behavior of the lattice self-energy calculated in the framework of 1PI, $\Sigma_{\mathrm{1PI},k}$, we have to consider only $\Sigma_{2,k}$ and $\Sigma_{\mathrm{loc},\nu}$ in Eq. (4.104). $\Sigma_{2,k}$, which is given in Eq. (4.107) in terms of the irreducible particle-hole vertex $\Gamma_{\mathrm{loc},r}$, is written as:

$$\Sigma_{2,k} = \frac{1}{\beta} \sum_{q} \sum_{r=d,m} A_r \frac{1}{\beta} \sum_{\nu'} \Gamma_{\mathrm{loc},r}^{\nu\nu'\omega} \left(\chi_{0,\mathbf{q}}^{\nu'\omega} F_{r,\mathbf{q}}^{\nu'\nu\omega} - \chi_{0,\mathrm{loc}}^{\nu'\omega} F_{\mathrm{loc},r}^{\nu'\nu\omega} \right) G_{\mathrm{loc},\nu+\omega}, \tag{4.115}$$

where the particle-hole bubbles $\chi_{0,\mathbf{q}}^{\nu\omega}$ and $\chi_{0,\mathrm{loc}}^{\nu\omega}$ are defined in Eqs. (4.110). Let us recall that $\Sigma_{2,k}$ does not depend on $\mathbf{k}$, but yields only a local correction to the DMFT self-energy $\Sigma_{\mathrm{loc},\nu}$, i.e., $\Sigma_{2,k} \equiv \Sigma_{2,\nu}$. As for the analysis of the $\frac{1}{i\nu}$-asymptotic behavior of the local DMFT self-energy $\Sigma_{\mathrm{loc},\nu}$ it is convenient to represent it in terms of the (local) equation of motion [see Eq. (2.194)][48]:

$$\Sigma_{\mathrm{loc},\nu} = \frac{Un}{2} + \frac{U}{\beta^2} \sum_{\nu'\omega} \chi_{0,\mathrm{loc}}^{\nu'\omega} F_{\mathrm{loc},\uparrow\downarrow}^{\nu\nu'\omega} G_{\mathrm{loc},\nu+\omega} = \frac{Un}{2} - \frac{U}{\beta^2} \sum_{\nu'\omega} \chi_{0,\mathrm{loc}}^{\nu'\omega} F_{\mathrm{loc},m}^{\nu\nu'\omega} G_{\mathrm{loc},\nu+\omega}, \tag{4.116}$$

where the last equality follows from:

$$\frac{U}{\beta^2} \sum_{\nu'\omega} \chi_{0,\mathrm{loc}}^{\nu'\omega} F_{\mathrm{loc},\uparrow\uparrow}^{\nu\nu'\omega} G_{\mathrm{loc},\nu+\omega} = 0, \tag{4.117}$$

in the SU(2) symmetric case. Eq. (4.117) can be easily proven by substituting the summation variables ν' and ω as $\nu' \to \nu + \omega$ and $\omega \to \nu' - \nu$ and considering the crossing relation $F_{\mathrm{loc},\uparrow\uparrow}^{\nu(\nu+\omega)(\nu'-\nu)} = -F_{\mathrm{loc},\uparrow\uparrow}^{\nu\nu'\omega}$ as given in Tab. 2.2.[49]

Let us now try to single out the ν dependence of each term in Eqs. (4.115) and (4.116) in the high-frequency regime, for obtaining a $\frac{1}{i\nu}$-expansion of the entire 1PI self-energy (cf. Sec.

---

[48]Note that the DMFT self-energy $\Sigma_{\mathrm{loc},\nu}$ exhibits already the correct asymptotic behavior as given in Eq. (4.114), i.e., its exact analytical expression for the $\frac{1}{i\nu}$-term is known to be $U^2 \frac{n}{2}\left(1 - \frac{n}{2}\right)\frac{1}{i\nu}$. However, as for the comparison with the asymptotic behavior of the DΓA self-energy in Eq. (4.109), which includes the local part, it is useful to represent $\Sigma_{\mathrm{loc},\nu}$ in a similar framework as $\Sigma_{2,k}$ [Eq. (4.100b)] and $\Sigma_{\mathrm{DΓA}}$ [Eq. (4.109)].

[49]Consider that $\chi_{0,\mathrm{loc}}^{\nu'\omega} G_{\mathrm{loc},\nu+\omega} = -G_{\mathrm{loc},\nu'} G_{\mathrm{loc},\nu'+\omega} G_{\mathrm{loc},\nu+\omega}$ is invariant under the transformation $\nu' \to \nu+\omega$ and $\omega \to \nu' - \nu$.
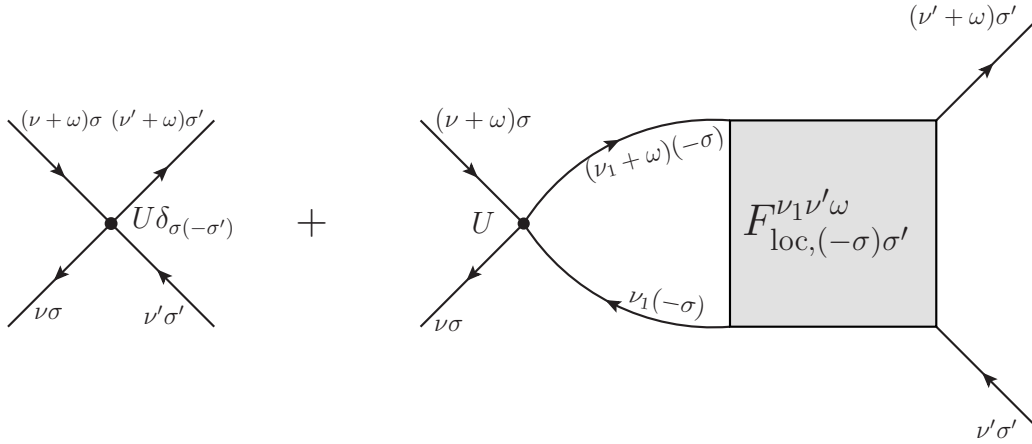
Figure 4.31: All possible diagrams for $F_{\text{loc},\sigma\sigma'}^{\nu\nu'\omega}$ that do not depend on ν.

4.3.1):

- $G_{\text{loc},\nu+\omega} \rightarrow \frac{1}{i\nu}$: In order to get the $\frac{1}{i\nu}$-contribution of the entire expression we are interested in constant contributions with respect to ν for all the remaining terms[50].

- $\Gamma_{\text{loc},r}^{\nu\nu'\omega}$, $r = d, m$: Since $G_{\text{loc},\nu+\omega}$ is already of the order $\frac{1}{i\nu}$, we have to identify the diagrammatic contributions to the irreducible vertex in the longitudinal particle-hole channel $\Gamma_{\text{loc},r}$, $r = d, m$ not showing any decay for $\nu \rightarrow \infty$, i.e., those which do *not* depend on ν. Considering first the full vertex $F_{\text{loc},r}^{\nu'\nu\omega}$, all corresponding ν-independent diagrams are depicted in Fig. 4.31. Since the diagram on the right-hand side of this figure is reducible in the longitudinal particle-hole channel, only the diagram on the left-hand side, i.e., the bare Hubbard interaction U can contribute to the ν-independent part of $\Gamma_{\text{loc},r}^{\nu'\nu\omega}$. Considering that:

$$\Gamma_{\text{loc},d}^{\nu\nu'\omega} = \Gamma_{\text{loc},\uparrow\uparrow}^{\nu\nu'\omega} + \Gamma_{\text{loc},\uparrow\downarrow}^{\nu\nu'\omega}, \tag{4.118a}$$

$$\Gamma_{\text{loc},m}^{\nu\nu'\omega} = \Gamma_{\text{loc},\uparrow\uparrow}^{\nu\nu'\omega} - \Gamma_{\text{loc},\uparrow\downarrow}^{\nu\nu'\omega}, \tag{4.118b}$$

the ν-independent part of $\Gamma_{\text{loc},r}^{\nu'\nu\omega}$ is given by $\Gamma_{\text{loc},d}^{\nu\nu'\omega} \sim +U$ and $\Gamma_{\text{loc},m}^{\nu\nu'\omega} \sim -U$, respectively.

- $F_{r,\mathbf{q}}^{\nu'\nu\omega}$ and $F_{\text{loc},r}^{\nu\nu'\omega}$: These terms are also present in the DΓA expression for the self-energy in Eq. (4.109). Since we are interested to compare the asymptotic behavior of the 1PI with the one of DΓA, we will for now keep this contributions in Eqs. (4.115) and (4.116) as they are.

---

[50]For the substitution $G_{\text{loc},\nu+\omega} \rightarrow \frac{1}{i\nu}$ note also that the largest contribution to the self-energy stems from the $\omega = 0$ term.

Inserting now the asymptotic forms of the different contributions in Eqs. (4.115) and (4.116) yields:

$$\Sigma_{2,k} + \Sigma_{\text{loc},\nu} = \frac{Un}{2} + \frac{1}{i\nu}\frac{1}{2}\frac{U}{\beta}\sum_{\nu'q}\left(-3F_{m,\mathbf{q}}^{\nu\nu'\omega} + F_{d,\mathbf{q}}^{\nu\nu'\omega}\right)\chi_{0,\mathbf{q}}^{\nu'\omega} + \left(F_{\text{loc},m}^{\nu\nu'\omega} - F_{\text{loc},d}^{\nu\nu'\omega}\right)\chi_{0,\text{loc}}^{\nu'\omega} + O\left(\frac{1}{[i\nu]^2}\right).$$
(4.119)

Considering that, as discussed above, $\Sigma_{1,k}$ does not contribute to the $\frac{1}{i\nu}$-asymptotic behavior of the 1PI self-energy $\Sigma_{\text{1PI},k}$ one has:

$$\Sigma_{\text{1PI},k} = \frac{Un}{2} + \frac{1}{i\nu}\frac{1}{2}\frac{U}{\beta}\sum_{\nu'q}\left(-3F_{m,\mathbf{q}}^{\nu\nu'\omega} + F_{d,\mathbf{q}}^{\nu\nu'\omega}\right)\chi_{0,\mathbf{q}}^{\nu'\omega} + \left(F_{\text{loc},m}^{\nu\nu'\omega} - F_{\text{loc},d}^{\nu\nu'\omega}\right)\chi_{0,\text{loc}}^{\nu'\omega} + O\left(\frac{1}{[i\nu]^2}\right).$$
(4.120)

This can be compared to the asymptotic behavior of the DΓA self-energy [Eq. (4.109)], where one should just replace G_{k+q} by $\frac{1}{i\nu}$. After performing this substitution in Eq. (4.109), the perfect equivalence of the $\frac{1}{i\nu}$-contributions of the 1PI and the DΓA self-energies is evident.

Moriya λ corrections for the 1PI approach

The high-frequency behavior of the 1PI ladder self-energy $\Sigma_{\text{1PI},k}$ exhibits the very same enhancement with respect to the exact $\frac{1}{i\nu}$-asymptotics [given in Eq. (4.114)], as the corresponding ladder DΓA self-energy. Since also the origin of this is the same as in DΓA (lack of two-particle self-consistency within the ladder approximation), it is logical to try to correct this problem by the same effective scheme adopted in DΓA. We recall that in the DΓA such a self-consistency at the two-particle level is effectively restored by means of the so-called Moriya λ corrections, which have been already discussed in section 4.3.1 and Refs. [27, 28]. The basic idea is to renormalize the mass of the nonlocal spin propagator (susceptibility) $\chi_{r,\mathbf{q}}^{\omega}$ (obtained from a one-shot calculation, and, hence, not self-consistently at the two-particle level) by means of a constant λ. Practically, the value of λ is determined (unambiguously) by the requirement that the self-energy obtained from the λ-corrected spin susceptibility $\chi_{r,\mathbf{q}}^{\lambda,\omega}$ exhibits the correct asymptotic behavior as given in Eq. (4.114). Hence, in order to apply the λ correction scheme also to the 1PI approach, one must first rewrite the expression for the 1PI self-energy, as given in Eq. (4.105), in terms of $\chi_{r,\mathbf{q}}^{\omega}$, $r = d, m$. To this end, we represent the (lattice) vertex $F_{r,\mathbf{q}}^{\nu\nu'\omega}$ by means of the (lattice) generalized susceptibility $\chi_{r,\mathbf{q}}^{\nu\nu'\omega}$ and the (lattice) bare susceptibility $\chi_{0,\mathbf{q}}^{\nu\omega}$ [defined in Eq. (4.110a)]:

$$F_{r,\mathbf{q}}^{\nu\nu'\omega} = \beta\delta_{\nu\nu'}\left(\chi_{0,\mathbf{q}}^{\nu\omega}\right)^{-1} - \left(\chi_{0,\mathbf{q}}^{\nu\omega}\right)^{-1}\chi_{r,\mathbf{q}}^{\nu\nu'\omega}\left(\chi_{0,\mathbf{q}}^{\nu'\omega}\right)^{-1}.$$
(4.121)

The nonlocal susceptibility $\chi^\omega_{r,\mathbf{q}}$ can be derived from the corresponding generalized suscepti-
bility $\chi^{\nu\nu'\omega}_{r,\mathbf{q}}$ in Eq. (4.121) as

$$\chi^\omega_{r,\mathbf{q}} = \frac{1}{\beta^2} \sum_{\nu\nu'} \chi^{\nu\nu'\omega}_{r,\mathbf{q}}, \tag{4.122}$$

i.e., summing over the fermionic Matsubara frequencies of the generalized susceptibility $\chi^{\nu\nu'\omega}_{r,\mathbf{q}}$
yields the physical response function $\chi^\omega_{r,\mathbf{q}}$.

The problem is now that, when inserting the expression for the nonlocal vertex function in Eq.
(4.121) into the 1PI self-energy equation (4.105), the generalized ($\chi^{\nu\nu'\omega}_{r,\mathbf{q}}$) rather than the phys-
ical ($\chi^\omega_{r,\mathbf{q}}$) susceptibility enters in the latter relation, making difficult a direct implementation
of the λ corrections explained above. Hence, we have to recast the generalized susceptibility
in Eq. (4.121) in terms of the physical one. Following the ideas of Refs. [27, 28, 227], this
can be achieved by separating the ladder for $F^{\nu\nu'\omega}_{r,\mathbf{q}}$ in the particle-hole (density or magnetic)
channel in Fig. 4.29 by the bare interaction U_r instead of the fully irreducible vertex $\Gamma^{\nu\nu'\omega}_{\mathrm{loc},r}$:

$$\chi^{\nu\nu'\omega}_{r,\mathbf{q}} = \chi^{*,\nu\nu'\omega}_{r,\mathbf{q}} - \frac{1}{\beta^2} \sum_{\nu_1\nu_2} \chi^{*,\nu\nu_1\omega}_{r,\mathbf{q}} U^{\nu_1\nu_2}_r \chi^{\nu_2\nu'\omega}_{r,\mathbf{q}}, \tag{4.123}$$

where the bare interaction matrix $U^{\nu\nu'}_r$ is constant, i.e., $U^{\nu\nu'}_r \equiv U_r$ with $U_d = +U$ and
$U_m = -U$ (U is the bare Hubbard interaction). The auxiliary susceptibility $\chi^{*,\nu\nu'\omega}_{r,\mathbf{q}}$ can be
obtained by solving Eq. (4.123), via a matrix inversion using the nonlocal version of the
Bethe-Salpeter equation reported in appendix B, Eq. (B.7). The result reads:

$$\chi^{*,\nu\nu'\omega}_{r,\mathbf{q}} = \left[\left(\chi^{\nu\omega}_{0,\mathbf{q}} \right)^{-1} \delta_{\nu\nu'} + \frac{1}{\beta^2} \left(\Gamma^{\nu\nu'\omega}_{\mathrm{loc},r} - U_r \right) \right]^{-1}, \tag{4.124}$$

where the outer matrix inversion is performed with respect to the fermionic Matsubara fre-
quencies ν and ν'. As for an interpretation of Eq. (4.124) one has to consider that the bare
interaction U_r in the corresponding channel ($r = d, m$) represents just the lowest-order (in
U) contribution to the local irreducible vertex function $\Gamma_{\mathrm{loc},r}$. Hence, the subtraction of U_r
from the irreducible vertex $\Gamma_{\mathrm{loc},r}$ in Eq. (4.124) leads to a ladder which is irreducible just in
the bare interaction U_r, i.e., removing one interaction vertex U from a diagram for $\chi^{*,\nu\nu'\omega}_{r,\mathbf{q}}$
does not split the diagram into two parts (see the corresponding definition in Ref. [227]).
The missing diagrams, which are reducible in the interaction U, are in turn recovered by
constructing a ladder from $\chi^{*,\nu\nu'\omega}_{r,\mathbf{q}}$ and the bare interaction U_r, yielding the full generalized
susceptibility in Eq. (4.123).

Iterating Eq. (4.123) leads to:

$$
\begin{aligned}
\chi_{r,\mathbf{q}}^{\nu\nu'\omega} =&\chi_{r,\mathbf{q}}^{*,\nu\nu'\omega} - \frac{1}{\beta^2}\sum_{\nu_1\nu_2}\left[\chi_{r,\mathbf{q}}^{*,\nu\nu_1\omega}U_r\chi_{r,\mathbf{q}}^{*,\nu_2\nu'\omega} + \frac{1}{\beta^2}\sum_{\nu_3\nu_4}\chi_{r,\mathbf{q}}^{*,\nu\nu_1\omega}U_r\chi_{r,\mathbf{q}}^{\nu_2\nu_3\omega}U_r\chi_{r,\mathbf{q}}^{*,\nu_4\nu'\omega}\right] = \\
=&\chi_{r,\mathbf{q}}^{*,\nu\nu'\omega} - \frac{U_r}{\beta^2}\sum_{\nu_1\nu_2}\chi_{r,\mathbf{q}}^{*,\nu\nu_1\omega}\chi_{r,\mathbf{q}}^{*,\nu_2\nu'\omega} + \frac{U_r^2}{\beta^2}\sum_{\nu_1\nu_4}\chi_{r,\mathbf{q}}^{*,\nu\nu_1\omega}\underbrace{\left(\frac{1}{\beta^2}\sum_{\nu_2\nu_3}\chi_{r,\mathbf{q}}^{\nu_2\nu_3\omega}\right)}_{\chi_{r,\mathbf{q}}^{\omega}}\chi_{r,\mathbf{q}}^{*,\nu_4\nu'\omega} = \\
=&\chi_{r,\mathbf{q}}^{*,\nu\nu'\omega} - U_r\left(1 - U_r\chi_{r,\mathbf{q}}^{\omega}\right)\frac{1}{\beta^2}\sum_{\nu_1\nu_2}\chi_{r,\mathbf{q}}^{*,\nu\nu_1\omega}\chi_{r,\mathbf{q}}^{*,\nu_2\nu'\omega}.
\end{aligned}
\tag{4.125}
$$

Inserting the last line of this equation into the expression for the full lattice vertex in Eq. (4.122) gives rise to the following representation of $F_{r,\mathbf{q}}^{\nu\nu'\omega}$:

$$
F_{r,\mathbf{q}}^{\nu\nu'\omega} = \left(\chi_{0,\mathbf{q}}^{\nu\omega}\right)^{-1}\left[\delta_{\nu\nu'} - \chi_{r,\mathbf{q}}^{*,\nu\nu'\omega}\left(\chi_{0,\mathbf{q}}^{\nu'\omega}\right)^{-1}\right] + U_r\left(1 - U_r\chi_{r,\mathbf{q}}^{\omega}\right)\gamma_{r,\mathbf{q}}^{\nu\omega}\gamma_{r,\mathbf{q}}^{\nu'\omega},
\tag{4.126}
$$

where the two-frequency "triangular" vertex $\gamma_{r,\mathbf{q}}^{\nu\omega}$ is defined as:

$$
\gamma_{r,\mathbf{q}}^{\nu\omega} = \left(\chi_{0,\mathbf{q}}^{\nu\omega}\right)^{-1}\frac{1}{\beta}\sum_{\nu'}\chi_{r,\mathbf{q}}^{*,\nu\nu'\omega}.
\tag{4.127}
$$

An explanation of the physical meaning of this vertex is given in Ref. [28].

Inserting now the vertex function $F_{r,\mathbf{q}}^{\nu\nu'\omega}$ from Eq. (4.126) into the expression for the self-energy in Eq. (4.105) yields the following result for $\Sigma_{1\text{PI},k}$:

$$
\Sigma_{1\text{PI},k} = \Sigma_{\text{loc},\nu} - \frac{1}{\beta}\sum_{r=d,m}A_m\sum_q\left\{\left(\chi_{0,\mathbf{q}}^{\nu\omega}\right)^{-1} - \chi_{r,\mathbf{q}}^{*,\nu\nu\omega}\left(\chi_{0,\mathbf{q}}^{\nu\omega}\right)^{-2} + U_r\left(1 - U_r\chi_{r,\mathbf{q}}^{\omega}\right)\left(\gamma_{r,\mathbf{q}}^{\nu\omega}\right)^2\right\}G_{k+q}+
$$
$$
+ \frac{1}{\beta}\sum_{r=d,m}A_m\sum_{\omega}F_{\text{loc},r}^{\nu\nu\omega}G_{\text{loc},\nu+\omega} - \Sigma_{1,k}^{(2)},
\tag{4.128}
$$

where $\chi_{r,\mathbf{q}}^{*,\nu\nu'\omega}$ is given in Eq. (4.124) and $\gamma_{r,\mathbf{q}}^{\nu\omega}$ is defined in Eq. (4.127). One can easily observe that the physical susceptibility $\chi_{r,\mathbf{q}}^{\omega}$ enters explicitly in Eq. (4.128) for the lattice self-energy of 1PI. Hence, the same Moriya λ corrections of DΓA [27, 28] can be directly introduced into this equation by just defining [see Eq. (4.21)]:

$$
\chi_{r,\mathbf{q}}^{\lambda_r,\omega} = \left[\left(\chi_{r,\mathbf{q}}^{\omega}\right)^{-1} + \lambda_r\right]^{-1},
\tag{4.129}
$$

where λ_d and λ_m are real positive numbers. Note that for the case of the half-filled Hubbard model on a bipartite (quadratic, cubic,...) lattice with nearest neighbor hopping only spin fluctuations play the dominant role for the behavior of the system. In this case λ_d can be neglected, i.e., $\lambda_d \equiv 0$, and we set $\lambda \equiv \lambda_m$, according to the similar discussion for the λ corrections of DΓA in Sec. 4.3.1. For our numerical calculations within the 1PI scheme, presented in the next section, only this situation will be considered.

4.4.3   Numerical results

Parts of the results and the discussion presented in the following section have been already published in the APS Journal "Physical Review B": PRB **88**, *115112 (2013).*

In this section, we present numerical results for nonlocal corrections to the self-energy of the two-dimensional Hubbard model obtained by means of the ladder 1PI formalism and compare them with the corresponding DF and DΓA results. Once more, we consider the relevant case of the Hubbard model on a (two-dimensional) square lattice with nearest-neighbor hopping t at half-filling, where the effect of nonlocal correlations beyond DMFT is expected to be particularly strong. Note that, in the following, all energy scales, such as the Hubbard interaction parameter U and the temperature $T = 1/\beta$, will be given in units of the half bandwidth $W/2 = 4t = 1$. Furthermore, one should bear in mind that due to the particle-hole symmetry of considered case, the self-energy evaluated for k-points at the Fermi-surface is purely imaginary as a function of Matsubara frequencies (besides the constant Hartree-contribution $\frac{Un}{2}$). Hence, in order to keep the notation as simple as possible, Σ refers to the *imaginary part* of the self-energy, i.e., $\Sigma \mathrel{\widehat{=}} \mathrm{Im}\Sigma$, in the sections below.

Before presenting our numerical results in the next two subsections, let us stress that the only possibility to perform a one-by-one comparison between the diagrammatic methods stands for the (non-self-consistent) one-shot calculations. Only in this case the exact relations between the three different approaches and their diagrammatic content can be precisely identified. Hence, this analysis is performed first. We want to emphasize here, that the one-shot results do not necessarily represent the final, physical results of the three methods. For instance, as discussed in sections 4.3.1 and 4.4.2.1 for DΓA and 1PI, respectively, the one-shot ladder self-energies ex-

hibit an enhanced high-frequency asymptotic behavior, typically corrected by an effective treatment of the two-particle self-consistency via (Moriya) λ corrections [27, 28, 31, 36]. As for DF, one observes that the (often) small nonlocal corrections, produced at the level of one-shot calculations, are typically strongly enhanced already by the implementation of the "inner" self-consistency (i.e., the self-consistency for the perturbation theory in dual space, without a change of the original local input [34, 221]). Hence, in a separate, final, subsection, we will look at the trends emerging when going beyond the one-shot calculations. We note already here, that because of the different ways the self-consistency is implemented (Moriyaesque λ corrections [27, 28, 36] in DΓA and 1PI discussed in Eqs. (4.19) and (4.128) vs. inner and outer self-consistency loops in DF [34, 123]), as well as the different possible levels of approximation (ladder or parquet diagrams, see table 4.1) an unambiguous identification of equivalent levels of approximation as in the one-shot case is in general not possible. Also for keeping the comparison among different methods as precise as possible, we present our numerical results on the Matsubara frequency axis only, avoiding the additional, and to some extent uncontrolled, effects of an analytic continuation.

4.4.3.1   One-shot calculations

In this subsection, we will focus on non-self-consistent one-shot calculations for nonlocal corrections to the (local) DMFT self-energy: this approach represents an expansion around DMFT, where the auxiliary local AIM [Eq. (4.31)] is not changed with respect to DMFT and the DMFT Green's functions (see caption of Fig. 4.5) are not renormalized by a feedback of the nonlocal self-energy. As one can understand from the discussion in the previous sections, examining (non-self-consistent) one-shot calculations corresponds to considering well-defined sets of diagrams for the lattice electrons. This way we are able to individuate the general trends obtained by the three approaches (1PI, DF and DΓA) emerging *solely* from their different diagrammatic content.
For the sake of conciseness, we will mainly discuss the numerical results obtained with ladder calculations, since (i) they are most frequently adopted in previous papers [28, 31, 35, 222], and (ii) the inclusion of ladder diagrams proved to be essential to correctly describe crucial features of the two- and
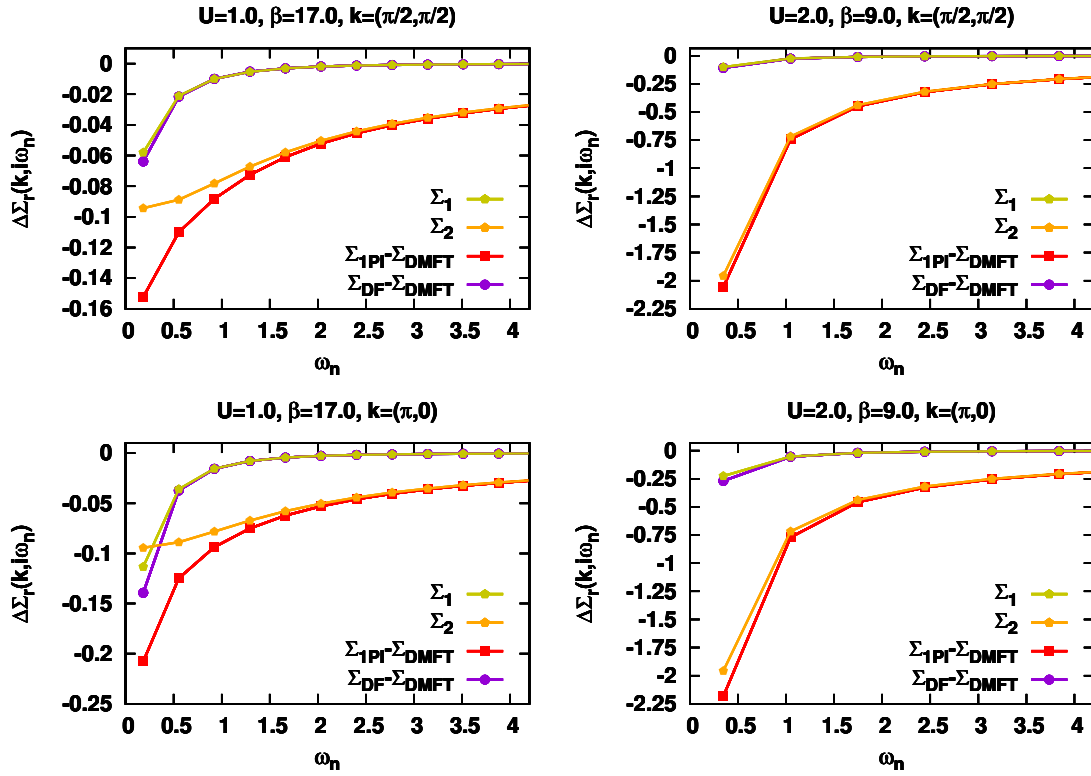
Figure 4.32: Nonlocal corrections $\Delta\Sigma_r(\mathbf{k}, i\omega_n) = \Sigma_r(\mathbf{k}, i\omega_n) - \Sigma_{\text{loc}}(i\omega_n)$ (r=1PI [Eq. (4.104)] and DF [Eq. (4.65)], respectively) to the DMFT (local) self-energy for the $d = 2$ Hubbard model on a square-lattice at half-filling for two different values of U, two different $\mathbf{k}$-points on the Fermi surface [i.e., $\mathbf{k}=(\frac{\pi}{2}, \frac{\pi}{2})$, nodal point, and $\mathbf{k} =(\pi, 0)$, anti-nodal point], and temperatures slightly above the corresponding T_N of DMFT (see phase-diagram in Fig. 4.16). For the 1PI results the single contributions Σ_1 [Eq. (4.100a)] and Σ_2 [Eq. (4.100b)] are also shown separately. Note, all self energies are purely imaginary except for the Hartree contribution $\frac{U}{2}$; this imaginary part is shown. The figure is reproduced from Ref. [36].

three-dimensional physics. Examples are the pseudogap [35] in $d = 2$ or the critical exponents of second-order phase transitions for $d < 4$ dimensions [31, 195], as already discussed in section 4.3.2.

We start our analysis by presenting n Fig. 4.32 our numerical results for one-shot calculations of the nonlocal corrections to the DMFT self-energy, $\Delta\Sigma_r(\mathbf{k}, i\omega_n) = \Sigma_r(\mathbf{k}, i\omega_n) - \Sigma_{\text{loc}}(i\omega_n)$ for r=1PI [Eq. (4.104)] and DF [Eq. (4.65)], respectively, on the Matsubara frequency axis. For the 1PI approach, we also show the two contributions Σ_1 [Eq. (4.100a)] and Σ_2 [Eq. (4.100b)] separately. Note, that since no self-consistent adaption of the underlying local model is

performed, the local self-energy inserted in the diagrams coincides with the DMFT one, i.e., $\Sigma_{\text{loc}}(i\omega_n) = \Sigma_{\text{loc}}^{\text{DMFT}}(i\omega_n)$. Specifically in Fig. 4.32, data for weak- ($U = 1.0$) and intermediate-to-strong coupling ($U = 2.0$) and for two different k-points on the Fermi surface are presented. The temperature has been chosen to be slightly above the onset of the antiferromagnetic ordering (Néel temperature, T_N^{DMFT}) obtained in DMFT, aiming at maximizing the possible effects of nonlocal correlations. One can see that, quite generally, the non-local corrections in the considered approaches increase the imaginary part of the self-energy, making its low-frequency- dependence less "metallic-like". Comparing the relative magnitudes of the nonlocal corrections shown in Fig. 4.32, the contribution of Σ_1 of the 1PI approach appears always rather small even though the U and T values have been selected very close to the anti-ferromagnetic instability of DMFT. The reason for this behavior is that in Σ_1 one has to perform k-summations over terms containing $G_{\text{DMFT}} - G_{\text{loc}}$, which yields small results since in a one-shot calculation, $\sum_{\mathbf{k}} G_{\text{DMFT}}(\nu, \mathbf{k}) - G_{\text{loc}}(\nu) = 0$ because of the DMFT self-consistency [Eq. (3.8)]. Let us also note that in one-shot calculations, the Σ_1-part of the 1PI correction [Eq. (4.100a)] almost exactly coincides with the DF correction $\Sigma_{\text{DF}} - \Sigma_{\text{DMFT}}$, except for the absence of the disputable denominator [226] in Eq. (4.65). For the data presented here, however, the effect of such denominator is found to be rather small. On the contrary, in Σ_2 a mixing of local and nonlocal contributions occurs, because one single Green's function G_{loc} enters instead of $G_{\text{DMFT}} - G_{\text{loc}}$ [see Eq. (4.100b)]. Hence, this explains why Σ_2 becomes significantly larger than Σ_1.

At the same time, as it was already mentioned in section 4.4.2.1, the con-tribution Σ_2 displays, similarly to the DΓA ladder diagrams, an enhanced high-frequency asymptotics, while Σ_1 decays faster than $\frac{1}{i\omega_n}$ and preserves the exact $\frac{1}{i\omega_n}$ asymptotic behavior of the self-energy when added to the local self-energy of DMFT. The reason for this is again that Σ_1 is constructed from $G_{\text{DMFT}} - G_{\text{loc}}$ only, which decays as $\frac{1}{(i\omega_n)^2}$. Σ_2 has an explicit $\frac{1}{i\omega_n}$ contribution from the G_{loc}-term, which leads to a (spurious) correction of the already ex-act $\frac{1}{i\omega_n}$ behavior of the DMFT self-energy. As in the DΓA case, the enhanced asymptotics can be corrected either by treating the full parquet set of di-agrams, or enforcing the self-consistency condition $\sum_{\mathbf{q}} \chi_{r,\mathbf{q}}^{\omega} = \chi_{\text{loc},r}^{\omega}$ [see Eq. (4.24)] at the ladder level via Moriyaesque λ corrections [28], see the results

in the next subsection.

In Fig. 4.33 we plot the self-energy obtained from one-shot ladder calculations for 1PI, DF and DΓA in comparison to DMFT. For 1PI and DΓA, nonlocal corrections are large as expected from the proximity to the DMFT Néel temperature. In the weak-coupling regime (i.e., for $U = 1.0$), one further observes that the 1PI correction is smaller than the corresponding DΓA correction. The reason for this is that the U appearing in the DΓA equation (4.109) is replaced by the irreducible vertex in the 1PI formula as it is illustrated in Eqs. (4.108), (4.109), (4.111) and (4.112) as well as in Fig. 4.25. At small values of the interaction parameter U, the (irreducible) vertex in the predominant (magnetic) channel is reduced [26,27,48] with respect to the bare interaction due to metallic screening. Therefore, nonlocal corrections obtained within the 1PI formalism tend to be smaller than the corresponding ones obtained in DΓA.

The situation is completely reversed in the intermediate-to-strong coupling regime ($U = 2.0$). Here, the local (irreducible) vertex is strongly enhanced [26,27,48,71] compared to the bare Hubbard interaction U, due to the formation of the local moment in the proximity of the Mott phase. Hence, the 1PI self-energy correction is larger than that obtained in DΓA. This observations suggest also some speculative considerations on the possible impact of different classes of diagrams onto other important results obtained with diagrammatic extensions of DMFT. Specifically, we will focus here on the existing estimate of T_N for the three-dimensional Hubbard model. In this respect we recall that in the present implementation of (the ladder versions of) 1PI and DΓA the calculation of the Néel-temperature T_N by means of a λ-corrected magnetic susceptibility is purely based on the asymptotic behavior of the (nonlocal) self-energy (see sections 4.3.1 and 4.4.2.1). However, this is the same in both approaches as it was shown in section 4.4.2.1, see in particular page 235 and following, and, hence, one would get the same transition temperatures. However, an improved scheme of λ corrections or a self-consistent treatment of these theories is expected to yield different T_N's due to the differences at low Matsubara frequencies in their self-energies. As we can see in Fig. 4.16, T_N for the half-filled Hubbard model in three dimension was found smaller in (ladder) DΓA than the one estimated in DCA [127,184] or in lattice quantum Monte Carlo [216] at weak-coupling, indicating a possible overes-
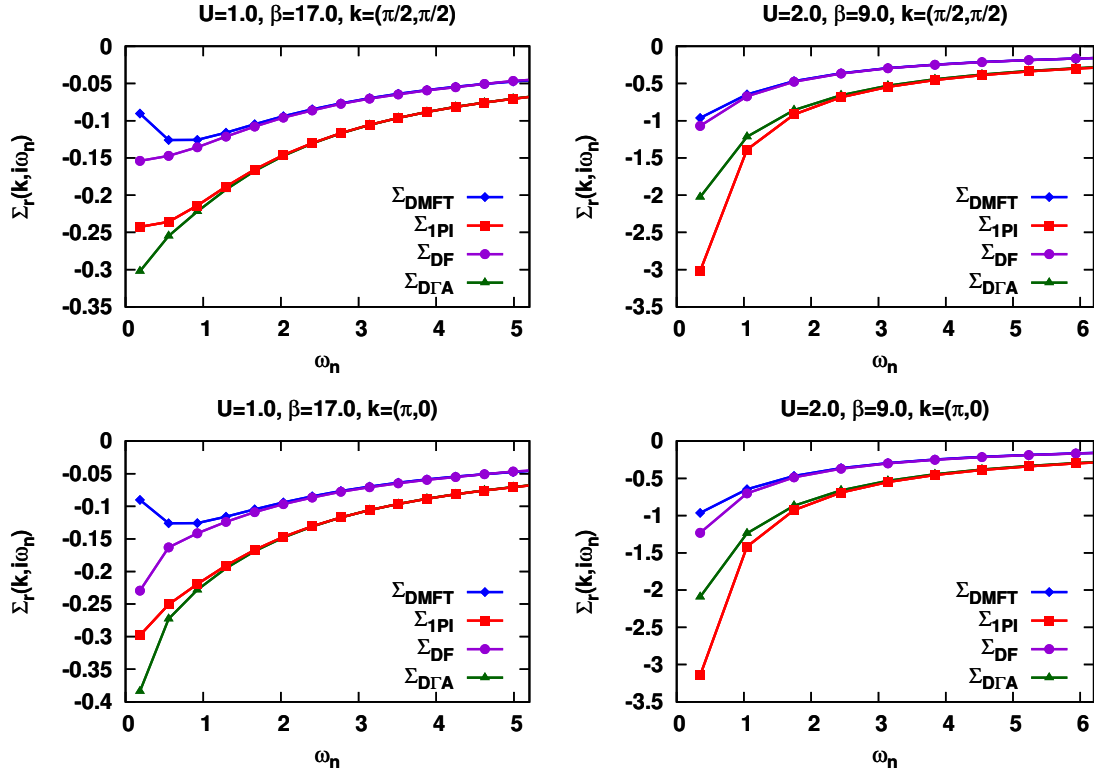
Figure 4.33: Self-energies (imaginary part) obtained with one-shot calculations for the 1PI approach vs. DF, DΓA and DMFT self-energies for the same parameters as in Fig. 4.32. The figure is reproduced from Ref. [36].

timation of the nonlocal correlation effects. Let us also emphasize here that similar values of T_N have been estimated by means ladder DF calculations in the weak-coupling regime [123]. As it was argued in section 4.3.1 and Ref. [31], nonlocal corrections to the charge- and particle-particle irreducible channels, which can be rigorously included only by performing the DΓA at the parquet level, might be responsible for such underestimation. Hence, the 1PI approach, which partly takes this corrections into account (see Fig. 4.30), is rather promising to improve the agreement between the diagrammatic and the cluster estimations of T_N in the Hubbard model, even at the level of ladder approximations. This may also hold true in the strong-coupling regime, where T_N was slightly larger in ladder DΓA than in the cluster methods, mirroring, to some extent, the inversion of the hierarchy in the magnitude of nonlocal corrections between between 1PI and DΓA at intermediate-to-strong coupling.
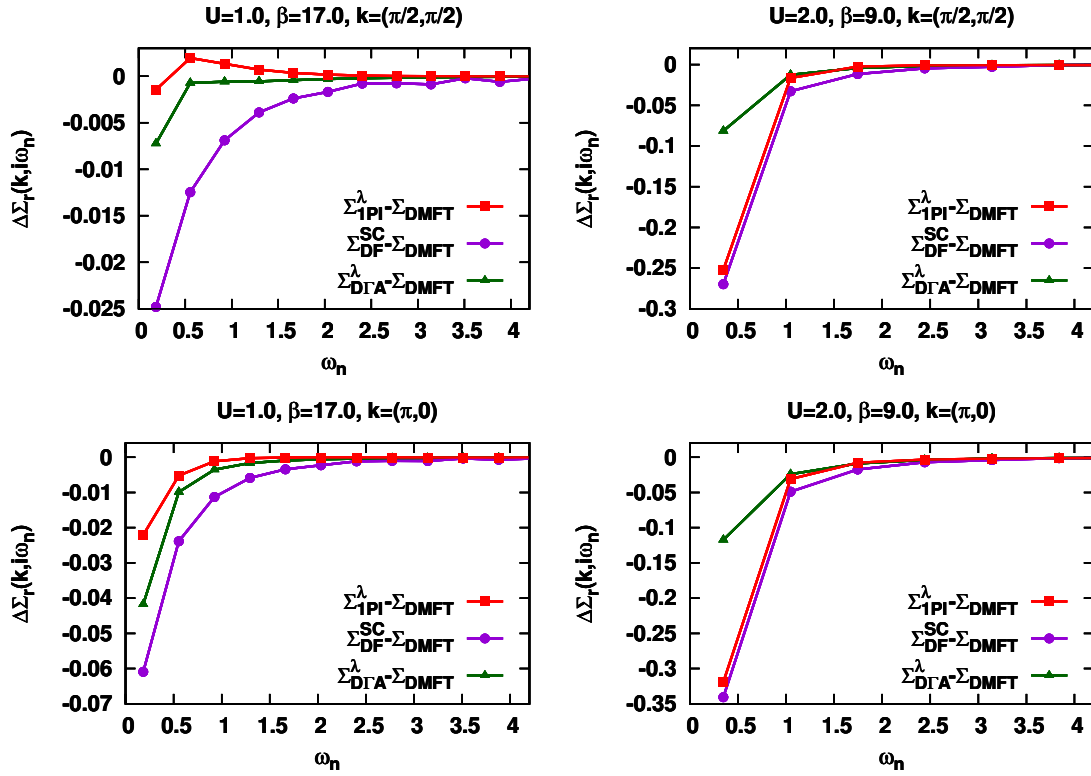
Figure 4.34: Nonlocal corrections $\Delta\Sigma_r(\mathbf{k}, i\omega_n) = \Sigma_r(\mathbf{k}, i\omega_n) - \Sigma_{\text{loc}}(i\omega_n)$ (r=1PI, DF and DΓA, respectively) as in Fig. 4.32, but for calculations including Moriyaesque λ corrections (1PI and DΓA) or self-consistency (DF). This figure is reproduced from Ref. [36].

As for the comparison with the (one-shot) DF self-energy, one clearly observes that it is smaller than the corresponding 1PI and DΓA ones. The reason for this is obviously the same as discussed for the contribution Σ_1 to the 1PI self-energy. However, one should consider, that the different ways of implementing self-consistency for 1PI, DF and DΓA can change this situation significantly (see next section).

4.4.3.2 Self-consistency and Moriyaesque λ corrections

The analysis of the one-shot results has shown the existence of a well-defined hierarchy in the relative magnitude of the nonlocal corrections. It is however expected that the overall size of the nonlocal corrections will be strongly modified by the inner and outer self-consistency loops in DF [35] on the one hand and the inclusion of the Moriyaesque λ corrections in DΓA and 1PI on the other. These effects are briefly analyzed in this subsection.
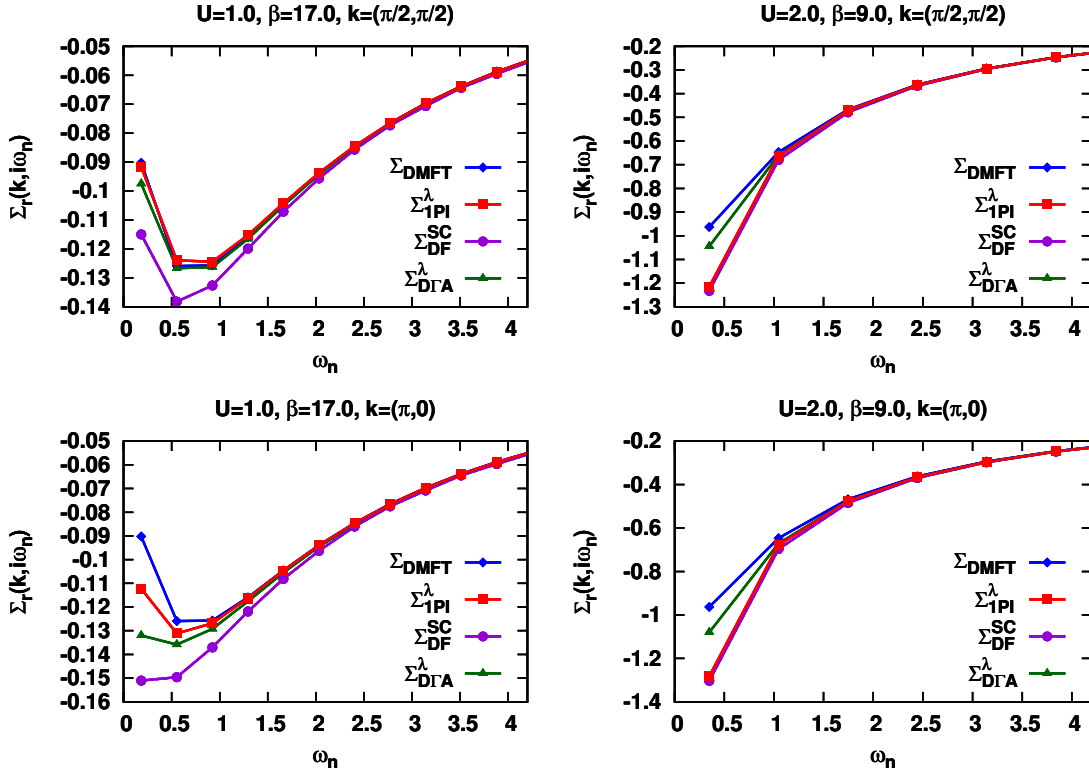
Figure 4.35: Self-energies obtained with the 1PI approach including λ corrections vs. self-consistent DF, λ-corrected DΓA and DMFT self-energies for the same parameters as in Fig. 4.34. This figure is reproduced from Ref. [36].

The results of the self-consistent DF, DΓA, and 1PI approaches are presented in Fig. 4.34. Comparing them to Fig. 4.32, one observes that the inclusion of the λ corrections in DΓA and 1PI (which reduces the value of T_N from the overestimated DMFT value) leads to a significant reduction of the nonlocal corrections to the self-energy (note the different scales in the two figures). This has been observed previously for DΓA [28, 36]. Hence, the λ-corrected results become much more similar to those obtained in *self-consistent* DF calculations. In particular, at strong coupling, 1PI and DF agree rather well. At the same time, the previously mentioned hierarchy in the relative magnitude of the nonlocal corrections to DMFT of 1PI and DΓA results is fully preserved by the Moriyaesque λ corrections (see Fig. 4.34): At weak coupling ($U = 1.0$) the 1PI corrections remain smaller than the DΓA ones due to the metallic screening of the irreducible vertex, while in the intermediate-to-strong coupling regime ($U = 2.0$) the enhancement of the same vertex due to the vicinity
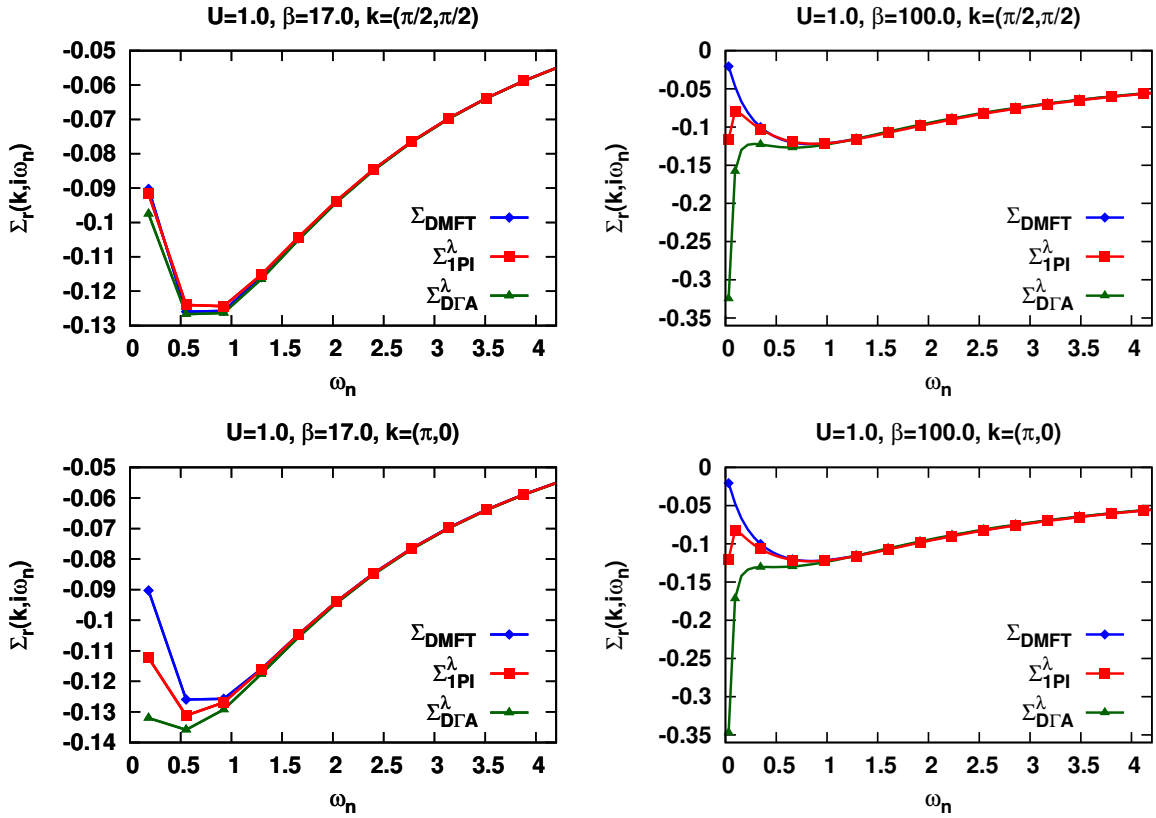
Figure 4.36: Self-energies for $U = 1.0$ obtained with the 1PI approach including λ correc-
tions vs. λ-corrected DΓA and DMFT self-energies for $\beta = 17.0$ (left panels) compared
to the low-temperature data $\beta = 100.0$ (right panels). Note that DF ladder calculations
cannot be performed at such low temperatures, since the ladder series diverges already at
the DMFT Néel temperature $T_N^{\mathrm{DMFT}} = 0.054$ ($\beta_N = 18.487$).

of the MIT leads to larger corrections for the 1PI approach with respect to the
DΓA. Note that the small value of the nonlocal part of the self-energy in the
1PI approach at $U = 1.0$ (especially in the nodal direction) may result from a
simplified way of considering self-consistent effects through the λ correction.
Since this correction is determined solely from the asymptotic behavior of the
self-energy at large frequencies, it may yield an overestimation of the effect of
non-ladder diagrams in the 1PI approach in the low-frequency region, calling
for a refined implementation of Moriya corrections adopted for the 1PI ladder
diagrams.

In Fig. 4.35 we present the corresponding results for the self-energies. For
$U = 1.0$ one can see, that at the considered temperature one observes metal-

lic behavior in all the approaches, except, perhaps, for the DF data in the $(\pi, 0)$ direction. We have verified, however, that even for this relatively small value of U the nonlocal 1PI corrections, though smaller than the DΓA and DF ones, eventually overcome the metallic behavior of the DMFT self-energy at sufficiently small temperatures consistent with the lattice QMC study in Ref. [228] and with the results from the self-consistent lattice theory proposed in Ref. [203]. Such a low-temperature insulating behavior at $U = 1.0$ is clearly found in the numerical data for both 1PI and DΓA at $\beta = 100.0$, shown in the right panels of Fig. 4.36. Note that ladder DF calculations cannot be performed at such low temperatures and the contribution of 2nd-order DF diagrams would not include long-range spatial correlations to open a low-temperature gap at small values of U [123]. We emphasize that, in this parameter regime, cluster extensions of DMFT would predict, instead, a low-temperature metallic phase below a larger, critical value of U (e.g., of about 1.5 according to the plaquette C-DMFT results of Ref. [229]). This confirms the necessity of including long-range spatial correlations beyond DMFT in order to capture correctly the low-temperature insulating behavior of the non-frustrated half-filled case down to very small values of the Hubbard interaction U. From a more physical point of view, our diagrammatic 1PI calculations would suggest that, differently from the DMFT or cluster DMFT case, the strong role played by long-range spin fluctuations makes quite hard, if not impossible, a clear-cut definition of the Mott-Hubbard transition in two-dimensions. Rather, a crossover between low-temperature insulating phases driven by antiferromagnetic correlations, whose nature gradually changes from Slater to Heisenberg [230–233], emerges from our analysis of the un-frustrated particle-hole symmetric case. Such general considerations can be also rather significant for realistic cases well beyond the model system considered here. For instance, an intrinsically intermixed insulating regime might be actually realized (see Refs. [112, 234], but see also Ref. [235]) in realistic situations of high-interest, as the correlated "Mott" antiferromagnetic phase of the doped/undoped cuprates.

Chapter 5

Summary and Outlook

5.1 Summary

In this thesis we have addressed the important problem of the theoretical many-body description of electronic correlations in lattice systems. In real materials strong correlations arise usually in compounds with partially filled d- or f-shells and are responsible for many fascinating phenomena such as, e.g., the Mott metal-to-insulator transition [236], quasiparticle renormalization effects [38, 194, 237, 238] or anomalies ("kinks") in the specific heat [239] and in the optical spectra and sum-rules [99, 105, 110, 111]. All these effects can be sufficiently well described by taking into account only local correlations, which can be accomplished by means of DMFT. However, some of the arguably most fascinating phenomena in condensed matter physics, such as unconventional superconductivity [17], (weak) localization effects [208, 210, 240–242] or (quantum) critical behavior [243, 244] originate from nonlocal correlations. In this situation DMFT is insufficient due to its intrinsic mean-field nature with respect to spatial degrees of freedom. Hence, extensions of DMFT, which are capable of including nonlocal correlations, are required for an accurate qualitative and quantitative description of the effects originating from nonlocal correlations. The main goal of this thesis is, hence, to point out routes from DMFT and its non-perturbative description of local correlations to more advanced many-body techniques capable of taking into account also nonlocal correlation effects.

In this respect, **chapter 1** gives a short introduction into the physics of correlated electron systems and introduces the methods to treat them, which is the main scope of this thesis. Furthermore, this chapter contains a survey over the main topics of the present thesis.

Chapter 2 provides for an introduction to the basic models for correlated electrons and

the quantum field theoretical techniques to treat them. Specifically, we start by recalling how the Hubbard model (2.22) can be deduced from the general solid state Hamiltonian (1.1) restricting ourselves just to the most relevant degrees of freedom, i.e., the correlated energy band(s) at the Fermi level, and taking into account just a local interaction between electrons at the same lattice site. Nevertheless, the physics of this model is characterized by both local and nonlocal correlation effects and can be –with good cause– considered as the simplest model for correlated electrons on a lattice. Furthermore, we introduced the Anderson impurity model (AIM) which describes just the local correlations between two electrons at a single impurity site hybridized with a non-interacting bath. Let us mention that, though the AIM has physical significance on its own, in the present thesis it mainly serves as a (dynamical) mean-field representation of the Hubbard Hamiltonian. When applying quantum field theory methods to these models the most relevant information is enclosed in the one- and two-particle Green's functions of the system. Their general properties and symmetry relations are extensively discussed in the second part of chapter 2, providing –to the best of our knowledge for the first time– a comprehensive and systematic presentation of this matter. For an illustration of the typical structure of the most important one- and two-particle Green's functions, we discuss their explicit expressions for the Hubbard model and the AIM at the end of chapter 2 for the two limiting cases of vanishing potential and kinetic energy, respectively, i.e., for the non-interacting system and the atomic limit.

As for the treatment of the realistic situation of a finite bandwidth and interaction we have to resort to approximations for calculating the Green's functions of the Hubbard model. In a parameter regime where the kinetic and the potential energy are of the same order of magnitude non-perturbative approaches are required. Hence, in **chapter 3** we introduce the dynamical mean field theory [24]. This method replaces the actual lattice problem with a self-consistent AIM, including in this way non-perturbatively all purely local correlation effects. In order to demonstrate the predictive power of DMFT, in situations where these local correlations are predominant even for real systems, we presented a DMFT study of the temperature dependence of the optical conductivity and sum rule in two optimally doped Bi-based high-temperature superconducting cuprates for temperatures much larger than the critical temperature of the superconducting phase-transition ($T \gg T_c$). Let us stress that the optical conductivity reduces to just the product of two one-particle Green's function. However, in general the inclusion of (local) frequency dependent vertex corrections beyond this bare bubble contribution is crucial for an accurate numerical description of other response functions, as it is demonstrated, e.g., for the frequency dependent magnetic susceptibility of LaFeAsO in Ref. [120]. In fact, the scope of the present thesis goes well beyond the

state-of-the-art DMFT analysis of one-particle Green's functions. Specifically, in the second part of chapter 3 we presented a comprehensive study of local two-particle DMFT Green's functions, i.e., generalized susceptibilities and vertex functions. They are crucial ingredients not only for calculating momentum-dependent response functions within the DMFT formalism, as mentioned above, but they also serve as an input for (almost) all diagrammatic extensions of DMFT, aiming at the inclusion of nonlocal correlations beyond the local ones of DMFT. Besides a general discussion of the structure of the local two-particle objects in terms of a comparison with perturbation theory, which provides very significant information for improving the numerical treatment, we also explicitly analyzed the different types of divergences occurring at all vertex levels (F, Γ_r and Λ). We found that, while the singularities of the principal features (background and diagonal structures) of the vertices F and Γ_r are governed by the corresponding divergence of the local magnetic susceptibility at the Mott metal-to-insulator transition, a completely different low-frequency singular behavior can be observed for Λ and Γ_r [71, 130]. For the latter, singularities occur for interaction values well before the Mott transition, possibly indicating a precursor of the MIT at low temperatures. They can be traced to large values of U and T and are found even in the atomic limit, where analytical derivations have been given explicitly. However, a conclusive interpretation of these low-frequency divergences of Γ_r and Λ is still missing, calling for further investigations of this fascinating and unexpected observation. In the third part of chapter 3 we have also presented a brief discussion of the corresponding attractive Hubbard model in terms of the mapping onto its repulsive counterpart, which is relevant as an effective model of the BCS-BE crossover [159–163, 245, 246].

In **chapter 4** of this thesis, we include nonlocal correlations beyond DMFT in our calculations. As argued in the first section of this chapter these nonlocal correlations are crucial for an accurate description of low-dimensional systems and systems in the vicinity of second-order phase transitions. In this respect the focus of this thesis has been on so-called diagrammatic extensions of DMFT which –in contrast to cluster extensions– are able to take into account correlations at all length scales on equal footing. This is necessary, e.g., for capturing the critical behavior of a system close to a second-order phase transition. After a survey of the common features of all diagrammatic methods, we focus on the DΓA, the formalism of which we present in more detail. First results for a simple benzene molecule obtained by means of the full DΓA scheme demonstrate the applicability of this method for describing nonlocal correlations. Since the full DΓA method, based on the self-consistent solution of the parquet equations, is numerically very demanding, we also discuss a simplified scheme, coined ladder DΓA which we applied to the interesting problem of the critical

behavior of the half-filled three dimensional Hubbard model close to the second-order phase transition to the antiferromagnetic state. It was shown that DΓA improves on the numerical value of the transitions temperature and corrects the mean-field like critical exponents of DMFT. Remarkably, they were found to be (within the numerical precision) coinciding with those of the three-dimensional Heisenberg model, as it can be expected for this universality class. In addition, we also observed significant effects of nonlocal correlations on the spectral quantities, where gaps open in parameter regimes predicted to be metallic by DMFT. Eventually, in the last section of chapter 4, we presented a completely new approach based on the functional integral formalism and the one-particle irreducible generating functional of the Hubbard model, coined 1PI approach, which allows for a comparison of the existing diagrammatic methods, i.e., DF and DΓA, within a unifying formalism. The corresponding diagrammatic analysis and the numerical results obtained for the half-filled two-dimensional Hubbard model on a square lattice indeed provide for a better understanding of the relation between DF, DΓA and 1PI, which might trigger new developments in the field of diagrammatic methods beyond DMFT. In this respect let us just mention the very recent attempts to combine DMFT with functional renormalization group techniques (fRG) [125], where the corrections to DMFT are computed through parquet-like diagrams generated via the fRG flow of one specific parameter rather than by an explicit construction [147].

Let us emphasize that, despite the successful application of the methods for describing electronic correlations on all length scale for specific many body problems, which were discussed in this thesis, a considerable number of important open questions remains to be addressed. Hence, a brief outlook on still unsolved physical problems and recent methodological developments is given in the following, final section.

5.2   Outlook

The methods and the corresponding applications presented in this thesis are at the frontier research of quantum many-body theory. Hence, it is difficult to make precise predictions on which specific aspects will be more significant for future developments in this field. Nevertheless, we will try in the following final section to figure out some relevant future issues, which are suggested by the results of this work.

Non-local interactions.   In this thesis we were exclusively concerned with the Hubbard model and the AIM, which exhibit a purely local interaction between the particles. As we have seen, from such a purely local interaction both local *and* nonlocal correlations emerge.

However, the real, "naked" interaction between the electrons in a crystal is given by the Coulomb repulsion [see Eq. (1.1)], which is long-range in its nature. In many situations the $\frac{1}{r}$ tail ($r = |\mathbf{r}|$) of this potential is of course well screened (leading to an exponentially damped Yukawa-like interaction $\frac{e^{-r/\lambda}}{r}$), which can justify the assumption of a purely local interaction as in the Hubbard model and the AIM, e.g., for the case of very localized orbitals at the Fermi-level. In general, however, neglecting nonlocal interaction contributions might represent a rather crude approximation for a given system as was shown recently, e.g., for the case of adatoms on semiconductor surfaces [40,247]. In such a situation, one should evidently supplement the Hubbard Hamiltonian with a nonlocal (e.g., nearest-neighbor) interaction V ("extended Hubbard model"), which further provides the opportunity of observing new physical phenomena, such as a tendency to a charge-ordered phase (instead of the spin-ordered state induced by the purely local interaction). We also note that the effects of a nonlocal interaction V can be translated formally into a dynamically screened local Coulomb interaction $U(\omega)$, if one performs a downfolding of the nonlocal to a purely local interaction. From a more technical point of view, we recall that for a theoretical description of this *extended* Hubbard model [248–250], the DMFT limit of an infinite coordination number z leads just to the static Hartree approximation for the nonlocal interaction V, if the proper scaling $V = \frac{V^*}{z}$ is adopted. However, if one is interested more in the physical consequences of the nonlocal interaction rather than in a formally clean derivation in the limit of $z \to \infty$, a different scaling such as $V = \frac{V^*}{\sqrt{z}}$ can be assumed. This leads to a divergent Hartree-contribution, which has to be subtracted, but, at the same time, gives rise to a non-trivial limit for this model, the so-called *extended* DMFT (EDMFT) approach. EDMFT can be applied for studying the competition between local and nonlocal interactions at a model level, allowing, e.g., for an understanding of satellite features in spectra due to plasmonic excitations [251]. As for the description of realistic materials (E)DMFT has been recently combined with the GW [252], an ab-inito method which treats the solid state problem (1.1) on the Hartree-Fock level where, however, the full Coulomb interaction has been screened by random phase approximation diagrams. An application of this combined method on the above-mentioned systems of adatoms on a semiconductor surface yields encouraging results [40], e.g., for the density of states, compared to experimental data.

Although the GW+DMFT approach [149,227,253–255] represents a conceptual improvement for calculating the electronic structure of real materials with respect to LDA+DMFT [21,256], which suffers from an intrinsically unsolvable double-counting problem, it still constitutes a rather ad-hoc merging of two (in their respective field successful) approaches without a unifying underlying principle. Hence, in the following, a new theory, which incorporates
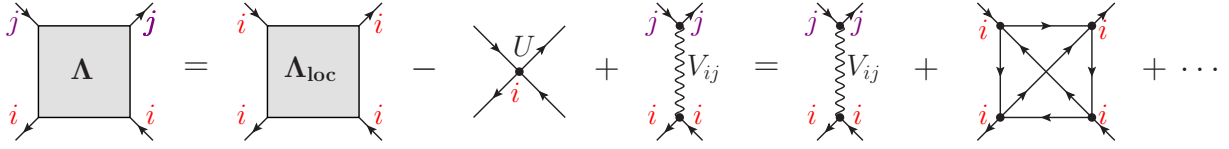
Figure 5.1: Fully irreducible vertex Λ for the ab initio version of DΓA: The lowest order contribution of the local vertex of "standard" DΓA, i.e., the Hubbard interaction parameter U, is replaced by the full nonlocal Coulomb interaction V (which is represented here as V_{ij}, i.e., in real space).

both the nonlocal interactions of GW and the local correlations of DMFT but also goes beyond the latter approaches by including nonlocal correlations, will be suggested.

DΓA for realistic materials. The basic idea of DΓA, as discussed in Sec. 4.2, is to replace the fully irreducible vertex of the system by its local counterpart (see Fig. 4.7b) obtained from a corresponding AIM ($\Lambda = \Lambda_{\mathrm{loc}}$). From Λ_{loc}, in turn, one can obtain all (momentum-dependent!) one- and two-particle Green's function of the lattice system via the self-consistent solution of the Parquet equations (see Sec. 4.2.2). According to the discussion in Secs. 3.2.3 and 4.2 and to Fig. 4.7b the lowest order contribution to Λ_{loc} is represented by the purely local Hubbard interaction U, if one considers the simplified Hubbard Hamiltonian (2.22) as model for the actual compound. A natural idea, aiming at an application of DΓA to real materials without being restricted to the case of a purely local interaction, is to replace this lowest order contribution to Λ_{loc} by the corresponding lowest order contribution to Λ of the real system, i.e., by the full Coulomb interaction (e.g., V_{ij} on a given Wannier-basis in real space). In practice, this means that the input of the Parquet solver will be changed from Λ_{loc} of DΓA to the fully irreducible vertex shown in Fig. 5.1, i.e., $V_{ij} + \Lambda_{\mathrm{loc}} - U$, in the so-called ab-initio DΓA [192]. Solving the parquet equations with this changed input, which includes the full Coulomb interaction as lowest order term, and the bare dispersion of our compound, reproduces *all* diagrams which are generated in GW, as well as the full set of DMFT diagrams [192]. In addition, nonlocal correlation effects which are considered *neither* in GW *nor* in DMFT are taken into account systematically.

New Physics accessible. The improved theoretical description of correlations might hold the key for the understanding of fascinating phenomena such as quantum criticality, (weak) localization or unconventional superconductivity. These physical problems are typically treated in the weak-coupling regime with perturbative methods such as fluctuation exchange (FLEX) [44, 257], weak-coupling perturbation theory, or renormalization group tech-

niques [125, 196]. Ab initio DΓA, which has been introduced in the previous paragraph, has the potential to provide for a qualitative and quantitative understanding of this striking physical phenomena even for strongly correlated systems, where conventional perturbative approaches are no longer applicable.

More precisely, a more sophisticated quantum many-body treatment of the solid state Hamiltonian (1.1), including nonlocal interactions and correlations, could be applied to several still unsolved physical problems. In this respect, let us focus here on the physics, previously mentioned, of quantum critical points (QCP) [176, 243, 258], i.e., critical points at zero temperature ($T = 0$). There is a large bunch of experimental results [259, 260] reporting the actual presence of QCPs in strongly correlated systems such as heavy fermion compounds. Even the high-temperature superconductivity of the cuprates has been related from several groups and in different perspective to a quantum critical point inside the superconducting dome [261, 262]. Currently, two theoretical approaches are applied to treat quantum criticality: (i) In the Hertz-Millis-Moriya theory, a perturbative approach, critical fluctuations on the time-axis are treated in the same way as the corresponding spatial fluctuations, leading to an increase of the dimension of the system by one [263]. (ii) On the other hand, in the local quantum criticality picture of Q. Si [264], a special role is assigned to temporal fluctuations, rendering the situation similar to that described by DMFT. Ab initio DΓA, including non-perturbatively both kind of fluctuations, could be used in the future to clarify whether one of these scenarios is correct or a more complex interplay between the two is occurring in a given material.

Appendix A

Symmetries

In this section the symmetry properties of the two-particle objects are reported for the particle-particle (pp) notation. We start with the corresponding symmetry relations for the generalized susceptibility:

Symmetry	Relation in pp-notation	Reference
Crossing symmetry	$\chi_{pp,\overline{\sigma\sigma'}}^{\nu\nu'\omega} - \delta_{\sigma\sigma'}\chi_{0,pp}^{\nu(\omega-\nu')\omega} = -\chi_{pp,\sigma\sigma'}^{\nu(\omega-\nu')\omega} + \chi_{0,pp}^{\nu\nu'\omega}$	Sec. 2.2.1.2, Eq. 2.37
Complex conjugation	$(\chi_{pp,\sigma\sigma'}^{\nu\nu'\omega})^* = \chi_{pp,\sigma'\sigma}^{(-\nu')(-\nu)(-\omega)} \overset{\mathrm{SU(2)}}{=} \chi_{pp,\sigma\sigma'}^{(-\nu')(-\nu)(-\omega)}$	Sec. 2.2.1.3, Eq. 2.39
SU(2) symmetry	$\chi_{pp,\sigma\sigma'}^{\nu\nu'\omega} = \chi_{pp,(-\sigma)(-\sigma')}^{\nu\nu'\omega} = \chi_{pp,\sigma'\sigma}^{\nu\nu'\omega}$ $\chi_{pp,\sigma\sigma}^{\nu\nu'\omega} = \chi_{pp,\sigma(-\sigma)}^{\nu\nu'\omega} - \chi_{pp,\sigma(-\sigma)}^{\nu(\omega-\nu')\omega} + \chi_{0,pp}^{\nu\nu'\omega}$	Sec. 2.2.2.2, Eqs. 2.87, 2.89
Time reversal symmetry	$\chi_{pp,\sigma\sigma'}^{\nu\nu'\omega} = \chi_{pp,\sigma'\sigma}^{\nu'\nu\omega} \overset{\mathrm{SU(2)}}{=} \chi_{pp,\sigma\sigma'}^{\nu\nu'\omega}$	Sec. 2.2.2.3, Eq. 2.95
Particle-hole symmetry $\left(\mu = \frac{U}{2} \text{ only}\right)$	$\left(\chi_{pp,\sigma\sigma'}^{\nu\nu'\omega}\right)^* = \chi_{pp,\sigma\sigma'}^{\nu\nu'\omega}$	Sec. 2.2.2.5, Eqs. 2.108-2.110
SU(2)$_\mathrm{P}$ symmetry $\left(\mu = \frac{U}{2} \text{ only}\right)$	$\chi_{pp,\sigma\sigma}^{\nu\nu'\omega} = \chi_{pp,\sigma(-\sigma)}^{\nu(\nu-\omega)(\nu+\nu'-\omega)} - \chi_{pp,\sigma(-\sigma)}^{\nu(\nu-\omega)(\nu-\nu')} + \chi_{0,pp}^{\nu\nu'\omega}$	Sec. 2.2.2.6, Eq. 2.136

Table A.1: Summary of the symmetry relations for the susceptibilities in pp-notation.

The corresponding symmetry relations for F_{pp} read:

Symmetry	Relation in pp-notation	Reference
Crossing symmetry	$$F_{pp,\overline{\sigma\sigma'}}^{\nu\nu'\omega} = -F_{pp,\sigma\sigma'}^{\nu(\omega-\nu')\omega}$$	Sec. 2.2.1.2, Eq. 2.37
Complex conjugation	$$\left(F_{pp,\sigma\sigma'}^{\nu\nu'\omega}\right)^* = F_{pp,\sigma'\sigma}^{(-\nu')(-\nu)(-\omega)} = F_{pp,\sigma\sigma'}^{(-\nu')(-\nu)(-\omega)}$$	Sec. 2.2.1.3, Eq. 2.39
SU(2) symmetry	$$F_{pp,\sigma\sigma'}^{\nu\nu'\omega} = F_{pp,(-\sigma)(-\sigma')}^{\nu\nu'\omega} = F_{pp,\sigma'\sigma}^{\nu\nu'\omega}$$ $$F_{pp,\sigma\sigma}^{\nu\nu'\omega} = F_{pp,\sigma(-\sigma)}^{\nu\nu'\omega} + F_{pp,\sigma(-\sigma)}^{\nu\nu'\omega} = F_{pp,\sigma(-\sigma)}^{\nu\nu'\omega} - F_{pp,\sigma(-\sigma)}^{\nu(\omega-\nu')\omega}$$	Sec. 2.2.2.2, Eqs. 2.87, 2.89
Time reversal symmetry	$$F_{pp,\sigma\sigma'}^{\nu\nu'\omega} = F_{pp,\sigma'\sigma}^{\nu'\nu\omega} = F_{pp,\sigma\sigma'}^{\nu'\nu\omega}$$	Sec. 2.2.2.3, Eq. 2.95
Particle-hole symmetry	$$\left(F_{pp,\sigma\sigma'}^{\nu\nu'\omega}\right)^* = F_{pp,\sigma\sigma'}^{\nu\nu'\omega}$$	Sec. 2.2.2.5, Eqs. 2.108-2.110
SU(2)$_\mathrm{P}$ symmetry $\left(\mu = \frac{U}{2} \text{ only}\right)$	$$F_{pp,\sigma\sigma}^{\nu\nu'\omega} = F_{pp,\sigma(-\sigma)}^{\nu(\nu-\omega)(\nu+\nu'-\omega)} - F_{pp,\sigma(-\sigma)}^{\nu(\nu-\omega)(\nu-\nu')}$$	Sec. 2.2.2.6, Eq. 2.136

Table A.2: Summary of the symmetry relations for the vertex function F in pp-notation.

Appendix B

Bethe-Salpeter equations

In this Appendix, we summarize the spin dependence of the three irreducible channels (i.e., ph, $\overline{ph}$, and pp) and present the derivations of the corresponding Bethe-Salpeter equations for the SU(2) symmetric case, partly following Ref. [44].

B.1 The longitudinal (=horizontal) channel ph

We start with the Bethe-Salpeter equations for the three different cases $\Gamma_{ph,\uparrow\uparrow\uparrow\uparrow} = \Gamma_{ph,\uparrow\uparrow}$, $\Gamma_{ph,\uparrow\uparrow\downarrow\downarrow} = \Gamma_{ph,\uparrow\downarrow}$ and $\Gamma_{ph,\uparrow\downarrow\downarrow\uparrow} = \Gamma_{ph,\overline{\uparrow\downarrow}}$. The three other non-vanishing spin-combinations, where all the spins are reversed, are equivalent due to SU(2)-symmetry. Diagrammatically, the Bethe-Salpeter equations take the forms shown in Fig. B.1. Algebraically they read as:

$$F_{\uparrow\uparrow}^{\nu\nu'\omega} = \Gamma_{ph,\uparrow\uparrow}^{\nu\nu'\omega} + \frac{1}{\beta} \sum_{\nu_1\sigma_1} \Gamma_{ph,\uparrow\sigma_1}^{\nu\nu_1\omega} G(\nu_1)G(\nu_1+\omega)F_{\sigma_1\uparrow}^{\nu_1\nu'\omega} \tag{B.1a}$$

$$F_{\uparrow\downarrow}^{\nu\nu'\omega} = \Gamma_{ph,\uparrow\downarrow}^{\nu\nu'\omega} + \frac{1}{\beta} \sum_{\nu_1\sigma_1} \Gamma_{ph,\uparrow\sigma_1}^{\nu\nu_1\omega} G(\nu_1)G(\nu_1+\omega)F_{\sigma_1\downarrow}^{\nu_1\nu'\omega} \tag{B.1b}$$

$$F_{\overline{\uparrow\downarrow}}^{\nu\nu'\omega} = \Gamma_{ph,\overline{\uparrow\downarrow}}^{\nu\nu'\omega} + \frac{1}{\beta} \sum_{\nu_1} \Gamma_{ph,\overline{\uparrow\downarrow}}^{\nu\nu_1\omega} G(\nu_1)G(\nu_1+\omega)F_{\overline{\uparrow\downarrow}}^{\nu_1\nu'\omega}. \tag{B.1c}$$

The plus sign in front of the second summand on the right hand side of these equations can be easily verified by comparison with second order perturbation theory: Indeed, replacing, e.g., both vertex functions Γ_{ph} and F in Eq. (B.1a) by their lowest order contribution U one obtains the second order diagram $\mathcal{P}_1$ shown in 3.10a which exhibits a plus sign [see Eq. (3.17a)].
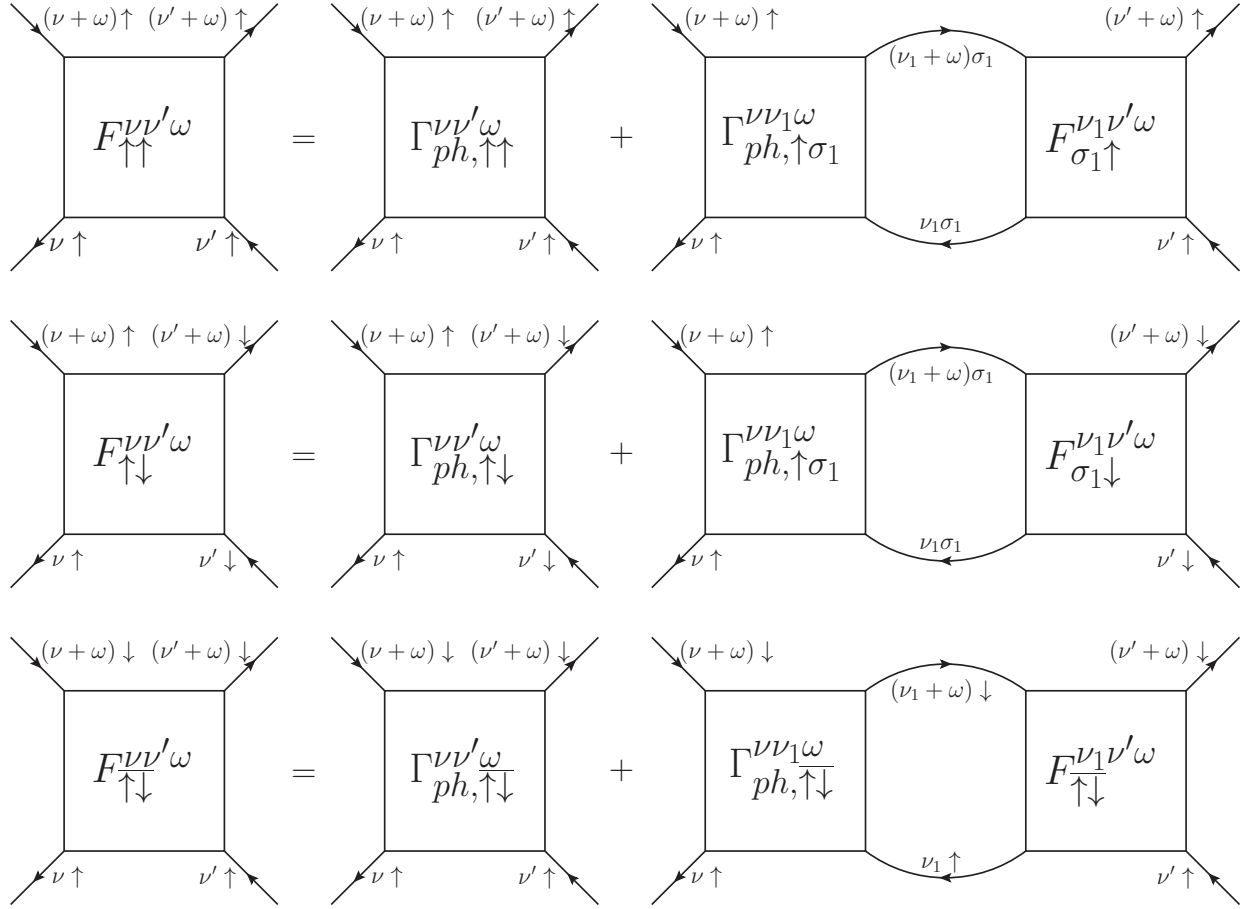
Figure B.1: Bethe-Salpeter equations in the longitudinal channel.

One can see that Eqs. (B.1a) and (B.1b) are coupled, while Eq. (B.1c) contains only $\Gamma_{ph,\sigma\sigma'}^{\nu\nu'\omega}$. In any case, we will postpone the calculation of this vertex function to the transversal particle-hole channel since $\Gamma_{ph,\overline{\sigma\sigma'}}$ and $\Gamma_{\overline{ph},\sigma\sigma'}$ are connected via the crossing relation derived in Eq. (2.165):

$$\Gamma_{ph,\uparrow\downarrow}^{\nu\nu'\omega} = -\Gamma_{\overline{ph},\uparrow\downarrow}^{\nu(\nu+\omega)(\nu'-\nu)}. \tag{B.2}$$

Considering only the coupled Eqs. (B.1a) and (B.1b) we find that, in the SU(2)-symmetric case, we can decouple them analytically by considering their sum and their difference, respectively:

$$F_{d(ensity)}^{\nu\nu'\omega} := F_{\uparrow\uparrow}^{\nu\nu'\omega} + F_{\uparrow\downarrow}^{\nu\nu'\omega}, \tag{B.3a}$$

$$F_{m(agnetic)}^{\nu\nu'\omega} := F_{\uparrow\uparrow}^{\nu\nu'\omega} - F_{\uparrow\downarrow}^{\nu\nu'\omega}, \tag{B.3b}$$

which correspond to Eqs. (2.167a) and (2.167b) for the Γ's.

Hence, we arrive at two decoupled equations for the density and magnetic channel:

$$F_d^{\nu\nu'\omega} = \Gamma_d^{\nu\nu'\omega} + \frac{1}{\beta} \sum_{\nu_1} \Gamma_d^{\nu\nu_1\omega} G(\nu_1) G(\nu_1 + \omega) F_d^{\nu_1\nu'\omega} \tag{B.4a}$$

$$F_m^{\nu\nu'\omega} = \Gamma_m^{\nu\nu'\omega} + \frac{1}{\beta} \sum_{\nu_1\sigma_1} \Gamma_m^{\nu\nu_1\omega} G(\nu_1) G(\nu_1 + \omega) F_m^{\nu_1\nu'\omega}. \tag{B.4b}$$

For the derivation of theses equations from Eqs. (B.1a) and (B.1b) we used the SU(2) symmetry, i.e., $\Gamma_{\uparrow\uparrow} = \Gamma_{\downarrow\downarrow}$ and $\Gamma_{\uparrow\downarrow} = \Gamma_{\downarrow\uparrow}$ (and similar for the F's). We can solve Eqs. (B.4) for the Γ's by an inversion of the matrix $(\mathbb{1} + \frac{1}{\beta}GGF)^{\nu\nu'\omega}$ in the $\nu\nu'$-space, i.e.,

$$\Gamma_{d,m}^{\nu\nu'\omega} = \sum_{\nu_1} F_{d,m}^{\nu\nu_1\omega} \big[(\mathbb{1} + \frac{1}{\beta}GGF_{d,m})^{-1} \big]^{\nu_1\nu'\omega}, \tag{B.5}$$

where the quantity which is inverted can be written as $\chi_{d,m}^{\nu\nu'\omega}/\chi_0^{\nu\nu'\omega}$ according to the definition in Eq. (2.160) and Fig. 2.8. The definition of χ_d and χ_m is analogue to Eqs. (2.167) for the Γ's and Eqs. (B.3) for the F's.

For the sake of completeness, we want to rewrite Eq. (B.5) into the form which was used for extracting the Γ's shown in this thesis. Combining the definition of the χ's in Eq. (2.160) with the Bethe-Salpeter equations for the F's [Eq. (B.4)] one finds the corresponding Bethe-Salpeter equations for the χ's:

$$\chi_{d,m}^{\nu\nu'\omega} = \chi_0^{\nu\nu'\omega} - \frac{1}{\beta^2} \sum_{\nu_1\nu_2} \chi_0^{\nu\nu_1\omega} \Gamma_{d,m}^{\nu_1\nu_2\omega} \chi_{d,m}^{\nu_2\nu'\omega}. \tag{B.6}$$

Solving these equations for $\Gamma_d^{\nu\nu'\omega}$ and $\Gamma_m^{\nu\nu'\omega}$ yields

$$\Gamma_{d,m}^{\nu\nu'\omega} = \beta^2 (\chi_{d,m}^{-1} - \chi_0^{-1})^{\nu\nu'\omega}. \tag{B.7}$$

B.2 The transverse (=vertical) channel $\overline{ph}$

Diagrammatically, the Bethe-Salpeter equations for the three different spin-combinations are shown in Fig. B.2. Algebraically these equations read as:
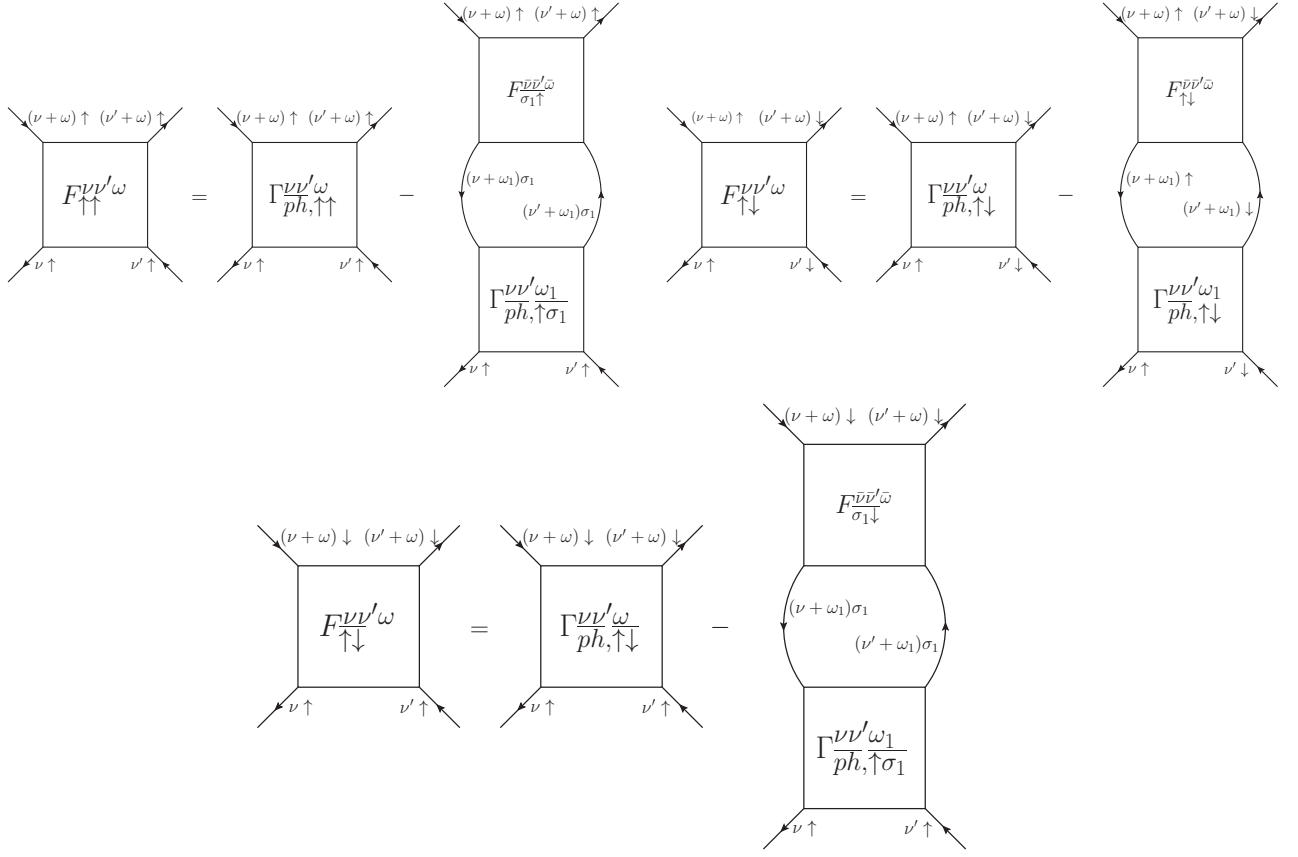
Figure B.2: Bethe-Salpeter equations in the transverse channel with $\bar{\nu} = \nu + \omega_1$, $\bar{\nu}' = \nu' + \omega_1$, $\bar{\omega} = \omega - \omega_1$.

$$F_{\uparrow\uparrow}^{\nu\nu'\omega} = \Gamma_{\overline{ph},\uparrow\uparrow}^{\nu\nu'\omega} - \frac{1}{\beta} \sum_{\omega_1\sigma_1} \Gamma_{\overline{ph},\uparrow\sigma_1}^{\nu\nu'\omega_1} G(\nu + \omega_1) G(\nu' + \omega_1) F_{\sigma_1\uparrow}^{(\nu+\omega_1)(\nu'+\omega_1)(\omega-\omega_1)} \tag{B.8a}$$

$$F_{\uparrow\downarrow}^{\nu\nu'\omega} = \Gamma_{\overline{ph},\uparrow\downarrow}^{\nu\nu'\omega} - \frac{1}{\beta} \sum_{\omega_1} \Gamma_{\overline{ph},\uparrow\downarrow}^{\nu\nu'\omega_1} G(\nu + \omega_1) G(\nu' + \omega_1) F_{\uparrow\downarrow}^{(\nu+\omega_1)(\nu'+\omega_1)(\omega-\omega_1)} \tag{B.8b}$$

$$F_{\uparrow\downarrow}^{\nu\nu'\omega} = \Gamma_{ph,\uparrow\downarrow}^{\nu\nu'\omega} - \frac{1}{\beta} \sum_{\omega_1\sigma_1} \Gamma_{\overline{ph},\uparrow\sigma_1}^{\nu\nu'\omega_1} G(\nu + \omega_1) G(\nu' + \omega_1) F_{\sigma_1\downarrow}^{(\nu+\omega_1)(\nu'+\omega_1)(\omega-\omega_1)}. \tag{B.8c}$$

As in the longitudinal channel, the minus sign in front of the second summand on the right hand side of these equations can be inferred from a comparison with second order perturbation theory [diagrams $\mathcal{P}_2$ and $\mathcal{P}_4$ in Fig. 3.10 as well as Eqs. (3.17b) and (3.18b)].

On can see that Eqs. (B.8a) and (B.8c) are coupled in the same way as it was the case for $\Gamma_{ph,\uparrow\uparrow}$ and $\Gamma_{ph,\uparrow\downarrow}$ in the longitudinal (horizontal) channel [see Eqs. (B.1a) and (B.1b)]. This

is not surprising since these functions are related to via the crossing symmetry relations, i.e.:

$$\Gamma_{\overline{ph},\uparrow\uparrow}^{\nu\nu'\omega} = -\Gamma_{ph,\uparrow\uparrow}^{\nu(\nu+\omega)(\nu'-\nu)}, \tag{B.9a}$$

$$\Gamma_{\overline{ph},\uparrow\downarrow}^{\nu\nu'\omega} = -\Gamma_{ph,\uparrow\downarrow}^{\nu(\nu+\omega)(\nu'-\nu)}, \tag{B.9b}$$

as it is reported for the full vertex functions F in Tab. 2.2 and for the Γ's in Eqs. (2.165) and (2.166). Therefore the only "new" (independent) quantity in the transverse (vertical) channel is $\Gamma_{\overline{ph},\uparrow\downarrow}$ [Eq. (B.8b)] which corresponds to $\Gamma_{ph,\overline{\uparrow\downarrow}}$ via the crossing relation Eq. (2.165). Hence, in the following we will discuss only Eq. (B.8b) in more detail. First of all we want to replace the sum over the bosonic Matsubara-frequency ω_1 with the sum over a fermionic Matsubara-frequency ν_1 by means of the transformation $\omega_1 = \nu_1 - \nu$, yielding:

$$F_{\uparrow\downarrow}^{\nu\nu'\omega} = \Gamma_{\overline{ph},\uparrow\downarrow}^{\nu\nu'\omega} - \frac{1}{\beta}\sum_{\nu_1}\Gamma_{\overline{ph},\uparrow\downarrow}^{\nu\nu'(\nu_1-\nu)}G(\nu_1)G(\nu_1+\nu'-\nu)F_{\uparrow\downarrow}^{\nu_1(\nu_1+\nu'-\nu)(\omega-\nu_1+\nu)}. \tag{B.10}$$

In the next step we introduce the transformation $\nu \to \nu$, $\nu' \to \nu+\omega$, and $\omega \to \nu'-\nu$ and make use of the SU(2)-symmetry relation reported in Tab. 2.2, $F_{\uparrow\downarrow}^{\nu(\nu+\omega)(\nu'-\nu)} = -(F_{\uparrow\uparrow}^{\nu\nu'\omega} - F_{\uparrow\downarrow}^{\nu\nu'\omega}) = -F_m^{\nu\nu'\omega}$. Furthermore we define $\widetilde{\Gamma}^{\nu\nu'\omega} = -\Gamma_{\overline{ph},\uparrow\downarrow}^{\nu(\nu+\omega)(\nu'-\nu)}$. After these manipulations (and a multiplication with -1) Eq. (B.10) reads as

$$F_m^{\nu\nu'\omega} = \widetilde{\Gamma}^{\nu\nu'\omega} + \frac{1}{\beta}\sum_{\nu_1}\widetilde{\Gamma}^{\nu\nu_1\omega}G(\nu_1)G(\nu_1+\omega)F_m^{\nu_1\nu'\omega}. \tag{B.11}$$

We observe that this is exactly the same equation as we already obtained for $\Gamma_m^{\nu\nu'\omega}$ [Eq. (B.4b)], which means that

$$\widetilde{\Gamma}^{\nu\nu'\omega} = \Gamma_m^{\nu\nu'\omega}, \tag{B.12}$$

Together with the definition of $\widetilde{\Gamma}$ this yields:

$$\Gamma_{\overline{ph},\uparrow\downarrow} = -\Gamma_m^{\nu(\nu+\omega)(\nu'-\nu)} \tag{B.13}$$

Hence, in the SU(2)-symmetric case, the transverse (vertical) channel does not provide any "new" information, and Γ_m and Γ_d represent, in fact, the only two independent functions for the two irreducible particle-hole channels.
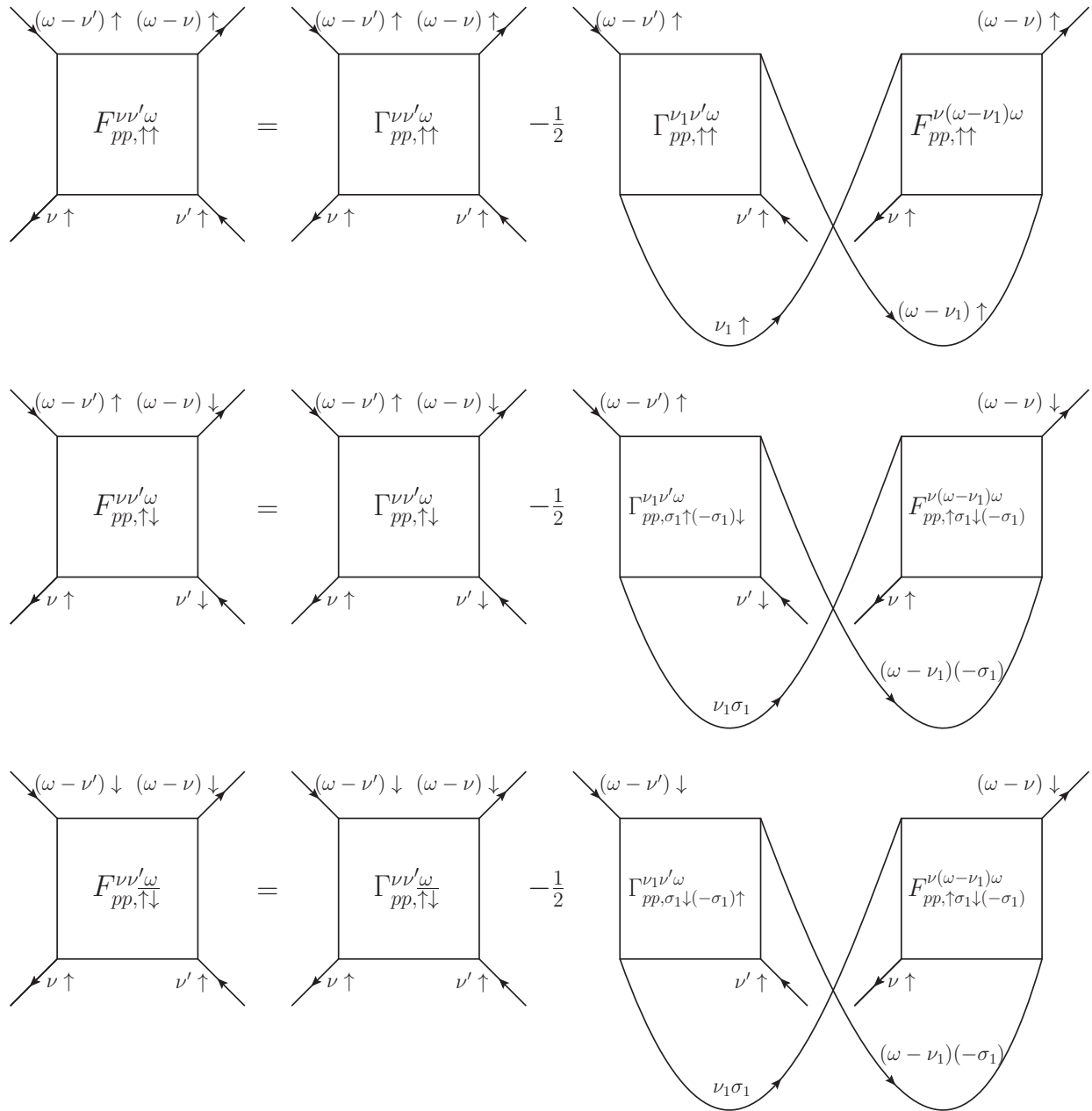
Figure B.3: Bethe-Salpeter equations in the particle-particle channel.

B.3   The particle-particle channel

The particle-particle channel is completely independent from the two particle-hole channels and fulfills a crossing relation on its own [Eq. 2.166)]. Diagrammatically, the Bethe-Salpeter equations for the three possible spin-combinations are depicted in Fig. B.3. Algebraically

these equations read as follows:

$$F_{pp,\uparrow\uparrow}^{\nu\nu'\omega} = \Gamma_{pp,\uparrow\uparrow}^{\nu\nu'\omega} - \frac{1}{2}\frac{1}{\beta}\sum_{\nu_1}\Gamma_{pp,\uparrow\uparrow}^{\nu_1\nu'\omega}G(\nu_1)G(\omega-\nu_1)F_{pp,\uparrow\uparrow}^{\nu(\omega-\nu_1)\omega} \tag{B.14a}$$

$$F_{pp,\uparrow\downarrow}^{\nu\nu'\omega} = \Gamma_{pp,\uparrow\downarrow}^{\nu\nu'\omega} - \frac{1}{2}\frac{1}{\beta}\sum_{\nu_1\sigma_1}\Gamma_{pp,\sigma_1\uparrow(-\sigma_1)\downarrow}^{\nu_1\nu'\omega}G(\nu_1)G(\omega-\nu_1)F_{pp,\uparrow\sigma_1\downarrow(-\sigma_1)}^{\nu(\omega-\nu_1)\omega} \tag{B.14b}$$

$$F_{pp,\overline{\uparrow\downarrow}}^{\nu\nu'\omega} = \Gamma_{pp,\overline{\uparrow\downarrow}}^{\nu\nu'\omega} - \frac{1}{2}\frac{1}{\beta}\sum_{\nu_1\sigma_1}\Gamma_{pp,\sigma_1\downarrow(-\sigma_1)\uparrow}^{\nu_1\nu'\omega}G(\nu_1)G(\omega-\nu_1)F_{pp,\uparrow\sigma_1\downarrow(-\sigma_1)}^{\nu(\omega-\nu_1)\omega}, \tag{B.14c}$$

where the minus sign in front of the second summand on the right hand side of the Bethe-Salpeter equations can be again inferred from comparison with second-order perturbation theory.

The factor $\frac{1}{2}$ appearing in Eqs. (B.14) prevents a double counting of diagrams which otherwise would be present in the particle-particle channel due to the indistinguishability of the particles. Fig. B.4 illustrates this state of affairs for the respective lowest order reducible contribution to Eqs. (B.14a) and (B.14b): (i) In Fig. B.4a the two *topologically distinct* lowest order diagrams for $\Gamma_{pp,\uparrow\uparrow}^{\nu\nu'\omega}$ and $F_{pp,\uparrow\uparrow}^{\nu(\omega-\nu')\omega}$, respectively, are shown. According to the Bethe-Salpeter equation one can connect, e.g., the first and the second diagrams of each box via two Green's functions in order to generate reducible contributions as shown in Fig. B.4b. However, these diagrams are topologically equivalent as one can easily verify by identifying the red and the blue lines and shifting the summation variable as $\nu_1 \to (\omega-\nu_1)$ in one of the diagrams. Hence, the Bethe-Salpeter construction of reducible contributions leads to a double counting which has to be corrected by the factor $\frac{1}{2}$ introduced in Eqs. (B.14a). A deeper understanding of this issue can be obtained by considering the crossing symmetry for $\Gamma_{pp,\uparrow\uparrow}$ and $F_{pp,\uparrow\uparrow}^{\nu\nu'\omega}$ as given in Tab. A.2: Exchanging the two outgoing or incoming lines in A_Γ (A_F) in Fig. B.4a one obtains the diagram B_Γ (B_F) which is consistent with the fact that A_Γ (A_F) belongs to $\Phi_{ph,\uparrow\uparrow}$ and B_Γ (B_F) is part of $\Phi_{\overline{ph},\uparrow\uparrow}$. Since $\Phi_{ph,\uparrow\uparrow}$ and $\Phi_{\overline{ph},\uparrow\uparrow}$ can be translated one into the other via crossing relations, they give rise to equivalent contributions in the Bethe-Salpeter equation, and, hence, to a double counting of diagrams. (ii) Similarly, for the Bethe-Salpeter equation (B.14b) the contributions corresponding to $\sigma_1 =\uparrow$ and $\sigma_1 =\downarrow$ lead to equivalent diagrams due to the crossing symmetry. This is illustrated for the lowest order irreducible diagrams (which is the bare U in the $\uparrow\downarrow$ case) in Fig. B.4c. There it is shown that the summation over σ_1 counts the emerging lowest order reducible ("bubble") diagram on the right hand side of this figure twice. The argumentation is completely analogous for
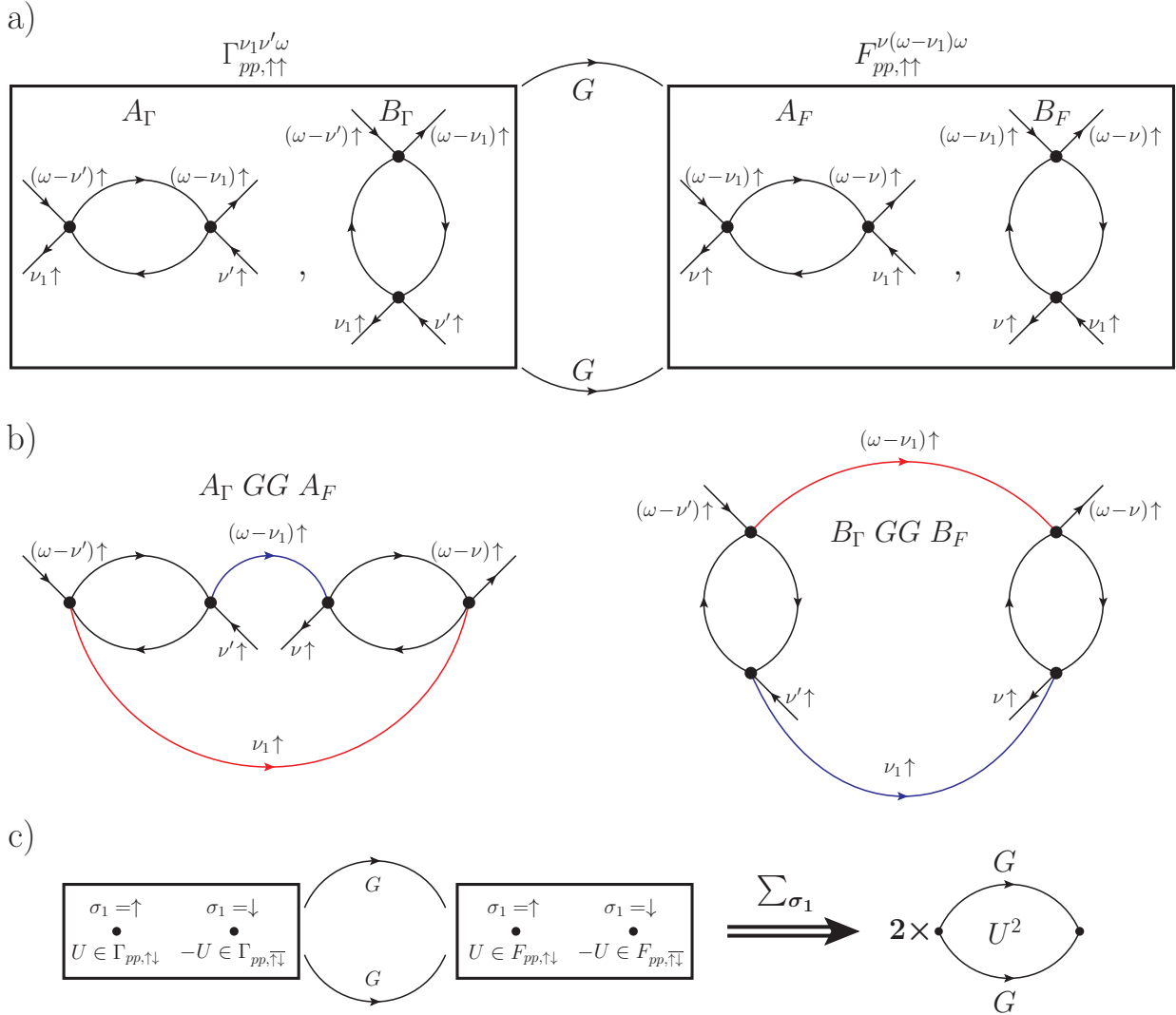
Figure B.4: a) Topologically distinct lowest order contributions to $\Gamma_{pp,\uparrow\uparrow}^{\nu\nu'\omega}$ and $F_{pp,\uparrow\uparrow}^{\nu\nu'\omega}$ in Eq. (B.14a) and Fig. B.3 (first line), respectively. The two diagrams shown in b), which are both constructed by means of the Bethe-Salpeter equation, are topologically equivalent. c) Diagrammatic representation of the lowest order diagrams for the Bethe-Salpeter equation (B.14b). The same bubble diagram is generated twice due to the internal spin sum over σ_1.

the Bethe-Salpeter equation (B.14c).

In the particle-particle channel, the $\uparrow\uparrow$-vertex is completely independent from the two other spin-combinations, while $\Gamma_{pp,\uparrow\downarrow}$ and $\Gamma_{pp,\overline{\uparrow\downarrow}}$ are not. In fact, they are coupled in the same way as $\Gamma_{ph,\uparrow\uparrow}$ and $\Gamma_{ph,\uparrow\downarrow}$, and, hence, it is possible to decouple them by introducing the linear

combinations:

$$F_{s(inglet)}^{\nu\nu'\omega} = F_{pp,\uparrow\downarrow}^{\nu\nu'\omega} - F_{pp,\overline{\uparrow\downarrow}}^{\nu\nu'\omega} \tag{B.15a}$$

$$F_{t(riplet)}^{\nu\nu'\omega} = F_{pp,\uparrow\downarrow}^{\nu\nu'\omega} + F_{pp,\overline{\uparrow\downarrow}}^{\nu\nu'\omega}, \tag{B.15b}$$

which correspond to Eqs. (2.167c) and (2.167d) for the Γ's and are completely analogous to the definition of the density and magnetic channel in Eqs. (B.3). By adding and subtracting Eqs. (B.14b) and (B.14c), one gets the Bethe-Salpeter equations for the singlet and the triplet channels:

$$F_s^{\nu\nu'\omega} = \Gamma_s^{\nu\nu'\omega} + \frac{1}{2}\frac{1}{\beta}\sum_{\nu_1\sigma_1}\Gamma_s^{\nu_1\nu'\omega_1}G(\nu_1)G(\omega-\nu_1)F_s^{\nu(\omega-\nu_1)\omega} \tag{B.16a}$$

$$F_t^{\nu\nu'\omega} = \Gamma_t^{\nu\nu'\omega} + \frac{1}{2}\frac{1}{\beta}\sum_{\nu_1\sigma_1}\Gamma_t^{\nu_1\nu'\omega_1}G(\nu_1)G(\omega-\nu_1)F_t^{\nu(\omega-\nu_1)\omega}. \tag{B.16b}$$

Applying the crossing relations in *pp*-notation, given in Tab. A.2, to $F_s^{\nu(\omega-\nu_1)\omega}$ and $F_t^{\nu(\omega-\nu_1)\omega}$ yields:

$$F_s^{\nu(\omega-\nu')\omega} = F_s^{\nu\nu'\omega}, \qquad\qquad F_t^{\nu(\omega-\nu')\omega} = -F_t^{\nu\nu'\omega}. \tag{B.17}$$

Inserting these crossing-relations into Eqs. (B.16) yields again the standard matrix multiplication-form of the Bethe-Salpeter equations. Furthermore, combining these equations with the definition of the susceptibility in Eq. (2.160) yields the corresponding Bethe-Salpeter equations for the generalized susceptibilities χ which read as

$$\chi_s^{\nu\nu'\omega} = -\chi_{0,pp}^{\nu\nu'\omega} - \frac{1}{2}\frac{1}{\beta^2}\sum_{\nu_1\nu_2}(\chi_{0,pp}^{\nu\nu_1\omega} - \chi_s^{\nu\nu_1\omega})\Gamma_t^{\nu_1\nu_2\omega}\chi_{0,pp}^{\nu_2\nu'\omega}, \tag{B.18a}$$

$$\chi_t^{\nu\nu'\omega} = \chi_{0,pp}^{\nu\nu'\omega} - \frac{1}{2}\frac{1}{\beta^2}\sum_{\nu_1\nu_2}(\chi_{0,pp}^{\nu\nu_1\omega} + \chi_t^{\nu\nu_1\omega})\Gamma_t^{\nu_1\nu_2\omega}\chi_{0,pp}^{\nu_2\nu'\omega}, \tag{B.18b}$$

where χ_s and χ_t are defined analogously to the F's in Eqs. (B.15b) and (B.15a). Solving Eqs. (B.18) for $\Gamma_s^{\nu\nu'\omega}$ and $\Gamma_t^{\nu\nu'\omega}$ yields

$$\begin{aligned} \Gamma_s^{\nu\nu'\omega} &= \beta^2\big[4(\chi_s - \chi_{0,pp})^{-1} + 2\chi_{0,pp}^{-1}\big]^{\nu\nu'\omega} \\ \Gamma_t^{\nu\nu'\omega} &= \beta^2\big[4(\chi_t + \chi_{0,pp})^{-1} - 2\chi_{0,pp}^{-1}\big]^{\nu\nu'\omega}. \end{aligned} \tag{B.19}$$

Considering, furthermore, the SU(2) symmetry relation

$$F_t^{\nu\nu'\omega} = F_{pp,\uparrow\uparrow}^{\nu\nu'\omega}, \tag{B.20}$$

as derived in Eq. (2.169b), implies that [in the SU(2) symmetric case] there are only two independent irreducible particle-particle vertices, namely, Γ_s and Γ_t.

However, according to Eqs. (2.168) and the discussion below, it should be sufficient to consider $\Gamma_{pp,\uparrow\downarrow}$ only, since Γ_s and Γ_t are just its symmetric and anti-symmetric part with respect to the fermionic frequency arguments. There is indeed a possibility to decouple the $\uparrow\downarrow$ from the $\overline{\uparrow\downarrow}$ Bethe-Salpeter equation without resorting to the singlet- and the triplet-channel: One can express the functions $\Gamma_{pp,\overline{\uparrow\downarrow}}$ and $F_{pp,\overline{\uparrow\downarrow}}$ appearing in Eq. (B.14b) for $\sigma_1 = \downarrow$ in terms of $\Gamma_{pp,\uparrow\downarrow}$ and $F_{pp,\uparrow\downarrow}$, respectively, by means of the crossing-relations

$$\Gamma_{pp,\overline{\uparrow\downarrow}}^{\nu\nu'\omega} = -\Gamma_{pp,\uparrow\downarrow}^{(\omega-\nu)\nu'\omega}, \qquad\qquad F_{pp,\overline{\uparrow\downarrow}}^{\nu\nu'\omega} = -F_{pp,\uparrow\downarrow}^{\nu(\omega-\nu')\omega}. \tag{B.21}$$

Hence, we can eliminate $\Gamma_{pp,\overline{\uparrow\downarrow}}$ from Eq. (B.14b) and obtain an equation containing $\Gamma_{pp,\uparrow\downarrow}$ only:

$$F_{pp,\uparrow\downarrow}^{\nu\nu'\omega} = \Gamma_{pp,\uparrow\downarrow}^{\nu\nu'\omega} - \frac{1}{\beta}\sum_{\nu_1}\Gamma_{pp,\uparrow\downarrow}^{\nu_1\nu'\omega}G(\nu_1)G(\omega-\nu_1)F_{pp,\uparrow\downarrow}^{\nu(\omega-\nu_1)\omega}. \tag{B.22}$$

Note that the factor $\frac{1}{2}$ and the spin summation have disappeared in this equation. This is completely consistent with the discussion below Eqs. (B.14): The factor $\frac{1}{2}$ was introduced in Eq. (B.14b) since the diagrams for $\sigma_1 = \uparrow$, generated by $\Gamma_{pp,\uparrow\downarrow}$ and $F_{pp,\uparrow\downarrow}$, are completely identical to those for $\sigma_1 = \downarrow$, generated by $\Gamma_{pp,\overline{\uparrow\downarrow}}$ and $F_{pp,\overline{\uparrow\downarrow}}$ which leads to a double counting of diagrams (see Fig. B.4c). Fixing $\sigma_1 = \uparrow$ in this equation (omitting the spin-summation) avoids this double-counting, and, hence, the factor $\frac{1}{2}$ has to be removed in that case. Physically, this result can be understood in the following way: The factor $\frac{1}{2}$ was introduced in the particle-particle channel to avoid double-counting of diagrams since the two particles are indistinguishable. This clearly holds for the $\uparrow\uparrow$-case. However, in the $\uparrow\downarrow$-case the spin can be fixed (i.e., no spin-summation in the Bethe-Salpeter equation) and hence, the two particles are now distinguishable by their spin.

Finally we write Eq. (B.22) in terms of the corresponding susceptibility $\chi_{pp,\uparrow\downarrow}^{\nu\nu'\omega}$

$$\chi_{pp,\uparrow\downarrow}^{\nu\nu'\omega} = -\frac{1}{\beta^2}\sum_{\nu_1\nu_2}(\chi_{0,pp}^{\nu\nu_1\omega} - \chi_{pp,\uparrow\downarrow}^{\nu(\omega-\nu_1)\omega})\Gamma_{pp,\uparrow\downarrow}^{\nu_1\nu_2\omega}\chi_{0,pp}^{\nu_2\nu'\omega}. \tag{B.23}$$

In contrast to Eqs. (B.18) this equation does not have the form of a matrix-multiplication

since it contains $\chi_{pp,\uparrow\downarrow}^{\nu(\omega-\nu_1)\omega}$ instead $\chi_{pp,\uparrow\downarrow}^{\nu\nu_1\omega}$ inside the sum. Nevertheless, it is possible to rewrite it by means of the substitution $\nu' \to \omega - \nu'$ and the transformation $\nu_2 \to \omega - \nu_2$ of the summation variable ν_2. Considering that $\chi_{0,pp}^{(\omega-\nu_2)(\omega-\nu')\omega} = \chi_{0,pp}^{\nu_2\nu'\omega}$ one gets

$$\chi_{pp,\uparrow\downarrow}^{\nu(\omega-\nu')\omega} = -\frac{1}{\beta^2}\sum_{\nu_1\nu_2}(\chi_{0,pp}^{\nu\nu_1\omega} - \chi_{pp,\uparrow\downarrow}^{\nu(\omega-\nu_1)\omega})\Gamma_{pp,\uparrow\downarrow}^{\nu_1(\omega-\nu_2)\omega}\chi_{0,pp}^{\nu_2\nu'\omega}. \tag{B.24}$$

With the definition $\widetilde{\chi}_{pp,\uparrow\downarrow}^{\nu\nu'\omega} = \chi_{pp,\uparrow\downarrow}^{\nu(\omega-\nu')\omega}$ (and the same for the Γ's) one gets the Bethe-Salpeter equation (B.24) in the usual form of a matrix multiplication

$$\widetilde{\chi}_{pp,\uparrow\downarrow}^{\nu\nu'\omega} = -\frac{1}{\beta^2}\sum_{\nu_1\nu_2}(\chi_{0,pp}^{\nu\nu_1\omega} - \widetilde{\chi}_{pp,\uparrow\downarrow}^{\nu\nu_1\omega})\widetilde{\Gamma}_{pp,\uparrow\downarrow}^{\nu_1\nu_2\omega}\chi_{0,pp}^{\nu_2\nu'\omega}, \tag{B.25}$$

It can be solved for $\widetilde{\Gamma}$ yielding

$$\widetilde{\Gamma}_{pp,\uparrow\downarrow}^{\nu\nu'\omega} = \beta^2\left[(\widetilde{\chi}_{pp,\uparrow\downarrow} - \chi_{0,pp})^{-1} + \chi_{0,pp}^{-1}\right]^{\nu\nu'\omega}. \tag{B.26}$$

Let us stress again, that from $\Gamma_{pp,\uparrow\downarrow}^{\nu\nu'\omega}$ all the other vertex functions irreducible in the particle-particle channel, i.e., $\Gamma_s^{\nu\nu'\omega}$ and $\Gamma_t^{\nu\nu'\omega} = \Gamma_{pp,\uparrow\uparrow}^{\nu\nu'\omega}$, can be obtained via the crossing relation Eq. (2.168).

Appendix C

Parquet equations

In this section we give the explicit form of the parquet Eq. (2.162) taking into account their frequency dependence in terms of the density, magnetic, singlet and triplet channel introduced in Sec. 2.2.4.2. In order to simplify the notation we use the definition of the reducible vertex Φ

$$\Phi_r^{\nu\nu'\omega} = F_r^{\nu\nu'\omega} - \Gamma_r^{\nu\nu'\omega}, \quad r = d, m, s, t. \tag{C.1}$$

Hence, the parquet equations read

$$\Lambda_d^{\nu\nu'\omega} = \Gamma_d^{\nu\nu'\omega} + \frac{1}{2}\Phi_d^{\nu(\nu+\omega)(\nu'-\nu)} + \frac{3}{2}\Phi_m^{\nu(\nu+\omega)(\nu'-\nu)} -$$
$$- \frac{1}{2}\Phi_s^{\nu\nu'(\nu+\nu'+\omega)} - \frac{3}{2}\Phi_t^{\nu\nu'(\nu+\nu'+\omega)} \tag{C.2}$$

$$\Lambda_m^{\nu\nu'\omega} = \Gamma_m^{\nu\nu'\omega} + \frac{1}{2}\Phi_d^{\nu(\nu+\omega)(\nu'-\nu)} - \frac{1}{2}\Phi_m^{\nu(\nu+\omega)(\nu'-\nu)} +$$
$$+ \frac{1}{2}\Phi_s^{\nu\nu'(\nu+\nu'+\omega)} - \frac{1}{2}\Phi_t^{\nu\nu'(\nu+\nu'+\omega)} \tag{C.3}$$

$$\Lambda_s^{\nu\nu'\omega} = \Gamma_s^{\nu\nu'\omega} - \frac{1}{2}\Phi_d^{\nu\nu'(\omega-\nu-\nu')} + \frac{3}{2}\Phi_m^{\nu\nu'(\omega-\nu-\nu')} -$$
$$- \frac{1}{2}\Phi_d^{\nu(\omega-\nu')(\nu'-\nu)} + \frac{3}{2}\Phi_m^{\nu(\omega-\nu')(\nu'-\nu)} \tag{C.4}$$

$$\Lambda_t^{\nu\nu'\omega} = \Gamma_t^{\nu\nu'\omega} - \frac{1}{2}\Phi_d^{\nu\nu'(\omega-\nu-\nu')} - \frac{1}{2}\Phi_m^{\nu\nu'(\omega-\nu-\nu')} +$$
$$+ \frac{1}{2}\Phi_d^{\nu(\omega-\nu')(\nu'-\nu)} + \frac{1}{2}\Phi_m^{\nu(\omega-\nu')(\nu'-\nu)}. \tag{C.5}$$

For the Λ_s and Λ_t particle-particle notation was adopted. Since at the level of Λ no dependency on an irreducible channel (ph, $\overline{ph}$ or pp) is present Λ_s and Λ_t can be expressed in terms of the Λ_d and Λ_m

$$\Lambda_s^{\nu\nu'\omega} = \frac{1}{2}\Lambda_d^{\nu\nu(\omega-\nu-\nu')} - \frac{3}{2}\Lambda_m^{\nu\nu'(\omega-\nu-\nu')}$$
$$\Lambda_t^{\nu\nu'\omega} = \frac{1}{2}\Lambda_d^{\nu\nu(\omega-\nu-\nu')} + \frac{1}{2}\Lambda_m^{\nu\nu'(\omega-\nu-\nu')}. \tag{C.6}$$

Appendix D

Covariance Splitting Formula

In this appendix we will present a slightly different way of deriving the decoupling of local and non-local degrees of freedom, as performed in Eqs. (4.48) and (4.47), which is based on the *covariance splitting formula* [219] rather than on a Hubbard-Stratonovich transformation, adopted in Eq. (4.42). This might improve the understanding of the physical meaning of the integral transformations presented in Sec. 4.4, Eq. (4.42). We start from the general formulation of the covariance splitting formula for Grassmann variables:

$$
\det A \int D[c^+, c]\, e^{-c_i^+ A_{ij}^{-1} c_j} F[c^+, c] = \det B \int D[\widetilde{c}^+, \widetilde{c}]\, e^{-\widetilde{c}_i^+ B_{ij}^{-1} \widetilde{c}_j} \times
$$
$$
\times \det C \int D[c^+, c]\, e^{-(c_i^+ - \widetilde{c}_i^+) C_{ij}^{-1} (c_j - \widetilde{c}_j)} F[c^+, c],
$$
(D.1)

where A, B and C are complex $N \times N$ matrices which obey the relation $A = B + C$. The indices i and j can be interpreted as multi-indices containing all degrees of freedom of the system, e.g., $\tau/\nu, \mathbf{R}_i/\mathbf{k}, \sigma, \ldots$ $F[c^+, c]$ is an arbitrary function of the Grassmann-fields c^+ and c which, in our case, will contain, amongst others, the non-Gaussian part of the action. Assuming that B contains the non-local and C the local degrees of freedom of our system, Eq. (D.1) represents exactly the splitting of these two types of variables. In order to make a connection with our previous considerations concerning the generating functional $Z[\eta^+, \eta]$ for the Hubbard model and the AIM [see Eqs. (4.33), (4.34) and (4.41)] we identify the matrices A, B and C with the corresponding bare Green's functions of the two models under

consideration in the following way:

$$A = G_0(\nu, \mathbf{k}) = \frac{1}{i\nu - \varepsilon_{\mathbf{k}} + \mu}, \tag{D.2a}$$

$$B = G_0(\nu, \mathbf{k}) - \mathcal{G}_0(\nu) = -G_0(\nu, \mathbf{k})\mathcal{G}_0(\nu)\left[\Delta(\nu) - \varepsilon_{\mathbf{k}}\right], \tag{D.2b}$$

$$C = \mathcal{G}_0(\nu) = \frac{1}{i\nu - \Delta(\nu) + \mu}. \tag{D.2c}$$

Furthermore, the function $F[c^+, c]$ contains the interactions term U as well as the fermionic source fields η^+ and η and reads as:

$$F[c^+, c] = \exp\left\{-\sum_i \int_0^\beta d\tau \; \left[U c_{i\uparrow}^+(\tau) c_{i\uparrow}(\tau) c_{i\downarrow}^+(\tau) c_{i\downarrow}(\tau) - c_{i\sigma}^+(\tau)\eta_{i\sigma}(\tau) - \eta_{i\sigma}^+(\tau) c_{i\sigma}(\tau)\right]\right\}. \tag{D.3}$$

It is now straightforward to show that, inserting Eqs. (D.2) and (D.3) into the splitting formula, Eq. (D.1), yields exactly the representation of the generating functional $Z[\eta^+, \eta]$ for the Hubbard model as given in Eq. (4.48), if we choose $b_\sigma(\nu) = \frac{1}{\sqrt{\beta}\mathcal{G}_0(\nu)}$ there[1]. Hence, the representation of the generating functional for the Green's functions of the Hubbard model, as given in Eq. (4.48), can be also interpreted in terms of the covariation splitting formula applied to the separation of local and non-local degrees of freedom in the action of the Hubbard model. While the Hubbard-Stratonovich transformation, Eq. (4.42) allows for a more flexible decoupling of the non-local degrees of freedom from a mathematical point of view [$b_\sigma(\nu)$ is an arbitrary function in that case], the covariance splitting formula, Eq. (D.1), where $b_\sigma(\nu) = \left[\sqrt{\beta}\mathcal{G}_0(\nu)\right]^{-1}$, might constitute a physically more transparent way of separating local and non-local degrees of freedom in the Hubbard model.

---

[1]Note that one has to transfer the prefactor $\det A$ from the left-hand side of Eq. (D.1) to the right-hand side, yielding a total factor $\det(A^{-1}BC) = \prod_{\nu,\mathbf{k},\sigma} \beta[\mathcal{G}_0(\nu)]^2 \left[\Delta(\nu) - \varepsilon_{\mathbf{k}}\right]$ there. This exactly coincides with the prefactor in Eq. (4.48) when setting $b_\sigma(\nu) = \frac{1}{\sqrt{\beta}\mathcal{G}_0(\nu)}$.

Appendix E

Functional derivatives of Γ_{AIM}

In this appendix we report the first and second functional derivatives of $\Gamma_{\mathrm{AIM}}[\phi^+, \phi]$ with respect to the Grassmann fields ϕ^+ and ϕ in real and momentum space, starting from the explicit expression for Γ_{AIM} in Eq. (4.70). In real space one has:

$$\frac{\delta \Gamma_{\mathrm{AIM}}[\phi_i^+, \phi_i]}{\delta \phi_{i\sigma}(\nu)} = -\frac{1}{\beta} \left[G_{\mathrm{loc}}(\nu) \right]^{-1} \phi_{i\sigma}^+(\nu) +$$
$$+ \frac{1}{\beta^3} \sum_{\nu_1 \omega, \sigma_1} \left(1 - \frac{1}{2}\delta_{\sigma\sigma_1} \right) F_{\mathrm{loc},\sigma\sigma_1}^{\nu_1 \nu \omega} \phi_{i\sigma}^+(\nu + \omega) \phi_{i\sigma_1}^+(\nu_1) \phi_{i\sigma_1}(\nu_1 + \omega), \qquad \text{(E.1a)}$$

$$\frac{\delta \Gamma_{\mathrm{AIM}}[\phi_i^+, \phi_i]}{\delta \phi_{i\sigma}^+(\nu)} = \frac{1}{\beta} \left[G_{\mathrm{loc}}(\nu) \right]^{-1} \phi_{i\sigma}(\nu) +$$
$$- \frac{1}{\beta^3} \sum_{\nu_1 \omega, \sigma_1} \left(1 - \frac{1}{2}\delta_{\sigma\sigma_1} \right) F_{\mathrm{loc},\sigma\sigma_1}^{\nu \nu_1 \omega} \phi_{i\sigma}(\nu + \omega) \phi_{i\sigma_1}^+(\nu_1 + \omega) \phi_{i\sigma_1}(\nu_1), \qquad \text{(E.1b)}$$

for the first derivatives of Γ_{AIM} and

$$\frac{\delta^2 \Gamma_{\mathrm{AIM}}}{\delta \phi_{i\sigma'}(\nu') \delta \phi_{i\sigma}(\nu)} = \frac{1}{\beta^3} \sum_{\omega} \left(1 - \frac{1}{2}\delta_{\sigma\sigma'} \right) F_{\mathrm{loc},\sigma\sigma'}^{(\nu'-\omega)\nu\omega} \phi_{i\sigma}^+(\nu + \omega) \phi_{i\sigma'}^+(\nu' - \omega), \qquad \text{(E.2a)}$$

$$\frac{\delta^2 \Gamma_{\mathrm{AIM}}}{\delta \phi_{i\sigma'}^+(\nu') \delta \phi_{i\sigma}(\nu)} = -\frac{1}{\beta} \left[G_{\mathrm{loc}}(\nu) \right]^{-1} \delta_{\nu\nu'} \delta_{\sigma\sigma'} +$$
$$+ \frac{1}{\beta^3} \delta_{\sigma\sigma'} \sum_{\omega, \sigma_1} \left(1 - \frac{1}{2}\delta_{\sigma\sigma_1} \right) F_{\mathrm{loc},\sigma\sigma_1}^{(\nu+\omega)\nu(\nu'-\nu)} \phi_{i\sigma_1}^+(\nu + \omega) \phi_{i\sigma_1}(\nu' + \omega) +$$
$$- \frac{1}{\beta^3} \sum_{\omega} \left(1 - \frac{1}{2}\delta_{\sigma\sigma'} \right) F_{\mathrm{loc},\sigma\sigma'}^{\nu\nu'\omega} \phi_{i\sigma}^+(\nu + \omega) \phi_{i\sigma'}(\nu' + \omega) \qquad \text{(E.2b)}$$

$$\frac{\delta^2 \Gamma_{\mathrm{AIM}}}{\delta \phi_{i\sigma'}(\nu') \delta \phi_{i\sigma}^+(\nu)} = \frac{1}{\beta} \left[G_{\mathrm{loc}}(\nu) \right]^{-1} \delta_{\nu\nu'} \delta_{\sigma\sigma'} +$$
$$- \frac{1}{\beta^3} \delta_{\sigma\sigma'} \sum_{\omega, \sigma_1} \left(1 - \frac{1}{2}\delta_{\sigma\sigma_1} \right) F_{\mathrm{loc},\sigma\sigma_1}^{\nu(\nu+\omega)(\nu'-\nu)} \phi_{i\sigma_1}^+(\nu' + \omega) \phi_{i\sigma_1}(\nu + \omega) +$$
$$+ \frac{1}{\beta^3} \sum_{\omega} \left(1 - \frac{1}{2}\delta_{\sigma\sigma'} \right) F_{\mathrm{loc},\sigma\sigma'}^{\nu\nu'\omega} \phi_{i\sigma'}^+(\nu' + \omega) \phi_{i\sigma}(\nu + \omega) \qquad \text{(E.2c)}$$

$$\frac{\delta^2 \Gamma_{\mathrm{AIM}}}{\delta \phi_{i\sigma'}^+(\nu') \delta \phi_{i\sigma}^+(\nu)} = \frac{1}{\beta^3} \sum_{\omega} \left(1 - \frac{1}{2}\delta_{\sigma\sigma'} \right) F_{\mathrm{loc},\sigma\sigma'}^{\nu(\nu'-\omega)\omega} \phi_{i\sigma}(\nu + \omega) \phi_{i\sigma'}(\nu' - \omega), \qquad \text{(E.2d)}$$

for the second derivatives of Γ_{AIM}.

For the corresponding relations in momentum space we adopt the four-vector notation intro-

duced in Sec. 4.3.1, which yields:

$$\frac{\delta \Gamma_{\mathrm{AIM}}[\phi^+, \phi]}{\delta \phi_{k\sigma}} = -\frac{1}{\beta} \left[G_{\mathrm{loc}}(\nu) \right]^{-1} \phi_{k\sigma}^+ +$$
$$+ \frac{1}{\beta^3} \sum_{k_1 q, \sigma_1} \left(1 - \frac{1}{2} \delta_{\sigma\sigma_1} \right) F_{\mathrm{loc},\sigma\sigma_1}^{\nu_1 \nu \omega} \phi_{(k+q)\sigma}^+ \phi_{k_1\sigma_1}^+ \phi_{(k_1+q)\sigma_1}, \qquad \text{(E.3a)}$$

$$\frac{\delta \Gamma_{\mathrm{AIM}}[\phi^+, \phi]}{\delta \phi_{k\sigma}^+} = \frac{1}{\beta} \left[G_{\mathrm{loc}}(\nu) \right]^{-1} \phi_{k\sigma} +$$
$$- \frac{1}{\beta^3} \sum_{k_1 q, \sigma_1} \left(1 - \frac{1}{2} \delta_{\sigma\sigma_1} \right) F_{\mathrm{loc},\sigma\sigma_1}^{\nu\nu_1\omega} \phi_{(k+q)\sigma} \phi_{(k_1+q)\sigma_1}^+ \phi_{k_1\sigma_1}, \qquad \text{(E.3b)}$$

for the first derivatives of Γ_{AIM} and

$$\frac{\delta^2 \Gamma_{\mathrm{AIM}}}{\delta \phi_{k'\sigma'} \delta \phi_{k\sigma}} = \frac{1}{\beta^3} \sum_q \left(1 - \frac{1}{2} \delta_{\sigma\sigma'} \right) F_{\mathrm{loc},\sigma\sigma'}^{(\nu'-\omega)\nu\omega} \phi_{(k+q)\sigma}^+ \phi_{(k'-q)\sigma'}^+, \qquad \text{(E.4a)}$$

$$\frac{\delta^2 \Gamma_{\mathrm{AIM}}}{\delta \phi_{k'\sigma'}^+ \delta \phi_{k\sigma}} = -\frac{1}{\beta} \left[G_{\mathrm{loc}}(\nu) \right]^{-1} \delta_{\nu\nu'} \delta_{\sigma\sigma'} +$$
$$+ \frac{1}{\beta^3} \delta_{\sigma\sigma'} \sum_{q,\sigma_1} \left(1 - \frac{1}{2} \delta_{\sigma\sigma_1} \right) F_{\mathrm{loc},\sigma\sigma_1}^{(\nu+\omega)\nu(\nu'-\nu)} \phi_{(k+q)\sigma_1}^+ \phi_{(k'+q)\sigma_1} +$$
$$- \frac{1}{\beta^3} \sum_q \left(1 - \frac{1}{2} \delta_{\sigma\sigma'} \right) F_{\mathrm{loc},\sigma\sigma'}^{\nu\nu'\omega} \phi_{(k+q)\sigma}^+ \phi_{(k'+q)\sigma'} \qquad \text{(E.4b)}$$

$$\frac{\delta^2 \Gamma_{\mathrm{AIM}}}{\delta \phi_{k'\sigma'} \delta \phi_{k\sigma}^+} = \frac{1}{\beta} \left[G_{\mathrm{loc}}(\nu) \right]^{-1} \delta_{\nu\nu'} \delta_{\sigma\sigma'} +$$
$$- \frac{1}{\beta^3} \delta_{\sigma\sigma'} \sum_{\omega,\sigma_1} \left(1 - \frac{1}{2} \delta_{\sigma\sigma_1} \right) F_{\mathrm{loc},\sigma\sigma_1}^{\nu(\nu+\omega)(\nu'-\nu)} \phi_{(k'+q)\sigma_1}^+ \phi_{(k+q)\sigma_1} +$$
$$+ \frac{1}{\beta^3} \sum_{\omega} \left(1 - \frac{1}{2} \delta_{\sigma\sigma'} \right) F_{\mathrm{loc},\sigma\sigma'}^{\nu\nu'\omega} \phi_{(k'+q)\sigma'}^+ \phi_{(k+q)\sigma} \qquad \text{(E.4c)}$$

$$\frac{\delta^2 \Gamma_{\mathrm{AIM}}}{\delta \phi_{k'\sigma'}^+ \delta \phi_{k\sigma}^+} = +\frac{1}{\beta^3} \sum_q \left(1 - \frac{1}{2} \delta_{\sigma\sigma'} \right) F_{\mathrm{loc},\sigma\sigma'}^{\nu(\nu'-\omega)\omega} \phi_{(k+q)\sigma} \phi_{(k'-q)\sigma'}, \qquad \text{(E.4d)}$$

for the second derivatives of Γ_{AIM}.

Appendix F

Functional determinant of Γ_{AIM}

In this appendix we provide an explicit expression for the matrix $D[\phi_i^+, \phi_i]$ [Eq. (4.84)], which is part of the Jacobian $M[\phi^+, \phi]$ [Eq. (4.74)] of the transformation of integral variables from $\widehat{c}^+/\widehat{c}$ to ϕ^+/ϕ in Eq. (4.73). Furthermore, we evaluate the trace of $\ln[\mathbb{1} + D]$ by performing an expansion of this expression up to the fourth order in ϕ_i^+ and ϕ_i. To this end we use the results for the second functional derivatives of Γ_{AIM} with respect to ϕ_i^+ and ϕ_i which are given in appendix E. For the sake of a better readability we introduce the following definition:

$$\widehat{F}_{\sigma\sigma'}^{\nu\nu'\omega} = \left(1 - \frac{1}{2}\delta_{\sigma\sigma'}\right) F_{\mathrm{loc},\sigma\sigma'}^{\nu\nu'\omega}, \tag{F.1}$$

and write the frequency arguments of ϕ_i^+ and ϕ_i as superscripts. Hence, $D[\phi_i^+, \phi_i]$ reads (in blockform) as:

$$D[\phi_i, \phi_i^+] = \frac{1}{\beta^2} G_{\mathrm{loc}}(\nu) \times$$

$$\times \sum_{\omega} \left(\begin{array}{c|c} \begin{array}{c} \widehat{F}_{\sigma\sigma'}^{\nu\nu'\omega}\phi_{i\sigma}^{+,(\nu+\omega)}\phi_{i\sigma'}^{(\nu'+\omega)} + \\ -\delta_{\sigma\sigma'}\sum_{\sigma_1}\widehat{F}_{\sigma\sigma_1}^{\nu(\nu+\omega)(\nu'-\nu)}\phi_{i\sigma_1}^{+,(\nu+\omega)}\phi_{i\sigma_1}^{(\nu'+\omega)} \\ \widehat{F}_{\sigma\sigma'}^{\nu(\nu'-\omega)\omega}\phi_{i\sigma}^{(\nu+\omega)}\phi_{i\sigma'}^{(\nu'-\omega)} \end{array} & \begin{array}{c} \widehat{F}_{\sigma\sigma'}^{\nu(\nu'-\omega)\omega}\phi_{i\sigma}^{+,(\nu'-\omega)}\phi_{i\sigma'}^{+,(\nu+\omega)} \\ \\ \widehat{F}_{\sigma\sigma'}^{\nu\nu'\omega}\phi_{i\sigma'}^{+,(\nu'+\omega)}\phi_{i\sigma}^{(\nu+\omega)} + \\ -\delta_{\sigma\sigma'}\sum_{\sigma_1}\widehat{F}_{\sigma\sigma_1}^{\nu(\nu+\omega)(\nu'-\nu)}\phi_{i\sigma_1}^{+,(\nu'+\omega)}\phi_{i\sigma_1}(\nu+\omega) \end{array} \end{array} \right),$$

$$\tag{F.2}$$

where SU(2) and time-reversal symmetry relations, given in Tab. (2.2), were used. Note that each of the four blocks in Eq. (F.2) is a matrix with respect to the frequency- and spin-arguments, i.e., the indices of the four sub-matrices are the combined indices $(\nu\sigma)$ and

$(\nu'\sigma')$.

In order to to evaluate $\operatorname{tr}\ln\left(\mathbb{1} + D[\phi_i^+, \phi_i]\right)$, as required, e.g., in Eq. (4.87), we expand the logarithm with respect to D:

$$\ln\left(\mathbb{1} + D\right) = D - \frac{1}{2}D^2 + \frac{1}{3}D^3 + \ldots + (-1)^{n+1}\frac{1}{n}D^n + \ldots. \qquad (F.3)$$

Now we are in a position to calculate $\operatorname{tr}\ln\left(\mathbb{1} + D[\phi_i^+, \phi_i]\right)$ by computing the trace of the single terms D^n in the expansion of $\ln\left(\mathbb{1} + D[\phi_i^+, \phi_i]\right)$ in Eq. (F.3). However, as for the functionals W_{AIM} in Eqs. (4.53) and (4.57) as well as Γ_{AIM} in Eq. (4.70) we restrict ourselves to terms up to the fourth order in the fields ϕ_i^+ and ϕ_i which correspond to the contributions D and D^2 in Eq. (F.3). The corresponding result for the first order term reads as:

$$\operatorname{tr}D = 2\frac{1}{\beta}\sum_{\nu,\sigma}\left[\frac{1}{\beta}\sum_{\omega}G_{\mathrm{loc}}(\nu+\omega)\widehat{F}_{\sigma\sigma}^{\nu\nu\omega} - \frac{1}{\beta}\sum_{\omega,\sigma'}G_{\mathrm{loc}}(\nu+\omega)\widehat{F}_{\sigma\sigma'}^{\nu(\nu+\omega)0}\right]\phi_{i\sigma}^+(\nu)\phi_{i\sigma}(\nu), \quad (F.4)$$

where SU(2)-, crossing-, and time-reversal-symmetry have been used for rendering the expression on the right hand side as simple as possible. The trace of the contribution, which is of second order in D, i.e., $\operatorname{tr}D^2$, is much more complicated and yields:

$$\frac{1}{2}\operatorname{tr}D^2 = \frac{1}{\beta^3}\sum_{\nu\nu'\omega}\sum_{\sigma\sigma'}\left[\left(\frac{1}{\beta}\sum_{\nu_1,\sigma_1}\widehat{F}_{\sigma\sigma_1}^{\nu\nu_1\omega}G_{\mathrm{loc}}(\nu_1)G_{\mathrm{loc}}(\nu_1+\omega)\widehat{F}_{\sigma_1\sigma}^{\nu_1\nu'\omega}\right)+\right.$$

$$+\left(\frac{1}{\beta}\sum_{\nu_1}\widehat{F}_{\sigma\sigma}^{\nu\nu_1\omega}G_{\mathrm{loc}}(\nu_1)G_{\mathrm{loc}}(\nu_1+\omega)\widehat{F}_{\sigma\sigma'}^{\nu_1\nu'\omega}\right)+$$

$$+\left(\frac{1}{\beta}\sum_{\nu_1}\widehat{F}_{\sigma'\sigma}^{\nu\nu_1\omega}G_{\mathrm{loc}}(\nu_1)G_{\mathrm{loc}}(\nu_1+\omega)\widehat{F}_{\sigma\sigma}^{\nu_1\nu'\omega}\right)+$$

$$-\left(\frac{1}{\beta}\sum_{\nu_1}\widehat{F}_{\sigma\sigma'}^{\nu\nu')(\nu_1-\nu)}G_{\mathrm{loc}}(\nu_1)G_{\mathrm{loc}}(\nu_1+\nu'-\nu)\widehat{F}_{\sigma'\sigma}^{\nu_1(\nu_1+\nu'-\nu)(\omega+\nu-\nu_1)}\right)+$$

$$+\left.\left(\frac{1}{\beta}\sum_{\nu_1}\widehat{F}_{\sigma\sigma_1}^{\nu(\nu+\nu'+\omega-\nu_1)(\nu_1-\nu)}G_{\mathrm{loc}}(\nu_1)G_{\mathrm{loc}}(\nu+\nu'+\omega-\nu_1)\widehat{F}_{\sigma'\sigma}^{\nu_1\nu'(\omega+\nu-\nu_1)}\right)\right]\times$$

$$\times\phi_{i\sigma}^+(\nu)\phi_{i\sigma}(\nu+\omega)\phi_{i\sigma}^+(\nu'+\omega)\phi_{i\sigma}(\nu'), \qquad (F.5)$$

where $\widehat{F}$ is defined in Eq. (F.1).

Bibliography

[1] M. Born and R. Oppenheimer, *Zur Quantentheorie der Molekeln*, Ann. Phys., **389**, 457 (1927).

[2] P. Hohenberg and W. Kohn, *Inhomogeneous Electron Gas*, Phys. Rev., **136**, B864 (1964).

[3] J. T. Chayes, L. Chayes, and M. B. Ruskai, *Density functional approach to quantum lattice system*, J. Stat. Phys., **38**, 497 (1985).

[4] R. O. Jones and O. Gunnarsson, *The density functional formalism: its applications and prospects*, Rev. Mod. Phys., **61**, 689 (1989).

[5] R. Dreizler and E. Gross, *Density Functional Theory*, Springer (Heidelberg) (1989).

[6] D. C. Langreth and M. J. Mehl, *Beyond the local-density approximation in calculations of ground-state electronic properties*, Phys. Rev. B, **28**, 1809 (1983).

[7] A. Becke, *Density-functional exchange-energy approximation with correct asymptotic behavior*, Phys. Rev. A, **38**, 3089 (1988).

[8] A. Becke, *A new mixing of Hartree-Fock and local density-functional theories*, J. Chem. Phys., **98**, 1372 (1993).

[9] A. Georges, *Lectures on the Physics of Highly Correlated Electron Systems VIII*, American Institute of Physics Conference Proceedings, **715**, 3 (2003).

[10] D. B. McWhan, T. M. Rice, and J. P. Remeika, *Mott Transition in Cr-Doped V_2O_3*, Phys. Rev. Lett., **23**, 1384 (1969).

[11] D. B. McWhan and J. P. Remeika, *Metal-Insulator Transition in $(V_{1-x}Cr_x)_2O_3$*, Phys. Rev. B, **2**, 3734 (1970).

[12] L. Baldassarre, A. Perucchi, D. Nicoletti, A. Toschi, G. Sangiovanni, K. Held, M. Capone, M. Ortolani, L. Malavasi, M. Marsi, P. Metcalf, P. Postorino, and S. Lupi, *Quasiparticle evolution and pseudogap formation in V_2O_3: An infrared spectroscopy study*, Phys. Rev. B, **77**, 113107 (2008).

[13] F. Rodolakis, P. Hansmann, J.-P. Rueff, A. Toschi, M. Haverkort, G. Sangiovanni, A. Tanaka, T. Saha-Dasgupta, O. Andersen, K. Held, M. Sikora, I. Alliot, J.-P. Iti, F. Baudelet, P. Wzietek, P. Metcalf, and M. Marsi, *Inequivalent routes across the Mott transition in V_2O_3 Explored by X-ray absorption*, Phys. Rev. Lett., **104**, 047401 (2010).

[14] A. Toschi, P. Hansmann, G. Sangiovanni, T. Saha-Dasgupta, O. K. Andersen, and K. Held, *Spectral properties of the Mott Hubbard insulator $(Cr_{0.011}V_{0.989})_2O_3$ calculated by LDA+DMFT*, Journal of Physics: Conference Series, **200**, 012208 (2010).

[15] S. Lupi, L. Baldassarre, B. Mansart, A. Perucchi, A. Barinov, P. Dudin, E. Papalazarou, F. Rodolakis, J. P. Rueff, J. P. Itiè, S. Ravy, D. Nicoletti, P. Postorino, P. Hansmann, N. Parragh, A. Toschi, T. Saha-Dasgupta, O. K. Andersen, G. Sangiovanni, K. Held, and M. Marsi, *A microscopic view on the Mott transition in chromium-doped V_2O_3*, Nature Communications, **1**, 105 (2010).

[16] P. Hansmann, A. Toschi, G. Sangiovanni, T. Saha-Dasgupta, S. Lupi, M. Maresi, and K. Held, *Mott-Hubbard transition in V_2O_3 revisited*, Phys. Status Solidi B, **250**, 1251 (2013).

[17] J. G. Bednorz and K. A. Müller, *Possible high T_C superconductivity in the Ba–La–Cu–O system*, Zeitschrift für Physik B Condensed Matter, **64**, 189 (1986).

[18] R. von Helmolt, J. Wecker, B. Holzapfel, L. Schultz, and K. Samwer, *Giant Negative Magnetoresistance in Perovskitelike $La_{2/3}Ba_{1/3}MnO_x$ Ferromagnetic Films*, Phys. Rev. Lett., **71**, 2331 (1993).

[19] S. Jin, T. H. Tiefel, M. McCormack, R. A. Fastnacht, R. Ramesh, and L. H. Chen, *Thousandfold Change in Resistivity in Magnetoresistive La-Ca-Mn-O films*, Science, **264**, 413 (1994).

[20] D. G. Koskimaki and K. A. Gschneider, *Handbook on the Physics and Chemistry of Rare Earths*, North Holland Publishing (1978).

[21] K. Held, *Electronic structure calculations using dynamical mean field theory*, Advances in Physics, **56**, 829 (2007).

[22] W. Metzner and D. Vollhardt, *Correlated Lattice Fermions in $d = \infty$ Dimensions*, Phys. Rev. Lett., **62**, 324 (1989).

[23] A. Georges and W. Krauth, *Numerical solution of the $d = \infty$ Hubbard model: Evidence for a Mott transition*, Phys. Rev. Lett., **69**, 1240 (1992).

[24] A. Georges, G. Kotliar, W. Krauth, and M. J. Rozenberg, *Dynamical mean-field theory of strongly correlated fermion systems and the limit of infinite dimensions*, Rev. Mod. Phys., **68**, 13 (1996).

[25] G. Kotliar and D. Vollhardt, *Strongly Correlated Materials: Insights from Dynamical Mean-Field Theory*, Physics Today, **57**, 53 (2004).

[26] A. Toschi, A. A. Katanin, and K. Held, *Dynamical vertex approximation: A step beyond dynamical mean-field theory*, Phys. Rev. B, **75**, 045118 (2007).

[27] K. Held, A. Katanin, and A. Toschi, *Dynamical Vertex Approximation - An Introduction*, Progress of theoretical physics, **176**, 117 (2008).

[28] A. A. Katanin, A. Toschi, and K. Held, *Comparing pertinent effects of antiferromagnetic fluctuations in the two- and three-dimensional Hubbard model*, Phys. Rev. B, **80**, 075104 (2009).

[29] A. Toschi, *Strong Electronic Correlation in Dynamical Mean Field Theory and beyond*, Habilitationsschrift, Vienna University of Technology (2011).

[30] A. Valli, *Electronic correlations at the nanoscale*, Ph.D. thesis, Vienna University of Technology (2013).

[31] G. Rohringer, A. Tosch, A. A. Katanin, and K. Held, *Critical Properties of the Half-Filled Hubbard Model in Three Dimensions*, Phys. Rev. Lett., **107**, 256402 (2011).

[32] J. W. Negele and H. Orland, *Quantum Many-Particle Systems*, Westview Press (1998).

[33] A. Altland and B. Simons, *Condensed Matter Field Theory*, Cambridge University Press (2008).

[34] A. N. Rubtsov, M. I. Katsnelson, and A. I. Lichtenstein, *Dual fermion approach to nonlocal correlations in the Hubbard model*, Phys. Rev. B, **77**, 033101 (2008).

[35] H. Hafermann, G. Li, A. N. Rubtsov, M. I. Katsnelson, A. Lichtenstein, and H. Monien, *Efficient Perturbation Theory for Quantum Lattice Models*, Phys. Rev. Lett., **102**, 206401 (2009).

[36] G. Rohringer, A. Toschi, H. Hafermann, K. Held, V. I. Anisimov, and A. A. Katanin, *One-particle irreducible functional approach: A route to diagrammatic extensions of the dynamical mean-field theory*, Phys. Rev. B, **88**, 115112 (2013).

[37] T. Matsubara, *A new approach to quantum-statistical mechanics*, Prog. Theor. Phys., **14**, 351 (1955).

[38] A. Abrikosov, L. Gorkov, and Dzyaloshinski, *Methods of Quantum Field Theory in Statistical Physics*, Dover (1975).

[39] N. Ashcroft and N. Mermin, *Solid State Physics*, Hartcourt College Publishers, New York (1976).

[40] P. Hansmann, T. Ayral, L. Vaugier, P. Werner, and S. Biermann, *Long-Range Coulomb Interactions in Surface Systems: A First-Principle Description within Self-Consistently Combined GW and Dynamical Mean-Field Theory*, Phys. Rev. Lett., **110**, 166401 (2013).

[41] F. Aryasetiawan, M. Imada, A. Georges, G. Kotliar, S. Biermann, and A. I. Lichtenstein, *Frequency-dependent local interactions and low-energy effective models from electronic structure calculations*, Phys. Rev. B, **70**, 195104 (2004).

[42] A. Hewson, *The Kondo Problem to Heavy Fermions*, Cambridge University Press (1993).

[43] P. Anderson, *Localized Magnetic States in Metals*, Phys. Rev., **124**, 41 (1961).

[44] N. E. Bickers, *Theoretical Methods for Strongly Correlated Electrons*, chapter 6, 237–296, Springer-Verlag New York Berlin Heidelbert (2004).

[45] S.-X. Yang, H. Fotso, H. Hafermann, K. M. Tam, J. Moreno, T. Pruschke, and M. Jarrell, *Parquet approximation for the 4×4 Hubbard cluster*, Phys. Rev. E, **80**, 046706 (2009).

[46] K.-M. Tam, H. Fotso, S.-X. Yang, T.-W. Lee, J. Moreno, J. Ramanujam, and M. Jarrell, *Soving the parquet equations for the Hubbard model beyond weak coupling*, Phys. Rev. E, **87**, 013311 (2013).

[47] S. Pairault, D. Sénéchal, and A.-M. S. Tremblay, *Strong-coupling perturbation theory of the Hubbard model*, Eur. Phys. J. B, **16**, 85 (2000).

[48] G. Rohringer, A. Valli, and A. Toschi, *Local electronic correlation at the two-particle level*, Phys. Rev. B, **86**, 125114 (2012).

[49] P. C. Martin and J. Schwinger, *Theory of Many-Particle Systems I*, Phys. Rev., **115**, 1342 (1959).

[50] A. Dolfen, *Strong Electronic Correlations in Low-Dimensional Systems*, Ph.D. thesis, RWTH Aachen University (2010).

[51] R. U. Sexl and H. K. Urbantke, *Relativität, Gruppen, Teilchen*, Springer-Verlag, Wien (1992).

[52] L. S. Brown, *Quantum Field Theory*, Cambridge University Press (1992).

[53] C. N. Yang and S. C. Zhang, *SO_4 symmetry in a Hubbard Model*, Mod. Phys. Lett. B, **4**, 759 (1990).

[54] G.-S. Tian, *Particle-hole transformations and sum rules for the Hubbard model*, Physics Letters A, **228**, 383 (1997).

[55] A. Masumizu and K. Sogo, *Ward-Takahashi relations for the SO(4) symmetry in the Hubbard model*, Phys. Rev. B, **72**, 115107 (2005).

[56] B. G. Wybourne, *Classical Groups for Physicists*, John Wiely & Sons Inc. (1974).

[57] V. S. Varadarajan, *Lie groups, Lie algebras, and their representations*, Springer (1984).

[58] H. Shiba, *Thermodynamic Properties of the One-Dimensional Half-Filled-Band Hubbard Model. II*, Prog. Theor. Phys., **48**, 2171 (1972).

[59] Y. Nagaoka, *Coexistence of Diagonal and Off-Diagonal Long-Range Order in Fermion Systems*, Prog. Theor. Phys., **52**, 1716 (1974).

[60] V. J. Emery, *Theory of the quasi-one-dimensional electron gas with strong "one-site" interactions*, Phys. Rev. B, **14**, 2989 (1976).

[61] R. Micnas, J. Ranninger, and S. Robaszkiewicz, *Superconductivity in narrow-band systems with loca nonretarded attractive interactions*, Rev. Mod. Phys., **62**, 113 (1990).

[62] E. H. Lieb, *Two Theorems on the Hubbard Model*, Phys. Rev. Lett., **62**, 1201 (1989).

[63] E. H. Lieb, M. Loss, and R. J. McCann, *Uniform density theorem for the Hubbard model*, J. Math. Phys., **34**, 891 (1993).

[64] S. Q. Shen, Z. M. Qiu, and G. S. Tian, *Ferrimagnetic Long-Range Order of the Hubbard Model*, Phys. Rev. Lett., **72**, 1280 (1994).

[65] G. S. Tian, *Two rigorous theorems on the momentum distribution functions of the Hubbard model at half-filling*, J. Phys. A: Math. Gen., **27**, 3635 (1994).

[66] G. S. Tian, *The symmetry of the momentum distribution functions in the Hubbard model at half-filling*, Solid State Commun., **92**, 277 (1994).

[67] G. Su, *Phase separation in the two-dimensional Hubbard model*, Phys. Rev. B, **54**, R8281 (1996).

[68] A. M. Zagoskin, *Quantum Theory of Many-Body Systems*, Springer-Verlag New York, Inc. (1998).

[69] F. Mandl and G. Shaw, *Quantum Field Theory*, Wiley-Interscience Publication (1984).

[70] H. Hafermann, C. Jung, S. Brener, M. I. Katsnelson, A. N. Rubtsov, and A. I. Lichtenstein, *Superperturbation solver for quantum impurity models*, Europhysics Letters, **85**, 27007 (2009).

[71] T. Schäfer, G. Rohringer, O. Gunnarsson, S. Ciuchi, G. Sangiovanni, and A. Toschi, *Divergent Precursors of the Mott-Hubbard Transition at the Two-Particle Level*, Phys. Rev. Lett., **110**, 246405 (2013).

[72] J. J. Binney, N. J. Dowrick, A. J. Fisher, and M. E. J. Newman, *The Theory of Critical Phenomena*, Oxford University Press Inc., New York (2002).

[73] P. Weiss, *L'hypthèse du champ moléculaire et la propriété ferromagnétique*, Journal de Physique, **6**, 661 (1907).

[74] E. Ising, *Beitrag zur Theorie des Ferromagnetismus*, Zeitschrift für Physik, **31**, 253 (1925).

[75] L. Landau, *Theory of phase transformations. I*, Zh. Eksp. Teor. Fiz., **7**, 19 (1937).

[76] L. Landau, *Theory of phase transformations, II*, Zh. Eksp. Teor. Fiz., **7**, 627 (1937).

[77] H. E. Stanley, *Introduction to Phase Transitions and Critical Phenomena*, Oxford University Press (1971).

[78] L. D. Landau and E. M. Lifshitz, *Statistical Physics Part 1*, Elsevier Ltd. (1980).

[79] P. G. J. van Dongen, *Extended Hubbard model at weak coupling*, Phys. Rev. B, **50**, 14016 (1994).

[80] P. G. J. van Dongen, *Extended Hubbard model at strong coupling*, Phys. Rev. B, **49**, 7904 (1994).

[81] A. Georges and G. Kotliar, *Hubbard model in infinite dimensions*, Phys. Rev. B, **45**, 6479 (1992).

[82] N. Blümer, *Mott-Hubbard Metal-Insulator Transition and Optical Conductivity in High Dimensions*, Ph.D. thesis, Universität Augsburg (2002).

[83] E. Gull, A. J. Millis, A. I. Lichtenstein, A. N. Rubtsov, M. Troyer, and P. Werner, *Continuous-Time Monte Carlo methods for quantum impurity models*, Rev. Mod. Phys., **83**, 349 (2011).

[84] R. Bulla, T. Costi, and T. Pruschke, *Numerical renormalization group method for quantum impurity systems*, Rev. Mod. Phys., **80**, 395 (2008).

[85] U. Schollwöck, *The density-matrix renormalization group*, Rev. Mod. Phys., **77**, 259 (2005).

[86] W. Münder, A. Weiselbaum, A. Holzner, J. von Delft, and C. L. Henely, *Correlation density matrices for one-dimensional quantum chains based on the density matrix renormalization group*, New J. Phys., **12**, 075027 (2010).

[87] U. Schollwöck, *The density matrix renormalization group in the age of matrix product states*, Ann. of Phys., **326**, 96 (2011).

[88] E. Müller-Hartmann, *Correlated fermions on a lattice in high dimensions*, Zeitschrift für Physik B Condensed Matter, **74**, 507 (1988).

[89] E. Müller-Hartmann, *The Hubbard model at high dimensions: Some exact results and weak-coupling theory*, Z. Phys. B, **76**, 211 (1989).

[90] E. Müller-Hartmann, *Fermions on a lattice in high dimensions*, Int. J. Mod. Phys. B, **3**, 2169 (1989).

[91] V. Zlatić and B. Horvatić, *The local approximation for correlated systems on high dimensional lattices*, Solid State Communications, **75**, 263 (1990).

[92] T. Timusk and B. Statt, *The pseudogap in high-temperature superconductors: an experimental survey*, Rep. Prog. Phys., **62**, 61 (1999).

[93] A. F. Ioffe and A. R. Regel, *Non-crystalline, amorphous and liquid electronic semiconductors.*, Progress in Semiconductors, **4**, 237 (1960).

[94] O. Gunnarsson, M. Calandra, and J. E. Han, *Colloquium: Saturation of electrical resistivity*, Rev. Mod. Phys., **75**, 1085 (2003).

[95] P. Hansmann, *LDA+DMFT: From bulk to heterostrcutures*, Ph.D. thesis, Technische Universität Wien (2010).

[96] V. J. Emery, *Theory of high–T_C superconductivity in oxides*, Phys. Rev. Lett., **58**, 2794 (1987).

[97] O. K. Andersen, A. I. Liechtenstein, O. Jepsen, and F. Paulsen, *LDA energy bands, low–energy hamiltonians, t', t'', $t_{perp.}(k)$, and $J_{perp.}$*, Journal of Physics and Chemistry of Solids, **56**, 1573 (1995).

[98] E. Pavarini, I. Dasgupta, T. Saha-Dasgupta, O. Jepsen, and O. K. Andersen, *Band-Structure Trend in Hole-Doped Cuprates and Correlation with $T_C^{max.}$*, Phys. Rev. Lett., **87**, 047003 (2001).

[99] A. Toschi and M. Capone, *Optical sum rule anomalies in the cuprates: Interplay between strong correlation and electronic band structure*, Phys. Rev. B, **77**, 014518 (2008).

[100] M. Hashimoto, T. Yoshida, H. Yagi, M. Takizawa, A. Fukumori, M. Kubota, K. Ono, K. Tanake, D. H. Lu, Z.-X. Shen, S. Ono, and Y. Ando, *Doping evolution of the electronic structure in the single-layer cuprate $Bi_2Sr_{2-x}La_xCuO_{6+\delta}$*, Phys. Rev. B, **77**, 094516 (2008).

[101] J. M. Tomczak, *Spectral and Optical Properties of Correlated Materials*, Ph.D. thesis, Ecole Polytechnique (2007).

[102] J. M. Tomczak and S. Biermann, *Optical properties of correlated materials: Generalized Peierls approach and its application to VO_2*, Phys. Rev. B, **80**, 085117 (2009).

[103] P. Wissgott, *Transport Properties of Correlated Materials from First Principles*, Ph.D. thesis, Vienna University of Technology (2012).

[104] P. Wissgott, J. Kuneš, A. Toschi, and K. Held, *Dipole matrix element approach versus Peierls approximation for optical conductivity*, Phys. Rev. B, **85**, 205133 (2012).

[105] D. Nicoletti, O. Limaj, P. Calvani, G. Rohringer, A. Toschi, G. Sangiovanni, M. Capone, K. Held, S. Ono, Y. Ando, and S. Lupi, *High-Temperature Optical Spectral Weight and Fermi-liquid Renormalization in Bi-Based Cuprate Superconductors*, Phys. Rev. Lett., **105**, 077002 (2010).

[106] A. J. Millis, A. Zimmers, R. P. S. M. Lobo, N. Bontemps, and C. C. Homes, *Mott physics and the optical conductivity of electron-doped cuprates*, Phys. Rev. B, **72**, 224517 (2005).

[107] M. M. Qazilbash, J. J. Hamlin, R. E. Baumbach, L. Zhang, D. J. Singh, M. B. Maple, and D. N. Basov, *Electronic correlations in the iron pnictides*, Nature Physics, **5**, 647 (2009).

[108] D. N. Basov, R. D. Averitt, D. van der Marel, M. Dressel, and K. Haule, *Electrodynamics of correlated electron materials*, Rev. Mod. Phys., **83**, 471 (2011).

[109] J. P. Carbotte and E. Schachinger, *Optical spectral weight distribution in d-wave superconductors*, Phys. Rev. B, **69**, 224501 (2004).

[110] J. P. Carbotte and E. Schachinger, *Optical Sum Rule in Finite Bands*, J. Low Temp. Phys., **144**, 61 (2006).

[111] A. Toschi, M. Capone, M. Ortolani, P. Calvani, S. Lupi, and C. Castellani, *Temperature Dependence of the Optical Spectral Weight in the Cuprates: Role of Electron Correlations*, Phys. Rev. Lett., **95**, 097002 (2005).

[112] A. Comanac, L. de' Medici, M. Capone, and A. J. Millis, *Optical conductivity and the correlation strength of high-temperature copper-oxide superconductors*, Nat Phys, **4**, 287 (2008).

[113] A. F. Santander-Syro, R. P. S. M. Lobo, N. Bontemps, Z. Konstantinovic, Z. Li, and H. Raffy, *Absence of a Loss of In-Plane Infrared Spectral Weight in the Pseudogap Regime of $Bi_2Sr_2CaCu_2O_{8+\delta}$*, Phys. Rev. Lett., **88**, 097005 (2002).

[114] H. J. A. Molegraaf, C. Presura, C. van der Marel, P. H. Kes, and M. Li, *Superconductivity-Induced Transfer of In-Plane Spectral Weight in $Bi_2Sr_2CaCu_2O_{8+\delta}$*, Science, **295**, 2239 (2002).

[115] A. F. Santander-Syro, R. P. S. M. Lobo, N. Bontemps, Z. Konstantinovic, Z. Z. Li, and H. Raffy, *Pairing in cuprates from high-energy electronic states*, Europhys. Lett., **62**, 568 (2003).

[116] G. Deutscher, A. F. Sandander-Syro, and N. Bontemps, *Kinetic energy change with doping upon superfluid condenstation in high-temperature superconductors*, Phys. Rev. B, **72**, 092504 (2005).

[117] M. Ortolani, P. Calvani, and S. Lupi, *Frequency-Dependent Thermal Response of the Charge System and the Restricted Sum Rules of $La_{2-x}Sr_xCuO_4$*, Phys. Rev. Lett., **94**, 067002 (2005).

[118] F. Carbone, A. B. Kuzemenko, H. J. A. M. an dE. van Heumen, V. Lukovac, F. Marsiglio, D. va der Marel, K. Haule, G. Kotliar, H. Berger, S. Courjault, P. H. Kes, and M. Li, *Doping dependence of the redistribution of optical spectral weight in $Bi_2Sr_2CaCu_2O_{8+\delta}$*, Phys. Rev. B, **74**, 064510 (2006).

[119] H. Park, K. Haule, and G. Kotliar, *Magnetic Excitation Spectra in $BaFe_2As_2$: A Two-Particle Approach within a Combination of the Density Functional Theory and the Dynamical Mean-Field Theory Method*, Phys. Rev. Lett., **107**, 137007 (2011).

[120] A. Toschi, R. Arita, P. Hansmann, G. Sangiovanni, and K. Held, *Quantum dynamical screening of the local magnetic moment in Fe-based superconductors*, Phys. Rev. B, **86**, 064411 (2012).

[121] M. Liu, L. W. Harriger, H. Luo, M. Want, R. A. Ewings, T. Guidi, H. Park, K. Haule, G. Kotliar, S. M. Hayden, and P. Dai, *Nature of magnetic excitations in superconducting $BaFe_{1.9}Ni_{0.1}As_2$*, Nature Physics, **8**, 376 (2012).

[122] L. Huang and Y. Wang, *Dynamical Screening Effect on Local Two-Particle Vertex Functions*, arXiv:1303.2818 (2013).

[123] H. Hafermann, *Numerical Approaches to Spatial Correlations in Strongly Interacting Fermion Systems*, Ph.D. thesis, Hamburg (2009).

[124] J. E. Hirsch and R. M. Fye, *Monte Carlo Method for Magnetic Impurities in Metals*, Phys. Rev. Lett., **56**, 2521 (1986).

[125] W. Metzner, M. Salmhofer, C. Honerkamp, V. Meden, and K. Schönhammer, *Functional renormalization group approach to correlated fermion systems*, Rev. Mod. Phys., **84**, 299 (2012).

[126] J. Jauch and F. Rohrlich, *The Theory of Photons and Electrons (Second Expanded Edition)*, Springer Verlag New York Heidelberg Berlin (1975).

[127] P. R. C. Kent, M. Jarrell, T. A. Maier, and T. Pruschke, *Efficient calculation of the antiferromagnetic phase diagram of the three-dimensional Hubbard model*, Phys. Rev. B, **72**, 060411(R) (2005).

[128] S. Hummel, *Asymptotic behavior of two-particle vertex functions in dynamical mean-field theory*, Master's thesis, Vienna University of Technology (2014), In preparation.

[129] M. J. Rozenberg, G. Kotliar, and X. Y. Zhang, *Mott-Hubbard transition in infinite dimensions. II*, Phys. Rev. B, **49**, 10181 (1994).

[130] T. Schäfer, *Electronic correlations at the two-particle level*, Master's thesis, Vienna University of Technology (2012).

[131] M. Kinza and C. Honerkamp, *Two-particle correlations in a functional renormalization group scheme using a dynamical mean-field theory*, Phys. Rev. B, **88**, 195136 (2013).

[132] M. Kinza, *Single Impurity Anderson Model and Dynamical Mean Field Theory - A Functional Renormalization Group Study*, Ph.D. thesis, RWTH Aachen (2013).

[133] D. J. Luitz, *Numerical methods and applications in many fermion systems*, Ph.D. thesis, Julius-Maximilians-Universität Würzburg (2012).

[134] C. Karrasch, R. Hedden, R. Peters, T. Pruschke, K. schönhammer, and V. Meden, *A finite-frequency functional renormalization group approach to the single impurity Anderson model*, J. Phys.: Condens. Matter, **20**, 345205 (2008).

[135] R. Bulla, *Zero Temperature Metal-Insulator Transition in the Infinite-Dimensional Hubbard Model*, Phys. Rev. Lett., **83**, 136 (1999).

[136] S.-X. Yang, H. Fotso, H. Hafermann, K.-M. Tam, J. Moreno, T. Pruschke, and M. Jarrell, *Dual Fermion Dynamical Cluster Approach for Strongly Correlated Systems*, arXiv:1104.3854v1 (2011), Appendix A.

[137] M. Eckstein, M. Kollar, and P. Werner, *Thermalization after an interaction Quench in the Hubbard Model*, Phys. Rev. Lett., **103**, 056403 (2009).

[138] M. Schirò and M. Fabrizio, *Quantum quenches in the Hubbard model: Time-dependent mean-field theory and the role of quantum fluctuations*, Phys. Rev. B, **83**, 165105 (2011).

[139] *Mathematica, Version 8.0.4.0, Wolfram Research, Inc. (1988).*

[140] V. Janiŝ, *Parquet approach to nonlocal vertex functions and electrical conductivity of disordered electrons*, Phys. Rev. B, **64**, 115115 (2001).

[141] V. Janiŝ and J. Kolorenĉ, *Mean-field theories for disordered electrons: Diffusion pole and Anderson localization*, Phys. Rev. B, **71**, 245106 (2005).

[142] S.-X. Yang, H. Fotso, H. Hafermann, K.-M. Tam, J. Moreno, T. Pruschke, and M. Jarrell, *Dual fermion dynamical cluster approach for strongly correlated systems*, Phys. Rev. B, **84**, 155106 (2011).

[143] J. Kuneŝ, *Efficient treatment of two-particle vertices in dynamical mean-field theory*, Phys. Rev. B, **83**, 085102 (2011).

[144] C. Karrasch, *The Functional Renormalization Group for Zero-Dimensional Quantum Systems in and out of Equilibrium*, Ph.D. thesis, RWTH Aachen (2010).

[145] C. Husemann and M. Slamhofer, *Efficient parametrization of the vertex function Ω scheme, and the t, t' Hubbard model at von Hove filling*, Phys. Rev. B, **79**, 195125 (2009).

[146] S. Góttel, S. Andergassen, C. Honerkamp, D. Schuricht, and S. Wessel, *Critical scales in anisotropic spin systems from functional renormalization*, Phys. Rev. B, **85**, 214406 (2012).

[147] C. Taranto, S. Andergassen, J. Bauer, A. A. Katanin, W. Metzner, G. Rohringer, and A. Toschi, *From infinite to two dimensions through the functional renormalization group*, arXiv:1307.3475 (2013).

[148] J. Bauer and A. C. Hewson, *Competition between antiferromagnetic and charge order in the Hubbard-Holstein model*, Phys. Rev. B, **81**, 235113 (2010).

[149] T. Ayral, P. Werner, and S. Biermann, *Spectral Properties of Correlated Materials: Local Vertex and Nonlocal Two-Particle Correlations from Combined "GW" and Dynamical Mean-Field Theory*, Phys. Rev. Lett., **109**, 226401 (2012).

[150] T. Ayral, S. Biermann, and P. Werner, *Screening and Non-local Correlations in the Extended Hubbard Model from Self-Consistent Combined GW and Dynamical Mean Field Theory*, Phys. Rev. B, **87**, 125149 (2013).

[151] E. Roddick and D. Stroud, *Effect of Phase Fluctuations on the Low-Temperature Penetration Depth of High-T_c Superconductors*, Phys. Rev. Lett., **74**, 1430 (1995).

[152] V. J. Emery and S. A. Kivelson, *Importance of phase fluctuations in superconductors with small superfluid density*, Nature, **374**, 434 (1995).

[153] V. J. Emery and S. A. Kivelson, *Superconductivity in Bad Metals*, Phys. Rev. Lett., **74**, 3253 (1995).

[154] E. W. Carlson, S. A. Kivelson, V. J. Emery, and E. Manousakis, *Classical Phase Fluctuations in High Temperature Superconducters*, Phys. Rev. Lett., **83**, 612 (1999).

[155] A. Paramekanti, M. Randeria, T. V. Ramakrishnan, and S. S. Mandal, *Effective actions and Phase fluctuations in d-wave superconducters*, Phys. Rev. B, **62**, 6786 (2000).

[156] L. Benfatto, A. Toschi, and S. Caprara, *The low-energy phase-only action in a superconductor: from weak to strong coupling*, Phys. Rev. B, **69**, 184510 (2004).

[157] L. Benfatto, A. Toschi, S. Caprara, and C. Castellani, *Coherence length in superconductors from weak to strong coupling*, Phys. Rev. B, **66**, 054515 (2002).

[158] A. Toschi, P. Barone, M. Capone, and C. Castellani, *Pairing and superconductivity from weak to strong coupling in the attractive Hubbard model*, New J. Phys., **7**, 7 (2005).

[159] A. Toschi, M. Capone, and C. Castellani, *Energetic balance of the superconducting transition across the BCS-Bose Einstein crossover in the attractive Hubbard model*, Phys. Rev. B, **72**, 235118 (2005).

[160] C. A. R. S. de Melo, M. Randeria, and J. R. Engelbrecht, *Crossover from BCS to Bose superconductivity: Transition temperature and time-dependent Ginzburg-Landau theory*, Phys. Rev. Lett., **71**, 3202 (1993).

[161] R. Haussmann, *Crossover from BCS superconductivity to Bose-Einstein condensation: A self-cosistent theory*, Z. Phys. B Condens. Matter, **91**, 291 (1993).

[162] F. Pistolesi and G. C. Strinati, *Evolution from BCS superconductivity to Bose condensation: Calculation of the zero-temperature phase coherence length*, Phys. Rev. B, **53**, 15168 (1996).

[163] B. Kyung, S. Allen, and A.-M. S. Tremblay, *Pairing fluctuations and pseudogap in the attractive Hubbard model*, Phys. Rev. B, **64**, 075116 (2001).

[164] I. Bloch, *Ultracold quantum gases in optical lattices*, Nature, **1**, 23 (2005).

[165] M. Greiner and S. Fölling, *Condensed-matter physics: Optical lattices*, Nature, **453**, 736 (2008).

[166] A. Privitera, M. Capone, and C. Castellani, *Finite-density corrections to the unitary Fermi gas: A lattice perspective from dynamical mean-field theory*, Phys. Rev. B, **81**, 014523 (2010).

[167] Y. Kamihara, H. Hiramatsu, M. Hirano, R. Kawamura, H. Yanagi, T. Kamiya, and H. Hosono, *Iron-Based Layered Superconducter: LaOFeP*, J. Am. Chem. Soc., **128**, 10012 (2006).

[168] Y. Kamihara, T. Watanabe, M. Hirano, and H. Hosono, *Iron-Based Layered Superconductor La[$O_{1-x}F_x$]FeAs ($x = 0.05 - 0.12$) with $T_c = 26K$*, J. Am. Chem. Soc., **130**, 3296 (2008).

[169] A. Ohtomo and H. Y. Hwang, *A high-mobility electron gas at the $LaAlO_3/SrTiO_3$ heterointerface*, Nature, **427**, 423 (2004).

[170] A. Ohtomo and H. Y. Hwang, *Corrigendum: A high-mobility electron gas at the $LaAlO_3/SrTiO_3$ heterointerface*, Nature, **441**, 120 (2006).

[171] N. Reyren, S. Thiel, A. D. Caviglia, L. F. Kourkoutis, G. Hammerl, C. Richter, C. W. Schneider, T. Kopp, A.-S. Rüetschi, D. Jaccard, M. Gabay, D. A. Muller, J.-M. Triscone, and J. Mannhart, *Superconducting Interfaces Between Insulating Oxides*, Science, **317**, 1196 (2007).

[172] P. Hansmann, X. Yang, A. Toschi, G. Khaliullin, O. K. Andersen, and K. Held, *Turning a Nickelate Fermi Surface into a Cupratelike One through Heterostructuring*, Phys. Rev. Lett., **103**, 016401 (2009).

[173] P. Hansmann, A. Toschi, X. Yang, O. Andersen, and K. Held, *Electronic structure of nickelates: From two-dimensional heterostructures to three-dimensional bulk materials*, Phys. Rev. B, **82**, 235123 (2010).

[174] J. C. Cuevas and E. Scheer, *Molecular Electronics: An Introduction to theory and experiment*, World Scientific Publishing (2010).

[175] M. Lewenstein, A. Sanpera, V. Ahufinger, B. Damski, A. Sen(De), and U. Sen, *Ultracold atomic gases in optical lattices: mimicking condensed matter physics and beyond*, Advances in Physics, **56**, 243 (2007).

[176] P. Gegenwart, Q. Si, and F. Steglich, *Quantum criticality in heavy-fermion metals*, Nature Physics, **4**, 186 (2008).

[177] G. R. Grimmett and D. R. Stirzaker, *Probability and Random Processes, 2nd Edition*, Clarendon Press, Oxford (1992).

[178] A. I. Lichtenstein and M. I. Katsnelson, *Antiferromagnetism and d-wave superconductivity in cuprates: A cluster dynamical mean-field theory*, Phys. Rev. B, **62**, R9283 (2000).

[179] G. Kotliar, S. Savrasov, G. Palsson, and G. Biroli, *Cellular Dynamical Mean Field Approach to Strongly Correlated Systems*, Phys. Rev. Lett., **87**, 186401 (2001).

[180] M. H. Hettler, A. N. Tahvildar-Zadeh, M. Jarrell, T. Pruschke, and H. R. Krshnamurthy, *Nonlocal dynamical correlations of strongly interacting electron systems*, Phys. Rev. B, **58**, R7479 (1998).

[181] M. Hettler, M. Mukherjee, M. Jarrell, and H. R. Krishnamurthy, *Dynamical cluster approximation: Nonlocal dynamics of correlated electron systems*, Phys. Rev. B, **61**, 12739 (2000).

[182] T. Maier, M. Jarrell, T. Pruschke, and M. H. Hettler, *Quantum Cluster Theories*, Rev. Mod. Phys., **77**, 1027 (2005).

[183] E. Gull, P. Staar, S. Fuch, P. Nukala, M. S. Summers, T. Pruschke, T. C. Schulthess, and T. Maier, *Submatrix updates for the continuous-time ausiliary-field algorithm*, Phys. Rev. B, **83**, 075112 (2011).

[184] S. Fuchs, E. Gull, L. Pollet, E. Burovski, and E. Kozik, *Thermodynamics of the 3D Hubbard Model on Approaching the Néel Transition*, Phys. Rev. Lett., **106**, 030401 (2011).

[185] D. D. Betts and G. E. Stewart, *Estimation of zero-temperature properties of quantum spin systems on the simple cubic lattice via exact diagonalization on finite lattices*, Can. J. Phys., **75**, 47 (1997).

[186] D. D. Betts, H. Q. Lin, and J. S. Flynn, *Improved finite-lattice estimates of the properties of two quantum spin models on the infinite square lattice*, Can. J. Phys., **77**, 353 (1999).

[187] M. Jarrell, T. Maier, C. Huscroft, and S. Moukouri, *Quantum Monte Carlo algorithm for nonlocal corrections to the dynamical mean-field theory*, Phys. Rev. B, **64**, 195130 (2001).

[188] A. Macridin, M. Jarrell, T. Maier, P. R. C. Kent, and E. D'Azevedo, *Psudogap and Antiferromagnetic Correlations in the Hubbard Model*, Phys. Rev. Lett., **97**, 036401 (2006).

[189] G. Sangiovanni and O. Gunnarsson, *Isotope effect in the pseudogap state of high-temperature copper ox superconductors*, Phys. Rev. B, **84**, 100505(R) (2011).

[190] E. Gull, M. Ferrero, O. Parcollet, A. Georges, and A. J. Millis, *Momentum-space anisotropy and pseudogaps: A comparative cluster dynamical mean-field analysis of the doping-driven metal-insulator transition in the two-dimensional Hubbard model*, Phys. Rev. B, **82**, 155101 (2010).

[191] T. Maier, M. Jarrell, and D. J. Scalapino, *Structure of the Pairing Interaction in the Two-Dimensional Hubbard model*, Phys. Rev. Lett., **96**, 047005 (2006).

[192] A. Toschi, G. Rohringer, A. Katanin, and K. Held, *Ab initio calculations with the dynamical vertex approximation*, Annalen der Physik, **523**, 698 (2011).

[193] C. Slezak, J. M., T. Maier, and J. Deisz, *Multi-scale extensions to quantum cluster methods for strongly correlated electron systems*, J. Phys.: Condens. Matter, **21**, 435604 (2009).

[194] G. D. Mahan, *Many-Particle Physics*, Kluwer Academic/Plenum Publishers, New York (2000).

[195] A. E. Antipov, E. Gull, and S. Kirchner, *Critical Exponents of Strongly Correlated Fermion Systems from Diagrmmatic Multi-Scale Methods*, arXiv:1309.5976 (2013).

[196] R. Shankar, *Renormalization-group approach to interacting fermions*, Rev. Mod. Phys., **66**, 129 (1994).

[197] A. Schiller and K. Ingersent, *Systematic $1/d$ Corrections to the Infinite-Dimensional Limit of Correlated Lattice Electron Models*, Phys. Rev. Lett., **75**, 113 (1995).

[198] M. V. Sadovskii, I. A. Nekrasov, E. Z. Kuchinskii, T. Pruschke, and V. I. Anisimov, *Pseudogaps in strongly correlated metals: A generalized dynamical mean-field theory approach*, Phys. Rev. B, **72**, 155105 (2005).

[199] E. Z. Kuchinskii, I. A. Nekrasov, and M. V. Sadovski, *Psueudogaps: introducing the length scale into dynamical mean-field theory*, Low Temp. Phys., **32**, 398 (2006).

[200] E. Z. Kuchinskii, I. A. Nekrasov, and M. V. Sadovskii, *Pseudogaps in strongly correlated metals: Optical conductivity within the generalized dynamical mean-field theory approach*, Phys. Rev. B, **75**, 115102 (2007).

[201] E. Z. Kuchinskii, I. A. Nekrasov, Z. V. Pchelkina, and M. V. Sadovskii, *Psueudogap behavior in Bi2212: Results of Generalize DMFT Approach*, JETP, **104**, 792 (2007).

[202] E. Z. Kuchinskii, I. A. Nekrasov, and M. V. Sadovskii, *Interplay of electron-phonon interaction and strong correlations: DMFT+Σ study*, Phys. Rev. B, **80**, 115124 (2009).

[203] T. Jabben, N. Grewe, and S. Schmitt, *Extensions of dynamical mean-field theory by inclusion of nonlocal two-site correlations with variable distance*, Phys. Rev. B, **85**, 165122 (2012).

[204] H. Kusunose, *Influence of Spatial Correlations in Strongly Correlated Electron Systems: Extension to Dynamical Mean Field Approximation*, J. Phys. Soc. Jpn., **75**, 054713 (2006).

[205] A. Valli, G. Sangiovanni, O. Gunnarsson, A. Toschi, and K. Held, *Dynamical Vertex Approximation for Nanoscopic Systems*, Phys. Rev. Lett., **104**, 246402 (2010).

[206] A. Valli, G. Sangiovanni, A. Toschi, and K. Held, *Correlation effects in transport properties of interacting nanostructures*, Phys. Rev. B, **86**, 115418 (2012).

[207] D. Rotter, A. Valli, G. Sangiovanni, and K. Held, *Double Exchange model for nanoscopic clusters*, Eur. Phys. J. B, **86**, 68 (2013).

[208] D. Vollhardt and P. Wölfle, *Diagrammatic, self-consistent treatment of the Anderson localization problem in $d \leq 2$ dimensions*, Phys. Rev. B, **22**, 4666 (1980).

[209] P. A. Lee and T. V. Ramakrishnan, *Disordered electronic systems*, Rev. Mod. Phys., **57**, 287 (1985).

[210] D. Vollhardt and P. Wölfe, *Electronic Phase Transitions*, chapter 1, 1–78, Elsevier Science Publishers B.V. (1992).

[211] H. Park, *The Study of Two-Particle Response Functions in Strongly Correlated Electron Systems with the Dynamical Mean-Field Theory*, Ph.D. thesis, Rutgers, The State University of New Jersey (2011).

[212] T. Moriya, *Spin Fluctuations in Itinerant Electron Magnetism*, Springer-Verlag Berlin Heidelberg (1985).

[213] N. Mermin and H. Wagner, *Absence of Ferromagnetism or Antiferromagnetism in One- or Two-Dimensional Isotropic Heisenberg Models*, Phys. Rev. Lett., **17**, 1133 (1966).

[214] M. F. Collins, *Magnetic Critical Scattering*, Oxford University Press, New York (1989).

[215] E. Kozik, E. Burovski, V. W. Scarola, and M. Troyer, *Néel temperature and thermodynamics of the half-filled Hubbard model by diagrammatic determinant Monte Carlo*, Phys. Rev. B, **87**, 205102 (2013).

[216] R. Staudt, M. Dzierzawa, and A. Muramatsu, *Phase diagram of the three-dimensional Hubbard model at half filling*, Eur. Phys. J. B, **17**, 411 (2000).

[217] J. K. Freericks and V. Zlatic, *Exact dynamical mean-field theory of the Falicov-Kimball model*, Rev. Mod. Phys., **75**, 1333 (2003).

[218] D. Werner, *Funktionalanalysis*, Springer-Lehrbuch (2011).

[219] M. Salmhofer, *Renormalization - An Introduction*, Springer-Verlag Berlin Heidelberg (1999).

[220] S. Brener, H. Hafermann, A. N. Rubtsov, M. I. Katsnelson, and A. I. Lichtenstein, *Dual fermion approach to susceptibility of correlated lattice fermions*, Phys. Rev. B, **77**, 195105 (2008).

[221] A. N. Rubtsov, M. I. Katsnelson, A. I. Lichtenstein, and A. Georges, *Dual fermion approach to the two-dimensional Hubbard model: Antiferromagnetic fluctuations and Fermi arcs*, Phys. Rev. B, **79**, 045133 (2009).

[222] G. Li, H. Lee, and H. Monien, *Determination of the lattice susceptibility within the dual fermion method*, Phys. Rev. B, **78**, 195105 (2008).

[223] H. Lee, G. Li, and H. Monien, *Hubbard model on the triangular lattice using dynamical cluster approximation and dual fermion methods*, Phys. Rev. B, **78**, 205117 (2008).

[224] H. Hafermann, M. Kecker, S. Brener, A. N. Rubtsov, M. I. Katsnelson, and A. I. Lichtenstein, *Dual Fermion Approach to High-Temperature Superconducting*, J Supercond Nov Magn, **22**, 45 (2009).

[225] C. Jung, A. Lieder, S. Brener, H. Hafermann, B. Baxevanis, A. Chudnovskiy, A. N. Rubtsov, M. I. Katsnelson, and A. I. Lichtenstein, *Dual-fermion approach to non-equilibirium strongly correlated problems*, Ann. Phys., **524**, 49 (2012).

[226] A. A. Katanin, *The effect of six-point one-particle reducible local interactions in the dual fermion approach*, J. Phys. A: Math. Theor., **46**, 045002 (2013).

[227] K. Held, C. Taranto, G. Rohringer, and A. Toschi, *Hedin Equations, GW, GW+DMFT, and All That*, Lecture Notes of the Autumn School 2011 Hands-on LDA+DMFT, Forschungszentrum Juelich GmbH (publisher) (2011).

[228] D. Rost, E. V. Gorelik, F. Assaad, and N. Blümer, *Momentum-dependent pseudogaps in the half-filled two-dimensional Hubbard model*, Phys. Rev. B, **86**, 155109 (2012).

[229] H. Park, K. Haule, and G. Kotliar, *Cluster Dynamical Mean Field Theory of the Mott Transition*, Phys. Rev. Lett., **101**, 186403 (2008).

[230] K. Borejsza and N. Dupuis, *Antiferromagnetism and single-particle properties in the two-dimensional half-filled Hubbard model: Slater vs. Mott-Heisenberg*, Europhys. Lett., **63**, 722 (2003).

[231] K. Borejsza and N. Dupuis, *Antiferromagnetism and single-particle properties in the two-dimensional half-filled Hubbard model: A nonlinear sigma model approach*, Phys. Rev. B, **69**, 085119 (2004).

[232] G. Sangiovanni, A. Toschi, E. Koch, K. Held, M. Capone, C. Castellani, O. Gunnarsson, S.-K. Mo, J. W. Allen, H.-D. Kim, A. Sekiyama, A. Yamasaki, S. Suga, and P. Metcalf, *Static versus dynamical mean-field theory of Mott antiferromagnets*, Phys. Rev. B, **73**, 205121 (2006).

[233] C. Taranto, G. Sangiovanni, K. Held, M. Capone, A. Georges, and A. Toschi, *Signature of antiferromagnetic long-range order in the optical spectrum of strongly correlated electron systems*, Phys. Rev. B, **85**, 085124 (2012).

[234] X. Wang, M. J. Han, L. de'Medici, H. Park, C. A. Marianetti, and A. J. Millis, *Covalency, double-counting, and the metal-insulator phase diagram in transition metal oxides*, Phys. Rev. B, **86**, 195136 (2012).

[235] P. Hansmann, N. Parragh, A. Toschi, G. Sangiovanni, and K. Held, *Importance of $d - p$ Coulomb interaction for high T_C cuprates and other oxides*, Unpublished.

[236] N. F. Mott, *Metal-Insulator Transition*, Rev. Mod. Phys., **40**, 677 (1968).

[237] P. Nozières and D. Pines, *Theory of quantum liquids*, Westview Press (USA) (1999).

[238] J. Sólyom, *Fundamentals of the Physics of Solids Vo 3*, Springer-Verlag Berlin Heidelberg (2011).

[239] A. Toschi, M. Capone, C. Castellani, and K. Held, *Kinks in the Electronic Specific Heat*, Phys. Rev. Lett, **102**, 076402 (2009).

[240] E. Abrahams, P. W. Anderson, D. C. Licciardello, and T. V. Ramakrishnan, *Scaling Theory of Localization: Absence of Quantum Diffusion in Two Dimensions*, Phys. Rev. Lett., **42**, 673 (1979).

[241] B. L. Altshuler and A. G. Aronov, *Electron-Electron interaction in disordered conductors*, Elsevier Science Publisher (1985).

[242] E. Abrahams and P. A. Lee, *Scaling description of the dielectric function near the mobility edge*, Phys. Rev. B, **33**, 683 (1986).

[243] S. Sachdev, *Quantum Phase Transitions*, Cambridge University Press (1999).

[244] P. Coleman, *Quantum Criticality*, Nature, **433**, 226 (2005).

[245] N. Andrenacci, A. Perali, P. Pieri, and G. C. Strinati, *Denity-induced BCS to Bose-Einstein crossover*, Phys. Rev. B, **60**, 12410 (1999).

[246] S. Allen and A.-M. S. Tremblay, *Nonperturbative approach to the attractive Hubbard model*, Phys. Rev. B, **64**, 075115 (2001).

[247] E. Tosatti and P. W. Anderson, *Charge and Spin Density Waves on Semiconductor Surfaces*, Jap. J. Appl. Phys. Suppl., **2**, 381 (1974).

[248] Q. Si and G. Kotliar, *Fermi-Liquid and Non-Fermi-Liquid Phases of an Extended Hubbard Model in Infinite Dimensions*, Phys. Rev. Lett., **70**, 3143 (1993).

[249] Q. Si and G. Kotliar, *Metallic non-Fermi-liquid phases of an extended Hubbard model in infinite dimensions*, Phys. Rev. B, **48**, 13881 (1993).

[250] Q. Si and J. L. Smith, *Kosterlitz-Thouless Transition and Short Range Spatial Correlations in an Extended Hubbard Model*, Phys. Rev. Lett., **77**, 3391 (1996).

[251] H. Martensson and P. O. Nilsson, *Investigation of the electronic structure of Ni by angle-resolved uv photoelectron spectroscopy*, Phys. Rev. B, **30**, 3047 (1984).

[252] L. Hedin, *New Method for Calculating the One-Particle Green's Function with Application to the Electron-Gas Problem*, Phys. Rev., **139**, A796 (1965).

[253] S. Biermann, F. Aryasetiawan, and A. Georges, *First-principles approach to the electronic structure of strongly correlated systems: combining the GW approximation and dynamical mean-field theory*, Phys. Rev. Lett., **90**, 086402 (2003).

[254] J. M. Tomczak, M. Casula, T. Miyake, F. Aryasetiawan, and S. Biermann, *Combined GW and dynamical mean-field theory: Dynamical screening effects in transition metal oxides*, EPL (Europhysics Letters), **100**, 67001 (2012).

[255] C. Taranto, M. Kaltak, N. Parragh, G. Sangiovanni, G. Kresse, A. Toschi, and K. Held, *Comparing quasiparticle GW+DMFT and LDA+DMFT for the test bed material SrVO₃*, Phys. Rev. B, **88**, 165119 (2013).

[256] G. Kotliar, S. Y. Savrasov, K. Haule, V. S. Oudovenko, O. Parcollet, and C. A. Marianetti, *Electronic structure calculations with dynamical mean-field theory*, Rev. Mod. Phys., **78**, 865 (2006).

[257] N. E. Bickers and D. J. Scalapino, *Conserving Approximations for Strongly Fluctuating Electron Systems*, Ann. Phys. (N. Y.), **193**, 206 (1989).

[258] F. Steglich, O. Stockert, and S. Wirth, *Special Issue: Quantum Criticality and Novel Phases*, Phys. Status Solidi B, **247**, 457 (2010).

[259] J. Custers, P. Gegenwart, H. Wilhelm, K. Neumaier, Y. Tokiwa, O. Trovarelli, C. Geibl, F. Steglich, C. Pépin, and P. Coleman, *The break-up of heavy electrons at a quantum critical point*, Nature, **424**, 524 (2003).

[260] S. Paschen, T. Lühmann, S. Wirth, P. Gegenwart, O. Trovarelli, C. Geibl, F. Steglich, P. Coleman, and Q. Si, *Hall-effect evolution across a heavy-fermion quantum critical point*, Nature, **432**, 881 (2004).

[261] C. Castellani, C. D. Castro, and M. Grilli, *Singular Quasiparticle Scattering in the Proximity of Charge Instabilities*, Phys. Rev. Lett., **75**, 4650 (1995).

[262] C. Castellani, C. D. Castro, and M. Grilli, *Non-Fermi-liquid behavior and d-wave superconductivity near the charge-density-wave quantum critical point*, Z. Phys. B, **103**, 137 (1997).

[263] J. A. Hertz, *Quantum critical phenomena*, Phys. Rev. B, **14**, 1165 (1976).

[264] Q. Si, S. Rabello, K. Ingersent, and J. L. Smith, *Locally crical quantum phase transitions in strongly correlated metals*, Nature, **413**, 804 (2001).

Acknowledgments

This thesis would not have been possible without the support of many people, which I experienced in the last four years.

First of all, I want to thank my advisor Alessandro Toschi for his almost "self-sacrificing" support. His deep physical understanding is combined with outstanding pedagogical skills. His introduction into theoretical solid state physics made me feel at home in this field pretty soon after I have started my PhD. I always profited (and still profit) from our innumerable scientific discussions, going sometimes even beyond the scope of condensed matter physics (and often beyond the usual working hours). His expertise is also in accordance with his personal qualities and his support during my –for health reasons in the year 2011 rather difficult– PhD time went well beyond just scientific supervision, even though with my "Wienerische Art zu raunzen" I made life sometimes difficult for him. For me, Alessandro has not only been my supervisor but also a mentor and a friend. Grazie mille, per il tuo sostegno, Alessandro!

I also want to thank Karsten Held, in whose group I started my PhD, for his constant support and advice. I was always impressed by his great physical intuition. Let me also mention, that he has given me the opportunity to co-organize a scientific workshop which I appreciate a lot.

I also want to thank all present and former members of Karstens and Alessandros groups for the nice and relaxed atmosphere, which made working here a real pleasure. I enjoyed the numerous interesting and inspiring physical discussion! Some of the people I started working with back in 2009 have already left Vienna: Giorgio Sangiovanni, Philipp Hansmann, Philipp Wissgott and Nico Parragh, who have been somehow the "veterans" of Karstens group here - it was a great time with you!

Special thanks go to Angelo Valli, with whom I wrote our great "vertex-paper" and worked on a solution of the parquet equations. He also helped me with the formatting of my thesis, not to forget the various interesting physical discussions through which I gained new insights. Let me also thank Thomas Schäfer whose master thesis I had the pleasure to co-supervise. I